Transactions of the ASME

Journal of Heat Transfer (ISSN 0022-1481) is edited and published quarterly at the offices of The American Society of Mechanical Engineers, United Engineering Center, 345 E. 47th St., New York, N. Y. 10017. ASME-TWX No. 710-581-5267, New York. Second-class postage paid at New York, N. Y., and at additional mailing offices.

CHANGES OF ADDRESS must be received at Society headquarters seven weeks before they are to be effective. Please send old label and new address.

PRICES: To members, $25.00, annually; to nonmembers, $50.00. Single copies, $15.00 each. Add $1.50 for postage to countries outside the United States and Canada.

INDEXED by the Engineering Index, Inc.

Journal of Heat Transfer

Published Quarterly by The American Society of Mechanical Engineers
VOLUME 102 • NUMBER 1 • FEBRUARY 1980

ANNOUNCEMENTS

TECHNICAL PAPERS

(continued on page 19)

TECHNICAL NOTES

DISCUSSIONS

K. H. Ardron
P. C. Hall

Central Electricity Generating Board,
Berkeley Nuclear Laboratories,
Berkeley,
Gloucestershire, GL 13 9PB
U.K.

Prediction of Void Fraction in Low Velocity Vertical Steam-Water Flow

A new drift flux relation is derived for low speed vertical bubble flows by balancing the hydrostatic pressure with the liquid eddy stresses; the effective eddy viscosity is related to the energy dissipated by the gas flow. Comparisons with steam-water data show that the observed variation of void fraction with gas flux, and the effects of pipe diameter, are well predicted by the model. However, to represent the pressure effects it is found necessary to postulate that the eddy viscosity increase systematically with pressure. Further experimental data are required to test this hypothesis.

1 Introduction

The calculation of void fraction and vapor separation rates in slow moving vertical bubbling flows (here defined as flows in which the gas forms the discontinuous phase, e.g., slug, churn-turbulent and ideal bubbly flow), is important for the analysis of postulated loss-of-coolant accidents in water-cooled nuclear reactors [1, 2, 18].

The general problem is to relate the void fraction in the two-phase mixture to the gas and liquid flow-rates, for conditions where buoyancy forces have an important influence on the motion of the gas phase. Several relationships have previously been proposed for use in the various flow regimes characteristic of vertical bubble flow [3, 4, 6, 12, 15–17]. In this paper these models are briefly reviewed and compared with typical steam-water data at low liquid flows. A new theoretical analysis is then described which accounts in a more consistent way for the contributions of slip and convection to gas upflows under these conditions.

2 Previous Work

Drift flux equations widely used to analyse the various bubble flow regimes are described below.

2.1 Correlations Based on Behringer's Model [3]. In this model the gas velocity is resolved into convective and buoyancy components, which are assumed not to interact. The correlations are of the form

$$\bar{u}_g = C_0 j + u_B, \tag{1}$$

where $C_0 j$ is the contribution to the mean gas velocity due to the bulk flow, and u_B is the bouyancy contribution.

Zuber and Findlay [4] noted that if a local drift velocity u_{gj} $(= u_g - j)$ can be defined at each point in the duct then it is possible to show that:

$$C_0 = \langle \alpha_g j \rangle / \langle \alpha_g \rangle \langle j \rangle;\ u_B = \langle \alpha_g u_{gj} \rangle / \langle \alpha_g \rangle. \tag{2}$$

When there is information on the radial distribution of the flow properties these expressions allow the calculation of C_0 or u_B. Usually, however, the terms can only be obtained empirically. Formulations commonly applied in the different bubble flow regimes are described below.

2.1.1 Ideal Bubbly Flow. The simplest case considered is an ideal bubbly flow in which there are uniform profiles of void fraction and velocity, and in which no interaction between bubbles occurs. Then:

$$u_g = u_{\ell i} + u_{\infty m}, \tag{3}$$

where $u_{\infty m}$ is the terminal rise velocity of bubble through two-phase mixture and $u_{\ell i}$ is the constant interstitial liquid velocity. Zuber and Hench [5] observed that in a column of void fraction $\alpha_g (= 1 - \alpha_\ell)$ the bouyancy force on a bubble is reduced by a factor of α_ℓ. Assuming a constant drag coefficient for a bubble, they used (3) to derive the expression:

$$u_g = j + \alpha_\ell{}^n u_\infty, \tag{4}$$

where $n = 3/2$. The terminal rise velocity of isolated bubbles in liquid only (u_∞) was obtained from the correlation of Harmathy [6]

$$u_\infty = 1.53 \left(\frac{\sigma g \rho_{\ell g}}{\rho_\ell{}^2} \right)^{1/4} \tag{5}$$

which is valid for bubbles of radii above about 5 mm rising in water.

To take into account the observed dependence of the bubble drag coefficient on its radius Zuber and Findlay [4] suggested that n in equation (4) should be varied between three and zero as bubble size is increased. Wallis [7] fitted a range of data for $0 < \alpha_g < 0.3$ using equations (4) and (5) by taking $n = 2$.

2.1.2 Churn-Turbulent Flow. As a result either of agglomeration of small bubbles because of Bernoulli forces, or of particular gas injection conditions, large nonspherical bubbles frequently occur in gas/liquid columns. These bubbles have turbulent wakes which promote strong interactions with their neighbors [8] producing an irregular collective motion termed "churn turbulent" flow.

Because of the non-uniformity of the velocity and void fraction profiles, and the strong interaction between bubbles, (3) and (4) are not valid in churn-turbulent flow. However, (1) and (2) are still applicable. Although it is not possible to evaluate the integrals in equation (2) from first principles, Zuber and Findlay calculated that for a wide range of centrally peaked profiles C_0 falls in the range $1.0 < C_0 < 1.5$. Hills [9] measured velocity and void fraction profiles in a vertical bubbling column in which there was upflow at the centre and downflow at the walls; his results also imply values of C_0 in this range. Thus it appears that C_0 can be bounded within fairly narrow limits.

A further difficulty in applying (1) and (2) directly arises in evaluating u_B, the weighted drift velocity. In fact Zuber and Findlay [4] were able to fit a range of churn-turbulent flow data for non-zero liquid fluxes by setting u_B equal to the terminal rise velocity of isolated bubbles given by equation (5), and by taking values of C_0 in the range of $1.2 < C_0 < 1.6$. Their proposed correlation was

$$\bar{u}_g = \langle j_g \rangle / \langle \alpha_g \rangle = C_0 \langle j \rangle + 1.53J \tag{6}$$

Steam-water data for zero liquid flux $[\langle j_\ell \rangle = 0]$, show a strong dependency on system pressure not predicted by equation (6) (See [10–12]). Zuber and Findlay proposed a second correlation for drift velocity to fit these data, which leads to a drift flux equation of the form

$$\bar{u}_g = \langle j_g \rangle / \langle \alpha_g \rangle = C_0 \langle j \rangle + K(\sigma_\ell \rho_{\ell g} g / \rho_g{}^2)^{1/4}, \tag{6a}$$

where the parameters K and C_0 are in the ranges $0.42 < K < 0.8$, $1.0 < C_0 < 1.2$.

2.1.3 Slug Flow. Slug flow is characterized by the presence of large discrete bubbles which almost fill the cross section of the duct. Nicklin, et al. [13] measured mean gas velocities in vertical slug flow, and were able to correlate their data with the expression

$$\bar{u}_g = C_0 \langle j \rangle + u_s \tag{7}$$

Contributed by the Heat Transfer Division for publication in the JOURNAL OF HEAT TRANSFER. Manuscript received by Heat Transfer Division January 19, 1979.

Here u_s is the velocity of a long slug bubble rising in a pipe filled with stationary liquid, given by $u_s = 0.35\sqrt{gD}$ [14, 15]. The parameter C_0 was observed to increase from 1.2 to 1.9 as the liquid Reynolds number decreased.

Griffith [16] analysed a range of void fraction measurements in the flow of boiling water in pipes and annuli. He correlated these data by using a similar equation to equation (7):

$$\bar{u}_g = C_0\langle j\rangle + 1.6K_1u_s, \tag{8}$$

with $C_0 = 1.2$. The constant K_1 depends on the channel geometry.

2.2 Drift Flux Correlations Based on Dimensional Analysis of Data. To establish a drift flux correlation applicable to large scale industrial equipment over a wide range of pressures, Wilson, et al. [17] measured $\langle\alpha_g\rangle$ in vertical steam-water flows in ducts up to 900 mm diameter, at pressures up to 130 bars. These data were correlated using an expression of the form:

$$\langle\alpha_g\rangle = C_1\left(\frac{\rho_g}{\rho_\ell}\right)^{C_2}\left(\frac{\langle j_g\rangle}{\langle j\rangle}\right)^{0.6}(Ku)^{C_3}\left(\frac{\sqrt{\sigma/g\rho_{\ell g}}}{D}\right)^{C_4} \tag{9}$$

where $C_1 = 0.564$ (0.619), $C_2 = 0.12$ (0.12), $C_3 = 0.67$ (0.47), $C_4 = 0.1$ (0.1) for $0 < Ku < 1.5$ ($1.5 < Ku < 10$). Subsequently Cunningham and Yeh [18] correlated (unpublished) steam-water data from a vertical 480-rod electrically heated pin bundle. Their correlation also had the form of (9) but with slightly revised constants C_n.

2.3 Comparisons of Correlations with Data. To test the applicability of the correlations described above for bubbly steam-water flow at low liquid fluxes comparisons have been made with results of tests in which steam was injected into vertical pipes containing saturated water at pressures up to 180 bar, [10, 11]. The liquid flux $\langle j_\ell\rangle$ was in all cases zero. Data of [10] are for a 238 mm dia pipe in which the height of the bubble column was less than four pipe diameters. Data of [11] are for a 63 mm dia pipe in which the bubble column height exceeded one hundred and 50 diameters. Typical results are plotted in Fig. 1 so as to display the independent effects of pressure and pipe diameter on void fraction. It can be seen that increasing the pressure[1] from 6 to 90 bar doubles $\langle\alpha_g\rangle$ for a fixed $\langle j_g\rangle$; similarly for a fixed pressure and $\langle j_g\rangle$ the effect of reducing pipe diameter from 238 mm to 63 mm is to increase $\langle\alpha_g\rangle$ by about 25 percent.

[1] To establish that the effect of pressure seen in these data was not due to changes in temperature dependent water properties, a series of tests were conducted as part of the present study (detailed in reference [19]). Results showed that raising pressure from 1 to 4 bar has the same influence on $\langle\alpha_g\rangle$ in a steam-water column as in an equivalent air-water column at constant temperature.

Fig. 1(*a*) shows that the correlations for ideal bubbly flow of the form of (4) are wholly inapplicable for the experimental conditions. These models imply that for zero liquid flux $\langle j_g\rangle$ is confined to be less than a fraction of the parameter J ($\simeq$0.1 m/s for water at 100°C). Also shown in Fig. 1(*a*) are predictions of the churn-turbulent flow correlation ((6)) proposed by Zuber and Findlay [4]. This allows $\langle j_g\rangle$ to increase unrestrictedly, but includes only a weak pressure effect and indicates no effect of pipe diameter. Fig. 1(*b*) compares the data with the second correlation proposed by Zuber and Findlay ((6*a*)), for a single choice for the parameters C_0 and K. Agreement is poor, particularly at low pressures, where because of the inverse dependency on ρ_g the proposed drift velocity diverges. No effect of pipe size is predicted.

Fig. 1(*c*) shows predictions of the slug flow correlations, (7) and (8). These relationships predict approximately the correct effect of pipe diameter, but have no pressure dependency whatever.

Finally, in Fig. 1(*d*) we have plotted predictions of the purely empirical correlation of Wilson, et al. ([9]). This expression gives much better agreement with data than any of the models based on (1), and correctly represents the observed trends with pressure and pipe diameter.

It is concluded that while equations of the form of (1) are reasonably well adapted for correlating void fraction data at low liquid fluxes (i.e., data form roughly linear plots in the $\langle j_g\rangle/\langle\alpha_g\rangle$, $\langle j_g\rangle$ plane) proposed correlations of this type are at present less satisfactory than the purely empirical equations of the form of (9).

3 Theory

Data comparisons shown above indicate that existing physically based models of bubble rise in vertical two-phase are inadequate at low liquid flows. In particular the effects of pressure and pipe size on $\langle\alpha_g\rangle$ are incompletely understood. To help explain these effects a fundamental model of bubble flows has been developed by solving equations of motion for the gas and liquid phases separately. Shear stresses in the liquid are calculated in terms of an eddy viscosity whose magnitude is related to the energy dissipated by the moving gas bubbles.

3.1 Calculation of Velocity Profile. Consider a steady axially symmetric flow in a vertical cylindrical pipe. The flow is assumed to be fully developed in the sense that the velocities and volume concentrations of the gas and liquid are independent of the axial position z. Neglecting mass transfer and compressibility effects, the non-dimensional time-averaged momentum equations for the gas and liquid phases are, respectively [20]

Nomenclature

C_0 = profile parameter $\langle\alpha_g j\rangle/\langle\alpha_g\rangle\langle j\rangle$
$C_{1,2,3,4}$ = constants in equation (9)
C_D = drag coefficient of bubble
D = pipe Diameter
F_{kd} = force on phase k per unit mixture volume due to interphase drag
g = acceleration due to gravity
h = enthalpy
H = function of k, defined after equation (27)
$i_1(k) = 2\int_0^1 (e^{k\lambda^2} - 1)/\lambda\, d\lambda$
$i_2(k) = 2\int_0^1 (1 - e^{-k\lambda^2})/\lambda d\lambda$ } exponential integrals tabulated in Table 1
j = total volumetric flux ($j = j_g + j_\ell$)
j_k = volumetric flux of phase k
j_k^* = dimensionless volumetric flux ($= j_k/\sqrt{gD}$)
J = velocity group ($= \sigma g\rho_{\ell g}/\rho_\ell^2)^{1/4}$
K = constant in equation (6*a*)
Ku = Kutateldaze Number ($= j_g/J$)
$k = \ell n(1/\alpha_{\ell c})$ Related to mean void fraction by equation (18)
n = index in equation (4)
p = pressure
$p^{(0)}$ = stagnation pressure
R_B = radial of sphere with volume of bubble
r = radius distance from pipe center
r^* = dimensionless distance ($= 2r/D$)
u = velocity
u_∞ = terminal rise velocity of isolated bubble in stagnant liquid
u_s = terminal rise velocity of a long slug bubble in a duct
u^* = dimensionless velocity ($= u/\sqrt{gD}$)
u_B = contribution to gas velocity due to slip
u_{gj} = drift velocity ($u_g - j$)
$\dot{W}$ = rate of working
z = axial co-ordinate
α_k = volumetric concentration of phase k
β = dimensionless pressure gradient ($= (dp/dz)/\rho_{\ell g}$)
$\beta' = \beta + \gamma$
γ = density Ratio ($= \rho_g/\rho_\ell$)
ϵ^* = dimensionless Turbulent Diffusivity
Λ = turbulence energy production function
ρ = density
σ = surface tension
τ_{rzk} = shear stress in phase k
τ_k^* = dimensionless shear stress ($= \tau_{rzk}/(\frac{1}{2}\rho_{\ell g}gD)$)
τ_w = shear stress at wall

Subscripts

c = value at pipe centre
g = property of gas phase
ℓ = property of liquid phase
$g\ell$ = difference between liquid and gas properties

Averages

$\langle G\rangle$ = area average $\left(= \frac{1}{A}\int_A g dA$, where A is duct area$\right)$

$\bar{G}_k$ = weighted average ($= \langle\alpha_k G_k\rangle/\langle\alpha_k\rangle$)

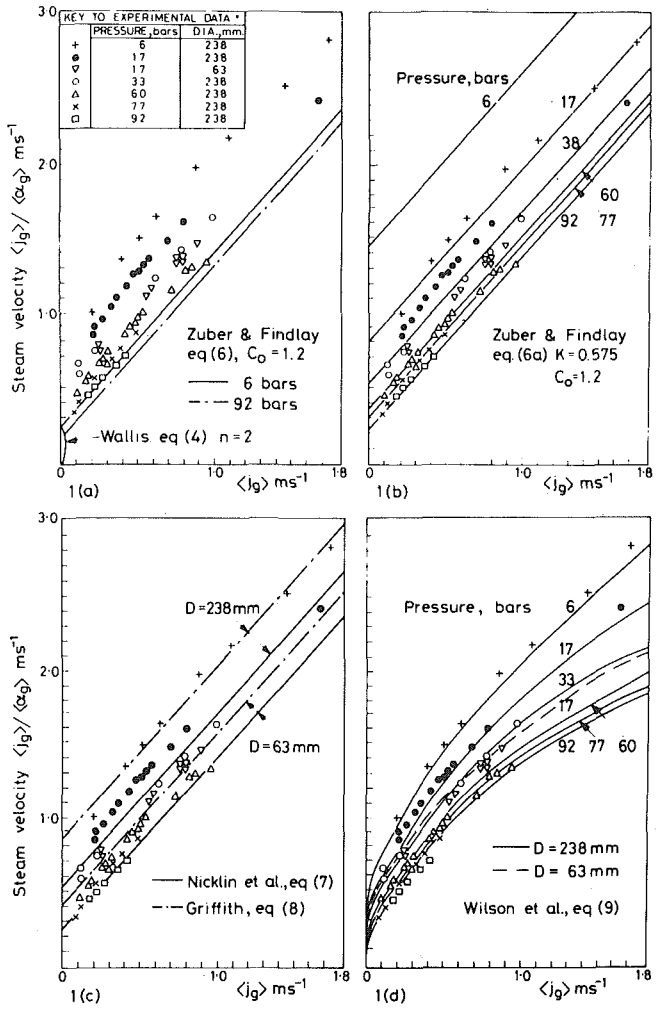

Fig. 1 Comparison of published drift flux correlations with experimental data of Styrikovich [10] and Filiminov [11]

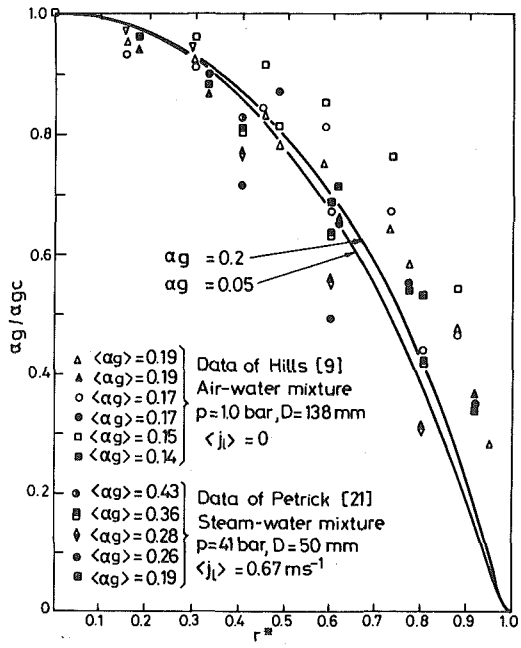

Fig. 2 Comparison of void fraction distribution predicted by equation (17) (solid curves) with air-water and steam-water data

$$(\beta + 1)\alpha_\ell = \frac{1}{r^*}\frac{d}{dr^*}(r^*\alpha_\ell \tau_\ell^*) + \frac{F_{\ell d}}{\rho_\ell g} \tag{10}$$

and

$$\beta'\alpha_g = \frac{1}{r^*}\frac{d}{dr^*}(r^*\alpha_g \tau_g^*) + \frac{F_{gd}}{\rho_\ell g} \tag{11}$$

In a bubbling column the shear stress in the liquid is expected to be dominated by the motion of turbulent eddies, whose energy comes from work done by the buoyancy forces. It is argued in Appendix A that at low liquid fluxes ($\langle j_g \rangle \simeq 0$) the Reynolds stresses so generated can be represented by:

$$\tau_\ell^* = \epsilon^* \frac{du_\ell^*}{dr^*} \tag{12}$$

where ϵ^* is an effective eddy diffusivity given by

$$\epsilon^* = \Lambda \langle j_g^* \rangle^{1/3} \tag{12a}$$

Λ depends on system properties, but is independent of void fraction and duct size.

We neglect shear stress within the gas phase, taking $\tau_g^* = 0$. Adding (10) and (11), noting that interphase forces are equal and opposite so that $F_{gd} = -F_{\ell d}$, and using (12) we get an ordinary differential equation for u_ℓ^*:

$$\beta' + \alpha_\ell(1 - \gamma) = \frac{1}{r^*}\frac{d}{dr^*}\left(r^*\alpha_\ell \epsilon^* \frac{du_\ell^*}{dr^*}\right) \tag{13}$$

Equations (12) and (13) are inapplicable in the viscous sub-layer close to the pipe walls since in this region the turbulent stresses decay rapidly, becoming comparable with the viscous stresses. Assuming, however, that the thickness of this "viscous layer" is small compared with the pipe radius, we can write an approximate "wall" boundary conditions for the solution u_ℓ^* of equation (13)

$$u_\ell^* = u_{\ell\delta}^* \text{ at } r^* \simeq 1 \tag{14}$$

$u_{\ell\delta}^*$ is the velocity at the outer edge of the sub-layer. Other boundary conditions are provided by noting that

$$du_\ell^*/dr^* = 0 \text{ at } r^* = 0 \tag{15}$$

while from the mass conservation for each phase, $k = g, k = \ell$

$$2\int_0^1 r^* u_k^* \alpha_k dr^* = \langle j_k^* \rangle = \text{constant, independent of } z \tag{16}$$

Integration of (13) requires a knowledge of the radial distribution of void fraction in the pipe. At present there is little information on the factors controlling this distribution for two-phase systems, but some experimental measurements are available for low speed bubble flows. Fig. 2 shows results for mean void fractions exceeding 0.15 obtained by Petrick [21] for 40 bar steam-water flow, and by Hills [8] for an air-water system at atmospheric pressure.

It is seen from Fig. 2 that a convenient representation of these data can be obtained using the distribution

$$\alpha_\ell = \alpha_{\ell c} \exp(kr^{*2}) \tag{17}$$

where $k = \ell n(1/\alpha_{\ell c})$. This function is adopted for the subsequent analysis.[2] It implies that the duct average void fraction $\langle \alpha_g \rangle$ is related to the center-line value by:

$$1 - \langle \alpha_g \rangle = \langle \alpha_\ell \rangle = 2\int_0^1 r^* \alpha_\ell dr^*$$

$$= (1 - e^{-k})/k = (\alpha_{\ell c} - 1)/\ell n \alpha_{\ell c}. \tag{18}$$

Inserting the distribution (17) into (13) and integrating, using the

[2] For non-zero liquid upflows a second peak in α_g is sometimes observed near the pipe wall [22, 23]. This is thought to be associated with the peak in turbulence energy which occurs close to the wall in pipe flows [24, 25]. Since these wall effects tend to become insignificant at liquid superficial velocities less than about 1 m/s they have been ignored for the present analysis.

boundary condition (15), we get

$$\beta' r^{*2}/2 + \alpha_{\ell c}(1-\gamma)(e^{kr^{*2}}-1)/2k = r^*\epsilon\alpha_\ell du_\ell^*/dr^* \quad (19)$$

It follows on integrating by parts, using (14) and (17), that

$$\int_0^1 \alpha_\ell du_\ell^*/dr^*\ dr^* = u_{\ell\delta}^* - \alpha_{\ell c}u_{\ell c}^* - k\langle j_\ell^*\rangle.$$

Using this identity (19) can be integrated between $r^* = 0$ and $r^* = 1$ to give

$$\beta' + (1-\gamma)\alpha_{\ell c}i_1(k)/k = 4\epsilon^*\{u_{\ell\delta}^* - \alpha_{\ell c}u_{\ell c}^* - k\langle j_\ell^*\rangle\}. \quad (20)$$

A second relation between $u_{\ell c}^*$, $u_{\ell\delta}^*$ and β' can be obtained by dividing both sides of (10) by $r^*\alpha_\ell$, and integrating between $r^* = 0$ and $r^* = 1$. This is

$$-\beta'(1-e^k)/k + (1-\gamma)i_2(k)/k = 4\epsilon^*(u_{\ell\delta}^* - u_{\ell c}^*). \quad (21)$$

At liquid velocities of a few meters per second the contribution of the wall shear stress to the total pressure gradient (inferred from turbulent friction factor data) is usually negligible compared with the hydrostatic contribution. Adopting a zero shear boundary approximation, we may write

$$\beta' = -\langle\alpha_\ell\rangle(1-\gamma). \quad (22)$$

3.2 Calculation of Slip Velocities. To determine the velocity of the gas relative to that of the liquid locally it is assumed that the gas is distributed in equal bubbles with an equivalent spherical radius R_B. The drag force bubbles per unit volume is given by

$$F_{gd} = \frac{\alpha_g}{\left(\frac{4}{3}\pi R_B{}^3\right)} \cdot \frac{1}{2} C_D \rho_\ell (u_g - u_\ell)^2 \pi R_B{}^2. \quad (23)$$

where the drag coefficient C_D is assumed to be the same for all bubbles. For bubbles greater than about one centimeter in diameter (spherical cap bubbles), rising in isolation, it is found experimentally that $C_D \simeq 2.6$, independent of bubble size and liquid properties [26]. If this value is adopted and (23) substituted into equation (11) we obtain an equation for the dimensionless relative velocity:

$$u_{g\ell}^* = u_g^* - u_\ell^* = 0.72\, R_B{}^{*1/2}(-\beta')^{1/2}. \quad (24)$$

3.3 The Drift Flux Equation. Using the known liquid velocity profile, and the relative velocity of bubbles given by (24), it is possible to relate the volume fluxes of the gas and liquid phases to the void fraction $\langle\alpha_g\rangle$. Firstly we observe that by definition:

$$\langle j_g^*\rangle + \langle j_\ell^*\rangle = \langle\alpha_g(u_g^* - u_\ell^*)\rangle + \langle u_\ell^*\rangle. \quad (25)$$

The mean liquid velocity is obtained by noting that

$$\langle u_\ell^*\rangle = 2\int_0^1 r^* u_\ell^* dr^* = u_{\ell\delta}^* - \int_0^1 r^{*2} du_\ell^*/dr^* dr^*, \quad (26)$$

Table 1 Functions used in drift-flux model (equation (27))

k	$\langle\alpha_g\rangle$	i_1†	i_2†	H
0.05	0.0246	0.050632	0.049382	5.21×10^{-5}
0.10	0.0484	0.102557	0.0975545	2.01×10^{-4}
0.15	0.0712	0.155818	0.144557	4.71×10^{-4}
0.20	0.0935	0.210462	0.190428	8.39×10^{-4}
0.30	0.136	0.324089	0.278920	1.89×10^{-3}
0.40	0.176	0.443843	0.363305	3.39×10^{-3}
0.50	0.213	0.570151	0.443842	5.30×10^{-3}
0.60	0.248	0.703491	0.520770	7.67×10^{-3}
0.80	0.312	0.993324	0.664669	1.37×10^{-2}
1.0	0.360	1.31790	0.796600	2.17×10^{-2}
1.5	0.482	2.3186	1.0827	5.00×10^{-2}
2.0	0.568	3.6839	1.3193	9.18×10^{-2}
3.0	0.736	8.2580	1.6889	0.225
4.0	0.755	17.667	1.9673	0.457
5.0	0.801	37.999	2.1878	0.860

† From Abromowitz and Stegun [29]

where we have used the wall boundary condition (14). Evaluating the integral on the right hand side of (26) using (19), and eliminating $u_{\ell\delta}^*$ and β' using (20, 21) and (22), we obtain an expression for $\langle u_\ell^*\rangle$. Inserting this in (25), eliminating $u_{g\ell}^*$ using (24) and (22), and using (12a) for ϵ^*, we obtain the general drift flux equation:

$$\langle j_g^*\rangle + \langle j_\ell^*\rangle\{1 - 1/\langle\alpha_\ell\rangle\} = \frac{1-\gamma}{4\Lambda\langle j_g^*\rangle^{1/3}} \cdot H(k) + 0.72\langle\alpha_g\rangle\sqrt{\langle\alpha_\ell\rangle R_B^*(1-\gamma)}. \quad (27)$$

where

$$H(k) = -\frac{2}{k} + \frac{1}{k^2}\left\{1 - e^{-k} + \frac{2}{k}(\cosh k - 1)\right\} + \frac{i_1(k) - i_2(k)}{k(e^k - 1)}.$$

The functions i_1, i_2 and H are calculated for different values of k (and $\langle\alpha_g\rangle$) in Table 1. The turbulence energy production function, Λ, and the non-dimensional bubble radius, R_b^*, remain as unknown parameters.

4 Comparisons with Data

In order to fit the available steam-water data using (27) it was found necessary to increase the turbulence production function Λ with vapor density in the manner shown in Fig. 3. For $\langle\alpha_g\rangle$ exceeding 0.15 and pipe sizes above $D = 70$ mm calculations were found insensitive to the values assumed for R_b (see below), and a fixed value of 1 cm was adopted for all cases.

Predictions of (27) made on this basis are compared with a wide range of steam-water data in Figs. 4 and 5. (In these tests the liquid flux $\langle j_\ell\rangle$ was zero, pressures range between 1 and 180 bars and duct diameters vary between 60 and 460 mm.) Although it should be emphasized that Λ has been adjusted to account for the observed pressure effects (cf., Fig. 3) both the shape of the theoretical curves, and the predicted effect of pipe diameter, follow directly from the analysis. Agreement with experiment is seen on the whole to be very good, although there are some systematic deviations at very high pressures for pipe sizes < 70 mm. These discrepancies may indicate that bubble size diminishes systematically with increasing pressure.

4.1 Discussion. The main difficulty in applying equation (27) to predict void fraction in bubble columns arises because of the absence of an analytic description of the two-order-of-magnitude variation of Λ with ρ_g which is needed to fit available steam-water data. In single phase flow Λ is of order $1/R_{cr}$, where R_{cr} is the Reynolds number for the onset of turbulence. In a vertical bubble flow, in which the liquid turbulence is created by gas pumping, the criterion of the onset of hydrodynamic instability is not known, and Λ cannot readily be estimated. However it seems possible that the large sinuous bubbles observed in these flows generate turbulence mainly through the working of shear forces at the gas-liquid interface. The turbulence energy might thus be expected to increase with vapour phase density, which is consistent with the implications of the model.

An interesting feature of the comparisons is the insensitivity of predictions to the value taken for the interphase relative velocity $u_{g\ell}^*$

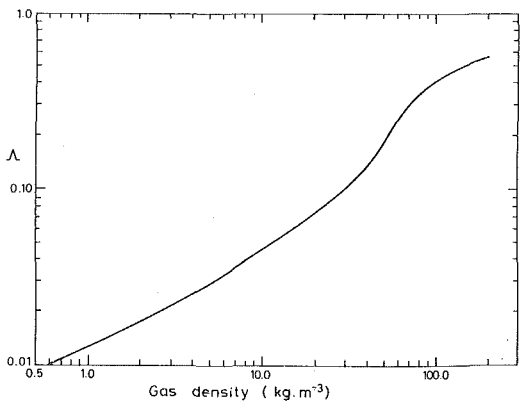

Fig. 3 Variation of turbulence production function Λ with vapor density for steam-water mixtures

(which forms the contribution to the gas flux represented by the second term on the right hand side of equation (27)). Fig. 6 shows the effect of varying $u_{g\ell}$* within realistic limits. The lower curve is the prediction obtained by taking $u_{g\ell}^* = R_B^* = 0$, (corresponding to the homogeneous approximation, where the mixture is regarded as a variable density continuum with no interphase relative motion). For the upper curve the slip has been maximised by setting the bubble diameter equal to the full pipe size. This suggests that (1) effects of pressure seen in Figs. 4 and 5 cannot be accounted for by adjusting the relative velocity within realistic limits, and (2) that for $\langle \alpha_g \rangle$ greater than about 0.15 the gas upflow [for $\langle j_\ell \rangle \approx 0$] is completely dominated by convection (profile effects), and that local slip is negligible.

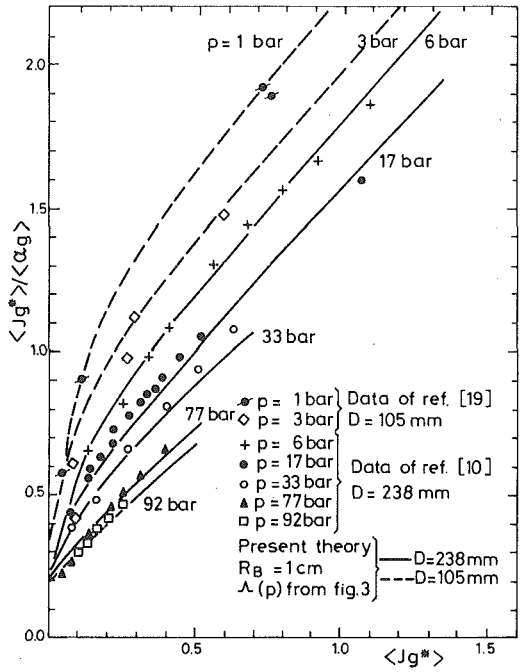

Fig. 4 Comparison of present model with steam-water data

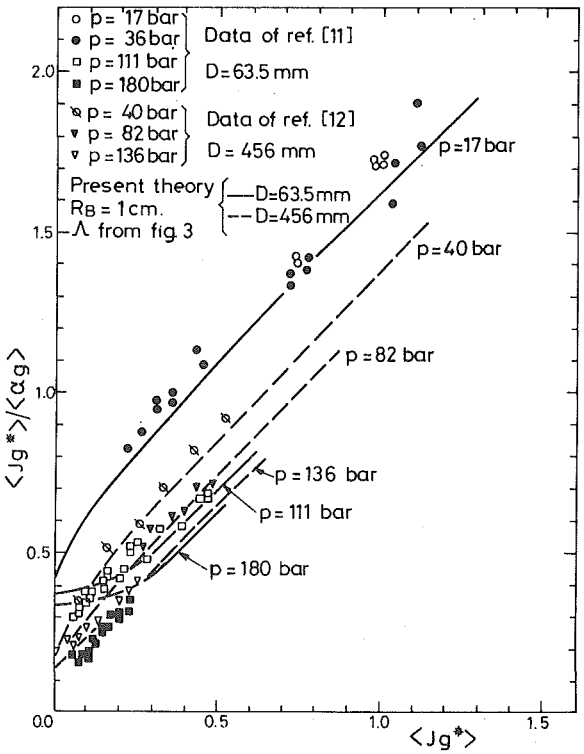

Fig. 5 Comparison of present model with steam-water data

It is clear that further investigations of the effect of gas density on turbulence intensities in bubble columns is needed before the present theory can be applied with complete confidence. Further data are also needed to support the adopted form for the radial distribution of voidage [equation (17)]. However the model provides a consistent physical description of bubble separation in low velocity liquid flows, and indicates the type of measurements that are needed to yield a full understanding of the process.

5 Conclusions

1 Physically based drift flux models currently used to calculate void fraction in vertical bubble flows resolve the gas flux into independent contributions due to liquid motion and slip. Data comparisons show that none of the representations satisfactorily describe the effects of pressure and pipe diameter observed in steam-water flows.

2 Data have been compared with predictions of a new drift flux model derived from a balance between the liquid eddy stresses and the hydrostatic pressure; the mean eddy viscosity is related to the energy dissipated by the moving gas bubbles. The model accurately predicts the variation of void fraction with gas flux, and the effects of pipe diameter, observed in steam-water flows. However, the pressure effect can only be represented by assuming the eddy viscosity increases with pressure.

3 Theoretical analysis suggests that gas upflow in a gas-liquid mixture is at low liquid flows dominated by the liquid velocity profile, and that the effects of slip are small.

4 Experiments are required to support the concept of a pressure dependent eddy viscosity for the liquid and provide a physical explanation of this pressure dependency.

Acknowledgment

This paper is published by permission of the Central Electricity Generating Board.

References

1 Yadigaroglu, G., "The Reflooding Phase of the LOCA in PWRs. Part I: Core Heat Transfer and Fluid Flow," *Nuclear Safety*, Vol. 19, No. 1, 1978, p. 20.

2 Yeh, H., and Hochreiter, L. E., "Mass Effluence During FLECHT Reflood Experiments," *Trans. ANS.*, Vol. 24, 1976, p. 301.

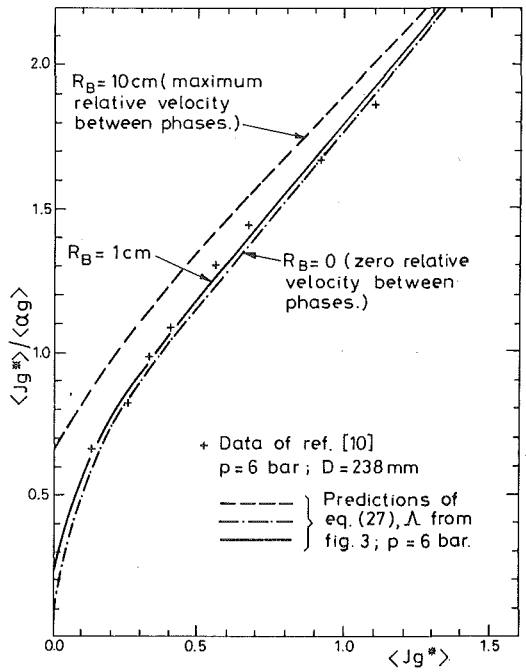

Fig. 6 Sensitivity of predicted gas flux to changes in the assumed bubble size

3 Behringer, H., "The Flow of Liquid Gas Mixtures in Vertical Tubes," *Zeit. Ges. Kalle-Ind.*, Vol. 43, 1936, p. 55 (AEC Translation No. 1777).
4 Zuber, N., and Findlay, J. A., "Average Volumetric Concentration in Two-Phase Flow Systems," ASME JOURNAL OF HEAT TRANSFER, Vol. 87, 1965, p. 453.
5 Zuber, N., and Hench, J., "Steady State and Transient Void Fraction of Bubbling Systems and Their Operating Limits," General Electric Co., Report 62-GL100, Schenectady, New York, 1962.
6 Harmathy, T., "Velocity of Large Drops and Bubbles in Media of Infinite and Restricted Extent," *AIChE Journal*, Vol. 6, 1960, p. 281.
7 Wallis, G. B., *One-Dimensional Two-Phase Flow*, McGraw-Hill, New York, 1969.
8 Zuber, N., Staub, F. W., Bijwaard, G., and Kroeger, P. G., "Steady State and Transient Void Fraction in Two Phase Flow Systems," General Electric Co. Report GEAP-5417, 1967.
9 Hills, J. H., "Radial Non-Uniformity of Velocity and Voidage in Bubble Columns," *Transactions of the Institution of Chemical Engineers*, Vol. 52, No. 1, 1974, p. 1.
10 Styrikovich, M. A., Surnov, A. V. and Vinokour, J. A., "Experimental Data on Hydrodynamics of a Two-Phase Layer," *Teploenergetika*, Vol. 8, No. 9, 1961, p. 56.
11 Filiminov, A. I., Przhizhalovski, M. M., Dik, E. P. and Petrova, S. N., "The Driving Head in Pipes with a Free Interface in the Pressure Range 17 to 100 At.," *Teploenergetika*, Vol. 4, 1957, p. 22.
12 Currier, F., Grenda, R., Littleton, W., Meyer, W., Wilson, J., and Yant, H., "Steam Separation Technology under the Euratom Program," Allis-Chalmers Atomic Energy Division, Report ACNP-63021, 1963.
13 Nicklin, E. J., Wilkes, J. O. and Davidson, J. F., "Two-Phase Flow in Vertical Tubes," *Transactions of the Institution of Chemical Engineers*, Vol. 40, 1962, p. 61.
14 Davies, R. M., and Taylor, G. I., "The Mechanics of Large Bubbles Rising Through Extended Liquids and Through Liquids in Tubes," *Proceedings of the Royal Society*, Vol. 200, Ser A, 1950, p. 375.
15 Dumitrescu, D. T., "Strömung an Einer Luftblase im Serkretchen Rohr," *Zeitschrift fuer Angewaudte Mathematik und Mechanik*, Vol. 23, No. 3, 1943, p. 139.
16 Griffith, P., "Prediction of Low Quality Boiling Voids," ASME JOURNAL OF HEAT TRANSFER, Vol. 86, 1969, p. 327.
17 Wilson, S. F., Littleton, W. E., Yant, H. W. and Mayer, W. C., "Primary Separation of Steam from Water by Natural Separation, Part I," Allis-Chalmers Atomic Energy Division, Report No. ACNP-65002, 1965.
18 Cunningham, S. P. and Hsu-Chieh Yeh, "Experiments and Void Correlation for PWR Small-Break LOCA Conditions," Vol. 17, 1973, p. 369.
19 Hall, P. C. and Ardron, K. H., "Prediction of Void Fraction in Low Velocity Vertical Bubbling Flows," CEGB Report RD/B/N3966, 1978.
20 Ishii, M., "Thermo-Fluid Dynamic Theory of Two-Phase Flow," Eyrolles, Paris, 1975.
21 Petrick, M., "A Study of Vapour Carry-under and Associated Problems," Argonne Nat. Lab. Report ANL-6581, 1962.
22 Malnes, D., "Slip Ratios and Friction Factors in the Bubble Flow Regime in Vertical Tubes," Report KR110, Kjeller Research Institute, Norway, 1966.
23 Serizwa, A., Kataska, I and Michiyoshi, I., "Turbulence Structure of Air-Water-Bubbly Flow—II Local Properties," *International Journal of Multiphase Flow*, Vol. 2, 1975, p. 235.
24 Rouhani, Z., "Effect of Wall Friction and Vortex Generation on the Radial Distribution of Different Phases," *International Journal of Multiphase Flow*, Vol. 3, 1976, p. 35.
25 Drew, D., Sim, S. and Lahey, R. T. Jnr., "Radial Phase Distribution Mechanisms in Two-phase Flow," 2nd CSNI Specialist Meeting on Transient Two-Phase Flow, Paris, 1978.
26 Haberman, W. L., Morton, R. K., "An Experimental Study of Bubbles Moving in Liquids," *Transactions of the American Society of Civil Engineers*, Vol. 121, 1956, p. 227.
27 Baird, M. H. I. and Rice, R. G., "Axial Dispersion in Large Unbaffled Columns," *Chem. Eng. J.*, Vol. 9, 1975, p. 171.
28 Landau, L. D., and Liftshitz, E. M., *Fluid Mechanics*, Pergamon Press, Oxford, 1959.
29 Abramowitz, A. and Stegun, I. A., "Handbook of Mathematical Functions," Nat. Bur. Standards, Washington D.C., 1969.

APPENDIX A

Calculation of an Effective Eddy Diffusivity for Vertical Bubble Flow

In a slow moving vertical two-phase flow bubble motion can excite strong recirculatory liquid movements with upflow at the pipe center and downflow at the walls. It is assumed that at *low liquid fluxes* wall effects can be ignored and that the radial transmission of momentum takes place mainly through the motion of turbulent eddies created by the working of interfacial forces. In the simplest model of turbulence, supposed homogeneous and isotropic, the Reynolds stress is expressed as

$$\tau_{rz} = \rho_\ell \nu_{\text{TURB}} \partial u_\ell / \partial r \tag{A1}$$

where ν_{TURB} is an effective turbulent diffusivity for momentum.

For the present case ν_{TURB} is estimated by equating the work done by the buoyancy forces to the energy dissipated by the eddies. The analysis is essentially the same as that given by Baird and Rice [27] to describe axial liquid/liquid mixing in bubble columns. Ignoring compressibility the *maximum* rate at which the bubbles can perform work on the liquid in an element of duct between elevations z and $z + \Delta z$ is

$$\Delta \dot{W}_g = -\langle j_g \rangle A \Delta p^{(0)} \tag{A2}$$

Here, $\Delta p^{(0)}$ is the stagnation pressure increase between stations z and $z + \Delta z$. Neglecting kinetic and gravitational heads in the gas phase $\Delta p^{(0)}$ is obtainable from the hydrostatic pressure gradient in the pipe:

$$\Delta p^{(0)} = -g \rho_\ell \langle \alpha_\ell \rangle \Delta z \tag{A3}$$

Since the volume of liquid in element Δz is $\langle \alpha_\ell \rangle A \Delta z$ it follows from (A2) and (A3) that the maximum power dissipated per unit liquid mass through the action of bubbles is given simply by

$$\dot{W}_\ell = \langle j_g \rangle g \tag{A4}$$

Now the work done by the rising bubbles must ultimately be converted into heat through the action of turbulent eddies in the liquid. Both large scale eddies, characteristic of the recirculating liquid flow and small-scale eddies created in the wakes of individual bubbles would be expected to exist in the bubbling mixture. We make the hypothesis that it is the *large eddies* (whose scale is of order the pipe diameter D), that are mainly responsible for the radial dispersion of momentum in the flow. If a fraction f of the work given by (A4) goes into creating these eddies dimensional arguments can be used to show that, (cf., Landau and Lifshitz [28]),

$$\nu_{\text{TURB}} = f \dot{W}_\ell^{1/3} D^{4/3} \tag{A5}$$

Defining a dimensionless eddy diffusivity by the equation

$$\tau_{rz}^* = \epsilon^* \partial u^* / \partial r^*$$

it follows from (A4) and (A5)

$$\epsilon^* = 4 \nu_{\text{TURB}} g^{-1/2} D^{3/2} = \Lambda \langle j_g^* \rangle^{1/3} \tag{A6}$$

where Λ is the turbulence energy production function

P. S. Kamath
R. T. Lahey, Jr.

Department of Nuclear Engineering
Rensselaer Polytechnic Institute
Troy, N. Y. 12181

A Turbine-Meter Evaluation Model for Two-Phase Transients

This work involves the development of an analytical model to calculate the transient two-phase mass flux in a conduit instrumented with a free-field turbind flow meter. The effects of rotor inertia, velocity and void profiles in the conduit, slip ratio, imperfect guidance of the flow by the rotor blades, bearing friction and windage losses have been incorporated into the model. The analytical Turbine-meter Evaluation Model for Two-Phase Transients (TEMPT) was programed and was used for numerical calculations. For a typical blowdown transient, the effects of velocity and void profiles, and rotor inertia were found to be the most significant parameters.

Introduction

Turbine-meters have been widely used in the chemical, nuclear and aerospace industries to measure single-phase fluid flow in conduits. For nuclear reactor applications, their use has been extended to the measurement of two-phase flows, as exemplified by such INEL programs as LOFT (Loss of Fluid Test) and Semiscale.

A turbine-meter is essentially a turbine rotor which rotates as the fluid flows through its blades. Its speed of rotation is measured by a sensor mounted on the shroud which registers a pulse for each passing blade. From this speed, the volumetric flow rate is inferred.

The behavior of turbine-meters, and their calibration equations, are reasonably well understood for steady and unsteady single-phase flows, and for well-mixed steady two-phase flows. Transient two-phase flows have normally been calculated using steady two-phase calibration equations. Previous transient analyses of turbine-meters in two-phase flows [1] have been concerned with determining the turbine-meter response for given transient vapor and liquid phase velocities. Of more practical interest is the determination of the fluid velocity for a given, (i.e., measured) turbine-meter response. This latter approach has been taken in this study. The output of the turbine-meter consists of a count rate (CR) from the sensor on the meter shroud. The rotation of the rotor is resisted by bearing and fluid friction, blade tip windage torques, and, in unsteady flows, by the moment of inertia of the rotor and the fluid contained in the blading. In addition, in two-phase flows, the effects on rotor torque of phasic slip and non-uniform velocity and void profiles have to be considered.

Discussion of Model

A fluid flowing through the blading of a free field turbine-meter imparts a transverse velocity ot the blades, thus causing them to rotate. This phenomena is known as the "turbine principle" and is described by Newton's Second Law of Motion for Rotation:

$$\begin{bmatrix}\text{outflow rate of angular momentum from the control volume}\end{bmatrix} - \begin{bmatrix}\text{inflow rate of angular momentum from the control volume}\end{bmatrix} + \begin{bmatrix}\text{storage rate of angular momentum in the control volume}\end{bmatrix} = \begin{bmatrix}\text{sum of the external torques on the control volume}\end{bmatrix} \quad (1)$$

For the case of two-phase flows, each term on the left-hand side of equation (1) will have contributions due to the liquid and vapor phases. As shown schematically in Fig. 1, the turbine meter also acts as a phase separator due to the relatively higher inertia of the liquid phase. Hence, non-uniform velocity and void profiles can be expected at the control volume boundary. This effect is incorporated into the analytical model through the use of correlation coefficients for the liquid and vapor phases, defined [2] by,

$$C_k \triangleq \frac{\langle \alpha_k V_k^2 \rangle}{\langle \alpha_k \rangle \langle V_k \rangle^2} \quad (2)$$

The control volume, shown in Fig. 1, is chosen so as to include a blade such that the pressure distribution on the blade surface drops out of the torque balance. Thus, the external torques on the control volume in Fig. 1 consist of bearing friction and windage loss torques.

The bearing friction torque can be expressed as [3],

$$T_{\text{bearing}} = \pi f \rho_\ell L_{jb} R_s^4 |\omega| \omega \quad (3)$$

where the liquid phase density, ρ_ℓ, is used, since the lubricating fluid is the liquid phase, and the friction factor is given by,

$$f = \frac{0.078}{\text{Re}_\ell^{0.43}} \quad (4)$$

where,

$$\text{Re}_\ell = \frac{\rho_\ell |\omega| R_s (R_{h_1} - R_s)}{\mu_\ell} \quad (5)$$

Fig. 2 illustrates the various dimensions used in these equations.

Noting that the bearing friction torque opposes the rotation of the rotor, equations (3–5) combine to yield,

$$\boldsymbol{T}_{\text{bearing}} = -0.245 (L_{jb} R_s^{3.57}) \rho_\ell^{0.57} |\omega|^{0.57} \nu_{\mu\ell}^{0.43} \times (R_{h_1} - R_s)^{-0.43} \boldsymbol{k} \quad (6)$$

The blade tip clearance drag torque (windage loss torque) is estimated

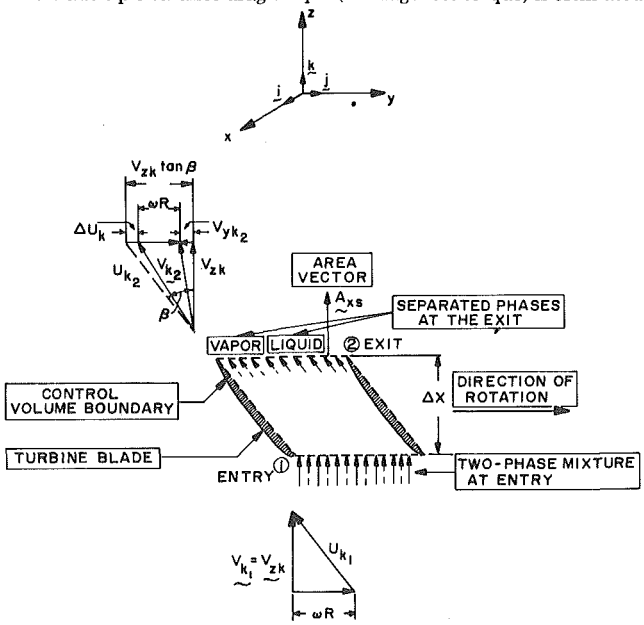

Fig. 1 Vector diagrams and control volume

Contributed by the Heat Transfer Division and presented at the Winter Annual Meeting, San Francisco, California, December 10–15, 1978. Manuscript received by the Heat Transfer Division August 17, 1978.

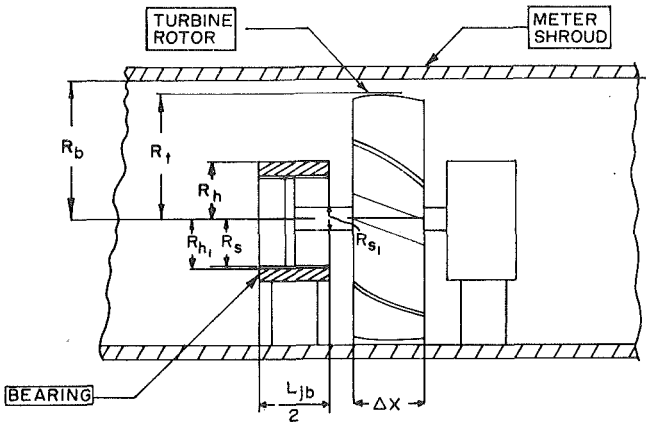

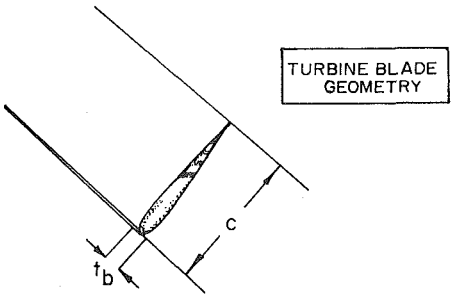

Fig. 2

by assuming that the rotor behaves like a journal bearing [3], hence,

$$T_{bT} = \frac{f\rho_\ell|\omega|\omega}{2} R_T{}^3 C t_b N \tag{7}$$

where the density ρ_ℓ of the liquid phase is used because it is assumed that mostly liquid exists on the shroud wall. Using the same friction factor as in equation (4) with,

$$\mathrm{Re}_\ell = \frac{\rho_\ell|\omega|R_T(R_b - R_T)}{\mu_\ell} \tag{8}$$

equations (4, 7) and (8) can be combined to yield,

$$\boldsymbol{T}_{bT} = -0.039(Ct_bN)\rho_\ell{}^{0.57}|\omega|^{0.57} \times \omega R_T{}^{2.57}\mu_\ell{}^{0.43}(R_b - R_T)^{-0.43}\boldsymbol{k} \tag{9}$$

The turbine blades, being of finite length, have finite guidance capacity which manifests itself as a slip in the rotor speed (see Fig. 1) which can be expressed as [4],

$$\Delta u_k = \eta_k |\, V_{y_{k2}}| \mathrm{Sgn}(V_{y_{k2}}) \tag{10}$$

where, $\mathrm{Sgn}(V_{y_{k2}}) \triangleq \begin{cases} +1, & V_{y_{k2}} \geq 0 \text{ (rotor deceleration)} \\ -1, & V_{y_{k2}} < 0 \text{ (rotor acceleration)} \end{cases}$

η_ℓ and η_v can be different, in general, due to the different inertias of the liquid and vapor phases.

Using equation (1) and the torques described above, an analytical transient turbine meter model was derived.

This model, which is described in detail in the Appendix, is of the form,

$$\frac{d\langle V_{z\ell}\rangle}{dt} + f_1(\langle\alpha\rangle, \langle\dot\alpha\rangle, p, \dot p, \omega)\langle V_{z\ell}\rangle = f_2(\langle\alpha\rangle, \langle\dot\alpha\rangle, p, \dot p, \langle V_{z\ell}\rangle, \omega, \dot\omega) \tag{11}$$

Equation (11) was programed on the computer and the resultant computer code, TEMPT, was exercised for a representative blowdown transient [5] given by,

$$p(t) = 14.82e^{-t} + 0.35 \quad \text{(Mpa)}$$
$$\alpha(t) = 1 - 0.999e^{-t}$$
$$CR(t) = 14te^{-5t} \quad (\mathrm{s}^{-1}) \tag{12}$$

Parametric runs were made to appraise the effect of the various terms in the model.

Effect of Correlation Coefficients

As the two-phase mixture flows through the turbine blading, the vapor phase will be turned to a greater degree than the liquid phase, leading to phase separation at the exit plane. In order to appraise this effect, it is convenient to reference our calculations to the homogeneous case. In this case,

$$C_\ell = C_v = 1.0 \tag{13}$$

Fig. 3 shows, as expected, that the effect of the liquid momentum predominates over that of the vapor. It is interesting to note that these effects are insignificant for small flow rates, since, as can be seen in equation (13A), C_ℓ and C_v appear only in the angular momentum terms.

Effect of Flow Deviation Factors

A typical single-phase flow value of η is [4], 0.2. The results of a parametric study are given in Fig. 4. A higher value of η_k implies that the fluid is less effective in driving the rotor and hence a higher mass flux is necessary for a given turbine-meter output.

It can be seen, as expected, that the momentum of the liquid phase is more important than that of the vapor phase. The effect is seen primarily in the rise part of the transient (fluid-driving-rotor), since the flow deviation factors have a smaller effect on the fluid tangential velocity for the decelerating portion of the transient (where the rotor drives the fluid).

Nomenclature

A_{xs} = effective flow area through the blading
C = chord length of the blade
C_k = correlation coefficients, C_ℓ and C_v for the liquid and vapor phases, respectively
f = fluid friction factor
G = mass flux
$\boldsymbol{i}, \boldsymbol{j}, \boldsymbol{k}$ = unit vectors in the x, y, and z directions, respectively, forming a right-hand triad
L_{jb} = length of the journal bearing
$\dot m_k$ = liquid and vapor phase mass flow rates, $\dot m_\ell$ and $\dot m_v$ across the control volume boundaries
N = number of blades on the rotor
p = absolute pressure at the location of the turbine meter
R = effective radius of the rotor
R_b = radius of the meter shroud or body
R_h = rotor hub radius
R_{h_1} = bearing radius
R_s = journal radius
R_{s_1} = shaft radius
R_T = blade tip radius
S = slip ratio
t = time
t_b = blade thickness
U_{k_1}, U_{k_2} = velocities of phase-k relative to the rotor at stations 1 and 2, respectively
V_t = turbine axial velocity ($\omega R/\tan\beta$)
V_{yk1}, V_{yk2} = velocities of phase-k in the y-direction at stations 1 and 2, respectively
V_{zk1}, V_{zk2} = velocities of phase-k in the z direction at stations 1 and 2, respectively
x, y, z = axes of the (right-hand) co-ordinate system
α = void fraction
$\alpha_k = \begin{cases} 1-\alpha, & \text{if } k = \ell \text{ (for liquid)} \\ \alpha, & \text{if } k = \mathrm{v} \text{ (for vapor)} \end{cases}$
β = blade angle
η_k = flow deviation factor, η_ℓ and η_v, for the liquid and vapor phases, respectively
μ_ℓ = dynamic viscosity of liquid phase
ρ_k = densities, ρ_ℓ and ρ_v of liquid and vapor phases, respectively
ω = angular velocity of the rotor
$\langle\xi\rangle = \frac{1}{A_{xs}}\int_{A_{xs}}\int \xi dA$, cross-sectional average of ξ
$|\xi|$ = absolute value of ξ
$\mathrm{Sgn}(\chi) = \begin{cases} +1, & \chi \geq 0 \\ -1, & \chi < 0 \end{cases}$

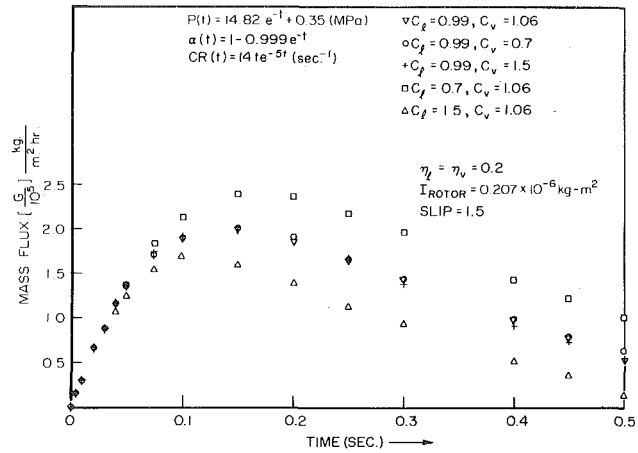

Fig. 3 The effect of distribution coefficient

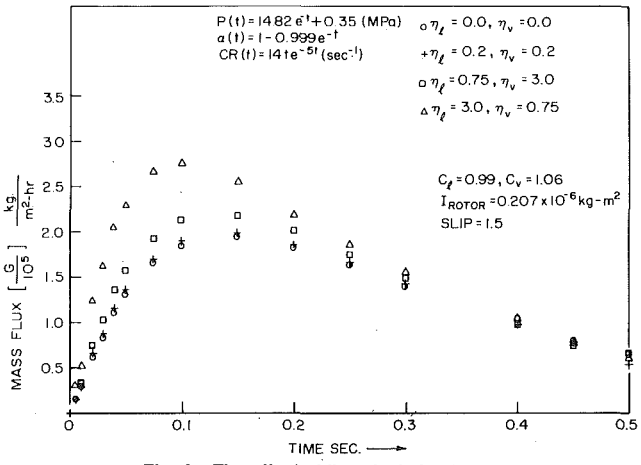

Fig. 4 The effect of flow deviation factor

Effect of the Moment-of-Inertia of the Rotor

The moment of inertia of the rotor makes the response of the rotor lag behind the flow rate, and thus, for the inverse problem the moment of inertia of the rotor predicts a flow rate that leads the measured response of the meter. Fig. 5 shows that both curves, the one with the I_{rotor} of 0.207×10^{-6} Kg − m^2 (best estimate value) and the other with 0.421×10^{-6} Kg − m^2, show significant differences from the quasi-steady solution in equation (17A), and from each other.

Effect of Drag Torques

Parametric calculations with the computer program TEMPT have indicated that the effect of the bearing friction and windage loss terms is quite small in comparison to the other terms during transients of interest.

Effect of Slip Ratio

For a given void fraction and turbine-meter response (e.g., equation (12)), an increase in the slip ratio implies an increase in the vapor velocity and a decrease in the liquid velocity. Since the mass flux is determined primarily by the inertia of the liquid phase, it is found in Fig. 6 that the higher the slip ratio, the lower the transient mass flux. However, as can be seen, this is not a very strong trend.

Moreover, the effect of the slip ratio (which appears in the angular momentum terms) is very small in the steeper parts of the transient because the inertial terms dominate in those regions. Calculations using a modified Bankoff variable slip model [6] showed no appreciable difference from the case of a constant slip of 1.5. This again indicates that the calculation is not sensitive to slip ratio and that a constant slip ratio can be used for transients similar to those given by equation (12).

Flow Reversal

The computer program TEMPT was tested for a transient with a flow reversal during depressurization, assuming that negative flow is indicated by a negative turbine counting rate, $cr(t)$.

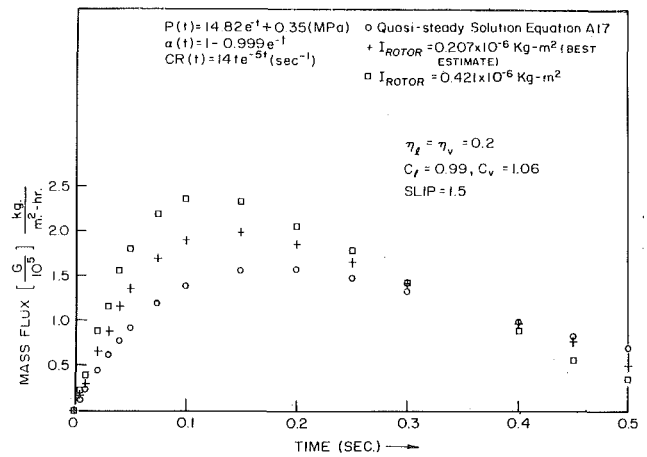

Fig. 5 The effect of rotor inertia

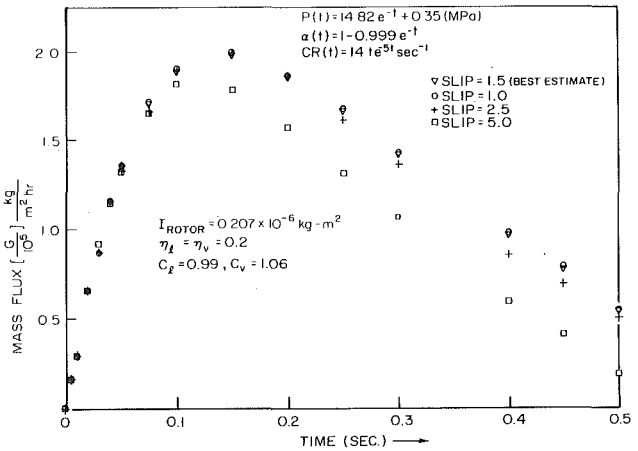

Fig. 6 The effect of slip ratio

The transient investigated was,

$$p(t) = 14.82e^{-t} + 0.35 \text{ (Mpa)}$$

$$\alpha(t) = 1 - 0.999e^{-t}$$

$$CR(t) = \cos\left(\frac{3\pi t}{2}\right) (\text{s}^{-1}) \tag{14}$$

The mass flow shown in Fig. 8 indicates that the quasi-steady solution, equation (17A), is not, in general, valid.

Conclusions

It has been shown that the quasisteady solution technique, which has been widely used for transient turbine-meter analysis in the past, is not generally valid for transients of practical concern. An analytical model has been developed with which accurate analysis of two-phase transients can be accomplished. A parameter study using this model has indicated that the most significant parameters are rotor inertia and void and velocity profile effects. It is hoped that experimental data will be taken in the future which can be used to determine the appropriate parameters to use.

Acknowledgments

The authors wish to acknowledge the help and advice given during the course of this study by Mr. R. Beardon (EG&G) and Dr. T. Chawla (ANL). In addition, the financial support given by EG&G to perform this study is gratefully acknowledged.

References

1 Estrada, H., and Sheppard, J. D., "Some Aspects of Interpreting Two-Phase Flow Measurements in Instrumented Spool Pieces," NUREG-0280, NRC-2.

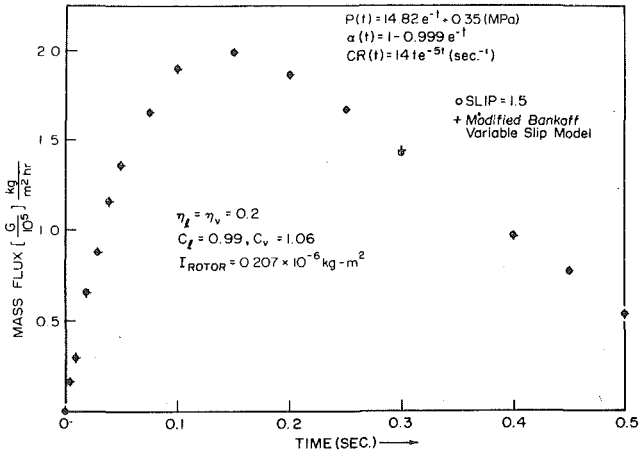

Fig. 7 The effect of variable slip

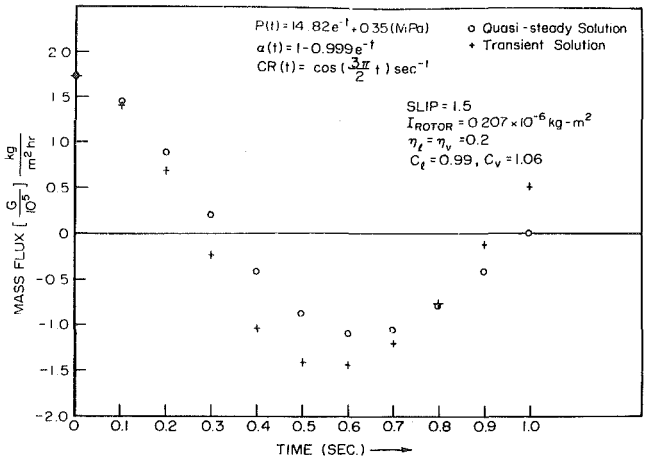

Fig. 8 Calculations of flow reversal

2 Yadigaroglu, G., and Lahey, R. R., "On the Various Forms of Conservation Equations in Two-Phase Flows," *International Journal of Multiphase Flow*, Vol. 2, 1976, pp. 477–494.

3 Thompson, K. E., and Grey, J., "Turbine Flow Meter Performance Model," ASME, *Journal of Basic Engineering*, Vol. 92, Dec. 1970, pp. 712–723.

4 Lee, W. F. Z., Kirik, M. J. and Bonner, J. A. "Gas Turbine Flow Meter Measurement of Pulsating Flow," ASME *Journal of Engineering for Power*, Vol. 97, No. 4, Oct. 1975, pp. 531–539.

5 Heiselmann, M. W., Arave, A. E., Goodrich, L. D. and Worley, L. C., "Design, Development and Testing Status of the LOFT Drag Disk Turbine Transducer," Report-No. 141-14, Aug. 1974.

6 Bankoff, S. G., "A Variable Density Single-Fluid Model for Two-Phase Flow with Particular Reference to Steam-Water Flow," ASME JOURNAL OF HEAT TRANSFER, Vol. 82, 1960.

7 Kamath, P. S., and Lahey, R. T., "A Turbine-Meter Evaluation Model for Two-Phase Transients," *Topical Report-NES-459*, Oct. 1977.

8 Rouhani, S., "Application of the Turbine-Type Flow Meters in the Measurement of Steam Quality and Void," presented at the Symposium on In-Core Instrumentation, Oslo, June 15, 1964.

APPENDIX

In this section, each term of equation (1) is evaluated for a two-phase fluid flowing through the control volume shown in Fig. 1.

The following assumptions are made in this analysis:

1 No inlet tangential velocity component (i.e., no inlet swirl)

2 The mass flow rates, void fractions and flow areas at the inlet and exit of the blading are equal, thus the fluid velocity component along the axis of the meter is invariant. That is,

$$V_{zk_1} = V_{zk_2} = V_{zk} \tag{1A}$$

3 Fig. 1 is the section of the blading at a representative radius, R, given by,

$$R = \left[\frac{R_h^2 + R_T^2}{2}\right]^{1/2} \tag{2A}$$

where all the forces are assumed [7] to act. Each term of equation (1) can now be written as:

$$\begin{bmatrix}\text{outflow rate of}\\ \text{angular momentum}\\ \text{from control}\\ \text{volume}\end{bmatrix} = (R\boldsymbol{i})X(\dot{m}_{\ell_2}\boldsymbol{V}_{y\ell 2}) + (R\boldsymbol{i})X(\dot{m}_{v2}\boldsymbol{V}_{yv_2}) \tag{3A}$$

where the mass flow rates are given by,

$$\dot{m}_{k_2} = \rho_k\alpha_k(V_{zk}A_{xs}) = \rho_k|V_{zk}|A_{xs}\alpha_k \text{ Cos } (0) = \rho_k|V_{zk}|A_{xs}\alpha_k \tag{4A},$$

and the tangential velocity components, obtained from Fig. 1 and equation (10), are,

$$V_{yk_2} = -V_{yk_2}|\boldsymbol{j} = -\left[\frac{V_{zk}\tan\beta}{(1-\eta_k \text{ Sgn}(V_{yk_2}))} - \frac{\omega R}{(1-\eta_k \text{ Sgn}(V_{yk_2}))}\right]\boldsymbol{j} = \left[\frac{\omega R}{(1-\eta_k \text{ Sgn}(V_{yk_2}))} - \frac{V_{zk}\tan\beta}{(1-\eta_k \text{ Sgn}(V_{yk_2}))}\right]\boldsymbol{j} \tag{5A}$$

Substituting equations (4A) and (5A) into equation (3A), and noting that the co-ordinate system is right-handed, and that, by definition [2],

$$\frac{\langle\alpha_k V_{zk}\rangle}{\langle\alpha_k\rangle\langle V_{zk}\rangle} = 1, \tag{6A}$$

the expression for the out-flow rate of angular momentum is obtained as,

$$\begin{bmatrix}\text{Outflow rate of}\\ \text{angular momentum}\\ \text{from the control}\\ \text{volume}\end{bmatrix} = R^2A_{xs}\omega\left[\frac{\rho_\ell|\langle V_{z\ell}\rangle|\langle 1-\alpha\rangle}{(1-\eta_\ell \text{ Sgn}(V_{y\ell_2}))} + \frac{\rho_v|\langle V_{zv}\rangle|\langle\alpha\rangle}{(1-\eta_v \text{ Sgn}(V_{yv_2}))}\right]\boldsymbol{k} - RA_{xs}\tan\beta\left[\frac{C_\ell\langle 1-\alpha\rangle\langle V_{z\ell}\rangle|\langle V_{z\ell}\rangle|}{(1-\eta_\ell \text{ Sgn}(V_{y\ell_2}))} + \frac{C_v\langle\alpha\rangle\rho_v\langle V_{zv}\rangle|\langle V_{zv}\rangle|}{(1-\eta_v \text{ Sgn}(V_{yv_2}))}\right]\boldsymbol{k} \tag{7A}$$

Let us now consider the inflow rates of angular momentum,

$$\begin{bmatrix}\text{Inflow rate of}\\ \text{angular momentum}\\ \text{into the control}\\ \text{volume}\end{bmatrix} = (R\boldsymbol{i})X(\dot{m}_{\ell i}V_{y\ell_1}) + (R\boldsymbol{i})X(\dot{m}_{v_1}V_{yv_1}) = 0 \tag{8A}$$

from the assumption of zero tangential velocity component at the inlet to the blading, we find that this term makes no contribution to the dynamic torque balance.

The storate rate is given by,

$$\begin{bmatrix}\text{storage rate of}\\ \text{angular momentum}\\ \text{in the control}\\ \text{volume}\end{bmatrix} = (R\boldsymbol{i})X\frac{d}{dt}(m_\ell V_{y\ell}) + (R\boldsymbol{i})X\frac{d}{dt}(m_v V_{yv}) + I_{\text{rotor}}\frac{d\omega}{dt} \tag{9A}$$

Introducing equations (5A) and (6A) into equation (9A), and noting that the co-ordinate system is right-handed, the expression for the storage rate is obtained,

$$\begin{bmatrix}\text{storage rate of}\\ \text{angular momentum}\\ \text{in the control}\\ \text{volume}\end{bmatrix} = \frac{R^2A_{xs}(\Delta x)}{(1-\eta_\ell \text{ Sgn}(V_{y\ell_2}))} \times\left[\rho_\ell\langle 1-\alpha\rangle\frac{d\omega}{dt} + \omega\langle 1-\alpha\rangle\frac{d\rho_\ell}{dt} - \rho_\ell\frac{\omega d\langle\alpha\rangle}{dt}\right]\boldsymbol{k}$$

$$-\frac{RA_{xs}\tan\beta(\Delta x)}{(1-\eta_\ell \operatorname{Sgn}(V_{y\ell_2}))}\left[\rho_\ell\langle 1-\alpha\rangle\frac{d\langle V_{z\ell}\rangle}{dt}+\langle V_{z\ell}\rangle\langle 1-\alpha\rangle\frac{d\rho_\ell}{dt}\right.$$
$$\left.-\rho_\ell\langle V_{z\ell}\rangle\frac{d\langle\alpha\rangle}{dt}\right]\boldsymbol{k}+\frac{R^2A_{xs}(\Delta x)}{(1-\eta_v \operatorname{Sgn}(V_{vk_2}))}\left[\rho_v\langle\alpha\rangle\frac{d\omega}{dt}\right.$$
$$\left.+\omega\langle\alpha\rangle\frac{d\rho_v}{dt}+\rho_v\omega\frac{d\langle\alpha\rangle}{dt}\right]\underline{k}\,\frac{RA_{xs}\tan\beta(\Delta x)}{(1-\eta_v \operatorname{Sgn}(V_{yv_2}))}$$
$$\times\left[\rho_v\langle\alpha\rangle\frac{d\langle V_{zv}\rangle}{dt}+\langle V_{zv}\rangle\langle\alpha\rangle\frac{d\rho_v}{dt}+\rho_v\langle V_{zv}\rangle\frac{d\langle\alpha\rangle}{dt}\right]\boldsymbol{k}$$
$$+I_{\text{rotor}}\frac{d\omega}{dt}\boldsymbol{k} \quad (10A)$$

From equation (6) and (9), the right-hand side of equation (1) is obtained,

$$\left[\begin{array}{l}\text{Sum of the exter-}\\ \text{nal torques on}\\ \text{the control}\\ \text{volume}\end{array}\right]=-\rho_\ell^{0.57}\mu_\ell^{0.43}|\boldsymbol{\omega}|^{0.57}\boldsymbol{\omega}$$
$$\times[0.039(Ct_bN)R_T^{2.57}(R_b-R_T)^{-0.43}$$
$$+0.245(L_{jb}R_s^{3.57})(R_{h_1}-R_s)^{-0.43}]\,\boldsymbol{k} \quad (11A)$$

Substituting equations (7A, 8A, 10A) and (A11) into equation (1), and eliminating the vapor phase velocity by using the slip ratio

$$S=\frac{\langle V_{zv}\rangle}{\langle V_{z\ell}\rangle} \quad (12A)$$

the governing differential equation is obtained,

$$\frac{d\langle V_{z\ell}\rangle}{dt}=|\langle V_{z\ell}\rangle|\left[\frac{V_t}{\Delta x}\right]-\langle V_{z\ell}\rangle$$
$$\times\left[\frac{R_1}{(S+R_1)}\frac{1}{\rho_\ell}\frac{d\rho_\ell}{dt}+\frac{S}{S+R_1}\frac{1}{\rho_v}\frac{d\rho_v}{dt}\right.$$
$$\left.+\frac{S-R_2}{S+R_1}\frac{1}{\langle\alpha\rangle}\frac{d\langle\alpha\rangle}{dt}+\frac{1}{S+R_1}\frac{dS}{dt}\right]$$
$$-\left[\frac{C_\ell R_1+C_vS^2}{(S+R_1)(\Delta x)}\right]\langle V_{z\ell}\rangle|\langle V_{z\ell}\rangle|$$
$$+V_t\left[\frac{R_1}{S+R_1}\frac{1}{\rho_\ell}\frac{d\rho_\ell}{dt}+\frac{S}{(S+R_1)}\frac{1}{\rho_v}\frac{d\rho_v}{dt}\right.$$
$$\left.+\frac{1-R_2}{S+R_1}\frac{1}{\langle\alpha\rangle}\frac{d\langle\alpha\rangle}{dt}\right]+\frac{dV_t}{dt}\left[\frac{1+R_1}{S+R_1}+\frac{I_{\text{rotor}}(1-\eta_v \operatorname{Sgn}(V_{yv_2}))}{(S+R_1)R^2A_{xs}(\Delta x)\rho_v\langle\alpha\rangle}\right]$$
$$+\frac{\mu^{0.43}\rho_\ell^{0.57}|\omega|^{0.57}\omega(1-\eta_v \operatorname{Sgn}(V_{yv_2}))}{(S+R_1)RA_{xs}(\Delta x)\rho_v\langle\alpha\rangle\tan\beta}$$
$$\times[0.039(Ct_bN)R_T^{2.57}(R_b-R_T)^{-0.43}$$
$$+0.245(L_{jb}R_S^{3.57})(R_{h_1}-R_s)^{-0.43}] \quad (13A)$$

where,

$$V_t\triangleq\frac{\omega R}{\tan\beta},\quad \frac{dV_t}{dt}=\frac{R}{\tan\beta}\frac{d\omega}{dt} \quad (14A)$$

and

$$R_1=\frac{\rho_\ell}{\rho_v}\frac{\langle 1-\alpha\rangle}{\langle\alpha\rangle}\frac{(1-\eta_v \operatorname{Sgn}(V_{yv_2}))}{(1-\eta_\ell \operatorname{Sgn}(V_{y\ell_2}))},$$
$$R_2\triangleq\frac{\rho_\ell}{\rho_v}\frac{(1-\eta_v \operatorname{Sgn}(V_{yv_2}))}{(1-\eta_\ell\, Sgn(V_{yl_2}))} \quad (15A)$$

The mass flux was obtained using the computer program, TEMPT, by solving equation (13A) numerically for $\langle V_{z\ell}\rangle$ and then using equation (12A),

$$G=\rho_\ell\langle 1-\alpha\rangle\langle V_{z\ell}\rangle+\rho_v\langle\alpha\rangle S\langle V_{z\ell}\rangle \quad (16A)$$

Equating all time derivatives in equation (13A) to zero and solving the resultant quadratic equation in $\langle V_{zl}\rangle$, the quasisteady solution is obtained as,

$$\langle V_{z\ell}\rangle=\frac{-B\pm\sqrt{B^2-4AC}}{2A} \quad (17A)$$

where the plus and minus signs are for forward and reverse flows in the conduit respectively, and the variables A, B and C are defined as,

$$A\triangleq\frac{C_\ell\rho_\ell\langle 1-\alpha\rangle}{(1-\eta_\ell \operatorname{Sgn}(V_{y\ell_2}))}+\frac{C_v\rho_v\langle\alpha\rangle S^2}{(1-\eta_v \operatorname{Sgn}(V_{yv_2}))} \quad (18.1A)$$

$$B\triangleq-\left[\frac{\rho_\ell\langle 1-\alpha\rangle}{(1-\eta_\ell \operatorname{Sgn}(V_{y\ell_2}))}+\frac{\rho_v\langle\alpha\rangle S}{(1-\eta_v \operatorname{Sgn}(V_{yv_2}))}\right]V_t \quad (18.2A)$$

and

$$C=\frac{\mu_\ell^{0.43}\rho_\ell^{0.57}|\omega|^{0.57}\omega}{RA_{xs}\tan\beta}[0.039(Ct_bN)R_T^{2.57}(R_b-R_T)^{-0.43}$$
$$+0.245(L_{jb}R_s)^{3.57}(R_{h_1}-R_s)^{-0.43}] \quad (18.3A)$$

The quasi-steady mass flux is obtained, as for the transient case, by using equation (16A). It is interesting to note that for $C_\ell=C_v=1.0$ (flat velocity and void profiles) and $\eta_\ell=\eta_v=0$ (perfect guidance by the blades), equation (17A) reduces to the so called Rouhani equation [8],

$$\rho_\ell\langle 1-\alpha\rangle|\langle V_{z\ell}\rangle|[V_t-\langle V_{z\ell}\rangle]+\rho_v\langle\alpha\rangle|\langle V_{zv}\rangle|[V_t-\langle V_{zv}\rangle]=0 \quad (19A)$$

Correlations for the Determination of the Inception Conditions of Density-Wave Oscillations for Forced and Natural Circulation Steam Generator Tubes

H. C. Ünal

Central Technical Institute TNO,
P.O. Box 342,
Apeldoorn, Netherlands

Accurate and simple correlations are presented to determine the inception conditions of density-wave oscillations in steam generator tubes. The correlations predict the power at the start of the density-wave oscillations within about 6.5 percent accuracy for long (i.e., L ≥ 10 m) forced circulation steam generator tubes and within about 20 percent accuracy for natural circulation and short forced circulation steam generator tubes. The ranges of the operating conditions and geometries for the data used to establish the correlations are as follows: Forced circulation tubes: Geometry: circular-straight tubes and serpentines, a circular coil and a rectangular straight tube; type of heating: electrical or sodium heating; the ratio of the heated length to diameter: 153–9502; pressure: 4.1–17.3 MN/m^2; outlet steam quality: 0.27–1.85; inlet subcooling: 2.8–245.9 K; mass velocity: 118–2088 kg/m^{2}s. Natural circulation tubes: Geometry and heating conditions: electrically heated circular tubes and annuli; ratio of the heated length to diameter: 34–489; pressure: 0.2–7.1 MN/m^2; outlet steam quality: 0.04–0.62; inlet subcooling: 0–244 K; mass velocity: 529–1230 kg/m^{2}s. The number of data considered is 106 for forced circulation tubes and 110 for natural circulation tubes.

Introduction

Although many types of dynamic instabilities can occur in a steam generator tube, a particular type of dynamic instability, i.e., Density-Wave Oscillations (DWO), is of practical importance for the design and safe operation of steam generators. The DWO are low-frequency flow oscillations of which the period is of the same order of magnitude as the transit time of a fluid particle in the steam generator tube. The DWO are due to multiple regenerative feedbacks between the flow rate, the vapor generation rate and the pressure drop [1], and are also referred to in the literature as mass flow-void feedback, time-delay or parallel channel instabilities. Both the DWO and other types of dynamic instabilities have been extensively studied in the last two decades. For a detailed review of the literature on the subject, the reader is referred to [2–3] and for a recently observed new type of dynamic instability to [4–5].

For the purpose of the present study it is considered sufficient to mention briefly the methods of correlating the DWO-data. In general, correlating the DWO-data consists of fitting them into a stability model, which is a simultaneous solution of one-dimensional non-steady-state, linearized or nonlinearized continuity, momentum and energy equations for a steam generator tube with appropriate boundary conditions and subsidiary equations [2–3]. The last-mentioned equations are correlations for the properties of water and steam, correlations for void fraction, heat transfer and pressure drop for different flow regimes in a steam generator tube, and a correlation for the thermal non-equilibrium condition in subcooled nucleate flow boiling. Almost all the stability models given in the literature are computer programs. It is well known that neither do the one-dimensional continuity, momentum and energy equations completely describe two-phase flow [3, 6], nor do the heat transfer, void and pressure drop correlations used in the stability models presented in the literature apply to non-steady state conditions [1, 3, 6, 7]. Furthermore, because of error margins in the aforesaid correlations and errors in the measurement of the inception conditions of the DWO, a stability model can not, in general, predict the power at the start of the DWO to better than about 10 percent accuracy. The accuracy of stability models given in the literature can be much less than 10 percent, as demonstrated by Neal and Zivi [1] and Bjørlo, et al. [7]. Neal and Zivi have compared six selected stability models with some or all of the 52 data of various investigators taken in forced and natural circulation steam generator tubes for a wide range of operating conditions and geometries. These models apply to the condition $X < 1$, and predict the power at the start of the DWO to within 95 percent accuracy. The authors obtained the best results with the model of [8], which predicts the power at the start of the DWO with 20 percent accuracy "about 70 percent of the time" [1]. For the rest of the time the model, however, gives the power with accuracy varying from 20 to 95 percent. Stability models which can be applied to a steam generator tube in which superheated steam is produced, are scarce in the literature [9–12]. It is reported in [13–14] that the model given in [9] does not fit the data well. A similar conclusion can also be drawn for the models of [10, 12].

It should be stressed that stability models presented so far in the literature have been of great scientific value. However for some special applications in engineering practice, improvements in the accuracy are considered very useful in the prediction of the power at the start of DWO, especially for a Forced Circulation Steam Generator Tube (FCSGT) in which superheated steam is produced. Correlations are therefore presented in this paper for different ranges of operating conditions and geometries for FCSGT's and Natural Circulation Steam Generator Tubes (NCSGT's). For long FCSGT's for which $L/d \geq 1272$ and $X > 1$, the accuracy obtained is about 6.5 percent. For short FCSGT's and NCSGT's, the accuracy is not better than about 20 percent.

Correlation of the DWO Data from FCSGT'S

The Data. The DWO tests reported in [12, 14–20] are considered. The ranges of operating conditions and geometries for these tests are summarized in Table 1. The aforementioned operating conditions are

Contributed by the Heat Transfer Division for publication in the JOURNAL OF HEAT TRANSFER. Manuscript received by the Heat Transfer Division April 17, 1978.

Table 1 Data for the inception conditions of the DWO for forced circulation systems

Geometry and dimensions of the test tube and type of heating	L/d	P MN/m²	X	G kg/m²s	ΔT_{sub} K
Electrically heated rectangular channel; d = 4.49 mm; L = 0.686 m; n = 18 [20]	153	4.1–11.0	0.273–0.726	436–2088	2.8–86.1
Sodium heated vertical tube of 7.86 mm ID, L = 10 m; n = 11 [16]	1272	6.2–14.1	1.14–1.34	706–1365	27–81.6
Sodium heated vertical tube of 11.4 mm ID, L = 14.58 m; n = 8 [18]	1279	16–17.3	1.51–1.62	—	87.3–93.7
Sodium heated vertical tube of 12.6 mm ID, L = 19.34 m; n = 33 [17]	1535	5.3–17.0	1.10–1.59	—	23.9–111.3
Sodium heated coil of 17 mm ID, D/d = 47.4; L = 43 m; n = 2 [19]	2529	9.9	1.44–1.46	835	104.2
Sodium heated serpentine of 9.4 mm ID, L = 39.65 m; n = 1	4220	16.7	1.85	—	127.6
Electrically heated serpentine consisting of three tubes of 18.2 mm, 21.8 mm and 29.9 mm ID, tubes with lengths of 24.1 m, 158.9 m and 26.6 m respectively; n = 33 [14–15]	9502	4.3–14.4	1.01–1.69	118–362 (at the inlet)	118.4–245.9

so-called inception conditions of the DWO, and were measured for the last stable test run before the DWO occurred in the test tube.

In the tests of [17] and [18] the total pressure drop in the test tube, which was one of the 139 tubes of a large capacity sodium heated steam generator, was constant. In these tests, the flow at the inlet of the test tube was not throttled and the mass velocity in the test tube was not measured. In the work reported by [14] and [15], three identical serpentines were arranged in parallel. Each serpentine used consisted of three tubes of different inside diameters. For this serpentine (L/d) is determined as the arithmetic sum of (L/d) for each tube. The flows at the inlet of the serpentines were throttled. In experiments reported by [19] two and by [12] three test tubes were arranged in parallel; [16] and [20] report a large bypass pipe built around the test tube. Thus a constant pressure drop is maintained in the test tube. For the tests of [12, 16, 19], the throttling of the flow at the inlet of the test tube was solely due to a flow measuring device (i.e., a turbine flow meter or an orifice) and was assumed to be negligible small for a long tube. In the work of [20], a venturi was used to measure the flow at the inlet of the test tube, of which inlet throttling was also considered negligible.

The Correlation. The dimensionless numbers which characterize fully the dynamics of two-phase flow are numerous and it is practically impossible to take all of them into account when correlating the data [21]. Therefore, in spite of a loss of generality, the number of them was reduced by considering only the most significant parameters, as presented in [17], with the result that the data for the outlet steam quality at the start of the DWO have been correlated using equation (1)

$$X = B_1 B_2 [B_3 + B_4 \ln (1 - P_r)]/B_5 \quad (1)$$

where

$$B_1 = 1 + 1.8 \exp [-11.4 (1 - P_r) \times (1 + 3.83.10^{-5} \exp (1.11.10^{-3} L/d))] \quad (2)$$

$$B_2 = 1 + 3.3 \exp (-4.5.10^{-3} L/d) \exp (-50\, \Delta H) \quad (3)$$

$$B_3 = (0.98 + 0.088.10^{-3} L/d)/[1 + 5.1 \exp (-5.3.10^{-3} L/d)] \quad (4)$$

$$B_4 = -0.14 \exp (0.23.10^{-3} L/d) \quad (5)$$

$$B_5 = 1 + 2.9.10^{-3} (10^{-3} L/d)^{2.77} \Delta H \quad (6)$$

For the data of [12, 14, 15, 17–19], the outlet steam quality was calculated with the measured outlet temperature and pressure, using a Steam Table [22], and for those of [16, 20], with a heat balance, assuming a thermodynamic equilibrium between the phases. From the data of [14, 15] it was not possible to deduce where the pressure was measured, at the inlet or the outlet of the test tube. It seems most probable that the above mentioned pressure is the outlet pressure. For the data of [14, 15], the outlet steam quality was therefore calculated using the pressure reported, without considering whether it was measured at the inlet or at the outlet of the test tube. This may introduce errors in the evaluation of the outlet-steam quality, though of only a few percent since for these data $P \gg \Delta P$, a condition which also applies to the data of [12, 16–20]. For the evaluation of h_i and h_{sat} in ΔH in equations (3) and (6), the value of the outlet pressure is used.

If the steam quality at the outlet of a FCSGT exceeds the outlet steam quality predicted by equation (1), the DWO will occur in the FCSGT. In accordance with this equation, it is sufficient to know only *two operating conditions,* namely inlet temperature and outlet

Nomenclature

D = coil diameter, m
d = equivalent tube inside diameter, m
d_1 = outside diameter of inner tube of annulus, m
d_2 = inside diameter of outer tube of annulus, m
F = cross-sectional area of steam generator tube, m²
F_o = cross-sectional area at the outlet of riser, m²
Fr = Froude number, $G^2/(\rho^2 dg)$
G = mass velocity at the start of DWO, kg/m²s
g = acceleration of gravity, m/s²
h_c = enthalpy of water at critical conditions, J/kg
h_i = inlet enthalpy at the start of DWO, J/kg
h_o = outlet enthalpy at the start of DWO, J/kg
h_{sat} = enthalpy of water at the state of saturation, J/kg
ΔH = dimensionless inlet enthalpy, $\Delta H = (h_{sat} - h_i)/h_{sat}$
L = heated length or heated length of a steam generator tube between the tube plates of a steam generator, m
n = number of data
P = outlet pressure at the start of DWO, N/m²
P_r = reduced outlet pressure at the start of DWO, i.e., P divided by critical pressure
Q = power at the start of DWO, W
QM = measured power at the start of DWO, W
QP = predicted power at the start of DWO, W
ΔP = total pressure drop in a steam generator tube, N/m²
r = latent heat of evaporation for water, J/kg
ΔT_{sub} = inlet subcooling at the start of DWO, K
X = outlet steam equality (i.e., thermodynamic quality) at the start of DWO, based on thermal equilibrium
ρ = density of saturated water, kg/m³

pressure in order to determine the outlet steam quality at the start of the DWO in a FCSGT of known dimensions. The outlet temperature is then also known for a FCSGT in which superheated steam is produced.

Quandt [20] has shown that for a short FCSGT very low inlet subcoolings affect substantially the outlet steam quality at the start of the DWO. From the 304 DWO data obtained in two sodium heated long FCSGT's of $L/d = 1467$ and 2229, the author comes to the conclusion [23] that the effect of very low subcoolings on the steam quality at the start of the DWO is negligible for long FCSGT's. The data from short FCSGT's are very scarce in the literature. The aforesaid effect could be taken into account in equation (1) only by the use of the few data (i.e., five data) of [20] for which $\Delta H = 0.0119$–0.0238 and $L/d = 153$, and is expressed with the parameter B_2 given by equation (3). (For the rest of the data of [20], ΔH varies between 0.087–0.31). Equation (1) is therefore not recommended for very low subcoolings (i.e., $\Delta H < 0.087$) if $L/d < 1272$. Note that $B_2 \cong 1$ if $L/d \geq 1272$ and $\Delta H \geq 0$ or if $153 \leq L/d \leq 1272$ and $\Delta H \geq 0.087$.

The power at the start of the DWO is expressed by the equation

$$Q = GF(h_{sat} - h_i + rX) = GF(h_o - h_i) \tag{7}$$

where X is given by equation (1). The results of the comparison of the data of [12, 14–20] with equation (7) is shown in Fig. 1. This equation predicts the power at the start of the DWO accurate within about 6.5 percent with a RMS error of 3.3 percent for all the 88 data of [12, 14–19] for which $X > 1$ and $1272 \leq L/d \leq 9502$, and accurate within 20 percent with a RMS error of 13.3 percent for the all the 18 data of [20] for which $X < 1$ and $L/d = 153$. The RMS error for all the data is 6.2 percent. The range of operating conditions and geometries for the data used to establish equation (1) and (7) are summarized below: Geometry of the test tubes: circular-straight tubes and -serpentines, a circular coil and a rectangular straight tube; type of heating; sodium or electrical heating; $L = 0.686$–200 m; $L/d = 153$–9502; $d = 4.49$–29.9 mm; $X = 0.27$–1.85; $P = 4.1$–17.3 MN/m^2; $G = 118$–2088 kg/m^{2}s; $\Delta T_{sub} = 2.8$–245.9 K.

Here it has to be mentioned that only the data for the last stable test run of the tests of [12, 14–20] have been analyzed in the present study. The other test runs need not be considered since these test runs were carried out in such a way that the outlet enthalpy (or outlet steam quality) of each test run was always less than the outlet enthalpy (or outlet steam quality) at the start of the DWO for a given inlet subcooling and outlet pressure.

The physical meaning of equation (7) is that the heat input per unit mass of fluid flowing in a FCSGT of known dimensions (i.e., L and d) is constant at the start of the DWO for a given pressure and inlet subcooling.

For a quick estimation of the inception conditions of the DWO for long FCSGT's (i.e., $1272 \leq L/d \leq 9502$), the following equation is recommended

$$h_o/h_c = 1.47 \tag{8}$$

In accordance with equation (8), the outlet enthalpy is constant at the start of the DWO without considering operating conditions and geometry. By the use of equations (7) and (8) it can be shown that the power at the start of the DWO can be predicted within 11 percent accuracy with a RMS error of 6.1 percent for all the 88 data of [12, 14–19]. The ranges of operating conditions and geometries for these data are: circular-straight-tubes and -serpentines, a circular coil; $L = 10$–200 m; $d = 7.86$–29.9 mm; $L/d = 1272$–9502; $X = 1.01$–1.85; $P = 4.3$–17.3 MN/m^2; $G = 118$–1365 kg/m^{2}s; $\Delta T_{sub} = 23.9$–245.9K. As discussed above, the stability models given in the literature in the form of computer programs do not in general predict the power at the start of the DWO for a long FCSGT (i.e., $L/d \geq 1272$) more accurately than the simple correlations presented here. A similar result was also found in [23] for long FCSGT's (i.e., $L/d \geq 1272$ and $X > 1$). In [23], 380 data were used. Most of these data were obtained from experiments carried out systematically in two long FCSGT's to determine the effects on the stability of all the operating conditions, geometry and inlet throttling.

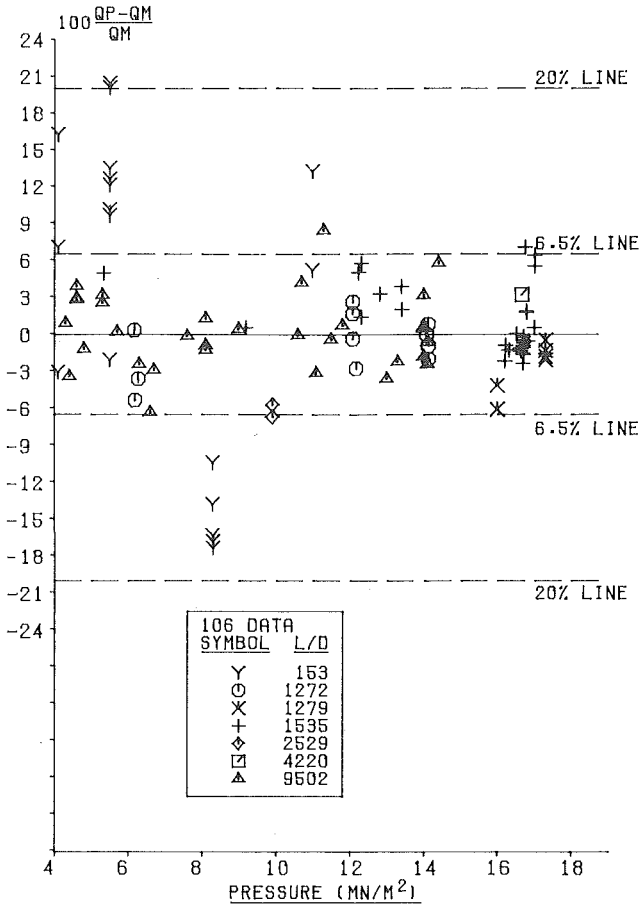

Fig. 1 Error in predicting power at the start of the DWO for FCSGTs

For $L/d < 4167$, inlet throttling does affect the outlet steam quality or the outlet enthalpy at the start of the DWO and this effect is among others a function of (L/d) [23]. Equations (1) and (8) can not therefore be applied to a FCSGT of $L/d < 4167$ if the flow at the inlet of the tube is throttled. The effect of inlet throttling on the inception conditions of the DWO for a FCSGT of $L/d > 4167$ appears to be negligible [23]. This can be also demonstrated indirectly by the use of the data of [14–15], which were obtained in a very long FCSGT of $L/d = 9502$. For these data, the error in predicting power at the start of the DWO in accordance with equation (7) is shown versus inlet-throttling coefficient (i.e., pressure loss coefficient of an orifice or a flow control valve fitted to the inlet of a tube) in Fig. 2. The conclusion drawn from Fig. 2 is that the effect of inlet throttling on the inception conditions of the DWO in very long FCSGT's seems to be negligible; in other words, the aforesaid effect is within the experimental accuracy.

Correlation of the DWO Data from NCSGT'S

The DWO data of [24–27] and those of Anderson as quoted from [1] are considered. The ranges of operating conditions and geometries of these 110 data are summarized in Table 2, and are as follows: Geometry and heating conditions: electrically heated vertical circular tubes and vertical annuli; $d = 8.51$–36 mm; $L = 0.91$–4.89 m; $L/d = 34$–489; $P = 0.2$–7.1 MN/m^2; $X = 0.04$–0.62; $G = 529$–1230 kg/m^{2}s; $\Delta T_{sub} = 0$–244 K.

The aforesaid data are correlated with equations (9) and (10) for circular tubes and annuli respectively.

$$X = 8C_1(L/d)^{0.22}P_r{}^{1.64}/(C_2C_3C_4) \tag{9}$$

$$X = 480C_1P_r{}^{0.93}D_1D_2D_3 \tag{10}$$

where

$$C_1 = \mathrm{Fr}(^{-1.88}P_r{}^{0.5}) \tag{11}$$

$$C_2 = 2.13 - 1.13 \exp(-586\Delta H^3 \mathrm{Fr}) \quad (12)$$

$$C_3 = 1 + 0.12 \exp[-2.76(F_o/F - 1)\mathrm{Fr}^{0.7}] \quad (13)$$

$$C_4 = 1 + 2.03.10^4[(L/d)\mathrm{Fr}^{-0.5}]^{-3.25} \quad (14)$$

$$D_1 = (d_1/d_2)^{(2.53/(1+4P_r^{2.52}))} \quad (15)$$

$$D_2 = (L/d)^{(-0.93/(1+\ 60.4P_r^{3.55}))} \quad (16)$$

$$D_3 = 1 + 1.69(1 - P_r)^{13.7} \exp(-38\ \Delta H) \quad (17)$$

Correlation of the DWO data from NCSGT's using two equations different from that given for FCSGT's seems justified in accordance with the work given in [23]: In [23] it is demonstrated that the DWO observed in two once-through FCSGT's are time-delay oscillations and that the transit time of a fluid particle in the different heat transfer regimes in the tubes, especially the transit time in the superheated steam region is of vital importance for the mechanism of the observed DWO. An empirical relationship is also established in [23] for the mechanism of the DWO using 176 data taken for quite an appreciable range of conditions. The pressure drops between the inlet and outlet of both of the aforesaid tubes were constant. In a natural circulation loop, the summation of the pressure drops along the loop equals to zero; it is logical then to assume that the transit time of a fluid particle in every part of the loop has to be considered for the mechanism of DWO. Nevertheless the above mentioned empirical relationship given in [23] suggests that the transit time in two-phase flow region in a natural circulation loop for which $X < 1$ is most significant for the mechanism of the DWO. This transit time strongly depends on void fraction and the void fraction in a vertical circular tube differs from that in a vertical annulus [5].

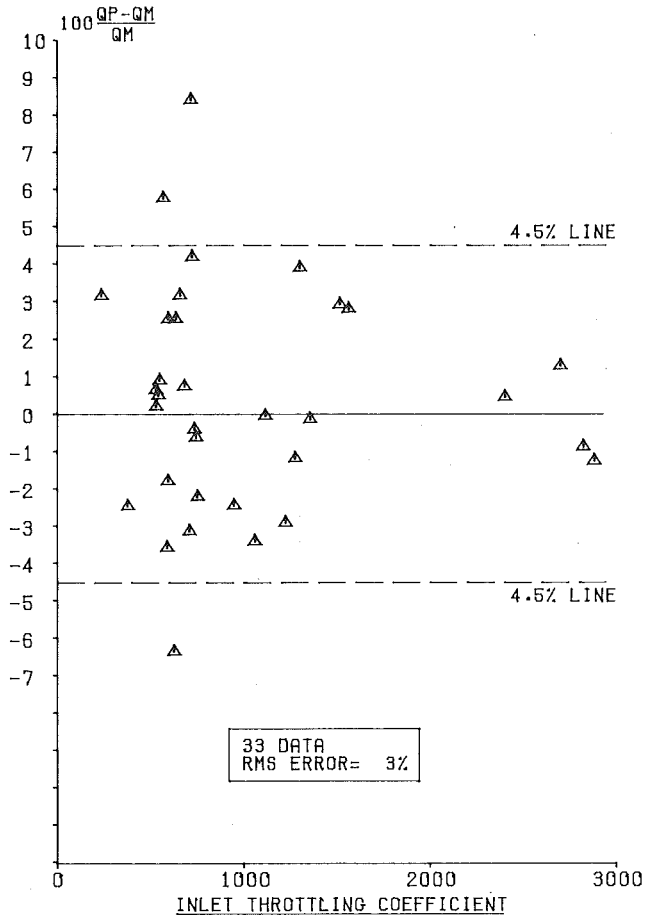

Fig. 2 Effect of inlet throttling on the inception conditions of the DWO

The Froude number is used in equations (9) and (10) in order to take into account the mass velocity in a nondimensional form. This number in a modified form is also used for correlating the void fraction data [28–29]. It is anticipated therefore equations [9] and [10] is not applicable to horizontal NCSGT's.

If the steam quality at the outlet of a NCSGT exceeds the outlet steam quality predicted by equation (9) (i.e., for a circular tube) or equation (10) (i.e., for an annulus) DWO occur in the NCSGT. The power at the start of the DWO is given by equation (7) in which X is expressed by equation (9) for circular tubes and by equation (10) for annuli. The physical meaning of the established correlation is that the heat input to the unit mass of the fluid flowing in a NCSGT of known dimensions (i.e., L, d and F_o/F) is constant at the start of the DWO for a given pressure, inlet subcooling and mass velocity.

The error in predicting power at the start of the DWO for the data of [24–27] and those of Anderson as quoted from [1] are shown versus pressure in Fig. 3. With five exceptions, the errors are within 20 percent. The RMS error for all the data is 10.6 percent.

In Figs. 1 and 3 all the data considered by Neal and Zivi [1] (i.e., some data of [25–26] from NCSGT's and all the data of [20] from a short FCSGT) to check six stability models are included. The correlations given here predict the power at the start of the DWO with 20 percent accuracy 95 percent of the time for all the data considered by Neal and Zivi [1]. It must be remembered however that an empirical correlation lacks generality and usually can not be used outside its range.

For the data of [26], the inlet throttling coefficient varies between 0.55 and 6.75. Although for 13 of the 62 tests of [24] the flow at the inlet of the test tube was throttled, the throttling coefficient is not reported and was assumed to be as small as those of [26]. It follows from equations (9) and (10), and Fig. 3 that the inception conditions of the DWO are not affected substantially if the flow at the inlet of a NCSGT is slightly throttled. In a NCSGT it is not possible to measure directly the effect of inlet throttling on the stability since the inlet throttling affects the mass velocity and thereby the pressure distribution in the tube. Furthermore the data obtained from NCSGT's in early experiments were not sufficient to form a general conclusion on the effect of the inlet throttling on the stability. In spite of this, it has been

Table 2 Data for the inception conditions of the DWO for natural circulation systems

Geometry of the test channel	L/d	d mm	P MN/m^2	X percent	G kg/m^{2}s	(ΔT_{sub}) K	n
circular tube [1]	34	26.6	2.10–4.19	4.75–12.1	668–800	8.6–25.7	3
circular tube [1]	58	15.8	2.82–3.51	6.00–7.37	742–763	16.9–19.9	2
annulus [25]	96	25.0	0.20–1.56	4.00–8.60	773–993	0.4–21.0	5
circular tube [26]	136	36.0	1.08–3.04	9.50–39.70	760–940	7.9–8.0	3
circular tube [26]	147	30.0	1.08–5.00	4.30–49.40	875–1230	10.0	4
annulus [25]	149	16.2	0.20–3.00	4.70–19.90	519–785	0–43.0	10
annulus [24]	216	12.7	6.16–7.09	8.30–26.9	671–1009	23.7–174.5 (in KJ/kg)	36
circular tube [26]	245	20.0	1.08–6.96	9.60–62.3	529–1140	1.9–16.0	19
annulus [24]	305	8.51	6.55–6.97	10.6–41.3	675–1117	60.7–290.5 (in KJ/kg)	26
circular tube [27]	489	10.0	5.0	18.7–35.1	549–624	164–244	2

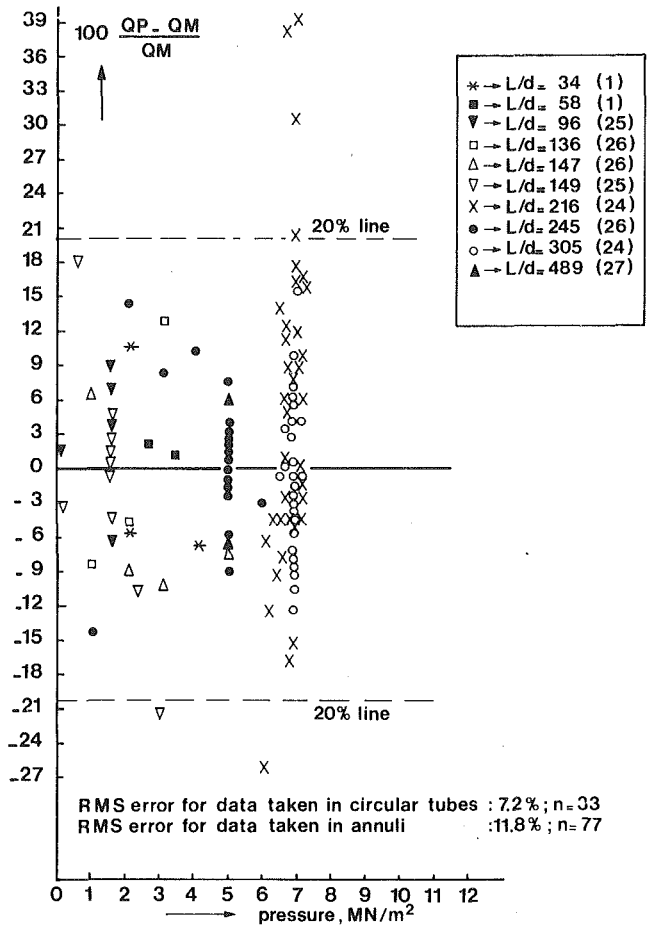

Fig. 3 Error in predicting power at the start of the DWO for NCSGTs

concluded long before in the literature that the inlet throttling affects the stability of a NCSGT. Therefore following the general conclusion given in the literature, equations (9) and (10) are not recommended if the flow at the inlet of a NCSGT is throttled.

In three tests reported in [26], the flow at the outlet of the riser was throttled in a circular steam generator tube of $L/d = 216$. For two of these tests, the pressure, inlet subcooling and mass velocity were kept approximately constant while the ratio of the outlet area of riser to the test section area was changed from 0.655 to 0.328. The power at the start of the DWO for these tests varied from 118.1 kW to 32.7 kW. From the above it is concluded that the outlet throttling has a substantial effect on the inception conditions of the DWO. This effect is taken into account in equation (9) by the use of the term C_3 given by equation (13).

Summary Conclusions

- Simple correlations are established to determine the inception conditions of the DWO for FCSGT's and NCSGT's. These correlations predict the power at the start of the DWO within about 6.5 percent accuracy for long FCSGT's (i.e., $L/d \geq 1272$ and $X > 1$) and within about 20 percent accuracy for short FCSGT's and NCSGT's. The range of operating conditions and geometries for the data correlated are as follows: Forced circulation systems: Geometry: circular-straight tubes and -serpentines, a circular coil and a rectangular straight tube; type of heating: electrical or sodium heating; L = 0.686–200 m; d = 4.49–29.9 mm; L/d = 153–9502; P = 4.1–17.3 MN/m²; X = 0.27–1.85; ΔT_{sub} = 2.8–245.9 K. Natural circulation systems: Geometry and heating conditions: electrically heated circular tubes and annuli; d = 8.51–36 mm; L = 0.91–4.89 m; L/d = 34–489; P = 0.2–7.1 MN/m²; X = 0.04–0.62; G = 529–1230 kg/m²s; ΔT_{sub} = 0–244 K. The number of data considered is 106 for FCSGT's and 110 for NCSGT's. Aforesaid correlations are invalid if the flow at the inlet of a NCSGT or a FCSGT for which $L/d < 4167$ is throttled. The correlation for the FCSGT's is recommended especially for $L/d \geq 1272$ and $X > 1$.
- The established correlations express the fact that the heat input per unit mass of the fluid flowing in a FCSGT or a NCSGT is constant at the start of the DWO for a given combination of operating conditions and geometry. If the value of the heat input per unit mass of the fluid exceeds the value of the aforesaid constant, the DWO occur in the tube.
- This study gives evidence that the inception conditions of the DWO can be predicted with simple equations, thus eliminating the use of time consuming complicated stability correlations in the form of a computer program for a wide range of operation conditions and geometries, as considered here. This evidence is particularly convincing for long FCSGT's for which $L/d \geq 1272$ and $X > 1$. Further experimental and theoretical verification of the presented correlations is recommended, however, since an empirical correlation is in general invalid outside its range.

Acknowledgments

This study is a government sponsored work carried out by TNO. The author is grateful to Mr. K. A. Warschauer, for his guidance in the preparation of this work. Thanks are also due to Messrs. K. A. Braun and M. L. G. v. Gasselt for their encouragement.

References

1 Neal, L. G., and Zivi, S. M., "Hydrodynamic Stability of Natural Circulation Boiling Systems," Vol. I, STL-372-14(1), 1965.

2 Bouré, J. A., Bergles, A. E., and Tong, L. S., "Review of Two-Phase Flow Instability," *Nuclear Engineering and Design*, Vol. 25, 1973, pp. 165–192.

3 *Proceedings of the Symposium on Two-Phase Flow Dynamics*, EUR-4288e, Vol. I and Vol. II, 1969.

4 Ünal, H. C., "Determination of Void Fraction, Incipient Point of Boiling and Initial Point of Net Vapor Generation in Sodium Heated Helically Coiled Steam Generator Tubes," ASME JOURNAL OF HEAT TRANSFER, 1978, Vol. 100, pp. 268–274.

5 Ünal, H. C., "Determination of the Drift Velocity and the Void Fraction for the Bubble- and Plug-Flow Regimes During the Flow Boiling of Water at Elevated Pressures," *International Journal of Heat and Mass Transfer*, Vol. 21, 1978, pp. 1049–1056.

6 Kirchenmayer, A., and Scholz, H. E., "Stability Problems of Boiling Water Reactors," *Proceedings of the Symposium on Two-Phase Flow Dynamics*, EUR-4288e, Vol. I, 1969, pp. 1059–1070.

7 Bjørlo, T., Eurola, T., Grumbach, R., Hansson, P., Olson, A., Rasmussen, J., and Romslo, K., "Comparative Studies of Mathematical Hydrodynamic Models Applied to Selected Boiling Channel Experiments," *Proceedings of the Symposium on Two-Phase Flow Dynamics*, EUR-4288e, Vol. I, 1969, pp. 981–1057.

8 Jones, A. B., and Dight, A. G., "Hydrodynamic Stability of a Boiling Channel," Part II, KAPL-2208, 1962.

9 Davies, A. L., and Potter, R., "Hydraulic Stability. An Analysis of the Causes of Unstable Flow in Parallel Channels," AEWW-R 446, 1966.

10 Vriesema, B., "Aspects of Molten Fluorides as Heat Transfer Agents for Power Generation," Ph.D. Thesis, Technical University of Delft, Netherlands, 1979.

11 Efferding, L. E., "DYNAM—A digital Computer Program for Study of the Dynamic Stability of Once-Through Boiling with Steam Superheat," GAMD-8656, 1968.

12 Waszink, R. P., and Efferding, L. E., "Hydrodynamic Stability and Thermal Performance Test of a 1-MWt Sodium-Heated Once-Through Steam Generator Model," ASME *Journal of Engineering For Power*, Vol. 96, 1974, pp. 189–200.

13 Fallows, T., Hitchcook, J. A., Jones, R. C., Lis, J., and Northover, E. W., "A Study of Oscillatory Instabilities in the Parallel Channels of A High Pressure Once-Through Boiler Rig," *Proceedings of the International Conference-Boiler Dynamics and Control in Nuclear Power Stations*, The British Nuclear Energy Society, 1973, pp. 14.1–14.8.

14 Deam, R., and Murray, J., "The Prediction of Dynamic Stability Limits in Once-Through Boilers Using DYMEL," Paper Presented at European Two-Phase Group Meeting, Erlangen, May 31–June 4, 1976.

15 Deam, R., Personnel communication.

16 Ünal, H. C., "An Investigation of the Inception Conditions of Dynamic Instabilities in Sodium Heated Steam Generator Pipes," in *Two-Phase Flows and Heat Transfer*, edited by Kakac, S., and Veziroglu, T. N., Vol. 3, Hemisphere Publishing Corporation, 1977, pp. 1425–1443.

17 Ünal, H. C., Van Gasselt, M. L. G., and Ludwig, P. W. P. H., "Dynamic Instabilities in Tubes of a Large Capacity, Straight-Tube, Once-Through Sodium Heated Steam Generator," *International Journal of Heat and Mass Transfer*, Vol. 20, 1977, pp. 1389–1399.

18 Brasz, J., "Hydrodynamic Instability and Performance Degradation

of a Straight-Tube Sodium Heated Steam Generator," *Proceeding of Condensed Papers of the Meeting—Two-Phase Flow and Heat Transfer Symposium-Workshop,* Ft. Lauderdale, Fla, Oct. 18–20, 1976, edited by Veziroglu, T. N., University of Miami, 1976, pp. 183–189.

19 Sano, A., Kanamori, A., and Tsuchiya, T., "Operating Experiences with 1 MW Steam Generator," Paper Presented at IAEA Study Group Meeting on Steam Generators for LMFBR's, Bensberg, Oct. 14–17, 1974.

20 Quandt, E. R., "Analysis and Measurements of Flow Oscillations," *Chemical Engineering Progress Symposium Series,* Vol. 57, Nr. 32, 1961, pp. 111–126.

21 Ishii, M., Jones, O. C. Jr., "Derivation and Application of Scaling Criteria for Two-Phase Flows", in *Two-Phase Flows and Heat Transfer,* edited by Kakac, S., and Mayinger, F., Vol. 1, Hemisphere Publishing Corporation, 1977, pp. 163–185.

22 The American Society of Mechanical Engineers, *1967 ASME Steam Tables,* ASME, New York.

23 Ünal, H. C., "Density Wave Oscillations in Sodium Heated Once-Through Steam Generator Tubes," submitted for publication in the ASME JOURNAL OF HEAT TRANSFER.

24 Levy, S., and Beckjord, E. S., "Hydraulic Instability in Natural Circulation Loop with Net Steam Generator at 1000 psia," GEAP-3215, 1959.

25 Spigt, C. L., "On the Hydraulic Characteristics of a Boiling Water Channel with Natural Circulation," Ph.D. Thesis, Technical University of Eindhoven, Netherlands, 1966.

26 Becker, K. M., Jahnberg, S., Haga, I., Hansson, P. T., and Mathisen, R. P., "Hydrodynamic Instability and Dynamic Burnout in Natural Circulation Two-Phase Flow. An Experimental and Theoretical Study," AE-156, 1964, Aktibolaget Atomenergi, Sweden.

27 Becker, K. M., Mathisen, R. P., Eklind, O., and Norman, B., "Measurements of Hydrodynamic Instabilities, Flow Oscillations and Burnout in a Natural Circulation Loop," AE-131, 1964, Aktiebolaget Atomenergi, Sweden.

28 Neal, L. G., "An Analysis of Slip in Gas-liquid Flow Applicable to the Bubble and Slug Flow Regimes," KR-62, Institutt for Atomenergi, Kjeller, Norway, 1963.

29 Zuber, N., Findlay, J. A., "Average Volumetric Concentration in Two-Phase Flow Systems," ASME JOURNAL OF HEAT TRANSFER, Vol. 87, 1965, pp. 453–468.

Vapor/Liquid Interaction and Entrainment in Falling Film Evaporators

D. Yung
Mem. ASME

J. J. Lorenz

Components Technology Division, Argonne National Laboratory, Argonne, Ill. 60439

E. N. Ganić
Department of Energy Engineering, University of Illinois at Chicago Circle, Chicago, Ill. 60680
Assoc. Mem. ASME

The problem of vapor/liquid interaction and entrainment in falling film evaporators is analyzed. Attention is focused primarily on horizontal tube falling film evaporators where liquid falls from one tube to the next in either a droplet or column mode. A criterion is presented for the onset of column formation, and equations are derived for the deflection of droplets and columns due to vapor crossflow. Based on an experimental study of drop detachment and breakup, a correlation is established for the resulting droplet sizes. For high vapor crossflow velocities, a criterion is presented for the inception of liquid entrainment by a process known as stripping. Based on the foregoing models, conditions are defined under which vapor/liquid interaction and entrainment are important for falling film evaporators.

Introduction

An evaporator concept widely used in desalination systems and recently proposed for use in Ocean Thermal Energy Conversion (OTEC) power plants is the falling film design, where a thin film of working fluid is evaporated on either horizontal or vertical tubes. With these types of designs vapor crossflow may cause serious problems, such as redistribution of the working fluid and incomplete wetting of tubes. Reliable evaporator design requires a clear understanding of the effect of vapor crossflow. The purpose of this paper is to study the basic mechanisms of vapor/liquid interaction and entrainment and to develop models applicable to the design and performance evaluation of falling film evaporators.

Compared to the vertical configuration, the horizontal design is considerably more vulnerable to vapor/liquid interaction. Thus attention is focused primarily on the latter design. In a typical horizontal tube falling film evaporator, working fluid is fed at the top of vertical banks of horizontal tubes. In the absence of vapor crossflow the unevaporated fluid from any given tube will fall directly onto the next lower tube. The qualitative structure of the falling liquid is dependent primarily on the feed flowrate. At relatively low feed flowrates the liquid falls in the form of droplets, see Fig. 1(*a*); and at relatively high flowrates the liquid falls in the form of columns, see Fig. 1(*b*). At still higher feed flowrates the liquid falls as unstable sheets and columns. These high flowrates are, however, generally outside the range of interest for most falling film evaporators because the required pumping power becomes excessive.

As a result of vapor crossflow, the droplets and columns falling from a given tube may be partially or totally deflected away from the next lower tube, thereby causing liquid redistribution and incomplete wetting of lower tubes in the bank. In addition to these deflection mechanisms, a number of entrainment mechanisms can also occur. For example if nucleate boiling is present in the film, a mist of small droplets is generated as bubbles burst through the film, and the small droplets are readily entrained by the flowing vapor. An entrainment mechanism common to both horizontal and vertical designs is that of shearing or "stripping" of the thin liquid film from the tube surface. In this paper models of the foregoing mechanisms are developed and conditions are defined under which vapor/liquid interaction and entrainment are important for falling film evaporators.

Droplet Mode

The following models in this and subsequent sections generally apply to horizontal tube falling film evaporators which are the most vulnerable to vapor/liquid interaction. It will be clearly stated when the models also apply to other evaporator designs. Furthermore, the present modelling is restricted to evaporators having working fluids of relatively low viscosity.

Droplet Spacing. In a horizontal tube evaporator, the physical form of the liquid falling from one tube to the next depends on the liquid flowrate and the distance between the tubes. When the flowrate is small and the tube spacing is large, the liquid is usually in the form of droplets which are generated at discrete points along the underside of the horizontal tube. The present problem of a thin film on the underside of a horizontal tube relates to the classic hydrodynamics problem known as Taylor instability [1], see Fig. 2. Taylor instability occurs when a heavier fluid is on top of a lighter fluid, such as liquid over vapor in the present case. The instability wave most likely to appear at the interface has a wave length:

$$\lambda = 2\pi \sqrt{\frac{n\,\sigma}{\rho_\ell g}} \tag{1}$$

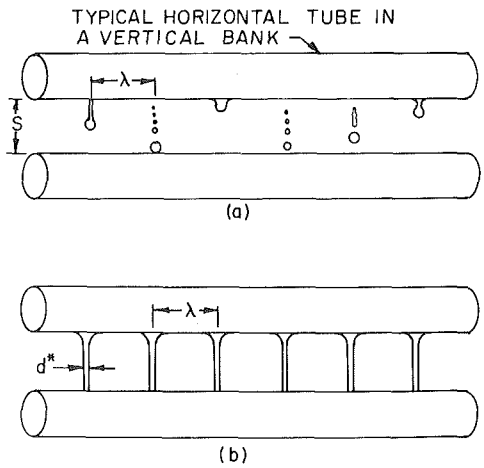

Fig. 1 Liquid falling in (*a*) droplet mode and (*b*) stable column mode

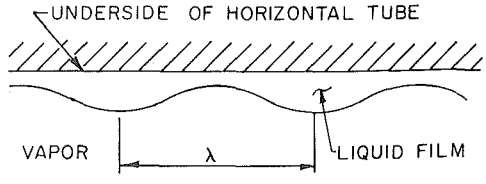

Fig. 2 Taylor instability at liquid/vapor interface

Contributed by the Heat Transfer Division and presented at the Winter Annual Meeting, San Francisco, California, December 10–15, 1978, of THE AMERICAN SOCIETY OF MECHANICAL ENGINEERS. Revised manuscript received by the Heat Transfer Division March 1, 1979. Paper No. 78-WA/HT-35.

where σ and ρ_ℓ are the surface tension and density of the liquid respectively, and g is the gravitational acceleration. The constant n in equation (1) has a value equal to 3 if the liquid layer is relatively thick [1] (thick film Taylor wavelength), and a value equal to 2 if the liquid layer is relatively thin [2] (thin film Taylor wavelength, as derived by Whitney and reported by Conti [2]).

Since the formation of droplets in the present case is a result of the growth of an instability wave at the interface, it is reasonable to expect that the spacing between the droplet generation sites is equal to the Taylor wavelength given by equation (1). In an earlier study [3] based on very limited data, the authors proposed that the spacing could be correlated with $n = 3$ in equation (1). However, a larger body of more recent data for water, ethyl alcohol, and ammonia [2] indicates that $n = 2$ is superior. With $n = 2$, equation (1) predicts the experimentally measured spacing to within 4 percent for ammonia[1] and 15 percent for ethyl alcohol and water. It should be pointed out that in the case of stable film boiling, which is the inverse of the present problem, the distance between vapor bubble columns has been found to be very well correlated by the *thick* film Taylor wavelength, $n = 3$, [4, 5].

Droplet Diameter. The mechanism of detachment of a drop from a liquid film is extremely difficult to treat analytically. To study the detachment mechanism, a simple experiment was performed with two different fluids: ethyl alcohol and water. In these tests, liquid at room temperature (20°C) was fed from a buret onto an unheated 3.8 cm dia horizontal aluminum tube. The liquid droplets falling from the underside of the tube were photographed by a high speed camera at 200 frames/s. Fig. 3 shows a typical sequence of photographs of a detaching drop. As a drop detaches from the film, a long narrow tail is formed, which, by the well known Rayleigh instability, eventually breaks up into four or five smaller droplets. The large drop in Fig. 3 will be referred to as the primary drop, and the four or five smaller drops as secondary drops. A slight increase in drop size and tail length was observed as the liquid flowrate was increased from essentially zero flow to the condition of incipient column formation. When plotted over the entire range of flowrates, the drop sizes exhibited a scatter of about ±5 percent from the mean value.

The mechanism by which the liquid breaks off from the film is essentially an interaction of gravity and surface tension forces. It is reasonable to expect that the diameter, d_p, of a primary drop can be correlated by an expression such as:

$$d_p = C_1 \sqrt{\frac{\sigma}{\rho_\ell g}} \tag{2}$$

where C_1 is a constant. The value of the constant C_1 was determined from our experiments with ethyl alcohol and water to be 3.0 with an uncertainty of ±5 percent. The secondary drops could also be correlated by a similar expression but with different constants. However, it was decided to express the diameter, d_s, of the secondary drops in terms of the ratio d_s/d_p. From the experimental data it was found that:

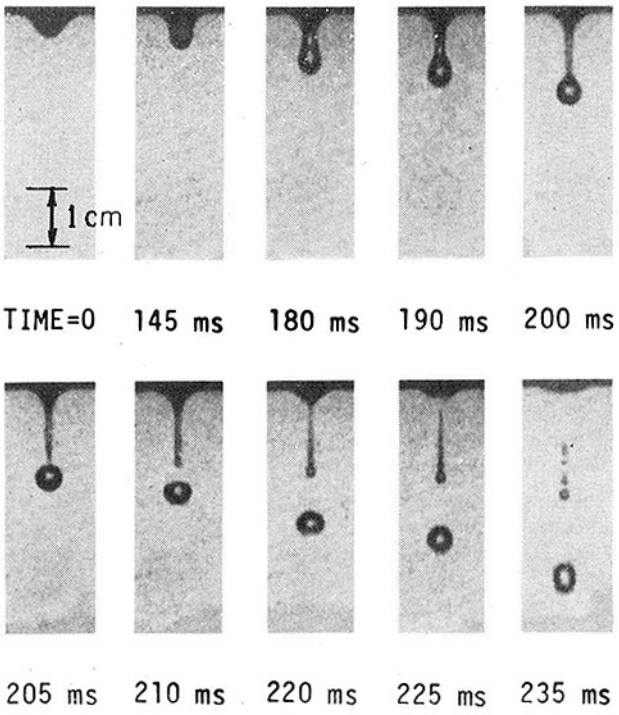

Fig. 3 Movie sequence of a drop detaching from a thin film; ethyl alcohol at 20°C

$$0.24 < \frac{d_s}{d_p} < 0.46 \tag{3}$$

It was estimated that the volume of the secondary droplets compared to the volume of the primary droplet is about 19 percent. It is expected that equation (2) and expression (3) can be applied to any fluid of low viscosity.

Droplet Deflection. Knowing the drop sizes, it is possible to calculate the droplet deflections due to vapor crossflow. In Fig. 4 the angle α is the actual drop deflection angle and θ is the critical angle beyond which the drop will not hit the lower tube. Deflection angles for which $\alpha < \theta$ are considered safe in the sense that the drop will impinge upon the lower tube, although it is recognized that nonuniform or incomplete wetting of the lower tube may still result. (Further remarks concerning the critical deflection angle will be given in a later section.) The angle θ has a simple relationship to the pitch-to-diameter ratio P/D as:

$$\theta = \tan^{-1}\left\{\frac{1}{2}\left[\frac{P}{D}\left(\frac{P}{D} - 1\right)\right]^{-1/2}\right\} \tag{4}$$

Based on the coordinates shown in Fig. 4, the equations of motion of a single droplet in the presence of vapor crossflow velocity u_g are:

[1] Dr. Conti informed the authors that the measured spacing for ammonia in Table 1 of his paper should be 1.73 cm instead of 1.5 cm as reported.

Nomenclature

A = column cross-sectional area, m^2
C_1 = constant, equation (2)
C_d = vapor drag coefficient
d = droplet diameter, m
d^* = effective column diameter, equation (15), m
D = tube diameter, m
F_d = vapor drag force, N
g = gravitational acceleration, m/s^2
L = column length, m
m = droplet mass, kg
n = constant, equation (1)
P = tube pitch, m
S = tube spacing, m
t = time, s
u = velocity, m/s
V = column volume, m^3
W = column weight, kg
We = Weber number, equation (9)
x = coordinate, Fig. 4, m
y = coordinate, Figs. 4 and 6, m
z = coordinate, Fig. 6, m
α = deflection angle, rad
θ = critical deflection angle, equation (4), rad
λ = wave length, equation (1), m
μ = viscosity, N·s/m^2
ρ = density, kg/m^3
σ = surface tension, N/m
Γ = flowrate, kg/s·m

Subscripts

i = incipient
g = gas or vapor
ℓ = liquid
p = primary
s = secondary

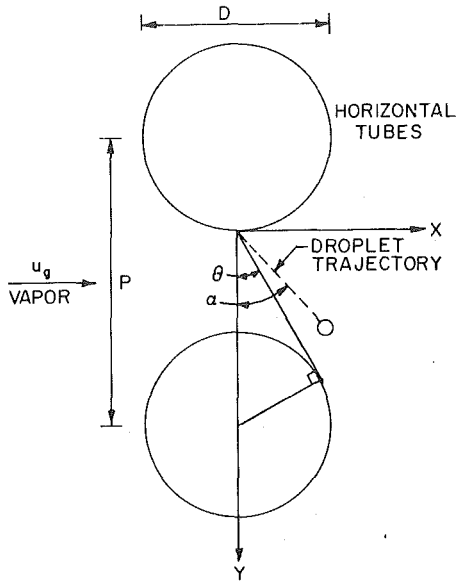

Fig. 4 Deflection of droplet due to vapor crossflow

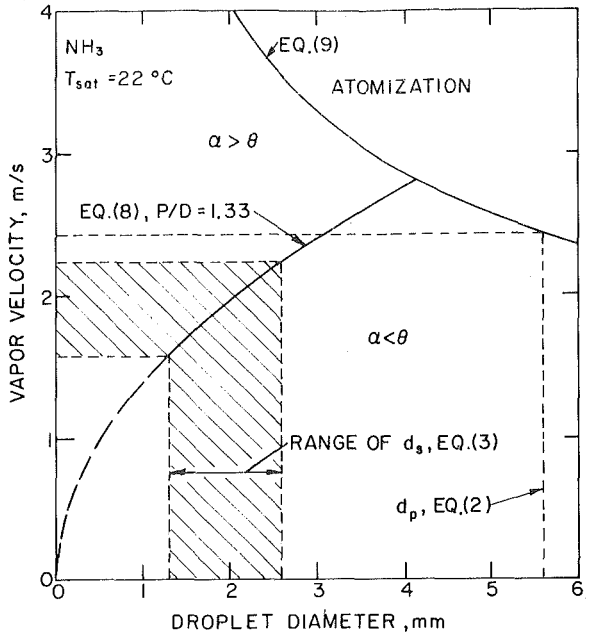

Fig. 5 Maximum allowable crossflow velocity for droplet deflection

$$x\text{-direction:} \quad m\frac{d^2x}{dt^2} = C_d\left(\frac{\pi d^2}{4}\right)\frac{1}{2}\rho_g u_g{}^2 \tag{5}$$

$$y\text{-direction:} \quad m\frac{d^2y}{dt^2} = m\,g \tag{6}$$

where m and d are the mass and diameter of the droplet, respectively, ρ_g is the vapor density and C_d is the drag coefficient. Also, the velocity u_g is the *between-tube* vapor velocity. The following assumptions are implied in the formulation of these equations: (1) the motion of the droplet in the y direction is mainly governed by gravity (i.e., vapor drag force in that direction is small); and (2) the motion of the droplet in the x direction is mainly due to the vapor drag force at a steady vapor crossflow velocity u_g (i.e., the reduction in drag force due to the motion of the droplet relative to u_g is negligible).

The drag coefficient C_d in equation (5) depends generally on the Reynolds number of the vapor flow. Equation (5) can be further simplified by restricting our solution to Reynolds number greater than 1000, which is usually the case. At Reynolds number between 10^3 and 10^5, the drag coefficient has a relatively constant value of 0.44 [6]. It should be pointed out that any reduction in drag coefficient due to evaporation is expected to be small [7].

The boundary conditions for equations (5) and (6) are $x = dx/dt = y = dy/dt = 0$ at $t = 0$. In setting $dy/dt = 0$ at $t = 0$, it is somewhat conservatively assumed that the droplet has no initial velocity as it departs from the tube. Equations (5) and (6) indicate that the trajectory of a deflected droplet is a straight line. The angle of deflection α, defined as $\alpha = \tan^{-1}(x/y)$, can be easily obtained from equations (5) and (6) as:

$$\alpha = \tan^{-1}\left[\frac{1}{3}\frac{\rho_g}{\rho_\ell}\frac{u_g{}^2}{dg}\right] \tag{7}$$

The maximum allowable vapor crossflow velocity u_g is obtained by setting the deflection angle α, equation (7), equal to the critical angle θ, equation (4), yielding:

$$u_g = \left(\frac{3}{2}\frac{\rho_\ell}{\rho_g}d\,g\right)^{1/2}\left[\frac{P}{D}\left(\frac{P}{D}-1\right)\right]^{-1/4} \tag{8}$$

To illustrate the use of equation (8), consider the case of an evaporator for Ocean Thermal Energy Conversion (OTEC) employing ammonia as the working fluid. In Fig. 5, the maximum allowable vapor crossflow velocity is plotted as a function of ammonia droplet diameter for $P/D = 1.33$. The dashed region for small drop diameters indicates a range where equation (8) is not strictly applicable because the Reynolds number is less than 1000; thus the curves are only projected values. Also plotted in Fig. 5 are ammonia droplet sizes calculated from equations (2) and (3) for primary and secondary droplets, respectively.

The atomization region in Fig. 5 indicates an area where droplets would not be able to exist because of disintegration at high vapor velocity. The atomization boundary is based on a Weber number of 12 [8], where the Weber number is defined as:

$$\mathrm{We} = \frac{\rho_g u_g{}^2 d}{\sigma} \tag{9}$$

The diameter d in this equation defines the maximum drop size that can exist for a given crossflow velocity. A drop which is larger than the maximum drop size corresponding to a given vapor velocity may disintegrate into many smaller droplets.

The safe region in Fig. 5 is the condition for which $\alpha < \theta$ (to ensure that the droplet impinges upon the lower tube) and lying below the atomization boundary (to avoid potential disintegration into much smaller droplets that can easily be deflected). If the crossflow velocity is kept below 1.6 m/s no droplets will be deflected from the lower tubes. For velocities exceeding 2.2 m/s all secondary droplets are deflected. Beyond 2.4 m/s the primary drops are also deflected, thus resulting in 100 percent deflection of liquid. To ensure good thermal performance, an evaporator should be designed such that all the droplets falling from a given tube impinge upon the next lower tube. Since a small droplet is more vulnerable to vapor crossflow than a larger one, the maximum allowable velocity should be based on the smallest secondary droplet; i.e., $d_s = 0.24\,d_p$ from equation (3). In the present example this maximum allowable velocity was seen to be 1.6 m/s and the corresponding drop diameter was 1.3 mm.

Column Mode

Onset of Column Formation. The onset of column formation was studied using water and ethyl alcohol with the experimental apparatus previously described. As before, liquid was fed atop the tube with a buret, creating a single droplet or column generation site on the underside. Since only a single tube was employed, this experiment simulated the asymptotic case of large tube spacing.

The onset of column formation was determined by gradually decreasing the flowrate and identifying the point at which the flow pattern changed from columns (characterized by continuous flow) to droplets (characterized by intermittency). By slowly playing back the high speed motion pictures, the inception point was clearly identifiable.

In a previous paper by the authors [3], the following expression for incipient column formation was derived by setting the droplet production frequency equal to the capillary wave oscillation frequency at the interface:

$$\Gamma_i = 0.81 \frac{\rho_\ell}{\lambda} \frac{\pi d_p^3}{6} \left(\frac{2\pi\sigma}{\rho_\ell \lambda^3}\right)^{1/2} \tag{10}$$

Equation (10) correlates the present experimental results for water and ethyl alcohol to within ± 10 percent. The coefficient in equation (10) is slightly different from the value reported previously [3] because it also reflects data for water which was not previously available.

The experimental set-up used herein to study the transition from droplets to columns is highly idealized: a single tube with a single droplet (or column) generation site. In a multiple-tube evaporator where liquid is fed over the entire length of the tubes, the transition phenomena is much more complicated. The transition from droplets to columns does not occur abruptly at a single feed flowrate, but occurs gradually over a range of flowrates. In the transition region, droplets and columns generally coexist in a random pattern over the length of the tube. This behavior is due, at least in part, to hydrodynamic instabilities and nonuniform liquid feed. In addition to liquid flowrate, column formation is dependent on other factors such as tube spacing and liquid viscosity.

On the basis of comparisons with the limited amount of reported data on flow patterns in multiple-tube configurations (e.g., Conti [2]), it appears that Γ_i from equation (10) represents the lower bound of the transition flow region. Accordingly, Γ_i from equation (10) should be regarded as the incipient condition where a few columns begin to form at random sites along the tube, rather than the onset of fully developed, well-ordered columns.

Column Deflection. Fig. 1(*b*) shows a sketch of the fully developed column mode. As in the case of droplets, the column spacing will be prescribed by the thin film Taylor wavelength, λ, from equation (1) with $n = 2$. A liquid column has a tapered shape but for analytical purposes it is convenient to model the column as a right circular cylinder having the same length and an effective diameter, d^*, such that the volumes are equivalent. The effective diameter is determined as follows. Referring to Fig. 6(*a*), the velocity at any position y below the tube is given by the "free-fall" expression:

$$u_\ell = (2\,g\,y)^{1/2} \tag{11}$$

Here it is conservatively assumed that the liquid velocity at $y = 0$ is negligibly small. The mass flowrate for a single column is $\lambda\Gamma$, where λ is column spacing and Γ is the liquid flowrate per unit length. Employing the foregoing in conjunction with the continuity equation, the following expression for the column cross-sectional area is obtained:

$$A = \frac{\lambda\Gamma}{\rho_\ell} (2\,g\,y)^{-1/2} \tag{12}$$

from which the column volume V can be determined by integration. Substituting $y = z \cos\alpha$ and integrating from $z = 0$ to L yields:

$$V = \int_0^L A\,dz = \frac{2\,\lambda\Gamma}{\rho_\ell} \left(\frac{L}{2\,g\cos\alpha}\right)^{1/2} \tag{13}$$

Then the effective diameter is determined from:

$$\frac{\pi\,d^{*2}}{4} L = V \tag{14}$$

Upon substituting V from equation (13) and letting $L = S/\cos\alpha$, the effective diameter can be expressed as:

$$d^* = \left(\frac{8\,\lambda\Gamma}{\pi\rho_\ell}\right)^{1/2} (2\,g\,S)^{-1/4} \tag{15}$$

Referring to Fig. 6(*b*), the column deflection angle, α, due to vapor crossflow can be determined from a balance of forces normal to the cylinder:

$$F_d = W \sin\alpha \tag{16}$$

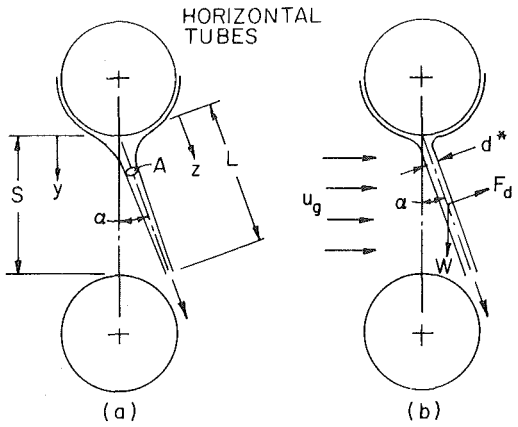

Fig. 6 Deflection of liquid column due to vapor crossflow

where F_d is the drag force based on the component of u_g normal to the cylinder (recall that u_g is the *between-tube* velocity):

$$F_d = \frac{1}{2} C_d\,L\,d^*\,\rho_g\,(u_g \cos\alpha)^2 \tag{16a}$$

and W is the weight of the column:

$$W = \rho_\ell\,g\,V \tag{16b}$$

After making the appropriate substitutions into equation (16) and with some rearrangement the following expression is obtained:

$$\frac{C_d\,d^*\,\rho_g\,u_g^2}{4\,\lambda\Gamma\,g} (2\,g\,S)^{1/2} = \frac{\tan\alpha}{\cos\alpha} \tag{17}$$

where d^* is defined by equation (15) and λ by equation (1) with $n = 2$.

The critical angle θ beyond which the column will no longer impinge upon the next lower tube is given by the same expression as for drops, i.e., equation (4). Substituting θ for α in equation (17) leads to an equation defining the maximum allowable velocity for columns. At this critical condition, equation (17) is plotted in Fig. 7 for $P/D = 1.33$ and ammonia as the working fluid. It can be seen that as the liquid flowrate increases and the column becomes "thicker," a greater vapor velocity is required to deflect the column. For this example, the between-tube distance was chosen to be $S = 1.7$ cm; but the results are not sensitive to this assumption since it can easily be shown that $u_g \sim S^{-1/8}$. The drag coefficient over the Re range of interest is $C_d = 1$.

As noted in the previous section, the transition from droplets to columns occurs over a range of flowrates rather than at a single value. The flowrate Γ_i, indicated in Fig. 7, defines the incipient condition where a few columns begin to form at random locations along the tube. A model defining the full extent of the transition region is not yet available; thus, the conditions for fully-developed, column-dominated flow cannot be predicted. In view of this, it will be conservatively assumed that droplets and columns coexist at all liquid flowrates greater than or equal to Γ_i. At any given liquid flowrate, the maximum design velocity will be dictated by the smaller of the respective allowable velocities for columns and secondary droplets. In Fig. 7, the maximum allowable vapor velocity for the smallest secondary droplets (i.e., equation (8) with $d_s = 0.24\,d_p$) is plotted along with equation (17) for columns. It can be seen that for liquid flowrates less than $\Gamma = 0.032$ kg/s·m, column deflection is controlling; whereas for greater liquid flowrates, droplet deflection is controlling.

Remarks on the Critical Deflection Angle

The safe region has been defined as the condition for which $\alpha < \theta$, where θ was defined as the critical deflection angle. However, it should be pointed out that deflection of liquid away from the next lower tube (i.e., $\alpha > \theta$) does not necessarily imply a loss in heat transfer performance because the liquid may eventually experience a good "hit" on

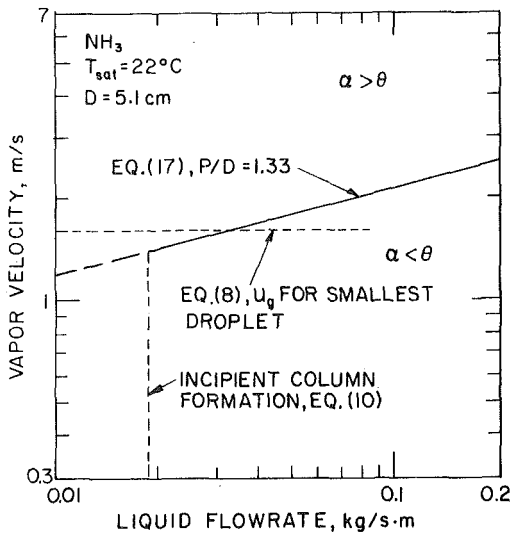

Fig. 7 Maximum allowable crossflow velocity for column deflection

a tube in the adjacent column. Nevertheless, it is expected that good wetting of the tubes, which is essential to good heat transfer performance, can be better achieved by a well-controlled liquid flow from one tube to the next rather than relying on random hits on tubes in adjacent columns.

In cases where the liquid is slightly deflected from the tube centerline and impinges on one side of the tube, part of the flow may still "climb up" and wet the other side. For such a case of nonuniform wetting, the circumferentially averaged heat transfer coefficient is probably not significantly different from the case of an evenly divided flow because the heat transfer coefficient is not a strong function of flowrate, except at very low flows [9]. However, there exists a certain deflection angle beyond which the liquid will no longer wet the opposite side, and thereby result in a loss of heat transfer performance. Using a very simple model, a few back-of-the-envelope calculations were made to estimate the deflection angle at which the inception of complete wetting occurs. This deflection angle was found to be approximately equal to $\theta/2$, implying a cross-flow velocity of about 80 percent of that given by equations (8) and (17). These calculations emphasize the fact that equations (8) and (17) define *maximum* allowable velocities which should not be exceeded in good design practice. Moreover, these calculations suggest the simple rule-of-thumb that the vapor crossflow velocities should be limited to about 80 percent of the values predicted by equations (8) and (17). A detailed analysis of the inception of complete wetting was beyond the scope of the present work, and will form the basis of a subsequent investigation.

Stripping

The previous sections dealt with the deflection of liquid as it falls from one tube to the next. This section considers entrainment phenomena associated with shearing or stripping of the thin liquid film directly from the tube surface. The models developed herein apply to both horizontal and vertical tube designs.

If the vapor velocity is sufficiently high, the liquid film on the tubes becomes unstable as a result of the well-known Helmholtz instability [10] phenomenon. The growth of instability waves eventually leads to the formation of liquid droplets which are easily stripped off by the flowing vapor. The inception criteria for droplet entrainment in thin films has been considered by numerous investigators. A review paper on this subject was published by Ishii and Grolmes [11]. Ishii and Grolmes proposed new criteria for droplet entrainment in two-phase co-current film flow, which were shown to agree well with all available experimental data. Their inception criteria relate the critical gas velocity (in dimensionless form) to the liquid Reynolds number and the flow direction (whether horizontal, upward, or downward flow). From their inception criteria, the lowest gas velocity to cause entrainment is given by:

$$\frac{u_g}{\sigma}\left(\frac{\rho_g}{\rho_\ell}\right)^{1/2}\left[\frac{\mu_\ell \rho_\ell^2\, \sigma^3}{(\rho_\ell - \rho_g)g}\right]^{1/5} = 1 \tag{18}$$

where μ_ℓ is the liquid viscosity. Although equation (18) is strictly applicable only to co-current gas-liquid flow, it should also apply to counter-current flow when the liquid velocity is small compared to the critical vapor velocity. In a falling film evaporator, the condition of small liquid velocity is usually satisfied and hence equation (18) is generally applicable.

For ammonia at 22°C, equation (18) indicates a vapor velocity of 4.7 m/s. If an evaporator is designed to satisfy the droplet and column deflection constraints discussed in the previous sections, then entrainment by stripping will not be a problem.

Nucleate Boiling

When nucleate boiling is present in the film, a mist of small droplets can be generated as bubbles burst through the film, and the small droplets can readily be entrained by the vapor crossflow. Petrovichev, et al. [12] have shown that the droplet generation rate depends on heat flux and film thickness. Furthermore, Newitt, et al. [13] have found that bubble size is also an important parameter affecting entrainment. Although representing pioneering efforts in the field, neither of these studies has yielded a generalized correlation for predicting droplet entrainment due to boiling. Fortunately, this mechanism is not expected to be significant for falling film evaporators, and therefore the lack of a generalized correlation is of no great consequence.

Droplet generation resulting from boiling in the film appears to be significant only at heat fluxes appreciably higher than those of interest for falling film evaporators. For example, the study by Petrovichev, et al. [12] covered heat fluxes in the neighborhood of 1×10^6 W/m^2, where violent surface boiling was present. On the other hand falling film evaporators generally operate at heat fluxes more than an order of magnitude lower, where little or no boiling is present. Thomas, et al. [14] reported data for an enhanced falling film evaporator for OTEC utilizing ammonia and having a special porous surface to promote boiling. Boiling was sufficient to create a fog of small droplets within the heat exchanger shell; however, the exiting ammonia vapor was found to contain less than 1 percent entrained liquid. Thus even in this extreme case, droplet entrainment does not present a significant problem for a falling film evaporator.

Splashing

Another possible entrainment mechanism is that due to splashing. Splashing can occur when a liquid impinges upon a solid surface. This process can generate drops of various sizes which are likely to be entrained by the vapor. The extent of splashing depends primarily on wettability and fluid velocity. Experiments with vertical banks of horizontal tubes (simulating an OTEC evaporator) indicated that splashing is not significant when the working fluid adequately wets the tubes [15]. Based on these test results and our own experimental observations with ethyl alcohol and water, it is expected that splashing is not important for good wetting fluids which fall from one tube to the next under the action of gravity. Splashing of good wetting fluids can be expected only when the liquid is sprayed at high velocity onto the tubes.

Conclusions

The spacing between droplet and column generation sites was adequately predicted by the most unstable thin film Taylor wavelength. Based on an experimental study of droplet detachment and breakup, a correlation was established for the resulting primary and secondary droplet sizes. An equation was derived for the maximum allowable vapor velocity for which a droplet will still hit the next lower tube. Good design practice dictates that the maximum crossflow velocity in the evaporator be based on the smallest droplet in the system (i.e., the smallest secordary droplet).

The transition from droplets to columns occurs over a range of liquid flowrates, rather than at a single value. In the transition region,

droplets and columns co-exist over the entire length of the tube. A criterion was derived for the onset of column formation. Following an approach similar to that for droplets, an equation was derived for the deflection of columns. At a given liquid flowrate the maximum crossflow velocity for design purposes will be dictated by the smaller of the respective allowable velocities for columns and secondary droplets.

A number of other entrainment mechanisms were studied: stripping, splashing, and boiling. If an evaporator is designed to satisfy the droplet and column deflection constraints, then entrainment by stripping will not be a problem. Entrainment due to splashing was judged to be insignificant for good wetting fluids. At the relatively low heat fluxes and wall superheats of interest for falling film evaporators, entrainment resulting from boiling also appears to be unimportant.

The vapor/liquid interaction and entrainment models developed in this paper are general, and should prove to be useful tools for the thermal design and performance evaluation of falling film evaporators.

References

1 Bellman, R. and Pennington, R. H., "Effects of Surface Tension and Viscosity on Taylor Instability," *Quarterly Applied Mathematics,* Vol. 12, 1954, pp. 151–162.

2 Conti, R. J., "Heat Transfer Enhancement in Horizontal Ammonia-Film Evaporator," *Proceedings, Sixth Ocean Thermal Energy Conversion* (OTEC) Conference, Washington, D.C., June, 1979.

3 Yung, D., Lorenz, J. J. and Ganić, E. N., "Vapor/Liquid Interaction and Entrainment in Shell-and-Tube Evaporators," ASME Paper No. 78-WA/HT-35.

4 Lienhard, J. H. and Sun, K., "Effects of Gravity and Size Upon Film Boiling From Horizontal Cylinders," ASME JOURNAL OF HEAT TRANSFER, Vol. 92, 1970, pp. 292–298.

5 Berghmans, J., "Film Boiling Near the Critical State," *International Journal of Heat and Mass Transfer,* Vol. 18, 1975, pp. 1127–1130.

6 Schlichting, H., *Boundary Layer Theory,* McGraw Hill, New York, 1968, p. 17.

7 Bailey, G. H., Stater, I. W., and Eisenklam, P., "Dynamic Equations and Solution for Particles Undergoing Mass Transfer," *British Chemical Engineers,* Vol. 15, 1970, pp 912–916.

8 Wallis, G. B., *One-dimensional Two-phase Flow,* McGraw Hill, New York, 1969, p. 377.

9 Lorenz, J. J., and Yung, D., "A Note on Combined Boiling and Evaporation of Liquid Films on Horizontal Tubes," ASME JOURNAL OF HEAT TRANSFER, Vol. 101, 1979, pp 178–180.

10 Yih, C. S., *Fluid Mechanics,* McGraw Hill, New York, 1969, pp. 497–498.

11 Ishii, M. and Grolmes, M. A., "Inception Criteria for Droplet Entrainment in Two-Phase Concurrent Film Flow," *AIChE Journal,* Vol. 21, No. 2, 1975, pp. 308–318.

12 Petrovichev, V. I., Kokorev, L. S., Didenko, A. Y., and Dubvrovskiy, G. P., "Droplet Entrainment in Boiling of Thin Liquid Films," *Heat Transfer—Soviet Research,* Vol. 3, No. 1, 1971, pp. 19–22.

13 Newitt, D. M., Dombrowski, N., and Knelman, F. H., "Liquid Entrainment: (1) The Mechanism of Drop Formation From Gas or Vapor Bubbles," *Transactions of the Institution of Chemical Engineers,* Vol. 32, 1954, pp. 244–261.

14 Thomas, A., Lorenz, J. J., Hillis, D. L., Yung, D. T. and Sather, N. F., "Performance Tests of the 1 MWt Shell-and-Tube and Compact Heat Exchangers for OTEC," *Proceedings, Sixth Ocean Thermal Energy Conversion (OTEC) Conference,* Washington, D.C., June 1979.

15 Snyder, E., "Design of 1 MWe Heat Exchangers for OTEC," *Proceedings, Fifth Ocean Thermal Energy Conversion (OTEC) Conference,* Miami Beach, Fla, Feb. 1978.

Salim Yilmaz
Research Engineer,
Heat Transfer Research, Inc.,
Alhambra, CA
Assoc. Mem. ASME

J. W. Westwater
Professor of Chemical Engineering,
University of Illinois,
Urbana, Il.,
Mem. ASME

Effect of Velocity on Heat Transfer to Boiling Freon-113

Measurements were made of the heat transfer to Freon-113 at near atmospheric pressure, boiling outside a 6.5 mm dia horizontal steam-heated copper tube. Tests included pool boiling and also forced flow vertically upward at velocities of 2.4, 4.0 and 6.8 m/s. The metal-to-liquid ΔT ranged from 13 to 125°C, resulting in nucleate, transition, and film boiling. The boiling curves for different velocities did not intersect or overlap, contrary to some prior investigators. The peak heat flux was proportional to the square root of velocity, agreeing with the Vliet-Leppert correlation, but disagreeing with the Lienhard-Eichhorn prediction of an exponent of 0.33. The forced-flow nucleate boiling data were well correlated by Rohsenow's equation, except at high heat fluxes. Heat fluxes in film boiling were proportional to velocity to the exponent 0.56, close to the 0.50 value given by Bromley, LeRoy, and Robbers. Transition boiling was very sensitive to velocity; at a ΔT of 55°C the heat flux was 900 percent higher for a velocity of 2.4 m/s than for zero velocity.

Introduction

Heat transfer in boiling is a very efficient means of energy transfer. An important class of heat exchange equipment involves boiling a liquid on the outside surface of metal tubes having an internal flow of warmer fluid such as condensing steam. Examples are kettle reboiler tube bundles and shellside boiling in both horizontal forced flow and horizontal thermosiphon reboilers. Design of reboilers involving boiling outside tubes and also design of finned surfaces cooled by boiling liquids require accurate knowledge of the entire boiling characteristic curves and their dependence on flow velocity and heating element size.

The purpose of this investigation was to determine the complete boiling characteristic curves including nucleate boiling, peak in the curve, transition boiling, and film boiling during pool and forced convection (cross-flow) boiling of saturated Freon-113 (trichlorotrifluoroethane) from a horizontal tube at atmospheric pressure. No published data exist in the literature for any fluid showing the effect of velocity for the entire boiling curve. Reference [1] gives what is believed to be a detailed literature survey. All published results, such as [2–21] are isolated studies, each restricted to a limited range of ΔT values which cover a single region of boiling only. In 1956, Pramuk and Westwater [22] agitated a boiling liquid with a three-bladed propeller and reported that all portions of the boiling curve were improved as the shaft speed increased. They did not measure the liquid velocity at the heater. Very little work has been done on forced convection boiling of liquids flowing normal to horizontal cylindrical heaters. Single tube geometry provides the closest link between the classical theory of pool boiling heat flux, which is reasonably well understood, with the case occurring in flow boiling. The single tube is the building block of a tube bundle, and more information might provide a base for attacking that far more complex problem. This original experimental work is of interest to the experimentalist and theoretician as well as to the practicing engineer.

Experimental. Two different heat transfer loops were used, one for pool boiling and one for forced flow. Photographs and complete details are available [1]. A brief description follows. The same removable test section containing the copper-tube heat source was used in both loops.

Pool Boiling Loop. Fig. 1 is a sketch of the pool boiling loop. The heated tube was 20 gauge, 6.4 mm OD, with a heated length of 127 mm, made of pure copper. The tube surface was electropolished initially. It was cleaned with Revere Ware copper cleaner and then polished before the start of each set of runs. The tube was stored in a nitrogen atmosphere to prevent oxidation by air except during actual tests. The tube was smooth and lustrous.

Contributed by the Heat Transfer Division for publication in the JOURNAL OF HEAT TRANSFER. Manuscript received by the Heat Transfer Division May 17, 1979.

The boiler test section was made of stainless steel. The internal dimensions were 394 mm high, 127 mm wide, and 38 mm front-to-back. A 25 mm thick window of Lexan polycarbonate was located in the front with a flush fit on the inner side. The test heater was parallel to the window. The tube was inclined slightly from the horizontal to facilitate steam condensate drainage. The tube was secured with Teflon seals at the boiler walls. The test fluid contacted only copper, stainless steel, Lexan, Teflon, and glass. The test section and the entire loop was heavily insulated with glass wool.

The test tube was heated by steam, available at pressures from 81 kPa below atmospheric to 760 kPa above atmospheric. The steam condensate from the test section was metered.

Vapor formed in the test section rose through a heated vapor riser and was condensed in a stainless steel heat exchanger of 0.40 m^2 area. The condensate was metered and returned to the boiler. Stainless steel encased thermistor probes were used to measure temperatures needed for heat balances and for monitoring the operation of the equipment. The thermistor outputs were on a digital thermometer which was calibrated repeatedly on a regular basis.

The temperature of the test tube was determined by using the tube as a resistance thermometer. A 25-amp DC was passed through the heating tube and then through a 0.000250 ohm magnanin standard resistance. Voltage drops across the tube and the standard resistance were measured within 0.001 mV by use of a Hewlett and Packard digital voltmeter. The two voltage taps, made of 24 gauge copper wire, were silver-soldered to the tube surface at about 124 mm apart. The heat generated by the current passing through the tube was about 0.15 w, a negligible amount compared to heat supplied by steam during a run. Calibration was done with the copper tube placed in the vapor space of four boiling liquids—Freon-113, isopropanol, n-octane, and n-decane, while heat was supplied by an electric cartridge heater.

For a typical pool boiling run, the boiler was filled with Freon-113 up to a level 15 cm above the heating tube. The power to the cartridge heater and vapor riser heaters were turned on. The test liquid was boiled vigorously for a half hour to heat piping and insulation to the saturation temperature and to purge the noncondensable gases from the system before starting steady-state operation. The steam pressure (and temperature in the heating tube) was slowly adjusted to the desired value for a particular run. The system was operated at the desired conditions for about one hour before any experimental measurements were recorded. Three heat balances were determined from (1) steam condensate, (2) Freon-113 boil-up, and (3) condenser cooling water. Heat losses from the equipment were calibrated and included in the heat balances.

The test liquid used in this study was 99.9 percent pure commercial grade Freon-113 as supplied by E. I. Du Pont de Nemours and Company. For pool boiling about four liters of liquid was needed for a

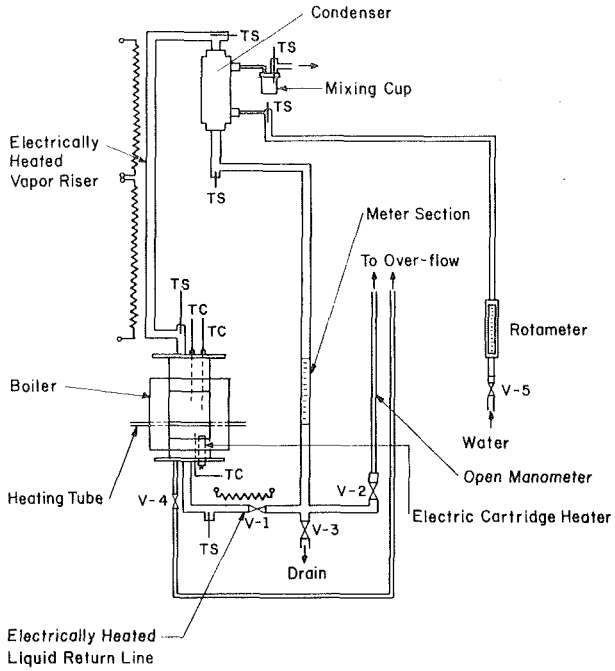

Fig. 1 Sketch of equipment for pool boiling tests

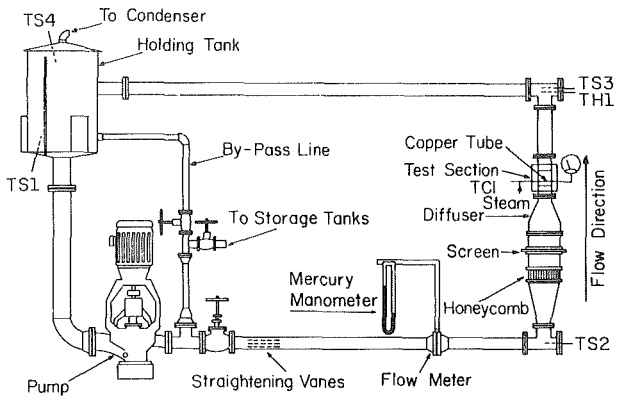

Fig. 2 Scale drawing of flow-loop for forced-flow boiling tests. The scale may be estimated from the pipe sizes: 15.2 cm dia suction side and 10.2 cm dia discharge side of the pump

particular run, and it was changed regularly and often. For flow boiling, about 570 liters of liquid was needed to fill the flow channels and half of the overhead surge tank, therefore the same 570 liters of Freon-113 was used for the entire flow boiling experiments. The pressure in the boiler was essentially atmospheric for pool boiling, and the liquid was at saturation temperature. For flow boiling, the pressure in the boiler ranged from 1.09 to 1.13 atmosphere, and the entering liquid was 4 to 5°C below the saturation temperature.

Flow-Boiling Loop. The flow-boiling loop is drawn to scale in Fig. 2. Circulation was provided by a 7.5 kw vertical in-line pump specified for 136 m^3/h of water at 105 kPa discharge pressure. An overhead surge and vapor-liquid separation tank with coils, baffles, and vortex breaker served as a liquid supply to the pump and as a temperature controller for the liquid in the loop. The flow rate was manually controlled by two globe valves downstream from the pump. Liquid velocity was measured with an orifice meter in a 10 cm dia pipe line. The test boiler was connected to the loop just above six transition sections as shown in Fig. 2. These six transition sections and another section just above the test boiler were designed to get a uniform symmetric turbulent velocity profile at the heating test tube placed horizontally in the test channel. These sections also minimized pressure drop and boundary layer separation (cavitation and wakes). Velocity profiles in the test section were determined for seven different flow rates with water at 25°C without the heating tube in the test section. Two Pitot tubes were traversed along the x- and y- axes of the horizontal plane where the test tube was to lie. Flat velocity profiles were obtained. Graphs of the velocity profiles along with detailed drawings and photographs of each section of the flow loop are available [1]. The velocity values used in this paper are the free or bulk stream velocities.

The vapor leaving the separation tank from the top went through an electrically heated vapor riser to the tubeside of a shell and tube heat exchanger with a heat transfer area of 0.85 m^2. The condensate was collected in a ten liter reservoir whose level was automatically controlled by a float-operated relay which operated a small pump to return the condensate to the holding tank. Nine thermistor probes were placed in the flow boiling heat transfer loop to monitor and measure the temperatures in the system. All piping was stainless steel, and all gaskets were Teflon.

For a typical flow boiling run, first the temperature of the liquid in the loop was increased to within 1°C of saturation while the liquid was being circulated. The pump was then turned off and the liquid in the overhead tank was boiled to purge the noncondensable gases from the system. Then the pump was turned on and the flow rate was adjusted to the desired value. Cooling water flow to the coils in the tank fixed the liquid temperature to within 4 to 5 °C of the boiling point. The system was operated at the desired conditions for about an hour before any data were recorded. The tube was steam-heated just as it was for the pool boiling loop. The tube temperature was measured the same way as for the pool boiling loop.

Results and Discussion

The goal of this investigation was to obtain reliable experimental data for the boiling heat transfer behavior of a pure liquid flowing upward across a horizontal cylindrical heater. This is the *first* study of the effect of velocity on the entire boiling curve for this geometry. The results are conveniently discussed in two parts: pool boiling and flow boiling.

Pool Boiling Results. The heat duty of the copper test tube was measured by three independent means:

$(Q/A)_{ST}$ heat flux based on steam condensate rate,

$(Q/A)_{F\text{-}113}$ heat flux based on Freon-113 boil-up, and

Nomenclature

a = empirical dimensional coefficient
b = empirical dimensionless exponent
D = outside diameter of tube
Fr = Froude number (U^2/gD), dimensionless
g = acceleration of gravity
h = boiling heat transfer coefficient
h_{Lv} = latent heat of vaporization
k_v = thermal conductivity of vapor
Nu_v = Nusselt number based on vapor (hD/k_v), dimensionless
q_c = heat flux during forced convection with no phase change
q_{FNB} = heat flux during flow nucleate boiling
q_{max} = peak heat flux in nucleate boiling
q_{max}^+ = dimensionless heat flux, $q_{max}/\rho_v h_{Lv} U$
q_{min} = minimum heat flux in film boiling
q_{PNB} = heat flux during nucleate pool boiling
Q/A = heat flux
$(Q/A)_{cw}$ = experimental heat flux for boiling, based on condenser duty
$(Q/A)_{F\text{-}113}$ = experimental heat flux for boiling, based on Freon boil-up
$(Q/A)_{ST}$ = experimental heat flux for boiling, based on steam condensate
ΔT = temperature difference, metal to liquid
U = liquid free stream velocity in test section
We_v = Weber number based on vapor density ($D\rho_v U^2/\sigma$), dimensionless
ρ_L = liquid density
ρ_v = vapor density
σ = surface tension

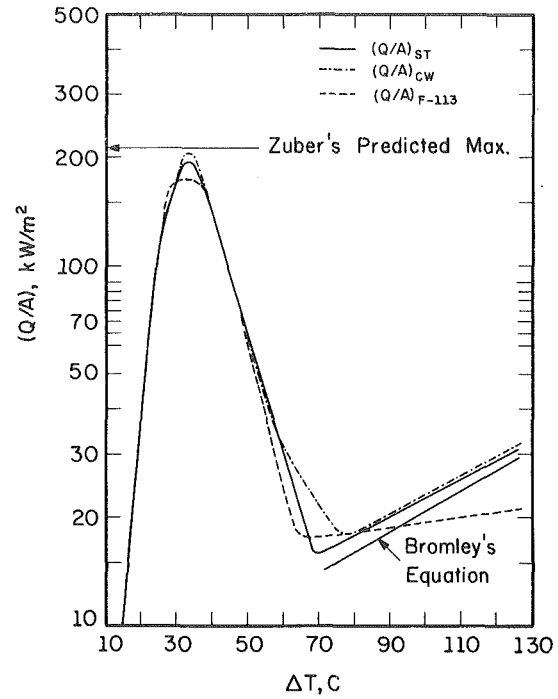

Fig. 3 Experimental pool boiling curves for Freon-113 based on three independent methods of heat flux measurement

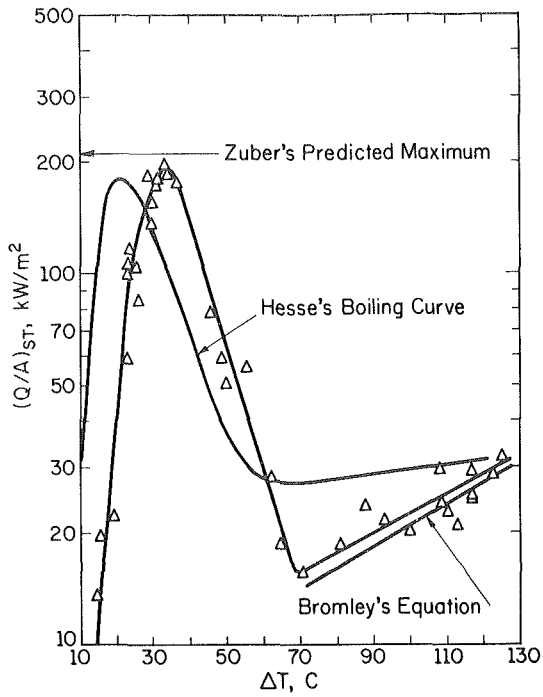

Fig. 4 Illustration of actual data based on use of measured steam condensate to obtain the heat flux. Pool boiling of Freon-113

$(Q/A)_{cw}$ heat flux determined from the cooling water heat duty in the condenser.

Fig. 3 shows these three heat fluxes (corrected for heat losses) as a function of the ΔT driving force for boiling. The independent methods agree well. The largest deviations occurred in the region of film boiling for which the heat loss corrections were largest. Fig. 3 indicates that the heat flux determination from the steam condensate was reliable and that using this method for flow boiling was satisfactory.

Fig. 4 shows the actual data points for pool boiling, with the heat flux based on the steam condensate measurement. Hesse [23] has previously used a 14 mm OD nickel tube, heated by flowing hot water inside, to boil Freon-113. His results are included in Fig. 4 for comparison. The peak heat flux for the present study was 196 kw/m^2 at ΔT = 33°C. This is close to the values of 201 kw/m^2 predicted by Zuber's equation for a flat plate [24] and 181 kw/m^2 predicted [25] by Lienhard and Dhir's equation. The data for film boiling are about 10 percent greater than predicted [26] by Bromley's equation.

Flow Boiling Results. Visual observations of the flow across the heating tube were made with and without boiling on the tube surface. First the effect of velocity was observed on liquid nonboiling Freon-113 flowing across the tube at about 46.0°C. (The normal boiling point is 47.6°C, but at the boiler pressure the saturation temperature was 50 to 51°C). At about U = 4.0 m/s, a clearly visible wake started to form behind the tube. The length of the wake was between 0.5 and 1 cm. At velocities less than 4.0 m/s, no wake formed. At the maximum flow velocity of 6.8 m/s, the wake extended 6 to 8 cm behind the tube. For the Freon-113 in flow nucleate boiling, the length of the wake was 0.5 to 0.75 cm for U = 2.4 m/s; 2.0 to 2.2 cm for U = 4.0 m/s; and 8 to 10 cm for U = 6.8 m/s.

The portion of the heating tube facing the incoming flow became coated with a thin, dark deposit after each set of runs in film boiling with forced flow. The rear portion of the tube had a thin gray coating. Film boiling tests had wall temperatures as high as 170°C. Whenever the tube was seen to be discolored, it was cleaned and polished. A study of boiling Freon-113 by Akagawa, et al. [27] showed that no fouling occurs with metal temperatures below 100°C (nucleate boiling) but that decomposition products of carbon, chlorine, and fluorine do form with metal temperatures above 350°C (film boiling). The region between 100 and 350°C could not be studied with their electrically heated platinum wire.

The incoming liquid at the test section was held at about 46.0°C, slightly below the saturation temperature of 51.0°C. This slight subcooling minimized cavitation at the pump and also assured that no vapor generation was being caused by the heat input of the pump. Three liquid flow velocities were used: 2.4, 4.0, and 6.8 m/s. Fig. 5 shows the individual data points for the free stream velocity of 4.0 m/s. The maximum heat flux was 583 kw/m^2 and occurred at a ΔT of 64°C. This peak value is about three times the peak value for pool boiling, 196 kw/m^2 at a ΔT of 33°C. The flow boiling peak value of 583 is less than 722 kw/m^2 predicted by Lienhard and Eichhorn's "high velocity" model equation [19]. The film boiling data are about 25 percent higher than the curve predicted by Bromley, LeRoy and Robber's equation [20].

In Fig. 6 smooth lines are shown for all the forced flow tests and for pool boiling. This is a master plot which summarizes the entire investigation. Predictions for the peak heat flux q_{max} and for film boiling are also plotted, for comparison. Velocity increases improved the nucleate boiling heat flux, and the curves shifted up with increasing velocity. This is in contradiction to observations by some previous investigators [3–6, 8] who reported that forced-convection nucleate boiling curves intersect or overlap with each other. The peak heat flux increased very noticeably as the flow velocity was increased. Lienhard and Eichhorn's "high velocity" equation for flow boiling q_{max} from wires was always higher than the experimentally obtained values in this study by about 25 percent. The q_{max} values followed a regular pattern and increased with increasing velocity from U = 0 (pool boiling) to U = 6.8 m/s as shown by the dashed locus drawn through the q_{max} values in Fig. 6. Also the ΔT for q_{max} increased as the flow velocity was increased.

In the transition boiling region, the boiling curves became steeper as the liquid velocity was increased. The second boiling crisis (minimum heat flux) was quite sensitive to velocity. The locus of these minimum values is shown also by a dashed line. It is interesting that the ratio of the maximum heat flux to the minimum heat flux is not constant. This ratio was about 12 for zero velocity. It decreased to about 4.4 for 2.4 m/s, to 3.9 for 3.0 m/s, and to 3.3 for 6.8 m/s. The intriguing possibility of a ratio of unity at infinite velocity must be considered. In other words, at a sufficiently high velocity, only one mode of boiling may exist, no matter what the ΔT.

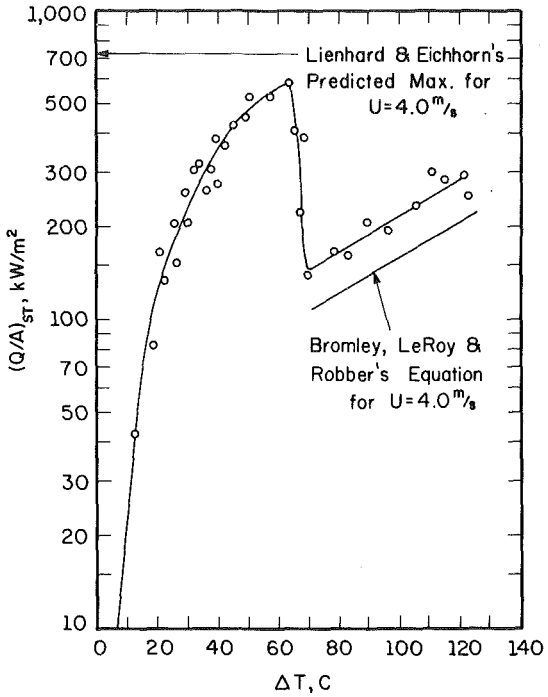

Fig. 5 Illustration of actual data during forced flow at 4.0 m/s

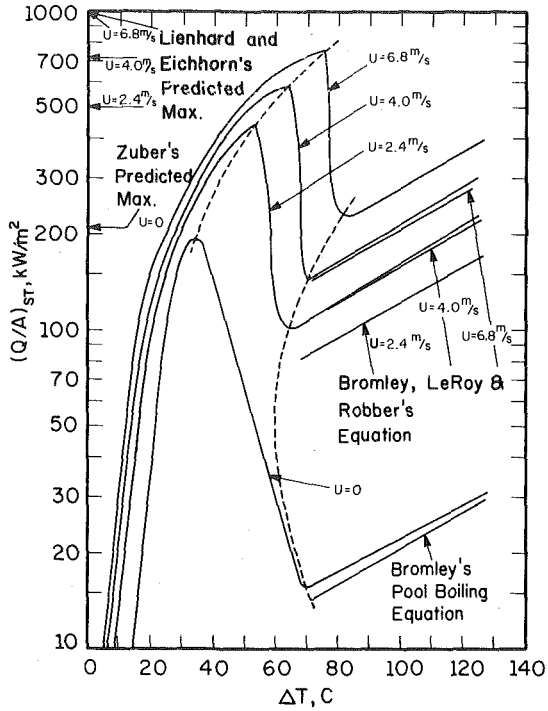

Fig. 6 Master plot showing experimental determination of the effect of velocity on the boiling curves. The loci of the first crisis (maximum flux) and second crisis (minimum flux) are shown by dashed lines. Freon-113 subcooled 4.5°C at 1.12 atmosphere flowing normal to a 6.4 mm dia cylinder

Although the minimum heat flux increased steadily with increasing velocity, the change in the ΔT at the minimum flux was less predictable. For example, at 4.0 m/s the minimum flux occurs at the same ΔT as for pool-boiling. The reason for this is unknown, but as can be seen in Fig. 4 there is some uncertainty in identifying exactly the minimum heat flux.

The heat flux during film boiling was improved greatly by increasing velocity. The value of $q_{\min}$ for $U = 6.8$ m/s was higher than the pool boiling $q_{\max}$. The film boiling predictions by Bromley, LeRoy, and Robbers were correct in that they were parallel to the experimental film boiling curves; however, they were 25 percent lower than the data of this study.

Figs. 7 , 8 and 9 show the experimental data of this investigation along with the empirical curves of the form

$$Q/A = a(\Delta T)^b \tag{1}$$

the arbitrary constants a and b were determined by least-squares fit. Equations such as these are useful in design work. They permit the designer to represent the complex bell-shaped, true boiling curve with a set of simple straight lines on logarithmic coordinates.

Fig. 7 is for nucleate boiling, and a pattern is evident. The coefficient a increases steadily as the liquid velocity increases. The exponent b decreases steadily.

Experimental nucleate flow boiling results of this study were compared with a correlation proposed by Rohsenow [28] who stated that nucleate flow boiling heat flux could be obtained by adding nucleate pool boiling heat flux to single-phase forced convection heat flux:

$$q_{\text{FNB}} = q_{\text{PNB}} + q_C \tag{2}$$

This equation was found to be quite good for all cases with ΔT less than 25°C. The method requires a knowledge of nucleate pool boiling Q/A versus ΔT; however, for forced flow nucleate boiling, ΔT and Q/A go well past the critical values for pool boiling. Thus there is no sure knowledge of what to use for q_{PNB} in equation (2) at values higher than the critical value for pool boiling.

Fig. 8 is for the transition region of boiling. No consistent pattern is evident for the effect of velocity on the constants a and b. Thus the transition region continues to be the poorest understood form of boiling.

Fig. 9 is for the film boiling region. The exponent b increases from 0.785 at zero velocity to 1.37 at 6.8 m/s. This is not a huge variation. In fact all four lines in Fig. 9 could be drawn parallel and give a useable fit; however, this would require large changes in the coefficient a.

Fig. 10 shows some examples in which the data for film boiling are correlated by equation (3)

$$\text{Nu}_v \propto \text{Fr}^{0.28} \tag{3}$$

The vapor Nusselt number Nu_v employs the thermal conductivity of the vapor, the tube diameter, and the experimental boiling heat transfer coefficient. The fit is excellent. From the definition of the Froude number (U^2/gD), we get equation (4)

$$h \propto U^{0.56} \tag{4}$$

The exponent 0.56 is close to the value of 0.5 proposed by Bromley, et al. [20]. In fact the present data can be force fit to the exponent 0.5, using the least-squares method, to yield equation (5) which is in the form used by Bromley, et al. for turbulent flow.

$$h = 3.68\left[\frac{Uk_v\rho_v h_{Lv}}{D\Delta T}\right]^{1/2} \tag{5}$$

The coefficient 3.68 is higher than the value of 2.7 used in [20]. Part of the discrepancy occurs because radiation heat transfer is included in equation (5) whereas it was excluded by Bromley, et al.

The peak of the boiling curve (burn out) is of great interest. The maxima of the flow-boiling curves in Fig. 6 may be correlated beautifully using the dimensionless groups shown in Fig. 11. The liquid velocity occurs in both the dimensionless heat flux (defined on the graph) and in the Weber number $D\rho_v U^2/\sigma$. The line is equation (6)

$$q_{\max}/\rho_v h_{Lv} U = 0.369\text{We}_v^{-0.26} \tag{6}$$

Rearrangement gives equation (7).

$$q_{\max} \propto U^{0.48} \tag{7}$$

The exponent 0.48 is in essential agreement with the value of 0.5 obtained by Vliet and Leppert [13] for water flowing normal to a 2.8 mm

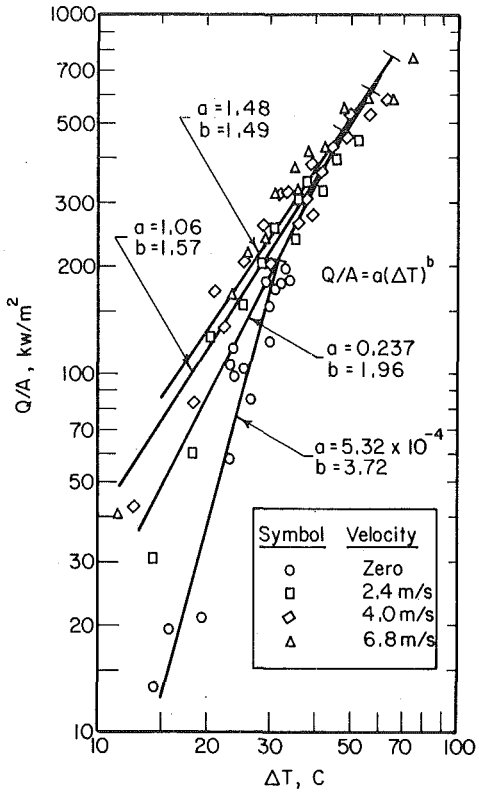

Fig. 7 Simplified best-fit straight lines for nucleate boiling data. A cross bar indicates the true end of each line

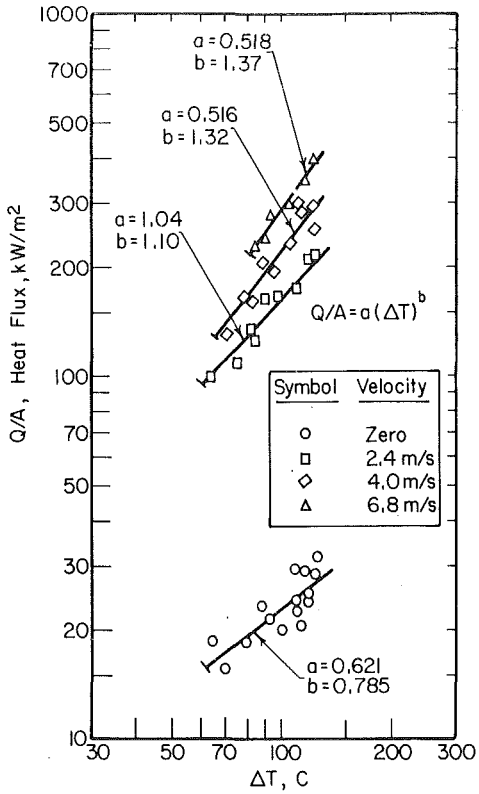

Fig. 9 Simplified best fit straight lines for film boiling data

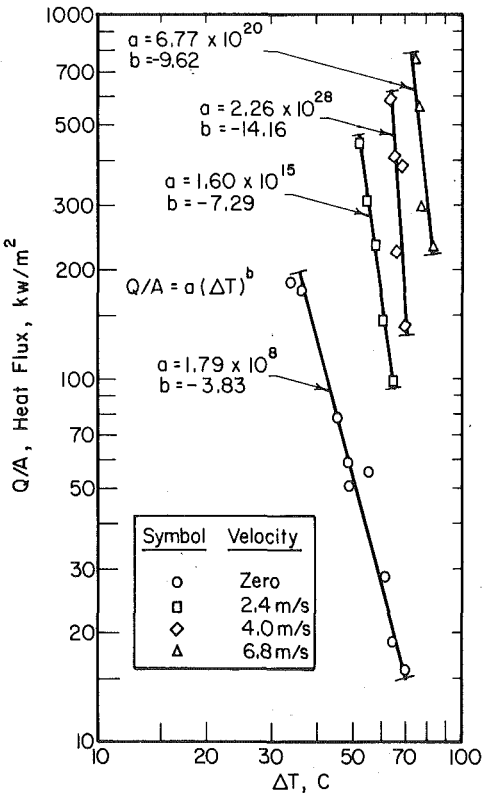

Fig. 8 Simplified best-fit straight lines for transition boiling data

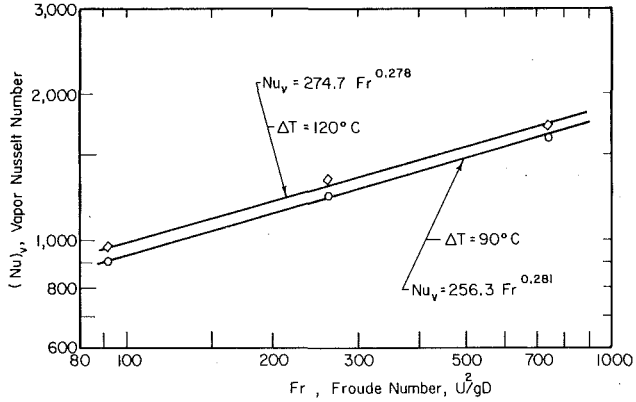

Fig. 10 Film boiling data correlated by Nusselt and Froude dimensionless groups

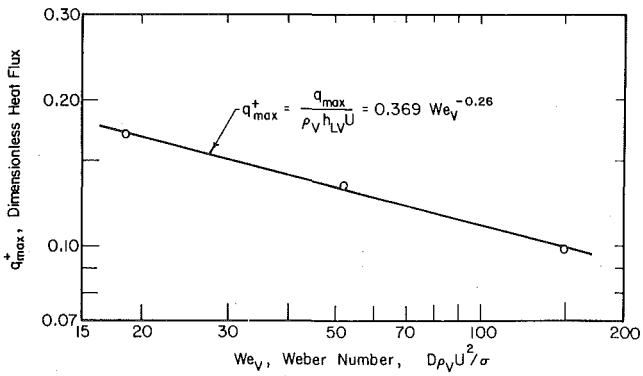

Fig. 11 Maximum heat flux correlated by dimensionless Weber number

OD stainless steel tube. The value 0.5 was also reported by Kutateladze and Burakov [15] for subcooled Dowtherm flowing parallel to heated flat plates. The same 0.5 was reported by Ornatskiy et al. [16] for water flowing normal to a jacketed cylinder. This exponent disagrees with the value of 0.33 proposed by Lienhard and Eichhorn [19] for various liquids boiling on wires. Weatherhead [11] obtained 0.33 for subcooled water on wires.

According to Eichhorn and Lienhard [29] for burnout of horizontal cylinders in a vertical cross-flow at low velocities, the structure of the escaping vapor changes from 3-dimensional jets (at low velocity) to a two-dimensional sheet when the velocity is at a critical value according to equation (8).

$$\text{Critical We}_v = (0.1)\frac{\rho_v}{\rho_L}\cdot\frac{gD^2(\rho_L - \rho_v)}{4\sigma} \tag{8}$$

For the present tube and Freon-113, this critical Weber number is less than unity. Fig. 11 shows that all the flow runs were made with Weber numbers much greater than that. Thus the vapor escape is predicted to be sheet-like rather than jet-like. This was in accord with the present observations.

Conclusions

1 For Freon-113 boiling outside a horizontal tube, the entire boiling curve is sensitive to liquid velocity and an increase in velocity always causes an increase in heat flux.

2 Boiling curves Q/A versus ΔT for different liquid velocities do not overlap or intersect.

3 The region of transition boiling becomes smaller as velocity is increased, suggesting that transition boiling will vanish at sufficiently high velocities.

4 The peak heat flux is proportional to the square root of the liquid velocity when the vapor Weber number is in the range between 15 and 200.

5 The heat flux in film boiling is proportional to the 0.56 power of velocity when the Froude number is in the range between 80 and 1000.

6 In nucleate boiling (except near the peak flux) a good estimate of the heat flux is given by simple addition of pool-boiling heat flux and forced-flow, non-phase-change, heat flux (Rohsenow's method).

7 The results of this investigation will improve the design of heat exchangers (compact plate-fin, shell-and-tube, etc.) where liquid velocity is created either by bubble generation due to boiling or by an external source (pump, gravity, etc.) . . . A first design method proposed by Panitsidis, et al. [30] for boiling of liquids in compact plate-fin heat exchangers now can be improved considerably by the results of this study.

Acknowledgments

Financial support was provided by means of a research grant from the National Science Foundation. The digital electronic thermometer was donated by E. I. Du Pont de Nemours and Company.

References

1 Yilmaz, Salim, "Effect of Velocity on Boiling Freon-113," PhD Thesis, Chemical Engineering Department, University of Illinois, 1979.

2 Leppert, G., Costello, C. P., and Hoglund, B. M., "Boiling Heat Transfer to Water Containing a Volatile Additive," *Trans. ASME,* Vol. 80, Oct., 1958, pp. 1395–1404.

3 Vliet, G. C., "Local Boiling Peak Heat Flux for Water Flowing Normal to Cylinders," PhD Thesis, Mechanical Engineering Department, Stanford University, 1962.

4 McKee, H. G., "Forced Convection Boiling from a Cylinder Normal to the Flow," PhD Thesis, Chemical Engineering Department, Oklahoma State University, 1967.

5 McKee, H. R., and Bell, K. J., "Forced Convection Boiling from a Cylinder Normal to the Flow," *Chemical Engineering Progress, Symposium Series,* Vol. 65, No. 92, 1969, pp. 222–230.

6 Bitter, R. C., "Heat Transfer from a Horizontal Tube with Transverse Flow of Evaporating Saturated R-11," International Institute of Refrigeration Commissions B-1, B-2 & E-1, Freudenstadt, Fed. Rep. of Germany, Supplement to International Institute of Refrigeration Bulletin, 1972, pp. 97–107.

7 Fand, R. M. et al, "Simultaneous Boiling and Forced Convection Heat Transfer from a Horizontal Cylinder to Water," ASME JOURNAL OF HEAT TRANSFER, Vol. 98, August 1976, pp. 395–400.

8 Lemmert, M. and Chawla, J. M., "Influence of Flow Velocity on Surface Boiling Heat Transfer Coefficient," *Heat Transfer in Boiling,* Hemisphere, Washington, 1977, pp. 237–247, Hahne, E. and Grigull, U., ed.

9 Diesselhorst, T., Grigull, U. and Hahne, E., "Hydrodynamic and Surface Effects on the Peak Heat Flux in Pool Boiling," *Heat Transfer in Boiling,* Hemisphere, Washington, 1977, pp. 99–135, Hahne, E. and Grigull, U. ed.

10 Beecher, N., MS Thesis, Chemical Engineering Department, Massachusetts Institute of Technology, 1948.

11 Weatherhead, R. T., "Boiling Burnout Heat Flux for Wires in Water Crossflow at Atmospheric Pressure," Boiling Burnout Progress Report No. 5, Argonne National Lab, June 30, 1955.

12 Kezios, S. P. and Lo, R. K. "Heat Transfer from Rods Normal to Subcooled Water Flow for Non-Boiling and Surface Boiling Conditions Up to and Including Burnout," Argonne National Laboratory Report ANL-5822, Jan., 1958.

13 Vliet, G. C. and Leppert, G., "Critical Heat Flux for Nearly Saturated Water Flowing Normal to a Cylinder," ASME JOURNAL OF HEAT TRANSFER, Vol. 86, Feb. 1964, pp. 59–67.

14 Vliet, G. C. and Leppert, G., "Critical Heat Flux for Subcooled Water Flowing Normal to a Cylinder," ASME JOURNAL OF HEAT TRANSFER, Vol. 86, February 1964, pp. 68–74.

15 Kutateladze, S. S., and Burakov, B. A., "The Critical Heat Flux for Natural Convection and Forced Flow of Boiling and Subcooled Dowtherm," *Problems of Heat Transfer and Hydraulics of Two-Phase Media,* Pergamon, Oxford, 1969, pp. 63–84, Kutateladze, S. S., ed.

16 Ornatskiy, A. P., Kichigan, A. M., and Kesova, L. A., "Burnout of Cylindrical Surfaces in Transverse Flow," *Heat Transfer Soviet Research,* Vol. 1, No. 6, 1969, pp. 119–123.

17 Cochran, T. H., and Andracchio, C. R., "Forced-Convection Peak Heat Flux on Cylindrical Heaters in Water and Refrigerant 113," NASA TN D-7553, Feb. 1974.

18 Min, T. K., "Boiling on Cylinders in Cross-Flow-Low Velocity Peak Heat Flux Measurements for Water and Methanol," MS Thesis, Mechanical Engineering Department, University of Kentucky, 1975.

19 Lienhard, J. H. and Eichhorn, R., "Peak Boiling Heat Flux on Cylinders in a Cross Flow," *International Journal of Heat and Mass Transfer,* Vol. 19, October 1976, pp. 1135–1142.

20 Bromley, L. A., LeRoy, N. R., and Robbers, J. A., "Heat Transfer in Forced Convection Film Boiling," Industrial and Engineering Chemistry, Vol. 45, No. 12, 1953, pp. 2639–2646.

21 Motte, E. I., and Bromley, L. A., "Film Boiling of Flowing Subcooled Liquids," *Industrial and Engineering Chemistry,* Vol. 49, No. 11, 1957, pp. 1921–1928.

22 Pramuk, F. S. and Westwater, J. W., "Effect of Agitation on the Critical Temperature Difference for a Boiling Liquid," *Chemical Engineering Progress, Symposium Series,* Vol. 52, No. 18, 1956, pp. 79–83.

23 Hesse, G., "Heat Transfer in Nucleate Boiling, Maximum Heat Flux and Transition Boiling," *International Journal Heat and Mass Transfer,* Vol. 16, No. 8, 1973, pp. 1611–1627.

24 Zuber, N., "Hydrodynamic Aspects of Boiling Heat Transfer," Doctoral Dissertation, University of California at Los Angeles, 1949.

25 Lienhard, J. H. and Dhir, V. K., "Hydrodynamic Prediction of Peak Pool-Boiling Heat Fluxes from Finite Bodies," ASME JOURNAL OF HEAT TRANSFER, Vol. 95, No. 2, 1973, pp. 152–158.

26 Bromley, L. A., "Heat Transfer in Stable Film Boiling," *Chemical Engineering Progress,* Vol. 46, No. 5, 1950, pp. 221–227.

27 Akagawa, K., Sakaguchi, T., and Fujii, T., "Influences of Fouling on Boiling Heat Transfer to Organic Coolants," Fifth International Heat Transfer Conference, Tokyo, Vol. 4, 1974, pp. 25–29.

28 Rohsenow, W. M., "Heat Transfer Associated with Nucleate Boiling," *Proceedings of Heat Transfer and Fluid Mechanics Institute,* Standford University Press, 1953, p. 123.

29 Eichhorn, R. and Lienhard, J. H., Private communication with J. W. Westwater, September 29, 1977.

30 Panitsidis, H., Gresham, R. D., and Westwater, J. W., "Boiling of Liquids in a Compact Plate-Fin Heat Exchanger," *International Journal of Heat and Mass Transfer,* Vol. 18, No. 1, 1975, pp. 37–42.

N. Kaji
Graduate Student.

Y. H. Mori
Research Associate.

Y. Tochitani[1]
Instructor.

K. Komotori
Professor.

Department of Mechanical Engineering,
Keio University,
3-14-1 Hiyoshi, Kohoku-Ku, Yokohama 223,
Japan

Augmentation of Direct-Contact Heat Transfer to Drops with an Intermittent Electric Field

The characteristics of the augmentation technique previously proposed by the authors has been studied experimentally with water drops 3.9 to 5.9 mm in diameter rising in methylphenyl silicone oil. Each drop is subjected to an intermittent electric field applied periodically perpendicular to its trajectory, and the drop responds by periodic elongation in the direction of the field. The dependence of heat transfer coefficient on the strength, frequency and duty ratio of the field is presented and discussed.

Introduction

Direct contact exchange between drops or bubbles and a surrounding fluid medium has an extensive applicability in both heat and mass transfer. The application of a steady electric field has been suggested by several researchers [1–3] to enhance the transfer through an increase of translational velocity of drops due to the Coulomb force or the circulations induced both inside and outside drops. When the continuous medium is a liquid with poor electrical conductivity, such an electrical augmentation seems to be more efficient than the conventional mechanical agitation because the former does not fruitlessly consume a large power to move the bulk of the continuous phase.

The authors recently proposed a new technique of electrical augmentation in which an intermittent electric field is periodically applied to yield an oscillation of drops (or bubbles) [4]. Some preliminary experiments were performed to verify the effectiveness of this technique with water drops rising in methylphenyl silicone oil. The electric field was applied perpendicular to the trajectory of drops, the direction of the field being alternated to prevent the drops from sliding in one direction toward one of the parallel electrodes between which the drops were put. In each duration with an appropriate strength of the field, drops were elongated parallel to the field due to the electric stress at their surfaces. The drops recovered a spherical form in the following duration with no field. A series of such deformations was very similar to usual $n = 2$ mode oscillation except that the mean distortion ratio (ratio of major to minor axis of drops) was not equal to but larger than unity. The effect of this electrically forced oscillation on heat transfer to drops was shown to be significant, provided the frequency as well as the strength of the field was adequate for a given system, surpassing that of the steady field as stated above. However, the range of the experiments was so limited that the characteristics of this augmentation method were not enough revealed.

This paper presents the results of further experimental study in which strength, frequency and duty ratio of the field as well as the drop diameter were varied systematically. Though the experiments were still restricted to the heat transfer to water drops in methylphenyl silicone oil, the principal features of the method obtained in this study seem to be applicable to various heat or mass transfer processes in dispersed fluid systems.

Experimental

The apparatus and procedure used were almost the same as described in [4].

Distilled water was employed as dispersed phase, and silicone oil KF 54 (Shin-Etsu Kagaku Co., Tokyo) as continuous phase. The temperature of silicone oil was maintained at 50.1 ± 0.1°C throughout the experiments. Two cylindrical nozzles 0.40 and 0.60 mm OD were used to obtain water drops of 4.9 and 5.9 mm dia, respectively. Smaller drops 3.9 and 4.4 mm dia were formed by injecting a little silicone oil to the tip of nozzle 0.40 mm dia. The frequency of formation of drops was so regulated that they could be considered isolated drops.

The intermittent electric field as shown in Fig. 1 was provided in a horizontal direction across the electrodes by use of a power supply unit designed originally by the authors [4]. There are three variable parameters concerning the electric field, i.e., strength E_f,[2] frequency f (= $1/2\Delta t$, a half of drop oscillation frequency) and duty ratio d (= $\Delta t_E/\Delta t$). The experiments were carried out in the ranges of strengths up to a critical value at which drops burst, frequencies from 0.95 to 7.40 Hz, and duty ratios from 0.16 to 0.82. The range of the latter two parameters were the most the power supply unit could yield.

The variation of distortion ratio D_p/D_n with time for each drop was known from the cine-photographs. The maximum value of D_p/D_n that a drop exhibits in each period is frequently used in this paper as an index of oscillation amplitude.

The enhancement of heat transfer by the field while drops are rising freely is evaluated in terms of a fractional increase of the overall heat transfer coefficient based on the surface area of spherical drop and averaged for an appropriate time interval covering a number of periods of the field, $2\Delta t$, just the same as in the previous work [4].

The properties of the system are presented in Table 1. The permittivity (at 4.7 Hz) and resistivity of silicone oil saturated with water and the interfacial tension between water and silicone oil were measured by the authors. Other properties were quoted from the technical data catalog of Shin-Etsu Kagaku Co. and reference tables.

[2] An overshooting ($E_i - E_f$) of about 46 percent of the final strength E_f is inevitable. In spite of this, E_f is exclusively used as the reference strength of the field in this paper as stated in [4].

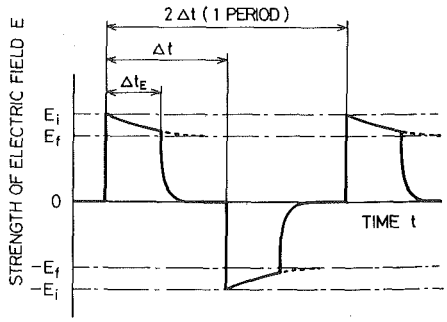

Fig. 1 Wave-form of strength of electric field

[1] Present address: Kanazawa Institute of Technology, Nonoichi, Ishikawa

Contributed by the Heat Transfer Division for publication in the JOURNAL OF HEAT TRANSFER. Manuscript received by the Heat Transfer Division March 20, 1979.

Table 1 Properties of the system (at 50°C unless otherwise noted)

	Water	Silicone oil KF 54
Density, kg/m^3	988	1055
Specific heat at constant pressure, kJ/kgK	4.18	1.63 (at 25°C)
Thermal conductivity, W/mK	0.642	0.147 (at 25°C)
Kinematic viscosity, mm^2/s	0.555	167
Permittivity, pF/m	709	25.6
Resistivity, MΩm	0.24	3.2×10^4
Interfacial tension, mN/m	27	

Table 2 Summarized data on heat transfer under no electric field

D_0, mm	3.9	4.4	4.9	5.9
U, mm/s	2.3	2.9	3.8	5.4
Re_c	0.054	0.076	0.111	0.187
Pe_c	105	150	218	366
α_0, W/m^{2}K	120	126	131	158
α_0*, W/m^{2}K	114	111	112	108
α_0', W/m^{2}K	231	241	256	267
$(1/\alpha_{0d}^*)/(1/\alpha_0)$	0.111	0.132	0.153	0.221
$(1/\alpha_{0d}')/(1/\alpha_0)$	0.041	0.049	0.057	0.082

Results and Discussion

Heat Transfer under No Electric Field. The data on heat-transfer experiments under no electric field are summarized in Table 2 to specify the conditions on which the effect of electric field was superposed. In the whole range of the experiments, drops were free from any oscillatory motion in shape and zigzag or helical motion in trajectory whenever no electric field was applied. The rise velocities U shown in Table 2 and the linear trajectory remained almost unchanged even under the fields with highest strengths. Here the values of overall heat transfer coefficient α_0 obtained under no electric field are compared to those deduced from some established correlations for heat transfer inside and outside drops, and the fraction of thermal resistance inside drops is estimated.

The dispersed-phase heat transfer coefficient α_{0d} and the continuous-phase heat transfer coefficient α_{0c} under no electric field are evaluated by assuming either a drop to be rigid or a circulation to take place inside the drop. Considering the range of present experiments for which $Re_c < 1$ and $Pe_c \gg 1$, α_{0d}^* and α_{0c}^* for rigid drop are predicted from the expressions of Newman [5] and Levich [6] respectively, while α_{0d}' and α_{0c}' for the drop with internal circulation are predicted from the expressions of Elzinga and Banchero (given in [7]) and Levich [8], respectively. By combining α_{0d}^* with α_{0c}^* or α_{0d}' with α_{0c}', the overall heat transfer coefficient for rigid drop, α_0^*, or for drop with internal circulation, α_0', can be deduced as given in Table 2. The actual overall heat transfer coefficient α_0 falls in the range between α_0^* and α_0', and tends to approach α_0^* with a decrease of D_0. This may be ascribed to the promotion of internal circulation with an increase of D_0.

The fraction of inside film resistance is presumed to be in the range between $(1/\alpha_{0d}^*)/(1/\alpha_0)$ and $(1/\alpha_{0d}')/(1/\alpha_0)$ presented in Table 2. Apparently the major resistance is present in the continuous-phase side around a drop in the system used in this study. Thus an electric field is primarily required to reduce this resistance to yield an effective augmentation of heat transfer.

Dependence on the Strength of Electric Field. Figs. 2(a) and 2(b) show the dependences of E_f of the maximum distortion ratio of drops, $(D_p/D_n)_{max}$, and of the fractional increase of heat transfer coefficient, α/α_0, respectively, while the frequency f and duty ratio d are maintained constant.[3] Plotted points of $(D_p/D_n)_{max}$ in each figure are averaged of measured values, the maximum discrepancy being ±0.02. On the other hand, the primary uncertainty in the measured results of heat transfer comes from the drop temperature measurements. Considering this and the other factors, the resultant accuracy of α/α_0 is likely to be within 0.1. Some correspondence can be seen between these dependences. A field with a certain strength yields a larger $(D_p/D_n)_{max}$ for larger drops and thus a larger α/α_0. As E_f increases, $(D_p/D_n)_{max}$ increases at an increasing rate till the drops burst at a critical strength E_{fcr} which depends on the drop diameter. The dependence of α/α_0 on E_f is not so straightforward as that of $(D_p/D_n)_{max}$.

At $f = 2.2$ Hz, for example, weak fields ranging up to a half of E_{fcr} cause only a limited increase of α. Further increase of E_f ranging up to three quarters of E_{fcr} results in a rapid rise of α in proportion to about the square of E_f. Above this range, the rate of increase of α reduces as E_f approaches E_{fcr}, though $(D_p/D_n)_{max}$ exhibits a quite sharp increase there.

At a higher frequency $f = 5.0$ Hz, the dependence of $(D_p/D_n)_{max}$ on E_f is similar to that for $f = 2.2$ Hz but a little reduced. In the lower range of E_f, α at $f = 5.0$ Hz surpasses that at $f = 2.2$ Hz, while this is reversed in the higher range of E_f. This fact may be explained qualitatively as follows. In the lower range of E_f where $(D_p/D_n)_{max}$ is as small as 1.2 or less, the heat transfer augmentation is primarily due to a small-scale turbulence, in the adjacent layer of drop surface, caused by an alternating displacement of the drop surface in the radial direction. Higher frequencies yield the higher intensities of turbulence provided the change in $(D_p/D_n)_{max}$ with the frequency is small. In the higher range of E_f, the heat transfer augmentation is rather related to such a large-scale flow alternating periodically as to enhance the exchange of liquid between inside and outside the boundary layer around the drop surface. Thus the augmentation in this range is more sensitive to the oscillation amplitude than that in the lower range of E_f.

[3] A small error in measuring E_f in authors' previous work [4] has been corrected in these figures.

Nomenclature

D_0 = equivalent spherical diameter of drop, mm
D_n = axis of drop normal to electric field, mm
D_p = axis of drop parallel to electric field, mm
d = duty ratio of electric field
E = strength of electric field, MV/m
E_i, E_f = strengths of electric field shown in Fig. 1, MV/m
E_{fcr} = critical field strength at which drops burst, MV/m
E_0 = strength of steady electric field, MV/m
f = frequency of electric field, Hz
f_{cr} = critical frequency of electric field at which α/α_0 peaks, Hz
p = normalized field strength
p_i, p_f = normalized field strengths corresponding to E_i, E_f
p_{cr} = critical normalized field strength at which drops burst
Pe = Peclet number
Re = Reynolds number
t = time, s
Δt = half period of electric field, s
Δt_E = pulse width of electric field, s
Δt_0 = time shown in Fig. 5, s
U = rise velocity of drop, mm/s
α = heat transfer coefficient, W/m^{2}K
α_0 = heat transfer coefficient under no electric field, W/m^{2}K
$\delta = (D_p - D_n)/(D_p + D_n)$
ϵ = permittivity, pF/m
ν = kinematic viscosity, mm^2/s
σ = interfacial tension, mN/m

Subscripts

c = continuous phase
d = dispersed phase
eq = equilibrium
max = maximum

Superscripts

$\bar{}$ = root mean square
$*$ = rigid drop
$'$ = drop with internal circulation

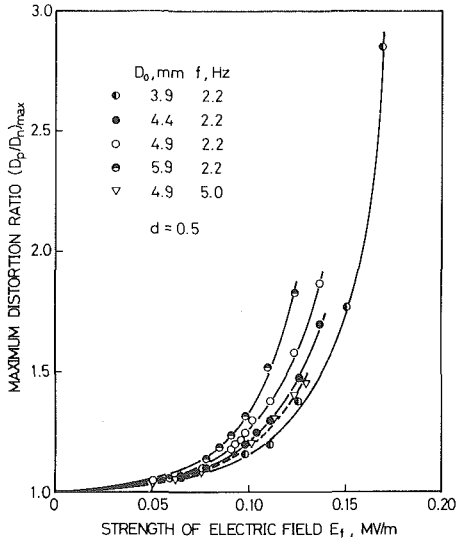

Fig. 2(*a*) Maximum distortion ratio of drops

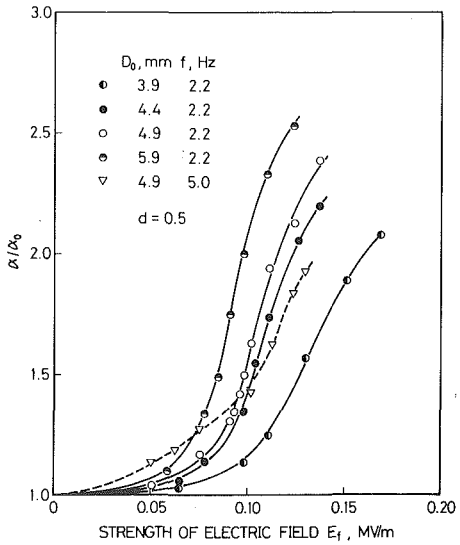

Fig. 2(*b*) Heat transfer coefficient

Fig. 2 Dependence on the strength of the field

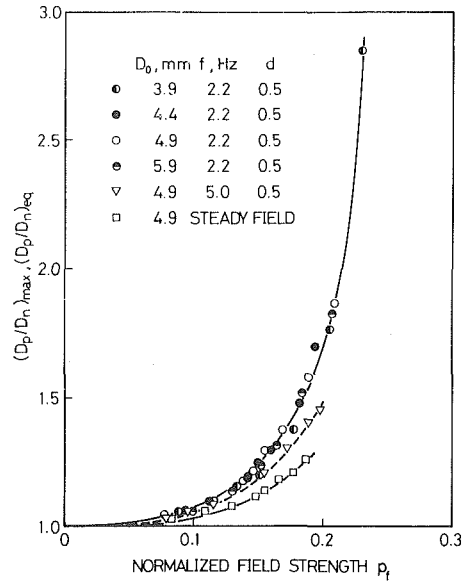

Fig. 3(*a*) Maximum distortion ratio of drops

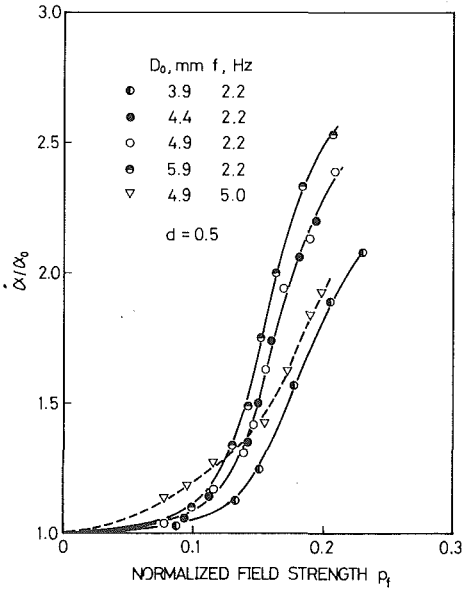

Fig 3(*b*) Heat transfer coefficient

Fig. 3 Dependence on the normalized field strength

It has been shown theoretically and experimentally that the quiescent distortion ratio of drop in the steady field or the alternating field (f = 60 Hz, sine wave) depends uniquely on the product of square of the field strength and the drop diameter when the system is specified [9–12]. Here $(D_p/D_n)_{max}$ and α/α_0 obtained in the experiments are to be correlated with the normalized field strength

$$p_f = E_f\sqrt{\epsilon_c D_0/2\sigma} \tag{1}$$

which was originally defined by Sample, et al. [11] using the steady strength E_0 instead of E_f in their analysis of quiescent distortion of conducting drops in the steady field. The correlations are demonstrated in Figs. 3(*a*) and 3(*b*).

Apparently there is a unique relation between $(D_p/D_n)_{max}$ and p_f while the frequency f and the duty ratio d are maintained constant. In Fig. 3(*a*) is also plotted the quiescent distortion ratio obtained in the steady field E_0. Though the steady field could be applied for a short time because of a sliding of drops toward one of the electrodes, the cine-photographs indicated that the distortion ratio shown in Fig. 3(*a*) can be considered an equilibrium one. The higher distortion ratios at f = 2.2 and 5.0 Hz than that under steady field at the same p_f are ascribed to some contribution of inertia to the oscillation of drops. Further discussion on the drop distortion versus field strength is given in Appendix.

On the contrary, α/α_0 cannot be represented uniquely by p_f as shown in Fig. 3(*b*). Though the difference between 4.4 and 4.9 mm dia drops almost disappears, α/α_0 increase, as a whole, with an increase in D_0 at a specified value of p_f.

Dependence on the Frequency of Electric Field. Figs. 4(*a*) and 4(*b*) show respectively the variations of $(D_p/D_n)_{max}$ and α/α_0 with frequency. There, drop diameter and strength of the field serve as parameters and are varied in some range respectively, while duty ratio is fixed at 0.5.

A peculiar dependence of the heat transfer coefficient α on the frequency as demonstrated in the previous paper [4] only for drop 4.9 mm dia has been confirmed to be qualitatively the same for every drop diameter as shown in Fig. 4(*b*). At a particular frequency the heat transfer coefficient α exhibits a peak with a steep slope on both sides. An increase of f in the range above that critical frequency results in a rapid decrease of α and then the convergence to a certain level. The peak becomes remarkable with an increase of either of drop diameter

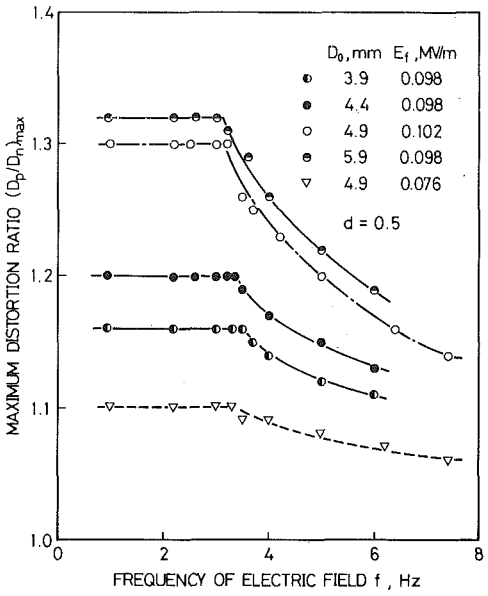

Fig. 4(*a*) Maximum distortion ratio of drops

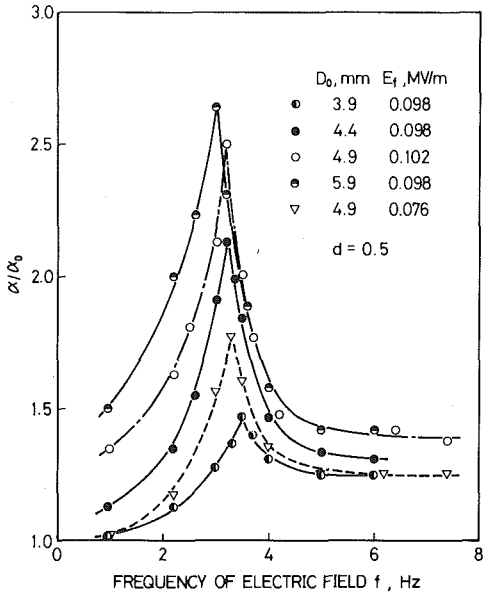

Fig. 4(*b*) Heat transfer coefficient

Fig. 4 Dependence on the frequency of the field

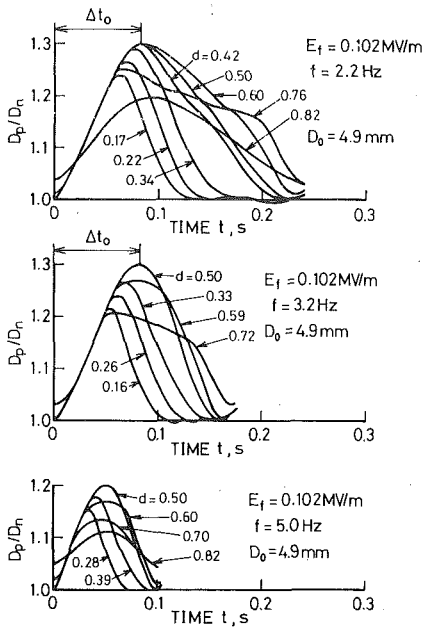

Fig. 5 Variation of drop distortion with time in a half period of the field

and the strength of the field. The critical frequency at the peak is hardly affected by the strength, and increases slightly with a decrease of drop diameter. The above characteristics can be explained by the variation of $(D_p/D_n)_{max}$ as shown in Fig. 4(*a*). In the range of f up to the critical frequency f_{cr}, $(D_p/D_n)_{max}$ takes a constant value depending on the drop diameter as well as the strength of the field. As f just exceeds f_{cr}, $(D_p/D_n)_{max}$ starts to decrease. Thus the critical frequency at which α takes a maximum coincides with the upper limit of the range in which $(D_p/D_n)_{max}$ takes a constant value.

The sharp peak of α at $f = f_{cr}$ as well as the apparent similarity in drop configuration between the oscillation in question and a usual $n = 2$ mode oscillation may be suggestive of $n = 2$ mode resonant oscillation of drops at $f = f_{cr}$. In the previous paper [4] the authors themselves suggested that the critical frequency f_{cr} coincides with a half of $n = 2$ mode resonant frequency. However, such an idea should be rejected for the following reasons. First, no excitation of oscillation amplitude $(D_p/D_n)_{max}$ occurs at $f = f_{cr}$ as shown in Fig. 4(*a*). Second, the natural frequency obtained by the observation of damped oscillation of drops is much higher than $2f_{cr}$ for every drop diameter employed in this study. These facts indicate that the oscillation at $f = f_{cr}$ is not a resonant oscillation. The dynamics of oscillation in question is interpreted as follows. When an electric field of the strength $E = E_i \sim E_f$ is applied as a quasi-step disturbance as shown in Fig. 1, a drop makes a "transient response" from a spherical shape to a spheroidal shape of a distortion ratio $(D_p/D_n)_{eq}$ that would be available under the steady electric field of the same strength. Succeeding cutoff of the field results in a transient response of the drop from spheroidal to spherical shape. If the duration Δt_E is enough long, D_p/D_n increases up to the maximum distortion ratio $(D_p/D_n)_{max}$, in a time Δt_0 (see Fig. 5), overshooting $(D_p/D_n)_{eq}$ to some extent, and then approaches $(D_p/D_n)_{eq}$ in the course of damped oscillation. The condition $f = f_{cr}$ yields the minimum Δt_E that ensures such a thorough distortion of the drop; i.e., $\Delta t_E = \Delta t_0$. As Δt_E becomes shorter than Δt_0, D_p/D_n does not increase up to the above mentioned level in that duration. Thus the oscillation of drops observed in this study is no more than a series of such a transient-response.

Dependence on the Duty Ratio of Electric Field. Fig. 5 illustrates the variation of distortion ratio with time in a half period of the field. When Δt_E and $\Delta t - \Delta t_E$ is long enough compared with the relaxation time for the drop distortion, drops exhibit a damped oscillation about the equilibrium shape corresponding respectively to $E = E_i \sim E_f$ or $E = 0$. As d so decreases that Δt_E becomes shorter than Δt_0 while the frequency is maintained constant, drops cannot exhibit such a thorough elongation that $(D_p/D_n)_{max}$ exceeds $(D_p/D_n)_{eq}$. On the contrary, as $\Delta t - \Delta t_E$ decreases with an increase of d, the drops cannot recover a spherical form. Unexpectedly the elongation is diminished in such a high range of d where Δt_E is enough long. There has not been made so far any satisfactory interpretation of this puzzling question. As shown in Fig. 4, the critical frequency f_{cr} for drops 4.9 mm dia is 3.2 Hz in the case of $d = 0.5$. Thus the dependences on d of both $(D_p/D_n)_{max}$ and α/α_0 have been examined at three typical frequencies below, equal to and above f_{CM}, respectively, i.e., 2.2, 3.2, and 5.0 Hz. Figs. 6(*a*) and 6(*b*) show a quite conspicuous correspondence between $(D_p/D_n)_{max}$ and α/α_0 at each of the three frequencies.

At a frequency lower than f_{cr}, there exists a region, extending symmetrically around $d = 0.5$, where both $(D_p/D_n)_{max}$ and α/α_0 are held constant respectively. In this region, both Δt_E and $\Delta t - \Delta t_E$ are equal to or above Δt_0 (0.08 s in the present case, see Fig. 5). This region is characterized by both Δt_E and $\Delta t - \Delta t_E$ being equal to or above Δt_0 (0.08 s in the present case, see Fig. 5) in it, and thus both the

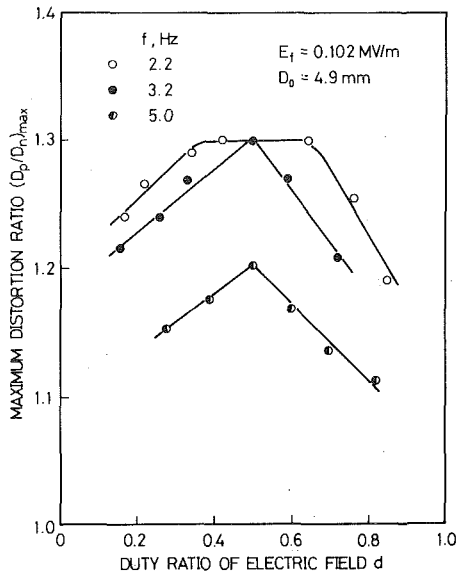

Fig. 6(*a*) Maximum distortion ratio of drops

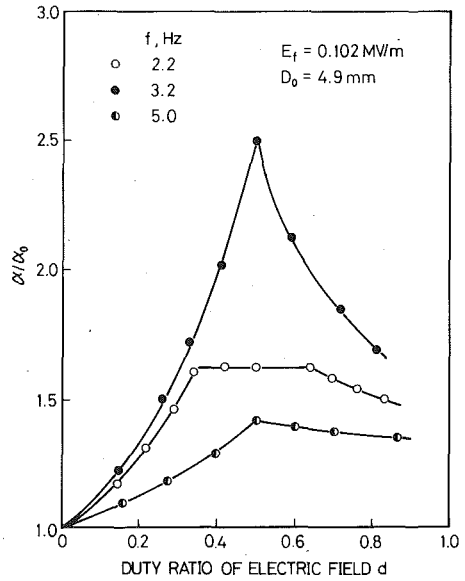

Fig. 6(*b*) Heat transfer coefficient

Fig. 6 Dependence on the duty ratio of the field

thorough elongation of drops and their recovery to a spherical form are simultaneously available there. As f approaches f_{cr} (3.2 Hz) this region vanishes, sharp peaks of $(D_p/D_n)_{max}$ and α/α_0 being left at $d = 0.5$.

These results lead to the following intuitive conclusion of practical importance; the heat transfer is maximized at the dual condition

$$f = f_{cr}, \quad d = 0.5 \tag{2}$$

that provides the relation

$$\Delta t_E = \Delta t - \Delta t_E = \Delta t_0 \tag{3}$$

Conclusions

The effect of an intermittent electric field as shown in Fig. 1 on the direct-contact heat transfer to drops has been examined experimentally. The principal conclusions reached from the study are as follows.

As the strength of the field increases exceeding a half of the critical strength at which drops burst, the heat transfer coefficient is raised rapidly. The heat transfer to larger drops is readily augmented at lower strengths.

At a particular frequency of the field the heat transfer coefficient exhibits a peak with a steep slope on both sides. The peak becomes remarkable with an increase of either of drop diameter and the strength of the field. This critical frequency is hardly affected by the strength, and increases slightly with a decrease of drop diameter. It is identified as the maximum frequency that permits a thorough deformation of drops and is distinguished from a half of a resonant frequency.

The heat transfer coefficient levels off as the frequency increases further away from the critical frequency. The heat transfer coefficient is more sensitive to both the drop diameter and the strength of field in the range below the critical frequency than in the range above it.

The heat transfer coefficient peaks at the duty ratio 0.5 when the frequency is higher than the critical frequency, while it assumes a constant value in a certain range around the duty ratio 0.5 when the frequency is lower than the critical frequency.

Acknowledgment

This work was subsidized by the Grant in Aid for Scientific Research of the Ministry of Education of Japan under Grant No. 346094. The authors wish to thank Messrs. H. Hanada, M. Takahashi and S. Furuse for their help in the experiments.

References

1 Bailes, P. J., and Thornton, J. D., "Electrically Augmented Liquid-Liquid Extraction in a Two-Component System I.—Single Droplet Studies," *Proceedings, International Conference on Solvent Extraction Chemistry,* Vol. 6, 1971, pp. 1431–1439.

2 Harker, J. H., and Ahmadzadeh, J., "The Effect of Electric Fields on Mass Transfer from Falling Drops," *International Journal of Heat and Mass Transfer,* Vol. 17, 1974, pp. 1219–1225.

3 Morrison, F. A., Jr., "Transient Heat and Mass Transfer to a Drop in an Electric Field," JOURNAL OF HEAT TRANSFER, Vol. 99, 1977, pp. 269–273.

4 Kaji, N., Mori, Y. H., Tochitani, Y., and Komotori, K., "Direct-Contact Heat Transfer to Drops in an Intermittent Electric Field," *Proceedings of the Sixth International Heat Transfer Conference,* Vol. 3, 1978, pp. 165–170.

5 Newman, A. B., "The Drying of Porous Solids: Diffusion Calculations," *Transactions of the American Institute of Chemical Engineers,* Vol. 27, 1931, pp. 310–333.

6 Levich, V. G., *Physicochemical Hydrodynamics,* Prentice-Hall, Englewood Cliffs, N. J., 1962, pp. 80–87.

7 Sideman, S., and Shabtai, H., "Direct-Contact Heat Transfer Between a Single Drop and Immiscible Liquid Medium," *The Canadian Journal of Chemical Engineering,* Vol. 42, 1964, pp. 107–117.

8 Levich, V. G., *Physicochemical Hydrodynamics,* Prentice-Hall, Englewood Cliffs, N. J., 1962, pp. 404–409.

9 Allan, R. S., and Mason, S. G., "Particle Behaviour in Shear and Electric Fields I. Deformation and Burst of Fluid Drops," *Proceedings of the Royal Society of London,* Series A, Vol. 267, 1962, pp. 45–61.

10 Garton, C. G., and Krasucki, Z., "Bubbles in Insulating Liquids: Stability in an Electric Field," *Proceedings of the Royal Society of London,* Series A, Vol. 280, 1964, pp. 211–226.

11 Sample, S. B., Raghupathy, B., and Hendricks, C. D., "Quiescent Distortion and Resonant Oscillations of a Liquid Drop in an Electric Field," *International Journal of Engineering Science,* Vol. 8, 1970, pp. 97–109.

12 Torza, S., Dox, R. G., and Mason, S. G., "Electrohydrodynamic Deformation and Burst of Liquid Drops," *Philosophical Transactions of the Royal Society of London,* Series A, Vol. 269, 1971, pp. 295–319.

APPENDIX

Some papers are available on the steady deformation of drops in an immiscible liquid subjected to an electric field which is steady or alternating at such a high frequency that the period of the field is much shorter than the relaxation time of the drop deformation, though the results are not in good quantitative agreement with each other. On the other hand, the oscillatory deformation of drops due to an electric field varying at lower frequencies has been only briefly mentioned in the work of Torza, et al. [12], except the authors' preliminary report [4]. Though the oscillation of drops observed under the field $f = 1$ Hz square wave is mentioned, no quantitative results are given there. Thus the oscillatory deformation observed in the present study is discussed below in some detail, to be compared with the steady deformation which has been studied more extensively.

Garton and Krasucki [10] and Sample, et al. [11] analyzed the steady deformation of conducting drops in a steady field by using the

prolate-spheroidal approximation and Legendre polynomial expansion method respectively, for representing the drop configuration. Allan and Mason [9] and Torza, et al. [12] dealt with the deformation in a steady or alternating (f = 60 Hz, sine wave) field when the two phases were perfect dielectrics and leaky dielectrics, respectively. Those theoretical expressions and the experimental results with water drops in silicone oil by Garton and Krasucki [10] and Torza, et al. [12] are compared in Fig. A1 with authors' results in an intermittent or steady field. Here, $(D_p/D_n)_{eq}$ obtained in an alternating field is plotted against the root-mean-square value of normalized field strength, $\bar{p}$, and $(D_p/D_n)_{max}$ obtained in an intermittent field is plotted against both p_i and p_f corresponding to E_i and E_f, respectively. The conditions of the systems assumed or used in those studies are summarized in Table A1. Fig. A1 shows that every theory underestimates the drop deformation and that an intermittent field with a moderate frequency yields a larger deformation of drops than the steady or alternating (f = 60 Hz) field, resulting in a burst of drops at lower critical strength.

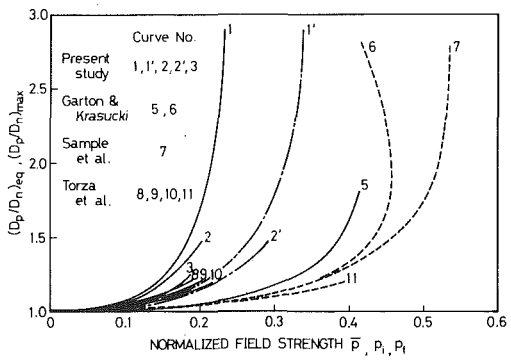

Fig. A1 Comparison of drop distortions in present and previous studies

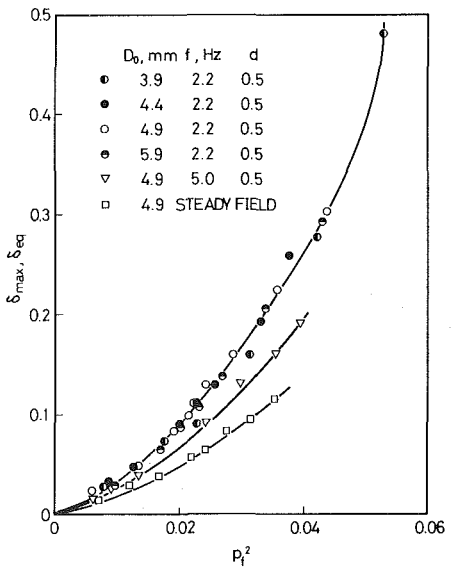

Fig. A2(a)

According to the theory of Allan and Mason [9] and Torza, et al. [12], the steady deformation of drops remaining nearly spherical is expressed as

$$\delta \sim \bar{p}^2 \tag{A-1}$$

where

$$\delta = (D_p - D_n)/(D_p + D_n)$$

Fig. A2(a) shows the relations between δ_{max} or δ_{eq} and $p_f{}^2$ obtained in the present study under an intermittent or steady field. Apparently the linearity between δ_{max} or δ_{eq} and $p_f{}^2$ does not exist in the whole range of the experiments. In Fig. A2(b), these relations in a limited range of p_f are enlarged and shown together with the relations between δ_{eq} and $\bar{p}^2$ obtained in the experiments by Allan and Mason [9] and Torza, et al. [12] under a steady or alternating (f = 60 Hz) field. The dependence of δ_{eq} on $\bar{p}^2$ (= $p_f{}^2$ for steady field) obtained in the present study under a steady field agrees quantitatively with the experimental results by Torza, et al. [12], both showing the approximate linearity between δ_{eq} and $\bar{p}^2$ in the lower range of $\bar{p}$, though they deviate from the theoretical prediction by Torza, et al. [12]. Under an intermittent field, the linearity between δ_{max} and $p_f{}^2$ approximately holds only in a more limited range of p_f.

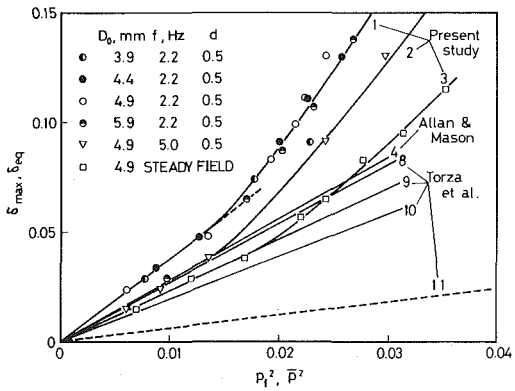

Fig. A2(b)

Fig. A2 Examination of linear variation of δ with p^2 predicted for steady deformation

Table A1 Conditions of systems in present and previous studies

	Curve No.	E/T*	f, Hz	ϵ_d/ϵ_c	σ, mN/m	ν_d/ν_c	p_{cr}
Present study	1†	E	2.2	28	27	3.7×10^{-3}	0.23
	1′	E	2.2	28	27	3.7×10^{-3}	0.34
	2	E	5.0	28	27	3.7×10^{-3}	—
	2′	E	5.0	28	27	3.7×10^{-3}	—
	3	E	0	28	27	3.7×10^{-3}	—
Allan and Mason [9]	4	E	0	∞	30	2×10^{-4}	—
Garton and Krasucki [10]	5	E	60	33	51	3×10^{-5}	0.41
	6	T	0	∞	—	—	0.45
Sample, et al. [11]	7	T	0	∞	—	—	0.535
Torza, et al. [12]	8	E	60	29	30	2×10^{-4}	—
	9	E	0	29	30	2×10^{-4}, 8×10^{-6}	—
	10	E	60	29	30	8×10^{-6}	—
	11	T	0, 60	29	30	2×10^{-4}, 8×10^{-6}	—

* E: experimental
T: theoretical
† Curves 1, 2 are related to p_f while 1′, 2′ are related to p_i.

A Parametric Analysis of the Performance of Internally Finned Tubes for Heat Exchanger Application

R. L. Webb
Associate Professor.

M. J. Scott
Graduate Assistant.

Department of Mechanical Engineering,
The Pennsylvania State University,
University Park, Penn. 16802

This paper presents a parametric analysis of the performance of internally finned tubes in turbulent forced convection for application to heat exchangers. The analysis compares the performance of an internally finned tube exchanger with that of an exchanger having internally smooth tubes. The calculations are performed for three important design cases.

By variation of the internal fin geometric parameters, we define the performance benefits and the preferred geometrical parameters which allow use of minimum tube material. The best axial internal fins offer less than 10 percent material savings for equal pumping power and heat duty. However, the material savings are increased to 49 percent using internal fins having a 30 deg helix angle. The heat exchanger UA may be increased 35 to 40 percent for equal pumping power and total tubing length. Pumping power reduction of 42 percent is obtained using five fins 2 mm in height with zero helix angle. The majority of the calculations are performed for water ($Pr = 3$) and include the effect of fin efficiency. The paper also compares the performance of internally finned and internally roughened tubes.

Introduction

Internally finned tubes have been developed for tube side heat transfer augmentation and are commercially available in copper and aluminum. The designer has little basis for selecting the "optimum" internal fin geometry, unless equipped with generalized heat transfer and friction correlations and quantitative relations for performance evaluation criteria. We recognize that "optimum" is a controversial term. In this work, "optimum" means to maximize (or minimize) the objective function for minimum tube material content.

Internally finned tubes are only one possibility for tube side augmentation. Other methods include internal roughness geometries, twisted tape inserts, and wire coil inserts. Whether an internally finned tube is the best choice depends on a quantitative assessment of the resulting heat exchanger design using the competing augmentation techniques. Our analysis will establish "optimum" internal fin geometries and compare the resulting performance with that of a competing augmentation technique (roughness).

Correlations for Internally Finned Tubes

A generalized correlation for the turbulent heat transfer and friction characteristics of internally finned tubes in single phase forced convection was not established until 1977. This is an empirical correlation developed by Carnavos [1] based on his air flow tests of 21 internal fin geometries. More recent data [2] on 11 geometries have established the Prandtl number dependence, via tests with water and ethylene glycol-water mixtures. These recent data span Prandtl numbers between 6 and 30. Carnavos concludes that internally finned and smooth tubes have the same Prandtl number dependence, $Nu \propto Pr^{.4}$ for heating.

Fig. 1 illustrates an internally finned tube and defines its geometric variables, D_i, p, e, t, and α (the helix angle). The helix angle is measured between the fin axis and the tube axis. In dimensionless terms, the variables are p/e, e/t, e/D_i, and α. Most analyses of internal fins use the number of fins (n) rather than the pitch (p) as a geometric parameter. The variables p and n are related by the equation $n = \pi D_i/p$. Use of the dimensionless variable p/e allows generalization of results, since a specified n fixes the tube diameter. If geometric similarity is maintained by keeping e/t = constant, analysis for different values of p/e and e/D_i is applicable to any tube diameter.

Carnavos uses the Dittus-Boelter equation as the basis for his heat transfer correlation. If the hydraulic diameter concept is applied to internally finned tubes, the Dittus-Boelter equation would directly apply. Carnavos develops a correction factor, $F_H \equiv Nu/Nu_{DB}$, to account for the deviation from the Dittus-Boelter equation based on hydraulic diameter. Carnavos' heat transfer correlation is given by equation (8) in Appendix I.

The friction correlation is developed on a similar basis by presenting a correction to the Blasius friction factor equation based on hydraulic diameter. The friction correlation is given by equation (13) in Appendix I.

Carnavos' air, water and glycol data for 11 tubes were correlated ±10 percent by equations (1) and (2) for $10{,}000 < Re < 80{,}000$. Equation (2) contains $s^{.75}\alpha$ rather than $\cos^{.5}\alpha$ as modified by Carnavos [2].

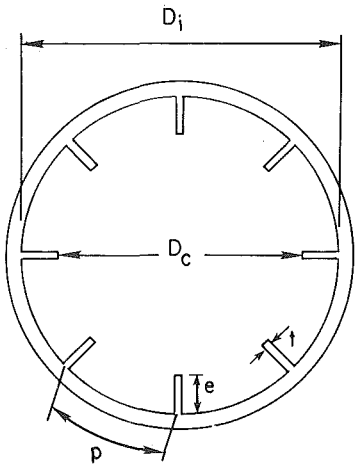

Fig. 1 Cross section of internally finned tube

Contributed by the Heat Transfer Division for publication in the JOURNAL OF HEAT TRANSFER. Revised manuscript received by the Heat Transfer Division July 19, 1979.

Selection of Geometrical Parameters and Operating Conditions

We wish to determine the geometric parameters, p/e and e/D_i, which require the minimum fin material content for a given performance objective. In the absence of fin efficiency considerations, common sense suggests that the fin material content is directly proportional to the fin thickness. Thus, minimum fin thickness is desirable. However, manufacturing considerations will establish a minimum practical fin thickness.

Examination of the 23 tube geometries tested by Carnavos [1,2] suggests that the maximum permissible aspect ratio is $e/t = 3.5$, which is more optimistic than offered by present manufacturing technology. As the fin height is increased, its thickness will be increased by the relation $t = e/3.5$, except we will assume a minimum practical fin thickness of $t_{\min} = .4$ mm (.016 in.). The maximum fin height to be considered is $e = 4$ mm, twice the value tested by Carnavos. We will also include an optimistic case for which the fin thickness is maintained at $t = .4$ mm for all fin heights.

The analytical calculations are performed for a copper tube of constant tube diameter ($D_i = 17.78$ mm = 0.70 in.) and wall thickness ($t_w = 0.711$ mm = 0.028 in.). The majority of the calculations are performed for $\mathrm{Re}_s = 25{,}000$ and water at Pr = 3. These calculations will include the effect of fin efficiency. The use of lower heat transfer coefficient fluids will yield higher fin efficiency.

Performance Evaluation Criteria

Using quantitative performance evaluation criteria, we may establish the heat exchanger performance as a function of the internally finned tube geometric variables. Our method compares the performance of the internally finned tube exchanger with that of an exchanger having internally smooth tubes. Both exchangers have equal entering flow conditions (temperature, pressure and mass flow rates). Similar criteria were previously outlined by Webb and Eckert [4] for internally roughened tubes. These criteria have been modified for internally finned tubes, as shown in Appendix II. Table 1 shows the criteria applied to internally finned tubes for three cases of interest:

Case A: Reduced tube material volume for equal pumping power and heat duty.

Case B: Increased heat duty (UA) for equal pumping power and total length of heat exchanger tubing (NL).[1]

Case C: Reduced pumping power for equal heat duty and total length of heat exchanger tubing (NL).

The parameter $r \equiv h_s A_s / h_0 A_0$ is the thermal resistance ratio for the reference smooth tube exchanger design. Normally, internally finned tubes would not be considered unless the dominant thermal resistance is on the tube side. If $r = 0.5$, the smooth tube exchanger has twice as much thermal resistance on the tube side as on the outside. If $r = 0$, a prescribed heat flux or temperature boundary condition exists, and the total resistance is on the tube side. The last column of Table 1 gives the ratio of the augmented-to-smooth tube side mass velocity required to meet the constraints. By continuity, $GNA_{fa} = G_s N_s A_{fn}$ where N is the number of tubes in parallel, and A_f is the cross sectional flow area per tube. The ratio of parallel flow circuits is $N/N_s = G_s A_{fn}/GA_{fa}$. Then, the ratio of the total lengths of heat exchanger tubing is $NL/N_s L_s = (G_s A_{fn} L)/(GA_{fa} L_s)$. The ratio N/N_s is the ratio of the flow frontal areas of the finned and smooth tube exchangers. In most cases, $N/N_s > 1$, so the finned tube exchanger will require greater frontal area than the smooth tube design. The objective functions are dependent on r for cases A and B. The Case A equations in Table 1 are for $r = 0$. See Appendix II for $r \neq 0$.

Analysis for Material Reduction (Case A, r = 0)

Fig. 2[2] shows the results for Case A with axial fins ($\alpha = 0$) at $\mathrm{Re}_s = 25{,}000$. For Case A, the pumping power and heat duty of the internally finned and smooth tube exchangers are equal. The objective function compared is V/V_s, the ratio of tube material volumes for the 0.711 mm (0.028 in.) wall thickness tube. The ratio V/V_s is plotted versus the mass velocity ratio, G_s/G, with the fin height (e) and the number of fins (n) as parameters. The "optimum" performance occurs at mini-

[1] N is the number of flow circuits in parallel, and L is the length of each flow circuit. Therefore, NL is the total length of tubing in the exchanger.

[2] In all cases the calculations were performed for $n = 5, 8, 12, 16, 25, 32$, and 40. "Tic marks" are drawn on all curves at the above n-values. The number of fins may be read from the graphs by counting the number of "tic marks" from the extreme left side of each curve where $n = 5$.

Table 1 Relative performance of internally finned tubes used in a two fluid heat exchanger

Case	Constraints	Objective Function	Relative Mass Velocity (G_s/G)
A	$\frac{P}{P_s} = \frac{Q}{Q_s} = 1, \mathrm{r} = 0$	$\frac{V}{V_s} = \frac{(f/f_s)^{1/2}}{(\mathrm{St}/\mathrm{St}_s)^{3/2}} \frac{A_n}{A_a} \frac{M}{M_s}$	$\frac{G_s}{G} = \frac{(f/f_s)^{1/2}}{(\mathrm{St}/\mathrm{St}_s)^{1/2}}$
B	$\frac{P}{P_s} = \frac{NL}{N_s L_s} = 1$	$\frac{UA}{U_s A_s} = \frac{1+r}{\left[\frac{(f/f_s)}{(A_a/A_n)^2}\right]^{1/3} \frac{\mathrm{St}_s}{\mathrm{St}} + r}$	$\frac{G_s}{G} = \left(\frac{f}{f_s} \cdot \frac{A_a}{A_n}\right)^{1/3}$
C	$\frac{Q}{Q_s} = \frac{NL}{N_s L_s} = 1$	$\frac{P}{P_s} = \frac{f/f_s}{(\mathrm{St}/\mathrm{St}_s)^3 (A_a/A_n)^2}$	$\frac{G_s}{G} = \frac{\mathrm{St}}{\mathrm{St}_s} \cdot \frac{A_a}{A_n}$

Nomenclature

A = heat transfer surface area, internally finned tube (A_a), smooth tube (A_n), surface area on outer tube surface (A_o)

A_f = flow area, internally finned tube (A_{fa}), smooth tube (A_{fn}), open core flow area is finned tube (A_{fc})

D = diameter, smooth tube or finned tube to base of fins (D_i), diameter of internally finned tube if fins melted down (D_e), hydraulic diameter ($D_h = 4 A_{fa} L/A_a$)

e = fin height

f = friction factor (based on D_h for internal fins), Blasius friction factor ($f_B = .046/\mathrm{Re}^{.2}$)

F_F, F_H = defined by equations (5) and (11)

G = mass velocity

h = heat transfer coefficient

L = length of flow circuit in heat exchanger

M = tube material volume per unit length of tube

n = number of internal fins

N = number of flow circuits in parallel

Nu = Nusselt number, ($\mathrm{Nu}_{DB} = .023\ \mathrm{Re}^{.8} \mathrm{Pr}^{.4}$)

p = transverse pitch of internal fins ($p = \pi D_i/n$)

P = pumping power; e.g. N-m/hr or horsepower

Pr = Prandtl number

Q = exchanger heat duty, e.g., Watts or Btu/hr

$r = h_s A_s / h_0 A_{0s}$

Re = Reynolds number, smooth tube ($D_i G_s/\mu$), internally finned tube ($D_h G/\mu$)

t = fin thickness

t_w = tube wall thickness

U = overall heat transfer coefficient

V = volume of tube material in heat exchanger

α = helix angle (angle between fin and tube axis)

μ = dynamic fluid viscosity

Subscripts

s = internally smooth tubes; heat exchanger with internally smooth tubes

o = outer surface of the tube

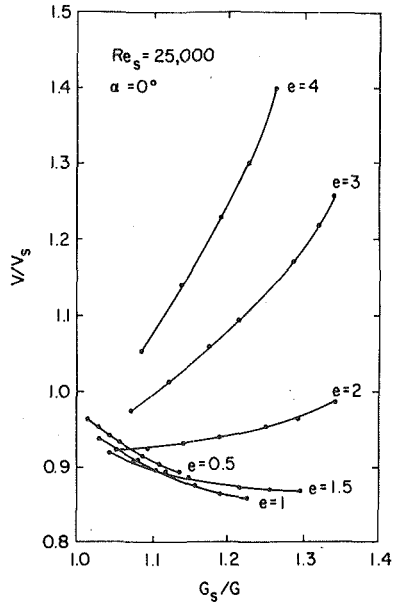

Fig. 2 V/V_s versus G_s/G for axial fins (Case A)

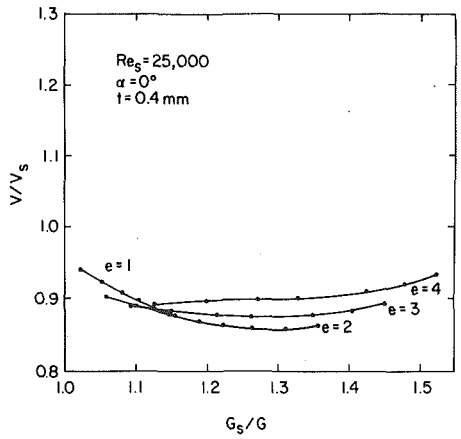

Fig. 3 V/V_s versus G_s/G for axial fins 0.4 mm thick (Case A)

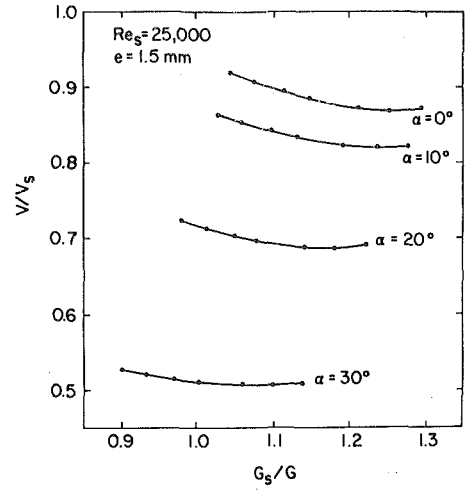

Fig. 4 V/V_s versus G_s/G for 1.5 mm high helical fins (Case A)

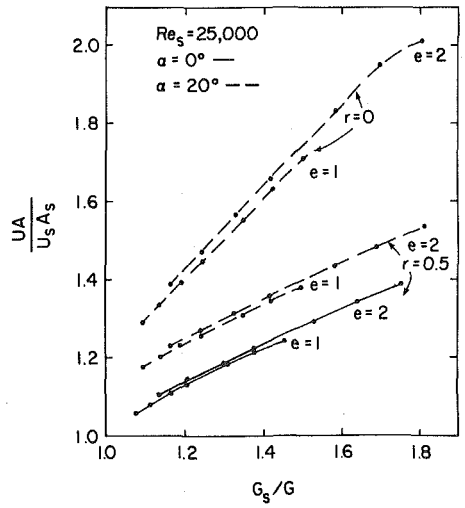

Fig. 5 UA/U_sA_s versus G_s/G for e = 1 and 2 mm high fins for r = 0 and 0.5 (Case B)

mum V/V_s. Fig. 2 shows that minimum material content occurs with e = 1 to 1.5 mm fin height. The material savings tend to increase with increasing number of fins. However, increasing n requires larger heat exchanger frontal area. The larger frontal area is compensated for by a reduced exchanger length. For e = 1.5, 16 fins give approximately the same material reduction as obtained with a greater number of fins. Since heat exchanger cost is usually more dependent on shell diameter than on length, 16 fins at e = 1.5 mm or 25 fins at e = 1 mm appear to be preferred geometries for axial fins. The material savings, about 12 percent, appear to be marginal.

The increasing values of V/V_s with increasing fin height are due to the increasing fin thickness with fin height. Fig. 3 is prepared to show the degree of this penalty. All parameters of Figs. 2 and 3 are the same, except Fig. 3 is for a constant fin thickness (t = .4 mm). Fig. 3 shows that constant thickness fins 2 mm or higher require greater tube material for equal pumping power and heat duty. There is no incentive to develop manufacturing techniques for 0.4 mm thick, high fins.

Equations (1) and (2) show that the internally finned tube performance is increased by making the fins with a helix angle (α), which causes the flow to spiral along the tube length. Fig. 4 shows V/V_s versus G_s/G with e = 1.5 for $0 < \alpha < 30$ deg. A 30 deg helix angle with 16 fins provides V/V_s = 0.51, compared to 0.88 for axial fins. Also, the 30 deg helix angle requires a smaller frontal area to satisfy the pumping power criterion. The use of helical fins offers a dramatic improvement in the material savings of internally finned tubes.

Performance Analysis for Increased Heat Duty (Case B)

In this application, the Case B performance analysis of Table 1 applies. We wish to determine the UA increase for constant pumping power and total tubing length (NL). Fig. 5 shows UA/U_sA_s versus G_s/G for two fin heights (e = 1 and 2 mm) and two helix angles (0 and 20 deg). The calculations are performed for r = 0 and 0.5. The greatest performance improvement is obtained with α = 20 deg. Approximately equal performance is obtained with the 1 and 2 mm high fins. For r = .5, 32 fins 1 mm height provides the same performance as 16, 2 mm high fins (UA/U_sA_s = 1.35). Both fin geometries require the same frontal area increase, 51 percent. The figure shows that relatively large frontal area increases are required to obtain a significant UA increase for the constant pumping power criterion. Fig. 5 also shows UA/U_sA_s for the r = 0 condition with e = 1 and 2 mm fin heights and α = 20 deg. Larger UA increases result when the total thermal resistance is on the tube side.

Compared to the smooth tube exchanger, the internal fin designs provide greater UA for the same total heat exchanger tubing length. Since the internal fin designs contain more tube material than the smooth tube exchanger, the designer is interested in the UA increase per unit of material increase. Table 2 shows the UA increase is approximately equal to the increase of tube material.

Rather than use internally finned tubes, the designer may consider the use of additional smooth tube surface. Compared to the 32 fin, e

Table 2 Comparison of UA/V for constant pumping power and total tubing length (α = 20 deg)

e	t	n	V/V_s	UA/U_sA_s	$\frac{UA/U_sA_s}{V/V_s}$
1 mm	0.4 mm	32	1.32	1.34	1.01
2	0.571	16	1.42	1.35	0.95

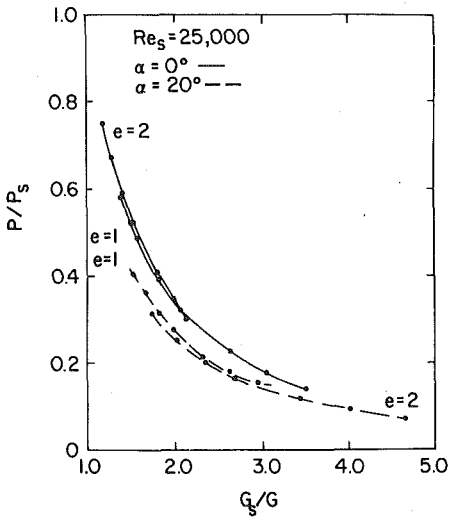

Fig. 6 P/P_s versus G_s/G for e = 1 and 2 mm high fins (Case C)

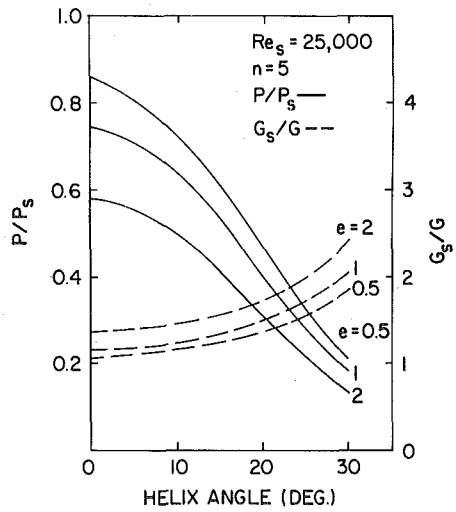

Fig. 7 P/P_s versus helix angle for 0.5, 1 and 2 mm high fins (Case C)

= 1 mm design, the designer may use 34 percent greater length of smooth tubes for the same total tube material volume. Equal friction power will be obtained if the modified smooth tube exchanger is 24 percent longer and has 8 percent larger frontal area. At this lower Reynolds number, the 34 percent larger surface area will provide 28.6 percent larger UA than the original smooth tube design. Therefore, for equal tube material volume and friction power, the internal fin exchanger provides a 33.5 percent larger UA versus 28.6 percent larger UA for the modified smooth tube exchanger, both having the same tube material content. Therefore, the allowable cost premium for the internally finned tubes is 1.34/1.286 = 1.04 for cost effectiveness equal to that provided by smooth tubes.

Analysis for Reduced Friction Power (Case C)

Fig. 6 shows the relative friction power (P/P_s) for e = 1 and 2 mm with α = 0 and 20 deg. This figure shows that large friction power reductions may be obtained. However, large frontal area increases are associated with small values of P/P_s. If the frontal area increase is to be minimized, a small number of fins is preferred. The preferred helix angle and fin height are revealed by examining Fig. 7, drawn for n = 5. The use of high fins with zero helix angle provides the smallest P/P_s with minimum frontal area increase (G_s/G). Because a small number of fins are used, it is possible to use a large fin height without incurring a significant material increase penalty. For example, with n = 5, e = 2 mm, and α = 0, we may obtain P/P_s = 0.58 with a frontal area increase of about 40 percent. This design will have 14 percent greater tube material than the reference smooth tube design.

Effect of Fin Efficiency on Calculated Results

The previous calculations were performed for water (Pr = 3) at Re_s = 25,000. The results include the effect of the temperature gradient (fin efficiency) in the fin. For n = 16 and α = 20 deg the fin efficiency ranged from 0.97 with e = 1 mm to 0.94 with e = 2 mm. At Re_s = 75,000, the corresponding fin efficiency range is 0.94 to 0.87. If fluids which yield lower heat transfer coefficients are used, higher fin efficiencies will result.

For 100 percent fin efficiency, the values of V/V_s are 1.24 to 5.1 percent smaller than the V/V_s values for water. At a larger Reynolds number (Re_s = 75,000), the V/V_s for 100 percent fin efficiency is 10 percent smaller for e = 2 mm, n = 16, and α = 20 deg. Therefore, the calculated V/V_s values will not be significantly smaller for lower heat transfer coefficient fluids.

Internal Fins versus Internal Roughness

Rough surfaces and internal fins are competing augmentation techniques. One manufacturer [6] is presently offering a two-dimensional rib roughness on the internal tube surface. The rib roughness is applied with a helix angle. No performance data have been published for this proprietary design. Webb and Eckert [4] have published the results of a performance analysis based on experimental data obtained with an internal two-dimensional rib roughness. The ribs of this roughness are oriented 90 deg to the flow and spaced ten times the rib height. Table 3 compares the performance of internal roughness and internal fins for the three design cases of interest. The comparison is made for Re_s = 25,000 and Pr = 3 using the preferred roughness and internal fin geometric parameters for each case.

Table 3 Performance comparison of internal fins and two-dimensional rib roughness D_i = 17.78 mm, t_w = .711 mm, Re_s = 25,000, Pr = 3

Augmentation Geometry	$\frac{V}{V_s}$	$\frac{G_s}{G}$	e mm	n	$\frac{UA}{U_sA_s}$	$\frac{G_s}{G}$	e mm	n	$\frac{P}{P_s}$	$\frac{G_s}{G}$	e mm	n
Two-dimensional rib roughness (p/e = 10)	0.54*	1.30	0.19	—	1.28**	1.40	0.12	—	0.64	1.40	0.06	—
Internal fins α = 0 deg	0.88*	1.22	1.5	25	1.22**	1.40	2	16	0.58	1.40	2	5
Internal fins α = 20 deg	0.69*	1.15	1.5	25	1.36**	1.41	2	16	0.31	1.77	2	5

* r = 0 ** r = 0.5

For Case A (reduced V/V_s) the performance is dependent on the resistance ratio, r. Our Case A comparison is for $r = 0$, which means all of the thermal resistance is on the tube side. The internal roughness provides a larger material reduction than axial internal fins (46 percent versus 12 percent). The comparison is improved using 20 deg helical fins, which give a 31 percent material reduction. The greater material requirement of the internal fins is due, in part, to their greater material content per unit length, 40 percent. The roughness elements contribute about 1 percent to the tubing material.

For Case B (increased heat duty), the 20 deg helical fins provide a 6 percent larger UA than the roughness for equal frontal area. However, the helical fins require 47 percent more tube material, due to the relatively greater tube material content per unit length.

The axial internally finned tubes appear to offer a performance advantage for Case C (reduced pumping power), $P/P_s = 0.58$ versus 0.64 for the roughness. Both designs require equal frontal area. Accounting for the 14 percent greater material content of the finned tube, the pumping power reduction per unit material content is approximately equal for both augmentation types.

The rib roughness has a stronger Prandtl number dependency than smooth or internally finned tubes. Therefore, its relative performance will improve with increasing Prandtl number. The rib roughness would appear to be well suited to high Prandtl number fluids, such as oils. A recent study [5] has shown that the performance of two-dimensional rib roughness improves if the ribs are applied at a helix angle, approximately 45 deg. This characteristic will improve the roughness performance, relative to internal fins.

An additional factor to be considered is the effect of fouling on the two competing augmentation techniques. Due to the larger internal surface area, a given fouling deposit thickness will cause a smaller performance decrement for internally finned than for internal roughness. The comparative fouling behavior of internally finned and internal roughness, of the preferred geometries, has not been established.

It may not be necessary to increase the exchanger frontal area if the reference exchanger is of multi-pass design. A two-pass smooth tube design may be replaced by a one-pass internal fin design ($G_s/G = 2$) yielding 60 percent pumping power savings. Similarly, a three pass smooth tube exchanger may be replaced by a two-pass internal fin design ($G_s/G = 1.5$) yielding $UA/U_sA_s = 1.4$ with no frontal area increase (Fig. 5).

Conclusions

1 This analysis has identified preferred internal fin geometric parameters and defines the benefits of internally finned tubes for three design cases.
2 Axial internal fins offer material savings less than 10 percent for constant pumping power and heat duty. The use of high fins ($e \geq 2$ mm) of reduced thickness is of no advantage.
3 Formation of the fins at a helix angle offers material savings on the order of 30 to 50 percent
4 The heat exchanger UA may be increased 35 to 40 percent using 16, 2 mm high fins at a 20 deg helix angle in the 17.78 mm tube.
5 To obtain reduced pumping power with minimum frontal area, a small number of relatively high axial fins are preferred. For $n = 5$, $e = 2$, a 42 percent pumping power reduction is predicted.
6 It is possible to select internal fin geometries which provide higher performance than two-dimensional rib roughness for Cases B and C. However, more tubing material is required. Roughness yields greater material reduction (Case A).

Acknowledgment

This study was supported by Department of Energy contract number EG-78-S-02-4649, under the technical cognizance of Mr. M. J. Perlsweig and Dr. W. H. Thielbahr

References

1 Carnavos, T. C., "Cooling Air in Turbulent Flow with Internally Finned Tubes," AIChE Paper No. 4, 17th National Heat Transfer Conference, Salt Lake City, UT, Aug. 1977.
2 Carnavos, T. C., "Heat Transfer Performance of Internally Finned Tubes in Turbulent Flow," AIChE Paper presented at the 18th National Heat Transfer Conference, San Diego, CA, Aug. 1979.
3 Kubanek, G. R. and Miletti, D. L., "Evaporative Heat Transfer and Pressure Drop Performance of Internally Finned tubes with Refrigerant 22," ASME Paper No. 77-WA/HT-25.
4 Webb, R. L. and Eckert, E. R. G., "Application of Rough Surfaces to Heat Exchanger Design," *Int. Journal of Heat and Mass Transfer*, Vol. 15, 1972, pp. 1647–1658.
5 Han, J. C., Glicksman, L. R., and Rohsenow, W. M., "An Investigation of Heat Transfer and Friction for Rib-Roughened Surfaces," *International Journal of Heat and Mass Transfer*, Vol. 21, No. 8, 1978, pp. 1133–1142.
6 Withers, Jr., J. G. and Klaus, K. R., U.S. Patent 3,847,212, "Heat Transfer Tube having Multiple Internal Ridges."

APPENDIX I

This appendix presents an assessment of the Carnavos correlations and attempts to define a physical significance for the correlating parameters.

The heat transfer correlation is given as:

$$\frac{\mathrm{Nu}}{\mathrm{Pr}^{0.4}} = 0.023\,\mathrm{Re}^{0.8}\left(\frac{A_{fa}}{A_{fc}}\right)^{0.1}\left(\frac{A_n}{A_a}\right)^{0.5} s^3\alpha \tag{3}$$

Let

$$\mathrm{Nu}_{DB} \equiv 0.023\,\mathrm{Re}^{0.8}\mathrm{Pr}^{0.4} \tag{4}$$

Equation (4) is the Dittus-Boelter equation defined for internally finned tubes using the hydraulic diameter (D_h) in the Nusselt and Reynolds number definitions. Thus, we may write

$$\frac{\mathrm{Nu}}{\mathrm{Nu}_{DB}} = \left(\frac{A_{fa}}{A_{fc}}\right)^{0.1}\left(\frac{A_n}{A_a}\right)^{0.5} s^3\alpha \equiv F_H \tag{5}$$

Examination of Carnavos' data shows that $0.64 < F_H < 0.96$. This means that the heat transfer coefficient of internally finned tubes is 4 to 36 percent below that predicted by the Dittus-Boelter equation based on hydraulic diameter. The empirical terms which comprise F_H are correction factors. These correction factors may be expressed in terms of the internally finned tube geometry using Fig. 1.

In Fig. 1, D_i is the diameter to the base of the fins, and D_c is the diameter of the "core region" flow area. The free flow area of the tube is $\pi D_e^2/4$, where D_e is inside diameter of the tube if the fins were melted down.

$$\frac{A_n}{A_a} \equiv \frac{\text{Surface area of plain tube of diameter } D_i}{\text{Surface area of internally finned tube}}$$

$$\frac{A_n}{A_a} = \frac{\pi D_i}{\pi Di + 2\mathrm{ne}/\cos\alpha} = \frac{D_iD_h}{D_e^2} \tag{6}$$

$$\frac{A_{fa}}{A_{fc}} = \frac{\text{Free flow area}}{\text{Core region flow area}}$$

$$\frac{A_{fa}}{A_{fc}} = \left(\frac{D_e}{D_c}\right)^2 = \left[\frac{D_i}{D_e}\left(1 - \frac{2e}{D_i}\right)\right]^{-2} \tag{7}$$

Substitution of equations (6) and (7) in (5) gives:

$$\frac{\mathrm{Nu}}{\mathrm{Nu}_{DB}} = \left[\frac{D_i}{D_e}\left(1 - \frac{2e}{D_i}\right)\right]^{-.2}\left(\frac{D_iD_h}{D_e^2}\right)^{0.5} s^3\alpha \tag{8}$$

Carnavos friction correlation is

$$f = \frac{0.046}{\mathrm{Re}^{0.2}}\left(\frac{A_{fa}}{A_{fn}}\right)^{0.5} s^{0.75}\alpha \tag{9}$$

Let

$$f_B = 0.046\,\mathrm{Re}^{-.2} \tag{10}$$

Equation (10) is the Blasius friction factor defined for internally finned tubes using the hydraulic diameter (D_h) in the Reynolds number definition. Thus, we have

$$\frac{f}{f_B} \equiv F_f = \left(\frac{A_{fa}}{A_{fn}}\right)^{0.5} s^{0.75}\alpha \tag{11}$$

$$\frac{A_{fa}}{A_{fn}} = \frac{\text{Free flow area}}{\text{Nominal flow area}} = \left(\frac{D_e}{D_i}\right)^2 \tag{12}$$

Substitution of equation (11) and (12) in (9) gives

$$\frac{f}{f_B} = \frac{D_e}{D_i} s^{0.75}\alpha \tag{13}$$

Equations (8) and (13) present Carnavos' heat transfer and friction correlations in terms of the internally finned tube geometric variables. The "melted down" diameter (D_e) is given by

$$D_e = \left(D_i^2 - \frac{4\text{net}}{\pi\cos\alpha}\right)^{1/2} \tag{14}$$

Consider the limiting case for very thin fins, e.g., $t \simeq 0$, for which $D_e = D_i$. Then equations (8) and (13) simplify to

$$\frac{Nu}{Nu_{DB}} = \left(1 - \frac{2e}{D_i}\right)^{-0.2} \left(\frac{D_h}{D_i}\right)^{0.5} s^3\alpha \tag{15}$$

$$\frac{f}{f_B} = s^{0.75}\alpha \tag{16}$$

If the zero thickness fins are axial ($\alpha = 0$), equation (16) shows that the hydraulic diameter correlation applies to the friction correlation. For smooth tubes, the Colburn analogy shows that $St \simeq f/2$ for Pr = 1. One may expect a similar relation for internally finned tubes. Comparison of equations (15) and (16) shows that such a Reynolds analogy relationship does not exist. This result is unexpected, since no flow separation should occur within the channel.

When the fins are applied in a helical manner, equations (15) and (16) show that the Nusselt number increase is greater than the friction increase. For example, with $\alpha = 30$ deg, the friction factor is increased 10 percent and the Nu is increased 54 percent relative to axial fins ($\alpha = 0$). In [1] Carnavos recommended $f/f_B \propto \cos^{.5}\alpha$ and modified the relation to $f/f_B = \cos^{.75}\alpha$ in [2]. This modification was primarily based on the data for two tubes having $\alpha = 27$ and 30 deg helix angles. The correlation underpredicts the friction factor for the $\alpha = 27$ deg tube. Therefore, there may be some uncertainty regarding the effect of helix angle.

APPENDIX II

This appendix presents derivation of the performance evaluation criteria for internally finned tubes. The criteria are modified from those for internally roughened tubes [4]. By definition,

$$\frac{1}{U_sA_s} = \frac{1}{h_sA_s} + \frac{1}{h_0A_{0s}} \tag{17}$$

Equation (17) can be written:

$$\frac{1}{U_sA_s} = \frac{1}{h_sA_s}(1 + r). \tag{18}$$

Similarly, for the internally finned tubes,

$$\frac{1}{UA} = \frac{1}{hA} + \frac{1}{h_0A_0} = \frac{1}{hA}\left(1 + r\frac{hA_a}{h_sA_n}\right) \tag{19}$$

Combining equations (18) and (19), we obtain the UA ratio for the internally finned and smooth tube heat exchangers

$$\frac{UA}{U_sA_s} = \frac{hA}{h_sA_s}\left(\frac{1 + r}{1 + r\dfrac{hA_a}{h_sA_n}}\right) \tag{20}$$

which can be written as

$$\frac{UA}{U_sA_s} = \frac{A}{A_s}\left(\frac{1 + r}{\dfrac{h_s}{h} + r\dfrac{A_a}{A_n}}\right) \tag{21}$$

The heat transfer coefficient can be written in terms of Stanton number:

$$\frac{h}{h_s} = \frac{\text{St}}{\text{St}_s}\frac{G}{G_s} \tag{22}$$

Substitution of equation (22) in (21) yields

$$\frac{UA}{U_sA_s} = \left(\frac{A}{A_s}\right)\frac{1 + r}{\dfrac{\text{St}_sG_s}{\text{St}G} + r\dfrac{A_a}{A_n}} \tag{23}$$

The friction power ratio for the internally finned and smooth tube exchangers is

$$\frac{P}{P_s} = \frac{f}{f_s}\frac{A}{A_s}\left(\frac{G}{G_s}\right)^3 \tag{24}$$

By elimination of G/G_s from equations (23) and (24), we obtain

$$\frac{UA}{U_sA_s} = \frac{(1 + r)}{\left[\dfrac{f/f_s}{(P/P_s)(A/A_s)^2}\right]^{1/3}\dfrac{\text{St}_s}{\text{St}} + \dfrac{r(A_a/A_n)}{A/A_s}} \tag{25}$$

The surface area ratio A/A_s is defined by

$$\frac{A}{A_s} = \frac{NL}{N_sL_s}\frac{A_a}{A_n} \tag{26}$$

Defining M/M_s as the tube material volume per unit tube length, the heat-exchanger tubing material volume ratio is

$$\frac{V}{V_s} = \frac{NL}{N_sL_s}\frac{M}{M_s} \tag{27}$$

The general equation (25) and equations (26) and (27) are employed to obtain the equations presented in Table 1. For example, in Case B, $P/P_s = NL/N_sL_s = 1$, and by equation (26), $A/A_s = A_a/A_n$. Substitution of these values in equation (26) gives the "objective function" equation for Case B in Table 1. The "relative mass velocity" equation of Table 1 is obtained from equation (24). A similar procedure is used to obtain the equations for Case C in Table 1.

An iterative solution is required for Case A when $r \neq 0$, since equation (25) cannot be explicitly solved for A/A_s. Using $P/P_s = UA/U_sA_s = 1$, equation (25) may be written

$$\frac{A}{A_s} = \frac{(f/f_s)^{1/2}/(\text{St}/\text{St}_s)^{3/2}}{\left[1 + r\left(1 - \dfrac{N_sL_s}{NL}\right)\right]^{3/2}} \tag{28}$$

Assume a value for N_sL_s/NL and calculate A/A_s from equation (28). Then solve for the new N_sL_s/NL using equation (26).

E. M. Sparrow
J. W. Ramsey
C. A. C. Altemani

Department of Mechanical Engineering
University of Minnesota,
Minneapolis, Minn. 55455

Experiments on In-line Pin Fin Arrays and Performance Comparisons with Staggered Arrays

Heat transfer and pressure drop experiments were performed for in-line pin fin arrays to obtain basic data to complement available information for staggered arrays. The experimental data were utilized as input to analyses aimed at establishing performance relationships between in-line and staggered arrays. In the experiments, mass transfer measurements via the naphthalene sublimation technique were employed to determine the row-by-row distribution of the heat (mass) transfer coefficient. Fully developed conditions prevailed for the fourth row and beyond. In general, the fully developed heat transfer coefficients for the in-line array are lower than those for the staggered array, but the pressure drop is also lower. The deviations between the two arrays increase with increasing fin height. With regard to performance, the in-line array transfers more heat than the staggered array under conditions of equal pumping power and equal heat transfer area. On the other hand, at a fixed heat load and fixed mass flow rate, the staggered array requires less heat transfer surface than the in-line array.

Introduction

This paper describes the second and final phase of a study of the heat transfer and pressure drop characteristics of pin fins. Typically, a pin fin is a cylinder attached perpendicular to a wall, with the transfer fluid passing in crossflow over the cylinder. In applications, pin fins may be positioned in arrays that are either staggered or in-line with respect to the flow direction.

The presently available heat transfer and pressure drop information for pin fins is both incomplete and characterized by highly specific geometrical attributes. The largest collection of such information is presented in the Kays-London compendium [1]. Among these, data are given for a single staggered array, the pin fins of which were formed from a continuous length of wire that looped back and forth across the flow cross section. The wire not only spanned the cross section but also ran along the attachment walls and thereby acted as a flow disturbance. Similarly, all of the five in-line arrays reported in [1] were marked by geometrical peculiarities. The only other pin fin data reported prior to the initiation of the present work are those of Norris and Spofford [2]. Those authors dealt with in-line arrays but did not describe their key geometrical characteristics. Furthermore, whereas the measured overall heat transfer rates related to both the fins and the attachment walls, only the fin surface area was employed in evaluating the heat transfer coefficients.

In both [1] and [2], only overall measurements were performed and, therefore, the reported results represent averages with respect to heat transfer from the entire fin array and from the attachment walls. In all cases, the fins spanned the entire height of the flow cross section, and air was the working fluid in all data runs.

The present research differs from the foregoing work in several fundamental ways. First, attention is focused here on the local (i.e., per row) heat transfer characteristics of the pin fins instead of on the overall performance of the heat exchanger. Second, the pin fins investigated here have tip clearance, and the ratio of the fin height to the flow passage height is one of the parameters of the study. Third, a systematic comparison is made between in-line and staggered arrays and, to this end, experiments on the two types of arrays are performed with consonant geometrical characteristics.

Another special feature of the present research is the use of mass transfer measurements as a means of determining heat transfer coefficients. The mass transfer experiments were performed with the naphthalene sublimation technique. In addition to the heat (mass) transfer experiments, measurements were also carried out to determine the per-row pressure drop associated with the presence of the pin fin array. Air was the working fluid in all of the experiments.

Experiments on staggered pin fin arrays were performed during the initial phase of this study and the results are reported in [3]. The second phase of the study, to be reported here, consists of two parts. First, heat (mass) transfer and pressure drop results for in-line pin fin arrays are determined by experiment and are presented along with corresponding results for staggered arrays. Then, this information is employed as input to analyses aimed at comparing the performance of the two types of arrays. Since these analyses and performance comparisons constitute a special feature of the research, it is relevant to discuss their background.

Invariably, the use of techniques and devices to obtain higher heat transfer causes an increase in pressure drop. It has been demonstrated by Bergles and co-workers [4–6] that the advantage or disadvantage of one system relative to another depends on the goals to be achieved and the constraints of the comparison. Possible goals may include, for example, increasing the heat transfer rate or reducing the pumping power or reducing the size of the heat exchanger. The constraints involve fixing several parameters such as mass flow rate, heat load, pressure drop, heat exchanger size, etc. For a particular goal and accompanying set of constraints, one system may be superior to another, but the situation may be reversed for another goal and other constraints.

In the analyses to be performed here, two cases will be considered. In one case, the relative heat transfer capabilities of the staggered and in-line arrays will be determined under the constraints of equal pumping power and equal heat transfer surface area. In the second case, the streamwise lengths (i.e., number of rows) of staggered-array and in-line-array heat exchangers will be calculated for the conditions of equal mass flow rate and equal heat load.

The experiments and their results will be described first because they provide information that is prerequisite to the analyses. The pin fin arrays used in the experiments were comprised of right circular cylinders situated in crossflow in a horizontal, flat rectangular duct. Three sets of arrays were employed during the course of the experiments, respectively characterized by ratios of fin height h to duct height H of 0.29, 0.58, and 0.875. The Reynolds number for the fin array, based on the cylinder diameter and on the velocity in the minimum free-flow area, was varied from 1000 to 9000. The corresponding variation of the Reynolds number of the duct flow approaching the fin array was from 5000 to 35,000.

Contributed by the Heat Transfer Division for publication in the JOURNAL OF HEAT TRANSFER. Manuscript received by the Heat Transfer Division March 29, 1979.

The Experiments

The experimental apparatus employed here is an adaptation of that of [3], thereby obviating the need for a highly detailed exposition. The description of the apparatus is facilitated by reference to the diagrams shown in Fig. 1. The upper diagram portrays the layout of the pin fin array as viewed looking downward at the flat rectangular duct, with its upper wall removed. In the lower diagram, a side view showing a longitudinal cut through the in-line pin fins is presented.

The open circles in the upper diagram depict the deployment of the cylinders that comprise the in-line arrays studied here, the geometry of which is characterized by the transverse and longitudinal spacings S_T and S_L and by the cylinder diameter D. These dimensions were selected so as to facilitate rational comparisons of the present results with the staggered-array results of [3]. For reference purposes, the upper diagram has been structured to enable visualization of the staggered array. The first row of the staggered array is depicted by the open circles, the second row by the blackened circles, the third row by the open circles, the fourth row by the blackened circles, etc. It is easily verified that the cylinders of the staggered array are deployed on equilateral-triangular centers.

For a rational comparison of the two arrays, it was deemed appropriate that the fin surface area per unit volume of flow passage be the same. This condition is fulfilled by the geometric relationship between the arrays that is shown in the upper diagram of Fig. 1. The first, third, fifth, etc. rows are identical for the two arrays, whereas in the second, fourth, sixth, etc. rows, the cylinders of one array are shifted sideways relative to those of the other arrays. Thus, the quantities S_T, S_L, and D are identical for the two arrays, with $S_T/D = 3$, $S_L/D = (\sqrt{3}/2)S_T/D \simeq 2.6$, $D = 0.556$ cm (7/32 in.).

Attention may now be focused on the lower diagram of Fig. 1. This diagram shows the wall attachment of the lower portion of the cylinders and the clearance gap between their upper ends and the top wall of the rectangular duct. The cylinder height exposed to the airflow is denoted by h and the duct height by H. The experiments encompassed h/H ratios of 0.29, 0.58, and 0.875, with $H = 1.91$ cm (0.75 in.). As seen in the diagram, the lower wall of the duct was backed by a base plate against which the cylinders bottomed out, thereby ensuring positive positioning. A recess machined into the underside of the lower wall served as a ventable air space, the presence of which ensured that the insertion and proper seating of cylinders was not resisted by air pressure.

The pin fin arrays used in the experiments contained a total of eighteen rows. This number of rows was more than sufficient for the attainment of fully developed conditions for both heat (mass) transfer and pressure drop.

The flat rectangular duct which served as the host flow passage for the pin fin array was 8.26×1.91 cm (3.25×0.75 in.) in cross section, with an overall length of 173 cm (68 in.). The initial portion of the duct functioned as a hydrodynamic development section, which was followed successively by the test section and the hydrodynamic redevelopment section. These sections were, respectively, about 33, 8, and 14 hydraulic diameters in length (hydraulic diameter ~ 3.1 cm, 1.22 in.). To enable very rapid access (~ a few seconds) to the test section for insertion and removal of mass transfer elements, part of the upper wall of the duct was made removable (see photograph in Fig. 1 of [3]). In addition, to facilitate the pressure drop studies, 25 static pressure taps were installed along the spanwise centerline of the upper wall.

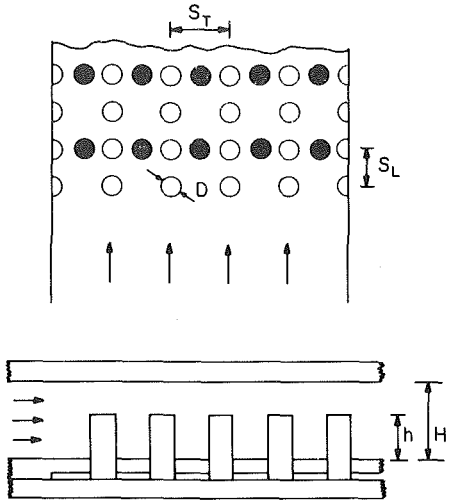

Fig. 1 Diagrams describing the pin fin arrays

The mass transfer elements were stainless steel cylinders whose exposed surfaces were coated with a thin layer of naphthalene. The naphthalene coating covered both the exposed cylindrical surface and the free end of the pin fin, but no coating was applied to the portions of the fin that were seated in the duct wall. There were two stages in the coating process—first, a dipping of the pin fin into a pool of molten naphthalene and then a machining of the solidified naphthalene to obtain the desired dimensions and surface smoothness. The details of the coating procedure are available in [3].

In each data run, only one naphthalene-coated pin fin was employed. The other pin fins of the array were stainless steel cylinders of diameter and height identical to the finished dimensions of the coated pin fin. In the successive data runs, the active element was consecutively placed in the first, second, third, etc. rows—positioned adjacent to the spanwise centerline of the row. In a set of supplementary runs undertaken to assess potential side wall effects, the mass transfer element was consecutively placed at all possible spanwise positions in a given row. These runs indicated the measured mass transfer to be spanwise uniform, thereby testifying to the negligible influence of the side walls.

The experiments were performed in the suction mode, with air being drawn into the test section from the temperature-controlled,

Nomenclature

A = heat transfer area per row
A_{min} = minimum cross sectional area for fluid flow
D = cylinder diameter
D_h = hydraulic diameter of unobstructed duct
$\mathcal{D}$ = naphthalene-air diffusion coefficient
H = duct height
h = fin height
h = heat transfer coefficient
K = per-row mass transfer coefficient, $\dot{m}/(\rho_{nw} - \rho_{nb})$
K_p = per-row pressure loss coefficient, equation (4)
$\dot{m}$ = mass transfer rate per unit area
N = number of rows
Nu = Nusselt number
P = pumping power, $(\dot{w}/\rho)\Delta p$
Pr = Prandtl number
p = static pressure
p_{atm} = atmospheric pressure
Δp = pressure drop
Δp_{array} = pressure drop due to array
Q = heat transfer rate for N rows
Q_{max} = maximum heat transfer rate, $\dot{w}c_p(T_w - T_{b1})$
Re = Reynolds number for the array, $V_{max}D/\nu$
Re_{duct} = Reynolds number of unobstructed duct, $\overline{V}D_h/\nu$
Sh = Sherwood number, $KD/\mathcal{D}$
Sc = Schmidt number
S_L = longitudinal spacing between fins
S_T = transverse spacing between fins
T_w = fin temperature
T_{bn} = bulk temperature of fluid approaching row n
V_{max} = maximum velocity, $\dot{w}/\rho A_{min}$
$\overline{V}$ = mean velocity in unobstructed duct
$\dot{w}$ = mass flow rate of air
ϵ = effectiveness, Q/Q_{max}
η = fin efficiency
ν = kinematic viscosity
ρ = air density
ρ_{nw} = naphthalene vapor density at fin surface
ρ_{nb} = naphthalene vapor density in bulk

Subscripts

fd = fully developed
IL = in-line array
S = staggered array

naphthalene-free laboratory room. The discharge (and the blower itself) were situated outside the laboratory.

The mass of the naphthalene-coated pin fin was measured both before and after a data run with a precise analytical balance capable of being read to 0.1 mg. Run times, selected to limit the mean change in diameter due to sublimation to 0.0025 cm (0.001 in.), ranged from 20 to 70 min. Each data run was followed by an auxiliary calibration procedure for determining the extraneous mass transfer which occurred during the periods of weighing and of test section assembly and disassembly. The pressure drop data were collected in data runs separate from those for the mass transfer measurements. Pressures were sensed with a capacitance-type meter having a smallest scale reading of 0.001 Hg. The air flow rates were measured with calibrated rotameters.

Experimental Results

Heat (Mass) Transfer Results. The per-fin mass transfer coefficient K was evaluated from the rate of mass transfer $\dot{m}$ per unit area and the difference in naphthalene vapor concentration between the fin surface and the approaching bulk flow, $\rho_{nw} - \rho_{nb}$. Of these, $\dot{m}$ was computed from the measured change in mass (corrected for extraneous losses, < 2 percent) in conjunction with the duration time of the run and the exposed surface area of the pin fin. The wall concentration was determined from the vapor pressure—temperature relation for naphthalene and the perfect gas law, while ρ_{nb} was zero for the conditions of the experiment. Once K was evaluated, its dimensionless counterpart, the Sherwood number (analogous to the Nusselt number), was obtained. These quantities are defined as

$$K = \dot{m}/(\rho_{nw} - \rho_{nb}), \quad \mathrm{Sh} = KD/\mathcal{D} \tag{1}$$

where D is the diameter of the pin fin and $\mathcal{D}$ is the naphthalene-air diffusion coefficient.

The Reynolds number chosen to parameterize the results is based on the velocity V_{max} which corresponds to uniform flow in the minimum free area A_{min}, that is, $V_{max} = \dot{w}/\rho A_{min}$. This velocity is fictive in that the flow in the inter-fin spaces will, in general, be different from that in the clearance gap above the fin tips. Such a fictive velocity is, however, used as a standard reference quantity in heat exchangers, and it was that fact which motivated its use here. The characteristic dimension used in the Reynolds number is the cylinder diameter D, so that

$$\mathrm{Re} = V_{max}D/\nu \tag{2}$$

It is also of some interest to report the Reynolds number Re_{duct} of the duct flow upstream of the pin fin array,

$$\mathrm{Re}_{duct} = \overline{V}D_h/\nu \tag{3}$$

where $\overline{V}$ is the mean velocity in the duct and D_h is the hydraulic diameter.

The row-by-row distributions of the Sherwood number are plotted in Figs. 2, 3, and 4, respectively for the short ($h/D = 1$, $h/H = 0.29$), intermediate ($h/D = 2$, $h/H = 0.58$), and tall cylinders ($h/D = 3$, $h/H = 0.875$). In each figure, data are presented for five Reynolds numbers spanning an overall range from about 1000 to 9000 (duct Reynolds numbers ranging from 5000 to 35,000). Curves have been faired to tie together the data for a fixed Reynolds number.

Examination of these figures shows that at any fixed Reynolds number, row-by-row variations of the Sherwood number are confined to the first few rows of the array. Beyond these initial rows, Sh becomes constant, signalling the attainment of fully developed conditions. Aside from the increase in Sh from the first to the second row, which is common to all cases, the detailed developmental pattern depends on the fin height, as will now be described. For the short pin fins (Fig. 2), the Sh distribution for a fixed Re attains a maximum at the second row (third row for the lower Re) and then decreases to a constant value which is less than or equal to the value at the first row. The respective Sh distributions for the intermediate height fins (Fig. 3) also attain their maxima at the second row, but the fully developed value is higher than that at the first row. In contrast, the Sh distributions for the tall fins (Fig. 4) attain their respective fully developed values via a monotonic increase.

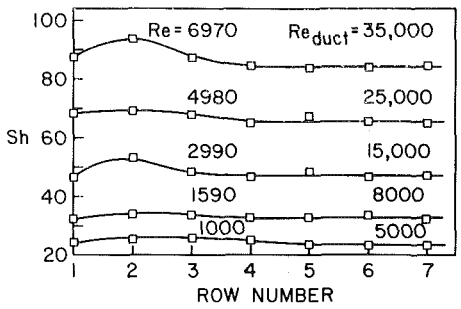

Fig. 2 Row-by-row distributions of the Sherwood number for $h/D = 1$, $h/H = 0.29$, and Sc = 2.5

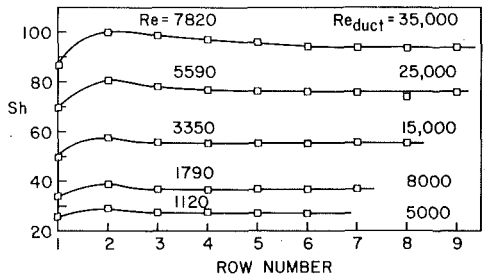

Fig. 3 Row-by-row distributions of the Sherwood number for $h/D = 2$, $h/H = 0.58$, and Sc = 2.5

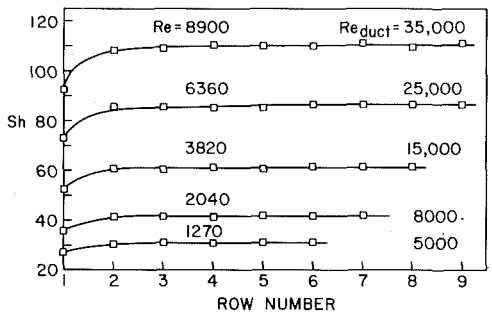

Fig. 4 Row-by-row distributions of the Sherwood number for $h/D = 3$, $h/H = 0.875$, and Sc = 2.5

For any practical purpose, the fully developed regime can be regarded as being in force for the fourth and all subsequent rows. Indeed, for the tallest fins, the second and all later rows can be taken as being in the fully developed regime.

The differing developmental patterns can be made plausible by considering the various processes which are responsible for the row-by-row variation of the Sherwood number. Relative to the first row, which is impinged by a fully developed duct flow, larger Sh values might be expected in subsequent rows because of the high level of turbulence experienced by a cylinder situated in the wake of another cylinder. A counteracting factor, tending to decrease the Sherwood number, is the tendency of flow to migrate to the clearance gap above the pin fins in order to escape the high resistance in the interfin spaces.

For the short fins, the clearance gap is large and the extent of the migration of fluid into the gap is sufficient to ultimately neutralize the augmentation caused by wake turbulence. There is lesser migration in the case of the intermediate fins and, as a consequence, the wake-turbulence augmentation is not fully neutralized. For the tallest fins, the outmigration plays a minor role, with the result that the Sh number increases in step with the wake turbulence.

It can also be seen in Figs. 2–4 that the Sherwood number increases substantially with the Reynolds number, and that there is also a tendency for it to increase with the fin height. These trends will shortly be brought to a sharper focus, when attention is directed to the fully developed results.

The row-by-row Sherwood number distributions for the in-line pin fin array will now be compared with those for the staggered array, the latter being taken from [3]. The comparisons are shown in Fig. 5 for the three fin heights and for Reynolds numbers that fall more or less in the middle of the range investigated here. Examination of the figure reveals that the staggered-array Sherwood numbers are generally higher than those for the in-line array. The extent of the differences is largest for the tallest pin fins and diminishes with decreasing fin height so that, for the shortest fins, the deviations are only a few percent. A second characteristic in evidence in the figure is that the development lengths are somewhat greater for the staggered array than for the in-line array, but even for the staggered array fully developed conditions prevail for the fifth and all subsequent rows. Since heat exchange devices employing pin fins typically encompass tens of rows, the differences in the development lengths are not of great importance and, therefore, it is more relevant to focus the comparison on the fully developed regime.

With a view to generalizing the fully developed (fd) results to apply to heat transfer as well as to mass transfer, the Sherwood numbers are first divided by $Sc^{0.4}$ ($Sc = 2.5$ for the naphthalene experiments). Then, upon invoking the analogy between heat and mass transfer, the quantity $Sh_{fd}/Sc^{0.4}$ is set equal to $Nu_{fd}/Pr^{0.4}$. The selection of the 0.4 power of Sc or Pr rather than the 1/3 power is based on the fact that it is more consonant with recent duct flow correlations in the range of Pr or Sc between 0.7 to 2.5. It should be noted that the Nusselt numbers obtained from the experimentally determined Sherwood numbers correspond to isothermal fins, i.e., to fins having an efficiency $\eta = 1$.

The fully developed heat (mass) transfer results are presented in Fig. 6 as a function of the Reynolds number. The figure is subdivided into four panels, with the lowermost panel showing the results for the in-line arrays and the other panels displaying comparisons between the in-line and staggered arrays. A common characteristic of all the results is the expected trend whereby Nu (and Sh) increases with the Reynolds number. The curves faired through the data are not quite straight lines, nor are straight lines expected for flows where separated regions (i.e., wakes) play an important role. For reference purposes, a global straight line passed through the data would have a 0.6 power dependence on the Reynolds number.

By examining the lowermost panel, it may be observed that the heat (mass) transfer coefficients for the in-line array are relatively insensitive to the fin height over the range investigated, the total spread being about eleven percent. This finding is highly convenient from the standpoint of practice since, in effect, it eliminates the fin height as a parameter (either in h/H or h/D) in characterizing the Nusselt number. It is, furthermore, a rather remarkable outcome in view of the changing character of the flow field with h/H and of the fact that the ratio of tip area to cylindrical area increases from 1/12 to 1/4 as h/D varies from three to one.

Also shown in the lower panel are results for cross flow over an in-line tube bank having the same S_T/D and S_L/D ratios as the in-line pin fins studied here ([7] Fig. H5.11). The tube bank Nusselt numbers lie about eight percent above those of the tallest pin fins. Since the tube bank may be regarded as the limit of a tall pin fin array, the eight percent deviation serves to reaffirm the aforementioned insensitivity of the results to fin height. Mention may also be made here of comparisons with results for channel-spanning pin fins presented in Kays and London (Figs. 10-68, 10-69, and 10-72) and by Norris and Spofford. In general, the present results for the tallest pin fins fall in the range from five to twenty percent below those of the cited references. This level of agreement has to be regarded as truly remarkable, especially in view of major geometrical differences and of the fact that the prior results were averages over an entire heat exchanger, encompassing both the fins and the duct wall.

Consideration may now be given to the upper panels of Fig. 6 and to the comparisons between the results for in-line and staggered pin fins. As expected on the basis of Fig. 5, the Nusselt numbers for the staggered array exceed those for the in-line array. The deviations are about fifteen percent for the tallest pin fins and diminish to about 3–4 percent for the shortest pin fins. This finding suggests that, at least for the tallest fins, it would be preferable to use a staggered array rather than an in-line array. However, as discussed in the Introduction, a rational choice should be based on the fulfillment of certain performance goals rather than on a comparison of heat transfer coefficients. This matter will be explored in greater depth in a later section of the paper.

Pressure Drop. The presence of the pin fin array gives rise to a pressure drop over and above that which would exist in the unobstructed duct. The array-induced pressure drop was determined from plots of the axial pressure distribution, a typical one of which is illustrated in Fig. 7 (the data correspond to $h/D = 2$, Re = 3,350). From the figure, it is seen that there are three distinct pressure regimes. Upstream of the pin fin array, the linearly decreasing pressure distribution is indicative of a fully developed duct flow. Within the array, the pressure decreases sharply (and, also, linearly). Immediately downstream of the array, there is a pressure recovery as the flow expands to fill the entire duct cross section, and this is followed by the re-establishment of a linear decrease corresponding to the redeveloped duct flow.

In the absence of the array, the straight lines passing through the upstream and downstream pressure data would be colinear. Their vertical displacement, designated as Δp_{array}, is, therefore, the net pressure drop due to the array. It encompasses all pressure-related

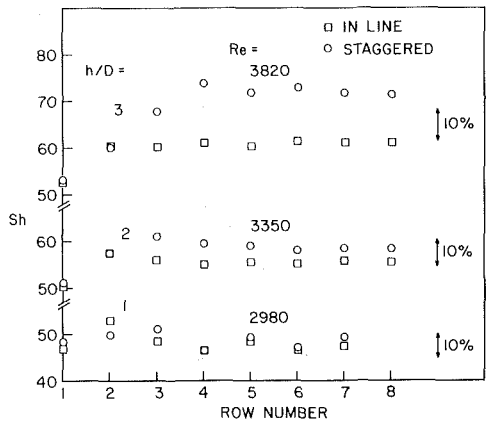

Fig. 5 Comparisons of row-by-row Sherwood number distributions for in-line and staggered arrays

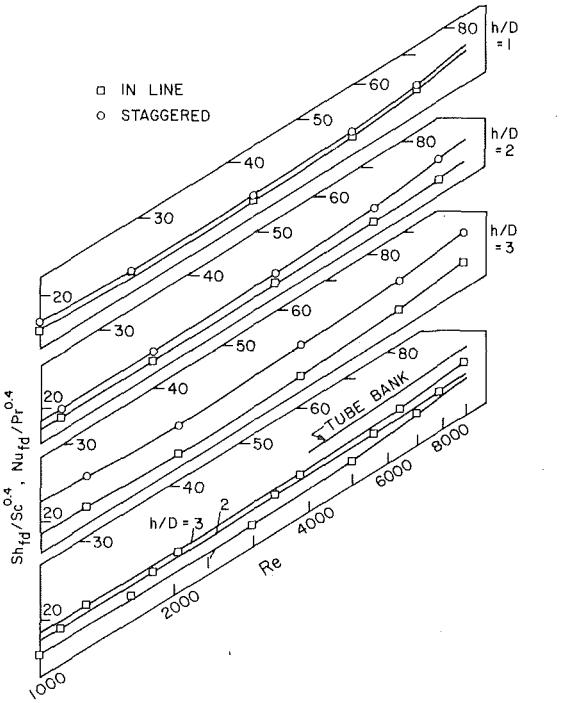

Fig. 6 Fully developed Sherwood and Nusselt numbers

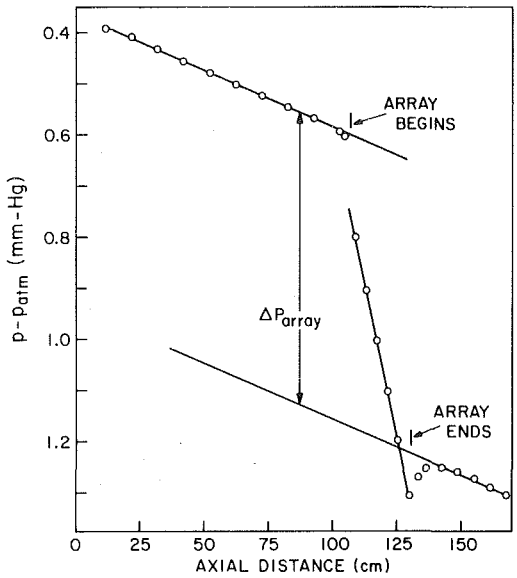

Fig. 7 Representative axial pressure distribution, $h/D = 2$, Re = 3,350

processes including skin friction, separation losses, entrance and exit losses, and the aforementioned recovery downstream of the array.

A dimensionless representation of the array pressure drop, stated on a per-row basis, is provided by a pressure loss coefficient K_p defined as

$$K_p = \Delta p_{\text{array}}/(\tfrac{1}{2}\rho V^2_{\max})N \tag{4}$$

where N is the number of rows in the array. The values of K_p are listed in Table 1 for the three fin heights and for the various Reynolds numbers that were investigated. At the bottom of the table are average K_p values—averaged over the Reynolds number range for each fin height. The averages listed just below the main body of the table are for the in-line array, and under these are the averages for the staggered array (taken from [3]).

It can be seen from the table that the array pressure drop is strongly affected by the height of the fin, increasing by a factor of five over the range of heights investigated here. On the other hand, K_p is relatively insensitive to the Reynolds number for a given height, which is plausible since inertial losses (proportional to velocity squared) should predominate over skin friction. The modest Reynolds number effects that are in evidence in the tabulation indicate that the three zones of separation—in the wake, at the wall attachment, and at the free end—respond somewhat differently to variations in $V_{\max}$. It is these different responses which are, presumably, responsible for the reversal in trend with Re as h/D increases.

The K_p values for the tallest fins may be compared with those for cross flow over an in-line tube bank having the same S_T/D and S_L/D values as those of the present in-line pin fins. From [7], the $\overline{K}_p$ for the Reynolds number range of Table 1 is 0.17, which compares very favorably with the value of 0.164 found here.

Of particular interest are the differences between the loss coefficients for the in-line and staggered arrays that are shown at the bottom of the table. In general, the losses sustained by the staggered array are greater than those for the in-line array, with the deviation between the two types of arrays increasing with the fin height. Specifically, for $h/D = 1$ and 3, the in-line loss coefficients are, respectively, 85 percent and 58 percent of those for the corresponding staggered cases.

The higher heat transfer coefficients for the staggered case are, therefore, accompanied by higher pressure drops. The next section of the paper deals with methodology and computations for making rational choices between the two types of arrays.

Performance Evaluations

As was discussed earlier, the selection of a particular augmentation device or technique, relative to other candidates, depends on the goals to be achieved and the constraints that are imposed. Here, the basic

Table 1 Per-row pressure loss coefficient K_p for in-line pin fin array

$h/D = 1$		$h/D = 2$		$h/D = 3$	
Re	K_p	Re	K_p	Re	K_p
1000	0.0304	1120	0.0842	1270	0.173
1590	0.0311	1790	0.0811	2040	0.167
2990	0.0342	3350	0.0817	3820	0.162
4980	0.0338	5590	0.0828	6360	0.160
6970	0.0352	7820	0.0817	8900	0.157
$\overline{K}_p$	0.0329		0.0823		0.164
$\overline{K}_{p\ \text{Stag}}$	0.0389		0.128		0.284

heat transfer and pressure drop information presented in the foregoing will be used to examine two standard situations. In one, the rate of heat transfer is to be maximized at fixed pumping power and fixed heat transfer surface area. In the other, a reduction in the length of the heat exchanger (i.e., reduction in surface area) is sought at a fixed heat duty and fixed mass flow.

The analysis to be presented here is focused on tall fins such that the fin heat transfer predominates over the heat transfer from duct walls, and similarly for the array pressure drop relative to that of the duct walls.

For both of the aforementioned performance evaluations, a necessary ingredient is a representation for the rate at which heat is transferred to the flowing fluid as it traverses N rows of fins. To facilitate the derivation, let T_{bn} denote the bulk temperature of the fluid approaching row n and assume that the fluid is well mixed between successive rows. The fins in all rows are regarded as having the same uniform temperature T_w; departures from temperature uniformity associated with a fin efficiency $\eta < 1$ can be easily accounted by replacing the actual per-row heat transfer area A with ηA.

In view of the foregoing, an energy balance for row n yields

$$hA(T_w - T_{bn}) = \dot{w}c_p(T_{b(n+1)} - T_{bn}) \tag{5}$$

or

$$\frac{T_{b(n+1)} - T_w}{T_{bn} - T_w} = 1 - (hA/\dot{w}c_p) \tag{6}$$

where, in writing equation (5), cognizance was taken for the fact that the experimentally determined heat (mass) transfer coefficients presented earlier in the paper were based on the difference between the wall temperature and the bulk temperature in the approaching fluid. If equation (6) is applied consecutively for $n = 1, 2, \ldots, N$, it follows directly that

$$\frac{T_{b(N+1)} - T_w}{T_{b1} - T_w} = [1 - (hA/\dot{w}c_p)]^N \tag{7}$$

in which T_{b1} is the known bulk temperature of the fluid at the inlet of the fin array. It should also be noted that since, in practice, N is much larger than five, h has been taken to be uniform and equal to its fully developed value.

The heat transferred to the fluid from N rows of fins can be written as

$$Q = \dot{w}c_p(T_{b(N+1)} - T_{b1}) \tag{8}$$

and, upon substitution of equation (7),

$$Q = \dot{w}c_p(T_w - T_{b1})(1 - [1 - (hA/\dot{w}c_p)]^N) \tag{9}$$

This representation for the heat transfer rate will be employed in the performance evaluations that follow.

Fixed Pumping Power and Heat Transfer Area. The pumping power required to propel a mass flow $\dot{w}$ through a pressure drop Δp is

$$P = (\dot{w}/\rho)\Delta p \tag{10}$$

Since $\dot{w} = \rho A_{\min} V_{\max}$, $V_{\max} = \nu \text{Re}/D$, and Δp is related to K_p via equation (4), it follows that

$$P = [\tfrac{1}{2}\rho\nu^3 N A_{\min}/D^3]\text{Re}^3 K_p \tag{11}$$

If consideration is given to in-line and staggered arrays having the same number of rows N, the same fin diameter D and height h, and the same spacings S_T and S_L, then the bracket on the right-hand side of equation (11) has the same numerical value for the two arrays. These constraints also imply equality of the heat transfer surface areas of the arrays. Then, to fulfill the condition that the pumping power be the same for the two arrays, it is necessary that

$$\mathrm{Re}_{IL} = \mathrm{Re}_S(K_{p,S}/K_{p,IL})^{1/3} \tag{12}$$

Thus, to compensate for differences in the pressure loss coefficients, the Reynolds numbers (i.e., mass flow rates) for the two arrays have to be different.

With the relationship between the Reynolds numbers thus established, the heat transfer rates will now be compared. When equation (9) is applied successively to the in-line and staggered arrays and it is noted that $\dot{w} = A_{\min}\mathrm{Re}/D$, then

$$\frac{Q_{IL}}{Q_S} = \frac{\mathrm{Re}_{IL}}{\mathrm{Re}_S}\frac{1-[1-(hA/\dot{w}c_p)_{IL}]^N}{1-[1-(hA/\dot{w}c_p)_S]^N} \tag{13}$$

Furthermore, it is readily shown that

$$hA/\dot{w}c_p = (\mathrm{Nu}/\mathrm{RePr})(A/A_{\min}) \tag{14}$$

Equation (13), supplemented by equation (12), compares the heat transfer rates for the in-line and staggered arrays under the dual constraints of fixed pumping power and fixed heat transfer surface area. For the numerical evaluation of equation (13), the experimental results for the tallest of the pin fin arrays will be used as input, specifically, Fig. 6, Table 1, and Table 1 of [3]. Also, for these fins,

$$A/A_{\min} = 1.42 \tag{15}$$

To begin the evaluation, calculation shows that $(K_{p,S}/K_{p,IL})^{1/3}$ is essentially independent of Reynolds number and equal to 1.2. Thus, according to equation (12),

$$\mathrm{Re}_{IL} = 1.2\,\mathrm{Re}_S \tag{16}$$

Then, a set of parametric values of Re_S is selected and equation (16) yields the corresponding values of Re_{IL}. These Reynolds numbers are then employed to read values of $\mathrm{Nu}/\mathrm{Pr}^{0.4}$ from Fig. 6, and the Nusselt numbers for air (Pr = 0.7) follow directly. With this information and with $A/A_{\min}$ from (15), values of $(hA/\dot{w}c_p)$ are obtained from equation (14). Finally, selections are made for the number of rows N, and values of Q_{IL}/Q_S are determined from equation (13).

The results of these computations are presented in Fig. 8, where Q_{IL}/Q_S is plotted as a function of Re_S for parametric values of the number of rows N. From the figure, it is seen that for all the cases investigated, the in-line array transfers more heat than the staggered array under conditions of equal pumping power and equal heat transfer surface area. The transfer increment provided by the in-line array increases with the number of rows, but, for all cases, $Q_{IL} < 1.2Q_S$. For a 100-row heat exchanger, where the effectiveness ϵ (= $Q/Q_{\max}$) is in the 80–95 percent range (depending on the Reynolds number), $Q_{IL}/Q_S \sim 1.15$.

Thus, there appears to be a clear advantage in employing an in-line array when it is desired to maximize the heat transfer rate at fixed pumping power and fixed heat transfer surface area. It should be noted, however, that the gain in heat transfer that can be achieved by using the in-line array is modest.

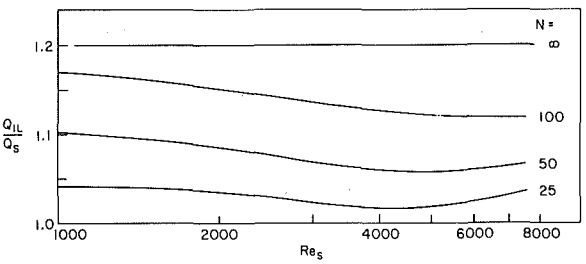

Fig. 8 Relative heat transfer performance for in-line and staggered arrays at fixed pumping power and heat transfer surface area

Fixed Heat Duty and Fixed Mass Flow. To characterize the heat duty, it is convenient to employ the effectiveness ϵ

$$\epsilon = Q/Q_{\max}, \quad Q_{\max} = \dot{w}c_p(T_w - T_{b1}) \tag{17}$$

and, with equation (9)

$$\epsilon = 1 - [1 - (hA/\dot{w}c_p)]^N \tag{18}$$

If the in-line and staggered arrays are to be compared for the same mass flow rate $\dot{w}$, then $Q_{\max}$ is the same for both cases. Furthermore, for the same heat duty (i.e., same Q), the ϵ values for the two arrays have to be the same. In addition, if the comparison is made for common values of D, h, H, S_T, and S_L, the constant mass flow constraint is identical to constant Reynolds number.

Computations will now be carried out to determine the size (i.e., number of rows N) of in-line and staggered array heat exchangers for fixed values of effectiveness and Reynolds number. As in the prior section, the computations are performed for the tallest of the experimentally investigated fins and for Pr = 0.7. To begin, parametric values of the Reynolds number are selected, and the corresponding values of $\mathrm{Nu}/\mathrm{Pr}^{0.4}$ and $hA/\dot{w}c_p$ are successively determined from Fig. 6 and equation (14). With this input and with a selected ϵ value, the number of rows N follows from equation (18).

The results for the number of rows are listed in Table 2 for Reynolds numbers of 1000, 4000, and 8000 and effectivenesses of 0.50 and 0.75. For the purpose of the ratios to be discussed shortly, the listed N values include fractional numbers of rows although such fractional rows are inconsistent with practice. Also listed in the table are the corresponding pressure drops.

The table shows that for a fixed heat duty and fixed mass flow rate, the staggered array has fewer rows (and, therefore, less heat transfer surface) than an in-line array. By ratioing the results given in Table 2, it is found that for all cases, the staggered array is fourteen percent shorter than the in-line array. Therefore, from the standpoint of minimum heat transfer surface the staggered array is advantageous.

It should be noted, however, that there is a pressure drop (and pumping power) penalty associated with the staggered array. For the cases displayed in Table 2, the pressure drops for the staggered arrays are about fifty percent larger than those for the corresponding in-line arrays. Thus, the first-cost economies associated with the lesser surface area of the staggered array have to be weighed against the higher operating costs associated with the increased pumping power.

Concluding Remarks

In this paper, basic heat transfer and pressure drop results were determined by experiment and then applied to heat exchanger performance evaluations. The experiments were performed with in-line pin fin arrays with a view to complementing earlier experimental results for geometrically comparable staggered arrays. The heat transfer coefficients for the in-line arrays are generally lower than those for the corresponding staggered arrays, but the pressure drop also is lower. The deviations between the two types of arrays are greatest for the tallest pin fins.

The performance evaluations were focused on two practically rel-

Table 2 Number of rows and pressure drop for fixed heat duty and mass flow rate

	(a) ϵ = 0.50			
	In-Line		Staggered	
Re	N	$\Delta p/\frac{1}{2}\rho V^2_{\max}$	N	$\Delta p/\frac{1}{2}\rho V^2_{\max}$
1000	20.4	3.53	17.6	5.23
4000	35.5	5.75	30.6	8.78
8000	43.9	6.89	37.9	10.2
		(b) ϵ = 0.75		
1000	40.8	7.06	35.1	10.4
4000	71.0	11.5	61.1	17.5
8000	87.7	13.8	75.7	20.4

evant situations. In one, the heat transfer performance of the two arrays was compared at fixed pumping power and fixed heat transfer surface area. In the second, the length of the heat exchanger (i.e., the heat transfer surface area) was compared at fixed heat duty and fixed mass flow rate.

The outcome of these performance evaluations is especially interesting in that it demonstrates that the selection of a heat transfer device, relative to other candidates, depends decisively on design goals and constraints rather than on ratios of heat transfer coefficients and friction factors. Thus, whereas the in-line array transfers more heat at fixed pumping power and surface area, the staggered array minimizes the surface area at a fixed heat duty and flow rate.

Acknowledgment

This research was performed under the auspices of NSF Grant ENG77-06762

References

1 Kays, W. M. and London, A. L., *Compact Heat Exchangers,* Second ed., McGraw-Hill, New York, 1964.

2 Norris, R. H. and Spofford, W. A., "High Performance Fins for Heat Transfer," *Trans. ASME,* Vol. 64, 1942, pp. 489–496.

3 Sparrow, E. M. and Ramsey, J. W., "Heat Transfer and Pressure Drop for a Staggered Wall-Attached Array of Cylinders with Tip Clearance," *International Journal of Heat and Mass Transfer,* Vol. 21, 1978, pp. 1369–1378.

4 Bergles, A. E., "Survey and Evaluation of Techniques to Augment Convective Heat and Mass Transfer," in *Progress in Heat and Mass Transfer,* Vol. 1, Pergamon Press, Oxford, 1969, pp. 331–424.

5 Bergles, A. E., Blumenkrantz, R. R., and Taborek, J., "Performance Evaluation Criteria for Enhanced Heat Transfer Surfaces," Fifth International Heat Transfer Conference, Vol. II, Paper FC6.3, pp. 239–243, 1974.

6 Bergles, A. E., Junkhan, G. H., and Bunn, R. L., "Performance Criteria for Cooling Systems on Agricultural and Industrial Machines," Report HTL-6, Department of Mechanical Engineering, Iowa State University, Ames, Iowa, Dec., 1974.

7 Fraas, A. P. and Ozisik, M. N., *Heat Exchanger Design,* Wiley, New York, 1965.

A. F. Emery
Professor,
Department of Mechanical Engineering,
University of Washington,
Seattle, Wash.

P. K. Neighbors
Sandia Laboratories,
Livermore, CA

F. B. Gessner
Professor,
Department of Mechanical Engineering,
University of Washington,
Seattle, Wash.

The Numerical Prediction of Developing Turbulent Flow and Heat Transfer in a Square Duct

Velocity and temperature profiles were computed for developing turbulent flow in a square duct with constant wall temperature, constant wall heat flux or asymmetric heating. The computations utilized an explicit numerical differencing scheme and an algebraic closure model based upon a three-dimensional mixing length. The computed local and fully-developed shear stresses and heat transfer are shown to be in good agreement with measured data and with predictions using the $k - \epsilon$ closure model.

Introduction

In the design of compact heat exchangers, square flow passages are sometimes employed as a convenient configuration for heat transfer purposes. When the flow is turbulent, the local heat transfer between the fluid and duct walls is dominated by the presence of secondary flows which are generated by Reynolds stress gradients acting in the corner region. These secondary flows appear in the form of two cells, centered about each corner bisector, which continue to grow laterally as the flow progresses downstream. Their presence is felt across the entire duct cross section when the flow is fully-developed. For a prescribed constant wall temperature, peripheral variations in local wall heat flux occur which are not present when the flow is laminar. For constant wall heat flux conditions, the local wall temperature varies in a manner that can lead to the formation of temperature "hot spots" in the corner region. Under these conditions, it is of primary importance to be able to predict local flow and heat transfer behavior accurately to avoid possible excessive wall temperatures.

In an early analysis of the problem by Diessler and Taylor [1], the law-of-the-wall was assumed to apply locally along velocity gradient lines between the wall and axial centerline of the duct for fully-developed flow conditions. An iterative procedure was then applied to determine lines of constant velocity in a plant normal to the axial mean flow direction (isotachs) and the associated local wall shear stress distribution. For a prescribed constant wall temperature, the peripheral variation in local wall heat flux was also evaluated. Neither the predicted local wall shear stress distribution nor the wall heat flux distribution model experimentally observed behavior because secondary flow effects were omitted in the analysis. The situation was improved considerably by Launder and Ying [2] who effected closure to the equations of motion by means of a prescribed length scale and a one-equation (k) model, in conjunction with algebraic relationships for the individual Reynolds stress components. The turbulent Prandtl number was specified as 0.9 in order to close the thermal energy equation, and predictions were restricted to fully-developed flow in a square duct with a prescribed constant wall temperature. Under these conditions, the predicted local wall heat flux and Stanton number variation with Reynolds number were found to agree well with the data of Brundrett and Burroughs [3]. Ramachandra and Spalding [4] have recently shown that even better agreement is possible than that noted by Launder and Ying when a two-equation ($k - \epsilon$) model is employed.

In the present paper, a turbulence model is prescribed which effects closure to the conservation equations via algebraic relationships for all of the turbulence correlations which appear in these equations. Although a length-scale formulation is employed which utilizes fourteen coefficients, application of the model involves specification of only one non-wall boundary condition, namely the variation of U on the first mesh line adjacent to a bounding wall, in contrast to three conditions (wall functions) which must be specified when the $k - \epsilon$ model is employed (the variation of U, k, and ϵ along the first mesh line). The first boundary condition can be specified by applying the law-of-the-wall on the first mesh line, which is now known to be a valid condition on the basis of recent measurements by Lund [5]. Currently prescribed boundary conditions for k and ϵ have not yet been verified experimentally, but the $k - \epsilon$ model still appears to perform well on the basis of recent comparisons between predictions and experiment [4, 6, 7]. At the present time, comparisons between predicted and measured heat transfer behavior in the developing flow region of a square duct have not appeared in open literature. It is the intent of this paper to present these and additional comparisons between predictions referred to an algebraic stress model and available experimental data. The selection of data for purposes of comparison is based on a recent survey of corner flow data by one of the authors [8], in which more than seventy data sets were examined and rated on the basis of their suitability for comparison with predicted results.

The Conservation Equations

For developing, incompressible turbulent flow in a square duct, both the local mean flow and the turbulence structure are three-dimensional, as shown in Fig. 1. If the boundary layer approximations are applied for this particular situation, the conservation equations can be written as:

$$\frac{\partial U}{\partial x} + \frac{\partial V}{\partial y} + \frac{\partial W}{\partial z} = 0 \tag{1}$$

$$U\frac{\partial U}{\partial x} + V\frac{\partial U}{\partial y} + W\frac{\partial U}{\partial z} = -\frac{1}{\rho}\frac{\partial \bar{P}}{\partial x} + \nu\left(\frac{\partial^2 U}{\partial y^2} + \frac{\partial^2 U}{\partial z^2}\right) - \frac{\partial \overline{uv}}{\partial y} - \frac{\partial \overline{uw}}{\partial z} \tag{2}$$

$$U\frac{\partial V}{\partial x} + V\frac{\partial V}{\partial y} + W\frac{\partial V}{\partial z} = -\frac{1}{\rho}\frac{\partial P}{\partial y} + \nu\left(\frac{\partial^2 V}{\partial y^2} + \frac{\partial^2 V}{\partial z^2}\right) - \frac{\partial \overline{v^2}}{\partial y} - \frac{\partial \overline{vw}}{\partial z} \tag{3}$$

$$U\frac{\partial W}{\partial x} + V\frac{\partial W}{\partial y} + W\frac{\partial W}{\partial z} = -\frac{1}{\rho}\frac{\partial P}{\partial z} + \nu\left(\frac{\partial^2 W}{\partial y^2} + \frac{\partial^2 W}{\partial z^2}\right) - \frac{\partial \overline{vw}}{\partial y} - \frac{\partial \overline{w^2}}{\partial z} \tag{4}$$

$$U\frac{\partial T}{\partial x} + V\frac{\partial T}{\partial y} + W\frac{\partial T}{\partial z} = \alpha\left(\frac{\partial^2 T}{\partial y^2} + \frac{\partial^2 T}{\partial z^2}\right) - \frac{\partial \overline{vt}}{\partial y} - \frac{\partial \overline{wt}}{\partial z} \tag{5}$$

where the pressure field is presumed to be of the form: $P(x, y, z) = \bar{P}(x) + P(y, z)$ following the method of Patankar and Spalding [9]. Closure to the above system of equations is effected by means of the initial conditions,

$$U(0, y, z) = U_0,\ T(0, y, z) = T_0 \tag{6a}$$

$$V(0, y, z) = W(0, y, z) = 0 \tag{6b}$$

Contributed by the Heat Transfer Division for publication in the JOURNAL OF HEAT TRANSFER. Manuscript received by the Heat Transfer Division June 5, 1979.

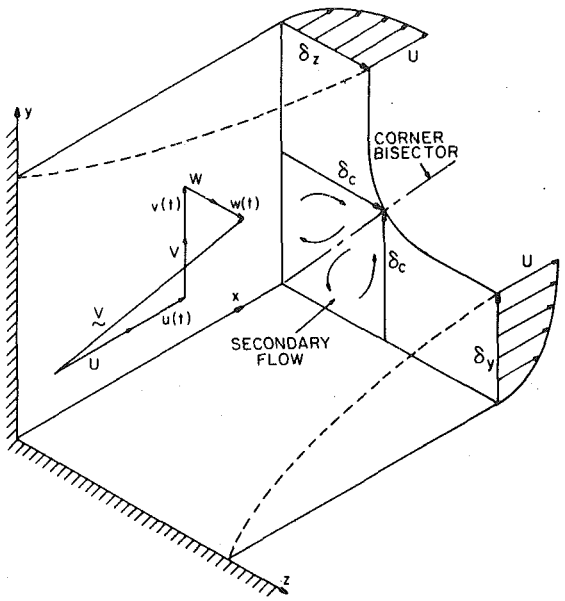

Fig. 1 Coordinate system and velocity components for developing turbulent flow in a square duct

with all Reynolds stress components equal to zero at the inlet and with the boundary conditions at the wall of

$$U = V = W = 0 \tag{6c}$$

and either

$$T = 0 \text{ for a constant wall temperature} \tag{6d}$$

or

$$-k\frac{\partial T}{\partial n} = q_w \text{ for a constant wall heat flux} \tag{6e}$$

and the algebraic stress model developed by Gessner and Emery [10], namely

$$\overline{v^2} = -\frac{(2F_{12}+\alpha_1-2)}{\alpha_2}\ell_p{}^2\left(\frac{\partial U}{\partial y}\right)^2 + \frac{F_{12}\ell_p{}^2}{\alpha_2}\left[\left(\frac{\partial U}{\partial y}\right)^2+\left(\frac{\partial U}{\partial z}\right)^2\right] \tag{7}$$

$$\overline{w^2} = -\frac{(2F_{12}+\alpha_1-2)}{\alpha_2}\ell_p{}^2\left(\frac{\partial U}{\partial z}\right)^2 + \frac{F_{12}\ell_p{}^2}{\alpha_2}\left[\left(\frac{\partial U}{\partial y}\right)^2+\left(\frac{\partial U}{\partial z}\right)^2\right] \tag{8}$$

$$\overline{uv} = -\ell_p{}^2\frac{\partial U}{\partial y}\left[\left(\frac{\partial U}{\partial y}\right)^2+\left(\frac{\partial U}{\partial z}\right)^2\right]^{1/2} \tag{9}$$

$$\overline{uw} = -\ell_p{}^2\frac{\partial U}{\partial z}\left[\left(\frac{\partial U}{\partial y}\right)^2+\left(\frac{\partial U}{\partial z}\right)^2\right]^{1/2} \tag{10}$$

$$\overline{vw} = -\frac{(2F_{12}+\alpha_1-2)}{\alpha_2}\ell_p{}^2\frac{\partial U}{\partial y}\frac{\partial U}{\partial z} \tag{11}$$

and the definition of the turbulent Prandtl number, from which

$$\overline{vt} = -\frac{\overline{uv}}{\mathrm{Pr}_t}\frac{\partial T/\partial y}{\partial U/\partial y} \tag{12}$$

$$\overline{wt} = -\frac{\overline{uw}}{\mathrm{Pr}_t}\frac{\partial T/\partial z}{\partial U/\partial z} \tag{13}$$

In equations (7–11) the coefficients α_1 and α_2 prescribed as 0.94 and 0.26, respectively, as suggested by Gessner and Emery [11] and correspond to the values of $C_{\phi 1}$ and $C_{\phi 2}$ chosen by Hanjalic and Launder [12]. However, the value of F_{12} was modified from the value suggested in [11] (0.600) to a lesser value (0.535) in order to avoid multiple secondary flow cells in an octant of the flow and overly distorted isotach patterns. The variation of Prandtl's mixing length, $\ell_p(x, y, z)$, was prescribed by equation (8) of [11] using the specified values for the coefficients, with the exception of C_{11}, which was changed from 0.4 to 0.5 so that the asymptotic value of ℓ_p/a would approach Buleev's [13] analytical value of 0.159 rather than the empirical value of 0.132 which was specified in [11]. This modification was made in order to predict axial centerline velocities which more closely approximated experimental values for fully-developed flow.

Although the prescribed length side is based on comparisons with data at Re = 250,000 and is not Reynolds number dependent, this aspect of the model is not a serious drawback for high Reynolds number flows. A comparison of axial velocity profiles measured by Melling and Whitelaw [14] at Re = 42,000 and by Gessner, et al. [15] at Re = 250,000 in a square duct shows that velocity profile development from an initially uniform flow is similar for both cases, and that the wall boundary layers do not begin to merge until $x/D_h \geq 24$. This same convert applies for velocity profile development in large-aspect-ratio (two-dimensional) ducts at high Reynolds numbers, where the development length is relatively insensitive to Reynolds number effects over the interval $1000{,}00 \leq \mathrm{Re} \leq 250{,}000$ (cf. Fig. 7 of [11]).

In order to illustrate the nature of the prescribed length scale, the variation of ℓ_p in the vicinity of a corner in the near entrance region of a square duct ($0 \leq x/D_h \leq 24$) is shown in Fig. 2(*a*). The closed contours of this figure model the observed peaking in the vicinity of the corner bisector [11], where δ_c is as defined in Fig. 1. The value of ℓ_p at δ_c ($\ell_p/\delta = 0.078$) closely approximates typical values observed in developing, incompressible turbulent boundary layers which have not yet merged. Between $x/D_h = 24$ and 72, the prescribed length-scale increases in the outer region of the boundary layer via a development length function [11] in order to model observed behavior as the wall boundary layers begin to merge and interact. At streamwise locations beyond x/D_h 72, no further changes in the length-scale appear to occur, and the analytical form developed by Buleev [13] for fully-developed flow is appropriate (Fig. 2(*b*)).

Numerical Method

For a given bulk Reynolds number, equations (1–11) were solved numerically in order to predict the developing velocity field. This

Nomenclature

a = duct half-width
C_{fx} = local skin friction coefficient
C_f = fully-developed skin friction coefficient
D_h = hydraulic diameter
h = heat transfer coefficient
k = thermal conductivity, turbulence kinetic energy
ℓ_p = Prandtl's mixing length
Nu = Nusselt number (hD_h/k)
Pr,Pr_t = Prandtl number, turbulent Prandtl number
P = mean static pressure
q_w = local wall heat flux
Re = Reynolds number ($2U_b a/\nu$)
St_x = local Stanton number
St = fully-developed Stanton number
T,t = temperature, fluctuating component
U,u = mean streamwise velocity, fluctuating component
V,v - mean transverse velocity, fluctuating component
W,w = mean transverse velocity, fluctuating component
x = streamwise coordinate
y,z = transverse coordinates
α = thermal diffusivity
δ,δ_c = boundary layer thicknesses
ϵ = dissipation rate
ρ = density
μ = dynamic viscosity
ν = kinematic viscosity
τ = local wall shear stress
$\overline{(\ )}$ = time or spatially averaged quantity

Subscripts

b = bulk
o = centerline
r = resultant
t = turbulent
ave = peripheral wall average
∞ = fully developed

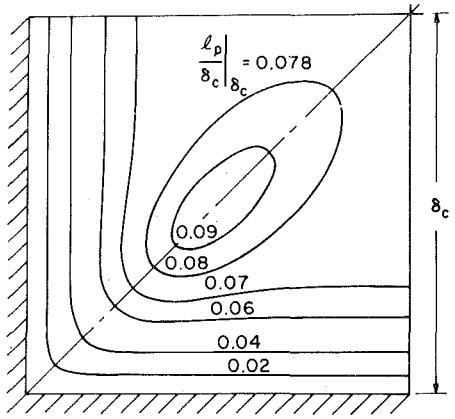

Fig. 2(*a*) $0 \leq x/D_h \leq 24$

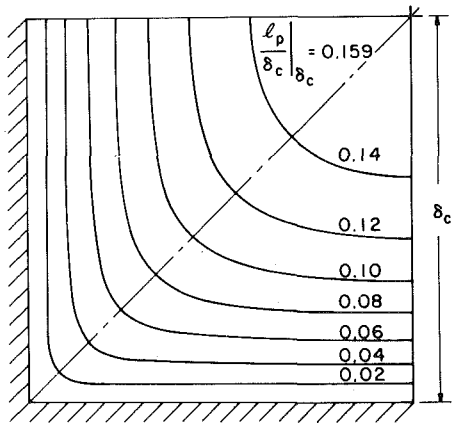

Fig. 2(*b*) $x/D_h \geq 72$

Fig. 2 Prescribed length scale variation for different streamwise locations

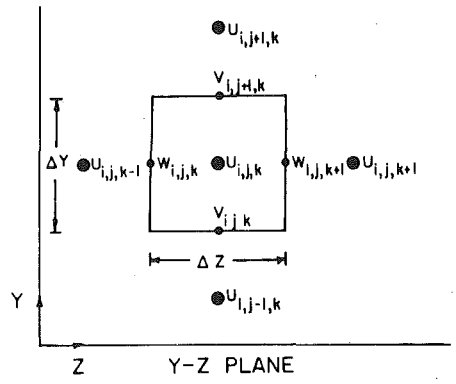

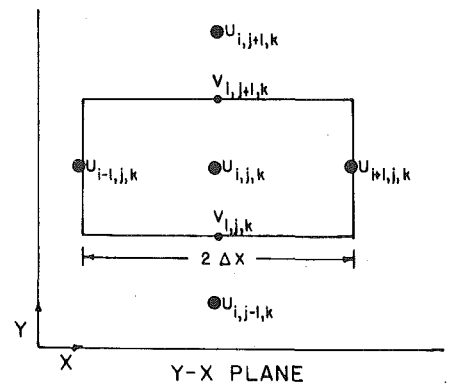

Fig. 3 Schematic of the nodal grid pattern

solution was then coupled with equations (5, 12) and (13) to predict the local temperature field using constant properties and assuming a constant value of 0.9 for the turbulent Prandtl number. Based upon the previous work of Pletcher [16] and Emery and Gessner [17], an explicit differencing method (DuFort-Frankel) was applied to the streamwise momentum and thermal energy equations, while the implicit method was used for the transverse momentum equations. In the finite difference form of the momentum equations, each Reynolds stress component was expressed in terms of components of a non-scalar (two-component) eddy viscosity model related to the length-scale formulation given by equations (6–10).

The local values of U, V, W and T were computed by using the grid shown in Fig. 3, where U and T are located at the center of a computational cell, and V and W are specified at the surface of the cell to ensure conservation of mass. Application of the DuFort-Frankel method to equation (2) leads to the finite difference form:

$$U_{i,j,k}\left[\frac{U_{i+1,j,k}-U_{i-1,j,k}}{2\Delta x}\right]+\overline{V}_{i,j,k}\left[\frac{U_{i,j+1,k}-U_{i,j,k}}{\Delta y}\right]+\overline{W}_{i,j,k}\left[\frac{U_{i,j,k+1}-U_{i,j,k}}{\Delta z}\right]=-\frac{1}{\rho}\left[\frac{\overline{P}_{i+1}-\overline{P}_{i-1}}{2\Delta x}\right]+\frac{\mu^*_{i,j+1/2,k}}{\rho}\left[\frac{U_{i,j+1,k}-U_{i,j,k}}{\Delta y^2}\right]-\frac{\mu^*_{i,j-1/2,k}}{\rho}\left[\frac{\overline{U}_{i,j,k}-U_{i,j-1,k}}{\Delta y^2}\right]+\frac{\mu^*_{i,j,k+1/2}}{\rho}\left[\frac{U_{i,j,k+1}-\overline{U}_{i,j,k}}{\Delta z^2}\right]-\frac{\mu^*_{i,j,k-1/2}}{\rho}\left[\frac{\overline{U}_{i,j,k}-U_{i,j,k-1}}{\Delta z^2}\right] \quad (13)$$

where

$$\overline{V}_{i,j,k}=\frac{V_{i,j+1,k}+V_{i,j,k}}{2},$$

$$\overline{W}_{i,j,k}=\frac{W_{i,j,k+1}+W_{i,j,k}}{2}$$

$$\overline{U}_{i,j,k}=\frac{U_{i+1,j,k}+U_{i-1,j,k}}{2}$$

and μ^* represents the effective viscosity given by

$$\mu^*_{i,j+1/2,k}=\mu+\mu_t=\mu+\rho\,\ell_p{}^2\left[\left(\frac{\partial U}{\partial y}\right)^2+\left(\frac{\partial U}{\partial z}\right)^2\right]^{1/2}\Bigg|_{i,j+1/2,k} \quad (14)$$

From the von Neumann-Fourier analysis, the stability restriction is found to be (for equal Δy and Δz)

$$(|V_{ij}|+|W_{ij}|)\,\Delta x < U_{ij}\sqrt{\Delta y^2+\Delta z^2} \quad (15)$$

where, for the case of strongly varying effective viscosities, the left-hand-side of equation (15) must be replaced by terms of the type

$$|V_{ij}|+\left|\frac{\partial \mu^*}{\partial y}\right|_{ij}$$

By rewriting equation (13) in the form:

$$\rho U_{i+1,j,k}=\rho U_{i,j,k}-\frac{\overline{P}_{i+1}-\overline{P}_{i-1}}{2U_{i,j,k}}+f(u,V,W,\mu^*) \quad (16)$$

integrating over the cross section, and imposing conservation of mass, it is possible to obtain a value for $\overline{P}_{i+1}$. This value is then used in equation (13) to determine the value of $U_{i+1,j,k}$.

The transverse velocities, V and W, were determined by using an implicit formulation of equations (3) and (4) in which $P(y, z)$ was taken to represent the local perturbation of the pressure field from the mean streamwise value, $P(x)$. The equations were solved by utilizing the continuity equation to yield an elliptic equation for $P(y, z)$ [9]. Once $P(y, z)$ was determined, the transverse momentum equations were used to solve for V and W. The decision to use an implicit method and a computational cell surface location for the transverse velocity components, as opposed to an explicit method, was based upon the observation that it is the secondary flow and its effect upon U and T which distinguish the duct flow from a two-dimensional channel flow. From this point of view, it is important to compute the secondary velocity components as accurately as possible and, taking into consideration the weakness of the transverse pressure field, $P(y,$

z), *an implicit method was judged to be the only satisfactory approach.*

In calculating the velocity components, special care was needed to ensure that the eddy viscosity values were consistently evlauated, especially in the neighborhood of the wall where the law-of-the-wall was used. Since experimental flows are usually turbulent from the duct entrance, either by design or because of naturally occurring inlet disturbances, the law of the wall, in conjunction with the seventh power law velocity profile, was applied at all axial positions to determine the wall shear stress which was then used in evaluating the axial velocity at the first nodal point from the wall. In particular, spatial averaging techniques were used in order to model the primary flow velocity gradients accurately [18]. It should also be noted that some stability problems were encountered when using the equations directly, and a weighted average value of μ_t (following the method of [15] and [16]) had to be used, namely,

$$\mu_{ti,j,k+1/2} = \frac{\ell_p{}^2{}_{i,j,k+1/2}}{2}\left(\frac{U_{i,j,k+1} - U_{i,j,k}}{\Delta z} - \frac{U_{i,j,k+2} - U_{i,j,k-1}}{3\Delta z}\right) \quad (17)$$

The finite difference form of the thermal energy equation that was employed was analogous to the axial momentum equation (13) with U replaced by T and μ replaced by k, using equations (12) and (13) to specify the eddy thermal diffusivity. The same stability restriction upon Δx and the same averaging procedure for k_t as for μ_t were employed.

In order to compute the local flow development from an initially uniform flow at $x/D_h = 0$ to a nominally fully-developed flow at $x/D_h = 120$, the typical CPU time on a CDC 6600 computer was 2.2 minutes for a 10×10 uniform mesh.[1] Additional computations were also made with a 20×20 uniform mesh, for which CPU time was approximately nine minutes.

Comparisons between Predictions and Experiment

Isotach Distributions. Predicted isotach distributions in a quadrant of the duct at two streamwide locations ($x/D_h = 24$ and 96) for Re = 75,000 are shown in Fig. 4, where a comparison is also made with experimental distributions measured by Alexopoulos [19] at nominally the same operating conditions ($x/D_h = 94$ and Re = 77,000). The predicted distributions at each streamwise location indicate that grid spacing effects do not have a significant influence on local primary flow behavior, except for a slight effect in the outer region of the boundary layer. Close comparison of the predicted distributions at $x/D_h = 96$ with Alexopoulos' results indicates differences of less than 2 percent throughout the entire flow field. This level of agreement is indicative of that which exists between predictions based on the present model and a data set obtained by the present authors at a higher Reynolds number (cf. Fig. 10(a) of [20]).

Secondary Flow Behavior. Fig. 5 shows predicted secondary flow velocity vectors corresponding to the isotach patterns shown in Fig. 4. At $x/D_h = 24$, there is a relatively weak, but well-defined secondary flow which does not yet have a pronounced influence on the local isotach distributions at this location (refer to Fig. 4(a)). Similar behavior was noted by Tatchell [6] in his comparisons between predicted and measured mean velocity distributions at $x/D_h = 35$ when a $k - \epsilon$ model was employed. At $x/D_h = 96$, the strength of the secondary flow has increased markedly (Fig. 5(b)), and transport effects are now reflected by the distorted isotachs shown in Fig. 4(b). With reference to Fig. 5, it can be seen that secondary flow predictions are sensitive to grid spacing effects, and that the magnitude of the secondary flow velocity vectors based on a 20×20 mesh grid are approximately 30 to 50 percent greater than those referred to a 10×10 mesh grid. The contrast is especially evident in the vicinity of the corner bisector. This sensitivity of secondary flow strength to grid spacing effects does not have marked influence on the local primary flow structure, however, (refer to Fig. 4(b)), and therefore all of the comparisons which follow are based on computations referred to a 10×10 mesh grid.

[1] This grid applies for a quadrant of the flow and does not include the image points about the solid boundaries and the lines of symmetry.

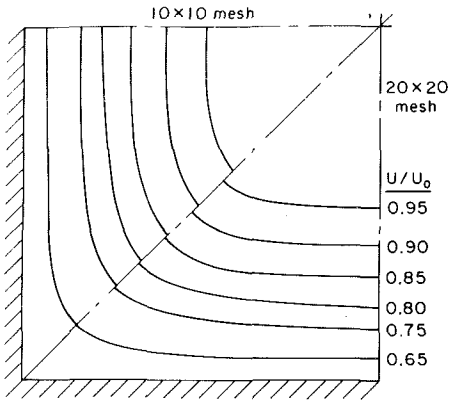

Fig. 4(a) $x/D_h = 24$

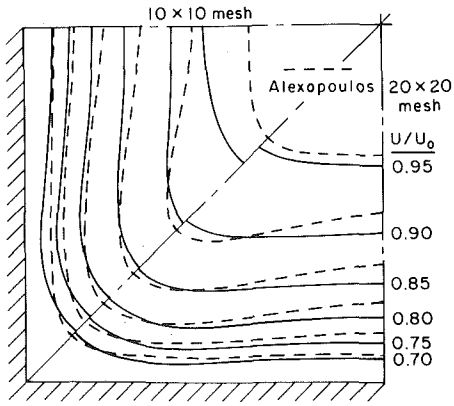

Fig. 4(b) $x/D_h = 96$

Fig. 4 Predicted and measured isotach distributions at $x/D_h = 24$ and 96 for Re = 75,000

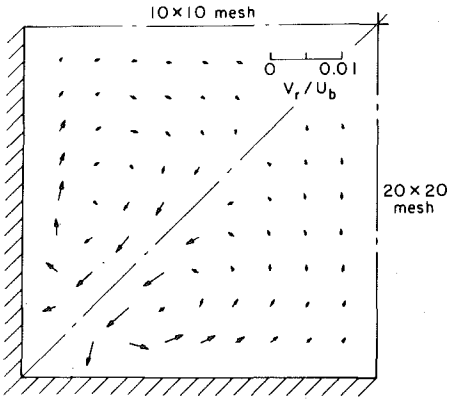

Fig. 5(a) $x/D_h = 24$

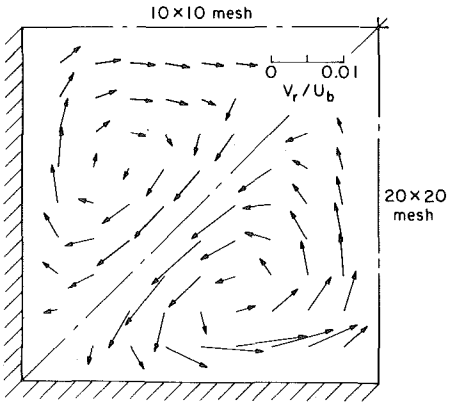

Fig. 5(b) $x/D_h = 96$

Fig. 5 Predicted secondary flow velocity vectors at $x/D_h = 24$ and 96 for Re = 75,000

Local Wall Shear Stress Behavior. Computed and measured local wall shear stress distributions for fully-developed flow in a square duct are compared in Fig. 6. The data of Leutheusser [21] are based on measurements at Re = 34,000 and Re = 84,000, with no significant differences between the two distributions. The predictions of Ramachandra and Spalding [4] at Re = 34,000, which are based on a $k - \epsilon$ level of closure, are in somewhat better agreement with Leutheusser's results than the present predictions at Re = 84,000. A more complete comparison between predictions based on various levels of closure and available experimental data has recently been presented elsewhere [20].

Heat Transfer Results. Heat transfer calculations were made for all Reynolds numbers with a 10×10 grid and for a few selected values of the Reynolds number with the 20×20 grid to investigate the effect of grid sizes. The 20×20 calculations gave nearly identical isotherm patterns, slightly higher heat transfer for $x < 20\ D_h$, and about 6 percent higher fully-developed Stanton numbers [18]. A comparison between predicted and measured isotherms for fully-developed flow in a square duct with a uniform wall temperature are shown in Fig. 7. The experimental distributions are based on data obtained by Alexopoulos [19]. In this instance, the level of agreement between predicted and measured distributions is not as good as that observed in Fig. 4(*b*) for the velocity field. In particular, a comparison of predicted isotachs and isotherms in the near corner region indicates that the secondary flow does not convect thermal energy as effectively as primary flow momentum (compare Figs. 4(*b*) and 7). In general, however, the predicted isotherms in Fig. 7 are in relatively good agreement with their experimental counterparts elsewhere in the flow.

Fig. 8 compares the predicted and measured local wall heat flux distributions at various streamwise locations along a square duct with a uniform wall temperature. The present predictions compare favorably with the experimental data of Brundrett and Burroughs [3], and with the predictions of Ramachandra and Spalding [4] which are based on the $k - \epsilon$ model. The lower set of distributions in Fig. 8 demonstrates that caution must be observed in making comparisons between predictions and data which ostensibly apply for fully-developed flow. At Re = 75,000, for example, the present predictions are indicative of a change in the local near-wall flow structure between $x/D_h = 60$ and $x/D_h = 120$, with an associated increase in peaking of the local wall shear stress distribution. This increase occurs, even though the prescribed length-scale model is invariant with x for $x/D_h \geq 60$. A further comparison between predictions at $x/D_h = 90$ for Re = 75,000 and Re = 250,000 indicates that a Reynolds number effect is also present, with local peaking being more pronounced at the higher Reynolds number.

The Nusselt number variation with Reynolds number for nominally fully-developed flow and heat transfer in a square duct is shown in Fig. 9. The data of Alexopoulos [19] are based on an axially constant heat flux, but with an essentially uniform peripheral duct wall temperature at each axial location, while the data of Lowdermilk, et al. [22] are referred to a uniform wall heat flux condition. It should also be noted that the results of Lowdermilk, et al. are average values over the duct length and are based on measurements in a square duct in which the thermal and hydrodynamic boundary layers developed simultaneously from $x/D_h = 0$ to a location only 53 hydraulic diameters downstream. In evaluating the local Nusselt number, the wall temperature was defined to be the average of the corner and mid-side temperature. In contrast, the Nusselt numbers evaluated by Alexopoulos were values at $x/D_h = 94$ where both the flow and heat transfer were nominally fully-developed. This difference in definitions could account for the slight, but consistent, differences between the two data sets. With reference to Fig. 9 it can be seen that the data lie consistently below the Dittus-Boelter correlation, which applies for circular pipe flow. It is also evident that the present predictions and those of Ramachandra and Spalding [4] agree well with Alexopoulos' data, although the present predictions are slightly low. It should be noted here that the computations were performed for both constant wall heat flux and constant wall temperature conditions, with no substantial differences between the Nusselt number results for fully-developed flow.

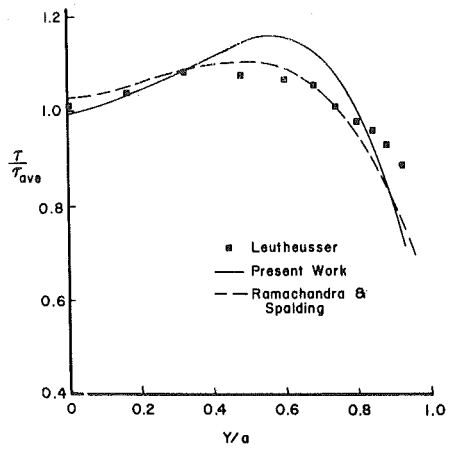

Fig. 6 Peripheral wall shear stress variation

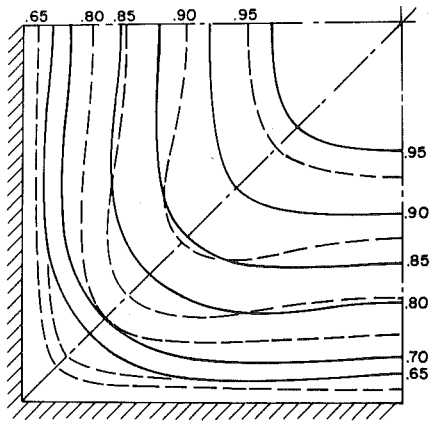

Fig. 7 Comparison of measured and predicted isotherms ($T - T_w / T_0 - T_w$) for constant wall temperature. (——Alexopoulos —numerical Predictions)

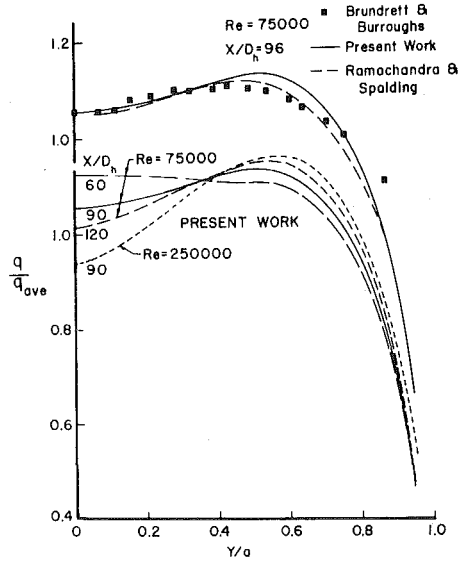

Fig. 8 Peripheral wall heat flux variation (note that there are two sets of curves with the lower set showing the development at Re = 75,000 and the effect of changing Re)

Entrance Region Behavior. Fig. 10 shows the calculated axial variation of the duct centerline velocity, skin friction coefficient, and Stanton number over a 10:1 Reynolds number range based on a prescribed constant wall temperature. The local peaking of the axial centerline velocity distributions is a result of shear layer interaction

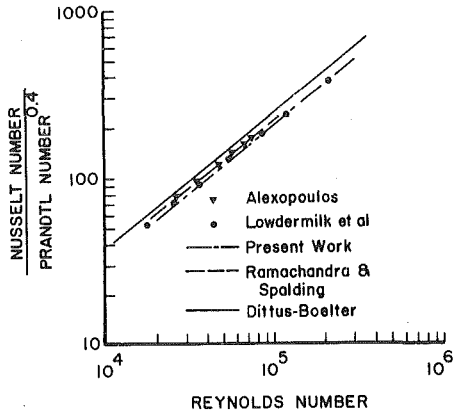

Fig. 9 Fully developed heat transfer in a square duct with isothermal walls

effects as the boundary layers developing along the four walls of the duct begin to merge (at $x/D_h = 32$ for Re = 250,000 [15]). The leftward shift of the peak as the Reynolds number decreases is in accord with the $k - \epsilon$ predictions of Tatchell [6], and with the experimental distributions measured by Melling and Whitelaw [14] and Gessner, et al. [15] at Re = 42,000 and 250,000, respectively.

Both the Stanton number and skin friction decrease initially in the duct, which is in accord with anticipated behavior, but then increase gradually as the flow progresses downstream. A similar trend has been observed experimentally for developing, two-dimensional flow in high-aspect ratio rectangular ducts (cf. Fig. 8 of [17]). This behavior is probably attributable to shear layer interaction effects between $x/D_h \simeq 20$ and 60, which lead to elevated mean rates of strain in the outer region of the boundary layer and slightly depressed strain rates near the wall in comparison to fully-developed values (cf. Fig. 5 of [15]). In the region before shear layer interaction effects influence the flow ($x/D_h \leq 20$), the Stanton number and $C_{fx}/2$ distributions are similar and differ by an amount in close accord with Colburn's correlation for turbulent flat plate flow [23]. As the flow progresses downstream, the distributions diverge, which implies that three-dimensional effects induced by the growth of secondary flow are now influencing local behavior at the wall. The predicted values of $C_{fx}/2$ at $x/D_h \simeq 80$ agree well with the data of Lowdermilk, et al. [22], but St_x values are slightly low in comparison to the data for reasons similar to those discussed earlier in conjunction with Fig. 9.

Predicted and measured local Nusselt number distributions in the near entrance region of an asymmetrically heated square duct are shown in Fig. 11. The data were obtained by Yang and Liao [24] in a duct composed of two uniformly heated opposite walls and two adiabatic side walls, and appear to be the only heat transfer data presently available for the entrance region of a square duct. The inlet of their experimental configuration ($x/D_h = 0$) was located a short (unspecified) distance downstream of an abrupt entrance section attached to a plenum chamber, and fine mesh screens were located approximately two hydraulic diameters upstream of the duct inlet to reduce the local turbulence level. The experimental inlet conditions do not correspond, therefore, to those employed in the present predictions. Fig. 11 does indicate, however, that similar trends exist between the present predictions and the experimentally measured distribution. In making the comparison it should be noted that Yang and Liao define a local Nusselt number in terms of a centerline wall temperature, which was also employed in the present predictions (mid-side value distribution) to facilitate a direct comparison. The local Nusselt number variation based on a peripherally averaged wall-temperature is included in Fig. 11 to demonstrate the relative influence of reference temperature on the results. This figure also shows that predicted values of Nu_x in the entrance region of an asymmetrically heated duct may be below their fully-developed counterparts, similar to observed behavior in Fig. 10 for a duct with uniform wall temperature.

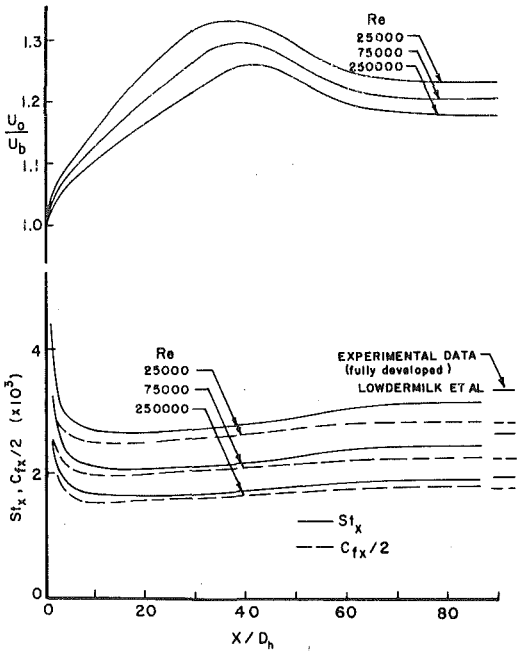

Fig. 10 Axial variation of the centerline velocity, skin friction coefficient, and Stanton number.

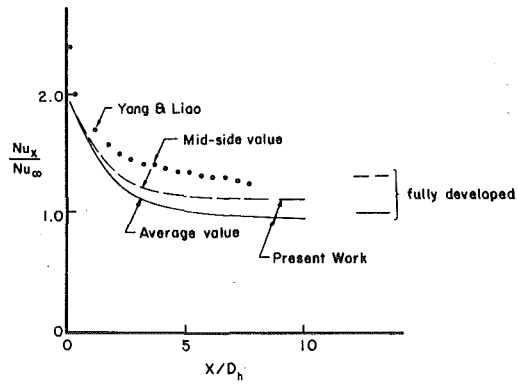

Fig. 11 Local Nusselt number variation for developing flow in an asymmetrically heated duct with constant wall flux

Conclusions

In the present paper comparisons have been made between predictions and experiment for both developing and fully-developed flow and heat transfer in a square duct. The present predictions are based on an algebraic closure model and compare favorably with those referred to the $k - \epsilon$ model. Both temperature and velocity field predictions for fully-developed flow display the transport effects of secondary flow and are in good agreement with data. Local wall shear stress and heat flux distributions exhibit observed peaking behavior between the duct midplane and corner region. Average Nusselt number predictions for fully-developed flow lie approximately ten percent below the Dittus-Boelter correlation, which is in accord with experimentally measured distributions. Predictions in the entrance region exhibit observed undershoot behavior of both the Stanton number and skin friction coefficients. For developing heat transfer in an asymmetrically heated square duct, the same trend is observed for the local Stanton number, and the predicted Stanton number variation in the near entrance region is qualitatively in accord with the limited experimental data presently available.

Acknowledgment

This study was sponsored by the National Science Foundation under NSF Grant ENG 76-11818. The authors would like to express their appreciation to the National Science Foundation for their support of this work.

References

1 Deissler, R. G., and Taylor, M. F., "Analysis of Turbulent Flow and Heat Transfer in Noncircular Passages," NACA Tech. Rep. R-31, 1959.

2 Launder, B. E., and Ying, W. M., "Fully-Developed Turbulent Flow in Ducts of Square Cross Section," Report TM/TN/A/11, Department of Mechanical Engineering, Imperial College of Science and Technology, London, 1971 (see also *Proceedings of the Institution of Mechanical Engineers,* Vol. 187, 37/73, 1978, pp. 455–461).

3 Brundrett, E., and Burroughs, P. R., "The Temperature Inner-Law and Heat Transfer for Turbulent Air Flow in a Vertical Square Duct," *International Journal of Heat and Mass Transfer,* Vol. 10, 1967, pp. 1133–1142.

4 Ramachandra, V., and Spalding, D. B., "Fluid Flow and Heat Transfer in Rectangular-Sectioned Ducts," Report HTS/76/21, Department of Mechanical Engineering, Imperial College of Science and Technology, London, Nov. 1976.

5 Lund, E. G., "Mean Flow and Turbulence Characteristics in the Near Corner Region of a Square Duct," M.S. Thesis, Department of Mechanical Engineering, University of Washington, 1977.

6 Tatchell, D. G., "Convection Processes in Confined, Three Dimensional Boundary Layers," Report HTS/75/20, Department of Mechanical Engineering, Imperial College of Science and Technology, London, July 1975.

7 Neti, S., "Measurements and Analysis of Flow in Ducts and Rod Bundles," Ph.D. Thesis, Department of Mechanical Engineering, University of Kentucky, 1977.

8 Gessner, F. B., "Preliminary Report: Corner Flow Data Evaluation," Department of Mechanical Engineering, University of Washington, Jan. 1979.

9 Patankar, S. V., and Spalding, D. B., "A Calculation Procedure for Heat, Mass and Momentum Transfer in Three-Dimensional Parabolic Flows," *International Journal of Heat and Mass Transfer,* Vol. 15, 1972, pp. 1787–1806.

10 Gessner, F. B., and Emery, A. F., "A Reynolds Stress Model for Turbulent Corner Flows—Part I: Development of the Model," ASME *Journal of Fluids Engineering,* Vol. 98, No. 2, 1976, pp. 261–268.

11 Gessner, F. B., and Emery, A. F., "A Length-Scale Model for Developing Turbulent Flow in a Rectangular Duct," ASME *Journal of Fluids Engineering,* Vol. 99, No. 2, 1977, pp. 347–356.

12 Hanjalic, J., and Launder, B. E., "A Reynolds Stress Model of Turbulence and Its Application to Thin Shear Flows," *Journal of Fluid Mechanics,* Vol. 52, Part 4, 1972, pp. 609–638.

13 Buleev, N. I., "Theoretical Model of the Mechanism of Turbulent Exchange in Fluid Flows," AERE Translation 957, Atomic Energy Research Establishment, Harwell, England, 1963.

14 Melling, A.. and Whitelaw, J. H., "Turbulent Flow in a Rectangular Duct," *Journal of Fluid Mechanics,* Vol. 78, Part 2, 1976, pp. 289–315.

15 Gessner, F. B., Po, J. K., and Emery, A. F., "Measurements of Developing Turbulent Flow in a Square Duct," in *Proceedings of the First Symposium on Turbulent Shear Flows* (edited by Durst, et al.), Springer-Verlag, 1979.

16 Pletcher, R. H., and Nelson, R. M., "An Explicit Scheme for the Calculation of Confined Turbulent Flows with Heat Transfer," *Proceedings of the 1974 Heat Transfer and Fluid Mechanics Institute,* Stanford University Press, 1974, pp. 154–170.

17 Emery, A. F., and Gessner, F. B., "The Numerical Prediction of Turbulent Flow and Heat Transfer in the Entrance Region of a Parallel Plate Duct," ASME JOURNAL OF HEAT TRANSFER, Vol. 98, No. 4, 1976, pp. 594–600.

18 Emery, A. F., Neighbors, P. K., and Gessner, F. B., "A Computational Procedure for Developing Turbulent Flow and Heat Transfer in a Square Duct," (accepted for presentation at the National Conference on Numerical Methods in Heat Transfer, University of Maryland, Sept. 1979).

19 Alexopoulos, C. C., "Temperature and Velocity Distributions and Heat Transfer for Turbulent Air Flow in a Square Duct," M.A. Sc. Thesis, Department of Mechanical Engineering, University of Toronto, 1964.

20 Gessner, F. B., and Emery, A. F., "The Numerical Prediction of Developing Turbulent Flow in Rectangular Ducts," (accepted for presentation at the Second Symposium on Turbulent Shear Flows, Imperial College of Science and Technology, London, July 1979).

21 Leutheusser, H. J., "Turbulent Flow in Rectangular Ducts," *Journal of the Hydraulics Division, Proceedings ASCE,* Vol. 89, HY3, 1963, pp. 1–19.

22 Lowdermilk, W. H., Weiland, W. F., Jr., and Livingood, J. N. B., "Measurement of Heat Transfer and Friction Coefficients for Flow of Air in Noncircular Ducts at High Surface Temperatures," NACA RM E53J07, 1954.

23 Colburn, A. P., "A Method of Correlating Forced Convection Heat Transfer Data and a Comparison with Fluid Friction," *Transaction of the American Institute of Chemical Engineers,* Vol. 29, 1933, pp. 174–210.

24 Yang, J. W., and Liao, N., "An Experimental Study of Turbulent Heat Transfer in Converging Rectangular Ducts," ASME JOURNAL OF HEAT TRANSFER, Vol. 95, 1973, pp. 453–457.

M. Faghri[1]
Department of Mechanical Engineering,
Tehran University of Technology,
Tehran, Iran

E. M. Sparrow
Department of Mechanical Engineering,
University of Minnesota,
Minneapolis, Minn. 55455
Fellow ASME

Simultaneous Wall and Fluid Axial Conduction in Laminar Pipe-Flow Heat Transfer

Consideration is given to a laminar pipe flow in which the upstream portion of the wall is externally insulated while the downstream portion of the wall is uniformly heated. An analysis of the problem is performed whose special feature is the accounting of axial conduction in both the tube wall and in the fluid. This conjugate heat transfer problem is governed by two dimensionless groups—a wall conductance parameter and the Peclet number, the latter being assigned values from 5 to 50. From numerical solutions, it was found that axial conduction in the wall can carry substantial amounts of heat upstream into the non directly heated portion of the tube. This results in a preheating of both the wall and the fluid in the upstream region, with the zone of preheating extending back as far as twenty radii. The preheating effect is carried downstream with the fluid, raising temperatures all along the tube. The local Nusselt number exhibits fully developed values in the upstream (non directly heated) region as well as in the downstream (directly heated) region. Of the two effects, wall axial conduction can readily overwhelm fluid axial conduction.

Introduction

The intense research activity on heat transfer in laminar duct flows has been given sharp focus by the Shah-London monograph [1], where the world literature on the subject has been brought together. From a study of the information contained there, it is apparent that only limited consideration has been given to problems where heat conduction in the duct wall interacts with the convective transfer between the wall and the fluid. Such interactive situations are often referred to as conjugate problems.

The impact of wall heat conduction on duct-flow convection is relatively greater in laminar flows than in turbulent flows. This is because, in general, the laminar heat transfer coefficients are substantially lower than the turbulent coefficients. Therefore, in the laminar case, the wall offers a heat flow path that is an attractive alternative to that offered by convection.

In this paper, an analysis is performed for a laminar pipe flow of a low Peclet number fluid which interacts with axial conduction in the pipe wall. A schematic diagram of the physical situation is pictured in Fig. 1. As shown in the figure, in one portion of the tube (designated as $x > 0$) there is either a uniform heating within the wall of the tube or a uniform heating at the outside surface of the tube. In the other portion ($x < 0$), the outside surface of the tube is insulated. However, the externally insulated portion receives heat via axial conduction through the wall and, in turn, passes it along to the fluid. Thus, the fluid may be heated in the region $x < 0$ as well as in the region $x > 0$.

In addition to the axial transport of heat through the wall, there is also appreciable axial conduction of heat in the fluid when the Peclet number is low. Thus, both wall and fluid conduction act together to preheat the fluid prior to its arrival at the directly heated portion of the tube. As will be demonstrated later, the distance to which the preheating penetrates into the upstream portion of the tube depends on both the Peclet number and on a dimensionless wall conduction parameter. Upstream of the penetration distance, the fluid has a uniform temperature T_0.

In the problem to be considered here, the heated portion of the tube will be of sufficient length to enable thermally developed conditions to be attained. As in conventional problems of uniform heat flux, thermal development is also characterized here by a linear temperature rise in both the fluid and the wall. Another feature of the present analysis is the focus on thin-walled tubes, so that radial temperature gradients in the wall need not be considered. The velocity profile at all axial stations is the fully developed Poiseuille parabola.

The temperature and heat flux at the solid-fluid interface are not known a priori and depend on the coupled mechanisms of heat transfer in the fluid and in the solid. Solutions of the problem were obtained by an elliptic finite-difference method employing an iterative scheme which dealt consecutively with the fluid and the tube wall. The results depend on two parameters—the Peclet number Pe and the wall conduction parameter $\beta = k_w t/kR$. In presenting the results, account was taken of the fact that the local convective heat flux q, the local wall temperature T_w, and the local bulk temperature T_b are all unknown functions of x. Consequently, numerical results are presented for each of these quantities, expressed in suitable dimensionless groups. Local Nusselt numbers are also presented.

A careful search of the literature failed to disclose any prior work on the problem that has been outlined in the preceding paragraphs. Papers that are related to the general topic will now be cited. For the case of a thermally inactive wall and a low-Peclet-number flow, the effect of axial conduction in the fluid was examined by a number of investigators, and the relevant literature has been brought together in Chapter 5 of [1]. Wall conduction effects have been studied for flows where there is no axial conduction in the fluid and for physical situations that differ from that investigated here. In [2–4], consideration was given to problems in which the conduction was confined to a finite length of heated wall, with an adiabatic boundary condition imposed at the upstream and downstream ends of the heated segment. A semi-infinite heated and conducting wall was considered in [5–7], with either a given temperature or adiabatic condition being prescribed at the upstream end of the wall. In [8], a slug-flow model (flat velocity profile) was employed to simplify the task of solving a sampling of wall conduction problems which are quite different from that investigated here.

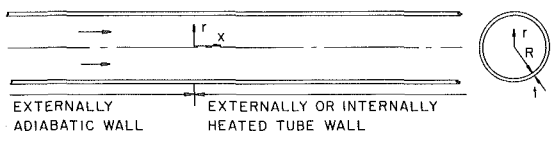

Fig. 1 Schematic diagram of the problem

[1] Work performed when the author was an adjunct associate professor at the University of Minnesota.

Contributed by the Heat Transfer Division and for publication in the JOURNAL OF HEAT TRANSFER. Manuscript received by the Heat Transfer Division June 1, 1979.

Analysis and Solution

Governing Equations. The conjugate heat transfer problem encompassing the flowing fluid and the tube wall is governed by the respective energy equations. Attention will first be focused on the energy equation for the wall. As noted earlier, consideration is being given here to relatively thin walls so that temperature variations across the thickness of the wall can be neglected and $T_w = T_w(x)$. For the heated portion of the wall ($x > 0$), the heating may take the form either of a uniform heat flux imposed on the outside surface of the tube or of a uniform generation of heat within the wall. Both of these heating conditions can be represented mathematically as a uniform heat input q_w which, for convenience, is based on the inside surface area of the tube wall. Then, if $q(x)$ denotes the local convective heat flux from the wall to the fluid, the wall energy balance becomes

$$k_w t(d^2T_w/dx^2) + q_w - q = 0 \tag{1}$$

Equation (1) corroborates the expectation that the convective heat flux to the fluid will be less than the heat input at any station x where there is a net upstream conduction of heat (i.e., where $d^2T_w/dx^2 < 0$). It may also be noted that $q_w = q$ at any x in the fully developed regime since dT_w/dx is a constant. The form of equation (1) is similar to that governing the temperature field in a fin.

If q is replaced by $k(\partial T/\partial r)_R$ and dimensionless variables are introduced, equation (1) becomes

$$\beta(d^2\theta_w/dX^2) + 1 - (\partial\theta/\partial\eta)_1 = 0 \tag{2}$$

where

$$\beta = k_w t/kR \tag{3}$$

is a measure of the strength of axial conduction in the wall. The term $(\partial\theta/\partial\eta)_1$ provides the coupling between the temperature field in the fluid and that in the wall.

For the portion of the wall that is not directly heated ($x < 0$), the dimensionless energy balance reduces to

$$\beta(d^2\theta_w/dX^2) - (\partial\theta/\partial\eta)_1 = 0 \tag{4}$$

Since $d^2\theta_w/dX^2$ is expected to be positive in this portion of the wall, equation (4) affirms that there is a convective heat transfer from the wall to the fluid.

The energy equation for the fluid, when written in dimensionless terms and with the Poiseuille velocity profile inserted, is

$$(1 - \eta^2)\frac{\partial\theta}{\partial X} = \frac{1}{\mathrm{Pe}}\left[\frac{1}{\eta}\frac{\partial}{\partial\eta}\left(\eta\frac{\partial\theta}{\partial\eta}\right) + \frac{\partial^2\theta}{\partial X^2}\right] \tag{5}$$

It may be noted that this equation contains both the radial and axial conduction terms, the latter being retained because of the focus on low Peclet number flows. Attention may also be called to the fact that the dimensionless axial coordinate used here is x/R, which results in a factor 1/Pe multiplying *both* conduction terms in equation (5). Had the more common coordinate $(x/R)/\mathrm{Pe}$ been used for X, then the Peclet number would have appeared in (5) only as a multiplier of the axial conduction term; however, it would also have made an appearance in equation (2), replacing β by β/Pe^2. It was deemed desirable to keep the β and Pe parameters separate and, therefore, X was chosen to be x/R.

The coupling between the wall and fluid temperature fields is via the derivative $(\partial\theta/\partial\eta)_1$ which appears in equations (2) and (4) and by the matching condition

$$\theta_{\eta=1} = \theta_w \text{ at any } x \tag{6}$$

In addition, due to symmetry

$$(\partial\theta/\partial\eta)_{\eta=0} = 0 \tag{7}$$

At sufficiently large upstream distances,

$$\theta = \theta_w = 0 \tag{8}$$

On the downstream side, fully developed conditions will be encountered at sufficiently large values of x, where

$$dT/dx = dT_w/dx = 2\pi R q_w/\dot{m}c_p, \quad \text{or } d\theta/dX = d\theta_w/dX = 4/\mathrm{Pe} \tag{9}$$

Total derivatives are employed in (9) because the axial gradient is independent of r. The upstream and downstream distances at which the respective boundary conditions (8) and (9) are to be imposed are not known in advance but are determined as part of the solution effort.

Solution Methodology. Solutions of the problem defined by the foregoing equations were obtained numerically by finite difference procedures. In view of the fact that boundary conditions have to be satisfied at both the upstream and downstream ends of the solution domain, a marching-type solution procedure, proceeding from upstream to downstream, cannot be used. Rather, a so-called elliptic procedure has to be used because all the unknowns (i.e., the temperatures at the nodal points) must be solved for simultaneously.

The general outline of the solution scheme will be discussed first, with details to follow. An iterative approach was used, with the discretized energy equations for the fluid and for the wall being solved consecutively (rather than simultaneously). Suppose, for instance, that n iterations have been completed and that the $(n + 1)$ iteration is about to begin. At this stage, the wall temperature distribution $\theta_w(X)$ has just been determined by solving the difference form of equations (2) and (4).

To start the $(n + 1)$ iteration, this $\theta_w(X)$ is imposed as a boundary condition on the fluid energy equation, which is then solved for $\theta(X,\eta)$. Attention is next turned to the tube wall energy equations in order to update $\theta_w(X)$. The just-obtained solution for $\theta(X, \eta)$ is fed into these equations via the term $(\partial\theta/\partial\eta)_1$, in a manner which will be detailed shortly. Then, the wall equations are solved for $\theta_w(X)$, and this information is used to initiate the $(n + 2)$ iteration. This procedure was continued until convergence was attained to at least four significant figures.

The difference scheme used here for solving the fluid energy equation is an adaptation of that to be accorded book-length description in a forthcoming text by Patankar [9]. The main feature of the adaptation was to revise the treatment of the outflow boundary, that is, the boundary at the downstream end of the solution domain. In the basic computer program, the difference equation for the most downstream control volume was written for a high Peclet number flow—the axial conduction term was omitted and the convection term was evaluated on an upwind basis. Neither of these conditions is

Nomenclature

c_p = specific heat
h = local heat transfer coefficient, $q/(T_w - T_b)$
k = thermal conductivity of fluid
k_w = thermal conductivity of tube wall
$\dot{m}$ = mass flow rate
Nu = local Nusselt number, $h(2R)/k$
Pe = Peclet number, $\overline{u}(2R)/\alpha$
q = local convective heat flow
q_w = uniform heat input to tube wall, $x > 0$
R = tube radius
r = radial coordinate
T = temperature
T_b = local bulk temperature
T_0 = temperature far upstream
T_w = local wall temperature
t = wall thickness
$\overline{u}$ = mean velocity of fluid
X = dimensionless coordinate, x/R
x = axial coordinate
α = thermal diffusivity of fluid
β = wall conductance parameter, $k_w t/kR$
η = dimensionless coordinate, r/R
θ = dimensionless temperature, $(T - T_0)/(q_w R/k)$
θ_b = dimensionless bulk temperature, $(T_b - T_0)/(q_w R/k)$
θ_w = dimensionless wall temperature, $(T_w - T_0)/(q_w R/k)$

Subscript
fd = fully developed

correct for a low Peclet number flow, and appropriate modifications were made.

For the fluid, a total of 1875 grid points were used. Twenty-five grid points were deployed at each of 75 axial stations. Furthermore, to obtain enhanced accuracy, the grid points were positioned nonuniformly. In the radial direction, the grid point density was highest near the tube wall, whereas in the axial direction the highest concentration of grid points was in the neighborhood of $X = 0$. In the positioning of the grid points, guidance was obtained from two limiting solutions for which results were available for comparison: low Peclet number heat transfer in the presence of an inactive wall and the classical uniform heat flux case (no Peclet number effect and no wall effect).

The discretization and solution methodology for the tube wall energy equations (2) and (4) will now be described. The second derivative $d^2\theta_w/dX^2$ was recast in difference from via Taylor series expansions, yielding a central-difference representation for a nonuniform array of points X_{i-1}, X_i, X_{i+1}. For the derivative $(\partial\theta/\partial\eta)_1$ at point X_i, the following representation was used

$$[(\partial\theta/\partial\eta)_1]_i = (\theta_{w,i} - \theta_{wa,i})/\Delta\eta_w \tag{10}$$

where the subscript wa denotes the wall-adjacent point, and $\Delta\eta_w$ is the radial step size between wa and w. Note that the numerical value of θ_{wa} is provided by the solution of the fluid energy equation.

With the discretizations noted above, the wall energy equations (2) and (4) can be written as

$$a_i\theta_{w,i} = a_{i-1}\theta_{w,i-1} + a_{i+1}\theta_{w,i+1} + b \tag{11}$$

The quantity b is a source term. It contains the wall-adjacent temperature $\theta_{wa,i}$ as well as the direct heat input (equal to one for equation (2) and to zero for equation (4)). At the upstream end of the solution domain, equation (11) is replaced by the condition $\theta_i = 0$, while at the downstream end a special difference equation was written to incorporate the condition $d\theta_w/dX = 4/\mathrm{Pe}$.

With known values of θ_{wa} from the immediately preceding solution of the fluid energy equation, the set of equations represented by equation (11) was solved by the tridiagonal matrix algorithm. This yielded a distribution $\theta_w(X)$ which was employed as a boundary condition for a new solution of the fluid energy equation.

The placement of the upstream and downstream boundaries of the solution domain was determined so that their further repositioning (respectively farther upstream and downstream) had no effect on the results to within plotting accuracy. The boundary placement was found to depend on both the Pe and β parameters; this dependence will be evident from the graphical presentation of the results.

Accuracy tests of the computational scheme were made by comparisons with the following literature information: (1) axially conducting fluid with a nonparticipating wall ([10] as tabulated in [1]), (2) uniform heat flux without axial conduction in wall or fluid (eigenvalues and related constants from [1]), (3) one-dimensional fin exchanging heat with a fluid environment with uniform heat transfer coefficient and bulk temperature. All of these tests were passed at a satisfactory level of agreement, within ½ percent or better.

Presentation Parameters. The numerical solutions were employed to evaluate various parameters for inclusion in the presentation of results. One of these is the local bulk temperature T_b which, in dimensionless form, can be expressed as

$$\theta_b = (T_b - T_0)/(q_wR/k) = \int\theta(1-\eta^2)\eta d\eta/\int(1-\eta^2)\eta d\eta \tag{12}$$

with the integral being extended over the range $0 \le \eta \le 1$. The linear bulk temperature rise that is characteristic of uniformly heated flows does not prevail under the conditions studied here, except in the fully developed regime.

To evaluate the bulk temperature at any axial station x in the fully developed regime, a cylindrical control volume of radius R may be used. The control volume extends sufficiently far into the non directly heated portion of the tube so that $T = T_0$ at its upstream face. The downstream face of the control volume is at x.

The heat entering the fluid via conduction through the three surfaces of the control volume is as follows: (1) upstream face, no conduction; (2) cylindrical surface,

$$(2\pi Rx)q_w + k_w(2\pi Rt)(dT/dx)_{fd} \tag{13}$$

(3) downstream face,

$$k(\pi R^2)(dT/dx)_{fd} \tag{14}$$

In equation (13), the first term represents the heat input to the wall between $x = 0$ and $x = x$, whereas the second term is the heat conducted axially through the wall cross section at $x = x$. The heat quantity that is expressed by equation (13) is transferred to the fluid along both the directly heated and non-directly heated portions of the wall. Equation (14) represents the fluid axial conduction at $x = x$.

When $(dT/dx)_{fd}$ is taken from equation (9) and the conductive inputs are equated to the enthalpy change experienced by the fluid, it follows that

$$\theta_{b,fd} = (4/\mathrm{Pe})X + 8/\mathrm{Pe}^2 + 16\beta/\mathrm{Pe}^2 \tag{15}$$

The first term on the right in equation (15) is the conventional linear rise that is characteristic of uniform heating in the absence of axial conduction. The second and third terms are, respectively, the contributions of the fluid and tube-wall axial conduction. Both contributions are accentuated at low Pe, and the latter is further accentuated at large values of the wall conductance parameter β.

The wall temperature T_w and its variation with x is another quantity of interest that will be reported in the presentation of results. The dimensionless counterpart of T_w is $\theta_w = (T_w - T_0)/(q_wR/k)$, and numerical values for θ_w are obtained directly from the solutions. In recognition of the fact that the local convective heat flux q will differ from the heat input q_w, information will be provided for the variation of q/q_w with x. In terms of the solution variables, this ratio is

$$q/q_w = (\partial\theta/\partial\eta)_1 \tag{16}$$

The local heat transfer coefficient and local Nusselt number have been evaluated from their definitions

$$h = q/(T_w - T_b), \quad \mathrm{Nu} = h(2R)/k = 2(\partial\theta/\partial\eta)_1/(\theta_w - \theta_b) \tag{17}$$

Results and Discussion

Although the heat transfer coefficient (or Nusselt number) is traditionally the main focus in a presentation of results, there are good reasons for not giving it top billing here. The essential fact is that in the present instance, the heat transfer coefficient contains three unknowns: q, T_w, and T_b, all functions of x. Thus, by giving the value of h (or Nu), a relationship between three unknowns is established, but there is no way of obtaining the actual values of these quantities. In view of this deficiency, there has to be a specific reporting of the results for q, T_w, and T_b, and this is accomplished in what follows. For completeness, Nusselt numbers are presented later.

Convective Heat Transfer. The convective heat flux to the fluid, plotted as the ratio q/q_w, is presented in Figs. 2(*a*), 2(*b*), 2(*c*), and 2(*d*) for Peclet numbers of 5, 10, 20, and 50, respectively. In each figure, results are given for a range of values of the wall conductance parameter β. It may be noted that larger parametric values of β have been employed for the higher Peclet numbers. This is because both β and Pe vary in the same way (i.e., inversely) with the thermal conductivity of the fluid. On the abscissa, there is a major dividing line at $x/R = 0$ to demark the regions of direct heating ($x > 0$) and non direct heating ($x < 0$).

Owing to crossing and overlapping of the curves in the $x > 0$ region and to the long tails in the $x < 0$ region for higher β values, it was necessary to give careful consideration to the structure of the figures in order to avoid confusion. The long tails are accommodated in an inset positioned at the upper left in the respective figures. To minimize crossing and overlapping for $x > 0$ in Fig. 2(*a*), the curves for higher β are referred to an ordinate scale that is displaced relative to that for lower β. However, to provide an interrelationship between

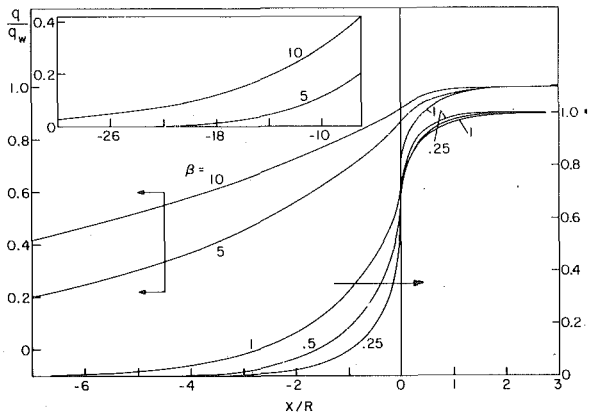

Fig. 2(*a*) Axial distributions of the convective heat flux, Pe = 5

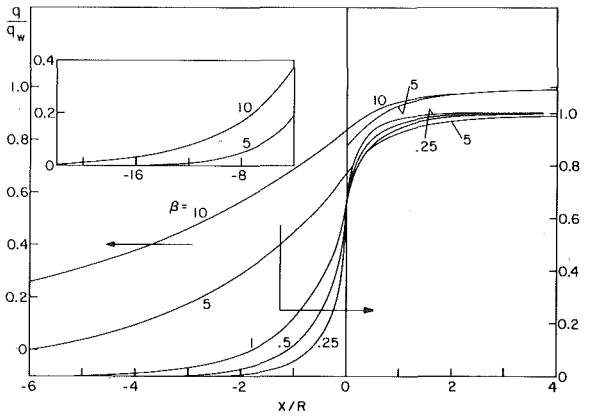

Fig. 2(*b*) Axial distributions of the convective heat flux, Pe = 10

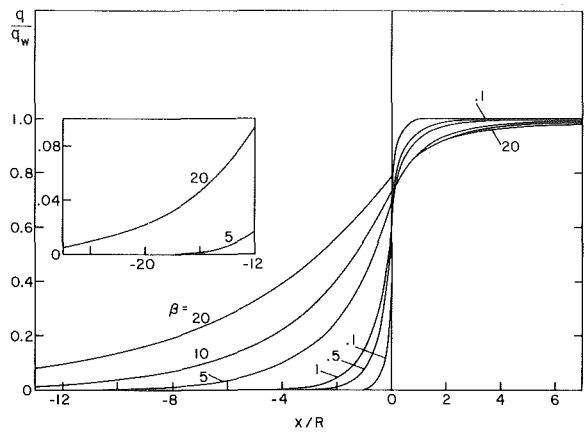

Fig. 2(*c*) Axial distributions of the convective heat flux, Pe = 20

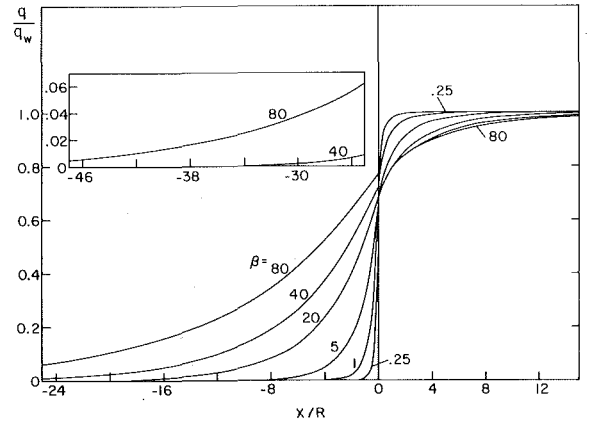

Fig. 2(*d*) Axial distributions of the convective heat flux, Pe = 50

the high and low β curves, the $\beta = 1$ curve is plotted in both sets. A similar arrangement is employed in Fig. 2(b), with $\beta = 10$ being displaced and with the $\beta = 5$ curve plotted in both sets. In Figs. 2(c) and 2(d), a common ordinate scale is used for all cases, but certain curves are interrupted in regions of heavy crossing.

In appraising the results, it is helpful to take note of the q/q_w distribution for the case of no axial conduction in the wall ($\beta = 0$). In that case, $q/q_w = 0$ for all negative x and $q/q_w = 1$ for all positive x.

From an examination of Fig. 2(a–d), certain general trends are in evidence along with some Peclet-number-related differences in detail. The main feature projected by these figures is the substantial amount of convective heat transfer that can occur along the non directly heated portion of the tube. Both the magnitude of this convective heating and the extent of the region where it occurs increase with increasing values of the wall conductance parameter β. As expected, the q/q_w curves drop off with increasing upstream distance as the heat supplied by axial conduction in the wall is drained away by convection to the flowing fluid. The rate of drop-off is markedly affected by the β parameter, becoming more and more gradual at larger β values. Correspondingly, the curves in the region of negative x are arranged in monotonic order with β.

In the region of direct heating ($x > 0$), q/q_w increases with increasing downstream distance and approaches unity as the *net* axial conduction dies away. Near $x = 0$, the departures of q/q_w from unity can be appreciable, and ignoring these deviations (for example, in interpreting experimental results) could lead to substantial errors. The crossing and overlapping of the curves in the $x > 0$ region indicates that there is not necessarily a monotonic ordering with β. A monotonic ordering is, in fact, established as x increases, with the curves for small β being closest to the line $q/q_w = 1$, as expected. The nonmonotonic ordering in the region of small x stems from the dual, but conflicting roles of wall axial conduction. One of these is to transport heat away from this region into the adjacent unheated portion of the tube. The second is to deliver heat to the region from locations that are farther downstream.

As a final comment with regard to Fig. 2(a–d), note may be taken of the effect of Peclet number on the q/q_w results. At a fixed value of β, it can be verified that the size of the upstream region where there is discernible convective heat transfer becomes larger as the Peclet number decreases. On the other hand, for $x > 0$, the region where $q/q_w < 1$ contracts at lower Pe.

Bulk and Wall Temperatures. The axial distributions of the dimensionless bulk and wall temperatures are presented in Fig. 3(a–d) for Pe = 5, 10, 20, and 50, respectively. In each of these figures, the bulk temperature is plotted with reference to the left-hand ordinate scale, while the wall temperature is referred to the right-hand ordinate. The various curves appearing in each figure are parameterized by the wall conductance parameter β. Insets have been provided to accommodate the long upstream tails for higher β curves.

From an overall examination of the figures, wall conduction is seen to have a dramatic effect in preheating both the wall and the fluid at axial stations upstream of the region of direct heating. The preheating effect is propagated downstream by the flowing fluid, resulting in substantial increases of both the bulk and wall temperatures all along the pipe. The impact of the wall conduction is readily gauged by comparing the curves for $\beta > 0$ with that for $\beta = 0$. Such a comparison shows that the extent of the temperature elevation grows rapidly with increasing β. It appears that the temperature distributions are more sensitive to β (i.e., greater elevation for a fixed β) when Pe is small. However, to put this finding in perspective, it may be noted that both β and Pe respond in the same way to changes in the thermal conductivity of the fluid, so that larger β values may be appropriate at higher Pe.

Particular attention may be directed to the bulk and wall temperatures at $x = 0$ where, for conventional no-axial-conduction conditions, $\theta_b = \theta_w = 0$. To provide perspective for the θ_b or θ_w values for $\beta > 0$, consider, for example, the case of Pe = 5 and $\beta = 5$, for which $\theta_b = 3.5$ and $\theta_w = 3.9$. For this same Peclet number and for $\beta = 0$, the corresponding values are 0.35 and 0.55. These results dramatize the necessity of taking proper account of the wall conduction, and they

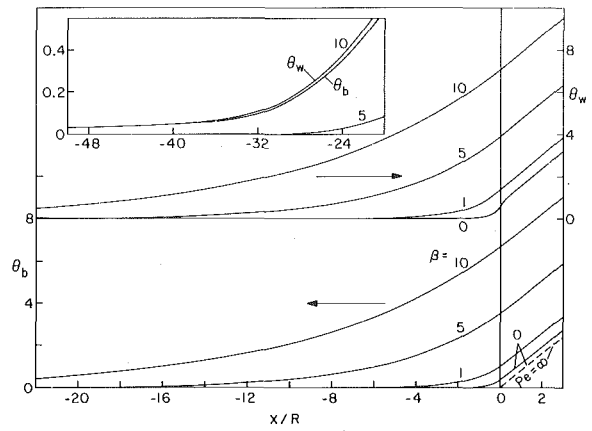

Fig. 3(*a*) Axial distributions of the bulk and wall temperatures, Pe = 5

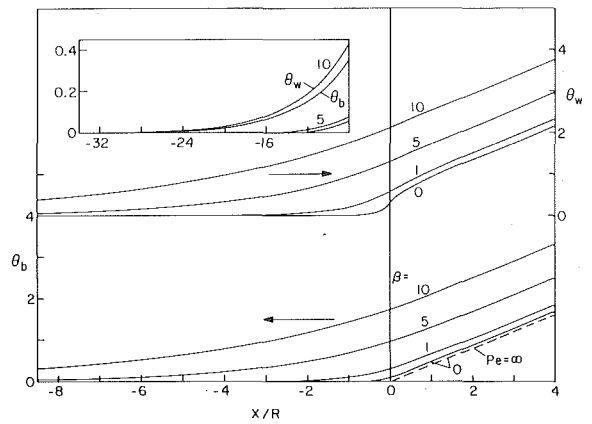

Fig. 3(*b*) Axial distributions of the bulk and wall temperatures, Pe = 10

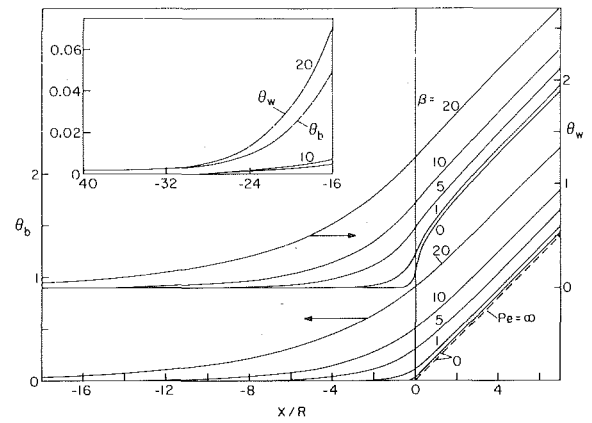

Fig. 3(*c*) Axial distributions of the bulk and wall temperatures, Pe = 20

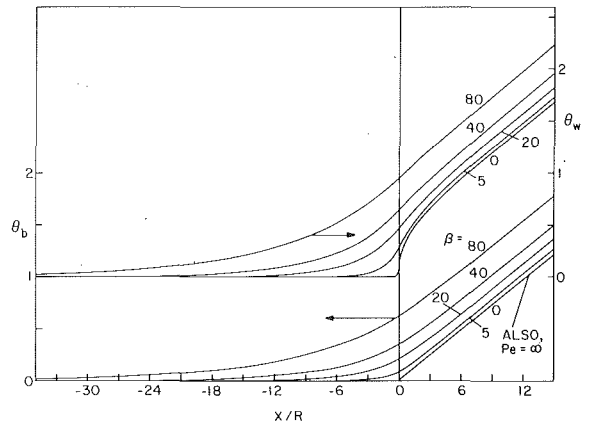

Fig. 3(*d*) Axial distributions of the bulk and wall temperatures, Pe = 50

also heavily underscore the potential errors that can be made by imposing $\theta_b = \theta_w = 0$ as a boundary condition at $x = 0$.

The penetration of the preheating into the upstream region is substantially increased as β increases. At large β values, significant preheating can extend as much as 20 radii upstream of the directly heated portion of the tube. At a given β value, the extent of the preheated region contracts with increasing Peclet number. However, as noted in the foregoing, higher Pe may imply higher β which, in turn, leads to an enlargement of the preheating zone.

All of the bulk temperature curves share a common shape, which is characterized by a steady, regular rise, a concave-upward curvature, and the ultimate attainment of a constant slope. Compared with the bulk, the wall temperature curves are considerably more responsive to changes in the convective heat transfer rate and the convective heat transfer coefficient which occur in the neighborhood of $x = 0$. These changes tend to be more rapid at lower β values, and this is reflected in the wall temperature curves. Thus, whereas the curves of θ_w are concave upward in the upstream region, they are either concave downward or linear in the downstream region.

Before leaving these figures, the bulk temperature results may be compared with two limiting cases. One of these is the fully developed bulk temperature distribution that was derived earlier in the paper and is expressed by equation (15). For Pe = 5, 10, and 20, the straight-line portions of the curves plotted in Figs. 3(*a–c*) are essentially overlapping with equation (15). For Pe = 50, a deviation between the numerical results of Fig. 3(*d*) and equation (15) is just discernible within the scale of the figure (equation (15) is not plotted in the figure to preserve clarity). This deviation serves as a signal to indicate the inadvisability of going on to higher Peclet number cases using an elliptic-type computation scheme—given the limitation of approximately 2000 grid points.

The other limiting case is that of no axial conduction in either the fluid or the wall, and the corresponding bulk temperature distribution is shown as a dashed line (labeled $\beta = 0$ and Pe = ∞) in the respective figures. The deviations between this line and the adjacent $\beta = 0$, Pe = finite curve is due to axial conduction in the fluid. These deviations are small compared to those that are brought about by wall axial conduction. Therefore, wall conduction effects which correspond to even moderate β values can overwhelm the effects of axial conduction in the fluid.

Nusselt Numbers. As was noted earlier, the local Nusselt number is not a convenient computational parameter in the present problem because it includes three unknowns, namely, $q(x)$, $T_w(x)$, and $T_b(x)$. However, as will soon be evident, the Nusselt number distributions do contain some interesting features. These distributions are presented in Fig. 4(*a–d*) for Pe = 5, 10, 20, and 50, respectively. In the first two of these figures, an inset is employed in order to extend the ordinate range to smaller values and thereby to accommodate upstream Nusselt number results for small β.

From an examination of these figures, three key characteristics of the Nusselt number distributions can be identified. They are: (1) a downstream fully developed regime in the directly heated portion of the tube where Nu = 48/11 = 4.364 for all cases, (2) an upstream fully developed regime in the non-directly heated portion of the tube where Nu takes on a constant value which depends on β, and (3) a peak value of Nu which occurs just downstream of the onset of direct heating.

At any given Peclet number, the peak value of Nu decreases monotonically as β increases. This trend reflects the increasing degree of upstream thermal boundary layer development which occurs as wall axial conduction plays a more active role. For all of the investigated Peclet numbers, the peak is situated between $x = 0$ and $x = 0.2R$. The location of the peak moves closer and closer to $x = 0$ as the Peclet number increases.

The attainment of a β-independent fully developed value of Nu at sufficiently large downstream distances is consistent with the vanishing of the *net* axial conduction, which occurs when the fluid and wall temperatures attain a linear variation. At a given Peclet number, the axial station marking the attainment of fully developed conditions

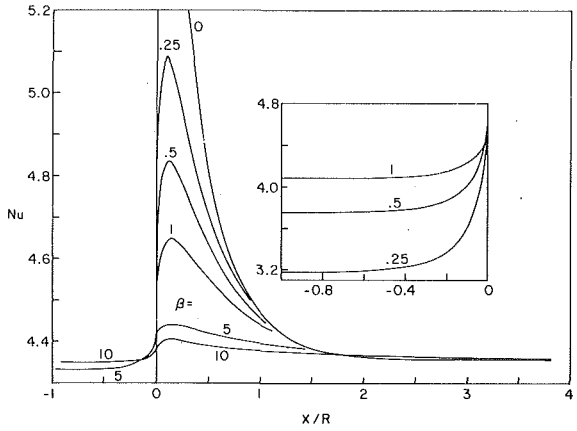

Fig. 4(*a*) Axial distributions of the local Nusselt number, Pe = 5

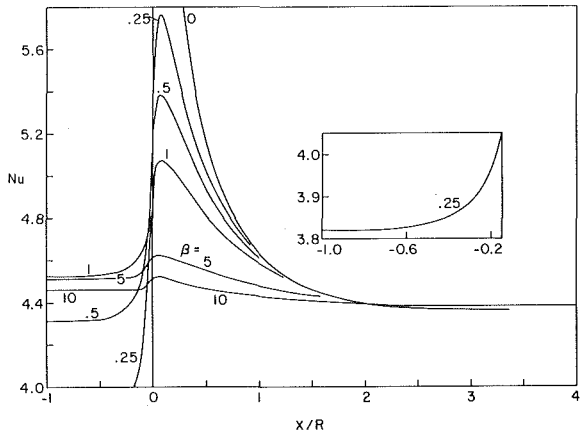

Fig. 4(*b*) Axial distributions of the local Nusselt number, Pe = 10

is very little affected by β. With increasing Peclet number, the development length increases.

Perhaps the most interesting feature of the Nusselt number results is the existence of fully developed values in the upstream region. These values are attained in a remarkably short distance upstream of $x = 0$—in most cases in a length less than half a radius. The magnitudes of these fully developed values show an interesting trend with β. Starting with small β, the Nu values increase, attain a maximum at a particular β, and then decrease with further increases in β. The just-described variation of Nu with β is fully in evidence in Figs. 4(b) and 4(c), but the β ranges of Figs. 4(a) and 4(d) permit only a part of the excursion to be seen.

Concluding Remarks

It has been shown that axial conduction in the tube wall can carry substantial amounts of heat upstream (i.e., opposite to the direction of fluid flow). As a consequence, the upstream portion of the wall, which is not externally heated, participates in an active convective exchange with the fluid. This results in a significant preheating of both the wall and the fluid in the upstream region. The preheated region can extend as much as twenty radii upstream of the point where active heating begins. The effects of the preheating are propagated downstream by the flowing fluid, so that there is a substantial increase in both the wall and bulk temperatures all along the tube. These findings underscore the limitations of the classical Graetz-type formulation.

It was found that the effect of wall axial conduction can readily overwhelm the effect of fluid axial conduction. Furthermore, the results demonstrate the impropriety of prescribing either the wall or the bulk temperature at the beginning of the directly heated region.

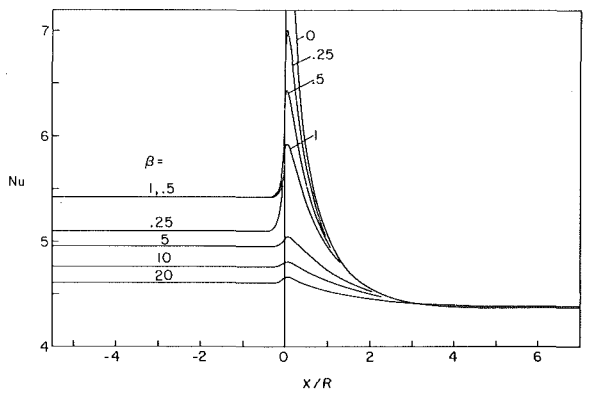

Fig. 4(*c*) Axial distributions of the local Nusselt number, Pe = 20

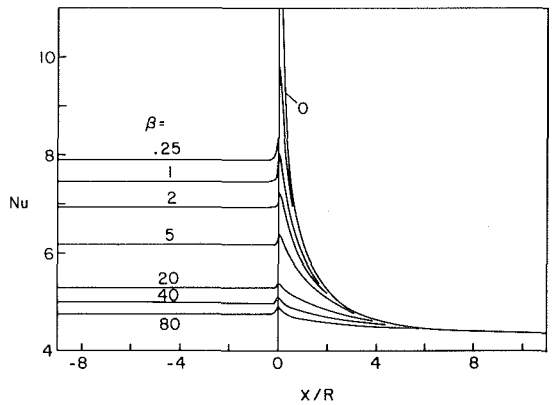

Fig. 4(*d*) Axial distributions of the local Nusselt number, Pe = 50

In the region of direct heating, the Nusselt number attains a fully developed value that is independent of the axial conduction. Fully developed Nusselt numbers also exist in the upstream (non-directly heated) region, the magnitudes of which depend both on the wall conductance parameter β and on the Peclet number.

Acknowledgment

This research was supported, in part, by NSF grant ENG 75-18141 A01, and, in part, by the Iranian Ministry of Higher Education.

References

1 Shah, R. K. and London, A. L., *Laminar Flow Forced Convection in Ducts,* Academic Press, New York, 1978.

2 Davis, E. J. and Gill, W. N., "The Effect of Axial Conduction in the Wall on Heat Transfer with Laminar Flow," *International Journal of Heat and Mass Transfer,* Vol. 13, 1970, pp. 459–470.

3 Mori, S., Sakakibara, M., and Tanimoto, A., "Steady Heat Transfer to Laminar Flow in a Circular Tube with Conduction in the Tube Wall," *Heat Transfer, Japanese Research,* Vol. 3, No. 2, 1974, pp. 37–46.

4 Mori, S., Shinke, T., Sakakibara, M., and Tanimoto, A., "Steady Heat Transfer to Laminar Flow Between Parallel Plates with Conduction in Wall," *Heat Transfer, Japanese Research,* Vol. 5, No. 4, 1976, pp. 17–25.

5 Aleksashenko, V. A., "Conjugate Stationary Problem of Heat Transfer with a Moving Fluid in a Semi-Infinite Tube Allowing for Viscous Dissipation," *Inzhenerno-Fizicheskii Zhurnal,* Vol. 14, No. 1, 1968, pp. 100–107.

6 Luikov, A. V., Aleksashenko, V. A., and Aleksashenko, A. A., "Analytical Methods of Solution of Conjugated Problems in Convective Heat Transfer," *International Journal of Heat and Mass Transfer,* Vol. 14, 1971, pp. 1047–1056.

7 Povarnitsyn, M. S. and Yurlova, E. V., "Calculation of the Temperature Field in a Plane Channel with Nonuniform Heating of Thermally Conducting Walls," *Inzhenerno-Fizicheskii Zhurnal,* Vol. 10, No. 1, 1966, pp. 120–126.

8 Chu, S. C. and Bankoff, S. G., "Heat Transfer to Slug Flows with Finite Wall Thickness," *Applied Scientific Research,* Vol. A14, 1965, pp. 379–395.

9 Patankar, S. V., *Numerical Heat Transfer and Fluid Flow,* Hemisphere Publishing Corporation, Washington, D.C. (in press).

10 Hennecke, D. K., "Heat Transfer by Hagen-Poiseuille Flow in the Thermal Development Region with Axial Conduction," *Wärme und Stoffübertragung,* Vol. 1, 1968, pp. 177–184.

E. M. Sparrow
Fellow, ASME

K. K. Koram
M. Charmchi

Department of Mechanical Engineering
University of Minnesota,
Minneapolis, Minn. 55455

Heat Transfer and Pressure Drop Characteristics Induced by a Slat Blockage in a Circular Tube

Complementary heat transfer and fluid flow experiments were performed to determine transfer coefficients and pressure drops associated with the presence of a slat-like blockage in a tube. Water was the working fluid for the heat transfer studies (Pr = 4), while for the fluid flow experiments, which were performed under isothermal conditions, air was employed. The flow was turbulent in all cases, with the Reynolds number ranging from 10,000 to 60,000. Three blockage elements were used which respectively blocked 1/4, 1/2, and 3/4 of the tube cross-sectional area. Downstream of the blockage, heat transfer coefficients were measured around the circumference of the tube as well as along its length. The heat transfer coefficients in the region just downstream of the blockage were found to be several times as large as those for a corresponding conventional turbulent pipe flow. With increasing downstream distance, the coefficients diminish and thermal development is completed (to within five percent) at about 10, 15, and 18 diameters from the respective blockages. The blockage-induced circumferential variations of the heat transfer coefficient are dissipated by about five diameters. The pressure losses induced by the blockage are high, with values for the respective blockages that are 1.2, 5.2, and 33.2 times the velocity head in the pipe flow in which the blockage is situated. These losses are comparable to those for a gate valve.

Introduction

This paper is concerned with the turbulent heat transfer and pressure drop characteristics downstream of a partial blockage in a circular tube. The blockages to be considered here are caused by the presence of a slat-like obstruction of the tube cross section. As is illustrated schematically at the upper right of Fig. 1, the slat spans the cross section and is centered on a diameter. The unblocked areas (i.e., the windows) above and below the blockage element are of equal size. Fluid approaching the blockage from left to right (Fig. 1, left-hand diagram) is deflected and accelerates as it passes through the windows. Directly behind the blockage, there is a zone of flow separation within which the fluid recirculates. This recirculating fluid washes a portion of the tube wall whose circumferential extent is more or less equal to the arcs of contact between the blockage and the wall. Farther downstream, the recirculation zone terminates and the flow reattaches to the wall. Then, the flow begins to redevelop and ultimately attains a fully developed state.

These complex blockage-activated fluid flow processes generally lead to substantially higher heat transfer coefficients than are encountered in conventional turbulent pipe flows. On the other hand, the pressure drop is substantially increased owing to the dissipation of mechanical energy due both to flow separation and to higher friction losses at the tube walls. Since the flow field associated with a slat-type blockage is not axisymmetric, the heat transfer coefficients will vary around the tube circumference as well as along the length.

Both heat transfer and fluid flow (i.e., pressure drop) experiments were performed during the course of the present investigation. The heat transfer studies were carried out with water as the working fluid, and the measurements enabled both the circumferential and axial distributions of the heat transfer coefficient to be determined in the tube downstream of the blockage. Heating was accomplished by ohmic dissipation in the tube wall. The heat transfer test section was not suitable for the fluid flow studies and, furthermore, the pressure drop information being sought was for isothermal flow conditions. Therefore, a second apparatus, designed specifically for pressure drop studies, was used, with air as the working fluid. For both sets of experiments, three blockage ratios (ratio of blocked area to total cross sectional area) were employed, namely, 1/4, 1/2, and 3/4. For each blockage, measurements were made for tube Reynolds numbers between 10,000 and 60,000.

The work reported here is the second and final stage of a study of non-axisymmetric blockages in turbulent pipe flow. The first part of the research was concerned with blockage elements having the form of a circular segment, as is illustrated at the lower right of Fig. 1. Heat transfer results for the segmental blockage are reported in [1].

Consideration of the two types of blockage elements pictured in Fig. 1 leads to the conclusion that the respective blockage-induced flow fields should be quite different, even when the blockage area ratios are identical. One major difference lies in the extent of the tube circumference that is washed by the recirculating flow downstream of the blockage. An estimate of this can be obtained by examining the arc length of the line of contact between the blockage and the pipe wall. For the slat blockage, the contact arc lengths are about 13, 26, and 44 percent of the total circumference, respectively for the 1/4, 1/2, and 3/4 area blockage ratios. For these same blockage ratios, the contact arc lengths for the segmental blockage are 37, 50, and 63 percent of the circumference. Therefore, compared with the slat blockage, a substantially larger portion of the tube wall is washed by the recirculating flow in the case of the segmental blockage.

Other anticipated differences in the fluid flow field induced by the two types of blockages can also be identified. The expected flow field differences should also give rise to differences in the heat transfer results. Comparisons will be made later to verify these expectations.

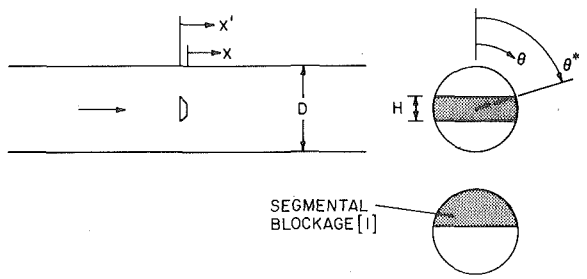

Fig. 1 Diagram of a slat blockage element and a segmental blockage element (lower right)

Contributed by The Heat Transfer Division for publication in the JOURNAL OF HEAT TRANSFER. Manuscript received by the Heat Transfer Division, January 11, 1979.

Aside from the research reported in [1], a literature search failed to uncover other studies dealing with the effect of an asymmetrical blockage on turbulent heat transfer in a circular tube. The axisymmetric heat transfer downstream of a conventional orifice plate with a central circular aperture has been experimentally investigated in [2] and [3].

The Experiments

As noted earlier, separate apparatuses were respectively employed in the heat transfer and pressure drop experiments. The heat transfer apparatus is an adaptation of that used in [1] and, therefore, it will be described in somewhat less detail than the pressure drop apparatus.

Heat Transfer Apparatus. The heat transfer experiments were carried out in a closed-loop apparatus with water as the working fluid. The heated test section, which formed the heart of the apparatus, consisted of a thin-walled stainless steel tube fitted with a slat-type blockage at its inlet cross section. Water was delivered to the test section by a long hydrodynamic development length. The development length and the test section were colinear and horizontal, as was an exit length situated downstream of the test section. These components were of identical internal diameter, 3.015 cm (1.187 in.), with lengths of 60, 33, and 10 diameters, respectively for the development section, test section, and exit section. The wall thickness of the test section was determined from measurements on samples cut from the ends, yielding an average value of 0.084 cm (0.033 in.) with more or less random variations up to ±0.0025 cm (0.001 in.).

The blockage elements were fabricated from a free-machining plastic (delrin), with a thickness (0.254 cm, 0.1 in.), a short flattened lip (0.04 cm, 0.015 in.), and a rear facing bevel[1] (30 deg) in accordance with ASME orifice-plate standards. Some of these features can be seen in the schematic side view of the blockage element shown in Fig. 1. Certain dimensional characteristics of the blockage elements are listed in Table 1. For each of the three elements, respectively with blockage area ratios of 1/4, 1/2, and 3/4, the table gives the slat width H (relative to the tube diameter D) and the edge angle θ^* (both H and θ^* are illustrated in Fig. 1). It may be noted that since the blockage is positioned in the widest part of the cross section (i.e., astride a diameter), H/D is always less than the area blockage ratio. For this same reason, the fraction of the circumference that is blocked off is also less than the area ratio.

For the ohmic heating of the test section tube, a bus bar system was designed to accommodate the high currents (up to 600 amperes) and, at the same time, to avoid adverse thermal impacts. In particular, the system was designed to avoid smoothing otherwise existing circumferential temperature variations in the test section tube and to suppress extraneous heat losses (gains) from (to) the test section along the bus bars. The general concern about heat losses (gains) led to a number of preventive features. These included the use of plastic (i.e., non-metallic) coupling between the test section and the adjacent piping, the absence of structural supports along the length of the test section, the selection of a plastic for fabrication of the blockage elements, the insulation of the test section with silica aerogel powder which has a thermal conductivity less than air, etc. Further details are available in [1].

Table 1 Characteristics of the slat-type blockages (see Fig. 1)

Blockage ratio	θ^*	H/D
1/4	78.6 deg	0.197
1/2	66.2 deg	0.404
3/4	50.6 deg	0.635

The test section was instrumented to enable heat transfer coefficients to be determined both around the circumference and along the length. At each of ten axial stations between $x/D = 1$ and 15, eight thermocouples were installed at 45 deg intervals, starting at $\theta = 0$ deg. At $x/D = 18$, 21, 27, and 32, there were two thermocouples per station, respectively at $\theta = 0$ and 180 deg. The thermocouples were fabricated from 30 gage calibrated iron-constantan wire. Measurements of the inlet and outlet bulk temperatures were made in multi-baffled, well-insulated mixing boxes.

Painstaking bleeding of air from the system was required as a prerequisite for a successful data run, and numerous bleed valves were installed for this purpose. The system also included a heat exchanger which facilitated extraction of the heat that was added to the flow as it passed through the test section. The mass flow rate was measured by a calibrated orifice meter.

Pressure Drop Apparatus. The pressure distributions and net pressure drop associated with the presence of the blockage were measured in an open-circuit airflow apparatus. Operation was in the suction mode. Air from the laboratory room was drawn through a hydrodynamic development length into the test section, from where it successively passed through a flowmeter and a control valve to a blower situated outside the laboratory.

The hydrodynamic development section and the test section were both cut from a single length of seamless brass tubing having an inside diameter of 1.905 cm (0.75 in.). The respective lengths of these sections were 50 and 60 diameters, and they were arranged horizontally along a common centerline. The mating of the sections was accomplished by means of flanges which were specially designed to house and precisely position the blockage element.

The blockage elements used for the pressure drop studies provided the same blockage area ratios as those for the heat transfer experiments, and the other characteristics of Table 1 are also applicable. However, owing to the smaller diameter tube used in the pressure drop work, the size of the elements was smaller. The blockage elements were 0.238 cm (3/32 in.) thick, had a flattened lip of 0.025 cm (0.010 in.), and a downstream bevel of 30 deg.

[1] The bevel was used to avoid flow reattachment on the lateral edges of the blockage element, thereby assuring that the element would function as a thin plate obstruction.

Nomenclature

A = cross sectional area of tube
A_0 = open area at blockage cross section
D = tube diameter
H = width of blockage, Fig. 1
$\overline{h}_x$ = circumferential average heat transfer coefficient, equation (1)
$h_x(\theta)$ = local coefficient at x,θ, equation (1)
K_A = blockage pressure loss coefficient based on velocity head in tube (area A), equation (6)
K_{A0} = blockage pressure loss coefficient based on velocity head in open area A_0, equation (6)
k = thermal conductivity
L = heated length of tube
$\dot{m}$ = mass flow rate
Nu_{fd} = fully developed Nusselt number
$\overline{\mathrm{Nu}}_x$ = circumferential average Nusselt number at x
$\mathrm{Nu}_x(\theta)$ = local Nusselt number at x,θ
ΔP_B = net pressure loss due to blockage
p = static pressure
p_{atm} = atmospheric pressure
p^* = extrapolated pressure at upstream face of blockage
$\overline{q}_x$ = circumferential average heat flux at x
$q_x(\theta)$ = local heat flux at x,θ
Re = Reynolds number, $4\dot{m}/\mu\pi D$
r_i = inner radius of tube wall
r_0 = outer radius of tube wall
S = power input per unit volume
T_{bx} = bulk temperature at x
$\overline{T}_{wx}$ = average inside wall temperature at x
$T_{wx}(\theta)$ = local inside wall temperature at x,θ
x = axial coordinate measured from downstream face of blockage
x' = axial coordinate measured from upstream face of blockage
V = mean velocity
θ = angular coordinate
θ^* = edge angle, Fig. 1
μ = viscosity
ρ = density
ρ^* = density evaluated at p^*

Pressure taps were installed both upstream and downstream of the blockage element at a total of twenty-two axial stations whose locations will be evident from the pressure distributions to be presented later. Since the most rapid pressure variations were expected to occur just downstream of the blockage, the taps were more concentrated in that region. On the upstream tube (i.e., the hydrodynamic development length), there was a single tap at each of the instrumented stations. On the other hand, on the test section tube, all stations were instrumented with two taps, respectively at $\theta = 0$ and 180 deg. Ideally, taps positioned at these circumferential locations should yield identical readings in each cross section. However, in separated flows, it is known that asymmetries can occur even when geometrical considerations indicate that symmetry should exist [4, 5].

After the pressure taps were installed, the bores of both the hydrodynamic development tube and the test section tube were carefully honed to remove burrs.

The pressure signals from the taps were conveyed via plastic tubing to a pressure selector switch, and the output of the switch was sensed by a Baratron capacitance-type pressure meter with a smallest scale reading of 0.001 mm Hg. In view of the pressure fluctuations induced by the unsteadiness of the separated flow, an electronic integrator was employed to obtain time-averaged pressure data. The integrator had an integration time of ten seconds. As many as five such averages were recorded at each tap and subsequently averaged. The averaging was performed at all taps as a matter of course, but it was not really necessary at the taps upstream of the blockage since the pressures were steady at those stations.

The rate of air flow through the apparatus was measured with one of two calibrated rotameters, depending on the range. In order to obtain a well-defined hydrodynamic inlet condition, a 51 cm (20 in.) diameter circular baffle plate was attached to the upstream end of the hydrodynamic development tube. The upstream face of the baffle plate was made flush with the exposed upstream edges of the tube, thereby providing a sharp-edge inlet.

Data Reduction

Heat Transfer Results. Two types of heat transfer coefficients will be evaluated from the measured temperature and heat transfer data. One of these is the circumferential-local heat transfer coefficient $h_x(\theta)$ which pertains to an angular position θ at axial station x. The other is the circumferential-average coefficient $\overline{h}_x$ which describes the average heat transfer performance at station x. These coefficients are defined as

$$h_x(\theta) = \frac{q_x(\theta)}{T_{wx}(\theta) - T_{bx}}, \quad \overline{h}_x = \frac{\overline{q}_x}{\overline{T}_{wx} - T_{bx}} \tag{1}$$

In the first of these equations, $q_x(\theta)$ and $T_{wx}(\theta)$ are, respectively, the local convective heat flux and the local inside wall temperature at x, θ. In the second, $\overline{q}_x$ and $\overline{T}_{wx}$ denote the circumferential average values of the heat flux and the inside wall temperature at station x. The quantity T_{bx} is the fluid bulk temperature at x. As illustrated in Fig. 1, the x coordinate is measured from the downstream face of the blockage element since heating begins at that point.

Whereas both the heat flux and wall temperature at the tube bore are needed for the evaluation of equations (1), neither of these quantities can be measured directly. The quantities that were actually measured include outside wall temperatures, the electric power input for the ohmic heating, and the rate of water flow through the test section. An analysis must, therefore, be carried out to deduce the desired inside-wall quantities from those that have been measured.

Two analytical models were employed. Since these are described at some length in [1], only a brief recounting is appropriate here. In both models, axial conduction in the tube wall and heat losses from the outer surface of the tube are neglected; these assumptions have been verified by calculation. In addition, since the ± three percent variations in the wall thickness did not follow a regular pattern, they could not be easily taken into account. Therefore, the analyses were based on a uniform wall thickness (equal to the mean value).

The first (and more complex) analysis starts with the governing equation for two-dimensional heat conduction in a circular annulus with internal heat generation, $\nabla^2 T + S/k_w = 0$, where S is the rate of ohmic heating per unit volume and k_w is the thermal conductivity of the wall. The solution of this equation is a straightforward application of the separation of variables method. There is, however, some novelty encountered in dealing with the discrete temperature data that are available on the outer circumference of the tube (from the thermocouple measurements). When the solution is properly executed, $q_x(\theta)$, $\overline{q}_x$, $T_{wx}(\theta)$, and $\overline{T}_{wx}$ can be evaluated at the tube bore.

A simpler model can be employed in which the net circumferential conduction in the tube wall, which is proportional to $\partial^2 T/\partial\theta^2$, is neglected. The rationale for omitting this term is that the thermal resistance for heat flow from the wall into the fluid should be much lower than the thermal resistance for circumferential heat flow in the tube wall. This model yields a one-dimensional radial heat conduction problem from which the temperature drop ΔT across the tube wall follows as

$$\Delta T = (Sr_0^2/4k_w)(r_i^2/r_0^2 - 1 - 2\ln(r_i/r_0)) \tag{2}$$

and the heat flux at the tube bore is

$$q_x(\theta) = \overline{q}_x = \text{constant} = P/\pi DL \tag{3}$$

where P is the power input and πDL is the area of the tube bore.

From a comparison of the results from the two analyses, it was found that the differences between them were smaller than the uncertainty associated with the variations of the tube wall thickness. Therefore, either analysis could have been used for the final data reduction. For convenience, the simpler analysis was selected, and $T_{wx}(\theta)$, $q_x(\theta)$, and $\overline{q}_x$ were evaluated with the aid of equations (2) and (3); $\overline{T}_{wx}$ was determined from a Simpson's Rule integration of $T_{wx}(\theta)$. The local bulk temperature T_{bx} needed in the evaluations of equations (1) was calculated from a straight-line relationship (appropriate to uniform heat flux) between the measured inlet and exit bulk temperatures.

The heat transfer coefficients $h_x(\theta)$ and $\overline{h}_x$ were recast in dimensionless terms via the Nusselt numbers $\mathrm{Nu}_x(\theta)$ and $\overline{\mathrm{Nu}}_x$

$$\mathrm{Nu}_x(\theta) = h_x(\theta)D/k, \qquad \overline{Nu}_x = \overline{h}_x D/k \tag{4}$$

The results were parameterized by the Reynolds number Re defined as

$$\mathrm{Re} = 4\dot{m}/\mu\pi D \tag{5}$$

All the data were taken at a Prandtl number of four, which lies in the middle of the Prandtl number range for water.

The fluid properties appearing in the Nusselt, Reynolds, and Prandtl numbers were evaluated at the mean bulk temperature. The bulk temperature rise from inlet to exit was typically about 1°C (2°F). The heating rates were adjusted so that the wall-to-bulk temperature difference in the fully developed regime was about 5°C (10°F), with smaller temperature differences in the thermal development region.

Pressure Distributions and Pressure Drop. A major focus of the fluid flow experiments was to determine the net pressure drop ΔP_B due to the presence of the blockage element. This information was deduced from working graphs in which the static pressure distribution along the hydrodynamic development length and the test section was plotted for each of the data runs. A typical working graph is presented in Fig. 2 (the graph is for Re = 40,000 and a blockage ratio of 1/2). In this figure, the pressure difference $p - p_{\mathrm{atm}}$ is plotted on the ordinate, where p is the pressure at axial station x', and p_{atm} is the pressure in the laboratory room from which the air was drawn. Note that for the fluid flow studies, the axial coordinate, denoted by x', is measured from the upstream face of the blockage since it is there that the flow separation is initiated. The x' coordinate is illustrated in Fig. 1; x' is negative for axial stations upstream of the blockage and positive for stations downstream of the blockage. The difference between x' and the x coordinate of the heat transfer results is about $0.1D$ for the present experiments and is, therefore, of no practical significance.

It is seen from Fig. 2 that the pressure distribution upstream of the

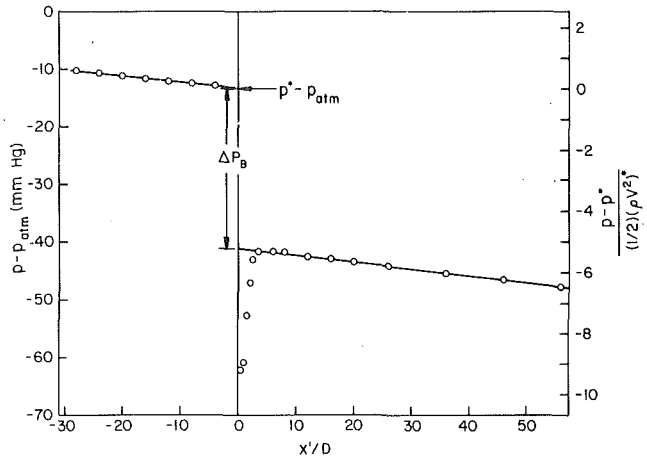

Fig. 2 Representative working graph illustrating determination of pressure loss due to the slat blockage element; 1/2 blockage, Re = 40,000. The right-hand ordinate gives the dimensionless pressure distribution

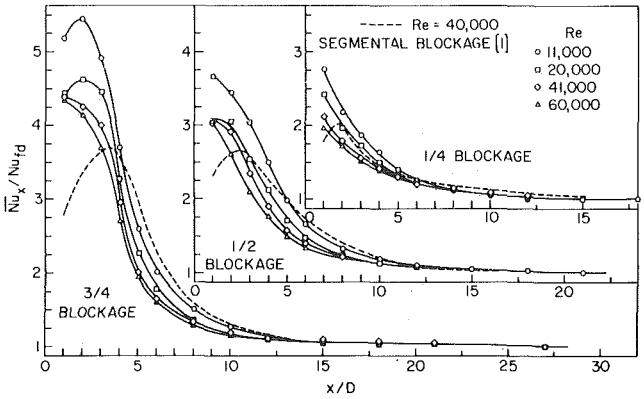

Fig. 3 Axial distributions of the circumferential average Nusselt number

blockage is linear, indicating hydrodynamically developed flow. Furthermore, downstream of the blockage, after a region of readjustment, fully developed conditions are restored as witnessed by linearity of the pressure distribution. Least squares straight lines were respectively passed through the upstream and downstream linear pressure data. As illustrated in Fig. 2, each line was extrapolated to $x' = 0$ to give the pressure that would have existed at that station had fully developed turbulent pipe flow existed in the respective tubes (i.e., in the absence of the blockage). The upstream and downstream extrapolations yield different pressures, as can be seen in Fig. 2. The difference between these two pressures is the net pressure loss ΔP_B due to the presence of the blockage. It is the net result of all pressure-related processes, including acceleration and deceleration, separation and reattachment, dissipation in the recirculating region, and post-reattachment redevelopment of the flow.

Since ΔP_B is primarily an inertial loss, it is natural to refer it to the velocity head $\frac{1}{2}\rho V^2$ in order to obtain a dimensionless result. Two reference velocities may be considered in evaluating the velocity head. One of these is the mean velocity of the fully developed pipe flow. The other is the mean velocity of the fluid passing through the free-flow area (i.e., the open area) in the plane of the blockage. In terms of the mass flow $\dot{m}$ and the respective areas A and A_0 of the tube cross section and the open area at the blockage plane, these velocities are $(\dot{m}/\rho A)$ and $(\dot{m}/\rho A_0)$.

For a liquid flow, the density ρ is essentially constant even if there is a large pressure drop across the blockage. However, for a gas, ρ may undergo moderate changes as a result of the blockage pressure drop. Therefore, it is appropriate to use a readily identifiable reference state to evaluate the density that appears in the velocity head. In practice, it is likely that the pressure would be known at some station upstream of the blockage. Then, by assuming that a fully developed pipe flow persists all the way to the upstream face of the blockage, a reference pressure p^* can be determined as illustrated in Fig. 2. It appears reasonable to employ the * state (p^* and T^*) as the reference state. With this, the loss coefficients can be defined as

$$K_A = \frac{\rho^* \Delta P_B}{\frac{1}{2}(\dot{m}/A)^2}, \quad K_{A0} = \frac{\rho^* \Delta P_B}{\frac{1}{2}(\dot{m}/A_0)^2} = K_A \left(\frac{A_0}{A}\right)^2 \tag{6}$$

Numerical values of these coefficients will be presented in a subsequent section.

Representative axial pressure distributions will also be presented in order to provide some insight into the fluid flow processes. These distributions will be plotted in dimensionless terms as

$$\frac{p - p^*}{\frac{1}{2}(\rho V^2)^*} = \frac{(p - p^*)\rho^*}{\frac{1}{2}(\dot{m}/A)^2} \tag{7}$$

where the velocity head corresponds to fully developed pipe flow at the * state.

Results and Discussion

In the presentation of results, the heat transfer will be dealt with first, followed by the pressure. The heat transfer presentation will include distributions of both circumferential average and circumferential local transfer coefficients along the length of the tube, as well as angular distributions of the circumferential local coefficient. Although the actual heat transfer data correspond to Pr = 4, the use of ratios in the presentation of the results generalizes their applicability to a range of Prandtl numbers, as demonstrated in [1] and [3]. For the pressure, values of the blockage loss coefficient will be tabulated and representative axial pressure distributions presented in graphical form.

Circumferential Average Heat Transfer Coefficients. The circumferential average Nusselt numbers $\overline{Nu}_x$ for the three blockages are respectively presented in the graphs that comprise Fig. 3. In each graph, the ratio $\overline{Nu}_x/Nu_{fd}$ is plotted as a function of the dimensionless axial coordinate x/D, with the Reynolds number as a parameter. The quantity Nu_{fd} is the experimentally determined fully developed Nusselt number, and the $\overline{Nu}_x/Nu_{fd}$ ratio is formed so that both numerator and denominator correspond to the same Reynolds number. Curves (i.e., solid lines) have been faired through the data to provide continuity. In addition, to facilitate comparisons, a dashed curve depicting the results of [1] for the segmental blockage for Re = 40,000 has been included in each graph. Dashed curves for other Reynolds numbers were not included in order to preserve the clarity of the figure (the 40,000 Re case is fully representative of the others).

There are a number of general characteristics which may be identified in Fig. 3. At small x/D, the Nusselt number takes on very high values, which decrease with increasing downstream distance. To help provide an appreciation of the truly high values of Nu_x that are attained at small x/D, it may be noted that for a conventional thermal entrance region (i.e., without blockage),[2] the measured value of Nu_x/Nu_{fd} at $x/D = 1$ is about 1.25 for Re = 40,000 and Pr = 4. The blockage-induced augmentation of the entrance region heat transfer coefficients is quite sensitive to the extent of the blockage, as witnessed by the different ordinate ranges employed for the various blockage ratios. In addition, the degree of augmentation is greatest at lower Reynolds numbers.

The detailed shapes of the $\overline{Nu}_x/Nu_{fd}$ distribution curves are worthy of note, especially when considered in relation to those for the segmental blockage (dashed lines). The curves for the $\frac{1}{4}$ and $\frac{1}{2}$ blockages are monotonic decreasing, although certain of the latter show inflections suggestive of an upstream maximum. For the $\frac{3}{4}$ blockage, the curves for the lower Reynolds numbers display maxima before commencing their monotonic decrease, whereas the others are inflected. This behavior is to be contrasted to that for the segmental blockage, where a maximum is in evidence for all cases. Similarly, the distribution curves for the conventional axisymmetric orifice with a central aperture all display maxima [2, 3].

[2] Distributions of Nu_x/Nu_{fd} versus x/D for the no-blockage case are presented in Fig. 2 of [1] for various Reynolds numbers and for Pr = 4.

To rationalize these findings, it is necessary to discuss the mechanisms which give rise to a maximum in the $\overline{Nu}_x$ distribution curve. There are two processes which can contribute to such a maximum. One is the reattachment of the separated flow on the tube wall. The other is the deflection of the flow by the blockage such that there is a jet-like impingement of the deflected fluid on the tube wall. For an axisymmetric orifice with a central aperture, only the first of the mechanisms is operative, whereas for asymmetric blockages (e.g., slat or segmental), both may exist.

For asymmetric blockages, the axial location of the maximum depends on where the separated flow reattaches and/or where the deflected flow impinges on the wall (if, indeed, it does impinge). As discussed in the Introduction, the extent of the separated region which washes the tube wall should be substantially smaller for a slat blockage than for a segmental blockage of the same area. Correspondingly, the reattachment should occur farther upstream and, in general, the interaction between the separated region and the wall should be of lesser importance. With regard to the deflected flow, it is difficult to predict the relative positions of the impingement points for the two types of blockages on the basis of physical reasoning alone. However, from the data for the circumferential local coefficients, it is found that the impingement, when it is strong enough to be felt, occurs farther upstream for the case of the slat blockage.

Thus, both of the processes which are potential contributors to the maximum in $\overline{Nu}_x$ occur farther upstream for the slat blockage than for the segmental blockage. Furthermore, if the contributing processes occur upstream of the first measurement station (i.e., upstream of $x/D = 1$), then a maximum will not be in evidence.

The foregoing discussion rationalizes the general differences in the shapes of the $\overline{Nu}_x$ distribution curves for the two types of blockages. Further insights will be conveyed shortly when results are presented for the circumferential local coefficient. With regard to the relative magnitudes of $\overline{Nu}_x$, the slat blockage gives rise to higher values than the segmental blockage at small x/D, with a reversed relationship at intermediate and large x/D.

Before leaving Fig. 3, it is appropriate to comment on two other matters. The first is the thermal entrance length $(x/D)_e$, which will be based on the criterion that $\overline{Nu}_x/Nu_{fd} = 1.05$. For a conventional (unblocked) turbulent pipe flow, $(x/D)_e = 3 - 4$ for Pr = 4. In the presence of a slat blockage, the $(x/D)_e$ values increase to 10, 15, and 18, respectively for the 1/4, 1/2, and 3/4 blockages. The second matter is the measured values of Nu_{fd}. These were compared with the well-accepted Petuhkov correlation [6], and the average deviation was found to be two percent.

Circumferential Local Heat Transfer Coefficients. Curves showing the axial variation of the Nusselt number at various fixed angular positions are presented in Fig. 4. The figure is subdivided into sections which, respectively, pertain to the three blockages. For the 1/2 and 3/4 blockages, results are given for both Re = 11,000 and 60,000 in order to portray the trends, whereas for the 1/4 blockage the trends are well portrayed by the curves for Re = 11,000. The results for the eight circumferential measurement stations ($\theta = 0, 45, \ldots$) have been collapsed into three curves, respectively for $\theta = 0$, 45, and 90 deg, by averaging out the slight thermal asymmetries at geometrically symmetric positions (e.g., $\theta = 0$ and 180 deg).

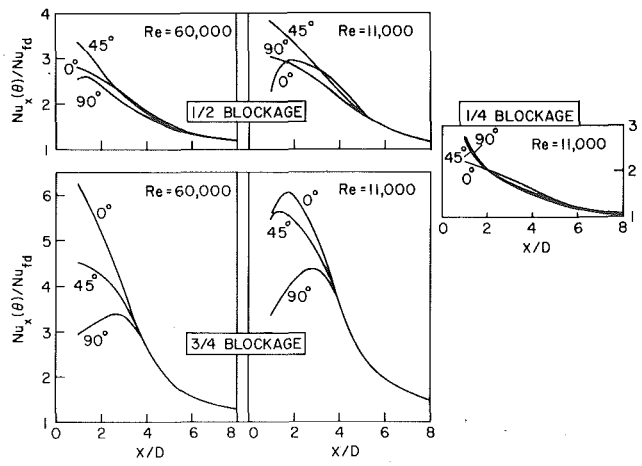

Fig. 4 Axial distributions of the circumferential local Nusselt number

In interpreting the results of Fig. 4, it is relevant to take note of the edge angles θ^* listed in Table 1. Then, upon consulting Fig. 1, it may be observed that only the $\theta = 90$ deg position (among those of Fig. 4) lies directly behind the blockage, although the 45 deg position for the 3/4 blockage just clears the edge of the blockage.

The curves for the 1/4 blockage do not show a maximum. This indicates that both reattachment and deflection-induced impingement have occurred at stations upstream of $x/D = 1$.

For the 1/2 blockage, there are maxima in evidence. At the higher Reynolds number, the separation zone is elongated, but the flow deflection is sharp. Therefore, there is a maximum at 90 deg but no maximum at 0 deg because impingement occurs for $x/D < 1$. At the lower Reynolds number, the smaller separated region and the more gradual deflection give rise to a maximum at 0 deg but not at 90 deg.

These trends are perpetuated and accentuated for the 3/4 blockage. The flow deflection is so sharp at Re = 60,000 that the impingement occurs upstream of $x/D = 1$, but the enlarged separation zone behind the blockage element gives rise to a maximum at $\theta = 90$ deg. At Re = 11,000, maxima occur at all three angular positions.

The results shown in Fig. 4 reinforce and illuminate those of Fig. 3.

An alternate portrayal of the circumferential local results is presented in Fig. 5. In this figure, $Nu_x(\theta)$ is plotted as a function of angular position at several fixed axial stations $x/D = 1, 2, \ldots, 5$. The figure is subdivided into three horizontal bands, each for a specific blockage. In each band, the angular distributions for the various axial stations are plotted serially, starting at $x/D = 1$. To help distinguish the successive sets of data, solid and dashed lines are alternated, along with circle and square data symbols. The local Nusselt numbers $Nu_x(\theta)$ at a given axial station are normalized by the average value $\overline{Nu}_x$ at that station. In view of symmetry, the angular coordinate is extended only over half the circumference, from $\theta = 0$ to 180 deg. The specific results shown in the figure are for Re = 40,000, but the trends and curve shapes are valid for all the Reynolds numbers investigated.

From an overall inspection of the figure, it is seen that the largest circumferential variations occur just downstream of the blockage, with the magnitude of the variations increasing with blockage ratio. The diverse shapes of the distribution curves reflect the different impacts of the various flow processes that were discussed earlier. With increasing downstream distance, the variations diminish rapidly, so that

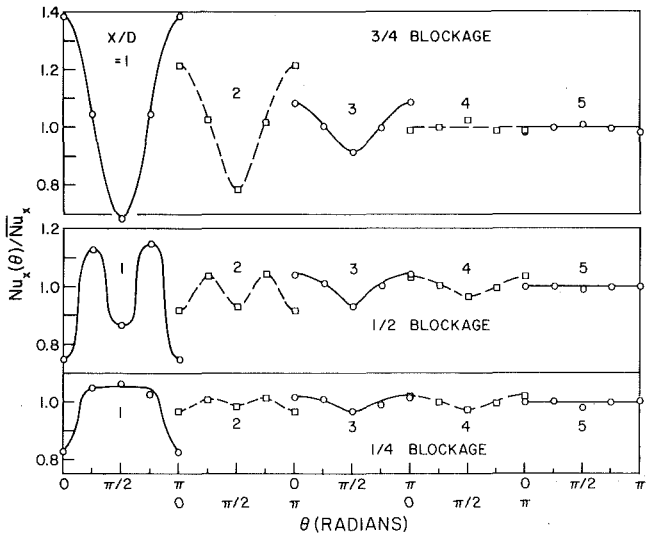

Fig. 5 Angular distributions of the Nusselt number at several fixed axial stations; Re = 40,000

Table 2 Blockage pressure losses

	1/4 Blockage		1/2 Blockage		3/4 Blockage	
Re	K_A	K_{A0}	K_A	K_{A0}	K_A	K_{A0}
10,000	1.21	0.68	5.10	1.28	32.5	2.03
18,000	1.22	0.69	5.14	1.29	33.3	2.08
26,000	1.17	0.66	5.03	1.26	32.6	2.04
32,000					34.3	2.14
40,000	1.20	0.68	5.24	1.31		
60,000	1.11	0.62	5.48	1.37		
Average	1.18	0.67	5.20	1.30	33.2	2.07

circumferential uniformity is attained at $x/D = 5$. Since the thermal entrance lengths are greater than $x/D = 5$, the attainment of circumferential uniformity does not imply thermally developed flow. It is also worthy of note that circumferential uniformity is attained much more rapidly for the slat blockage than for the segmental blockage. In particular, the long-lived circumferential variations encountered in [1] for the 1/4 segmental blockage do not occur here.

Pressure Drop and Pressure Distributions. The coefficients K_A and K_{A0} which express the net pressure loss due to the presence of the blockage were evaluated in accordance with equations (6) and are listed in Table 2. The table contains results for the three blockage ratios (1/4, 1/2, and 3/4) and for Reynolds numbers ranging from 10,000 to 60,000. For the 3/4 blockage, the largest Reynolds number that could be attained with the available blower was about 30,000. In addition to the K values for each specific case, the average K for each blockage is also given (bottom line of table).

It should be noted that K_A is based on the velocity head of the fully developed pipe flow upstream of the blockage and that K_{A0} is based on the velocity head of the flow passing through the open area in the plane of the blockage. The respective flow cross sections for these velocity heads are A and A_0. For assessing the relative impacts of the various blockage ratios on the system pressure drop and pumping power, it is K_A that is relevant.

Inspection of the table reveals that the pressure loss coefficient K_A is markedly affected by the degree of blockage, increasing from about 1.2 to 5.2 to 33.2 as the blockage ratio increases from 1/4 to 1/2 to 3/4. On the other hand, K_A is relatively insensitive to Reynolds number. The slight variation of K_A with the Reynolds number is believed to be data scatter, since there is no regular trend in evidence. For practical purposes, it appears that the average value of K_A for each blockage ratio can be used without a significant error penalty.

The numerical values of K_A are high, indicating that the slat blockage is a significant source of pressure drop. This can be appreciated by noting that the K_A values of Table 2 are comparable to those for a partially open gate valve [7]. Another perspective on the magnitude of blockage-induced pressure loss can be obtained by calculating the equivalent length of an unobstructed pipe in which a fully developed flow would incur a pressure drop equal to that caused by the blockage. In round numbers, the equivalent lengths are 50, 210, and 1330 diameters, respectively for the 1/4, 1/2, and 3/4 blockages. For the large blockages, these lengths are impressively large.

Table 2 shows that, as expected, K_{A0} is both smaller than K_A and less dependent on the blockage ratio. Presumably, the dependence on blockage ratio could be eliminated if the velocity head were based on the (unknown) vena contracta velocity.

A comparison of K_A values for the slat and segmental blockages is presented in Table 3, with the latter taken from [8]. In general, the slat blockage induces somewhat higher losses, which is in keeping with the higher heat transfer coefficients it induces in the region just downstream of the blockage (Fig. 3).

Representative axial pressure distributions will now be presented in terms of the dimensionless variable defined in equation (7). Since p^* and $(\rho V^2)^*$ are constants for a given data run, the axial distribution of this variable is a true reflection of the behavior of the pressure itself. For the 1/4 and 1/2 blockages, the pressure results to be presented are for Re = 40,000, while for the 3/4 blockage, the pressure results for the highest available Reynolds number, 32,000, will be used. The dimensionless pressure distribution for the 1/2 blockage is already available in Fig. 2 when reference is made to the right-hand ordinate;

Table 3 Comparison of average K_A values

Blockage	1/4	1/2	3/4
Slat	1.18	5.20	33.2
Segmental	0.72	4.53	32.9

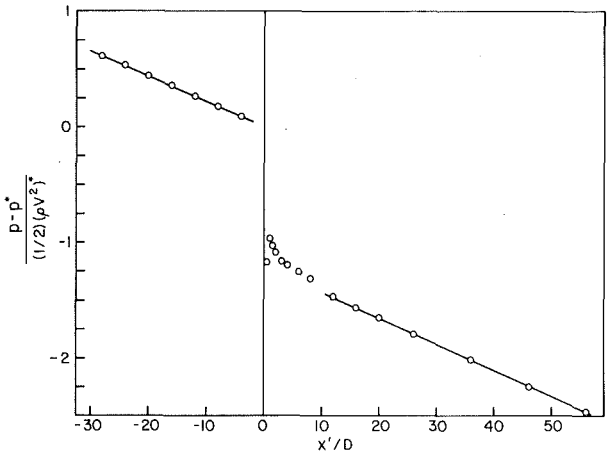

Fig. 6 Dimensionless axial pressure distribution for 1/4 blockage and Re = 40,000

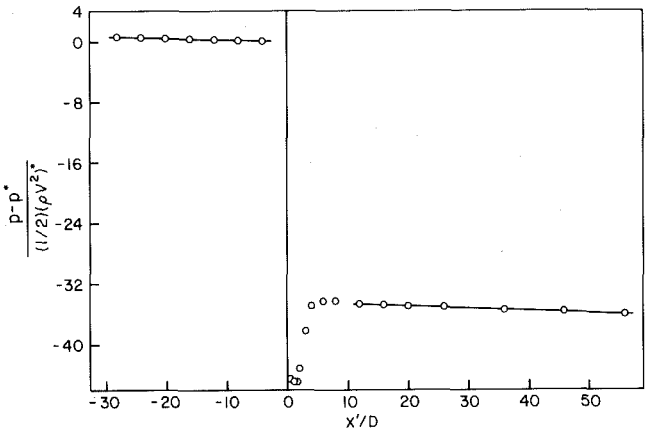

Fig. 7 Dimensionless axial pressure distribution for 3/4 blockage and Re = 40,000

the distribution curves for the 1/4 and 3/4 blockages are respectively presented in Figs. 6 and 7.

All of the pressure distributions have similar shapes. The pressure drops slowly in the fully developed pipe flow upstream of the blockage and then precipitously due to the acceleration of the fluid as it is constricted and deflected by the blockage. This is followed by a pressure recovery as the mainflow progressively fills more and more of the pipe cross section. The recovery ceases when the mainflow fills the entire cross section, and then the pressure begins to drop as the flow redevelops and continues to drop as friction takes its toll in the fully developed regime.

The pressure minimum downstream of the blockage occurs in the range between $x'/D = 0$ and $\frac{1}{2}$ for the $\frac{1}{4}$ and $\frac{1}{2}$ blockages, whereas for the $\frac{3}{4}$ blockage the minimum point has moved out to $x'/D = 1$. Pressure recovery is completed at $x'/D = 1$ for the $\frac{1}{4}$ blockage and respectively at $x'/D = 6$ and 8 for the two larger blockages. The onset of the linear pressure variation, signalling redevelopment of the flow, occurs at about $x'/D = 12$ for all cases. This redevelopment appears to be remarkably rapid, especially in view of the severe disturbances that are inflicted on the flow by the larger blockages.

As was mentioned earlier, two pressure taps (at $\theta = 0$ and 180 deg) had been installed at each downstream measurement station in order to enable unexpected asymmetries to be identified. Slight differences were observed at the first several measurement stations (up to $x'/D \sim 4$), but there was no regular pattern. Furthermore, the differences were such that the corresponding data symbols overlapped considerably. In view of this, it was decided to average the data from the two taps and to plot a single data symbol at each measurement station.

Concluding Remarks

The present experiments on slat-type blockages conclude a two-part study of the heat transfer and pressure characteristics downstream of a partial blockage in a circular tube. The results found here differ in various ways from those for the segmental blockages which were investigated in the first part of the study. The peak heat transfer coefficients induced by the slat blockage are greater than those for the segmental blockage, as is the pressure loss. The heat transfer primacy of the slat blockage persists for several pipe diameters downstream of the blockage, but the situation is reversed at larger downstream distances. The blockage-induced circumferential variations of the heat transfer coefficient are dissipated within five pipe diameters for the slat, but persist to much greater distances for the segment.

The pressure drop studies performed here indicate that the blockage-induced pressure loss is highly sensitive to the extent of the blockage but, when made dimensionless by the velocity head, is insensitive to the Reynolds number. For the three blockage area ratios investigated, respectively $\frac{1}{4}$, $\frac{1}{2}$, and $\frac{3}{4}$, the pressure loss was 1.2, 5.2, and 33.2 times the velocity head of the pipe flow in which the blockage was situated. These losses are comparable to those of a partially opened gate valve. A linear pressure distribution was re-established at about twelve pipe diameters downstream of the blockage, thereby indicating a rather rapid redevelopment of the flow.

References

1 Koram, K. K., and Sparrow, E. M., "Turbulent Heat Transfer Downstream of an Unsymmetric Blockage in a Tube," ASME JOURNAL OF HEAT TRANSFER, Vol. 100, 1978, pp. 588–594.

2 Boelter, L. M. K., Young, G., and Iverson, H. W., "An Investigation of Aircraft Heaters, XXVII—Distribution of Heat Transfer Rate in the Entrance Section of a Circular Tube," NACA TN 1451, 1948.

3 Krall, K. M., and Sparrow, E. M., "Turbulent Heat Transfer in the Separated, Reattached, and Redevelopment Regions of a Circular Tube," ASME JOURNAL OF HEAT TRANSFER, Vol. 88, 1966, pp. 131–136.

4 Abbot, D. E., and Kline, S. J., "Experimental Investigation of Subsonic Flow over Single and Double Backward Facing Steps," *Journal Basic Engng*, Vol. 84, 1962, pp. 317–325.

5 Seki, N., Fukusako, S., and Hirata, T., "Effect of Stall Length on Heat Transfer in Reattached Region Behind a Double Step at Entrance to an Enlarged Flat Duct," *Int. Journal Heat Mass Transfer*, Vol. 19, 1976, pp. 700–702.

6 Petukhov, B. S., "Heat Transfer and Friction in Turbulent Pipe Flow with Variable Physical Properties," *Advances in Heat Transfer*, Vol. 6, 1970, pp. 503–560.

7 Rohsenow, W. M., and Hartnett, J. P., editors, *Handbook of Heat Transfer*, McGraw-Hill, New York, Table 2, 1973, p. 7–19.

8 Lau, S. C., "Flow Field Phenomena Downstream of a Segmental Blockage in a Turbulent Pipe Flow," M. S. Thesis, Department of Mechanical Engineering, University of Minnesota, Minneapolis, Minn., 1978.

E. G. Hauptmann
Professor,
Department of Mechanical Engineering,
The University of British Columbia,
Vancouver, B.C., Canada V6T 1W5
Mem. ASME

A. Malhotra
Centre for Energy Studies,
Mechanical Engineering Department,
Indian Institute of Technology,
New Delhi, India 110029

Axial Development of Unusual Velocity Profiles due to Heat Transfer in Variable Density Fluids

Velocity profiles exhibiting maxima away from the axis of symmetry have been calculated for supercritical carbon dioxide flowing vertically in a heated circular duct. The analysis was carried out at the two-dimensional level and the turbulent fluxes are represented by a two equation model of turbulence. The existence of such velocity profiles has been accepted previously but the nature of their growth along a pipe was not known previous to this work.

Introduction

It has been recognized for more than a decade that fluid velocity profiles in variable property boundary layers can be strikingly different from those normally encountered in forced convection situations (see Hsu and Smith [1]). For example, velocity profiles in heated pipe flows of fluids near the critical state sometimes exhibit maxima away from the axis of symmetry. The apparent cause of this anomalous behavior is a buoyancy effect induced as a result of density variations. This phenomenon has interested investigators working on convective heat transfer near the critical state primarily because under such circumstances density variations are particularly severe.

These anomalous velocity profiles (which Wood [2] termed "unusual") have an immediate and significant influence on heat transfer behavior. Nevertheless there is much that remains unknown in this area because experimental data are scarce and so far only preliminary attempts at an analytical treatment have been made. Theoretical predictions of such velocity profiles have been made by Hsu and Smith [1], Hall [3], Tanaka, et al. [4] and Malhotra and Hauptmann [5]. All the preceding analyses were, however, simplified to a one-dimensional level by neglecting streamwise convection in the flow and are therefore limited in their usefulness. Further, a major part of the development of unusual velocity profiles takes place in the thermal entrance length which cannot be handled at the one-dimensional level.

The present study undertakes an investigation of this phenomenon through a considerably expanded two-dimensional numerical procedure. The work is centered around carbon dioxide near the critical state although the principles and analysis presented here are generally applicable to any variable density type of flow.

Preliminary Concepts

A physical understanding of the problem may be obtained by looking at a situation in which streamwise convection is negligible. Consider a single phase fluid with strongly varying properties flowing in a vertical pipe. The one-dimensional momentum equation applicable to this flow may be written as

$$\frac{\partial \tau}{\partial r} + \frac{\tau}{r} + \frac{dp}{dx} \pm \rho g = 0 \tag{1}$$

The ± sign corresponds to upflow and downflow, respectively. If the fluid is heated at the walls, a density gradient will be set up by virtue of the fact that fluid close to the wall is hotter than that in the core. The resulting radial shear stress distribution can be found by integrating equation (1) (and dropping the + sign for convenience).

$$\tau = \frac{R-y}{R}\left(\tau_0 - \frac{I}{R}\right) + \frac{I}{R-y} - \frac{I(y)}{R-y}, \tag{2}$$

where

$$y = R - r,$$

$$I = \int_0^R \rho g(R-y)dy,$$

$$I(y) = \int_0^y \rho g(R-y)dy.$$

It will be noticed on a brief examination of the preceding equations that if density is constant then radial shear stress variation is

$$\tau = \tau_0 \frac{(R-y)}{R} \tag{3}$$

When the shear stress distribution is linear as exhibited by equation (3), shear stress is always positive. Hence velocity gradients must also be positive in such a flow, and the resulting velocity profile will always have a maximum at the axis of symmetry. Under appropriate conditions of density variation, however, equation (2) shows a change in the sign of shear stress, leading to an unusual velocity profile. In the case of heated, vertical upward flow with density variations of the kind shown in Fig. 1, equation (2) will sometimes lead to a solution in which radial shear stress may change its sign only once. However, it has been found experimentally that this reversal of sign may occur more than once [2] as a result of streamwise convection.

Mathematical Model

The present theoretical model involves a simultaneous solution of equations for the conservation of mass, momentum and energy as well as additional equations for turbulence kinetic energy and its dissipation rate. The last two equations were added to replace the traditional mixing-length type of models for turbulent fluxes. A full description of the so-called turbulent kinetic energy-dissipation (K-ϵ) model has been given by Launder [6]. With traditional mixing length models, presence of maxima away from the axis of symmetry lead to

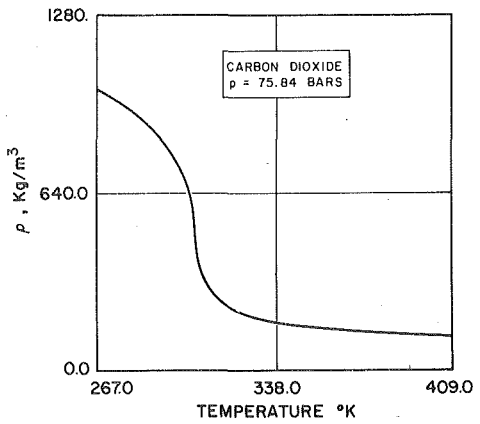

Fig. 1 Density of carbon dioxide as a function of temperature [7]

Contributed by the Heat Transfer Division for publication in the JOURNAL OF HEAT TRANSFER. Manuscript received by the Heat Transfer Division March 15, 1978.

zero heat fluxes at locations where such maxima appear. Use of the K-ϵ model avoids this limitation.

The complete set of equations governing the present problem involve twelve unknowns as follows

Continuity:

$$\frac{\partial}{\partial x}(\rho u r) + \frac{\partial}{\partial y}(\rho v r) = 0 \tag{4}$$

Momentum:

$$\rho u \frac{\partial u}{\partial x} + \rho v \frac{\partial u}{\partial y} = -\frac{dp}{dx} + \frac{1}{r}\frac{\partial}{\partial y}\left[r\left(\mu \frac{\partial u}{\partial y} - \rho\overline{u'v'}\right)\right] \pm \rho g \tag{5}$$

Energy:

$$\rho u \frac{\partial h}{\partial x} + \rho v \frac{\partial h}{\partial y} = u\frac{dp}{dx} + \frac{1}{r}\frac{\partial}{\partial y}\left[r\left(k\frac{\partial t}{\partial y} - \rho\overline{h'v'}\right)\right] + \left(\mu - \frac{\rho\overline{u'v'}}{\partial u/\partial y}\right)\left(\frac{\partial u}{\partial y}\right)^2 \tag{6}$$

Turbulence Energy:

$$u\frac{\partial K}{\partial x} + v\frac{\partial K}{\partial y} = \frac{1}{\rho r}\frac{\partial}{\partial y}\left(r\rho\frac{K^2}{\epsilon\sigma_K'}\frac{\partial K}{\partial y}\right) - \overline{u'v'}\frac{\partial u}{\partial y} - \epsilon \tag{7}$$

Turbulence Dissipation:

$$u\frac{\partial \epsilon}{\partial x} + v\frac{\partial \epsilon}{\partial y} = \frac{1}{\rho r}\frac{\partial}{\partial y}\left(r\rho\frac{K^2}{\epsilon\sigma_\epsilon'}\frac{\partial \epsilon}{\partial y}\right) + \left(C_{\epsilon 1}\frac{P}{\epsilon} - C_{\epsilon 2}\right)\frac{\epsilon^2}{K} \tag{8}$$

Turbulent Fluxes:

(a) $\overline{u'v'} = C_\mu \dfrac{K^2}{\epsilon}\dfrac{\partial u}{\partial y}$ for $y \geq y_1$; $\overline{u'v'}$

$$= \kappa^2 y^2 [1 - \exp(-y+/A)]^2 \left(\frac{\partial u}{\partial y}\right)^2$$

for $y \leq y_1$ (9)

(b) $$\frac{\overline{h'v'}}{\overline{u'v'}} = \frac{1}{\mathrm{Pr}_t}\frac{\partial h/\partial y}{\partial u/\partial y} \tag{10}$$

Pressure Equation:

$$G = \int_0^r \rho u dA \tag{11}$$

Property Relationships:

$$\mu = \mu(h, p)\ k = k(h, p),\ C_p = C_p(h, p);\ \rho = \rho(h, p). \tag{12}$$

Equation (11) does not clearly reveal its function as a pressure equation, but it can readily be converted through the use of the momentum equation to eliminate velocity u. The property relationships are contained in the form of tabulated data which are numerically interpolated at the required fluid state.

The equations for the turbulence model were derived for variable property fluids by closely examining and extending arguments previously used for constant property flows [6]. Equation (9) contains two definitions for turbulent fluxes: one based on the K-ϵ model for the turbulent region of the flow; the Van Driest hypothesis for the near-wall and transitional region. The turbulent Prandtl number was assigned a constant value of 0.9. The sensitivity of computed results to this assumption as well as a full description of the turbulence model is given in [7]. The empirical constants in equations (7–9) are deduced from experimental measurements of certain constant-property turbulence parameters, but are thought to be equally valid in variable property flows and have values

$$C_\mu = 0.09,\quad \sigma_\epsilon' = 11.11,\quad \sigma_K' = 11.11$$
$$C_{\epsilon 2} = 1.9,\quad A = 28,\quad \kappa = 0.4$$

The constant $C_{\epsilon 1}$ is determined from the following relationship [7].

$$\kappa^2\left[1 + \frac{3y}{R} + \frac{3y^2}{R^2}\right] = \sigma_\epsilon'[C_{\epsilon 2} - C_{\epsilon 1}]C_\mu^{3/2} \tag{13}$$

These equations require boundary conditions and starting profiles before a solution can be achieved. The wall boundary conditions for the continuity, momentum and energy equations follow from the no-slip condition at the wall and a known value of wall heat flux. The near-wall boundary conditions for the turbulence energy and dissipation equations follow from the assumption that near the wall, production and dissipation of turbulence energy are in balance and that the effective viscosity determined from K-ϵ equations is identical with that found from the Van-Driest hypothesis. A constant property, fully developed velocity profile and a constant enthalpy profile was used at the starting location. Starting profiles for turbulence energy K and dissipation ϵ were found by empirical approximations of existing experimental data. The complete set of equations were then solved by the Pletcher-DuFort Frankel finite difference method [8, 9] for two-dimensional parabolic flows. Complete details of the solution method along with a demonstration of its accuracy and capabilities were given by Malhotra [7]. It may be noticed that the turbulence equations do not in any way reflect the contribution of buoyancy. This practice is an extension of past experience gathered at the one-dimensional level. Moreover at the present time there is no known practical way of accounting for buoyancy in the turbulence model for near-wall confined flows. However, as will be shown later, it was deduced from the computer results that for certain heat transfer calculations it will be necessary to account for such an effect in the future.

Results and Discussion

Experimental data for velocity profiles are scant in near-critical fluids. However, Wood has devoted a substantial part of his thesis to such measurements in CO_2. Most of Wood's data were taken at operating conditions that resulted in normal velocity profiles, although a few unusual velocity profiles were also encountered (under essentially similar operating conditions).

Wood conducted experiments in an Inconel pipe with an inside diameter of 0.0229 m and a total length of 1.435 m. It was mounted vertically and the flow was upward. The heated section of the pipe was 0.7645 m long. The tube upstream of the heated section served to establish a fully developed velocity profile. He conducted a series of runs by varying the mass flow rates and inlet bulk temperatures. Profile measurements were made at one location only (30.7 diameters downstream from the beginning of the heated section).

Nomenclature

A^+ = constant in Van Driest's expression
$C_{\epsilon 1}$, $C_{\epsilon 2}$ = constants in the dissipation equation
C_μ = constant in $K - \epsilon$ model
σ_K, σ_ϵ = constants in $K - \epsilon$ model
g = acceleration due to gravity
h = enthalpy
k = thermal conductivity
K = turbulence kinetic energy
G = mass flow rate
p = pressure
Pr_t = turbulence Prandtl number
r = radial distance from axis of symmetry
R = radius
t = temperature
u = velocity
u' = fluctuating component of velocity
v = velocity in direction perpendicular to predominant flow direction
v' = fluctuating component of velocity in direction perpendicular to predominant flow direction
x = streamwise distance measured from location where heating starts
y = cross-stream distance measured from the wall
τ = shear stress
μ = viscosity
μ_t = turbulent viscosity
ρ = density
ϵ = dissipation rate of turbulence kinetic energy

Subscript

0 = indicating value of quantity at wall

Superscript

( ) = time-averaged quantity

Conditions corresponding to two of his experimental runs are shown in Figs. 2 and 3. Fig. 2 shows a normal velocity profile at a pressure of 74.12 bars (P/P_c = 1.0037) and an inlet temperature of 299 81 K. Property variations in this run are severe due to the proximity of the critical point, but an unusual velocity profile was not observed due to a relatively high mass flow rate. Fig. 2 also shows results computed by the methods described in the previous section. The agreement was considered good even though deviations in velocity profile (of about 10 percent) can be seen close to the wall. At the wall, velocity in both cases is zero and it is reasonable to expect deviations in velocity profiles would start reducing in the near-wall region. A detailed comparison of the entire near wall region is not possible because of lack of measurements for this part of the flow.

Another set of measurements due to Wood, made at a lower mass flow rate, illustrates an unusual velocity profile. Computations corresponding to this data are shown in Fig. 3. The encouraging feature in this computation is the correct prediction of trend in a flow where a variety of different types of velocity profiles are possible. The discouraging feature is that actual magnitudes of velocity were not well predicted. The main reason why better agreement could not be achieved in this flow is the close proximity of the pseudocritical temperature, leading to uncertainties in both calculated and experimental results. In order to attain an unsual profile, Wood had to take inlet temperatures within 0.005 percent of the pseudocritical temperature. At this temperature density variations are severe so that the slightest errors in temperature will result in significant errors in density. This effect is shown in Fig. 4. In most supercritical flows, similar differences normally occur over smaller regions and therefore affect the computation to a smaller degree. The slight difference in temperature in Fig. 4 could have been rectified by redesignating certain empirical constants that go into the mathematical model, but this was not done in order to maintain consistency. In addition, a certain degree of inaccuracy in property data could further contribute to errors in both calculated and measured results. The same difficulty was faced by Wood in reducing his experimental data. He found that when the profile in Fig. 3 was integrated, it did not yield correct mass flow rate. The computed profile has this in its favour. Given the density, it yields the correct mass flow rate since mass flow constraint is an integral part of the mathematical procedure.

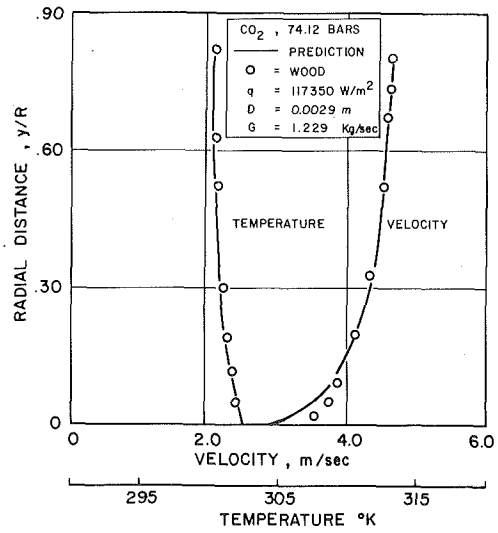

Fig. 2 Velocity and temperature profiles for supercritical carbon dioxide

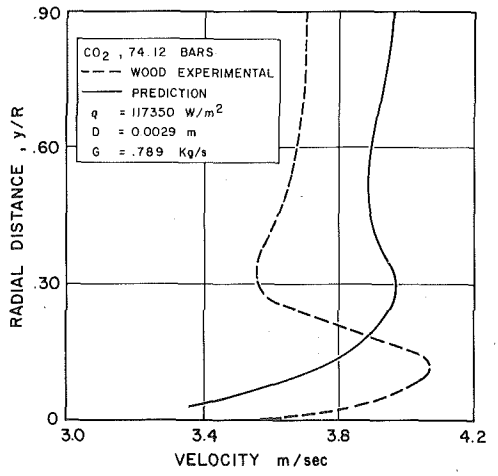

Fig. 3 Unusual velocity profile in supercritical carbon dioxide

Fig. 5 illustrates the development of velocity profiles as the fluid progresses along the pipe. Transformation from a normal to an unusual velocity profile takes several diameters (more than 20 in this case) before the fluid can develop maxima away from the axis of symmetry. The fully developed flow cannot be achieved under such conditions. However, if the pipe is long enough the fluid will eventually heat itself out of variable density regions (away from the critical region) and eventually return to a nearly fully-developed state.

Implications to Heat Transfer

Buoyant influences in variable property forced convection situations can clearly be determined when experiments are carried out in pipe flow by changing the orientation of the flow with respect to

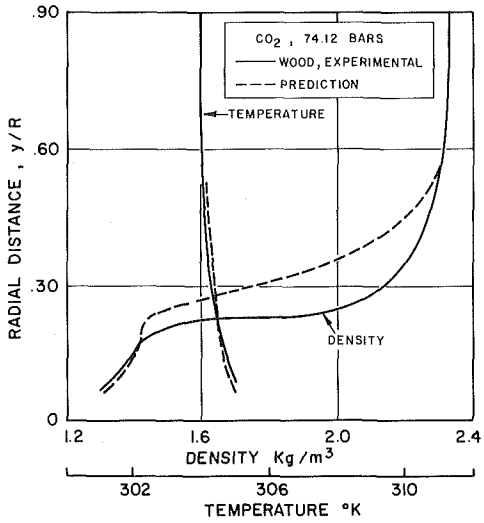

Fig. 4 Temperature and density profiles in supercritical carbon dioxide corresponding to data in Fig. 3

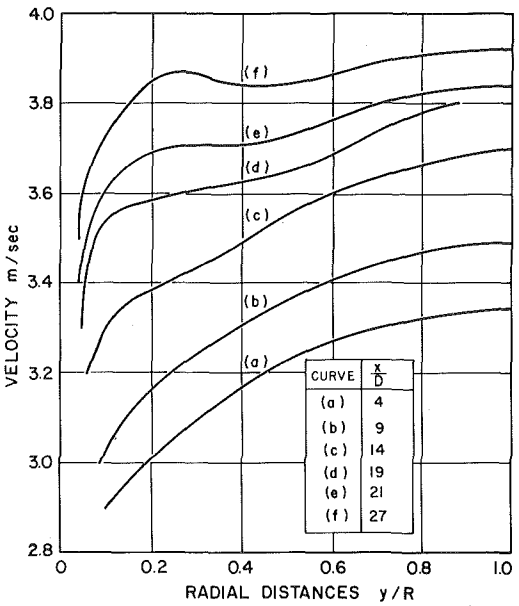

Fig. 5 Development of unusual velocity profiles in supercritical carbon dioxide at conditions corresponding to Figs. 3 and 4

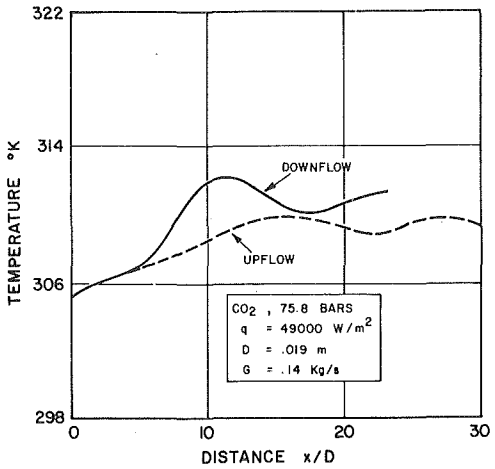

Fig. 6 Wall temperatures for upflow and downflow

gravity, all other conditions remaining the same. Such experiments have been carried out by several investigators [10, 11]. It was found that as buoyant effects become significant, observed upflow wall temperatures are higher than downflow wall temperatures. In the past, it has been speculated that this difference between wall temperatures can be traced to modification in velocity profiles. The source of this speculation lies in the fact that sometimes zero shear stresses can be expected in vertical upflow at locations other than the axis of symmetry, thereby leading to an inhibition in shear-generated turbulence. However, when calculations are made with the present procedure it leads to higher temperatures for downflow (see Fig. 6). Radial variations in shear stress τ are illustrated in Fig. 7. It may be noted for upflow that shear stress becomes equal to zero at approximately $y/R = 0.1$. However, the wall shear stress for upflow is 2.5 times as large for downflow. A larger value of wall shear stress here is a consequence of accelerative influences in the near wall region which arise in order to compensate for deceleration in the core. As a result calculated wall temperatures are lower in upflow. The inference drawn from this calculation is that modification of the velocity profile in itself does not lead to a correct representation of observed behavior but rather to a reversal of observed trends.

It is felt that buoyancy generated turbulence effects should be included in theoretical models to rectify this error. Buoyancy forces lead to an additional term in equation (7), approximately equal to $\beta\overline{u'h'}g$. This term could not be included in the present work since there is insufficient experimental information on its magnitude even for constant property flows. Methods for estimating this correlation for variable property flows await development. The effect of this correlation in heated flows is to inhibit turbulence in situations of stable stratification, which is the case in upflow. A more detailed discussion of buoyancy effects can be found in [5].

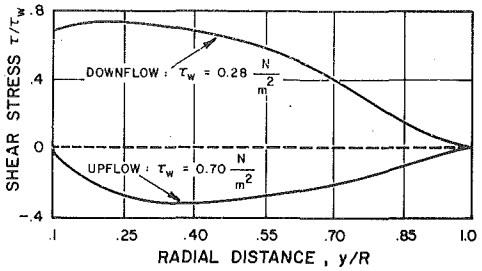

Fig. 7 Computed radial shear stress profiles for carbon dioxide at p/p_c = 1.027 at a location $x/D = 30$

Acknowledgments

The Authors gratefully acknowledge the assistance of the computing and other facilities extended by the University of British Columbia and the support of the National Research Council of Canada.

References

1 Hsu, Y. Y., and Smith, J. M., "The Effect of Density Variations on Heat Transfer in the Critical Region," ASME JOURNAL OF HEAT TRANSFER, Vol. 83, 1961, pp. 176–182.

2 Wood, R. D., "Heat Transfer in the Critical Region: Experimental Investigation of Radial Tmperature and Velocity Profiles," Ph.D. Thesis, Northwestern University, Evanston, Ill., 1963.

3 Hall, W. B., "The Effects of Buoyancy Forces on Forced Convection Heat Transfer in a Vertical Pipe," *Simon Engineering Lab. Report NE1,* University of Manchester, 1968.

4 Tanaka, H., Tsuge, A., Hirata, M., and Nishiwaki, N., "Effects of Buoyancy and Acceleration Owing to Thermal Expansion on Forced Turbulence Convection in Vertical Circular Tubes," *Int. J. Heat Mass Transfer,* Vol. 16, 1973, pp. 1267–1288.

5 Malhotra, A. and Hauptmann, E. G., "Heat Transfer to a Supercritical Fluid During Turbulent, Vertical Flow in a Circular Duct," International Seminar on Turbulent Buoyant Convection, I.C.G.M.T., Yugoslavia, 1976.

6 Launder, B. E. and Spalding, D. B., *Lectures in Mathematical Models of Turbulence,* Academic Press, London and New York, 1972.

7 Malhotra, A., "An Analytical Investigation of Forced Convection Heat Transfer to Supercritical Carbon Dioxide Flowing in a Circular Duct," Ph.D. Thesis, University of British Columbia, Vancouver, B.C. 1977.

8 Pletcher, R. H., "On a Finite Difference Solution for the Constant Property Turbulent Boundary Layer," *AIAA Journal,* Vol. 7, 1969, pp. 305–311.

9 Pletcher, R. H. and Nelson, M. N., "Heat Transfer to Laminar and Turbulent Flow in Tubes with Variable Fluid Properties," *Proceedings of the Fifth International Heat Transfer Conference,* Tokyo, Vol. II, 1974, pp. 146–150.

10 Jackson, J. D. and Evans-Lutterodt, K., "Impairment of Turbulent Forced Convection Heat Transfer to Supercritical Pressure CO_2 Caused by Buoyancy Forces," Res. Report N.E. 2, University of Manchester, England, 1968.

11 Bourke, P. J., Pulling, D. J., Gill, L. E., and Denton, W. H., "Forced Convective Heat Transfer to Turbulent CO_2 in the Supercritical Region," *Int. J. Heat Mass Transfer,* Vol. 13, 1970, pp. 1339–1348.

D. R. Smart
Quality Assurance Engineer.

Diesel Division,
General Motors of Canada, Ltd.
London, Ontario, Canada

K. G. T. Hollands
Professor.

G. D. Raithby
Professor.

Thermal Engineering Group,
Department of Mechanical Engineering,
University of Waterloo,
Waterloo, Ontario, Canada

Free Convection Heat Transfer across Rectangular-Celled Diathermanous Honeycombs

Experimentally obtained Nusselt number-Rayleigh number plots are presented for free convective heat transfer across inclined honeycomb panels filled with air. The honeycomb cells were rectangular in shape with very long cell dimensions across the slope and comparatively short dimensions up the slope. Elevation aspect ratios, A_E, investigated were 3, 5 and 10; angles of inclination, θ, measured from the horizontal, were 0, 30, 60, 75 and 90 deg. The effect on the Nusselt number, of the emissivities of the plates bounding the honeycomb, and of the emissivity of honeycomb material, was also investigated. The measurements confirmed that the critical Rayleigh number and the post-critical heat transfer depend on the radiant properties of the honeycomb cells. The critical Rayleigh numbers at $\theta = 0$ were well predicted by the methods of Sun and Edwards. For $0 < \theta \leq 75$ deg, the critical Rayleigh numbers and the Nusselt-Rayleigh relations were both found to be essentially the same as their horizontal counterparts provided the Rayleigh number was first scaled by cos θ. For $\theta = 90$ deg, the form of the Nusselt-Rayleigh relation was found to be very different from that for $\theta \leq 75$ deg and similar to that observed for square-celled honeycombs for $\theta \geq 30$ deg. The $\theta = 90$ deg data were found to be closely correlated by an equation of the form recently proposed by Bejan and Tien.

Introduction

Recently Cane, et al. [1] reported an extensive set of measurements on free convective heat transfer across an inclined air layer heated from below and constrained internally with a thin-walled square-celled, diathermous honeycomb. The present paper extends this set of measurements to rectangular-celled honeycombs, covering, in essence, the limiting case where the plan aspect ratio of the honeycomb approaches infinity. As sketched in Fig. 1 the rectangular honeycomb is made up of a set of thin partitions positioned at right angles to the inclined plates bounding the air layer. The aspect ratios defining the shape of the rectangular cells so formed are defined by $A_E = L/D$, (the elevation aspect ratio) and $A_p = w/D$, (the plan aspect ratio). In the present set of experiments the cell width w was made equal to the full plate width, W. Since $W \gg L$, for practical purposes the experiments should correspond to the limit $A_p \to \infty$. Interest in this problem stems from the fact that the partitions can suppress the free convective currents which would otherwise occur in the air layer, thereby decreasing the heat transfer across the layer. If the partitions and top plate are transparent to solar radiation the system acts as an excellent solar trap for use in flat plate solar collectors [2, 3]. Other applications include the use of honeycombs in double glazed windows and in other air cavities, such as occur in buildings.

Previous studies relating to this problem are discussed in [1] and [4]. More recently Arnold, et al. [5, 6] reported measurements on liquid-filled rectangular honeycombs. Since, in the case of an air-filled honeycomb there exists a strong thermal radiation effect on the free convection [7, 1] which would not be experienced in an opaque liquid, their results are not necessarily directly applicable to air-filled honeycombs. This notwithstanding, the conclusion in [5] that the Nusselt number becomes independent of A_p for $A_p \geq 4$ should apply approximately to the air layer implying that the present results will be applicable to any situation having $A_p \geq 4$. Cormack, et al. [8, 9] and Imberger [10] report analytical, numerical and experimental studies for the case of a single cell having $A_p = \infty$ and $\theta = 90$ deg and adiabatic side-walls. Their analytical work was recently extended considerably by Bejan and Tien [11]. Catton, et al. [12] have reported an analysis over a range in A_E for $A_p = \infty$ and $\mathrm{Pr} = \infty$. Koutsoheras and Charters [13] report an extensive two-dimensional numerical analyses of the problem and Kay and Charters [14] report measurements over the range $\frac{1}{3} \leq A_E \leq 1$. Recently Meyer, et al. [15] reported an interferometric investigation.

The present set of experiments differs from earlier work in that it covers a wide range of variables ($3 \leq A_E \leq 10$, $0 \leq \theta \leq 90$ deg, and $10^3 \leq \mathrm{Ra} \leq 10^7$) and also examines the effect of the emissivities ϵ_{pc} and ϵ_{ph} of the plates bounding the air layer, and of the emissivity, ϵ_w, of the partitions (also called side-walls). Particular emphasis was placed on measurements at angles, θ, in the range 60 deg $\leq \theta \leq 90$ deg since it was anticipated that, for a given quantity of partition material, rectangular honeycombs should be more effective at suppressing convection than square-celled honeycombs at angles near vertical, whereas near horizontal square-celled honeycombs should be superior. This is based on the argument that for θ near 90 deg, there is little or no tendency for rolls with their axis oriented in the upslope direction to form, thereby negating any need for partitions running in this direction. These expectations were confirmed by the present experiments.

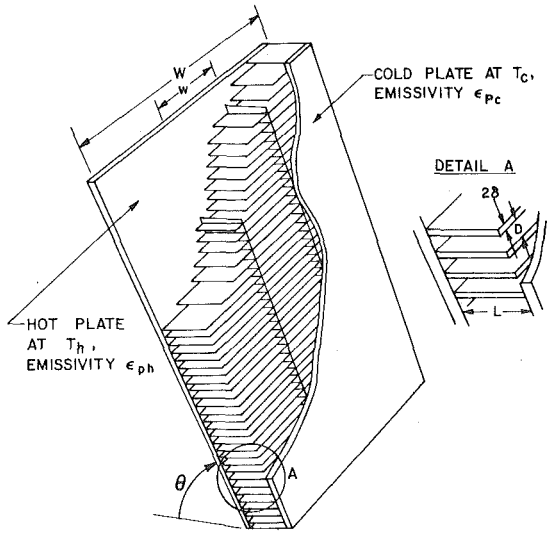

Fig. 1 Sketch defining rectangular honeycomb dimensions

Contributed by the Heat Transfer Division for publication in the JOURNAL OF HEAT TRANSFER. Manuscript received at ASME Headquarters March 21, 1979.

Description of Experiment

The apparatus and procedure used were identical, (except for a minor revision described shortly) to that used by Cane, et al. [1] for measurements on square-celled honeycombs. The vertical partitions were constructed by winding thin strips of polyethylene film back and forth around pins placed in a framework mounted at the edge of the copper plates, while maintaining a constant space $D = 12.7 \pm .5$ mm between adjacent partitions. Changing the dimension L (which required changing both the plate spacing and the width of the film) permitted changing of A_E. The top and bottom of the partitions were made to just touch the adjacent plates. Two types of polyethylene film were used. The first—essentially the same as that used by Cane, et al. [1]—was .038 mm thick, diathermous, and had the following estimated total hemispheric radiant properties for black body radiation at $T_m = 305$K: $\tau_w = .82$ $\rho_w = .07$ and $\alpha_w = \epsilon_w = 0.11$. The second film was 0.15 mm thick and had a black filler to make it opaque. It had total hemispheric radiant properties, as measured on a Gier-Dunkle DB 100 Reflectometer, of: $\tau_w = 0$, $\rho_w = .1$, $\alpha_w = \epsilon_w = 0.9$. Provision was made for varying the emissivities of the bounding plates ϵ_{pc}. Ordinarily the plates are polished copper with a measured emissivity of 0.065. For some of the tests the plates were sprayed with black paint giving them a measured emissivity of 0.9. The thermal conductivity of polyethylene was taken at .54W/mK with an uncertainty of about ±10 percent [16]. High accuracy in assessing this latter value was not important since approximate calculations of conduction along the partitions, from hot plate to cold plate indicated this conduction to be small compared to conduction through the gas.

Assuming a grey radiant analysis applies to the honeycomb cell, and assuming that $T_h/T_c \simeq 1$ (so that linearization of the radiant effects is permitted), dimensional analysis gives:

$$\mathrm{Nu} = \mathrm{Nu}\ (\mathrm{Ra}, \mathrm{Pr}, \theta, A_E, C, H, N, \epsilon_w, \epsilon_{ph}, \epsilon_{pc}) \tag{1}$$

The quantities τ_w and ρ_w were not listed since, as discussed in [1], due to the symmetry about the planes of the partitions, the partitions (although diathermous), can be treated as opaque with equivalent reflectance $\rho_{w,e} = \tau_w + \rho_w$; since $\tau_w + \rho_w = 1 - \epsilon_w$ specification of ϵ_w fixes $\rho_{w,e}$. Moreover A_p was fixed once and for all at $A_p = 44$ which was considered sufficiently large to represent the limit $A_p \to \infty$. Consequently A_p has also been omitted from the list of parameters. The Prandtl number of course was fixed at that for air at moderate temperature: $\mathrm{Pr} \simeq 0.71$. Apart from Ra, and θ, values for each of the other parameters were constant for each of the six experimental setups used, as given in Table 1. The values shown in this table are closely representative of those found in honeycomb solar energy collectors. As noted in [1], an error analysis indicated that the maximum expected error on the Nusselt number is estimated to be 3 percent, and for the Rayleigh number, about 2 percent. Further details on the experiments and full tabulation of data are given in [17].

Results and Discussion

The results for each of the experimental setups are shown in Figs. 2–7, in terms of Nu-Ra plots. The lower plots in each figure gives Nu as a function of the product Ra cos θ for $\theta \leq 75$ deg; the upper gives Nu versus Ra for the vertical orientation, $\theta = 90$ deg. Also shown for the lower set of plots as a solid line is the Nu-Ra relationship which would exist if no honeycomb were present, based upon the correlation of Hollands, et al. [18].

The Nu-Ra data presented in the figures display two distinctly different shapes, called here, the gradual rise and the abrupt rise. For example in Fig. 2, for $\theta = 90$ deg, the Nusselt number rises gradually with Ra over the measurement range; however, for $\theta = 0$ the Nusselt number remains very close to unity until a critical value of Ra is reached, Ra_c, after which it rises abruptly tracing out a curve which is concave downward. In the vertical orientation, $\theta = 90$ deg, the plates are aligned with the gravity so that the full component of gravity drives a vigorous base flow. The gradual rise of Nu with Ra is associated with this flow regime. When the plates are normal to the gravity vector ($\theta = 0$ deg) there is no base flow so that heat transfer is strictly by conduction at low Ra. With increasing Ra, the density of the fluid at the top of the air layer becomes increasingly larger than that at the bottom until at $\mathrm{Ra} > \mathrm{Ra}_c$ cellular motion, associated with Benard instability, abruptly appears, giving rise to the sharp increase in Nu characterizing the second type of Nu-Ra relation.

At other angles in the range 0 deg $< \theta \leq 75$ deg, the Nu-Ra relations all display the trends associated with the abrupt rise. Since $g \cos \theta$ is the component of gravity responsible for driving this motion, the value of $\mathrm{Ra}_c \cos \theta$ should be the same for all angles in this range. Reference to the figures indicates that this is generally borne out experimentally, lending additional support to the arguments relating the curve shape with the type of motion in the honeycomb.

Nomenclature

a = correlation constant, see equation (5b)
A_E = elevation aspect ratio of honeycomb cell, = L/D
A_p = plan aspect ratio of honeycomb cell, = w/D
b = correlation constant, see equation (5b)
c = correlation constant, see equation (5b)
C = first dimensionless side-wall conduction number, = $k_f L/(k_w \delta)$
D = spacing, measured in the upslope direction, between adjacent rectangular honeycomb partitions, (see Fig. 1)
g = acceleration due to gravity
$h_T = q_T/\Delta T$
$h_{T,s}$ = value of h_T measured at low Rayleigh number, with $\theta = 0$, when air is assumed to be in a stationary condition.
H = second dimensionless sidewall conduction number, = $k_f \delta/(k_w L)$
k_f = thermal conductivity of air, evaluated at T_m
k_w = thermal conductivity of honeycomb partition or side-wall material, (of polyethylene in the present experiments), evaluated at T_m.
L = perpendicular distance from hot plate to cold plate (see Fig. 1)
m = constant, equal to −0.386
n = correlation constant, see equation (5b)
N = dimensionless radiation to conduction number, = $4\sigma T_m{}^3 L/k_f$
Nu = Nusselt number, = $1 + (h_T - h_{T,s})L/k_f$
Pr = Prandtl number, = ν/λ
q_T = total measured heat flux across air layer, including effects of conduction along partitions, radiation, and gaseous conduction and convection
Ra = Rayleigh number, = $g\beta\Delta T L^3/(\nu\lambda)$
Ra_c = critical Rayleigh number
$(\mathrm{Ra}_c)_0$ = critical Rayleigh number at $\theta = 0$ deg
S = definite integral due to Sun [19]; in general it is a function of A_E and A_p only; for $A_p = \infty$, it is given (approximately) by equation (3).
T_c, T_h = temperature of cold and hot isothermal plates which form the bounding surfaces to air layer, respectively.
$T_m = (T_h + T_c)/2$
$\Delta T = T_h - T_c$
W, w = spacing measure in cross-slope direction, (see Fig. 1).
α_w = total hemispheric absorptivity of honeycomb partitions to a black body at T_m
β = volumetric expansion coefficient of air at T_m
$\gamma_1\gamma_2$ = constants in equation (6), (see Table 2)
δ = semi-thickness of honeycomb partitions, see Fig. 1.
ϵ_w = total hemispheric emissivity of honeycomb partitions at T_m
ϵ_{pc}, ϵ_{ph} = total hemispheric emissivity of the cold and hot plates bounding the air layer, respectively
θ = angle of inclination of air layer from horizontal, see Fig. 1
λ = thermal diffusivitiy of air at T_m
ν = kinematic viscosity of air at T_m
ρ_w = total hemispheric reflectance of honeycomb partitions to black body radiation at T_m
$\rho_{w,e}$ = equivalent value of ρ_w, obtained by treating wall as opaque, = $\tau_w + \rho_w$
σ = Stefan-Boltzmann constant
τ_w = total hemispheric transmittance of honeycomb partitions to black body radiation at T_m

Table 1 Description of the rectangular honeycombs and plate emissivities investigated

Experimental Set up No.	2δ mm	L mm	D mm	A_E	ϵ_w	ϵ_{ph}	ϵ_{pc}	C	N	$H \times 10^5$
1	0.038	63.5	12.7	5	0.13	0.065	0.065	166	15.2	1.5
2	0.038	127.	12.7	10	0.13	0.065	0.065	332	30.4	.75
3	0.038	38.1	12.7	3	0.13	0.065	0.065	100	9.1	2.5
4	0.15	63.5	12.7	5	0.9	0.065	0.065	42	15.2	6
5	0.15	63.5	12.7	5	0.9	0.9	0.065	42	15.2	6
6	0.15	63.5	12.7	5	0.9	0.9	0.9	42	15.2	6

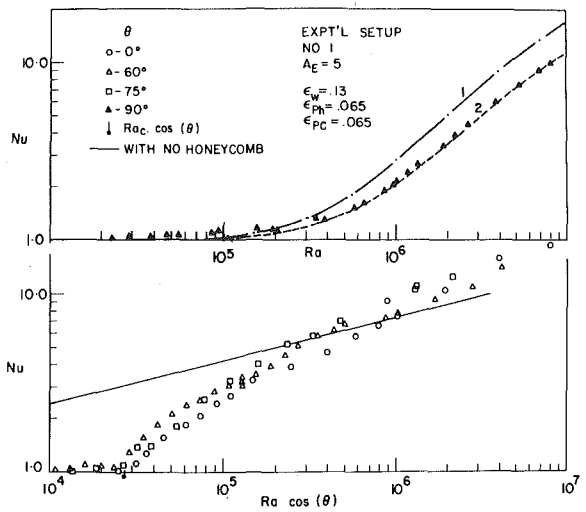

Fig. 2 Experimental results in terms of Nu versus Ra cos θ (lower graph) or versus Ra (upper graph) for experimental set-up No. 1

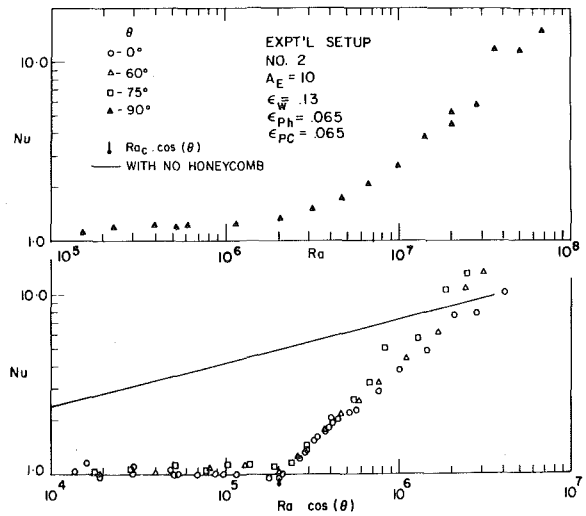

Fig. 3 Experimental results in terms of Nu versus Ra cos θ (lower graph) or versus Ra (upper graph) for experimental set-up No. 2

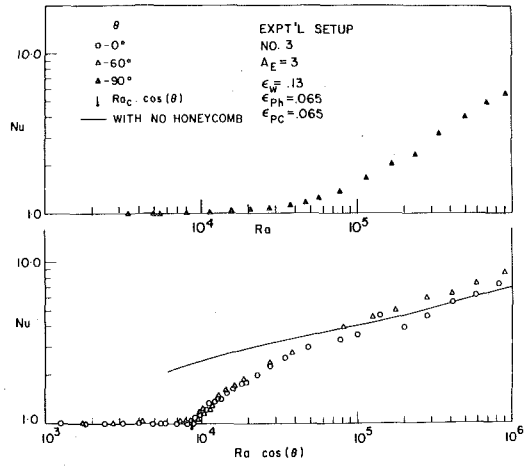

Fig. 4 Experimental results in terms of Nu versus Ra cos θ (lower graph) or versus Ra (upper graph) for experimental set-up No. 3

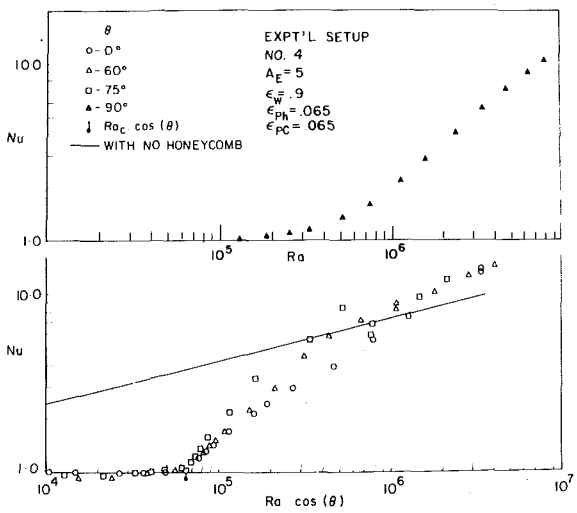

Fig. 5 Experimental results in terms of Nu versus Ra cos θ (lower graph) or versus Ra (upper graph) for experimental set-up No. 4

For θ not equal to zero a base-flow must always exist, driven by the component of gravity $g \sin \theta$. Clearly from a heat transfer point of view, this base flow is unimportant (i.e., Nu $\approx$ 1) in all the present experiments for 0 deg $< \theta \leq$ 75 deg up to the critical Rayleigh number. The fact that the Nu data for 0 deg $\leq \theta \leq$ 75 deg, for Ra $>$ Ra$_c$, collapse very nearly onto a single curve for each experiment when Ra cos θ is used as the abscissa suggests that the flow induced by the top-heavy instability remains mainly responsible for the heat transfer.

A comparison of the present curve-shapes for rectangular honeycombs with those of Cane, et al. [1] for square-celled honeycombs shows some striking differences. Similar trends are observed for θ = 0 deg and θ = 9θ deg, except that Ra$_c$ for θ = 0 deg is delayed to a much higher value using the square-celled honeycombs of the same value of A_E. However, the shapes of the curves are markedly different for intermediate angles of inclination; the square-celled honeycombs all showed the gradual rise but the rectangular-cells all display the abrupt rise associated with the top-heavy instability. The reason for this different character is that the flow induced by the top-heavy instability tends to generate both longitudinal rolls (i.e., rolls with axes along the upslope) and transverse rolls (i.e., rolls with axes across the slope), with an equal preference for each type of roll at θ = 0 deg, but with a preference for the longitudinal rolls for 0 $\leq \theta \leq \sim$ 75 deg and a preference for the transverse rolls at $\sim$ 70 deg $\leq \theta \leq$ 90 deg [19]. The walls of the rectangular-celled honeycomb restrict only the transverse rolls; they permit longitudinal rolls and therefore have a relatively low critical Rayleigh number—so low that the base flow is not yet of sufficient strength to have significant heat transfer. However the square-celled side walls restrict both longitudinal and transverse cells yielding very high values for the critical Rayleigh number which governs top-heavy instability. Before this critical Rayleigh number

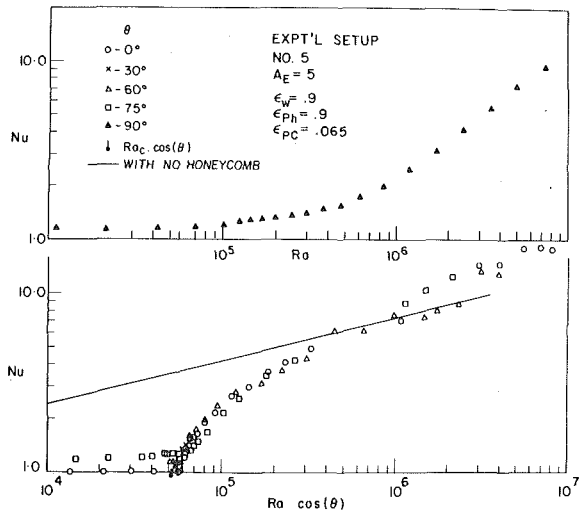

Fig. 6 Experimental results in terms of Nu versus Ra cos θ (lower graph) or versus Ra (upper graph) for experimental set-up No. 5

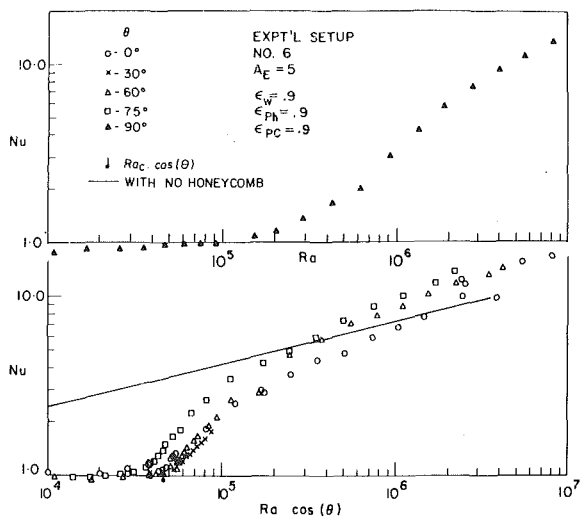

Fig. 7 Experimental results in terms of Nu versus Ra cos θ (lower graph) or versus Ra (upper graph) for experimental set-up No. 6

is achieved, base flow, which is dampened but not prohibited by the upslope partitions, is sufficiently strong to drive significant heat transfer and therefore its characteristic gradual rise is observed.

Fig. 8 permits a comparison of the convection suppression abilities of rectangular vis-a-vis square-celled honeycombs. The smooth curves are fits to Cane, et al.'s data for square-celled honeycombs; the open and closed circle points are for the present data. All data were generated with the same thickness and type of partition material and with the same bounding plate emissivities. Comparison of the two honeycombs for the same elevation aspect ratio, A_E, is afforded by comparing the circles with the smooth line. As expected, the square-cells permit greater convection suppression; however their advantage decreases as the angle θ increases until at $\theta = 90$ deg there is little difference between the two. It must be remembered, however, from a practical point of view, that in this latter comparison, the square-celled honeycomb contains twice the amount of partition material as the rectangular one—and hence is likely to involve twice the material cost. A comparison for the same amount of honeycomb material is afforded by comparing the closed circles with the smooth line, corresponding to $A_E = 10$ for the rectangular and $A_E = 5$ for the square-cells. In this instance, the square honeycomb is still superior for $\theta < 70$ deg; the two are roughly equivalent at $\theta = 75$ deg; and at $\theta = 90$ deg, the rectangular honeycomb is superior. As already explained, this results from the absence of any tendency for the longitudinal rolls to form at $\theta = 90$ deg, and the consequent redundancy of the partitions in the upslope direction in the square-celled honeycomb. These partitions are more usefully placed parallel to the transverse partitions in order to suppress the base flow/transverse rolls by confining them to a smaller eddy size.

The effect of honeycomb wall emissivity, ϵ_w, (at least for $A_E = 5$) is seen by comparing experimental setups 1 and 4 in Figs. 2 and 5. For $\theta \leq 75$ deg, the critical Rayleigh number is seen to have increased by a factor of 2.3 by increasing the wall emissivity from 0.13 to 0.9, in agreement with Edwards and Sun [7] who first noted the stabilizing effect of a high emissivity wall, for $\theta = 0$. However at $\theta = 90$ deg, very little effect due to a change in ϵ_w is to be noted.

The effect of plate emissivity $\epsilon_{p,c}$ and $\epsilon_{p,h}$ can be seen by comparing experimental setups 4, 5, and 6. Taking both bounding plates at high emissitivity (setup 6) as a starting point, the critical Rayleigh number is increased 11 percent by giving one of the plates a low emissivity (run 5), while giving both plates a low emissivity gives a further increase in Ra_c of 26 percent. One can only speculate as to the reason for this observed stabilizing effect of lowering the bounding plate emissivities. It is known that the radiant field tends to establish a roughly linear temperature distribution in the partitions if the bounding plates are black, whereas when they have a very low emissivity, it tends to establish a uniform temperature in the central region (equal to the average temperature), with high gradients near each bounding plate [22]. Since the radiant field's wall temperature distribution must, to some extent, be imposed on the air temperature, this may have the effect of effectively decreasing the length dimension over which a temperature difference operates on the air, to the dimension of the high gradient regions. Since the effective Rayleigh number corresponding to this dimension is also decreased, the net effect would be a stabilizing one.

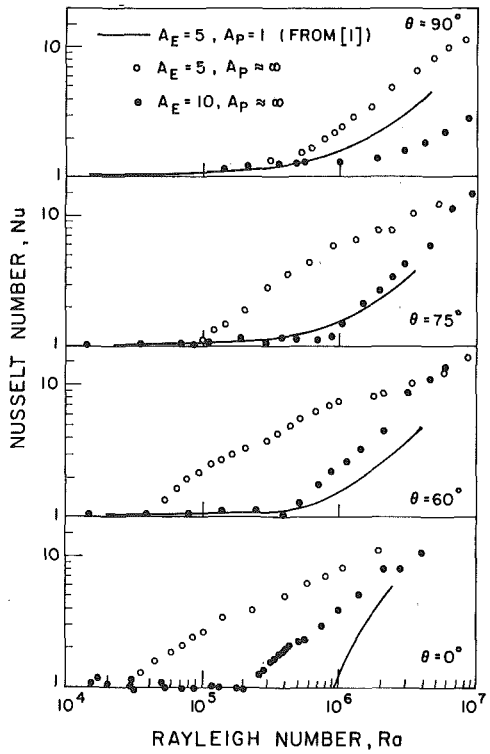

Fig. 8 This graph shows a comparison of the relative convection suppression capabilities of square and rectangular honeycombs. The smooth line is for a square celled honeycomb with $A_E = 5$; the open circles are for a rectangular honeycomb of the same A_E, the closed circles are for a rectangular honeycomb containing the same amount of honeycomb material

A comparison of the present results for air with the results of Arnold, et al. on liquids [5, 6] is of interest. Only the $A_E = 5$ cases fall within the range of validity of their equations. Their calculated value of $Ra_c \cos\theta$ is 18,200 which is quite different from the values of about 55,000 determined in the present experiments. Consequently the error

in the Nusselt-number calculated from their horizontal equation is about 100 percent at Ra ≈ 55,000. Similar difference are found with their vertical orientation equation. These differences can be explained as being due to the opacity of the liquid to thermal radiation, and to the different side-wall conduction. However, similar shapes of the Nu-Ra curves are to be observed for both air and liquids.

Correlation Equations

For Critical Rayleigh Number at $\theta < 70$ Deg. Table 2 gives the values of the critical Rayleigh number Ra_c at $\theta = 0$, (denoted by $(Ra_c)_0$) obtained by fairing a curve through those data points having $1 \leq Nu \leq 1.2$ and extrapolating the curve to Nu = 1. Based on analytical methods developed and tabulated by Sun [9], Buchberg, et al. [4] give an approximate equation for this $(Ra_c)_0$, which for the present instance of large A_p, reduces to:

$$(Ra_c)_0 = A_E{}^2\left[768 + \frac{1536A_E}{C} + 48\,\epsilon_w N A_E \frac{(1-S)}{1-S(1-\epsilon_w)}\right] \quad (2)$$

In this equation, the quantity S is the value of a definite integral containing both A_p and A_E as parameters. Although graphed in [4], for the purposes of engineering calculations, a fitted functional relation for S appears to be a more satisfactory representation. For the limit $A_p \to \infty$, and $A_E \geq 2$ such a fitted function, accurate to within 1 percent was found in the present study to be:

$$S = 1.0102 - \frac{1.4388}{A_E} - \frac{9.4653}{A_E{}^2} + \frac{31.440}{A_E{}^3} - \frac{27.515}{A_E{}^4} \quad (3)$$

Values of $(Ra_c)_0$ calculated from equations (2) and (3) are tabulated in Table 2 along with the measured values. Despite the fact that the analysis does not incorporate the effects of ϵ_{ph} and ϵ_{pc}, the agreement with measurement is seen to be quite good. The maximum deviation occurs when $\epsilon_{ph} = \epsilon_{pc} = .9$, being 34 percent in this instance. Aside from this case, predictions are within 21 percent. Better comparisons are obtained for the cases where the wall emissivities are low. More precise predictions will have to await the development of a stability theory which incorporates ϵ_{ph} and ϵ_{pc} as variables.

The preceding has been restricted to the case $\theta = 0$. However, inspection of Figs. 2–7 shows the product $Ra_c \cos\theta$ is approximately independent of θ provided $\theta \leq 75$ deg. Hence it appears that Ra_c at any angle in this range can be estimated closely from

$$Ra_c = (Ra_c)_0/\cos\theta \quad (4)$$

where $(Ra_c)_0$ is given by equation (2).

Nusselt Number for $\theta \leq 75$ Deg. Since all of the Nu-Ra plots for $\theta \leq 75$ deg are generally the same shape, a single form of equation was sought to fit all this data. The form chosen was similar to that used by Hollands [21] for square-celled horizontal honeycombs:

$$Nu = 1 + c(Ra\cos\theta)^{1/3}\left[1 - \exp\left\{-(a + b\,\theta)\left[\left(\frac{Ra}{Ra_c}\right)^n - 1\right]\right\}\right] \quad (5a)$$

where a, b, c and n are constants chosen so as to minimize the sum of the squares of the deviations of the data from the equation, over the 347 data points having $\theta \leq 75$ deg. This procedure resulted in:

$$a = 0.18 \qquad b = 1.2 \times 10^{-3}\ \text{deg}^{-1}$$
$$c = 0.131 \qquad n = 0.513 \quad (5b)$$

In equation (5a) the Ra_c's are to be obtained from equation (2), thereby bringing in the dependence of Nu on A_E, C, ϵ_w and N. The root mean square error in Nu associated with equation (4) is about 18 percent. The range of validity of the equation is $Ra_c < Ra < 100\,Ra_c$. For $Ra < Ra_c$, Nu is to be taken as equal to unity.

Nusselt Number for $\theta = 90$ Deg. An equation recently developed by Bejan and Tien [11] describing the Nu-Ra relation for a horizontal cavity with adiabatic top and bottom boundaries and different end temperatures should be exactly applicable to the present problem for the case $\theta = 90$ deg, $C = \infty$, $H = \infty$ (i.e., $k_w = 0$) and $\epsilon_w N = 0$ (i.e., no radiant coupling). In the present experiments there is undoubtly some coupling between the radiant and convective fields; there is also, doubtless, some conduction between adjacent cells, since it will be noted that in the central core, hot fluid in the upper half of the cell travelling toward the cold plate is in counterflow with cold fluid in the lower half of the next cell up. However the general form of the flow field outlined by Bejan and Tien—namely streamlined flow in the central core and a boundary layer-like resistance at the end walls is very likely applicable to the present set of experiments. Hence the *form* of their equation, with some adjustment to its constants may be anticipated to fit the present data. Their equation is:

$$Nu = 1 + \left\{\left[\gamma_1\left(\frac{Ra}{A^4}\right)^2\right]^m + \left[\gamma_2 Ra^{1/5}A^{2/5}\right]^m\right\}^{1/m} \quad (6)$$

in which $\gamma_1 = 2.756 \times 10^{-6}$ and $\gamma_2 = 0.623$. Fig. 2 shows the comparison of this equation (line 1) with the data for experimental setup No. 1. Agreement is seen to be only fair, but by adjusting the constants γ_1 and γ_2 so as to pass the curve (line 2) through the data at two points excellent agreement is obtained over the whole measured Rayleigh number range. This fitting procedure was repeated for the five remaining runs with equally accurate fits obtained in each case. The resulting values of γ_1 and γ_2 for each run are summarized in Table 2. Unfortunately, no clear trend in the values of γ_1 and γ_2 with the radiant conditions can be noted. However, for practical purposes a designer could choose the γ-values most closely fitting the aspect ratio and radiant conditions of the experiment.

Conclusions

1 Critical Rayleigh numbers at $\theta = 0$ deg are predicted well by the equations of Buchberg, et al., provided the emissivities of the bounding plates are low; if either or both bounding plates have high emissivity, the equations overpredicts by up to 34 percent.

2 For $0 \leq \theta \leq 75$ deg the Nu-Ra relations are characterized by a sudden rise in Nusselt from unity occurring at a critical Rayleigh number, indicating a top-heavy-type instability. With reasonable accuracy, this critical Rayleigh number can be determined from the critical Rayleigh number at $\theta = 0$ by dividing the latter by $\cos\theta$. The form (i.e., shape) of this Nu-Ra relation is quite different from that observed for square-celled honeycombs of the same aspect ratio, where (except at $\theta = 0$ deg) a much more gradual rise was observed.

3 A correlation equation (equation (5)) is given which relates Nu to Ra and Ra_c over the range $0 \leq \theta \leq 75$ deg and $Ra_c \leq Ra \leq 100\,Ra_c$.

4 For $\theta = 90$ deg the form of the Nu-Ra relation is quite different from that at lower angles, having the same gradual rise as that observed for square-celled honeycombs at lower angles. This "gradual-rise" form is attributable to the heat transport associated with

Table 2 Summary of values of $(Ra_c)_0$, γ_1 and γ_2 for the various experimental set-ups

Experimental Set-Up Number	1	2	3	4	5	6
A_E	5	10	3	5	5	5
ϵ_w	0.13	0.13	0.13	0.9	0.9	0.9
ϵ_{ph}	0.065	0.065	0.065	0.065	0.9	0.9
ϵ_{pc}	0.065	0.065	0.065	0.065	0.065	0.9
Measured $(Ra_c)_0$	27,500	204,000	8660	65,200	51,800	46,500
$(Ra_c)_0$ Predicted by equation (2)	30,500	206,000	8780	62,500	62,500	62,500
Percent Diff. in $(Ra_c)_0$'s	+11	+1	+1	−4.3	+21	+34
$\gamma_1 \times 10^6$	1.324	3.952	1.274	0.970	1.524	4.76
γ_2	0.474	0.502	0.415	0.594	0.430	0.511

the base flow, rather than a top-heavy instability. The form agrees well with that obtained from analysis by Bejan and Tien and, with adjusted values for its constants, their equation fits the data at this angle very well.

5 For the same elevation aspect ratio, the square-celled honeycomb gives better convection suppression characteristics than the rectangular honeycomb of large plan aspect ratio. However, if the two are compared for the same amount of honeycomb material, the rectangular celled honeycomb is superior at $\theta = 90$ deg, although the square-celled is still superior for $\theta \leq 60$ deg.

Acknowledgments

The authors wish to acknowledge with gratitude the financial support provided through the United States Department of Energy, Division of Solar Energy, Solar Heating and Cooling Branch, under grant number EY-76-C-02-2597. The National Research Council of Canada provided the funds for the original construction of the apparatus.

References

1 Cane, R. L. D., Hollands, K. G. T., Raithby, G. D., Unny, T. E., "Free Convection Heat Transfer Across Inclined Honeycomb Panels," ASME JOURNAL OF HEAT TRANSFER, Vol. 99, No. 1, 1977, pp. 86–91.

2 Francia, G., "A New Collector of Solar Radiant Energy—Theory and Experimental Verification," *Proceedings, U.N. Conference on New Sources of Energy,* Rome, Vol. 4, 1961, pp. 554–558.

3 Hollands, K. G. T., "Honeycomb Devices in Flat-Plate Solar Collectors," *Solar Energy,* Vol. 9, No. 3, 1965, pp. 159–164.

4 Buchberg, H., Catton, I., and Edwards, D. K., "Natural Convection in Enclosed Spaces—A Review of Application to Solar Energy Collection," ASME JOURNAL OF HEAT TRANSFER, Vol. 98, No. 2, 1976, pp. 182–188.

5 Arnold, J. N., Edwards, D. K., and Catton, I., "Effect of Tilt and Horizontal Aspect Ratio on Natural Convection in Rectangular Honeycombs," ASME JOURNAL OF HEAT TRANSFER, Vol. 99, 1977, pp. 120–122.

6 Arnold, J. N., Edwards, D. K. and Wu, P. S., "Effect of Cell Size on Natural Convection in High *L/D,* Tilted Rectangular Cells Heated and Cooled on Opposite Faces," ASME Paper No. 78-WA/HT-5, 1978.

7 Edwards, D. K. and Sun, W. M., "Effect of Wall Radiation on Thermal Instability in a Vertical Cylinder," *International Journal of Heat and Mass Transfer,* Vol. 14, 1971, pp. 15–18.

8 Cormack, D. E., Leal, L. G., and Imberger, J., "Natural Convection in a Shallow Cavity with Differentially Heated End Walls, Part 1, Asymptotic Theory," *Journal of Fluid Mechanics,* Vol. 65, 2, 1974, pp. 209–229.

9 Cormack, D. E., Leal, L. G., and Seinfeld, J. H., "Natural Convection in a Shallow Cavity with Differentially Heated End Walls, Part 2. Numerical Solutions," *Journal of Fluid Mechanics,* Vol. 65, 2, 1974, pp. 231–246.

10 Imberger, J., "Natural Convection in a Shallow Cavity, with Differentially Heated End Walls, Part 3, Experimental Results," *Journal of Fluid Mechanics,* Vol. 65, No. 2, 1974, pp. 247–260.

11 Bejan, A. and Tien, C. L., "Laminar Natural Convection Heat Transfer in a Horizontal Cavity with Different End Temperatures," ASME JOURNAL OF HEAT TRANSFER, Vol. 100, No. 4, 1978, pp. 640–647.

12 Catton, I., Ayyaswany, P. S., and Clever, R. M., "Natural Convection Flow in a Finite Rectangular Slot Arbitrarily Orientated with Respect to the Gravity Vector," *International Journal of Heat and Mass Transfer,* Vol. 17, 1974, pp. 173–184.

13 Koutsoheras, W., and Charters, W. W. S., "Natural Convection Phenomena in Inclined Cells with Finite Side-walls—a Numerical Solution," *Solar Energy,* Vol. 19, No. 5, 1977, pp. 433–438.

14 Kay, H. K., and Charters, W. W. S., "Convective Effects in Slot Collectors," *Proceedings of the International Solar Energy Society Congress,* New Delhi, India—Jan. 1978, Pergamon Press, pp. 965–970.

15 Meyer, B. A., El-Wakil, M. M., Mitchell, J. W., "An Interferometric Investigation of Heat Transfer in Honeycomb Solar Collector Cells," *Proceedings, International Solar Energy Society Congress,* New Delhi, 1978, Pergamon Press, pp. 956–959.

16. Hanson, D., and Bernier, G. A., "Thermal Conductivity of Polyethylene—the Effect of Crystal Size, Density, and Orientation," *Polymer Engineering and Science,* Vol. 12, No. 3, 1972, pp. 204–208.

17 Smart, D. R., "Convection Suppression and Heat Transfer in Air Layers Constrained by Slit Type Honeycombs with Application to Flat Plate Solar Collector Design," M.A.Sc. Thesis, University of Waterloo, 1977.

18 Hollands, K. G. T., Unny, T. E., Raithby, G. D., Konicek L., "Free Convection Across Inclined Air Layers," ASME JOURNAL OF HEAT TRANSFER, Vol. 98, No. 2, 1976, pp. 189–193.

19 Hart, J., "Stability of the Flow in a Differentially Heated Inclined Box," *Journal of Fluid Mechanics,* Vol. 47, 1971, pp. 547.

20 Sun, W. M., "Effect of Arbitrary Wall Conduction and Radiation of Free Convection in a Cylinder," Ph.D. Thesis, University of California, Los Angeles, 1970.

21. Hollands, K. G. T., "Natural Convection in Horizontal Thin-Walled Honeycomb Panels," JOURNAL OF HEAT TRANSFER, Vol. 95, 1973, pp. 439–444.

22 Hollands, K. G. T. et al., "Methods for Reducing Heat Losses from Flat Plate Solar Collectors—Phase III," University of Waterloo Report 702-02, Waterloo Research Institute of the University of Waterloo, Waterloo, Canada, 1979.

T. C. Chawla
S. H. Chan[1]
F. B. Cheung
D. H. Cho

Reactor Analysis and Safety Division,
Argonne National Laboratory,
Argonne, IL 60439

Combined Natural Convection and Radiation in a Volumetrically Heated Fluid Layer

The effect of radiation in combination with turbulent natural convection on the rates of heat transfer in volumetrically heated fluid layers characterized by high temperatures has been considered in this study. It is demonstrated that even at high Rayleigh numbers the radiation mode is as effective as the turbulent natural convection mode in removing the heat from the upper surface of the molten pools with adiabatic lower boundary. As a result of this improved heat transfer, it is shown that considerably thicker molten pools with internal heat generation can be supported without boiling inception. The total Nusselt number at a moderate but fixed value of conduction-radiation parameter, can be represented as a function of Rayleigh number in a simple power-law form. As a consequence of this relationship it is shown that maximum nonboiling pool thicknesses vary approximately inversely as the 0.9 power of internal heat generation rate. A comparison between exact analysis using the integral formulation of radiation flux and Rosseland approximation shows that the latter approximation bears out very adequately for optically thick pools with conduction-radiation parameter $\gtrsim 0.4$ inspite of the fact that individual components of Nusselt number due to radiation and convection, respectively, are grossly in error. These errors in component heat fluxes are compensating due to the total heat balance constraint. However, the comparison between Rosseland approximation and exact formulation gets poorer as the value of conduction-radiation parameter decreases. This increase in error is principally incurred due to the error in estimating wall temperature differences.

Introduction

The study of heat transfer in volumetrically heated fluid layers is of fundamental importance to a number of technological applications, such as nuclear reactor safety, environmental sciences, geophysics and astrophysics. For example, in the nuclear reactor safety application, the volumetrically heated fluid layer occurs in the hypothetical core meltdown accidents initiated by loss of flow in a liquid metal cooled fast breeder reactor (LMFBR). The fluid layer consisting of molten fuel with decay heating, has temperatures in excess of 3100 K, so that the contribution of thermal radiation to heat transfer in the fluid layer could be significant. The majority of previous studies in these high temperature applications have considered natural convection as the only mode of heat transfer. Notable among these studies are Cheung [1], Kulacki and Nagle [2], Kulacki and Emara [3], Tritton and Zarraga [4], Baker, et al. [5], and Suo-Anttila and Catton [6]. The heat transfer correlations in these studies are derived mostly from experimental data obtained at low temperatures and consequently these correlations do not account for the effect of radiation heat transfer. In one recent experimental study conducted by Stein, et al. [7] to determine downward heat flux in a molten UO_2 pool, it was discovered that heat transfer from the pool could not be accounted for by available thermal convection models, suggesting that the internal radiation may be a very significant mode of heat transfer. The effect of radiation on the rates of heat transfer in molten pools of oxide fuels has been considered recently by Cho, et al. [8] and by Anderson [9]. Both of these analyses have utilized the Rosseland diffusion approximation to estimate the heat flux. In the former analysis, however, the effect of local variation of eddy diffusivity has been neglected. As a result of this assumption, Cho, et al. has shown that Anderson's analysis underestimates the heat flux at high Rayleigh numbers. It is, however, well known that the Rosseland approximation is valid in the interior of a medium but does not provide a correct description of radiation transport near the boundaries since it does not include any terms for radiation transport from the boundary surfaces. One of the purposes of the present study is to perform more exact analysis applicable to the complete range of optical depths of interest to LMFBR safety for combined natural convection and radiation transport so that the accuracy that can be obtained using the Rosseland approximation is assessed.

In addition, we wish to demonstrate that radiation heat transport, particularly in the LMFBR safety area, has a significant contribution compared to natural convection, even at high Rayleigh numbers. This, as we will point out subsequently in more detail, has a considerable significance to heat removal capability of molten core debris in post-accident heat removal (PAHR).

Formulation of the Problem

The approach presently utilized (see, for example, [5]) in the heat transfer analysis of heat generating molten fuel layers in PAHR studies is to consider first the experimental correlations for heat transfer for the molten layer having equal temperatures at the upper and lower boundaries and then conceptually separate the layer at the plane of the maximum temperature into an upper and lower sublayers. All the heat generated within upper sublayer transfers upward, and all the heat generated in the lower sublayer transfers downward. As a consequence of this conceptual subdivision, heat transfer in each sublayer is studied independently considering one boundary to be insulated (the division line at the maximum temperature) and the other boundary at the fixed temperature. One of the primary parameters of interest is the range of thicknesses of fuel layers corresponding to various rates of internal heat generation that correspond to nonboiling thickness of the fuel, that is the thickness in which the maximum temperature at the lower insulated boundary remains at the boiling temperature of the fuel while the temperature of the upper boundary is at the melting temperature of the fuel. For thicker layers, boiling will significantly change the nature of heat transfer and the consideration of PAHR capability.

In view of the above discussions, we consider a horizontal layer of molten heat-generating fuel with an adiabatic lower boundary at an unknown temperature T_1 and the upper boundary at temperature $T_2 < T_1$. The Rayleigh numbers of interest to the present application

Contributed by the Heat Transfer Division for publication in the JOURNAL OF HEAT TRANSFER. Manuscript received by the Heat Transfer Division May 29, 1979.

[1] Department of Mechanical Engineering, University of Wisconsin-Milwaukee, Milwaukee, Wisc. 53201.

are quite high ($>10^{10}$) and, as has been shown experimentally [2], the thermal convection is characterized by intense turbulent mixing in the region away from wall and consequently the temperature profile is mostly uniform except for a very sharp gradient near the upper wall. These large temperature gradients are characterized by very low thermal conductivity of the fuel material. It has been demonstrated by comparison with the experimental data obtained at high Rayleigh numbers but at low temperatures, that heat transfer is principally controlled by eddy heat transport [1, 10]. In one-dimensional treatment, which we shall adopt in the present analysis, the heat transport by time-mean circulation has been shown to be identically zero [10]. At high temperatures, of interest in PAHR, turbulent mode of heat transfer must be accompanied by radiation heat transport in the medium. Consequently, the governing energy equation can be written as

$$\frac{d}{dy}\left[K(1+\epsilon_H/\alpha)\frac{dT}{dy}\right]-\frac{dq_r}{dy}+q_v=0, \tag{1}$$

where eddy diffusivity ϵ_H is given by Cheung's model [1]:

$$\frac{\epsilon_H}{\alpha}=0.051\mathrm{Ra}^{*0.87}, \tag{2a}$$

with

$$\mathrm{Ra}^*=\frac{q\beta(T-T_2)L^3}{\alpha\nu}\left[\left(\frac{y}{L}\right)\left(1-\frac{y}{L}\right)\right]^{3.448} \tag{2b}$$

The above expression raised to power 0.87 represents spatial variation of eddy diffusivity. The radiation flux q_r is prescribed by assuming the participating medium is gray, nonscattering, with the absorption coefficient κ and the thermal conductivity K independent of temperature. The bounding surfaces consist of two parallel black walls which extend indefinitely in all horizontal directions and are isothermal but at different temperatures. Due to lack of experimental data on radiation properties of the molten pools of oxide fuels over the temperature range of interest, no justification can be provided for these simplifying assumptions other than the fact that they will minimize the complications in a coupled radiation turbulent-diffusion problem while still displaying the essential features of the effect of radiation on heat transfer processes occurring in molten pools. In view of these assumptions, the radiation flux q_r is given as [11]:

$$q_r(\eta)=2n^2\sigma T_1^4E_3(\eta)-2n^2\sigma T_2^4E_3(\eta_0-\eta)+2\int_0^{\eta}n^2\sigma T^4(\eta')E_2(\eta-\eta')d\eta'-2\int_{\eta}^{\eta_0}n^2\sigma T^4(\eta')E_2(\eta'-\eta)d\eta' \tag{3}$$

The boundary condition that equation (1) must satisfy are

$$q(0)=\left[-K\frac{dT}{dy}+q_r\right]_{y=0}=0 \tag{4a}$$

$$T(L)=T_2 \tag{4b}$$

It is convenient to nondimensionalize equation (1) through (3) by introducing the following dimensionless quantities:

$$\eta=\kappa y,\quad \theta(\eta)=\frac{T(\eta)}{T_R},\quad \theta_1=\frac{T_1}{T_R},\quad \theta_2=\frac{T_2}{T_R}, \tag{5}$$

$$N=\frac{K\kappa}{4n^2\sigma T_R^3},\quad q_r^*=\frac{q_r}{n^2\sigma T_R^4},\quad q_v^*=\frac{q_v}{n^2\sigma T_R^4\kappa},\quad \epsilon_H^*=\frac{\epsilon_H}{\alpha}$$

With the above definition, equations (1, 2b, 3), and (4) reduce, respectively, to

$$\frac{d}{d\eta}\left[(1+\epsilon_H^*)\frac{d\theta}{d\eta}\right]-\frac{1}{4N}\frac{dq_r^*}{d\eta}+\frac{q_v^*}{4N}=0 \tag{6}$$

$$\epsilon_H^*=0.051\mathrm{Ra}^{*0.87},\quad \mathrm{Ra}^*=\frac{g\beta T_R(\theta-\theta_2)L^3}{\alpha\nu}\left[\frac{\eta}{\eta_0}\left(1-\frac{\eta}{\eta_0}\right)\right]^{3.448} \tag{7}$$

$$q_r^*(\eta)=2\theta_1^4E_3(\eta)-2\theta_2^4E_3(\eta_0-\eta)+2\int_0^{\eta}\theta^4(\eta')E_2(\eta-\eta')d\eta'-2\int_{\eta}^{\eta_0}\theta^4(\eta')E_2(\eta'-\eta)d\eta' \tag{8}$$

$$\left[-4N\frac{d\theta}{d\eta}+q_r^*\right]_{\eta=0}=0 \tag{9a}$$

$$\theta(\eta_0)=\theta_2 \tag{9b}$$

In view of boundary condition (9a), it is more convenient to solve equation (6) in its heat flux form by integrating it once with respect to η. Thus

$$4N(1+\epsilon_H^*)\frac{d\theta}{d\eta}-q_r^*+q_v^*\,\eta=0 \tag{10}$$

where the radiation flux q_r^* is given either by the exact formulation (8) or by the Rosseland approximation given as [11]:

$$q_r^*=-\frac{16\theta^3}{3}\frac{d\theta}{d\eta} \tag{11}$$

Heat Transfer Parameters. The mean Nusselt number at the upper surface is defined as [1]

$$\mathrm{Nu}=\frac{(q_vL)L}{2K(T_1-T_2)} \tag{12}$$

Substituting from equation (10) at $\eta=\eta_0$ and using the fact that $\epsilon_H^*(\eta_0)=0$ we obtain

$$\mathrm{Nu}_T=\frac{\eta_0}{8N(\theta_1-\theta_2)}\left[-4N\frac{d\theta}{d\eta}+q_r^*\right]_{\eta=\eta_0} \tag{13}$$

or

$$\mathrm{Nu}_T=\mathrm{Nu}_c+\mathrm{Nu}_r \tag{14}$$

where for a given temperature difference between the upper and lower walls equation (13) assumes that the heat balance expressed by equation (10) is satisfied exactly. Since in any numerical computations

Nomenclature

$E_n(\eta)$ = nth exponential integral
g = acceleration due to gravity
K = thermal conductivity of fluid
L = thickness of the horizontal fluid layer
N = conduction-radiation parameter
n = refractive index of the fluid
Nu = Nusselt number defined by equation (12)
Nu_T = total Nusselt number defined by equation (13)
Nu_c^* = Nusselt number due to convection alone
q = heat flux
q_v = volumetric heat generation rate
R = stretching parameter in the coordinate transformation
Ra = Rayleigh number $g\beta q_vL^5/(2K\alpha\nu)$
T = absolute temperature
T_R = arbitrary reference temperature, chosen equal to T_2 in numerical calculations
y = position coordinate along the pool thickness from the bottom wall
z = transformed coordinate
α = thermal diffusivity of fluid
β = isobaric coefficient of thermal expansion
δ = thermal boundary layer thickness
ϵ_H = eddy diffusivity for turbulent natural convection
η = optical depth from the lower wall
η_0 = optical thickness of the pool
θ = nondimensional temperature
κ = absorption coefficient
σ = Stefan-Boltzmann constant

Subscripts

r = radiation component
1,2 = values of a variable at the lower and upper wall, respectively

Superscripts

* = nondimensional quantities

heat fluxes will suffer from inaccuracies of the truncation errors, the two Nusselt numbers expressed by equation (12) and that by equation (13) are not likely to be identical. However, they must not differ from each other by more than an acceptable level of engineering tolerance. To make this distinction, we have appended a subscript T to the latter definition of Nu.

Results and Discussions

The principal parameters of interest to PAHR studies in LMFBR safety are the maximum nonboiling thickness, L, of molten oxide fuel pools corresponding to various rates of internal heat generation, q_v (due to fission decay heating) and the corresponding Nusselt numbers at the upper wall. With this objective in mind, internal heat generation rates were varied from a value of $q_v = 2$ cal/cm^3 s to 14 cal/cm^3 s to cover the range of interest. It may be noted that the rate of change in decay heat after the initial decay in a nuclear reactor is slow and, therefore, the internal heat generation due to decay heating can be assumed with negligible error as quasi-steady. For this calculation the upper surface temperature was kept fixed at the melting point of fuel, namely, $T_2 = 3138$ K and for a given value of q_v, the pool thickness was varied until the temperature at the lower wall reached the boiling point of fuel, namely, $T_1 = 3760$ K. Over this temperature range, the values of various properties of the fuel utilized in the present study are: $K = 0.0072$ cal/(cm s K), $\alpha = 0.00665$ cm^2/s, $\nu = 0.00497$ cm^2/s, $\beta = 4 \times 10^{-5}$ K^{-1}, $\kappa = 50$ cm^{-1}, $n = 2.3$, $\sigma = 1.3681 \times 10^{-12}$ cal/cm^2 s K^4 and $N = 0.40245$. Because of very sharp temperature gradients near the upper wall, one would need to stretch the wall region near the upper wall with the use of transformation $\eta = \eta_0[1 - (e^z - 1)/R]$ to obtain closely spaced mesh points. The calculations were carried out by using the method of spline collocation [12–15] with R varying between 2500–4500 until the Nusselt number calculated on the basis of total heat flux (equation (13)) differed from that calculated by using internal heat generation (equation (12)) by less than 1.5 percent for the pool of the largest thickness calculated in the present study.

Since it is also the objective of the present paper to study the effect of radiation using the exact integral formulation for radiation flux and compare the results with those obtained either employing Rosseland approximation or using natural convection alone without radiation, the above procedure for finding maximum nonboiling thickness of a pool with a fixed value of q_v was carried out in a single computer run for each of the above approximations. The results of these calculations are presented in Tables 1 and 2 and Figs. 1–3. Table 1 gives the comparison of maximum nonboiling pool thickness using three approximations. Using the results corresponding to the exact integral formulation of radiation flux as bench mark values, it is seen that pool thicknesses corresponding to natural convection alone are underestimated by as much as 61 percent. On the other hand, pool thicknesses using the Rosseland approximation are overestimated by only about 4 percent and thus indicate the applicability of the Rosseland approximation for estimating pool thicknesses to a very acceptable level of accuracy. As expected, the relative deviation increases slightly as pool thickness decreases thus implying that accuracy obtainable using the Rosseland approximation improves as the pool thickness (i.e., optical thickness) increases.

The explanation for the large deviations of the results between natural convection and combined radiation-convection is presented in Table 2. Table 2 compares the Nusselt numbers at the upper wall as a function of Rayleigh number, Ra. Both the Rayleigh and Nusselt numbers are based on maximum nonboiling pool thickness corresponding to the exact integral formulation and fixed power (Table 1), while temperature differences between the lower and upper walls correspond to the particular approximation to which they pertain. Besides the total Nusselt numbers based on heat flux (see equation (13)), we have also displayed component Nusselt numbers in Table 2. It is clearly seen from Table 2 that the rates of heat transfer are considerably increased due to the presence of radiation combined with natural convection. As much as 56 percent improvement in heat transfer is found compared to natural convection alone. This large increase in heat transfer clearly accounts for the corresponding large increases in nonboiling pool thicknesses. The majority of this increase in heat transfer occurs due to radiation and only a small fraction of

Table 1 Maximum nonboiling pool thickness as a function of internal heat generation rate corresponding to natural convection and combined radiation—natural convection using the Rosseland approximation and exact integral formulation for the heat flux corresponding to $N = 0.4$

	Maximum Nonboiling Pool Thickness, L (cm)		
	Natural	Combined radiation-convection	
q_v W/cm^3	Convection Only	Rosseland Approximation	Exact
8.374	21.46 (−60.8%)	56.55 (+3.3%)	54.74
16.748	11.57 (−60.7%)	30.54 (+3.6%)	29.47
25.122	8.05 (−60.7%)	21.27 (+3.8%)	20.49
33.496	6.21 (−60.7%)	16.44 (+3.9%)	15.82
41.87	5.08 (−60.7%)	13.45 (+4.0%)	12.93
50.24	4.30 (−60.8%)	11.4 (+4.1%)	10.96
58.62	3.74 (−60.7%)	9.93 (+4.3%)	9.52

Table 2 A comparison of various Nusselt numbers at the upper wall as a function of Rayleigh number (both based on maximum nonboiling pool thickness corresponding to exact formulation of radiation heat flux) for natural convection and combined radiation-convection using both exact integral formulation for radiation flux and Rosseland approximation corresponding to $N = 0.4$

Maximum Nonboiling Pool thickness (cm)	Rayleigh Number Ra	Natural Convection	Combined Radiation—Convection						
			Rosseland Approximation			Exact			
		Nu_c*	Nu_T	Nu_c	Nu_r	Nu_T	Nu_c	Nu_r	Nu
9.52	9.04×10^{10}	63.16 (−55.4%)	145.14 (+2.39%)	33.65 (−49.6%)	111.49 (+50%)	141.00 (−0.53%)	66.70	74.30	141.75
10.96	1.56×10^{11}	71.53 (−55.5%)	164.72 (2.36%)	38.19 (−49.5%)	126.53 (+50%)	160.01 (−0.57%)	75.66	84.35	160.92
12.93	2.98×10^{11}	82.75 (−55.7%)	191.00 (+2.31%)	44.28 (−49.5%)	146.72 (+49.9%)	185.56 (−0.60%)	87.72	97.85	186.69
15.82	6.53×10^{11}	98.79 (−55.8%)	228.50 (+2.26%)	52.98 (−49.6%)	175.52 (+49.9%)	222.20 (−0.57%)	105.09	117.77	223.46
20.49	1.79×10^{12}	124.01 (−56.9%)	287.33 (+2.17%)	66.62 (−49.5%)	220.71 (49.8%)	279.31 (−0.68%)	131.96	147.35	281.23
29.47	7.33×10^{12}	170.53 (−56.0%)	395.83 (+2.03%)	91.78 (−49.5%)	304.06 (+49.6%)	384.99 (−0.77%)	181.77	203.22	387.96
54.74	8.10×10^{13}	293.04 (−56.2%)	681.20 (+1.80%)	157.94 (−49.1%)	523.26 (+49.4%)	660.34 (−1.32%)	310.12	350.22	669.17

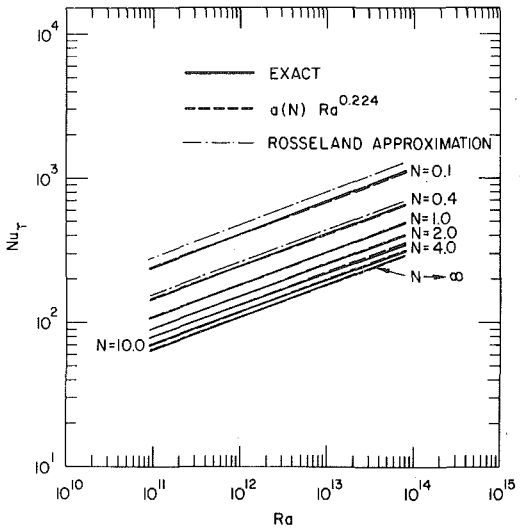

Fig. 1 The plot of Nusselt number as a function of Rayleigh number with *N* as a parameter

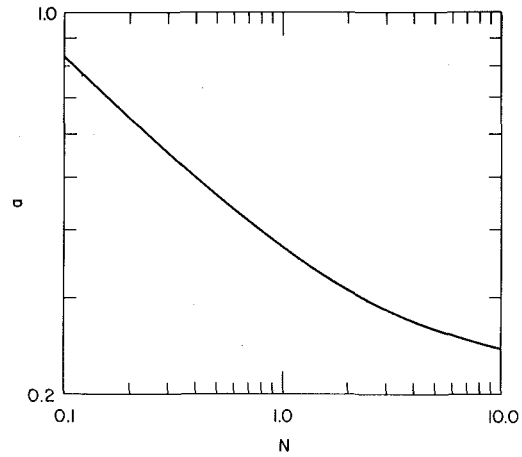

Fig. 2 The variation of parameter *a* as a function of conduction—radiation parameter

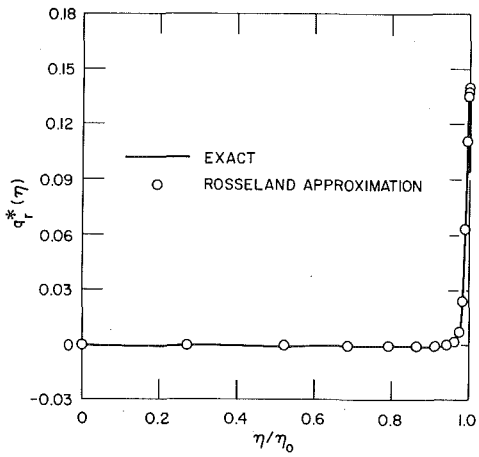

Fig. 3 A comparison of radiation heat flux as a function of dimensionless distance from the adiabatic wall corresponding to the exact integral formulation and Rosseland approximation at q_v = 8.0 cal/cm³ s and pool thickness of 15.82 cm

it is contributed through an increase in convection due to the interaction with radiation. It may be further seen by comparing the values of component Nusselt numbers that heat transfer by radiation, in contrast to Anderson's results [9], is as important as turbulent natural convection, in spite of very high values of Rayleigh number. The near equality (deviation being less than 6 percent) of the convective component of combined radiation-convection with the Nusselt number for natural convection alone, suggests rather weak interaction between radiation and convection at $N = 0.4$. As a consequence of this weak interaction, the plots of total Nusselt numbers function of Rayleigh numbers corresponding to all three approximations are parallel to each other, implying that they all have the same slope, this can be clearly seen in Fig. 1. This behavior can be further elaborated upon as follows: Fig. 1 suggests that both the Nusselt numbers due to combined radiation-convection and convection alone ($N \to \infty$) can be represented by the following relationships

$$\mathrm{Nu}_T = \mathrm{Nu}_c + \mathrm{Nu}_r = a(N)\mathrm{Ra}^b \tag{15}$$

$$\mathrm{Nu}_c{}^* = c\mathrm{Ra}^b \tag{16}$$

where $\mathrm{Nu}_c{}^*$ denotes the Nusselt number due to convection alone. Since $\mathrm{Nu}_c{}^* \simeq \mathrm{Nu}_c$ (see Table 2) it therefore follows that

$$\mathrm{Nu}_r \simeq (a - c)\mathrm{Ra}^b, \tag{17}$$

implying that the radiation component of Nusselt number has the same slope as that of total Nusselt number due to combined radiation-convection or that of Nusselt number due to convection alone. It is apparent that parameter a in equation (15) is a function of conduction-radiation parameter N as can be seen from the plots given in Fig. 1 of total Nusselt numbers as a function of Rayleigh number with N as a parameter varying from a value of 0.1 to 10. This figure clearly demonstrates that slope b of these plots is nearly constant over a wide range of values of N. Evaluating constants a, b from numerical data presented in Fig. 1, equation (15) approximately becomes

$$\mathrm{Nu}_T \simeq \mathrm{Nu} \simeq a(N)\mathrm{Ra}^{0.224}, \tag{18}$$

where parameter a as a function of N is displayed in Fig. 2. This plot clearly shows that a will reach an asympototic value as $N \to \infty$. This asympototic value as computed from Fig. 1 is 0.222. With this value of a, equation (18) agrees with the empirical expression $\mathrm{Nu}_c{}^* = 0.2015\ \mathrm{Ra}^{0.226}$ obtained by Kulacki and Emara [3] within about 5 percent of relative deviation. The value of a corresponding to $N \simeq 0.4$ is 0.4994 which produces deviation of less than 2 percent between values predicted by equation (18) and the exact tabulated values in Table 2. For a whole range of values of N, Fig. 1 shows a comparison between formula (18) and the exact solution. It is clear from this figure that approximate expression (18) represents a very satisfactory formula for the range of values of N displayed in this figure.

With Nu defined by equation (13) and Rayleigh number Ra defined as $\mathrm{Ra} = g\beta q_v L^5/(2K\alpha\nu)$ it is seen from equation (18) that $L \sim q_v{}^{-0.88}$. A comparison of numerical results in Table 2 shows that at $N \simeq 0.4$ the Rosseland approximation predicts total Nusselt number within 3 percent of relative deviation from the total Nusselt number predicted by exact integral formulation of radiation flux. However, at $N = 0.1$, the relative deviation increases to about 10 percent which can be clearly seen in Fig. 1. We may, however, note that the individual components due to radiation and convection are in considerable error as can be seen in Table 2. These errors compensate each other to an extent due to the total heat balance constraint dictated by equation (10).

This comparison between the exact formulation of radiation and the Rosseland approximation is further highlighted in Fig. 3. Fig. 3 gives the variation of radiation flux as a function of nondimensional distance from the lower wall. Both the exact and Rosseland approximations predict about the same results throughout the thickness of the pool except near the boundaries, where the Rosseland approximation overpredicts considerably. This is typical behavior for the optically thick limit approximation which is not applicable near the boundaries.

Conclusions

It is demonstrated that in volumetrically heated pools characterized by the high temperatures of interest in post accident heat removal studies the radiation mode is equally or more dominant than heat transfer by turbulent natural convection, even at very high Rayleigh numbers. Due to the presence of radiation in combination with turbulent natural convection, it is shown that considerably thicker molten pools can be supported without boiling inception. The exact analysis using the integral formulation of radiation flux shows that for optically thick pools, corresponding to $N \simeq 0.4$, the Rosseland approximation compares very favorably both in the determination of maximum nonboiling pool thicknesses and total Nusselt numbers at the upper wall because of compensating errors in the individual components of radiative and conductive heat fluxes due to the total heat balance constraint. However, the agreement between the Rosseland approximation and the exact formulation is poorer as the value of N decreases.

Acknowledgment

The authors greatly appreciate the assistance afforded by George Hauser in preparing the plots. This work was performed under the auspices of the U.S. Department of Energy.

References

1 Cheung, F. B., "Natural Convection in a Volumetrically Heated Fluid Layer at High Rayleigh Numbers," *International Journal of Heat and Mass Transfer*, Vol. 20, 1977, pp. 499–506.

2 Kulacki, F. A. and Nagle, M. Z., "Natural Convection in a Horizontal Fluid Layer with Volumetric Energy Sources," ASME JOURNAL OF HEAT TRANSFER, Vol. 97, 1975, pp. 204–211.

3 Kulacki, F. A. and Emara, A. A., "Heat Transfer Correlations for use in PAHR Analysis and Design," *Transactions of American Nuclear Society*, Vol. 22, 1975, pp. 447–448.

4 Tritton, D. J. and Zarrage, M. N., "Convection in Horizontal Fluid Layers with Heat Generation Experiments," *Journal of Fluid Mechanics*, Vol. 30, 1967, pp. 21–32.

5 Baker, L., Jr., Faw, R. E. and Kulacki, F. A., "Postaccident Heat Removal—I. Heat Transfer within an Internally Heated, Nonboiling Liquid Layer," *Nuclear Science and Engineering*, Vol. 61, 1976, pp. 222–230.

6 Suo-Anttila, A. J. and Catton, I., "The Effect of a Stabilizing Temperature Gradient on Heat Transfer from a Molten Fuel Layer with Volumetric Heating," ASME JOURNAL OF HEAT TRANSFER, Vol. 97, 1975, pp. 544–548.

7 Stein, R. P., Baker, L. Jr., Gunther, W. H. and Cook, C., "Heat Transfer from Heat Generating Molten UO_2: Interpretations of the Available Experimental Data," Paper No. 79-HT-115, ASME-AICHE National Heat Transfer Conference, San Diego, Aug. 5–9, 1979.

8 Cho, D. H., Chan, S. H. and Hauser, G. M., "Radiative Heat Transfer in a Horizontal Molten Fuel Layer with Volumetric Heating," *Transactions of American Nuclear Society*, Vol. 30, 1978, pp. 473–474.

9 Anderson, E. E., "Radiative Heat Transfer in Molten UO_2 Based on the Rosseland Diffusion Method," *Nuclear Technology*, Vol. 30, 1976, pp. 65–70.

10 Cheung, F. B., "Heat Source-Driven Thermal Convection at Arbitrary Prandtl Numbers," to appear in *Journal of Fluid Mechanics*.

11 Sparrow, E. M. and Cess, R. D., *Radiation Heat Transfer*, Augment edition, Hemisphere Publishing, Washington, 1978.

12 Chawla, T. C., Chan, S. H. and Hauser, G. M., "Solution of Radiation-Conduction Problems with Collocation Method Using B-Splines as Approximating Functions," to appear in *International Journal of Heat and Mass Transfer*.

13 Chawla, T. C., Leaf, G., Chen, W. L. and Grolmes, M. A., "The Application of Collocation Method Using Hermite Cubic Splines to Nonlinear Transient One-Dimensional Heat Conduction Problems," ASME JOURNAL OF HEAT TRANSFER, Vol. 97, 1975, pp. 562–569.

14 Chawla, T. C., Leaf, G. and Chen, W. L., "A Collocation Method Using B-Splines for One-Dimensional Heat or Mass Transfer—Controlled Moving Boundary Problems," *Nuclear Engineering and Design*, Vol. 35, 1975, pp. 163–180.

15 Chawla, T. C., Chan, S. H. AND Hauser, G. M., "Heat Transfer in Thermally Developing, Absorbing, Emitting and Scattering Slug and Couette Flows Between Parallel Plates with Collocation Method," ASME Paper No. 79-HT-20, ASME-AIChE National Heat Transfer Conference, San Diego, Aug. 5–9, 1979.

W. W. Yuen
Assistant Professor of Mechanical Engineering,
University of California,
Santa Barbara, CA 93106

C. L. Tien
Professor of Mechanical Engineering,
University of California,
Berkeley, CA
Fellow, ASME

A Successive Approximation Approach to Problems in Radiative Transfer with a Differential Formulation

The radiation intensity in a gray participating medium is expressed in a differential form. The energy equation for radiative transfer becomes an infinite-order differential equation. Utilizing the method of weighted residuals and introducing some appropriate formulations for the intensity boundary conditions, a method of successive approximations is developed. The solution method is applied to a one-dimensional problem with linear-anisotropic scattering. This problem is chosen because of its practical importance and the availability of exact solutions. A first-order closed-form result, which has never been derived analytically before, is obtained and shown to have good accuracy. Successive higher-order approximate solutions are also presented. These solutions are easily attainable algebraically and converge quickly to the exact result. To illustrate the possible applicability of the solution method for multidimensional problems, the first-order solution to a simple two-dimensional problem is presented. Results show that based on the present approach, reasonably accurate approximate solutions can be generated with some simple mathematical developments.

Introduction

The major difficulty in the analysis of radiative heat transfer in a participating medium lies in the mathematical complexity of the integral transport equation. Except for some simple one-dimensional problems [1, 2], exact solution is extremely difficult to obtain. A great deal of research effort in the past, therefore, had been directed to the development of an effective approximation technique for this complex problem. Milne [3], Eddington [4], Deissler [5], Traugott [6], Cheng [7] and many others have proposed different approximation methods for the radiative transfer problem. Their success, however, is quite limited. While most of them are effective in an accurate heat-flux prediction for the one-dimensional planar problem, they are subject to some common difficulties. First, most of the proposed approximation methods cannot be readily generalized to obtain solutions with better accuracy. High-order approximations based on these methods are either not available or almost impossible to obtain because of the extreme mathematical complexity. Secondly, all of the proposed methods are very difficult, if not impossible, to adopt for problems with multidimensional geometry. A few attempts have been reported [7–10], but they are all either too complicated mathematically or too restrictive in application because of some highly simplifying physical assumptions.

The purpose of this investigation is to reformulate the radiative transfer problem as a boundary-value problem. The governing integral equation is transformed into an infinite-order differential equation. The intensity boundary condition is expressed as an infinite set of linear relations in terms of the medium's temperature and its derivatives at the physical boundary. Utilizing the method of weighted residuals, which, in its various forms, has been used extensively to obtain approximate solutions for many problems in fluid mechanics and heat transfer [11], successive approximate solutions can be readily generated. In contrast to the existing approximation methods, the present solution method has the distinct advantage that solutions with increasing degree of accuracy can be obtained with little difficulty. The general philosophy of the solution technique also appears to be adaptable to problems with multi-dimensional geometry.

To illustrate the effectiveness of the proposed solution method, the problem of radiative heat transfer in a one-dimensional, gray, absorbing, emitting and linear-anisotropic scattering medium will be considered. This problem is chosen mainly because of its practical importance in many engineering problems such as energy transport in porous media and in fire and smoke. Solution to this problem will also demonstrate the superiority of the present method, since none of the existing approximation methods have ever been applied successfully to problems with anisotropic scattering. Based on the method of weighted residuals, successive approximate solutions, converging quickly to the exact result, will be developed. Also obtained is a closed-form solution, which is convenient for practical engineering calculations. To demonstrate the potential effectiveness of the present method for multidimensional problems, the first-order approximation of a simple two-dimensional radiative heat transfer problem with planar geometry is developed. The result is shown to compare favorably with the available exact solution

Contributed by the Heat Transfer Division for publication in the JOURNAL OF HEAT TRANSFER. Manuscript received by the Heat Transfer Division October 11, 1978.

The One-Dimensional Problem

Physical Model. The physical model chosen for the present analysis is a uniform plane parallel gray medium with two black walls. The medium is assumed to consist of particles which scatter radiative energy anisotropically. For simplicity, the anisotropic scattering property of the medium is approximated by retaining only the first two terms of the Legendre polynomial series expansion for the general phase function (for details, consult [12]). Such scattering is termed linearly anisotropic and has the following mathematical representation

$$p(\cos\theta_0) = 1 + x_0 \cos\theta_0 \quad -1 \le x_0 \le 1 \tag{1}$$

where p is the phase function, θ_0 the angle between the incoming and the scattered ray and x_0 a coefficient which indicates physically the amount of anisotropic scattering in the medium.

Governing Equations. With the coordinate system as illustrated in Fig. 1, the equation of transfer can be written as

$$\frac{di}{ds} = -\beta i + a i_b + \frac{\gamma}{4\pi}\int_{\omega'=4\pi} i(\omega')p(\omega,\omega')d\omega' \tag{2}$$

where i denotes the radiation intensity, i_b the blackbody intensity, a the absorption coefficient, γ the scattering coefficient, β the extinction coefficient, s the pathlength and ω the solid angle.

Substituting equation (1) into equation (2) and utilizing the axisymmetric property of the planar geometry, the last term of equation (2) can be integrated over ϕ' from 0 to 2π giving

$$\mu \frac{di}{d\tau_z} + i = (1 - \omega_0) i_b + \frac{\omega_0}{2} \int_{-1}^{1} i d\mu + \frac{\omega_0 x_0}{2} \mu \int_{-1}^{1} i \mu d\mu \quad (3)$$

where ω_0 represents the single scattering albedo, τ_z the optical thickness defined by

$$d\tau_z = \beta dz \quad (4)$$

with z being the axis of symmetry and $\mu \equiv \cos\theta$.

Assuming that there is no heat generation, the energy equation for the present one-dimensional system is given simply by

$$\frac{d}{d\tau_z} \int_{-1}^{1} i \mu d\mu = 0. \quad (5)$$

Utilizing equation (5), equation (3) can be integrated over μ from -1 to 1 to yield the following familiar relation

$$i_b = \frac{1}{2} \int_{-1}^{1} i d\mu \quad (6)$$

Substituting equation (6) into equation (3) gives

$$\mu \frac{di}{d\tau_z} = i_b - i + \frac{\omega_0 x_0}{2} \mu \int_{-1}^{1} i \mu d\mu \quad (7)$$

Equation (7) can now be rearranged and differentiated successively to obtain the following set of equations

$$\begin{aligned} i &= i_b - \mu \frac{di}{d\tau_z} + \frac{\omega_0 x_0}{2} \mu \int_{-1}^{1} i \mu d\mu \\ \frac{di}{d\tau_z} &= \frac{di_b}{d\tau_z} - \mu \frac{d^2 i}{d\tau_z{}^2} \\ \frac{d^n i}{d\tau_z{}^n} &= \frac{d^n i_b}{d\tau_z{}^n} - \mu \frac{d^{n+1} i}{d\tau_z{}^{n+1}} \quad (n = 1, 2, 3, \ldots) \end{aligned} \quad (8)$$

Note that equation (5) has been used to eliminate all but one of the scattering terms appearing in equations (8).

Combining equations (8) and after some algebraic manipulation, the radiation intensity can be written in the following differential form

$$i = \sum_{k=0}^{\infty} (-1)^k \mu^k \frac{d^k i_b}{d\tau_z{}^k} - \frac{\omega_0 x_0 \mu}{1 - \frac{\omega_0 x_0}{3}} \sum_{k=1}^{\infty} \left(\frac{1}{2k+1} \right) \frac{d^{2k-1} i_b}{d\tau_z{}^{2k-1}} \quad (9)$$

Substituting equation (9) into equation (5), the governing equation for the one-dimensional problem based on the present differential formulation becomes

$$\left(\frac{1}{1 - \frac{\omega_0 x_0}{3}} \right) \sum_{k=1}^{\infty} \left(\frac{1}{2k+1} \right) \frac{d^{2k} i_b}{d\tau_z{}^{2k}} = 0 \quad (10)$$

Equation (10) has the advantage of being a differential equation instead of an integral equation under the traditional formulation. It is, however, of infinite order. In principle, its solution requires an infinite number of boundary conditions.

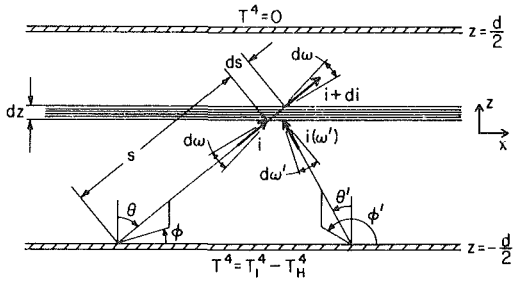

Fig. 1 Coordinate system for radiative transfer in a plane parallel geometry

Boundary Conditions. For the present one-dimensional problem and in fact most problems in radiative heat transfer of practical interest, temperatures of the bounding surfaces are specified. In terms of the radiative intensity, boundary conditions for the present problem are

$$i\left(-\frac{L}{2}, \mu\right) = \frac{\sigma T_1{}^4}{\pi} \quad 0 \le \mu \le 1 \quad (11)$$

$$i\left(\frac{L}{2}, \mu\right) = \frac{\sigma T_2{}^4}{\pi} \quad -1 \le \mu \le 0 \quad (12)$$

where σ is the Stefan-Boltzman constant, T_1 the lower wall temperature, T_2 the upper wall temperature and $L = \beta d$ with d representing the distance between the bounding walls. Utilizing equation (9), equations (11) and (12), evaluated at the different values for μ, can be considered as an infinite set of linear relations in terms of the blackbody intensity and its derivatives at the two boundaries. These relations, together with equation (10), thus constitute a complete mathematical description of the present one-dimensional problem.

Approximate Solution. Exact solution to equation (10) and its associated boundary condition is clearly impossible to obtain. But a series of successive approximate solutions, converging to the exact result, can be constructed by the following procedure.

In the Nth approximation, the blackbody intensity in the medium is assumed to be a finite-order power series of the following form:

$$i_b{}^{(N)} = \sum_{k=0}^{4N-1} A_k \tau_z{}^k \quad (13)$$

Physically, i_b is expected to be a monotonically increasing smooth function. It also approaches a linear distribution in the limit of $L \to \infty$. Equation (11) should thus be a fairly accurate representation of the blackbody intensity even for moderate values of N.

Equation (13) is obviously not a solution to the governing conservation equation. In fact, when $i_b{}^{(N)}$ is substituted into equation (10), a residual ϵ_N will be resulted as follows:

$$L_N(i_b{}^{(N)}) = \epsilon_N \quad (14)$$

where L_N is an operator defined by

Nomenclature

A_j = coefficients defined in equation (13)
a = absorption coefficient
B_0, B_1 = coefficients defined in equation (32)
d = distance between the two walls for the parallel plate system
F_0, F_1 = functions defined by equations (32) and (33)
i = radiation intensity
i_b = blackbody intensity
$i_b{}^{(N)}$ = Nth approximation of the blackbody intensity
$j = \sqrt{-1}$, equation (23)
$L = \beta d$, optical thickness between the two walls of the parallel plate system
L_N = differential operator in the Nth order approximation, equation (15)
ℓ_x, ℓ_y, ℓ_z = directional cosines
$\underline{\ell}$ = vector with components (ℓ_x, ℓ_y, ℓ_z)
P = phase function
$q^{(1)}$, $q_x^{(1)}$, $q_z^{(1)}$ = first approximation of the heat flux
S = distance along a line of sight
T = temperature
T_1 = temperature of the lower wall
T_2 = temperature of the upper wall
u, v, w = coefficients defined in equations (34) and (35)
W_k = weighting factors for the method of weighted residuals, equation (16)
x_0 = coefficient defined in equation (1)
x, z = spatial coordinate
β = extinction coefficient
γ = scattering coefficient
ϵ_N = residuals in the Nth approximation, equation (14)
θ_0 = scattering angle measured from forward direction to direction of observer, equation (1)
θ = polar angle, Fig. 1
λ = constant defined in equation (23)
$\mu = \cos\theta$
σ = Stefan-Boltzmann constant
τ_x, τ_z = ax, az defined in equation (4)
$\underline{\tau}$ = vector with components (τ_x, τ_y, τ_z)
ω, ω' = solid angle
ω_0 = single scattering albedo

$$L_N = \sum_{k=1}^{2N} \left(\frac{1}{2k+1}\right) \frac{d^{2k}}{d\tau_z{}^{2k}} \tag{15}$$

To determine the best estimate for the constants A_k's, the present work utilizes the commonly used method of weighted residuals [11]. Multiply equation (14) by a weighting factor W_k and integrate over the one-dimensional space. The Nth order approximation requires that ϵ_N be small in the following sense:

$$\int_{-L/2}^{L/2} W_k L_N(i_b{}^{(N)}) d\tau_z = 0 \quad (k = 1, 2, \ldots, 2N) \tag{16}$$

The exact form of the weighting factor generally depends on the nature of the considered problem. For the present one-dimensional analysis, since $i_b{}^{(N)}$ is assumed to be a power series in τ_z, a natural choice for the weighting factor is

$$W_k = \tau_z{}^{k-1} \tag{17}$$

In the Nth approximation, equation (10) is thus approximated by the following $2N$ algebraic relations

$$\int_{-L/2}^{L/2} \tau_z{}^{k-1} L_N(i_b{}^{(N)}) d\tau_z = 0 \quad (k = 1, 2, \ldots, 2N) \tag{18}$$

Physically, it is interesting to note that equation (18) can be interpreted as the conservation of the first $2N$ multi-order moments of the radiation intensity within the medium [13]. Mathematically, equation (18) is identical to requiring that equation (10) is satisfied at $2N$ distinct values of τ_z. In the limit of $N \to \infty$, equations (18) and (10) are clearly equivalent.

To generate the remaining set of equations needed for the determination of A_k's, $2N$ relations must be generated from the boundary conditions. The task of approximating equations (11) and (12) by a finite set of relations is not entirely new. A great number of efforts have been made in this area, because all of the existing approximation techniques require some forms of approximation for the intensity boundary conditions. A survey of the existing works suggests that the following two ideas appear to be the most applicable for the present consideration:

1 *Marshak's Boundary Conditions.* Proposed by Marshak [14], the boundary conditions for the present Nth order approximation are

$$\int_0^1 i\left(\frac{L}{2}, \mu\right) \mu^{2k-1} d\mu = \frac{\sigma T_1{}^4}{2k\pi} \quad (k = 1, 2, \ldots, N)$$
$$\int_1^0 i\left(\frac{L}{2}, \mu\right) \mu^{2k-1} d\mu = \frac{\sigma T_2{}^4}{2k\pi} \tag{19}$$

Physically, equations (19) can be interpreted as the conservation of multi-order moments of the radiation intensity across the two boundaries. It is compatible with the physical interpretation of equations (18).

2 *Variational Boundary Conditions.* In his work with the Spherial Harmonics techniques, Pomraning [15] showed that the radiative transfer equation and its associated boundary conditions can be characterized simply by a Lagrangian. Applying the variational principle, the intensity boundary condition can be written in the following form.

$$\int_0^1 d\mu\mu \left[i\left(-\frac{L}{2}, \mu\right) - \frac{\sigma T_1{}^4}{\pi}\right] \delta i\left(-\frac{L}{2}, -\mu\right) + \int_{-1}^0 d\mu\mu \left[\frac{\sigma T_2{}^4}{\pi} - i\left(\frac{L}{2}, \mu\right)\right] \delta i\left(\frac{L}{2}, -\mu\right) = 0 \tag{20}$$

where $\delta i(-L/2, -\mu)$ and $\delta i(L/2, -\mu)$ stand for the variation of the trial intensity function at the lower and the upper walls, respectively. In the Nth approximation, if the variation of the blackbody intensity i_b and its first $(N-1)$ derivatives at the two boundaries are assumed to be independent, it can be readily shown that equation (20) is reduced to a set of $2N$ equations.

Equations (18), together with either equations (19) or (20) thus constitute a complete set of equations based on which the coefficient A_k's can be evaluated.

Results and Discussion. For the present one-dimensional problem, calculation shows that both Marshak's boundary conditions and the variational boundary conditions are effective in generating accurate low-order approximate solutions. The first-order approximation using Marshak's boundary conditions, for example, yields the following radiative heat flux expression

$$q^{(1)} = \frac{\sigma T_1{}^4 - \sigma T_2{}^4}{1 + \left(\frac{3}{4} - \frac{\omega_0 x_0}{4}\right) L} \tag{21}$$

In the limit of $\omega_0 \to 0$, equation (21) reduces to the familiar diffusion approximation [5]. It is interesting to note that the same expression was developed semi-empirically by Dayan and Tien [16] by matching exact solutions in the optically thick and thin limits. Equation (21) compares very well with the available exact solution [16] for all values of the optical thickness and the scattering albedo.

With the variational boundary condition, the first-order approximation gives a slightly different expression for the radiative heat flux as follows:

$$q^{(1)} = \frac{\sigma T_1{}^4 - \sigma T_2{}^4}{\frac{3}{4}(2)^{1/2} + \left(\frac{3}{4} - \frac{\omega_0 x_0}{4}\right) L} \tag{22}$$

While equation (22) is less accurate than equation (21) in the optically thin limit, it is superior in the optically thick limit. When $\omega_0 = 0$, for example, equation (22) agrees quite closely with the optically thick asymptotic heat flux expression obtained from an exact calculation [1, 2].

Results for the radiative heat flux based on the first three approximations and Marshak's boundary conditions, together with the exact result, are presented in Table 1. Some typical results of the temperature profile are shown in Fig. 2. It can be readily observed that the successive approximate solutions converge quickly to the exact solution, independent of the value of the optical thickness and the scattering albedo. It is important to emphasize that for each approximation, the solution is obtained by solving a simple finite-order matrix equation for the constants A_k, a relatively easy task.

The Two-Dimensional Problem

Physical Model. To illustrate the effectiveness of the present method for multidimensional radiative transfer, the present work considers the same parallel-plate system as in the previous one-dimensional problem. For simplicity, the scattering coefficient is now assumed to be zero, and the two-dimensional effect is considered to be generated by the following temperatures at the two boundaries

$$\sigma T_1{}^4 = e^{j\lambda\tau_x}, \quad T_2 = 0 \tag{23}$$

where $j = \sqrt{-1}$ and λ is a constant which can be interpreted as the inverse wave-length of the sinusoidal temperature variation at the lower wall. In spite of its simplicity, the present problem has important practical applications, because by superposition its solution can be generalized to parallel-plate radiative transfer problems with arbitrary wall temperatures. This problem also serves as a good indication on the effectiveness of the present method because exact solution [17, 18] is available to check the accuracy of the approximate solution.

Governing Equations. Following a similar procedure as in the one-dimensional problem, the radiation intensity for the present two-dimensional system can be written in the following differential form:

$$i(\underline{\tau}, \underline{\ell}) = \sum_{k=0}^{\infty} (-1)^k (\underline{\ell} \cdot \text{grad})^k i_b \tag{24}$$

where

$$\underline{\ell} \cdot \text{grad} = \frac{1}{a}\left[\ell_x \frac{\partial}{\partial x} + \ell_z \frac{\partial}{\partial z}\right]$$

with ℓ_x, ℓ_z being the directional cosines in the x and z direction, respectively. The energy conservation equation becomes

Table 1 Comparison of the first, second and third approximations of the dimensionless heat flux $q_z/(\sigma T_1^4 - \sigma T_2^4)$ with the exact solution for the one-dimensional problem with anisotropic scattering

	$\omega_0 x_0 = -0.7$		$\omega_0 x_0 = 0.0$		$\omega_0 x_0 = 0.7$	
L	First, Second and Third	Exact	First, Second and Third	Exact	First, Second and Third	Exact
0.1	0.915		0.930		0.946	
	0.907	0.901	0.921	0.916	0.937	0.931
	0.901		0.916		0.931	
0.5	0.684		0.727		0.777	
	0.668	0.661	0.709	0.704	0.756	0.750
	0.662		0.702		0.748	
1.0	0.520		0.571		0.635	
	0.507	0.505	0.556	0.553	0.616	0.611
	0.504		0.553		0.612	
3.0	0.265		0.308		0.367	
	0.261	0.260	0.302	0.302	0.359	0.358
	0.260		0.302		0.358	
10.0	0.098		0.118		0.148	
	0.097		0.117		0.147	
	0.097		0.117	0.109	0.147	

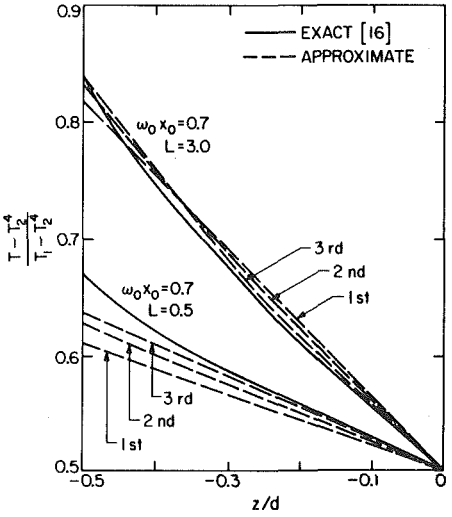

Fig. 2 The comparison of the first, second and third approximation for some typical temperature profile with the exact result [16] for the one-dimensional problem with anisotropic scattering

$$\sum_{k=1}^{\infty} \left(\frac{1}{2k+1}\right) (\text{div} \cdot \text{grad})^k i_b = 0 \tag{25}$$

where div·grad is the two-dimensional Laplacion given by

$$\text{div} \cdot \text{grad} = \frac{1}{a^2}\left(\frac{\partial^2}{\partial x^2} + \frac{\partial^2}{\partial z^2}\right) \tag{25a}$$

Based on equation (25) a series of approximate solutions can again be constructed utilizing the method of weighted residual and imposing the appropriate set of boundary conditions.

Approximate Solution and Discussion. To adopt the solution method presented in the previous sections to the present two-dimensional problem, a number of important modifications are clearly required. The simple power series expansion, for example, does not appear to be an adequate trial solution for the two-dimensional blackbody intensity because, in the limit of $L \to \infty$, i_b should be a function of $\sinh \lambda\tau_z$ and $\cosh \lambda\tau_z$. A different series expansion which possesses the above limiting behavior should be chosen. Correspondingly, a different set of weighting functions W_k should be introduced. The two-dimensional generalization of the operator L_N, as expressed by equation (9) for the one-dimensional case, must be constructed with care. Since the new series expansion for i_b might possess non-vanishing derivatives of all order, some sort of truncation procedure must be introduced in the development of approximate solutions. It can also be shown (as was done for the spherical harmonic method in its application to the neutron transport theory [19]) that without some additional assumptions, the Marshak boundary condition cannot be applied to the multidimensional problem in a mathematically consistent manner. The variational boundary condition is more suitable. It must be emphasized that the applicability of the present solution method to multidimensional problems will remain an open question until all of the above modifications are adequately resolved. A detailed consideration, however, would be quite lengthy and beyond the scope of the present work. Many of these modifications are currently under investigation; and these results will be presented in future publications. For the purpose of demonstrating the potential applicability of the proposed solution method, the present work will consider only a simple first-order approximate solution. As will be demonstrated, the first-order result already gives good agreement with the available exact solution.

Utilizing the symmetry of the present two-dimensional system, the first-order approximation for the blackbody intensity is assumed to be

$$i_b^{(1)} = (A_0 + B_0 e^{\lambda\tau_z} + B_1 e^{-\lambda\tau_z}) e^{j\lambda\tau_x} \tag{26}$$

Similar to equation (8), the governing conservation equation is approximated by

$$\int_{-1/2}^{1/2} L_1(i_b^{(1)}) d\tau_z = 0 \tag{27}$$

where L_1 is a two-dimensional operator defined as

$$L_1 = \frac{1}{a^2}\left[\frac{\partial^2}{\partial x^2} + \frac{\partial^2}{\partial z^2}\right] \tag{28}$$

Substitution of equation (26) into equation (27) immediately yields

$$A_0 = 0 \tag{29}$$

The remaining constants B_0 and B_1 must now be determined from the boundary conditions.

Generalizing the development of Pomraning [15], the variational boundary condition for the present two-dimensional problem can be written as

$$\int_0 d\omega \ell_z \left[i\left(\tau_x, -\frac{L}{2}, \ell_{x'}\, \ell_z\right) - \frac{e^{j\lambda\tau_x}}{\pi}\right] \delta i\left(\tau_{x'} - \frac{L}{2}, -\ell_{x'} - \ell_z\right) + \int_0 d\omega \ell_z \left[-i\left(\tau_{x'} \frac{L}{2'} \ell_{x'} \ell_z\right)\right] \delta i\left(\tau_{x'} \frac{L}{2'} - \ell_{x'} - \ell_z\right) = 0 \tag{30}$$

where $\int_0 d\omega$ and $\int_0 d\omega$ represent integration over the upper and lower hemisphere respectively. Substituting equations (23) and (26) into equation (30), keeping only terms up to the first derivative in τ_z and carrying out all the necessary integration, the following equation is obtained.

$$\left[\frac{1}{16} F_0\left(-\frac{L}{2}\right) + \frac{1}{8} F_1\left(-\frac{L}{2}\right) - \frac{1}{4}\right] \delta F_0\left(-\frac{L}{2}\right) + \frac{1}{64} \lambda^2 F_0\left(-\frac{L}{2}\right) \delta F_0\left(-\frac{L}{2}\right) - \left[\frac{1}{8} F_0\left(-\frac{L}{2}\right) + \frac{9}{32} F_1\left(-\frac{L}{2}\right) - \frac{1}{2}\right] \delta F_1\left(-\frac{L}{2}\right) + \left[\frac{1}{16} F_0\left(\frac{L}{2}\right) - \frac{1}{8} F_1\left(\frac{L}{2}\right)\right] \delta F_0\left(\frac{L}{2}\right)$$

$$+\frac{1}{64}\lambda^2 F_0\left(\frac{L}{2}\right)\delta F_0\left(\frac{L}{2}\right)+\left[\frac{1}{8}F_0\left(\frac{L}{2}\right)-\frac{9}{32}F_1\left(\frac{L}{2}\right)\right]\delta F_1\left(\frac{L}{2}\right)=0 \quad (31)$$

The functions F_0 and F_1 are introduced in equation (31) for convenience; they are defined as

$$F_0(\tau_z)=4\pi(B_0e^{\lambda\tau_z}+B_1e^{-\lambda\tau_z}) \quad (32)$$

$$F_1(\tau_z)=\frac{4\pi}{3}\lambda(B_0e^{\lambda\tau_z}-B_1e^{-\lambda\tau_z}) \quad (33)$$

Now, in the use of the variational method one usually assumes that all variations at the boundaries of the system are independent. But the definition of F_0 and F_1 involve only two constants and, since there are just two boundaries in the present problem, variations of F_0 and F_1 at each boundary are clearly not totally independent. For simplicity, the present work assumes that at the two boundaries F_0 and F_1 are linearly related according to

$$F_1\left(\frac{L}{2}\right)-uF_0\left(\frac{L}{2}\right)=0 \quad (34)$$

$$vF_1\left(-\frac{L}{2}\right)+wF_0\left(-\frac{L}{2}\right)=1 \quad (35)$$

where u, v and w are constant and, from a simply physical consideration, can be shown to be positive. Using equations (34) and (35) in equation (31) to eliminate all the F_1 terms and setting the coefficient of $F_0(L/2)\delta F_0(L/2)$, $\delta F_0(-L/2)$ and $F_0(-L/2)\delta F_0(-L/2)$ to be zero yields the following algebraic equations for u, v and w.

$$\left(\frac{1}{16}+\frac{\lambda^2}{64}\right)-\frac{9}{32}u^2=0 \quad (36)$$

$$\left(\frac{1}{16}+\frac{\lambda^2}{64}\right)-\frac{9}{32}\left(\frac{w}{v}\right)^2=0 \quad (37)$$

$$\frac{1}{8v}-\frac{1}{4}+\frac{w}{v}\left(\frac{9}{32v}-\frac{1}{2}\right)=0 \quad (38)$$

The solution of equations (36) to (38) is

$$u=\left(\frac{2}{9}+\frac{\lambda^2}{18}\right)^{1/2} \quad (39)$$

$$v=\frac{1+\frac{9}{4}\left(\frac{2}{9}+\frac{\lambda^2}{18}\right)^{1/2}}{2+4\left(\frac{2}{9}+\frac{\lambda^2}{18}\right)^{1/2}} \quad (40)$$

$$w=\left(\frac{2}{9}+\frac{\lambda^2}{18}\right)^{1/2}\left[\frac{1+\frac{9}{4}\left(\frac{2}{9}+\frac{\lambda^2}{18}\right)^{1/2}}{2+4\left(\frac{2}{9}+\frac{\lambda^2}{18}\right)^{1/2}}\right] \quad (41)$$

Equations (34) and (35) can now be solved to yield

$$B_0=\frac{\frac{1}{4\pi}\left(u-\frac{\lambda}{3}\right)e^{-\lambda(L/2)}}{v\left[\left(u-\frac{\lambda}{3}\right)^2e^{-\lambda L}-\left(u+\frac{\lambda}{3}\right)^2e^{\lambda L}\right]} \quad (42)$$

$$B_1=\frac{-\frac{1}{4\pi}\left(u+\frac{\lambda}{3}\right)e^{\lambda(L/2)}}{v\left[\left(u-\frac{\lambda}{3}\right)^2e^{-\lambda L}-\left(u+\frac{\lambda}{3}\right)^2e^{\lambda L}\right]} \quad (43)$$

Physically, the interesting quantities are the temperature and the radiative heat flux. In terms of the constants B_0 and B_1, they are

$$i_b^{(1)}=[B_0e^{\lambda\tau_z}+B_1e^{-\lambda\tau_z}]e^{j\lambda\tau_x} \quad (44)$$

$$q_x^{(1)}=-\frac{4\pi}{3}j\lambda[B_0e^{\lambda\tau_z}+B_1e^{-\lambda\tau_z}]e^{j\lambda\tau_x} \quad (45)$$

$$q_z^{(1)}=-\frac{4\pi}{3}\lambda[B_0e^{\lambda\tau_z}-B_1e^{-\lambda\tau_z}]e^{j\lambda\tau_x} \quad (46)$$

In a recent work, Breig and Crosbie [17, 18] obtained the exact solution for the radiative heat flux and the gas temperature at the two bounding walls for the present problem. Comparisons between equation (46) and the exact result at the upper and lower walls are shown in Figs. 3 and 4, respectively. The agreement is quite satisfactory. Even though exact solutions for q_z and q_x at arbitrary values of τ_z and τ_x are not available, it is reasonable to expect that they should be of the same order of accuracy as at the two boundaries. The temperature profile prediction, however, is less satisfactory. It can be shown that equation (44), when evaluated at the lower wall, yields an incorrect asymptotic value in the limit of $\lambda \to \infty$. The accuracy improves at the region near the upper wall. A comparison between equation (44) and the exact solution for the gas temperature at the upper wall, for example, is shown in Fig. 5.

To further demonstrate the relative accuracy and efficiency of the present solution method compared with the existing approximation techniques, the two-dimensional problem with a constant temperature at the upper wall and a step temperature at the lower wall is now considered based on the above first-order result. This problem is chosen largely because an exact solution generated by the Monte Carlo technique [20] and a fairly accurate approximate solution generated

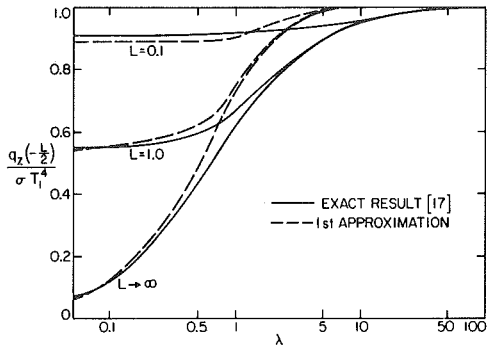

Fig. 3 Comparison between the first approximation and the exact result of the radiative heat flux at the lower boundary for the two-dimensional problem

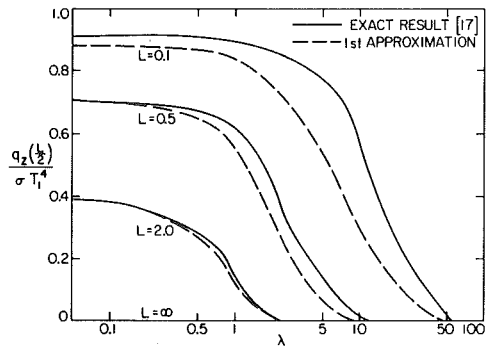

Fig. 4 Comparison between the first approximation and the exact result of the radiative heat flux at the upper wall of the two-dimensional problem

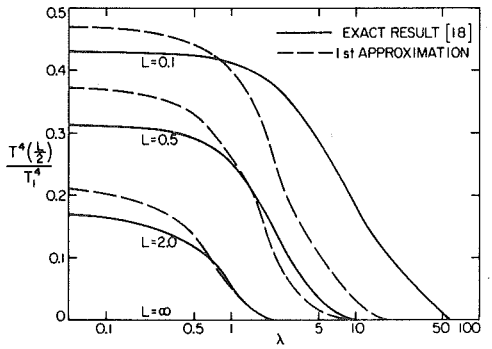

Fig. 5 Comparison between the first approximation and the exact result of the dimensionless gas temperature at the upper boundary for the two-dimensional problem

by a modified differential method [21] are both available in the literature. They can thus serve conveniently as a basis for a direct comparison.

Specifically, the boundary conditions for this sample two-dimensional problem are assumed to be the following normalized forms:

$$\sigma T_1^4 = \begin{cases} 1 & x > 0 \\ -1 & x < 0 \end{cases} \tag{47a}$$

$$\sigma T_2^4 = 0 \tag{47b}$$

By a Fourier series expansion, it can be readily shown that equation (47a) can be written as

$$\sigma T_1^4 = \lim_{L_x \to \infty} \frac{4}{\pi} \sum_{n=0}^{\infty} (2n+1) \sin \lambda_n \tau_x \tag{48}$$

with

$$\lambda_n = \frac{(2n+1)\pi}{L_x} \tag{49}$$

Utilizing equation (46) and a simple superposition, the first-order approximations for the radiative heat flux at the upper and lower walls are obtained. They are

$$q_z\left(\tau_{x'} - \frac{L}{2}\right) = \lim_{L_x \to \infty} \sum_{n=0}^{\infty} \left(-\frac{16}{3}\lambda_n\right) \times [B_0(\lambda_n)e^{-\lambda_n(L/2)} - B_1(\lambda_n)e^{\lambda_n(L/2)}] \sin \lambda_n \tau_x \tag{50}$$

$$q_z\left(\tau_x, \frac{L}{2}\right) = \lim_{L_x \to \infty} \sum_{n=0}^{\infty} \left(-\frac{16}{3}\lambda_n\right) \times [B_0(\lambda_n)e^{\lambda_n(L/2)} - B_1(\lambda_n)e^{-\lambda_n(L/2)}] \sin \lambda_n \tau_x \tag{51}$$

Physically, the interesting heat flux results are those near the point $\tau_x = 0$. For $\tau_x/L \leq 5.0$, calculations show that the $L_x \to \infty$ results are practically indistinguishable from the results with $L_x/L = 100$. Assuming $L_x/L = 100$, the heat flux at various locations of the upper and lower walls with $L = 0.1, 0.5, 1.0, 2.0$ and 5.0 are tabulated and presented in Tables 2 and 3. By some additional superposition with the one-dimensional result, the corresponding heat flux values for the problem with the unnormalized boundary conditions considered in [20] and [21] can be easily generated. The agreement is excellent for all cases. In a direct comparison with the modified differential method [21], results in Tables 2 and 3 have the same degree of accuracy as those presented graphically in [21]. But the present first-order approximation represents a substantial reduction in mathematical complexities. Equation (46) can also be applied to generate heat flux results for planar systems with arbitrary wall temperature with relatively little effort.

Table 2 The heat flux at different locations of the lower wall for the sample two-dimensional problem with boundary conditions as described by equation (47)

τ_x/L							
L	0	1.0	2.0	3.0	4.0	5.0	∞
0.1	∞	1.000	0.966	0.942	0.925	0.914	0.880
0.5	∞	0.869	0.771	0.727	0.708	0.700	0.697
1.0	∞	0.700	0.591	0.561	0.553	0.551	0.551
2.0	∞	0.483	0.403	0.391	0.390	0.390	0.390
5.0	∞	0.241	0.209	0.207	0.207	0.207	0.207

Table 3 The heat flux at different locations of the upper wall for the sample two-dimensional problem with boundary conditions as described by equation (47)

τ_x/L							
L	0	1.0	2.0	3.0	4.0	5.0	∞
0.1	0	0.452	0.644	0.731	0.779	0.808	0.880
0.5	0	0.436	0.600	0.658	0.681	0.690	0.697
1.0	0	0.338	0.510	0.541	0.549	0.551	0.551
2.0	0	0.303	0.376	0.388	0.390	0.390	0.390
5.0	0	0.177	0.205	0.207	0.207	0.207	0.207

Concluding Remarks

A successive approximation approach is proposed for the solution of problems in radiative transfer based on a differential formulation. The problem is applied successfully to a one-dimensional problem including the effect of anisotropic scattering. Both first-order closed-form results and higher-order approximate solutions are presented. These solutions are easily attainable algebraically and converge quickly to the exact result.

Application of the present solution method to multidimensional problems encounters some difficulties. Important questions concerning the proper selection of trial solution, the approximation of the intensity boundary condition and the development of a consistent truncation criteria for the multi-dimensional governing equation are still unresolved and require further investigation. Nevertheless, a direct generalization of the one-dimensional first-order approximation method to a two-dimensional problem with planar geometry is demonstrated to be successful. The heat flux prediction agrees well with the available exact results and results generated by other approximation techniques. The closed-form solution is mathematically simple and can be used to generate heat transfer results for problems with arbitrary wall temperature distribution.

References

1 Heaslet, M. A. and Warming, R. F., "Radiative Trasnport and Wall Temperature Slip in an Absorbing Planar Medium," *International Journal Heat Mass Transfer*, Vol. 8, 1965, pp. 979–994.

2 Heaslet, M. A. and Warming, R. F., "Radiative Transportant in An Absorbing Medium II. Prediction of Radiative Source Function," *International Journal Heat Mass Transfer*, Vol. 10, 1967, pp. 1413–1427.

3 Milne, E. A., "Thermodynamics of Stars," *Handbuch der Astrophysik*, Vol. 3, Spring-Verlag, Berlin, 1930, pp. 65–135.

4 Eddington, A. S., *The Internal Constitution of Stars*, Dover Publication, Inc., New York, 1959.

5 Deissler, R. G., "Diffusion Approximation for Thermal Radiation in Gases with Jump Boundary Conditions," ASME JOURNAL OF HEAT TRANSFER, Vol. 86, 1964, pp. 240–246.

6 Traugott, S. C., "A Differential Approximation For Radiative Transfer with Application to Normal Shock Structure," *Proc. 1963 Heat Transfer Fluid Mech. Inst.*, 1963, pp. 1–13.

7 Cheng, P., "Two-dimensional Radiating Gas Flow by a Moment Method," *AIAA Journal*, Vol. 2, 1964, pp. 1662–1664.

8 Olfe, D. B., "A Modification of the Differential Approximation for Radiative Transfer," *AIAA Journal*, Vol. 5, 1967, pp. 638–643.

9 Taitel, Y., "Formulation of Two-Dimensional Radiant Heat Flux for Absorbing—Emitting Plane Layer with Non-isothermal Bounding Walls," *AIAA Journal*, Vol. 7, 1969, pp. 1832–1837.

10 Pomraning, G. C., *The Equation of Radiation Hydrodynamics*, Pergamon Press, New York, 1973.

11 Finlayson, B. A., *The Method of Weighted Residuals and Variational Principles*, Academic Press, New York, 1972.

12 Hottel, H. C. and Sarofim, A. F., *Radiative Transfer*, McGraw-Hill, New York, 1967.

13 Yuen, W. W., "A Differential Formulation of Radiative Transfer and Its Application to One-Dimensional and Two-Dimensional System," Ph.D. Dissertation, University of California, Berkeley, May 1977.

14 Marshak, R. E., "Note on the Spherial Harmonic Method as Applied to the Milne Problem for a Sphere," *Phys. Rev.*, Vol. 71, 1947, p. 443.

15 Pomraning, G. C., "Variational Boundary Conditions for the Spherical Harmonics Approximation to the Neutron Transport Equation," *Annals of Physics*, Vol. 27, 1964, pp. 193–215.

16 Dayan, A. and Tien, C. L., "Heat Transfer in Gray Planar Medium with Linear Anisotropic Scattering," ASME JOURNAL OF HEAT TRANSFER, Vol. 97, 1975, pp. 391–396.

17 Breig, W. F. and Crosbie, A. L., "Two-Dimensional Radiative Equilibrium: Boundary Emissive Powers for a Finite Medium Subjected to Cosine Varying Radiation," *Journal of Quantitative Spectroscopy Radiative Transfer*, Vol. 14, 1974, pp. 1209–1237.

18 Breig, W. F. and Crosbie, A. L., "Two-Dimensional Radiative Equilibrium: Boundary Fluxes for A Finite Medium Subjected to Cosine Varying Radiation," *Journal of Quantitative Spectroscopy Radiative Transfer*, Vol. 15, 1975, pp. 163–179.

19 Davidson, B. and Sykes, J. B., *Neutron Transport Theory*, The Claredon Press, Oxford, 1957.

20 Murakami, M., "Direct Monte Carlo Simulation of Two-Dimensional Radiative Heat Transfer in Absorbing-Emitting Medium Bounded by the Non-Isothermal Gray Walls," *Proceedings of the Ninth International Symposium on Space Technology and Science*, Agne Publ. 1971, pp. 407–416.

21 Modest, M. F., "Two-Dimensional Radiative Equilibrium of a Gray Medium in a Plane Layer Bounded by Gray Nonisothermal Walls," ASME JOURNAL OF HEAT TRANSFER, Vol. 96, 1974, pp. 483–488.

M. F. Modest
Associate Professor
Mem. ASME

F. H. Azad
Research Assistant,
Student Mem. ASME

Department of Mechanical Engineering,
Aeronautical Engineering and Mechanics
Rensselaer Polytechnic Institute
Troy, NY 12181

The Influence and Treatment of Mie-Anisotropic Scattering in Radiative Heat Transfer[1]

The influence of highly anisotropic Mie scattering on radiative heat transfer is investigated. Exact solutions for temperature distributions and radiative flux are found for scattering functions with up to 35 terms in their Legendre polynomial series expansion. Approximation by linear anisotropic scattering is found to describe radiative transfer excellently as long as the phase function is relatively smooth and as long as there is only insignificant backscattering. The linear-anisotropic differential approximation also yields very accurate results (within its limitations) and can account for backscattering as well.

Introduction

In recent years considerable research has been conducted on the analysis of radiative heat transfer in scattering media. Some of the engineering applications for such analyses are heat transfer in high-temperature porous materials, luminous flames, rocket exhaust plumes, particle suspensions, powder and fibrous insulations, diffuse solar energy, etc.

Many of the previous investigations have only considered the relatively simple case of isotropic scattering, e.g. [1–2]. While some problems are accurately described by isotropic scattering, this simplification was primarily made to avoid the enormous complexity that accompanies calculations with anisotropic scattering effects. A number of investigations deal with the somewhat more realistic case of linear anisotropic scattering. All of these papers deal with one-dimensional geometries, usually planar, and a gray medium. Dayan and Tien [3] obtained numerical and exponential-kernel solutions for linear anisotropic scattering in a gray slab at radiative equilibrium. Buckius and Tseng [4] investigated the effect of Fresnel reflection at the boundaries of an isothermal gray slab. Buckius and King [5] used the exponential kernel method combined with linear anisotropic scattering to predict diffuse solar radiation.

Rayleigh scattering, important for atmospheric calculations, was investigated by Dayan and Tien [6] for a gray isothermal slab. Rayleigh scattering with incident radiation such as sunshine was treated by Evans et al. [7] for conservative scattering and by Kubo [8] for a plane layer at radiative equilibrium.

Investigations dealing with realistic scattering phase functions, such as strong forward or backward scattering, generally resorted to simplified methods such as the two-flux method employed by Bergquam and Seban [9] or the modified two-flux model used by Domoto and Wang [10]. Somewhat more accurate should be the six-flux method introduced by Chin and Churchill [11]. Wang [12] treated linear-anisotropic scattering in a semi-infinite medium using the exponential-kernel approximation.

Few papers deal with exact solutions to higher-order anisotropic scattering. Hottel, et al. [13] use a four-term phase function but report only specialized results. Love and Grosh [14] employed the full Mie equations for small size parameters and solved the integro-differential equations by Gaussian quadrature for an isothermal slab. Later Hsia and Love [15] extended the results to include quadratic temperature profiles. Viskanta and Toor [16] studied solar transmission in semi-infinite water bodies, using isotropic, Rayleigh and experimental scattering phase functions. They note that the choice of phase function has only a minor influence on the results. Daniel, et al. [17] used the same experimental phase function to compare the "exact" (discrete-ordinate) method with approximate schemes. Using the Monte Carlo method, Stockham and Love [18] treated scattering from a rocket exhaust plume. These papers report specialized results and no general conclusions can be drawn. Finally, Barkstrom [19] developed a finite-difference method for anisotropic scattering without, however, reporting any results.

Thus it appears that in previous investigations researchers have either limited themselves—without physical justification—to simple scattering phase functions, or—if realistic phase functions were employed—to reporting specialized results. It obviously would be of great help to the researcher if it could be established under what conditions the enormous simplification of linear anisotropic scattering could be introduced without significant loss of accuracy. A first step in this direction was undertaken by Potter [20] who used an experimental phase function for atmospheric radiation and showed that removal of the sharp forward-scattering peak results in negligible error.

It is the purpose of this paper to demonstrate that the approximation of the phase function by linear anisotropic scattering yields results of adequate accuracy for nearly all practically important cases. This is achieved by investigating heat transfer rates through a plane gray layer bounded by black plates. Phase functions are calculated from the Mie theory with size parameters up to 20 and containing up to 35 terms after expansion into a Legendre polynomial series. The results for isothermal slabs and slabs at radiative equilibrium show that the approximation of linear anisotropic scattering is nearly always excellent. Furthermore, comparison with the differential approximation for anisotropic scattering (Modest and Azad [21]) demonstrates that extremely simple results can be obtained which are accurate for planar geometries as well as any optically thick situations, if an equivalent linear-anisotropic phase function and an equivalent scattering coefficient are introduced.

Analysis

Exact Solution. The equation of transfer for planar absorbing, emitting and anisotropically scattering medium (Fig. 1) is, e.g. [3]:

$$\vec{s} \cdot \nabla I = \kappa I_b - \beta I + \frac{\sigma}{4\pi} \int_{4\pi} I(\vec{s}') \Phi(\vec{s} \cdot \vec{s}') d\omega', \qquad (1)$$

where I is the intensity (monochromatic or, for a gray medium, wavelength-integrated), I_b is the black-body intensity, κ is the absorption coefficient, σ the scattering coefficient, $\beta = \kappa + \sigma$ the extinction coefficient, $\vec{s}$ a unit direction vector, and Φ the scattering phase function. If Φ is calculated from Mie theory, it may be expanded into a series of Legendre polynomials as outlined by Chu and Churchill [22]:

$$\Phi(\vec{s} \cdot \vec{s}') = \sum_{n=0}^{N} a_n P_n(\vec{s} \cdot \vec{s}'), \quad (a_0 \equiv 1), \qquad (2)$$

where the series may be truncated after N significant terms. Employing equation (2) and evaluating the integral over all azimuthal

[1] Supported by the National Science Foundation under NSF Grant ENG 77-12628.

Contributed by the Heat Transfer Division for publication in the JOURNAL OF HEAT TRANSFER. Manuscript received by the Heat Transfer Division July 27, 1979.

Table 1 Radiative properties of typical particle clouds (all evaluated for number density $N_p = 10^4$, wavelength $\lambda = 3.1416\ \mu m$)

Cloud	#1 Constant Radius $r = 5\ \mu m$ $m = 2 - i$	#2 Size Distribution $n(r)$ from equation (30) $m = 2 - i$	#3 Constant Radius $r = 5\ \mu m$ $m = 2$	#4 Size Distribution $n(r)$ from equation (30) $m = 2$
Mie Theory				
Absorption Coefficient κ [cm^{-1}]	8.307×10^{-3}	1.524×10^{-3}	0	0
Scattering Coefficient σ [cm^{-1}]	1.073×10^{-2}	1.674×10^{-3}	6.420×10^{-2}	3.363×10^{-3}
Extinction Coefficient β [cm^{-1}]	1.904×10^{-2}	3.198×10^{-3}	6.420×10^{-2}	3.363×10^{-3}
Albedo ω	0.5634	0.5235	1	1
Terms Needed for Phase Function, N	26	35	27	33
Linear Approximation				
Modified Scattering Coefficient σ^* [cm^{-1}]	2.039×10^{-3}	4.185×10^{-4}	3.210×10^{-2}	1.682×10^{-3}
Backward Scattered Fraction (Diff. Appr. Only) δ_b	0	0	0 or .0491	0.096
Modified a_1*	7/19	3/5	1	1

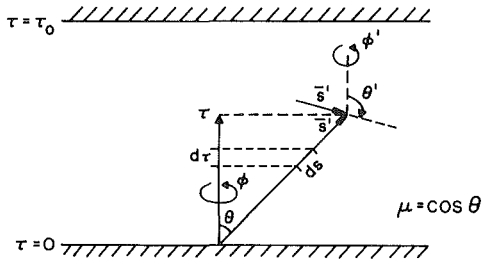

Fig. 1 Physical model and coordinate systems

angles, equation (1) reduces for the one-dimensional slab to

$$\mu \frac{dI}{d\tau}(\tau, \mu) = (1 - \omega) I_b(\tau) - I(\tau, \mu) + \frac{\omega}{2} \int_{-1}^{1} I(\tau, \mu') \sum_{n=0}^{N} a_n P_n(\mu) P_n(\mu') d\mu' = (1 - \omega) I_b(\tau) - I(\tau, \mu) + \frac{\omega}{4\pi} \sum_{n=0}^{N} a_n i_n(\tau) P_n(\mu). \quad (3)$$

Here τ is the optical distance normal to the plates, $d\tau = \beta dx$, $\omega = \sigma/\beta$ is the single-scattering albedo, and $\mu = \cos\theta$ is the cosine of the angle between the direction under consideration and the normal to the surfaces. Furthermore, the abbreviation

$$i_n(\tau) \equiv 2\pi \int_{-1}^{1} I(\tau, \mu) P_n(\mu) d\mu \quad (4)$$

was introduced in equation (3). Note that i_0 is the integrated intensity, while i_1 is the heat flux between the plates. Equation (3) is readily integrated to yield

$$I(\tau, \mu) = I_1 e^{-\tau/\mu} + (1 - \omega) \int_0^{\tau} I_b(\tau^*) e^{-(\tau - \tau^*)/\mu} \frac{d\tau^*}{\mu} + \frac{\omega}{4\pi} \sum_{n=0}^{N} a_n P_n(\mu) \int_0^{\tau} i_n(\tau^*) e^{-(\tau - \tau^*)/\mu} \frac{d\tau^*}{\mu}, \quad \mu \geq 0; \quad (5)$$

$$I(\tau, \mu) = I_2 e^{(\tau_o - \tau)/\mu} - (1 - \omega) \int_{\tau}^{\tau_o} I_b(\tau^*) e^{(\tau^* - \tau)/\mu} \frac{d\tau^*}{\mu} - \frac{\omega}{4\pi} \sum_{n=0}^{N} a_n P_n(\mu) \int_{\tau}^{\tau_o} i_n(\tau^*) e^{(\tau^* - \tau)/\mu} \frac{d\tau^*}{\mu}, \quad \mu \leq 0;$$

where I_1 and I_2 are the intensities emanating from the boundaries and τ_o is the optical distance between the plates. In order to generate simultaneous integral equations in the unknown intensity functions $i_n(\tau)$, one may multiply equation (5) by $2\pi P_m(\mu)$ and integrate over all μ. This yields, after some manipulation:

$$i_n(\tau) = 2\pi I_1 G_{on}(\tau) + (-1)^n 2\pi I_2 G_{on}(\tau_o - \tau) - 2\pi(1 - \omega) \left[\int_0^{\tau} I_b(\tau^*) G'_{on}(\tau - \tau^*) d\tau^* + (-1)^n \int_{\tau}^{\tau_o} I_b(\tau^*) G'_{on}(\tau^* - \tau) d\tau^* \right] - \frac{\omega}{2} \sum_{m=0}^{N} a_m \left[\int_0^{\tau} i_m(\tau^*) G'_{mn}(\tau - \tau^*) d\tau^* + (-1)^{m+n} \int_{\tau}^{\tau_o} i_m(\tau^*) G'_{mn}(\tau^* - \tau) d\tau^* \right], \quad n = 0, 1, \ldots, N, N+1, \ldots \quad (6)$$

In this equation the abbreviation

$$G_{mn}(\tau) = G_{nm}(\tau) \equiv \int_0^1 e^{-\tau/\mu} P_m(\mu) P_n(\mu) d\mu; \quad (7a)$$

$$G'_{mn}(\tau) = \frac{dG_{mn}}{d\tau}(\tau), \quad (7b)$$

has been introduced. The functions G_{mn} are directly related to the exponential integrals $E_n(\tau) \equiv \int_0^1 e^{-\tau/\mu} \mu^{n-2} d\mu$, (see equation (12)).

For $n \leq N$ equation (6) constitutes a set of $N + 1$ simultaneous integral equations for the unknown $i_n(\tau)$ ($I_b(\tau)$ is either known a priori or must be determined in connection with overall conservation of energy). For $n > N$ equation (6) gives higher order Legendre moments of the intensity in terms of known functions.

In this investigation two special cases will be treated in some detail: (1) constant temperature gray slab bounded by black walls of zero temperature, and (2) radiative equilibrium in a gray slab bounded by black walls at different temperatures. For the isothermal slab equation (6) reduces to

Nomenclature

a_n = coefficients in series expansion of phase function
E_n = exponential integral
G_{mn} = geometric parameters, equation (7)
i_n = coefficients for series expansion of intensity, equation (4)
I_b, I = (black body) intensity
m = complex index of refraction
$\vec{n}_w$ = surface normal
N = number of terms in series expansion of phase function
N_p = particle cloud number density
P_n = Legendre polynomial
q = radiative heat flux
r = particle radius
$\vec{s}$ = direction unit vector
T = temperature
x = Mie size parameter, $= 2\pi r/\lambda$
α_n = coefficient defined in equation (18)
β = extinction coefficient
δ_f, δ_b = forward, backward scattered fractions
ϵ_w = surface emissivity
κ = absorption coefficient
λ = wavelength
μ = direction cosine, $= \vec{n}_w \cdot \vec{s}$
μ_f, μ_b = limiting value of μ for forward and backward scattering
ω = single scattering albedo, or solid angle
Φ = scattering phase function
Φ_n, Ψ_n = nondimensional intensity functions
σ = scattering coefficient, or Stefan-Boltzmann constant
τ, τ_o = optical length

$$\Phi_n(\tau) \equiv \frac{i_n(\tau)}{\sigma T^4} = 2(1-\omega)[2\delta_{on} - G_{on}(\tau) - (-1)^n G_{on}(\tau_o - \tau)]$$
$$- \frac{\omega}{2} \sum_{m=0}^{N} a_m \left[\int_o^\tau \Phi_m(\tau^*) G'_{mn}(\tau - \tau^*) d\tau^* \right.$$
$$\left. + (-1)^{m+n} \int_\tau^{\tau_o} \Phi_m(\tau^*) G'_{mn}(\tau^* - \tau) d\tau^* \right], \quad (8)$$

where δ_{ij} is the Kronecker delta. For the case of radiative equilibrium equation (6) becomes, on the other hand,

$$\Psi_n(\tau) \equiv \frac{i_n(\tau) - 4\sigma T_1^4 \delta_{on}}{4\sigma(T_2^4 - T_1^4)} = (-1)^n \frac{1}{2} G_{on}(\tau_o - \tau)$$
$$- \frac{1}{2} \int_o^\tau \Psi_o(\tau^*) G'_{on}(\tau - \tau^*) d\tau^*$$
$$- \frac{1}{2}(-1)^n \int_\tau^{\tau_o} \Psi_o(\tau^*) G'_{on}(\tau^* - \tau) d\tau^*$$
$$- \frac{\omega}{2} \sum_{m=1}^{N} a_m \left[\int_o^\tau \Psi_m(\tau^*) G'_{mn}(\tau - \tau^*) d\tau^* \right.$$
$$\left. + (-1)^{m+n} \int_\tau^{\tau_o} \Psi_m(\tau^*) G'_{mn}(\tau^* - \tau) d\tau^* \right]. \quad (9)$$

These equations are inconvenient for numerical calculations as they contain terms such as $G'_{oo}(\tau) \equiv E_1(\tau)$ which become unbounded at $\tau = 0$. In view of this and in order to avoid the calculation of G'_{mn} in addition to the G_{mn}, it is advantageous to integrate equations (8) and (9) by parts:

$$\Phi_n(\tau) = 4(1-\omega)\delta_{on} + \frac{\omega a_n}{2n+1} \Phi_n(\tau)$$
$$- 2(1-\omega)[G_{on}(\tau) + (-1)^n G_{on}(\tau_o - \tau)]$$
$$- \frac{\omega}{2} \sum_{m=0}^{N} a_m \left\{ \Phi_m(0)[G_{mn}(\tau) + (-1)^n G_{mn}(\tau_o - \tau)] \right. \quad (10)$$
$$+ \int_o^\tau \Phi'_m(\tau^*) G_{mn}(\tau - \tau^*) d\tau^*$$
$$\left. - (-1)^{m+n} \int_\tau^{\tau_o} \Phi'_m(\tau^*) G_{mn}(\tau^* - \tau) d\tau^* \right\};$$

$$\Psi_n(\tau) = (1-\omega)\Psi_o(\tau)\delta_{on} + \frac{\omega a_n}{2n+1} \Psi_n(\tau)$$
$$- \frac{1}{2} \sum_{m=0}^{N} [\delta_{om} + \omega(1-\delta_{om})] a_m \left\{ \Psi_m(0)[G_{mn}(\tau) \right.$$
$$- (-1)^n G_{mn}(\tau_o - \tau)]$$
$$+ \int_o^\tau \Psi'_m(\tau^*) G_{mn}(\tau - \tau^*) d\tau^*$$
$$\left. - (-1)^{m+n} \int_\tau^{\tau_o} \Psi'_m(\tau^*) G_{mn}(\tau^* - \tau) d\tau^* \right\}. \quad (11)$$

In this form the equations for Φ_n and Ψ_n, respectively, allow straightforward and quickly converging solutions for any albedo ω (including $\omega = 1$) by successive approximations, provided the geometric parameters $G_{mn}(\tau)$ can be evaluated efficiently. Employing the various recursion formulae for Legendre polynomials, a set of recursion formulae for the G_{mn} can be developed and turn out to be:

$m = 0$:
$$G_{oo}(\tau) = E_2(\tau), \quad (12a)$$
$$G_{o1}(\tau) = E_3(\tau), \quad (12b)$$
$$G_{o2}(\tau) = \frac{3}{2} E_4(\tau) - \frac{1}{2} E_2(\tau), \quad (12c)$$
$$G_{o3}(\tau) = \frac{5}{2} E_5(\tau) - \frac{3}{2} E_3(\tau), \quad (12d)$$
$$G_{on}(\tau) = -\frac{2n-1}{n(n+1)} \left\{ \tau[G_{o,n-1}(\tau) - G_{o,n-3}(\tau)] \right.$$
$$+ \left[\frac{n(n-2)}{2n-1} + \frac{(n-1)(n-3)}{2n-5} \right] G_{o,n-2}(\tau)$$
$$\left. + \frac{(n-3)(n-4)}{2n-5} G_{o,n-4}(\tau) \right\}, \quad n \geq 4; \quad (12e)$$

$m = 1$:
$$G_{1n}(\tau) = \frac{n+1}{2n+1} G_{o,n+1}(\tau) + \frac{n}{2n+1} G_{o,n-1}(\tau), \quad n \geq 1; \quad (13)$$

$m \geq 2$:
$$G_{mn}(\tau) = \frac{2m-1}{m} \left[\frac{n+1}{2n+1} G_{m-1,n+1}(\tau) \right.$$
$$\left. + \frac{n}{2n+1} G_{m-1,n-1}(\tau) \right] - \frac{m-1}{m} G_{m-2,n}(\tau), \quad n \geq 1. \quad (14)$$

Note that in these recursion formulae knowledge of $G_{m-1,n+1}$ is required for the calculation of G_{mn}. Thus, in order to calculate G_{NN} the case of $m = 0$ must be carried out to $G_{o,2N}$, etc. As the G_{mn} are geometric parameters, they may be calculated a priori for all values of m, n and τ and do not enter the iterative process (they do, however, require substantial amounts of computer storage for large N). It is easily seen that the recurrence relations (12) to (14) are numerically stable (a certain relative error at a low level will penetrate to higher levels of n and m at the same relative magnitude, without increasing or diminishing). Note also that the G_{mn} need to be calculated only once if several problems are considered (e.g., different temperature profiles, system optical thickness, etc.).

The numerical solution of equations (10) and (11) was performed as follows: First approximations for i_o and i_1 were obtained from the differential approximation which is discussed in the next section. In these calculations a linear anisotropic phase function was used and i_n for $n \geq 2$ were set to zero. Improved values of Φ_n (or Ψ_n) were then obtained by iterating equations (10) (or (11)). In this process, Φ'_n (or Ψ'_n) were computed by numerical differentiation, and a combination of several Newton-Cotes quadrature formulae was used for the variable ranges of integration. The number of nodes that are necessary is determined by the integrands in equations (10) and (11), i.e., $\Phi'_n G_{mn}$ (or $\Psi'_n G_{mn}$). The G_{mn} are basically exponentially decaying functions with their maxima at or close to the point under consideration. Fig. 2 demonstrates the behavior of the G_{mn} for a few values of m and n. The Φ_n and Ψ_n, on the other hand, are slightly oscillatory functions, becoming more oscillatory with increasing n. Some Ψ_n are depicted in Fig. 3 to demonstrate their typical behavior. Thus, for optically thin situations when the G_{mn} decay gradually, the oscillations in Φ_n and Ψ_n determine the necessary number of nodes. In optically thick situations the G_{mn} decay rapidly, necessitating a number of nodes to be close to the point under consideration and, thus, increasing the overall number of nodes. In the sample cases discussed below 21 spatial nodes were used for the optically thin case of $\tau_o = 0.1$, resulting in four-significant-figure convergence for the heat flux. For $\tau_o = 5$, 21 nodes yielded accuracies of only three significant figures so that 41 nodes were used, which improved accuracy to four figures and also improved convergence. Note that in the choice for the number of nodes only the accuracy of Φ_o and Φ_1 (or Ψ_o and Ψ_1) was considered, because they are physically meaningful (i.e., integrated intensity and radiative flux). The accuracy of, say, Φ_N may be substantially worse.

To check the accuracy of the numerical integration and the convergence of the successive approximations, it is a good idea to calculate the heat flux at a boundary independently from equation (10) or (11). This can be achieved by realizing that, at the lower boundary

$$q(0) \equiv i_1(0) = \sigma T_w^4 + 2\pi \int_{-1}^{o} I(0, \mu)\mu d\mu, \quad (15)$$

or

$$\begin{Bmatrix} \Phi_1(0) \\ \Psi_1(0) \end{Bmatrix} = \frac{1}{2} \sum_{n=0}^{\infty} (-1)^{n+1}(2n+1) \int_o^1 P_n(\mu)\mu d\mu \begin{Bmatrix} \Phi_n(0) \\ \Psi_n(0) \end{Bmatrix}. \quad (16)$$

After some manipulation, employing recursion formulae for Legendre polynomials, equation (16) may be reduced to

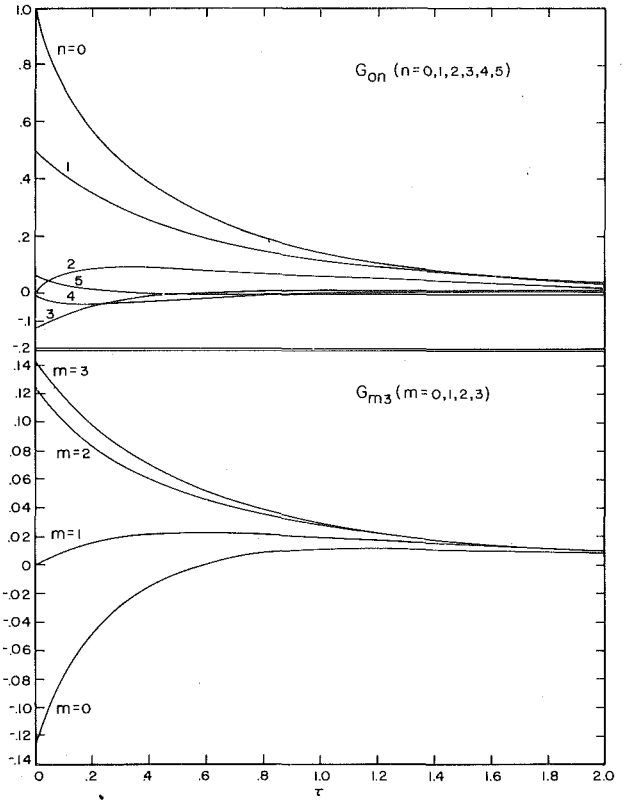

Fig. 2 Some typical G_{mn} as functions of optical distance

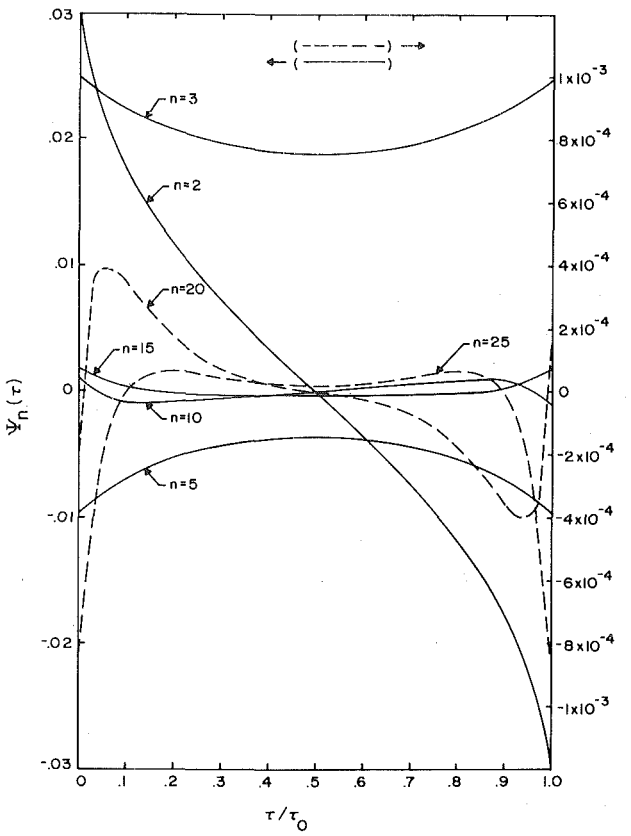

Fig. 3 Some typical Ψ_n as functions of position (radiative equilibrium, cloud No. 2, $\tau_0 = 1.0$)

$$\begin{Bmatrix}\Phi_o(0)\\ \Psi_o(0)\end{Bmatrix} = -2\begin{Bmatrix}\Phi_1(0)\\ \Psi_1(0)\end{Bmatrix} - 2\sum_{n=1}^{\infty}\alpha_n\begin{Bmatrix}\Phi_{2n}(0)\\ \Psi_{2n}(0)\end{Bmatrix}, \quad (17)$$

where

$$\alpha_n \equiv (4n+1)\int_0^1 P_{2n}(\mu)\mu d\mu = -\frac{(4n+1)(2n-3)}{(4n-3)(2n+2)}\alpha_{n-1}. \quad (18)$$

The series in equation (17) converges very quickly and, therefore, provides a convenient mechanism to check the accuracy of the overall solution.

Approximate Solutions

It is obvious from the above discussion that exact solutions employing the full Mie-scattering phase function are extremely involved, and are close to impossible if nonplanar and/or multidimensional problems are considered. The question arises how accurate the results from equation (6) would be (for any possible situation), if the phase function in equation (2) is replaced by an equivalent, linear one:

$$\Phi^*(\vec{s}\cdot\vec{s}') \cong 1 + a_1^*\vec{s}\cdot\vec{s}', \quad (19)$$

while, at the same time, replacing σ by an equivalent scattering coefficient σ^*. Furthermore, how would such equivalent values be determined? Finally, can the differential approximation [21] be modified to yield satisfactory results?

If one desires to approximate a scattering phase function by a linear function such as equation (19), one generally encounters a number of difficulties: The phase function may display strong forward scattering (e.g., Fig. 4), strong backward scattering, or both (e.g., Fig. 5); furthermore, the phase function may be highly oscillatory (e.g., Fig. 5). Placing a straight line through an oscillatory function appears intuitively acceptable: underprediction of scattering in one direction is compensated for by overprediction in a slightly different direction. Forward and backward scattering peaks may be accounted for by approximating the scattering term in equation (1) as follows:

$$\frac{1}{4\pi}\int_{4\pi} I(\vec{s}')\Phi(\vec{s}\cdot\vec{s}')d\omega' \simeq \delta_f I(\vec{s}) + \delta_b I(-\vec{s})$$

$$+ (1-\delta_f-\delta_b)\frac{1}{4\pi}\int_{4\pi} I(\vec{s}')\Phi^*(\vec{s}\cdot\vec{s}')d\omega', \quad (20)$$

i.e., the fraction δ_f is considered to be scattered straight forward (rather than within a narrow cone), the fraction δ_b is scattered straight back, while the rest is scattered in a linear-anisotropic fashion. Thus

$$\delta_f = \frac{1}{2}\int_{\mu_f}^{1}\left[\Phi(\mu) - \frac{\sigma^*}{\sigma}\Phi^*(\mu)\right]d\mu, \quad (21)$$

$$\delta_b = \frac{1}{2}\int_{-1}^{\mu_b}\left[\Phi(\mu) - \frac{\sigma^*}{\sigma}\Phi^*(\mu)\right]d\mu. \quad (22)$$

The equivalent linear-anisotropic values for σ and Φ should satisfy

$$\int_{\mu_b}^{\mu_f}\left[\Phi(\mu) - \frac{\sigma^*}{\sigma}\Phi^*(\mu)\right]d\mu = 0, \quad (23)$$

or

$$\sigma^* = \sigma(1-\delta_f-\delta_b). \quad (24)$$

Obviously, there is a good deal of uncertainty involved in the choice of the cut-off angle μ_f for forward scattering, μ_b for backward scattering, and with the placement of

$$\frac{\sigma^*}{\sigma}\Phi^*(\mu) = \frac{\sigma^*}{\sigma}(1 + a_1^*\mu), \quad (25)$$

in the central portion of the phase function (compare Fig. 5). One may want to investigate the sensitivity of the results on different choices for μ_f and μ_b. Joseph, et al. [23] suggested taking a number of moments of the phase function to determine δ_f and a_1^*. However, their work is limited to pure scattering with negligible backscattering. This method gave rather poor approximations for the four sample phase functions discussed below, once even yielding the impossible case of $a_1^* > 1$, or negative backscattering (these results are not included in Figs. 4 and 5 to avoid overcrowding).

Equation (20) may be readily incorporated into the exact solution of equation (1) but would not result in any simplification due to the

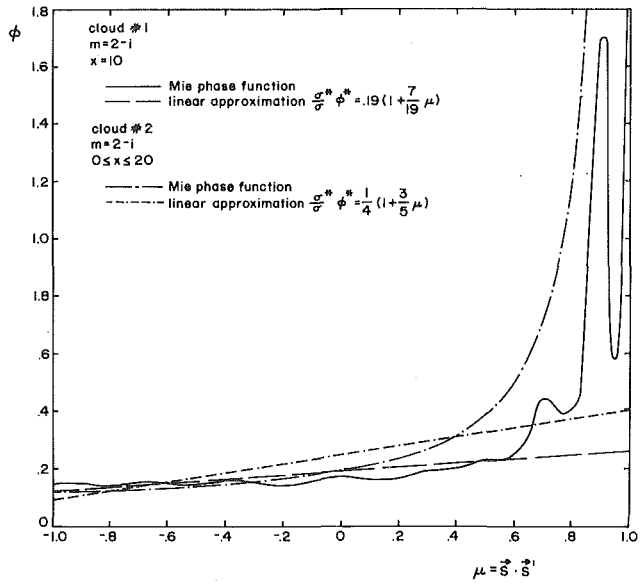

Fig. 4 Mie scattering phase function and linear approximation for absorbing particles

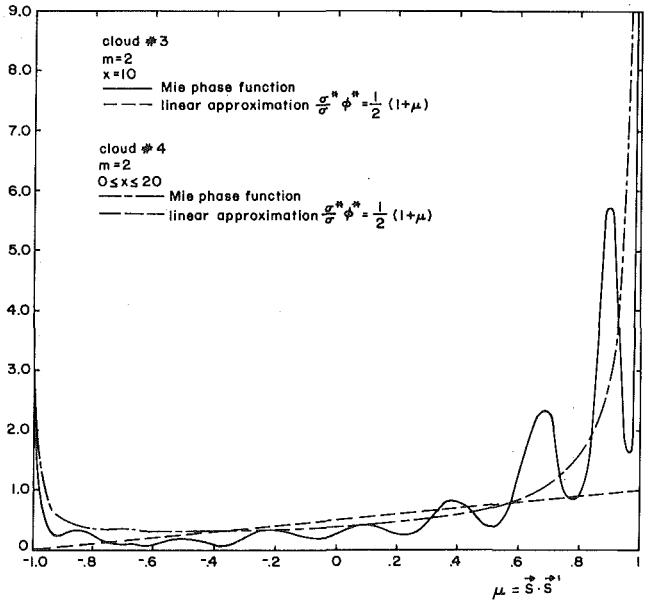

Fig. 5 Mie scattering phase function and linear approximation for nonabsorbing particles

backscattering term. Thus, in order to achieve a simplified exact solution with an approximate phase function, one must set $\delta_b \equiv 0$. Physically this means that only the amount $\sigma^* I$ is scattered (linear-anisotropically) while the rest $(\sigma - \sigma^*)I$, is not scattered at all but transmitted. Equation (6) is then directly applicable with $N = 1$, and with σ and a_1 replaced by the equivalent quantities σ^* and a_1^*, e.g., $d\tau = (\kappa + \sigma^*)dx$, etc.

If results are obtained by the simple differential approximation [21], backscattering can also be accounted for. In this approximation it is assumed that, in optically thick media, the intensity can deviate only by a small amount from isotropic conditions, i.e., [21, 23]

$$I(\vec{s}) \simeq \frac{1}{4\pi}[i_o + 3\vec{q} \cdot \vec{s}]. \tag{26}$$

Combining equations (1, 20) and (26) yields

$$\nabla \cdot \vec{q} = \frac{dq}{dx} = \kappa[4\pi I_b - i_o] \tag{27}$$

$$\nabla i_o = \frac{di_o}{dx} = -3\left[\kappa + \sigma\left\{1 - \delta_f + \delta_b - \frac{a_1^*}{3}(1 - \delta_f - \delta_b)\right\}\right]\vec{q}. \tag{28}$$

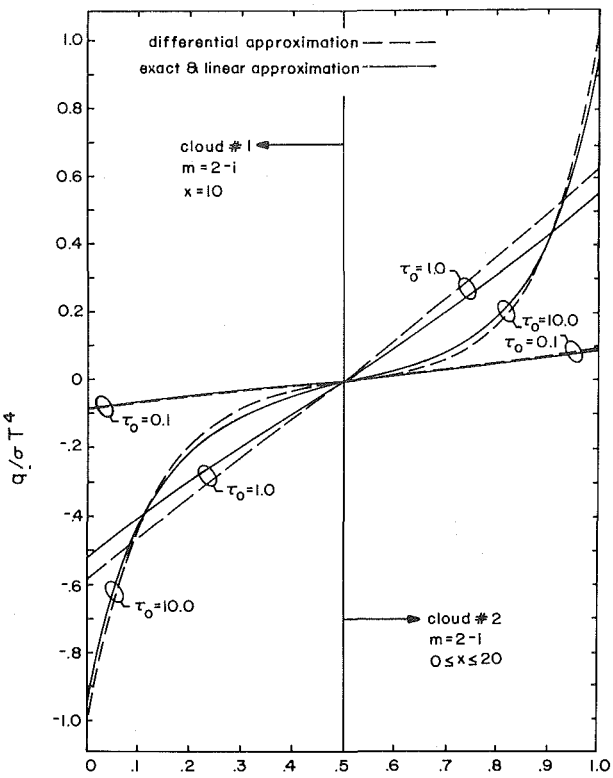

Fig. 6 Nondimensional heat flux rates in an isothermal slab (clouds No. 1 and 2)

Note that equations (27) and (28) are also valid for the general multidimensional case, together with the customary boundary conditions [21]

$$2\vec{q} \cdot \vec{n}_w = \frac{\epsilon_w}{2 - \epsilon_w}[4\pi I_{bw} - i_o] \tag{29}$$

where $\vec{n}_w$ is the outward surface normal and ϵ_w is the emissivity of the surface.

Results and Discussion

Equations (10) and (11) have been solved for four different and typical particle clouds for a wide range of optical thicknesses. Two types of particles are considered, one nonabsorbing with an index of refraction $m = 2$, and one absorbing with $m = 2 - i$. The particles are either in clouds of constant radius $r = 5$ μm, or in clouds with a distribution function

$$n(r) = 27{,}230\, r^2 \exp(-1.7594r), \tag{30}$$

which has its maximum at $r = 5$ μm. All the particle clouds have a number density of 10^4 particles/cm^3, and the Mie calculations are carried out for a typical wavelength of $\lambda = 3.1416$ μm, resulting in a size parameter of $x = 2\pi r/\lambda = 10$ for the constant-radius clouds, and a range of significant size parameters of $0 \le x \le 20$ for clouds with particle size distribution. The radiative properties for the four different particle clouds are summarized in Table 1, and the scattering phase functions are plotted in Figs. 4 and 5, along with linear approximations. The number of terms in the phase function expansion was arbitrarily cut off after N terms by the criterion $a_{N+1} < 10^{-3}$ (retaining smaller terms would have no effect as long as fluxes are calculated to within four significant figures). Absorption and scattering coefficients for constant-radius and size distribution clouds differ considerably. This is primarily due to the fact that the average particle size in equation (30) is less than 5 μm, being 2.23 μm for the volume or mass-averaged radius, and 1.52 μm for the number-averaged radius. (Note the dilemma encountered if—as frequently done—a particle cloud is to be approximated by a single size.)

Fig. 6 depicts local radiative heat transfer rates in an isothermal slab laden with particle clouds No. 1 and 2, i.e., absorbing particles

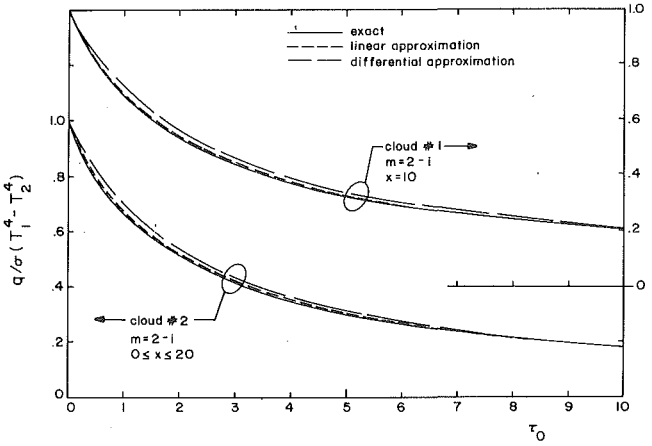

Fig. 7 Nondimensional heat flux rates for a slab at radiative equilibrium (clouds No. 1 and 2)

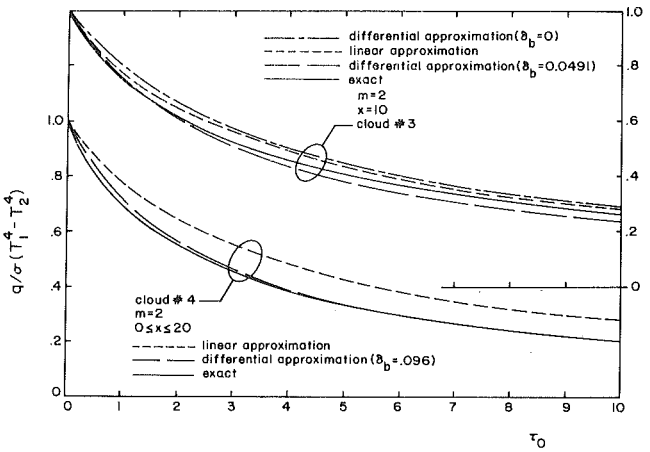

Fig. 9 Nondimensional heat flux rates for a slab at radiative equilibrium (clouds No. 3 and 4)

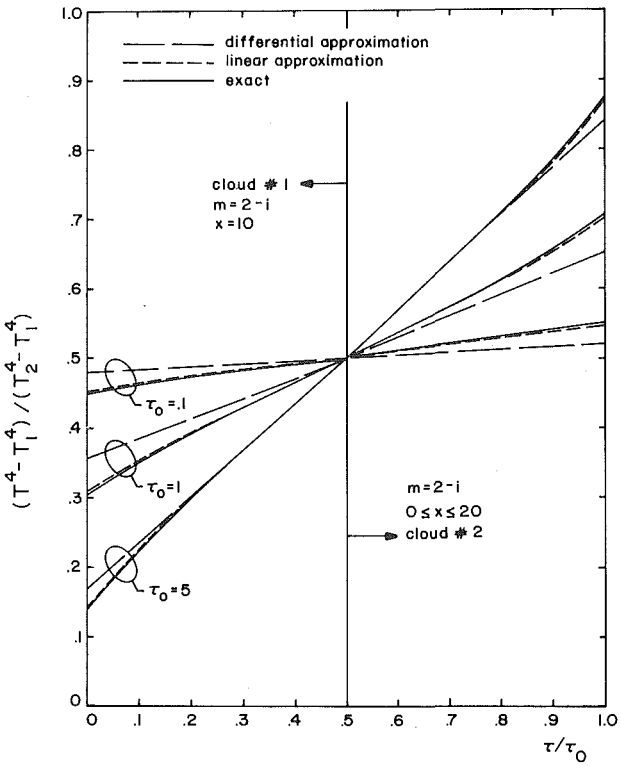

Fig. 8 Nondimensional temperature profiles for a slab at radiative equilibrium (clouds No. 1 and 2)

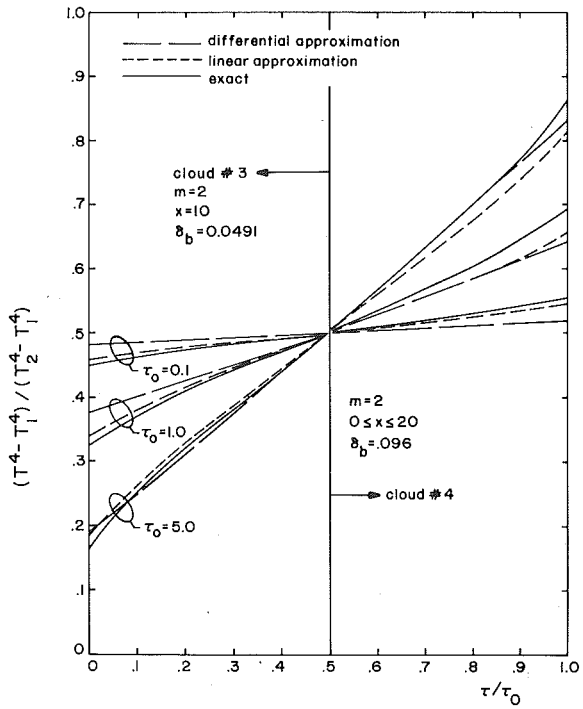

Fig. 10 Nondimensional temperature profiles for a slab at radiative equilibrium (clouds No. 3 and 4)

($m = 2 - i$) of constant radius (No. 1, left) and particle size distribution (No. 2, right), with the corresponding phase functions depicted in Fig. 4. In these cases there is negligible back scattering, and the linear-anisotropic model results in negligible error. Also the differential approximation yields acceptable results with a maximum error of 10 percent at intermediate optical thickness. Similar results hold for radiative equilibrium. Fig. 7 depicts heat flux rates, and again the linear-anisotropic model yields extremely accurate results while, as expected, the differential approximation overpredicts heat fluxes slightly. Temperature profiles, shown in Fig. 8, follow similar trends, with the maximum error for the differential approximation occurring at small τ_o (as in the case for nonscattering media). Results for particle clouds No. 1 and 2 are very similar, with the only difference that the phase function for cloud No. 2 is smoother as the various diffraction peaks for different particle sizes have been integrated out. Note that the ripples in the phase function for cloud No. 1 do not cause any noticeable error in the linear-anisotropic approximation.

For dielectric particles $\kappa \equiv 0$ neither emission nor absorption takes place in the medium. Thus, only radiative equilibrium is considered here. As the more complicated nature of the phase function for clouds No. 3 and 4 suggests (Fig. 5), the linear-anisotropic model becomes less accurate in these cases. The primary reason for this inaccuracy is that backscattering is not accounted for. Neglect of backscattering results in overprediction of heat fluxes for single particle size as well as size distribution (Fig. 9). Note that the differential approximation takes the backscattering into account and predicts the heat fluxes for cloud No. 4 with excellent accuracy. For the single particle size the evaluation of the equivalent parameters becomes rather dubious (due to large oscillations in $\Phi(\mu)$), and loss of accuracy results. The linear approximation in Fig. 5 underpredicts backscattering for $\mu \gtrsim -.7$, while it overpredicts backscattering for larger values of μ. In optically thick planar media ($\tau_o \gg 1$) only intensity scattered back within a narrow cone, say $\mu < -.9$, will eventually travel back to the surface of emission, while for optically thin situations ($\tau_o \ll 1$), nearly all backscattered radiation $\mu < 0$ may return to the surface of emission. Thus the best value for δ_b (or μ_b) will depend on the geometry and

on the optical thickness. Fig. 9 shows the results for two different values of δ_b for cloud No. 3. In one case a $\mu_b \simeq -.7$ is assumed which, as expected, yields good results for $\tau_o > 1$. If one argues that underprediction of backscattering for $\mu < -.7$ is compensated for by overprediction for $\mu > -.7$, i.e., $\delta_b \cong 0$, one may expect the results to be more accurate for optically thin situations. This is not the case, however, as it is the nature of the differential approximation to overpredict heat fluxes in optically thin media, an error which is partially compensated for by assuming $\delta_b > 0$. Thus, if the differential approximation with linear-anisotropic scattering is to be employed for highly oscillatory phase functions, great care must be taken to find a best estimate for the value of δ_b. Luckily, one is unlikely to encounter clouds of particles of uniform size in practice. For completeness temperature profiles are also included for clouds No. 3 and 4 (Fig. 10). Of course, if $\omega = 1$, the medium can maintain any temperature distribution (as there is no emission or absorption). Thus Fig. 10 strictly depicts the integrated intensity, or the temperature distribution that results in the limiting process as $\omega \to 1$.

Summary and Conclusion

Exact solutions have been found for radiative heat transfer between parallel plates separated by an absorbing, emitting and Mie-anisotropically scattering medium. A number of representative Mie-phase functions were employed to investigate the relative importance of highly anisotropic scattering on radiative heat transfer. The exact solutions have been compared with a linear-anisotropic model using (1) the exact relations, (2) the differential approximation. In the absence of significant backscattering the linear-anisotropic model always yields excellent results, as does the differential approximation within its limitations (planar and/or optically thick medium). Significant backscattering cannot be accommodated by the exact relations with a linear-anisotropic model, resulting in inaccuracies. The differential approximation, on the other hand, can be modified to include backscattering, resulting in excellent accuracy (again, within its limitations). Finally, in order to extract accurate results from the exact linear-anisotropic model as well as the differential approximation, the actual scattering phase function must be well behaved, as is the case for clouds of particles of varying size. For clouds of particles of constant size, with erratic scattering phase functions, the definition of equivalent linear-anisotropic parameters becomes dubious. Fortunately, such clouds are rare and unimportant in practice. The fact that linear-anisotropic scattering appears to be an adequate model for most practical cases will make it possible to investigate radiative transfer in Mie-anisotropically scattering media in nonplanar and/or multi-dimensional configurations.

References

1 Edwards, R. H. and Bobco, R. P., "Radiant Heat Transfer from Isothermal Dispersions with Isotropic Scattering," ASME JOURNAL OF HEAT TRANSFER, Vol. 89, 1967, pp. 300–308.

2 Armaly, B. F. and El-Baz, H. S., "Influence of the Refractive Index on the Radiative Source Function of an Isotropically Scattering Medium," *Journal of Quantitative Spectroscopy and Radiative Transfer*, Vol. 18, 1977, pp. 419–424.

3 Dayan, A. and Tien, C. L., "Heat Transfer in a Gray Planar Medium with Linear Anisotropic Scattering," ASME JOURNAL OF HEAT TRANSFER, Vol. 97, 1975, pp. 391–396.

4 Buckius, R. O. and Tseng, M. M., "Radiative Heat Transfer in a Planar Medium with Anisotropic Scattering and Directional Boundaries," *Journal of Quantitative Spectroscopy and Radiative Transfer*, Vol. 20, 1978, pp. 385–402.

5 Buckius, R. O. and King, R., "Diffuse Solar Radiation on a Horizontal Surface for a Clear Sky," *Solar Energy*, Vol. 21, 1978, pp. 503–509.

6 Dayan, A. and Tien, C. L., "Radiative Transfer with Anisotropic Scattering in an Isothermal Slab," *Journal of Quantitative Spectroscopy and Radiative Transfer*, Vol. 16, 1976, pp. 113–125.

7 Evans, L. B., Chu C. M., and Churchill, S. W., "The Effect of Anisotropic Scattering on Radiant Transport," ASME JOURNAL OF HEAT TRANSFER, Vol. 87, 1965, pp. 381–387.

8 Kubo, S., "Effects of Anisotropic Scattering on Steady One-Dimensional Radiative Heat Transfer Through an Absorbing-Emitting Gray Medium," *Journal Physical Society Japan*, Vol. 41, 1976, pp. 894–898.

9 Bergquam, J. B. and Seban, R. A., "Heat Transfer by Conduction and Radiation in Absorbing and Scattering Materials," ASME JOURNAL OF HEAT TRANSFER, Vol. 93, 1971, pp. 236–239.

10 Domoto, G. A. and Wang, W. C., "Radiative Transfer in Homogeneous Nongray Gases with Nonisotropic Particle Scattering," ASME JOURNAL OF HEAT TRANSFER, Vol. C-96, 1974, pp. 385–390.

11 Chin, J. H. and Churchill, S. W., "Anisotropic Multiply Scattered Radiation from an Arbitrary, Cylindrical Source in an Infinite Slab," ASME JOURNAL OF HEAT TRANSFER, Vol. 89, 1967, pp. 167–172.

12 Wang, L., "Anisotropic Nonconservative Scattering in a Semi-infinite Medium," *The Astrophysical Journal* Vol. 174, 1972, pp. 671–678.

13 Hottel, H. C., Sarofim, A. F., Evans L. B., and Vasalos, I. A., "Radiative Transfer in Anisotropically Scattering Media: Allowance for Fresnel Reflection at the Boundaries," Trans ASME JOURNAL OF HEAT TRANSFER, Vol. C-90, 1968, pp. 56–62.

14 Love, T. J. and Grosh, R. J., "Radiative Heat Transfer in Absorbing, Emitting and Scattering Media," ASME JOURNAL OF HEAT TRANSFER, Vol. 87, 1965, pp. 161–166.

15 Hsia, H. M. and Love, T. J., "Radiative Heat Transfer between Parallel Plates Separated by a Nonisothermal Medium with Anisotropic Scattering," ASME JOURNAL OF HEAT TRANSFER, Vol. C-89, 1967, pp. 197–204.

16 Viskanta, R. and Toor, J. S., "Effect of Multiple Scattering on Radiant Energy Transfer in Waters," *Journal Geophysical Research*, Vol. 78, No. 18, 1973, pp. 3538–3551.

17 Daniel, K. J., Laurendeau N. M., and Incropera, F. P., "Prediction of Radiation Absorption and Scattering in Turbid Water Bodies," ASME JOURNAL OF HEAT TRANSFER, Vol. 101, 1979, pp. 63–67.

18 Stockham, L. W. and Love, T. J., "Radiative Heat Transfer from a Cylindrical Cloud of Particles," *AIAA Journal* Vol. 6, 1968, pp. 1935–1940.

19 Barkstrom, B. R., "A Finite Difference Method of Solving Anisotropic Scattering Problems," *Journal of Quantitative Spectroscopy and Radiative Transfer*, Vol. 16, 1976, pp. 725–739.

20 Potter, J. F., "The Delta Function Approximation in Radiative Transfer Theory," *Journal of the Atmospheric Sciences*, Vol. 27, 1970, pp. 943–949.

21 Modest, M. F. and Azad, F. H., "The Differential Approximation for Radiative Transfer in an Emitting, Absorbing and Anisotropically Scattering Medium," to appear in *Journal of Quantitative Spectroscopy and Radiative Transfer*.

22 Chu, C. M. and Churchill, S. W., "Representation of an Angular Distribution of Radiation Scattered by a Spherical Particle," *Journal of the Optical Society of America*, Vol. 45, 1955, pp. 958–962.

23 Joseph, J. H. and Wiscombe, W. J., "The Delta-Eddington Approximation for Radiative Flux Transfer," *Journal of the Atmospheric Sciences*, Vol. 33, 1976, pp. 2452–2459.

Radiation Properties for Polydispersions: Application to Coal

R.O. Buckius
D. C. Hwang

Department of Mechanical and Industrial Engineering, University of Illinois at Urbana-Champaign, Urbana, IL 61801

The extinction and absorption coefficients and the asymmetry factor for polydispersions of absorbing spherical particles are analyzed. The results are based upon Mie's theory for single spherical particles and particle size distributions found in practical systems. Dimensionless spectral radiation properties are shown to be independent of the explicit size distribution and functions only of the average radii and the index of refraction. The Planck and Rosseland mean coefficients are also presented and the dependence on temperature is explicitly denoted for a large practical temperature range. The results for coal with optical properties which are wavelength dependent indicate the usefulness of the dimensionless and mean properties.

Introduction

Many practical engineering systems require the knowledge of the radiative properties of a particulate medium. The radiation transfer through atmospheric aerosols is of considerable interest in atmospheric transmission calculations [1, 2]. Radiant energy transfer through combustion products is of importance in fire safety considerations as well as in pollution detection [3]. An essential element in modeling coal dust combustion systems is the radiation transfer and, therefore, accurate values for the radiation properties are needed [4, 5]. In general, the calculation of radiation properties requires information about the particulate concentration, composition, shape and size distribution.

The properties of interest in radiation heat transfer analyses are the absorption and scattering coefficients and the phase function for the particles. Throughout this work the particles are treated as spherical and separated by a large distance as compared to the radius, so that the properties are described by Mie's solution to Maxwell's equations [1, 2]. The phase function is required if detailed directional information is sought; yet in many heat transfer computations, only the asymmetry factor is desired. The asymmetry factor is given as a weighted mean of the phase function defined below which characterizes the forward and backward dependence of the phase function. Comparisons of an approximate phase function using this asymmetry factor with more detailed representations of the phase function indicate the usefulness of this parameter [6, 7].

Much of the existing literature deals with monodisperse size distributions. The basic radiation properties have been presented by many authors and have been extensively discussed by van de Hulst [2]. The consideration of polydisperse particle distributions has not been as extensive, focusing primarily upon particular applications [8]. Results for small carbon particles for three different distributions have been presented [9] and for large carbon smokes for a class of size distributions [3, 10]. Properties for polydispersions found in terrestrial and planetary atmospheres have also been presented [1]. Scattering coefficients for various polydispersions of dielectric spheres have been presented [11] which shows the importance of an average radius as compared to actual size distribution.

The objective of the present work is to present the extinction coefficient, absorption coefficient and asymmetry factor for polydispersions of absorbing spherical particles. A technique is presented to eliminate the need for the detailed size distribution and require only average radii of the size distribution. Mean coefficients for heat transfer calculations are also presented with specific results for coal.

Contributed by the Heat Transfer Division for publication in the JOURNAL OF HEAT TRANSFER. Manuscript received by the Heat Transfer Division June 5, 1979.

Theory

The radiative properties for a polydisperse cloud of spherical particles are expressed in terms of the extinction efficiency, absorption efficiency, and phase function for a single particle. The extinction and absorption coefficients are given as

$$\beta(\lambda, \bar{n}, N) = \int_0^\infty \pi r^2 N(r) Q_{\text{ext}}(x, \bar{n}) dr \tag{1a}$$

$$\kappa(\lambda, \bar{n}, N) = \int_0^\infty \pi r^2 N(r) Q_{\text{abs}}(x, \bar{n}) dr \tag{1b}$$

and the scattering coefficient, $\gamma(\lambda, \bar{n}, N)$, is the difference between the extinction coefficient and the absorption coefficient. The asymmetry factor for a polydispersion is defined as

$$\langle \cos\theta \rangle = \frac{1}{\gamma(\lambda, \bar{n}, N)} \int_0^\infty \pi r^2 N(r) Q_{\text{sca}}(x, \bar{n}) \overline{\cos\theta}\, dr \tag{1c}$$

All symbols have been defined in the Nomenclature. The functional dependence of the radiative properties on wavelength, index of refraction and particle size distribution is explicitly denoted.

The radiative properties for an isotropic sphere in a homogeneous medium have been described by Mie's theory. These results have been discussed by many authors [1, 2] and the expressions will not be presented here. The expressions for Q_{ext}, Q_{abs}, and $\overline{\cos\theta}$ are in terms of infinite series of Ricatti-Bessel functions with real and complex arguments. The computational scheme used throughout this work includes a downward recurrence relation for the generation of the logarithmic derivative of $\psi(z) = (\frac{1}{2}\pi z)^{1/2} J_{n+1/2}(z)$ [12]. The Bessel functions of the first kind of half order were generated by a downward recurrence relation [13, 14].

Dimensionless radiation properties are obtained from considerations of the limiting expressions in the size parameter, x. As $x \to \infty$, the radiation properties are

$$\beta(\lambda, \bar{n}, N) = 2 \int_0^\infty \pi r^2 N(r) dr \tag{2a}$$

$$\kappa(\lambda, \bar{n}, N) = C_1(\bar{n}) \int_0^\infty \pi r^2 N(r) dr \tag{2b}$$

$$\langle \cos\theta \rangle = C_2(\bar{n}) \tag{2c}$$

where $C_1(\bar{n})$ and $C_2(\bar{n})$ are expressed in terms of weighted integrals over angle of the Fresnel relations [2] and are the only weak functions of the index of refraction for many practical combustion systems, especially when the difference between n and k is not small. As $x \to 0$, the radiation properties are

$$\beta(\lambda, \bar{n}, N) = \kappa(\lambda, \bar{n}, N) = \frac{2\pi}{\lambda} Im\left(-4\frac{\bar{n}^2 - 1}{\bar{n}^2 + 2}\right) \int_0^\infty \pi r^3 N(r) dr \tag{3a,b}$$

$$\langle \cos\theta \rangle = \frac{1}{30}\left(\frac{2\pi}{\lambda}\right)^2 \left|\frac{\bar{n}^2 + 2}{\bar{n}^2 - 1}\right|^2 \left\{3\frac{\bar{n}^2 - 1}{\bar{n}^2 + 2}\left(\overline{\frac{\bar{n}^2 - 1}{2\bar{n}^2 + 3}}\right)\right.$$

$$+\left(\frac{\overline{n}^2-1}{\overline{n}^2+2}\right)\overline{(\overline{n}^2-1)}\Bigg\}\frac{\int_0^\infty \pi r^8 N(r)dr}{\int_0^\infty \pi r^6 N(r)dr} \quad (3c)$$

Therefore, if the dimensionless extinction and absorption coefficient are defined as

$$\beta^*(\lambda,\overline{n}) = \frac{\beta(\lambda,\overline{n},N)}{\int_0^\infty \pi r^2 N(r)dr} \quad (4a)$$

$$\kappa^*(\lambda,\overline{n}) = \frac{\kappa(\lambda,\overline{n},N)}{\int_0^\infty \pi r^2 N(r)dr} \quad (4b)$$

and if average radii are denoted by

$$r_{32} = \frac{\int_0^\infty r^3 N(r)dr}{\int_0^\infty r^2 N(r)dr}$$

$$r_{86}^2 = \frac{\int_0^\infty r^8 N(r)dr}{\int_0^\infty r^6 N(r)dr} \quad (5)$$

then as $x \to \infty$, the properties are

$$\beta^*(\lambda,\overline{n}) = 2 \quad (6a)$$

$$\kappa^*(\lambda,\overline{n}) = C_1(\overline{n}) \quad (6b)$$

$$\langle\cos\theta\rangle = C_2(\overline{n}) \quad (6c)$$

and as $x \to 0$, the properties are

$$\beta^*(\lambda,\overline{n}) = \kappa^*(\lambda,\overline{n}) = \frac{2\pi r_{32}}{\lambda} Im\left(-4\frac{\overline{n}^2-1}{\overline{n}^2+2}\right) \equiv 24 x_{32} F_\kappa(\overline{n}) \quad (7a,b)$$

$$\langle\cos\theta\rangle = \frac{1}{30}\left(\frac{2\pi}{\lambda}\right)^2 r_{86}^2 \left|\frac{\overline{n}^2+2}{\overline{n}^2-1}\right|^2 \left\{3\frac{\overline{n}^2-1}{\overline{n}^2+2}\left(\overline{\frac{\overline{n}^2-1}{2\overline{n}^2+3}}\right) + \left(\frac{\overline{n}^2-1}{\overline{n}^2+2}\right)\overline{(\overline{n}^2-1)}\right\} \equiv \frac{1}{30} x_{86}^2 F_c(\overline{n}) \quad (7c)$$

where x_{ij} is the particle size parameter based upon the average radius, r_{ij}^{i-j}. The correct limiting expressions given in (7) are obtained from expansion coefficients presented in [15]. These limiting expressions suggest that the dimensionless extinction and absorption coefficients and the asymmetry factor are independent of the actual size distribution and only a function of average radii. Also, since $C_1(\overline{n})$ and $C_2(\overline{n})$ are in many cases only weak functions of $\overline{n}$, the dependence of $[\beta^*(\lambda,\overline{n})/x_{32}F_\kappa(\overline{n})]$ and $[\kappa^*(\lambda,\overline{n})/x_{32}F_\kappa(\overline{n})]$ with $x_{32}F_\kappa(\overline{n})$ and $[\langle\cos\theta\rangle/x_{86}{}^2F_c(\overline{n})]$ with $x_{86}{}^2F_c(\overline{n})$ in these limits are approximately independent of $\overline{n}$ explicitly. These possibilities have been explored through numerical computations.

The dependence of these ratios on the size distribution and the index of refraction was studied for distributions and indices of refraction found in practical systems [1, 3]. The general form for the size distribution considered was

$$N(r) = ar^b e^{-cr} \quad (8)$$

Calculations over a large range of size distributions (obtained by a variation of c between $10^4 m^{-1}$ and $10^7 m^{-1}$ for the b values presented) and therefore the size parameter, were carried out to include the above limits as well as the intermediate values. Figs. 1 and 2 present the results for the radiation properties for $\overline{n} = 1.5 - 0.5i$ which has been used in carbon considerations [3]. The figures confirm the fact that the dimensionless properties are independent of the size distribution in each limit. There is also little variation of the radiation properties with size distribution for intermediate values of the size parameter. A rectangular size distribution was also tested and these results are consistent with the above conclusions. For the cases considered, the effect of the size distribution on extinction and absorption properties is approximately 10 percent while in the case of the asymmetry factor a variation up to approximately 25 percent was observed at intermediate values of the size parameter.

The index of refraction for practical systems is a function of wavelength. The extinction and absorption properties for two values of the index of refraction are presented in Fig. 3. The values chosen are the extremes for coals in the near infrared [16]. At small values of $x_{32}F_\kappa(\overline{n})$, the independence of the $[\beta^*(\lambda,\overline{n})/x_{32}F_\kappa(\overline{n})]$ and $[\kappa^*(\lambda,\overline{n})/x_{32}F_\kappa(\overline{n})]$ is observed while at large value of $x_{32}F_\kappa(\overline{n})$, $[\beta^*(\lambda,\overline{n})/x_{32}F_\kappa(\overline{n})]$ is independent of $\overline{n}$ and dependence of the $[\kappa^*(\lambda,\overline{n})/x_{32}F_\kappa(\overline{n})]$ on $\overline{n}$ is not large. This variation is a result of the dependence of the Fresnel relations on $\overline{n}$. The variation with $\overline{n}$ at intermediate values of $x_{32}F_\kappa(\overline{n})$ is much greater. Therefore, for moderate variations of $\overline{n}$ and very general particle size distributions, the radiation properties can be expressed in terms of only average radii.

Heat transfer calculations require mean coefficients over wavelength. This is especially true for particulate media where variation of the radiation properties with wavelength is not large and can be accurately quantified by mean coefficients. If $\pi^*(\lambda,\overline{n})$ denotes either $\beta^*(\lambda,\overline{n})$ or $\kappa^*(\lambda,\overline{n})$ and $\pi^*_{p\text{ or R}}$ denotes $\beta^*_{p\text{ or R}}$ or $\kappa^*_{p\text{ or R}}$, then the Planck mean coefficients are

$$\pi^*_p = \frac{\pi}{\sigma T^4}\int_0^\infty \pi^*(\lambda,\overline{n})\, i_{\lambda b} d\lambda \quad (9)$$

and the Rosseland mean coefficients are

$$\frac{1}{\pi^*_R} = \int_0^\infty \frac{1}{\pi^*(\lambda,\overline{n})}\frac{di_{\lambda b}}{di_b}d\lambda. \quad (10)$$

The limiting expressions for the Planck and Rosseland coefficients

Nomenclature

a, b, c = size distribution constants
$C_1(\overline{n}), C_2(\overline{n})$ = constants which are functions of $\overline{n}$, equation (2)
C_3, C_4 = constants, equations (11) and (12)
$\overline{\cos\theta}$ = asymmetry factor for a single particle
$\langle\cos\theta\rangle$ = asymmetry factor for a polydispersion
$F_c(\overline{n})$ = function of $\overline{n}$ for $\langle\cos\theta\rangle$, equation (7c)
$F_\kappa(\overline{n})$ = function of $\overline{n}$ for β and κ, equation (7a, b)
$Im()$ = imaginary part
$i_{\lambda b}$ = blackbody spectral intensity
i_b = blackbody intensity
k = imaginary part of the index of refraction
n = real part of the index of refraction
$\overline{n}$ = index of refraction $(= n - ik)$
$N(r)$ = size distribution
Q = efficiency for a single particle
r = radius
r_{ij}^{i-j} = average radius
T = temperature
x = size parameter $(= 2\pi r/\lambda)$
x_{ij} = size parameter based upon the average radius
y = variable, equation (13)
z = power in empirical correlation
β = extinction coefficient
γ = scattering coefficient
κ = absorption coefficient
λ = wavelength
π = radiation property
σ = Stefan-Boltzman constant

Subscripts

abs = absorption
ext = extinction
p = Planck
R = Rosseland
sca = scattering
0 = limit as $x \to 0$
∞ = limit as $x \to \infty$

Superscripts

* = dimensionless
$^-$ = complex conjugate

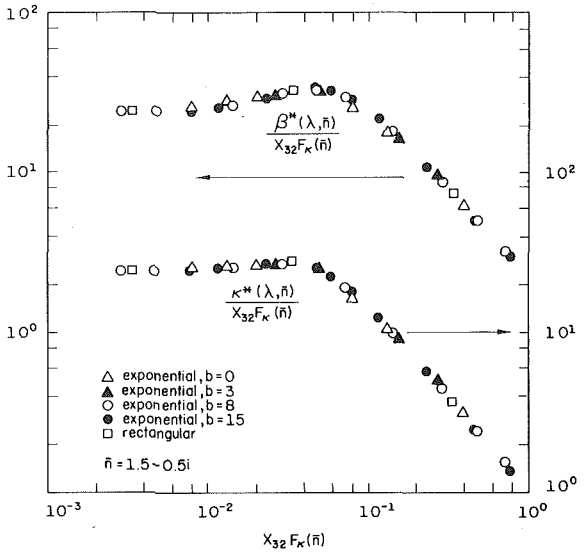

Fig. 1 Effect of size distribution on extinction and absorption properties

are obtained from the limiting expressions of the radiation properties given in equations (6) and (7). If $\bar{n}$ is independent of wavelength and temperature then $C_1(\bar{n})$, $C_2(\bar{n})$ and $F_\kappa(\bar{n})$ are constants for a particular medium. The resulting limiting expressions as $x \to \infty$ are

$$\pi^*_{p\text{ or R}} = C_3 \tag{11}$$

where C_3 denotes the same constant for the Planck and Rosseland mean coefficient but is two for the extinction coefficient and $C_1(\bar{n})$ for the absorption coefficient. In the limit as $x \to 0$, the expressions are

$$\pi^*_{p\text{ or R}} = C_4 r_{32} T \tag{12}$$

where C_4 denotes the same constant for extinction and absorption but is *different for the Planck and Rosseland mean coefficients.* Thus, within the assumptions above, the variation of $[\pi^*_{p\text{ or R}}/r_{32}T]$ with $r_{32}T$ is independent of the size distribution and since it depends only upon $r_{32}T$ in the limits, the dependence on temperature at intermediate values must be assessed. It is shown to be small for the case for coal over a large temperature range.

The computation of the extinction and absorption coefficient per unit volume of medium requires the number of particles per unit volume. This number concentration multiplied by the coefficients given in equations (1) give the radiative properties for medium. The dimensionless extinction and absorption coefficient have been defined with respect to the area of the polydispersion so that these dimensionless quantities (denoted by the superscript,*) multiplied by the volume concentration of the polydispersion divided by r_{32} give the radiative properties for the polydispersion. If the wavelength dependence is desired then results as shown in Fig. 1 are needed and if heat transfer calculations are to be made then the coefficients presented in equations (11) and (12) are necessary.

Application

The radiation properties presented in the previous section are determined for coal. The indices of refraction for coals in the infrared [16] and for carbons [9, 16, 17] have been presented by other authors. The properties have been determined for three coals with different carbon content and different carbon/hydrogen ratios. The real and imaginary part of the index of refraction for all the coals are relatively constant from 1 μm to 5 μm and increases from 5 μm to 10 μm. The magnitude differences between the coals is not large. The spectral optical properties for the three coals in [16] have been used throughout this work.

The dimensionless radiation properties are shown in Figs. 4 and 5. The shaded areas represent over 300 calculations for wavelengths from 1 μm to 10 μm and size distributions used in the previous section.

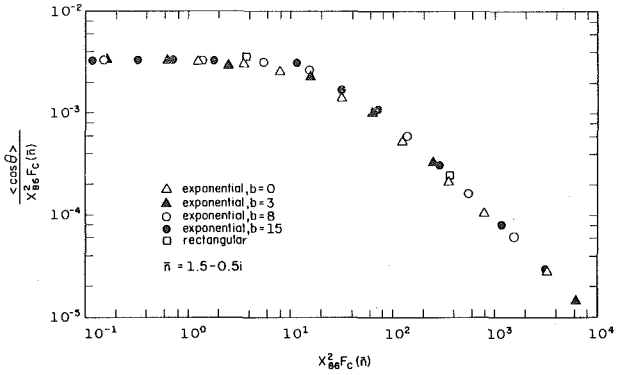

Fig. 2 Effect of size distribution on the asymmetry factor

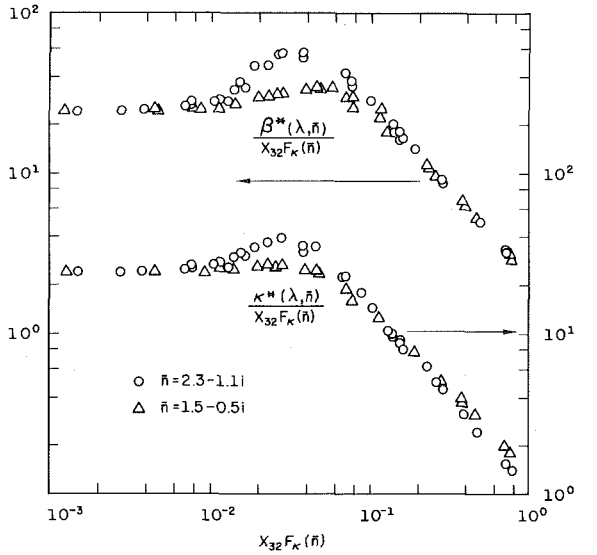

Fig. 3 Effect of index of refraction on extinction and absorption properties

The results are similar to those presented in Fig. 3. The large variation in $\beta^*(\lambda, \bar{n})$ and $\kappa^*(\lambda, \bar{n})$ at moderate size parameters results from variations in the optical constants for the coals while in the limiting size parameter regions, the dimensionless properties show little variation. Therefore, if spectral radiation properties for coal are desired, the results from these figures are desired.

An empirical equation for the spectral coal properties was determined. The procedure to obtain the expressions is based upon the asymptotic behavior at small and large values of the size parameter. The general form for the empirical equation is

$$\frac{1}{y^z} = \frac{1}{y_0^z} + \frac{1}{y_\infty^z} \tag{13}$$

and the parameters are presented in Table 1. The results are valid for the range of size parameters given in the figures. The details of the correlation procedure have been presented in [18]. The resulting empirical correlations are presented in Figs. 4 and 5.

These empirical equations for the spectral extinction and absorption coefficients are then used to determine the Planck and Rosseland mean coefficients. The data available are between 1 μm and 10 μm so that, for wavelength integrations at low temperatures, a significant portion of the energy is at longer wavelengths. The optical constants for the coals were extended to longer wavelengths based upon the slope of the optical constants from 5 μm to 10 μm. The extensions for both n and k were taken of the form $a\lambda^b$ as suggested by variations observed for soots [17]. Various reasonable extensions were tested and the differences in mean coefficients were approximately 15 percent. The optical properties were used in the calculation of $F_\kappa(\bar{n})$ and $F_c(\bar{n})$ and the mean coefficients were evaluated. The radiative properties

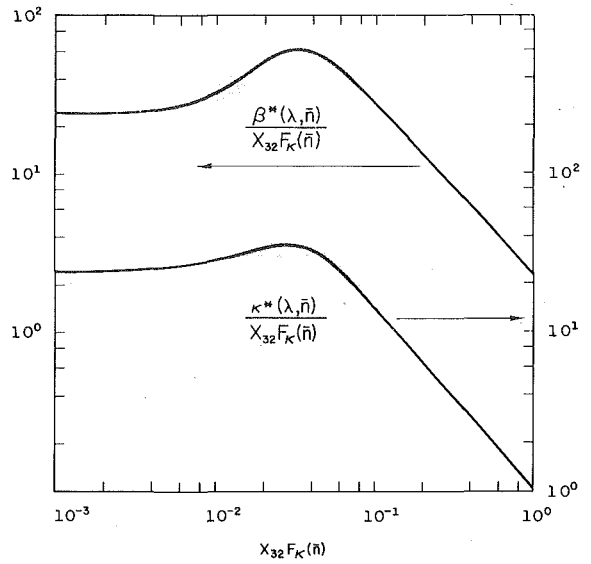

Fig. 4 Extinction and absorption properties for coal. The shaded area represents results for various size distributions and coal optical properties [16]

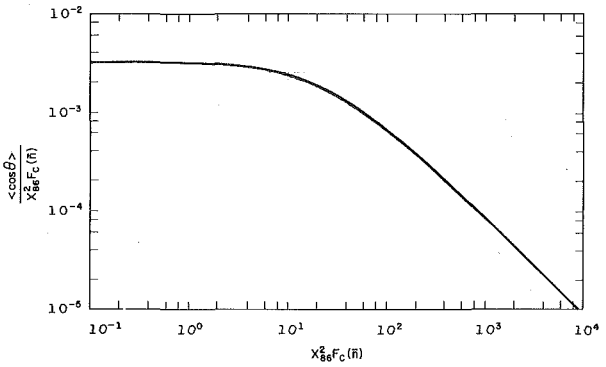

Fig. 5 Asymmetry factor for coal. The shaded area represents results for various size distributions and coal optical properties [16]

are assumed to be independent of temperature as reported by Howarth, et al. [19] for soot.

The results are presented in Fig. 6 and the empirical correlations in Table 1. The range of temperatures considered was between 750K and 2500K. The curves support the conjecture that $[\pi^*_{p \text{ or } R}/r_{32}T]$ depends only upon $r_{32}T$ and not temperature explicitly. The calculations indicated a slight effect on temperature but within the variations in properties and size distribution effects observed above. There is also a small contribution from the different coals since the optical properties differed. The variation in the small particle limit is approximately 20 percent and increased to approximately 30 percent at intermediate size parameters. The largest variation was observed for coal 3 but no consistent trends were found.

The extinction and absorption coefficients were found to be different for the Planck and Rosseland expressions in the small particle limit. Yet, due to the averaging over wavelength with optical properties which are wavelength dependent, the slight dependence of the properties upon temperature and the incorporation of all size distri-

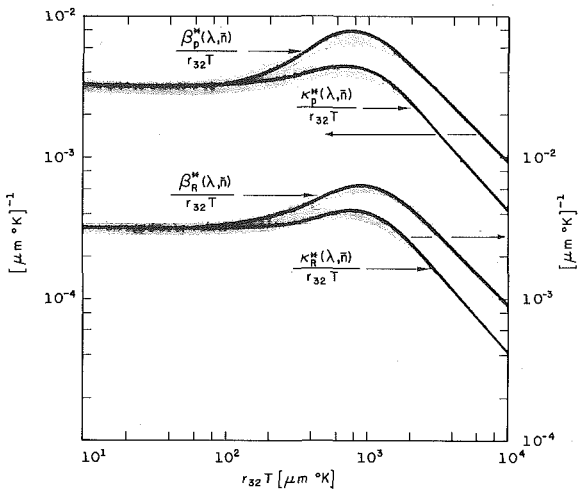

Fig. 6 Planck and Rosseland mean coefficients for coal. The shaded area represents results for variations in temperature between 750 and 2500 K and three coals [16]

Table 1 Empirical correlations for coal properties

$$\text{with } \frac{1}{y^z} = \frac{1}{y_0{}^z} + \frac{1}{y_\infty{}^z}$$

$y^{(1)}$	y_0	y_∞	z
$\frac{\beta^*(\lambda,\bar{n})}{x_{32}F_\kappa(\bar{n})^{(2)}}$	$24\left[1+\left(\frac{x_{32}F_\kappa(\bar{n})}{0.016}\right)^2\right]$	$\frac{2.25}{[x_{32}F_\kappa(\bar{n})]^{1.1}}$	1.2
$\frac{\kappa^*(\lambda,\bar{n})}{x_{32}F_\kappa(\bar{n})}$	$24\left[1+\left(\frac{x_{32}F_\kappa(\bar{n})}{0.0275}\right)^2\right]$	$\frac{1}{[x_{32}F_\kappa(\bar{n})]^{1.16}}$	1.6
$\frac{\langle\cos\theta\rangle}{x_{86}{}^2F_c(\bar{n})^{(3)}}$	0.033	$\frac{0.9}{x_{86}{}^2F_c(\bar{n})}$	1.0
$\frac{\beta_p{}^*}{r_{32}T}$	$0.0032\left[1+\left(\frac{r_{32}T}{355}\right)^{1.9}\right]$	$\frac{10.99}{(r_{32}T)^{1.02}}$	1.2
$\frac{\beta_R{}^*}{r_{32}T}$	$0.0032\left[1+\left(\frac{r_{32}T}{485}\right)^{1.75}\right]$	$\frac{10.99}{(r_{32}T)^{1.02}}$	1.2
$\frac{\kappa_p{}^*}{r_{32}T}$	$0.0032\left[1+\left(\frac{r_{32}T}{725}\right)^{1.65}\right]$	$\frac{13.75}{(r_{32}T)^{1.13}}$	1.5
$\frac{\kappa_R{}^*}{r_{32}T}$	$0.0032\left[1+\left(\frac{r_{32}T}{650}\right)^{2.3}\right]$	$\frac{15.65}{(r_{32}T)^{1.143}}$	1.15

(1) * quantities dimensionless, $r_{32}T[\mu m\ K]$ (2) $F_\kappa(\bar{n})$ defined in equation (7*a*,*b*) (3) $F_c(\bar{n})$ defined in equation (7*c*).

butions indicate that the difference between the Planck mean and Rosseland mean coefficients was very small. Therefore, the Planck and Rosseland mean coefficients were taken as the same in the small particle limit.

Conclusions

The present analysis has considered the radiation properties for polydispersions of absorbing spherical particles. The dimensionless extinction and absorption coefficient have been shown to depend primarily upon the average radius. These coefficients and the asymmetry factor are represented as only functions of the index of refraction including the moderate size parameter range. The Planck and Rosseland mean coefficients have been presented in a form independent of temperature and particle size distribution for a large practical range of temperatures and size distributions. Results for coal verify these conclusions. Empirical correlations for coal allow these results to be applied directly to coal combustion problems.

Acknowledgment

This research was performed under the auspices of NSF Grant ENG 77-26973. The contributions of Mr. G. T. Randall to the initial Mie calculations are gratefully acknowledged.

References

1 Diermendjian, D., *Electromagnetic Scattering of Spherical Polydispersions,* American Elsevier Publishing, New York, 1969.

2 Van de Hulst, H. C., *Light Scattering by Small Particles,* John Wiley and Sons, New York, 1957.

3 Tien, C. L., Doornik, D. G., and Rafferty, D. A., "Attenuation of Visible Radiation by Carbon Smokes," *Combustion Science and Technology,* Vol. 6, 1972, pp. 55–59.

4 Krazinski, J. L., Buckius, R. O., and Krier, H., "A Model for Flame Propagation in Low Volatile Coal Dust-Air Mixtures," ASME JOURNAL OF HEAT TRANSFER, Vol. 100, Feb. 1978, pp. 105–110.

5 Krazinski, J. L., Buckius, R. O., and Krier, H., "Coal Dust Flames: A Review and Development of a Model for Flame Propagation," *Progress in Energy and Combustion Science,* Vol. 5, 1979, pp. 31–71.

6 Evans, L. B., Chu, C. M., and Churchill, S. W., "The Effect of Anisotropic Scattering on Radiant Transport," ASME JOURNAL OF HEAT TRANSFER, Aug. 1965, pp. 381–387.

7 Irvine, W. M., "Multiple Scattering by Large Particles," *Astrophysical Journal,* Vol. 142, 1965, pp. 1563–1575.

8 Hottel, H. C. and Sarofim, A. F., *Radiative Transfer,* McGraw-Hill Book Co., New York, 1967.

9 Stull, V. R. and Plass, G. N., "Emissivity of Dispersed Carbon Particles," *Journal of the Optical Society of America,* Vol. 50, 1960, pp. 121–129.

10 Blokh, A., "The Problem of Flame as a Disperse System," in *Heat Tranefer in Flames,* ed. N. H. Afagan and J. M. Beer, Scripta Book Co., Washington, 1974.

11 Dobbins, R. A. and Jizamian, G. S., "Optical Scattering Cross Sections for Polydispersions of Dielectric Spheres," *Journal of the Optical Society of America,* Vol. 56, No. 10, Oct. 1966, pp. 1345–1350.

12 Kattawar, G. W. and Plass, G. N., "Electromagnetic Scattering from Absorbing Spheres," *Applied Optics,* Vol. 6, No. 8, Aug. 1967, pp. 1377–1382.

13 Wyatt, P. J., "Scattering Electromagnetic Waves from Inhomogeneous Spherically Symmetric Objects," *Physical Review,* Vol. 12, No. 5, Sept. 1962, pp. 1837–1843.

14 Stegun, I. A. and Abramowitz, M., "Generation of Bessel Functions on High Speed Computers," *Mathematical Tables and Aids to Computation,* Vol. 11, No. 60, Oct. 1957, pp. 255–257.

15 Olsen, R. L., Rodgers, D. V. and Hodge, D. B., "The aR^b Relation in the Calculation of Rain Attenuation," *IEEE Transactions on Atennas and Propagation,* Vol. AP-26, No. 2, March 1978, pp. 318–329.

16 Foster, P. J. and Howarth, C. R., "Optical Constants of Carbons and Coals in the Infrared," *Carbon,* Vol. 6, 1968, pp. 719–729.

17 Dalzell, W. H. and Sarofim, A. F., "Optical Constants of Soot and Their Application to Heat-Flux Calculations," ASME JOURNAL OF HEAT TRANSFER, Feb. 1969, pp. 100–104.

18 Churchill, S. W. and Usagi, R., "A Standardized Procedure for the Production of Correlations in the Form of a Common Empirical Equation," *Industry Engineering Chemical, Fundamentals,* Vol. 13, No. 1, 1974, pp. 39–44.

19 Howarth, C. R., Foster, P. J., and Thring, N. W., "The Effect of Temperature on the Extinction of Radiation by Soot Particles," *International Heat Transfer Conference,* Vol. 15, 1966, pp. 122–128.

C. M. Kinoshita
P. J. Pagni

Department of Mechanical Engineering,
University of California,
Berkeley, CA 94720

Laminar Wake Flame Heights

One important measure of material fire hazard is the flame height a given polymer produces upon burning in a specified ambience. Six systems are considered here—two fuel geometries: wall-mounted and free standing; and three flow fields: forced, free and mixed-mode. In each case, the extent of the combusting gas downstream of a pyrolyzing slab is obtained as a function of the fuel's thermochemical properties. The flow is modeled as a steady, laminar, two-dimensional, nonradiative boundary layer. The combustion is described by a single Shvab-Zeldovich energy-species equation assuming unit Lewis number and a fast one-step overall gas phase reaction. Numerical methods are employed due to the abrupt change in boundary conditions at the end of the pyrolyzing slab. However, an approximate similarity solution is found for forced flow which yields explicit flame heights. Based on these results, explicit functional fits to numerical flame heights are obtained for free and mixed-mode flows. Comparisons between theory and experiment indicate quantitative agreement.

Introduction

The development of laminar, forced, free, and mixed-mode convection flames above both wall-mounted and free-standing vertical burning surfaces is examined. This study is a natural extension of previous investigations of laminar combusting boundary layers [1–7]. The limits of pure forced and pure free flow combustion downstream of vertical pyrolyzing surfaces have been examined by Pagni and Shih [4] and by Faeth and co-workers [5, 6], while mixed-mode diffusion flames adjacent to a burning fuel slab have been analyzed by Shih and Pagni [7]. The present investigation extends the analysis of mixed-mode combustion into the region above the fuel source and provides accurate explicit expressions for flame heights in all six cases considered. Good agreement is obtained with experiments.

The six systems analyzed are illustrated schematically in Fig. 1. The two geometries given in Figs. 1(a) and 1(b) are: (1a) combustion adjacent to an inert, adiabatic, vertical extension above the fuel slab, referred to as "wall-wake" or "wall-plume" combustion, and (1b) combustion above a free-standing fuel slab referred to as "wake" or "plume" combustion. Three flow regimes are considered for each geometry: (1) forced flow: $\xi_x \ll 1$, (2) free flow: $\xi_x > 1$, and (3) forced and free mixed-mode flow: $\xi_x = 0(1)$. In each case a uniform stream of oxidizer approaches the vertical fuel plate and reacts with pyrolyzed fuel in a thin diffusion flame.

All systems have two regions: a pyrolysis zone where energy transfer to the fuel produces mass transfer into the flow and partial fuel consumption occurs, and an extended flame zone where pyrolysis ceases and the combustion process is completed. The abrupt change in boundary conditions between these regions disallows similarity; hence, numerical techniques are employed. For pure forced flow combustion, however, an approximate similarity model is developed which yields flame heights in terms of known combustion parameters. The analyses are presented in order of increasing complexity, viz., pure forced, pure free, and then mixed-mode combusting flow.

Forced Flow Combustion

Analyses. The boundary-layer equations which govern two-dimensional, laminar flows with fast kinetics are well known, hence the mathematical treatment is abbreviated. Making the usual Shvab-Zeldovich and boundary-layer assumptions, the continuity, momentum, and coupled energy-species equations for forced flow combustion, neglecting dissipation and radiation, are, in turn,

$$\frac{\partial}{\partial x}(\rho u) + \frac{\partial}{\partial y}(\rho v) = 0$$

$$\rho u \frac{\partial u}{\partial x} + \rho v \frac{\partial u}{\partial y} = \frac{\partial}{\partial y}\left(\mu \frac{\partial u}{\partial y}\right) \tag{1}$$

$$\rho u \frac{\partial J}{\partial x} + \rho v \frac{\partial J}{\partial y} = \frac{\partial}{\partial y}\left(\rho D \frac{\partial J}{\partial y}\right)$$

in which J is the normalized energy-species variable. The stoichiometry is given by an assumed single-step overall chemical reaction,

$$\nu_f \text{ fuel} + \nu_{ox} \text{ oxidizer} \rightarrow \nu_p \text{ products} + Q \tag{2}$$

where Q denotes the energy released by ν_f moles of fuel in the reaction.

At the pyrolyzing surface, the streamwise velocity vanishes, the enthalpy is specified and energy and fuel balances yield the transverse velocity and the wall fuel concentration:

$$\rho_w v_w = \frac{\lambda}{c_p L}\frac{\partial h}{\partial y}\bigg|_w, \quad x \leqslant \ell$$

and

$$\rho_w v_w = \frac{\rho D}{Y_{fw} - Y_{f\ell}}\frac{\partial Y_f}{\partial y}\bigg|_w, \quad x \leqslant \ell. \tag{3}$$

The boundary conditions downstream of the pyrolyzing surface, $x > \ell$, depend on the specific system under consideration. For wall-wake combustion, the velocity vanishes at the adiabatic, inert wall along with the enthalpy and fuel gradients, whereas, for wake combustion, the transverse gradients of streamwise velocity, enthalpy, and fuel are zero along the axis of symmetry as is the transverse velocity. In

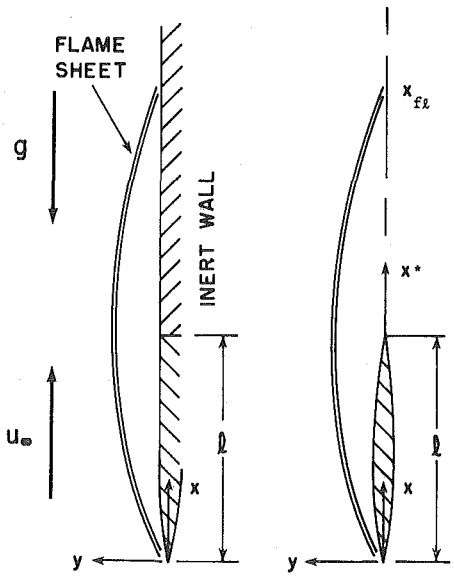

Fig. 1 System schematic of steady, laminar, mixed-mode combustion above a burning vertical fuel slab: (a) wall-wake combustion; (b) wake combustion

Contributed by the Heat Transfer Division for publication in the JOURNAL OF HEAT TRANSFER. Manuscript received by the Heat Transfer Division October 17, 1979.

all instances, the streamwise velocity, enthalpy, and oxidant approach their prescribed values in the free stream.

The following dimensionless variables are appropriate:

$$X \equiv \frac{x}{\ell}, \; Y \equiv \frac{\mathrm{Re}_\ell^{1/2}}{\ell} \int_0^y \frac{\rho}{\rho_\infty} dy,$$

$$U \equiv \frac{u}{u_\infty}, \; V \equiv \frac{\mathrm{Re}_\ell^{1/2}}{\rho_\infty u_\infty} \left(\rho v + u \int_0^y \frac{\partial \rho}{\partial x} dy \right) \tag{4}$$

in which $\mathrm{Re}_\ell \equiv u_\infty \ell / \nu_\infty$ is the slab Reynolds number. Assuming constant Pr and $\rho\mu$, the governing equations become

$$\frac{\partial U}{\partial X} + \frac{\partial V}{\partial Y} = 0,$$

$$U \frac{\partial U}{\partial X} + V \frac{\partial U}{\partial Y} = \frac{\partial^2 U}{\partial Y^2}, \tag{5}$$

$$U \frac{\partial J}{\partial X} + V \frac{\partial J}{\partial Y} = \frac{1}{\mathrm{Pr}} \frac{\partial^2 J}{\partial Y^2}.$$

In the pyrolysis region, $X \leqslant 1$, the boundary conditions, assuming $Y_{\mathrm{ox}_w} = 0$, are

$$U = 0, \; V = -\frac{B}{\mathrm{Pr}} \frac{\partial J}{\partial Y}\bigg|_w, \; J = 1 \text{ at } Y = 0 \tag{6}$$

$$U = 1, J = 0 \quad \text{as } Y \to \infty \tag{7}$$

where the mass transfer number is defined as

$$B \equiv [Q Y_{\mathrm{ox}\infty} / \nu_{\mathrm{ox}} M_{\mathrm{ox}} - h_w]/L \tag{8}$$

In the extended flame region, $X > 1$, equation (7) continues to apply, while equation (6) is replaced with

$$U = V = \frac{\partial J}{\partial Y} = 0 \text{ at } Y = 0, \tag{9}$$

for wall-wake combustion and

$$\frac{\partial U}{\partial Y} = V = \frac{\partial J}{\partial Y} = 0 \text{ at } Y = 0 \tag{10}$$

for wake combustion.

Temperature and species fields are readily obtained from $J(X, Y)$ using the flame-sheet approximation, i.e., fuel only exists inside and oxidizer only outside the flame. At the flame, $Y_f = Y_{\mathrm{ox}} = \beta = 0$, and $J_{f\ell}(X_{f\ell}, Y_{f\ell}) = r/(1 + r)$, which implicitly identifies the flame location. The mass consumption number, r, [4] is defined as the ratio of the relative available oxygen to the stoichiometrically required oxygen,

$$r \equiv Y_{\mathrm{ox}\infty} \nu_f M_f / Y_{fw} \nu_{\mathrm{ox}} M_{\mathrm{ox}}. \tag{11}$$

The surface fuel concentration, for $X \leqslant 1$, is known *a priori* [7] as

$$Y_{fw} = [Y_{ft} B - Y_{\mathrm{ox}\infty}(\nu_f M_f / \nu_{\mathrm{ox}} M_{\mathrm{ox}})]/(1 + B) \tag{12}$$

The flame height is that downstream location where all of the pyrolyzed fuel is consumed, here approximated as where the reaction sheet intersects $Y = 0$. Thus the flame height, $X_{f\ell}$, is implicitly given by

$$J_w(X_{f\ell}, 0) = J_{f\ell} = r/(1 + r). \tag{13}$$

Approximate Solution for Downstream Forced Flow. While the abrupt change in boundary conditions renders the flow field non-similar near the trailing edge of the fuel slab, it is likely that the combusting system again approaches self-similarity far downstream. An approximate profile of the Shvab-Zeldovich variable, J, in the extended flame zone is now found by coupling the pyrolysis zone similarity solution with a downstream similarity solution for $X \gg 1$. The assumption that the flame extension is large compared to the fuel slab length suggests the similarity variable,

$$\eta \equiv Y/2X^{1/2}. \tag{14}$$

The stream function, $\psi = f(\eta)X^{1/2}$, is defined by

$$U \equiv \frac{\partial \psi}{\partial Y} \text{ and } V \equiv -\frac{\partial \psi}{\partial X}. \tag{15}$$

The downstream velocity is then $U = f'(\eta)/2$. If it is assumed that $J/J_w(X)$ is only a function of η, i.e., $J/J_w(X) \equiv \theta(\eta)$, then

$$\theta'' + \mathrm{Pr}[f\theta' - 2f'\theta(J_w' X / J_w)] = 0 \tag{16}$$

is obtained by substituting these definitions into the energy-species equation (5). Primes denote differentiation with respect to the independent variables of $f(\eta)$, $\theta(\eta)$, and $J_w(X)$. To determine if a similarity solution can be found, i.e., if $J_w' X / J_w$ is independent of X, consider the integral form of the energy-species equation downstream of the fuel slab for an inert, adiabatic wall or symmetric wake:

$$\frac{d}{dx} \int_0^\infty \rho u J dy = 0, \; x > \ell. \tag{17}$$

Substituting θ, f' and equations (4) and (14) into equation (17) shows that indeed $J_w' X / J_w = -1/2$.

The downstream energy-species equation is now

$$\theta'' + \mathrm{Pr}(f\theta' + f'\theta) = 0 \tag{18}$$

subject to

$$\theta(0) = 1, \theta'(0) = 0, f(0) = 0. \tag{19}$$

The solution is simply

$$\theta(\eta) = \exp\left(-\mathrm{Pr} \int_0^\eta f(\eta)\, d\eta\right) \tag{20}$$

where $f(\eta)$ is obtained from the transformed momentum equation,

Nomenclature

B = mass transfer number, $(Q Y_{\mathrm{ox}\infty}/\nu_{\mathrm{ox}} M_{\mathrm{ox}} - h_w)/L$
c_p = specific heat
D = species diffusivity
D_3 = dimensionless heat of combustion, $Q Y_{\mathrm{ox}\infty}/\nu_{\mathrm{ox}} M_{\mathrm{ox}} h_w$
f = similarity stream function
Gr_x = Grashof number, $g(T_w - T_\infty)x^3/\nu_\infty^2 T_\infty$
g = acceleration of gravity
h = specific enthalpy, $\int_{T_\infty}^{T} c_p\, dT$
J = normalized Shvab-Zeldovich variable, $(\beta - \beta_\infty)/(\beta_w - \beta_\infty)$ or $(\gamma - \gamma_\infty)/(\gamma_w - \gamma_\infty)$
L = effective latent heat of pyrolysis
ℓ = fuel slab length
M_i = molecular weight of specie i
Pr = Prandtl number
Q = energy released by combustion of ν_f moles of gas phase fuel
Re_x = Reynolds number, $u_\infty x/\nu_\infty$
r = mass consumption number, $Y_{\mathrm{ox}\infty}\nu_f M_f / Y_{fw}\nu_{\mathrm{ox}} M_{\mathrm{ox}}$
S = total flux of J in extended flame zone
U = dimensionless streamwise velocity
u = streamwise velocity
V = dimensionless transverse velocity
v = transverse velocity
X = dimensionless streamwise coordinate
x = streamwise coordinate
Y = dimensionless transverse coordinate
y = transverse coordinate
Y_i = mass fraction of specie i
$\beta = Y_f/\nu_f M_f - Y_{\mathrm{ox}}/\nu_{\mathrm{ox}} M_{\mathrm{ox}}$
$\gamma = -h/Q - Y_{\mathrm{ox}}/\nu_{\mathrm{ox}} M_{\mathrm{ox}}$
η = similarity variable
θ = Shvab-Zeldovich variable
λ = conductivity
μ = viscosity
ν = kinematic viscosity or stoichiometric coefficient
ξ_x = mixed convection number, $\mathrm{Gr}_x/\mathrm{Re}_x^2$
ρ = density
ϕ = enthalpy ratio, h/h_w

Subscripts

f = fuel
$f\ell$ = flame
ox = oxidizer
t = transferred gas
w = fuel surface
∞ = ambient

Superscripts

* = measured from the downstream edge of the fuel slab

$$f''' + ff'' = 0 \tag{21}$$

with the boundary conditions,

$$f(0) = 0, f'(\infty) = 2$$

and

$$f'(0) = 0 \text{ or } f''(0) = 0 \tag{22}$$

for wall-wake or wake combustion, respectively. For wall-wake combustion, the system is identical to the Blasius problem for flow over a flat plate and although no closed-form expression for $f(\eta)$ exists, numerical solutions are well known [8]. For wake combustion, the solution for $f(\eta)$ is

$$f(\eta) = 2\eta. \tag{23}$$

These results are simply the two asymptotes for $X \gg 1$, i.e., flat plate flow for wall-wake combustion and uniform flow for wake combustion.

In the pyrolysis region, the energy-species equation in integral form is

$$\frac{d}{dx}\int_0^\infty \rho u J dy = \rho_w v_w J_w - \rho D \left.\frac{\partial J}{\partial y}\right|_w, \; 0 < x < \ell. \tag{24}$$

Substituting equations (4) and (6) into equation (24) and integrating along the length of the fuel slab yields

$$S \equiv \int_0^\infty UJdY = \left(\frac{1+B}{B}\right)\int_0^1 V_w dX \text{ at } X = 1. \tag{25}$$

Equation (17) indicates that S remains constant throughout the extended flame zone; i.e., J is conserved. J is generated along the pyrolyzing surface and is never consumed in the flow field. The extended flame region is effectively coupled to the pyrolysis region through a single source of J, with strength S, located at the trailing edge of the slab.

The flame height is obtained by considering the variation of J_w for $X > 1$ or $X^* > 0$. From equation (25),

$$J_w(X^*) = S/(X^{*1/2}\int_0^\infty f'\theta d\eta) \tag{26}$$

where X^* is the streamwise coordinate measured from the trailing edge of the fuel slab. The flame height is the X^* at which $J_w = J_{f\ell}$; i.e.

$$X^*_{f\ell} = S^2/(J_{f\ell}\int_0^\infty f'\theta d\eta)^2. \tag{27}$$

Numerical integration of equations (20, 21) yields $\int_0^\infty f'\theta_{(\text{wall-wake})}d\eta \approx 1.5\,\text{Pr}^{-0.6}$, while equations (20) and (23) give analytically $\int_0^\infty f'\theta_{(\text{wake})}d\eta = (\pi/\text{Pr})^{1/2}$; so that

$$X^*_{f\ell(\text{wake})}/X^*_{f\ell(\text{wall-wake})} \approx 0.72\,\text{Pr}^{-0.2}, \tag{28}$$

i.e., wake flame heights are ~3/4 (wall-wake flame heights).

The B number dependence of $S(\text{Pr}, B)$ can be made explicit by fitting total pyrolysis rate computations,

$$S \approx 0.56\,\text{Pr}^{-0.6}\,B^{-1.15}\,(1+B)\,\ell\text{n}\,(1+B),\; 0.5 \leqslant B \leqslant 5,\; 0.5 \leqslant \text{Pr} \leqslant 2 \tag{29}$$

Since the generation of J by diffusion decreases with increased blowing, the B dependence of S is weaker than the B dependence of the total pyrolysis rate, as shown by the pre-integral factor in equation (25). Substituting equations (13) and (29) and the $\int_0^\infty f'\theta d\eta$ fit into equation (27) yields an approximate explicit expression for the wall-wake flame height,

$$X^*_{f\ell(\text{wall-wake})} \approx 0.14\,[(1+r^{-1})(1+B^{-1})\,B^{-0.15}\,\ell\text{n}\,(1+B)]^2 \tag{30}$$

for $0.5 \lesssim B \lesssim 5.0$, $0.5 \lesssim \text{Pr} \lesssim 2.0$ and all r. As examples, equation (30) gives $X^*_{f\ell} = 19$ and 1.9 respectively for polystyrene ($r = 0.14$, $B = 1.3$) and cellulose ($r = 0.59$, $B = 0.8$). Equation (30) also fits the numerical $X^*_{f\ell}$ shown in Fig. 2 within 15 percent for $0.1 \leqslant r \leqslant 0.5$. The dominant parameter in equation (30) is r which entered only through $J_{f\ell}$. $X^*_{f\ell}$ increases strongly as r decreases, since small r implies that much fuel is available relative to that which is required by stoichiometry and thus long flames are produced.

Additional Results. Numerical solutions were also obtained using the Patankar-Spalding finite difference method (GENMIX) [9, 10] which employs streamwise marching integration. The computations were initiated near the leading edge of the pyrolyzing slab ($X = 0.01$) assuming standard, cubic, forced-flow profiles for U and J. Mass transfer (blowing) effects at the pyrolyzing surface were included. Employing 50 cross-stream grid nodes, the step-by-step procedure traversed the pyrolysis region and continued into the extended flame zone. The ratio of the streamwise step size to the current boundary-layer thickness was initialized at 0.01 and gradually increased along the length of the plate. At the trailing edge of the slab, the step size ratio was reset to 0.01 and again progressively increased downstream. As a check on the numerics, the surface gradients on the pyrolyzing slab at the trailing edge gave agreement with similarity results [11] within one percent. Detailed profiles and surface fluxes were calculated; flame height results are emphasized here.

Fig. 2 presents flame heights measured from the downstream edge as functions of B parameterized in r for (a) wall-wake and (b) wake combustion obtained with equation (27) and S from similarity solutions, an integral approach [4], and GENMIX. Good agreement between this approximate solution and GENMIX is observed for flame heights in excess of one slab length. It appears that the simple model based on conservation of J and large X asymptotic profiles is valid for synthetic polymer fuels. For short flames, this approximate solution overpredicts flame heights, as expected, since large $X^*_{f\ell}$ is an

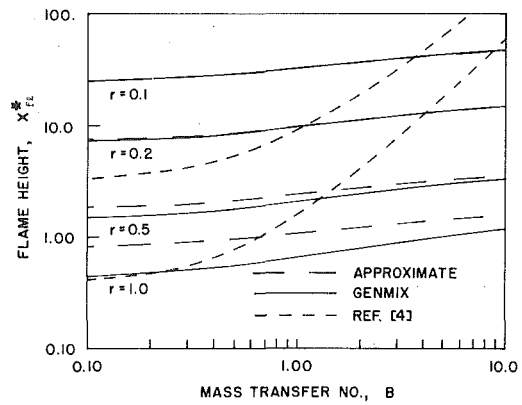

Fig. 2(*a*) Dimensionless flame height in a wall-wake measured from trailing edge of fuel slab versus mass transfer number parameterized in mass consumption number for Pr = 0.73

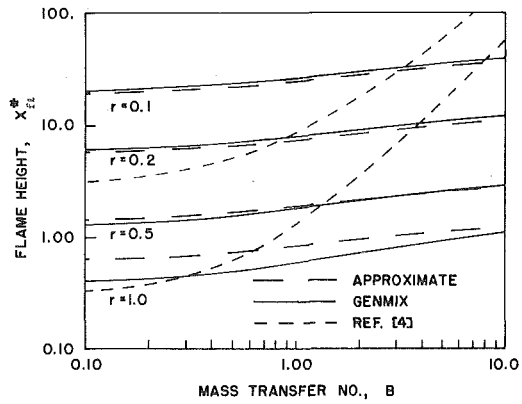

Fig. 2(*b*) Dimensionless flame height in a wake measured from trailing edge of fuel slab versus mass transfer number parameterized in mass consumption number for Pr = 0.73

essential model assumption; indeed, the accuracy as low as $X^*_{f\ell} \sim 1$ is surprisingly good. The previous approach [4] shows agreement with the GENMIX results only for short flame heights, $X^*_{f\ell} < 1$, typical of natural polymer fuels.

Many trends agree with those obtained from the previous integral analysis [4], namely: flame heights increase with increasing B number and decreasing r number, wall-wake flames are longer than wake flames, and the dimensionless flame height is independent of Reynolds number. Quantitative differences are obvious, however; the present analysis shows a much weaker dependence of flame height on B number. Briefly, the integral analysis assumed polynominal profiles for fuel and velocity fields normalized on wall/centerline values which had to be obtained as functions of X from local elemental balances. While the approximate polynomials might suffice in the integral equations, they are not adequate to determine proper wall/centerline values from differential expressions. Such an approach can only succeed when the flow is similar. The poor representation of the detailed profiles in the non-similar region led to loss of conservation of the total flux of fuel which became worse the further the flame extended beyond the pyrolysis zone. The excess pyrolyzate results reported [4] for the end of the pyrolysis zone were correct. Here S is held constant throughout the extended flame zone, $X^* \geq 0$. This emphasis on S, the total flux of the Shvab-Zelovich energy-species variable J, is responsible for the agreement with the numerical solution and for the difference from the previous approximate integral approach.

The constancy of the total flux of the Shvab-Zeldovich variable downstream of the fuel slab demands that a balance be maintained between velocity and J in the extended flame zone. Any decrease in average velocity is thus accompanied by an increase in J; a longer distance is then required for J to decay down to $J_{f\ell}$. Thus longer flames result whenever the velocity is retarded, as in the case of the wall-wake, Fig. 2(a), compared with the wake, Fig. 2(b). The approximate solution for wake combustion neglects the velocity defect that may exist for some distance downstream of the slab. This velocity defect will produce longer flames, therefore the slightly larger GENMIX results in Fig. 2(b) are expected even at large $X^*_{f\ell}$. The approximate flame height ratio given by equation (28) is thus a lower bound. The overprediction at short $X^*_{f\ell}$ is primarily caused by placing the source in the approximate model, S, at the trailing edge of the fuel slab rather than upstream in the pyrolysis region. A simple procedure for more accurately locating the source is not obvious.

Comparisons with Experiment. Flame heights in the wall-wake of PMMA samples burning in O_2/N_2 mixtures were measured in a small wind tunnel 12 cm wide by 5 cm high. Slabs of PMMA of lengths 1.3 and 1.6 cm and width 9.0 cm were approximately flush mounted in the martinite floor of the test section. Y_{ox_∞} was varied from 30 to 100 percent producing B numbers from 2.0 to 8.0 and r numbers from 0.25 to 0.65 [12]. Data were taken at two free-stream velocities, 85 cm/s and 170 cm/s, determined by corrected volume flow rate measurement. Gas and wall temperatures were monitored. Steady-state flame heights were recorded with an 8 mm movie camera. Fig. 3, which plots the dimensionless flame height, $X^*_{f\ell}$, versus free stream oxygen mass fraction, Y_{ox_∞}, shows good agreement between theory, equation (30), and experiment. Radiation is probably responsible for the experiments slightly exceeding predictions. Though thin, these flames are very luminous. Net radiation to the pyrolyzing surface would, by decreasing L, increase B, and through the B dependence of Y_{fw} decrease r and thus increase $X^*_{f\ell}$. The data confirm that larger r numbers, produced by higher ambient oxygen concentrations, yield shorter flames and that the dimensionless flame height is independent of Reynolds number.

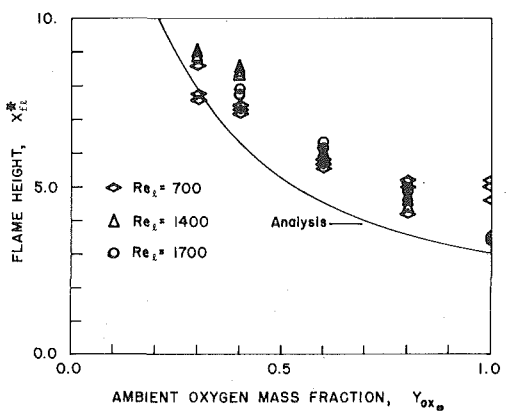

Fig. 3 Comparison of experimental and theoretical dimensionless flame heights for PMMA in wall-wake combustion as function of ambient oxygen mass fraction

Free Flow Combustion

Analyses. The equations which govern free flow combustion near an upright burning surface are identical to the forced flow relations, equation (1), with the obvious modification of a buoyancy term in the momentum equation,

$$\rho u \frac{\partial u}{\partial x} + \rho v \frac{\partial u}{\partial y} = \frac{\partial}{\partial y}\left(\mu \frac{\partial u}{\partial y}\right) + g\,(\rho_\infty - \rho). \tag{31}$$

Here the appropriate dimensionless variables are

$$X \equiv \frac{x}{\ell},\ Y \equiv \frac{\mathrm{Gr}_\ell^{1/4}}{\ell}\int_0^y \frac{\rho}{\rho_\infty}\,dy$$

$$U \equiv \frac{u\ell}{\mathrm{Gr}_\ell^{1/2}\nu_\infty},\ V \equiv \frac{\ell}{\mathrm{Gr}_\ell^{1/4}\rho_\infty\nu_\infty}\left(\rho v + u\int_0^y \frac{\partial \rho}{\partial x}\,dy\right) \tag{32}$$

in which $\mathrm{Gr}_\ell \equiv g(T_w - T_\infty)\ell^3/\nu_\infty^2 T_\infty$, is the slab Grashof number. The natural convection momentum equation then becomes

$$U\frac{\partial U}{\partial X} + V\frac{\partial U}{\partial Y} = \frac{\partial^2 U}{\partial Y^2} + \phi \tag{33}$$

where, assuming uniform mixture specific heat and molecular weight across the boundary layer, ϕ is the enthalpy ratio, h/h_w, which in the flame-sheet approximation is

$$\phi = D_3 + (1 - D_3)J,\ Y \leq Y_{f\ell}$$

and (34)

$$\phi = (1 + D_3/r)J,\ Y \geq Y_{f\ell}.$$

Equations (34) introduce the single new parameter needed to describe free flow combustion,

$$D_3 \equiv \frac{QY_{ox_\infty}}{\nu_{ox}M_{ox}h_w}, \tag{35}$$

a dimensionless heat of combustion. The transformed continuity and energy-species equations are identical to equation (5) while the boundary conditions are given by equations (6–10) with the exception that

$$U = 0 \text{ as } Y \to \infty. \tag{36}$$

The strong coupling between velocity and thermal fields in combusting plumes makes it more difficult to formulate simple approximate solutions, however, using the forced flow results, equations (28) and (30) as guides, the following fits, accurate to 10 percent, were obtained from GENMIX results:

$$X^*_{f\ell(\text{wall-plume})} \approx 0.24[(1 + r^{-1})r^{-0.16}(1 + B^{-1})B^{-0.06}\ell\mathrm{n}(1 + B)D_3^{-0.03}]^{4/3} \tag{37}$$

and

$$X^*_{f\ell(\text{plume})}/X^*_{f\ell(\text{wall-plume})} \approx 0.9 \tag{38}$$

for $0.1 \lesssim r \lesssim 0.5$, $0.5 \lesssim B \lesssim 5$, $2 \lesssim D_3 \lesssim 60$, and $\mathrm{Pr} = 0.73$.

Results. Numerical computations were performed by GENMIX using natural convection profiles as initial conditions for the marching process [13], the details of which closely parallel the forced flow calculations. The combined body force and pressure gradient term, ϕ, was treated as an apparent pressure gradient in the finite difference code. The surface gradients at the trailing edge of the pyrolyzing slab

once more compared well with similarity results as a check of the numerics. The free flow flame heights, plotted in Fig. 4 as functions of B parameterized in r for both plume and wall-plume combustion, show trends analogous with forced convection results. Although the previous integral analysis [4] indicated variations with Grashof number, the present analysis shows that Gr_ℓ can be eliminated from both the nondimensional problem, equations (33–36), and X, equation (32), so that flame heights are independent of Grashof number. Both the excess and total pyrolyzate are $\sim Gr_\ell^{1/4}$, so that the unburned fraction is also independent of Gr_ℓ.

Comparisons with Experiment. The free convection flame heights from equations (37) and (38), given in Table 1, show reasonable agreement with both experimental results and other numerical results. The shortness of the experimental alcohol flame heights compared with either prediction may be due to quenching [5] or low luminosity. The polymer experimental flame heights suggest, as in the forced case, a role for radiation since the more luminous polymer flames are larger while the less luminous alcohol flames are shorter than predicted. The wall-plume alcohol data and analysis [5] differed from the present study by fixing the wall temperature at T_w for all X. Here $\phi(X, 0)$ increases approximately exponentially from 1 for $X^* \leq 0$ to $(D_3 + r)/(1 + r)$ at $X^*_{f\ell}$. Note that the r defined in [5, 6] does not include Y_{fw} and that slightly different alcohol B values were used in [5], in [6] and in Table 1.

Mixed-Mode Combustion

Analyses. The phenomenon of mixed-mode combustion spans the limits of pure forced and pure free flow combustion. The governing equations are identical to those for free convection, equations (1) and (31). Adopting the dimensionless variables used in the forced flow limit, equation (4), the momentum equation becomes

$$U\frac{\partial U}{\partial X} + V\frac{\partial U}{\partial Y} = \frac{\partial^2 U}{\partial Y^2} + \xi_\ell \phi \tag{39}$$

where $\xi_\ell \equiv Gr_\ell/Re_\ell^2$ is the mixed convection ratio or inverse Froude number. The transformed continuity and energy-species equations (5) remain unchanged. The choice of the forced flow transformations is dictated by the simpler boundary conditions, equations (6–10).

Results. The only new parameter introduced in mixed-mode flames is ξ_ℓ. Consistent with the two cases already examined, no additional parameters emerge from the analysis of the diffusion dominated extended flame zone downstream of the pyrolysis region. Numerical solutions using GENMIX in the pure forced flow manner are shown in Fig. 5 as a function of mixed convection ratio, ξ_ℓ, parameterized in r, at a fixed mass transfer number, $B = 1.0$, with $Pr = 0.73$ and $D_3 = 4.0$ for both wake and wall-wake geometries. The limits of pure forced flow, $\xi_\ell \to 0$, and pure free flow, $\xi_\ell \to \infty$ are shown for comparison. The smooth transition from forced to free as ξ_ℓ increases suggests that mixed-mode combustion is approximately a simple superposition of the two limiting flame cases. A local similarity analysis in the pyrolysis region [7] suggested otherwise. However, such an approximation over-predicts surface velocity gradients and under-predicts surface J gradients yielding larger velocities near the wall and larger flame standoff distances than the GENMIX results. Thus the local similarity approximation overestimated the unburned fraction of total pyrolyzate for ξ_ℓ far from the forced limit. This study finds the unburned fraction monotonically increasing with ξ_ℓ, correctly approaching the free limit for $\xi_\ell > 1$.

As discussed in the forced flow section, downstream conservation of the total flux of J requires that increases in the average velocity lead to faster decays in the average value of J and thus to shorter flames. Such is the case with free flow where acceleration occurs in the extended flame zone due to buoyancy. This explains the decrease in flame height shown in Fig. 5 as ξ_ℓ increases in spite of the increase in unburned fraction of total pyrolyzate in the pyrolysis region [4, 7]. As in both flow limits, flame heights in mixed-mode combustion are primarily dependent on r, increasing with decreasing r number. Fitting numerical results similar to Fig. 5 over $0.5 \lesssim B \lesssim 5.0$ and $0.1 \lesssim r \lesssim 0.5$, for $Pr = 0.73$ and $D_3 = 4.0$ yields the following interpolation between the pure flow flame height limits,

$$\frac{X^*_{f\ell(\text{mixed})}}{X^*_{f\ell(\text{free})}} \approx (1.0 - \xi_\ell^{0.2})\frac{X^*_{f\ell(\text{forced})}}{X^*_{f\ell(\text{free})}} + \xi_\ell^{0.2}, \quad \xi_\ell \leq 1$$
$$\approx 1.0, \qquad \xi_\ell > 1 \tag{40}$$

with an accuracy of 15 percent. Thus mixed-mode flame heights are readily obtained from equations (28, 30, 37, 38) and (40).

Table 1 Free flow flame height comparisons

					Wall-Plume		Plume	
Material	Monomer	r	B	D_3	Experiment	Analysis	Experiment	Analysis
propanol	C_3H_7OH	0.12	4.2	25	10[a]	15, 13[a]	9[b]	13, 11[b]
ethanol	C_2H_5OH	0.15	3.6	36	8[a]	11, 10[a]	9[b]	9.6, 9.4[b]
methanol	CH_3OH	0.22	2.9	56	4[a]	5.7, 5.3[a]	5[b]	5.2, 4.3[b]
PMMA	$C_5H_8O_2$	0.21	1.6	6.6	6[c]	5.5	—	5.0
POM	CH_2O	0.47	1.2	9.4	3[c]	1.9	—	1.7

[a] Ahmad and Faeth [5], [b] Groff and Faeth [6], [c] This laboratory

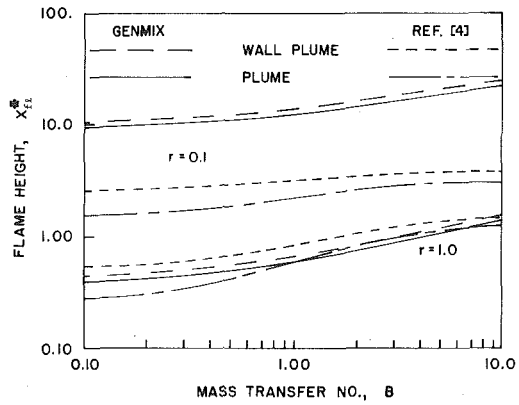

Fig. 4 Dimensionless flame height measured from trailing edge of fuel slab versus mass transfer number parameterized in mass consumption number for free convection with $D_3 = 4.0$ and $Pr = 0.73$

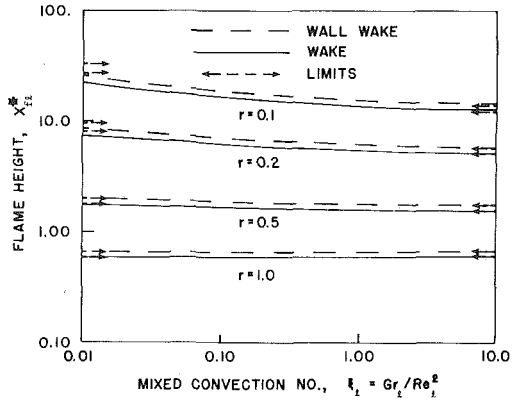

Fig. 5 Dimensionless flame height measured from trailing edge of fuel slab versus mixed-convection ratio parameterized in mass consumption number for $B = 1.0$, $D_3 = 4.0$ and $Pr = 0.73$

Conclusions

In summary, from the detailed steady, laminar, two-dimensional, nonradiating, combusting boundary layer analyses of six systems (wall-wake, wake, wall-plume, plume, mixed-mode wall-wake and mixed-mode wake), emphasizing the constancy of the flux of the Shvab-Zeldovich energy-species variable J in the extended flame region, the following conclusions are drawn:

1 For forced flow, $X^*_{f\ell}(r, B, \mathrm{Pr})$ and is independent of Re_ℓ. Explicit expressions are presented which quantify the strong increase in $X^*_{f\ell}$ as r decreases and the moderate increase in $X^*_{f\ell}$ as B increases. The Pr dependence is very weak. Good agreement with experiment is obtained.

2 For free flow, $X^*_{f\ell}(r, B, \mathrm{Pr}, D_3)$ and is independent of Gr_ℓ. Explicit fits to numerical results are given which quantify the r and B dependence as in forced flow. The dependence on D_3 and Pr is weak. Free flow flames are generally shorter than forced flow flames for the same fuel and ambience. Reasonable agreement with experiment is obtained.

3 For mixed-mode flow, $X^*_{f\ell}(r, B, \mathrm{Pr}, D_3, \xi_\ell)$ with the forced and free limits approached at $\xi_\ell \lesssim 10^{-2}$ and $\xi_\ell \gtrsim 1$ respectively. The mixed-mode case appears to be a simple superposition of forced and free flow.

4 Wall-mounted flames are longer than free-standing flames for the same fuel and ambience. This difference depends on flow type and Pr, i.e., wall-wake flames are ~30 percent longer than wake flames, wall-plume flames are ~10 percent longer than plume flames.

Future effort will be directed at extending these analyses to include radiation and turbulence. More experimental results for comparison would be valuable. It is hoped that flame height measurement under controlled conditions will become one of the standard procedures for assessing material fire hazard.

Acknowledgments

Mr. R. Beier obtained the experimental data reported in Fig. 3. The authors appreciate support from the Products Research Committee and from the National Bureau of Standards—Fire Research Center. The conclusions are those of the authors and not of the Products Research Committee nor the National Bureau of Standards.

References

1 Emmons, H. W., "The Film Combustion of Liquid Fuel," *Zeitschrift fuer Angewandte Mathematik und Mechanik,* Vol. 36, 1956, pp. 60–71.

2 Kosdon, F. J., Williams, F. A., and Buman, C., "Combustion of Vertical Cellulosic Cylinders in Air." *Twelfth Symposium (International) on Combustion,* The Combustion Institute, 1969, pp. 253–264.

3 Kim, J. S., de Ris, J., and Kroesser, F. W., "Laminar Free-Convective Burning of Fuel Surfaces," *Thirteenth Symposium (International) on Combustion,* The Combustion Institute, 1971, pp. 949–961.

4 Pagni, P. J., and Shih, T. M., "Excess Pyrolyzate," *Sixteenth Symposium (International) on Combustion,* The Combustion Institute, 1976, pp. 1329–1342.

5 Ahmad, T., and Faeth, G. M., "An Investigation of the Laminar Overfire Region Along Upright Surfaces," ASME JOURNAL OF HEAT TRANSFER, Vol. 100, 1978, pp. 112–119.

6 Groff, E. G., and Faeth, G. M., "Laminar Combustion of Vertical Free-Standing Fuel Surfaces," *Combustion and Flame,* Vol. 32, 1978, pp. 139–150.

7 Shih, T. M., and Pagni, P. J., "Laminar Mixed-Mode, Forced and Free, Diffusion Flames," ASME JOURNAL OF HEAT TRANSFER, Vol. 100, 1978, pp. 253–259.

8 Schlichting, H., *Boundary-Layer Theory,* 6th ed., McGraw-Hill, 1968, p. 193.

9 Patankar, S. V., and Spalding, D. B., *Heat and Mass Transfer in Boundary Layers,* Morgan-Grampian, West Wickham, 1967.

10 Spalding, D. B., "A General Computer Program for Two-Dimensional Boundary Layer Problems," Report No. HTS/73/48, Department of Mechanical Engineering, Imperial College of Science and Technology, 1973.

11 Shih, T. M., "Excess Pyrolyzate from Diffusion Flames," Ph.D. Thesis, Mech. Engr. Dept., University of California, Berkeley, 1977.

12 de Ris, J., "Fire Radiation—A Review," *Seventeenth Symposium (International) on Combustion,* The Combustion Institute, 1979, pp. 1003–1016.

13 Sparrow, E. M., Patankar, S. V., and Abdel-Wahed, R. M., "Development of Wall and Free Plumes Above a Heated Vertical Plate," ASME JOURNAL OF HEAT TRANSFER, Vol. 100, 1978, pp. 184–190.

Spray Quenching in a Ventilated Duct Fire

I. S. Habib

Professor of Mechanical Engineering,
The University of Michigan—Dearborn,
Dearborn, Mich. 48128
Mem. ASME

Analysis of the interaction between cold liquid sprays, a flowing hot gas, and an ignited duct wall is presented. This situation simulates what could be the result of a fire spread in an underground ventilated wood lined corridor or a coal mine entry. Spread of an ignition front is defined as the rate of propagation of a specific ignition temperature along the solid wall. Radial wall conduction, heat and mass transfer associated with the liquid sprays, convection at the wall, and surface, luminous, and nonluminous radiative interchange are accounted for. The zone method of solution is chosen as it can accommodate real gas effects in the analysis, and the adaptability of this approach to include luminous flames proved to be successful. Wall friction is included through the use of a friction coefficient. The results presented show in the direction of flow the variation in the temperature of the duct, the gas, and the liquid droplets. Also presented is the quenching distance along the duct at which wall ignition ceases as a function of spray distribution, air flow rate, and other pertinent parameters. The results give qualitative and quantitative assessment of the parameters which control a fire spread identified by the model presented.

Introduction

The mechanism of fire spread in ventilated ducts lined with a combustible material is quite complex. The interdependency of liner ignition, luminous and nonluminous radiative interchange, wall conduction and convection, and the possible presence of cold liquid sprays yield a problem which requires simplifications and reasonable assumptions in order to obtain, however limited, adequate qualitative and quantitative results.

Modeling techniques have been presented for flame propagation in combustible mixture and in duct fires. Krazinski, et al. [1] presented a model describing steady, laminar flames propagation in coal dust-air mixture. They included radiative transport, two-phase energy equation and heterogeneous carbon gasification of the coal particles. Edwards, et al. [2] developed a theoretical model describing fire spread in the axial direction along the surface of a cylindrical coal-lined duct. They included only surface radiation along with convection and radial conduction at the solid surface. In their analysis they define a flame spread as the rate of the propagation of a specific ignition temperature along the solid surface. Pagni and Han [3] studied the temperature fields in solids beneath spreading flames using a steady state two-dimensional analysis. Steward [4] discussed in some detail a line fire which is a fire with one dimension very much larger than the other two so a two-dimensional analysis can be invoked. Richmond and Liebman [5] presented a physical description of coal mine explosions with experimental results in the form of wave diagrams. In their work they found that flame speed and air speed are practically equal up to 100 m/s. Emmons and Shen [6] analyzed the fire spread in paper arrays and conducted measurements on the rate of fire spread in a solid fuel array consisting of horizontal paper strips standing on edge, separated by various amounts of space. They concluded that ignition transients show evidence of several burning modes and in some cases the steady burning can also occur in two different ways at different speeds: namely, a vertical fire front and a front inclined at about 45 deg; both are stable and move at different speeds. Other work [7–9] presented discussion and analysis related to fire spread and ignition of thermally irradiated material.

There has been limited fundamental investigation of the extinction of a ventilated duct wall fire by liquid sprays. Previous investigations of fire extinction by water have dealt mainly with pool fires and wood crib fires [10–12]. Furthermore, these studies focused on the extent of penetration of the water drops through the fire plume to the burning fuel surface and also dealt with the effect of burning rate and water application rate on extinction. Magee and Reitz [9] investigated experimentally the extinguishment of radiation augmented plastic fires by water sprays. They dealt with single slabs of four different plastics which were subjected to turbulent burning, two as a vertical wall and four as a pool fire. They identified critical conditions for extinguishment of each plastic.

In the present analysis we consider the case of an ignited and ventilated duct wall in which a flame and an ignition front propagate along the duct. The objective is to determine the quenching distance at which wall ignition ceases as a function of liquid spray distribution, liquid to gas ratio, and duct length to diameter ratio, and also to obtain the gas, wall and droplets temperature history in the direction of the flow. The interaction of conductive, convective, and radiative (surface, luminous, and non-luminous) heat transfer in the duct with heat and mass transfer from cold liquid sprays is considered.

Analysis

The model chosen for analysis is shown in Fig. 1. It represents the flow of atmospheric air with a velocity V through a burning segment in a circular duct; instantaneously the air is exposed to a cold liquid spray as it passes the burning duct wall. The wall is considered to be a combustible substance such as coal or wood and assumed to lose heat by conduction radially while axial conduction is ignored. The droplets are assumed to be spherical and the flow involves a one-dimensional quasi-steady transport of heat and mass with no shattering and no coalescence of the droplets, and no liquid deposition by migration or settling on the duct walls; hence the spray is thin.

Gas Stream and Wall Conditions. The zonal method is used in this analysis as the approach can accommodate real gas effects including luminous radiation. An energy balance on a volume zone (Fig. 1) yields

$$[\dot{m}_g(h_g + V_g{}^2/2)]_1 + [\Sigma \dot{m}_d(h_d + V_d{}^2/2)]_1 + \sum_j \vec{G}_j G_i E_{g,j} + \sum_j \vec{S}_j G_i E_{s,j} + \vec{S}_e G_i E_e + \vec{S}_o G_i E_o - 4K_i V_i E_{g,i} - hA_s(T_{g,i} - T_{s,i}) = [\dot{m}_g(h_g + V_g{}^2/2)]_2 + [\Sigma \dot{m}_d(h_d + V_d{}^2/2)]_2 + d/dt\,[(\Sigma m_d(h_d + V_d{}^2/2]_i. \quad (1)$$

The terms in equation (1) respectively represent: gas stream energy at inlet, droplets energy at inlet, radiant energy emitted by volume zones and absorbed by volume V_1, radiant energy leaving surface zones at the duct wall (S_j), at entrance (S_e), and at outlet (S_o) of the duct and absorbed by volume V_i, and then followed by volume zone emission and a convection heat transfer term. The right hand side of the equation represents, respectively, the gas stream energy at outlet,

Contributed by the Heat Transfer Division for publication in the JOURNAL OF HEAT TRANSFER Manuscript received by the Heat Transfer Division.

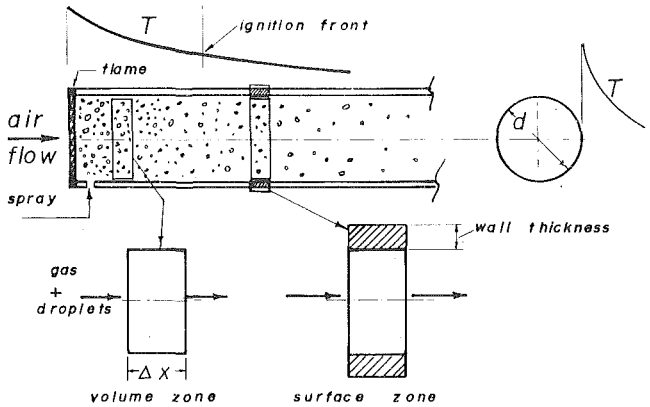

Fig. 1 The model chosen for the study (physical properties of coal are used)

droplets energy at outlet, and the time rate of change of droplets energy within the control volume or zone. An energy balance on a surface zone gives

$$Q_{s,i} = \sum_J \vec{S}_j S_i E_{s,i} + \vec{S}_e S_i E_e + \vec{S}_o S_i E_o + \sum \vec{G}_j S_i E_{g,j} - A_s E_{s,i} + hA_S(T_{g,i} - T_{s,i}) + W \quad (2)$$

where $Q_{s,i}$ represents the wall heat flux for a surface zone, and the rest of the terms are respectively: tube wall emission from surface zones, inlet surface emission, outlet surface emission, and volume zone emission, which are incident on a specific surface zone. The next three terms represent wall zone emission, convection heat transfer, and a heat source to account for an exothermic reaction. This term depends upon the wall mass depletion rate times the heat of reaction of the wall material; thus W is a rate of heat release.

Radiative Properties. While the zonal method is suitable for radiation from a nonluminous radiating gas, its adaptability to luminous flames proved to be successful [13–15] although the soot radiation is continuous over the spectrum. Accordingly, in this analysis the emittance of the gas is represented by [13–71]

$$\epsilon_m = \sum_n a_{g,n}(T)\,(1 - e^{-K_n L}) \quad (3)$$

where the equivalent absorption coefficient K_n is taken as the sum of the absorption coefficient of soot with concentration c and of the gas, and is represented by

$$K_n = \exp(q_{2,n}c + q_{1,n}) \quad (4)$$

The weighting factor $a_{g,n}$ is chosen to be a linear function of temperature of the form

$$a_{g,n}(T) = b_{1,n} + b_{2,n}T \quad (5)$$

Scattering in the analysis is ignored, and the duct wall emissivity is taken to be unity. Values for $b_{1,n}$ and $b_{2,n}$ are obtained from [13]. The total absorption coefficient K_i is expressed as

$$K_i = \sum_n a_{g,n}(T)K_n \quad (6)$$

p_c and p_w represent the partial pressures of carbon dioxide and water vapor respectively. The ratio of p_w/p_c is taken equal to one in the present analysis.

Wall Conduction and Convection. The transient heat loss from the wall is modeled as a semi-infinite solid bounded internally by a cylindrical surface for which the heat flux is given by [18]

$$Q_s = -k\left(\frac{\partial\theta}{\partial r}\right)_{r=r_0} = \frac{4k\theta_0}{r_0\Pi^2}\int_0^\infty e^{-\alpha u^2 t}\frac{du}{u[J_0^2(r_0u) + Y_0^2(r_0u)]} \quad (7)$$

Because the largest zone width chosen in this analysis is less than 2 cm, and a gas velocity of the order of 200 cm/s prevails, the duration of the flowing gas within each zone will be very short. Hence equation (7) for small times becomes

$$Q_s = -\frac{2\theta_0 k}{r_0}\left\{\frac{1}{\ln(4\phi) - 2\gamma} - \frac{\gamma}{[\ln(4\phi) - 2\gamma]^2}\right\} \quad (8)$$

where

$$\phi = \frac{\alpha t}{r_0^2},\ \gamma = 0.57722 = \text{Euler constant}$$

$$\theta = T - T_s, \qquad \theta_0 = T_s - T$$

Previous experimental and theoretical study on the interaction of convection with radiation for the case of the turbulent flow of a radiating gas [19] showed that the effect of radiation tends to increase the convection heat transfer coefficient by as much as 10 percent. Accordingly, for the present study, it is found adequate to use the relations for Nusselt number presented in [20] after augmenting it by 10 percent. This modification to the convection heat transfer coefficient is intended to improve the convection accuracy and does not imply that the level of radiation is prescribed a priori. Radiation effect is obtained through the solution of equations (1) and (2); see Table 1.

Nomenclature

A = area; A_d = droplet surface area; A_s = wall area
C_d = drag coefficient; c_p = specific heat at constant pressure
D = mass diffusivity of the vaporizing liquid; d = duct diameter
E = emissive power
F = friction factor $\equiv \tau_w/(\rho_{fm}V^2/2)$
G/L = gas to liquid ratio on a mass basis; L/G = liquid to gas ratio
$\vec{G}G, \vec{G}S$ = directed flux area; volume zone, volume and surface zones
h = heat transfer coefficient; h_0 = enthalpy of gas; h_d = enthalpy of droplet
J_0 = Bessel function of the first kind of order zero
K_n = equivalent absorption coefficient; K_i = total absorption coefficient for volume zone V_i
k = thermal conductivity; k_m = mass transfer coefficient
L = duct length
M = mass of droplet; $\dot{m}_g$ = mass flow rate of gas; $\dot{m}_d$ = mass flow rate of droplets of one size; $\Sigma\dot{m}_d$ = total mass flow rate of droplets summed over all sizes
$\mathcal{M}$ = molecular weight
Nu = Nusselt number
P = pressure; P_s = static pressure
Pr = Prandtl number = $(c_p\mu/k)_{fm}$
Q_d = heat received at droplet surface; Q_s = wall heat flux
R = universal gas constant; R_M, r_m = mass mean droplets radius r_d = drop radius, $r_{d,0}$ = initial droplet radius
r_0 = duct radius
Re = Reynolds number = $2r_dU\rho_{fm}/\mu_{fm}$
$\vec{SS}$ = directed flux area, surface to surface zones
Sc = Schmidt number = $\mu_{fm}/D\rho_{fm}$
Sh = Sherwood number
S = heat release per unit volume
T = temperature; $\overline{T} = (T_g + T_1)/2$; t = time; T_1 = gas initial temperature
U = velocity difference between gas and the droplet
V_g, V_G = gas velocity; V_d, V_D = droplet velocity, V_i = zone volume
W = equivalent heat source
w = vaporization rate
Y_0 = Bessel function of the second kind of order zero
α = thermal diffusivity
δ = vapor film thickness
μ = viscosity; droplet size in microns
ρ = density
σ_G = geometric standard deviation
τ_w = wall shear stress
ψ = volume of mass depleted

Subscripts

d,D = pertaining to droplet; droplet surface
f = vaporizing liquid vapor
fm = pertaining to the gas and vapor mixture
i = pertaining to zone i
$1d$ = liquid at surface of droplet
l = liquid
s,S = gas static conditions
g,G = gas
cs = cross-sectional

Table 1 Radiation effect on wall temperatures

$(Q_{r,i}/hA_sT_{s,i})$, percent
$L/G = 1.0$; $L = 6.3$m; $r_m = 50\mu$; $T_i = 555$ K; $S = 6.4 \times 10^{-4}$ KJ/cm^3
$V_g = 3$m/s, $\sigma = 2.3$, Droplets initial temperature = 311 K

	Distance Along the Duct, cm					
L/D	5.4	18.0	56.2	81.6	107.0	138.7
1.9	65.3	58.0	45.5	34.4	24.4	15.0
3.47	63.3	54.0	34.2	22.2	13.3	6.6
6.86	53.4	43.0	16.8	7.7	3.4	1.3
13.72	46.4	29.9	4.8	1.4	0.5	0.2

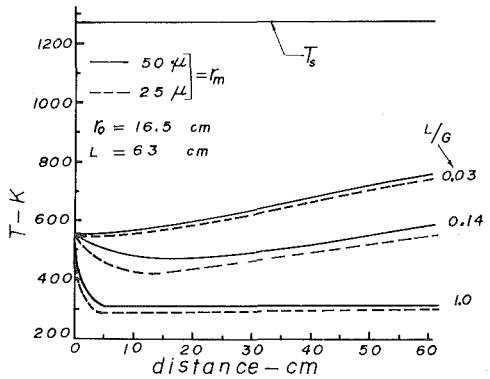

Fig. 2 Gas and wall temperature along the duct (T_i = 555 K; V_g = 3 m/s; S = 0.5 KJ/cm^3; F = 0.04; P_s = 1 atm; σ = 2.3, droplets initial temperature = 311 K)

Pertinent Conservation Equations and Droplet Size Distribution. The continuity, momentum, and equation of state for the gas and the equations of heat, momentum, and mass transfer from the droplets have been presented before in [21–23], and a summary of these equations is given in the appendix of this paper.

With respect to droplets sizes, a logarithmic normal distribution function was used to describe the droplets sizes and mass distribution (22–23). Five sizes were conveniently chosen from the log-normal scale such that the percent of drops smaller than a given radius is equal to 10, 30, 50, 70, and 90 percent. The number of drops was chosen such that each size constitutes twenty percent of the total liquid mass.

Results and Conclusions

Equations (1–8) along with the spray conservation equations listed in the appendix have been solved simultaneously by iteration for each zone. For the case of a short duct (L = 63 cm), the maximum zone width was 0.1 cm while for the long duct the maximum width was 1.2 cm. In all the calculations, the gas is assumed to be leaving the duct into an ambient of 333 K. In most cases, five iterations were sufficient for the convergence of the results.

Fig. 2 shows the gas temperature and the duct wall temperature in the direction of flow for three liquid to gas ratios and for two different spray distributions. The heat release, S, from wall ignition is chosen in this case to be 0.5 KJ/cm^3. An ignition temperature of 666 K is selected with a flame temperature of 1218 K. As long as the wall temperature T_s is above 666 K, the heat release rate W in equation (2) takes the form

$$W = \dot{x}\left(\frac{S}{\Delta x} + \rho C_p \frac{dT_s}{dx}\right)\psi \qquad (9)$$

where S is the heat release due to heat of reaction stated usually as KJ/cm^3 or KJ/gm (S for wood varies from 0.08 to 0.12 KJ/cm^3), and $\dot{x}$ is the rate of propagation of the ignition front along the duct wall. Initially a short duct is chosen with a length L = 63 cm and a radius r_0 = 16.5 cm. A flame is assumed to have been started at x = 0 covering the duct cross-section, and at the same time a continuous flow of cold liquid spray is injected into the gas stream at a specific rate. For the conditions specified in Fig. 2, the wall temperature in the direction of flow remains above the ignition temperature, and hence combustion prevails with the wall temperature T_s equal to the flame temperature. The gas flow, assumed to enter the flame region at 555 K, undergoes

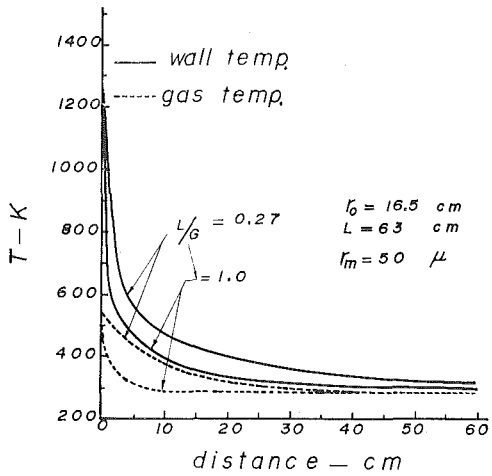

Fig. 3 Gas and wall temperature along the duct (T_i = 555 K; V_g = 3 m/s; S = 6.4 × 10^{-4} KJ/cm^3; F = 0.04; P_s = 1 atm; σ = 2.3 droplets initial temperature = 311 K)

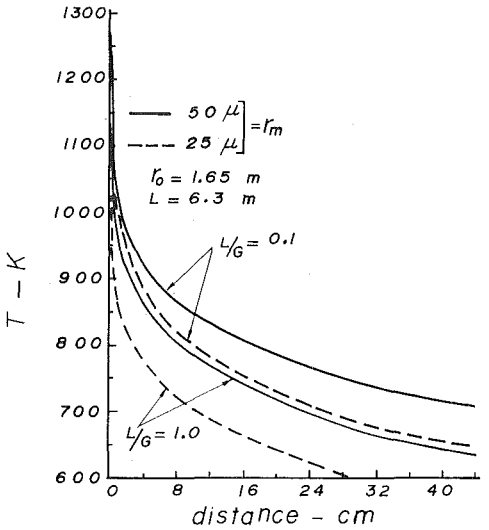

Fig. 4 Early stages of gas and wall temperature (T_i = 555 K; V_g = 3 m/s; S = 6.4 × 10^{-4} KJ/cm^3; F = 0.04; P_s = 1 atm; σ = 2.3, droplets initial temperature = 311 K)

a sudden drop in temperature[1] around the region of spray injection for the cases where the L/G ratios are high. This drop in temperature is attributed to the sudden evaporation of the cold liquid droplets. As would be expected a spray distribution with a smaller mass mean ratio is shown to be more effective as a cooling medium.

Further downstream, the gas temperature starts increasing. This is due to the magnitude of the heat input from the wall to the gas being greater than the cooling effect of the droplets remaining in the gas stream. The radiation parameters chosen for all the cases presented here are taken from [13] and arbitrarily selected to be:

Soot Concentration = 0.001 Kg/m^3

P_w/P_c = 1 = ratio of partial pressure of water vapor to the partial pressure of carbon dioxide

n	$b_{1,n}$	$b_{2,n}$	$q_{1,n}$	$q_{2,n}$
1	.5478	−.0001869	−1.252	558.55
2	.3846	0.0002071	−0.221	665.38
3	—	—	2.608	839.62

Fig. 3 shows the wall and the gas temperatures in the direction of flow for a heat release = 6.4 × 10^{-4} KJ/cm^3. Again here, temperature in excess of 666 K represents combustion and the effect of L/G ratio is shown to be effective in reducing the wall temperature to a level below ignition in a shorter distance. For the conditions shown, the gas appears to approach the wet bulb temperature.

[1] The gas also experienced a sudden drop in velocity as a result of the drag by the droplets; however, an increase in velocity followed [23].

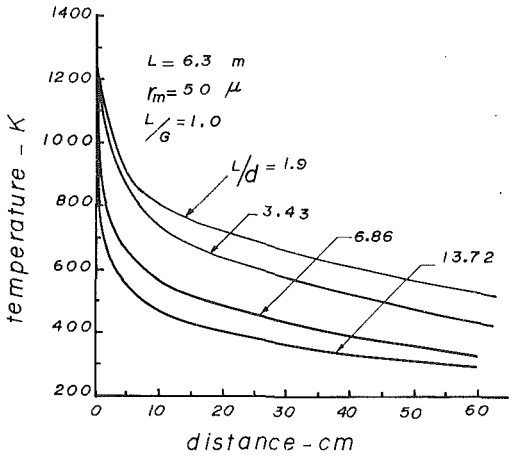

Fig. 5 Effect of L/d ratio on wall temperature (T_l = 555 K; V_g = 3 m/s; S = 6.4 × 10^{-4} KJ/cm³; F = 0.04; P_s = 1 atm; σ = 2.3, droplets initial temperature = 311K)

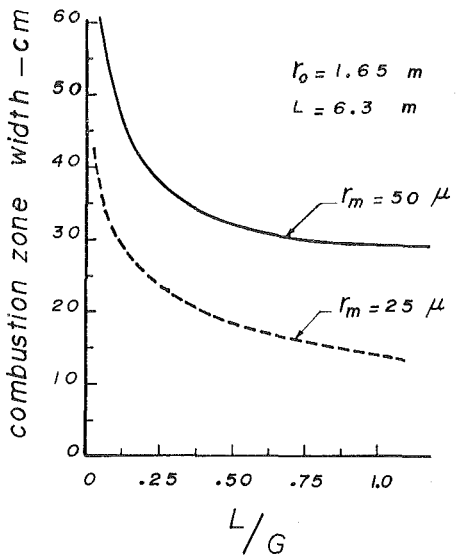

Fig. 6 Combustion zone width versus L/G ratio (T_l = 555 K; V_g = 3 m/s; S = 6.4 × 10^{-4} KJ/cm³; F = 0.04; P_s = 1 atm; σ = 2.3, droplets initial temperature = 311 K)

Fig. 4 shows the results of spray cooling in a large duct of length = 6.3 m and radius = 1.65 m. The effectiveness of spray distribution is demonstrated towards the duct entrance for two L/G ratios. A fine spray with r_m = 25 μ and for L/G = 0.1 is almost as effective as a spray with r_m = 50 μ but with L/G = 1.0. The effect of the duct length to diameter ratio is shown in Fig. 5 for an L/G ratio = 1.0. The larger the ratio L/d the more effective the spray cooling. This is to be expected as the radiative interchange between surface and volume zones is highly dependent upon geometry, specifically the length and the diameter of the duct. The quantitative importance of radiation can be obtained from equation (2). Designating $Q_{r,i}$ as the net radiative interchange for a surface zone, equation (2) when solved for $T_{s,i}$ yields

$$T_{s,i} = T_{g,i} - Q_{s,i}/hA_s + Q_{r,i}/hA_s + W/hA_s \quad (10)$$

$Q_{s,i}/hA_s$, $Q_{r,i}/hA_s$, and W/hA_s represent the effect on wall temperature in degrees due to wall conduction, radiative interchange, and the rate of heat release, respectively. Table 1 shows the effect of radiation on wall temperature as a percentage ($Q_{r,i}/hA_sT_{s,i}$) for various L/D ratios and at various locations along the duct. For zones located in the proximity of the flame front, it can be seen that radiation is predominant. This effect drops sharply with distance for high L/D ratios. Fig. 6 shows the combustion zone width versus the L/G ratio in a duct of radius = 1.65 m and length = 6.3 m and for two spray distributions. This figure shows essentially the L/G ratio needed to arrest the propagation of the ignition front. It is important to emphasize here that, for the parameters chosen in the analysis, the radial conduction from the duct wall did not affect the wall and the gas temperature significantly. This is attributed to the short residency time of the gas in each zone which can justify a model with adiabatic walls. Finally, above results are considered significant in the design, selection, and location of spray nozzles required for the control of fire propagation in ducts.

References

1 Krazinski, J. L., Buckius, R. D., and Krier, H., "A Model for Flame Propagation in Coal-Duct-Air Mixtures," ASME Paper No. 77-HT-18, 1977.

2 Edwards, J. C., Perlee, H. E., and Chaiken, R. F., "Flame Spread in a Duct Fire," ASME Paper No. 76-HT-56, 1976.

3 Pagni, P. J., and Han, J. T., "Temperature Fields in Solids Beneath Spreading Flames," ASME Paper No. 73-HT-61, 1973.

4 Steward, F. R., "Fire Spread Through a Fuel Bed," *Heat Transfer in Fires*, Blackshear, P. L., Editor, 1974.

5 Richmond, J. K. and Liebman, I., "A Physical Description of Coal Mine Explosion," *Fifteenth Symposium (International) on Combustion*, Tokyo, Japan, Aug. 25–31, pp. 115–126.

6 Emmons, H. W. and Shan, T., "Fire Spread in Paper Arrays," *Thirteenth Symposium (International) on Combustion*, Aug. 23–29, Salt Lake City, Utah, 1979, pp. 917–926.

7 Lee, S. I. and Hellman, J. M., "Heat and Mass Transfer in Fire Research," *Advances in Heat Transfer*, Vol. 10, Academic Press, New York, 1974.

8 Blackshear, P. L., *Heat Transfer in Fires*, Scripta Book Co., Washington, D.C., 1974.

9 Magee, R. S. and Reitz, R. D., "Extinquishment of Radiation Augmented Plastic Fires by Liquid Sprays," *Fifteenth Symposium (International) on Combustion*, Aug. 25–31, Tokyo, Japan, 1974, pp. 337–347.

10 Yao, C. and Kalelkar, A. S., *Fire Technology*, 6, 254, 1970.

11 Kalelkar, A. S., "Understanding Sprinkler Performance: Modeling of Combustion and Extinction," 75th Annual Meeting National Fire Protection Association, San Francisco, Calif., May 1971.

12 Rasbash, D. J., *Fire Research Abstracts and Reviews*, 4, Jan–May, 1962.

13 Taylor, P. D. and Foster, P. J., "Some Gray Gas Weighting Coefficient for CO_2–H_2O–Soot Mixtures," *International Journal Heat Mass Transfer*, Vol. 18, 1975, pp. 1331–1332.

14 Taylor, P. D. and Foster, P. J., "The Total Emissivities of Luminous and Non-Luminous Flames," *International Journal Heat Mass Transfer*, Vol. 17, 1974, pp. 1591–1605.

15 Johnson, R. R. and Beer, J.M., "The Zone Method Analysis of Radiant Heat Transfer: A Model for Luminous Radiation," *Journal of the Institute of Fuel*, Sept. 1973.

16 Hottel, H. C. and Sarofim, A. F., *Radiative Transfer*, McGraw-Hill, 1967.

17 Nakra, N. K. and Smith T. F., "Combined Radiation-Convection for a Real Gas," ASME JOURNAL OF HEAT TRANSFER, Vol. 99, 1977, pp. 60–65.

18 Carslaw, H. S. and Jaeger, J. C., *Conduction of Heat in Solids*, Second Ed., Oxford University Press, 1959, p. 336.

19 Habib, I. S. and Greif, R., "Heat Transfer to a Flowing Non-Gray Radiating Gas: An Experimental and Theoretical Study," *International Journal Heat Mass Transfer*, Vol. 13, 1979, pp. 1571–1582.

20 Kays, W. M., *Convective Heat and Mass Transfer*, McGraw-Hill, 1966.

21 Habib, I. S., "Fuel Droplets Evaporation in a Moving Gaseous Medium," *International Journal Heat Mass Transfer*, Vol. 13, pp. 1378–1383, 1970.

22 Habib, I. S., "The Rapid Cooling of a Hot Gas Discharge by Liquid Sprays," *Applied Scientific Research*, Vol. 28, July 1973.

23 Habib, I. S., "The Interaction of a Hot Gas Flow and a Cold Liquid Spray in Channels," ASME JOURNAL OF HEAT TRANSFER, Vol. 98, 1976 pp. 421–426.

APPENDIX

Gas Momentum Equation. The momentum equation when applied to the gas mixture including the droplets can be written in the following form

$$P_1A_1 + \frac{(P_1 + P_2)}{2}(A_2 - A_1) + \dot{m}_{g1}V_{g1} = P_2A_2 + \dot{m}_{g2}V_{g2} + \Sigma \text{ Drag} + \mathcal{F} \quad (A1)$$

Σ Drag represents the total drag forces exerted by the gas on the total number of droplets.

$$\Sigma\text{Drag} = \sum_i \left(C_d A_{cs} \rho_{fm} \frac{U^2}{2}\right)_i \quad (A2)$$

$\mathcal{F}$ is the frictional forces between the gas and the duct wall expressed as

$$\mathcal{F} = \frac{F\rho_{fm}V^2A_s}{2} = \tau_w A_s \tag{A3}$$

Continuity Equation

$$\dot{m}_{g1} + \sum\dot{m}_{d1} = \dot{m}_{g2} + \sum\dot{m}_{d2} + \frac{d}{dt}\sum\dot{m}_{d\sigma} \tag{A4}$$

$$\dot{m}_{g2} - \dot{m}_{g1} \equiv w \tag{A5}$$

$$\frac{d}{dt}\sum\dot{m}_{d\sigma} = \sum\dot{m}_{d1} - \sum\dot{m}_{d2} - w \tag{A6}$$

Equation of State. When a mixture of gases is treated as a perfect gas mixture the equation of state can be stated in the form

$$\rho_{fm} = \left[\frac{P_s\mathcal{M}}{RT}\right]_{fm} \tag{A7}$$

Liquid Droplets Relations

Mass Transfer. The mass transfer rate from the droplet is expressed by the following expressions

$$dM/dt = (4/3)\pi d(\rho_d r_d{}^3)/dt = w = \frac{2\pi D\mathcal{M}_f r_d}{R\bar{T}}\,\alpha \mathrm{Sh}\mathrm{P}_{1d} \tag{A8}$$

where

$$\alpha = \frac{P_s}{P_{1d}}\ln\frac{P_s}{P_s - P_{1d}} \tag{A9}$$

and Sh is given by Ranz-Marshall relation

$$\mathrm{Sh} = \frac{2r_d R\bar{T}k_m}{D\mathcal{M}_f} = 2 + 0.6\,(\mathrm{Sc})^{1/3}\,(\mathrm{Re})^{1/2} \tag{A10}$$

Heat Transfer

$$Q_d = hA_d(T_g - T_1)Z \tag{A11}$$

where

$$Z = z(e^z - 1) \tag{A12}$$

and

$$z = \frac{wc_{p,f}\delta}{4\pi r_d(r_d + \delta)k_{fm}} \tag{A13}$$

with

$$\delta = 2r_d/(\mathrm{Nu} - 2) \tag{A14}$$

In equation (A11) the average droplet heat transfer coefficient, h, is expressed by

$$\mathrm{Nu} = \frac{2r_d h}{k_{fm}} = 2 + 0.6(\mathrm{Pr})^{1/3}\,(\mathrm{Re})^{1/2} \tag{A15}$$

The total heat transfer from the gas will then be equal to that expressed by equation (A11) summed over the total number of the droplets.

An energy balance on the liquid droplet yields the following expression for the change in the droplet temperature.

$$\frac{dT_1}{dt} = \frac{1}{Mc_{p,1}}(Q_d - w\lambda) \tag{A16}$$

Momentum Trasfer. The aerodynamic drag force acting on the droplet will force the velocity of the droplet to approach that of the flowing gas. For a spherical droplet we have

$$\text{Drag Force} = -M\frac{dV_d}{dt} = C_d A_{cs}\rho_{fm}\frac{U^2}{2} \tag{A17}$$

or

$$\frac{dV_d}{dt} = -\frac{3}{8}C_d\frac{\rho_{fm}}{\rho_1}\frac{U^2}{r_d} \tag{A18}$$

where C_d is the drag coefficient and taken for evaporating droplets as (21–23)

$$C_d = 27(\mathrm{Re})^{-0.84} \tag{A19}$$

For a standard deviation = 2.3, the following spread in droplets sizes are obtained for mass mean radii equal to 50μ and 25μ, respectively.

$r_m = 50\mu$	$r_m = 25\mu$
17.19	8.59
32.32	16.16
50.00	25.00
77.36	38.68
145.45	72.72

Long-Time Solutions to Heat-Conduction Transients with Time-Dependent Inputs

Graduate Student.

G. E. Myers

Professor.

Department of Mechanical Engineering,
the University of Wisconsin-Madison
Madison, Wis. 53706

An economical method for obtaining long-time solutions to one, two, or three-dimensional heat-conduction transients with time-dependent forcing functions is presented. The conduction problem is spatially discretized by finite differences or by finite elements to obtain a system of first-order ordinary differential equations. The time-dependent input functions are each approximated by continuous, piecewise-linear functions each having the same uniform time interval. A set of response coefficients is generated by which a long-time solution can be carried out with a considerably lower cost than for conventional methods. A one-dimensional illustrative example is included.

Introduction

Long-time solutions of one, two, or three-dimensional heat-conduction transients with time-dependent input forcing functions are often required in building air-conditioning calculations and in the development of load models for solar-energy studies. Several methods are available to solve this kind of problem. Analytical methods of solving the governing heat equation using superposition principles are treated in standard heat-conduction books [1, 2]. This approach is quite acceptable for regular geometries such as homogeneous plane walls when the input functions are relatively simple. In many practical applications, however, the geometry may not be regular, the thermal properties may not be uniform, and the input functions may not be simple. In these cases analytical techniques become rather cumbersome if not impossible.

Widespread use of computers has made discretization techniques, such as finite differences, and more-recently finite elements, much more convenient [1]. They can be used for complicated problems that do not lend themselves very readily to analytical methods. In both of these techniques the conduction problem is discretized by using a set of n nodal points and arriving at a system of n simultaneous first-order ordinary differential equations to be solved for the temperature-time history at each of the n nodal points. The solution is then typically approximated using the Euler or the Crank-Nicolson technique for moving ahead step-by-step in time. Once the temperature distribution at a time step has been computed, other desired outputs, such as heat flows, may be determined. A major drawback of this approach is that it is often necessary to take very small time steps to avoid numerically-induced oscillations [1, 3, 4] in the solution. Furthermore, the complete internal temperature distribution must be computed at each time step even though one might only desire a single temperature or a heat flow at one surface as an output. Finally, if it is desired to determine the response of the same structure to another input time history, it is necessary to solve the complete problem over again. Thus, although it is possible to obtain long-time solutions using these techniques, they can be expensive.

Stephenson and Mitalas [5, 6] used superposition and transform theory to develop the thermal-response-factor method. This technique avoids the computation of internal temperatures by relating the desired outputs at any time to the previous inputs through a set of response-factor coefficients. Later Stephenson and Mitalas [7] presented the z-transfer-function method as an improvement over the thermal-response-factor method. This technique relates current outputs to current and previous inputs but also incorporates outputs previously computed. The ASHRAE handbook of fundamentals [8] lists z-transfer-function coefficients for some particular building structures to facilitate heat-transfer calculations for buildings. The z-transfer-function method overcomes the necessity to calculate internal temperature distributions. It also provides a set of coefficients for the structure that can be used to analyze other input time histories without completely resolving the entire problem. However, at present it is restricted to certain one-dimensional, composite-plane-wall problems. Its extension to more general problems (e.g., irregular two-dimensional regions, time-dependent energy generation) appears to be rather difficult.

Pawelski [9] needed response coefficients in his solar energy studies for more general cases than the z-transfer-function method could handle. Using an Euler finite-difference model, he computed the outputs for a particular input history and then deduced the unknown response coefficients by a statistical least-squares fit.

The technique described in the next section begins with either a finite-difference or a finite-element model of the heat-transfer problem and produces response coefficients. Exact response coefficients for the discrete model are obtained without using z-transform theory or making any further approximations. This technique also allows a wider variety of problems to be solved than can be handled by present methods.

Theoretical Development

This paper is concerned with heat-conduction transients described by the partial differential equation

$$\frac{\partial}{\partial x}\left(k\frac{\partial t}{\partial x}\right)+\frac{\partial}{\partial y}\left(k\frac{\partial t}{\partial y}\right)+\frac{\partial}{\partial z}\left(k\frac{\partial t}{\partial z}\right)+g'''=\rho c\frac{\partial t}{\partial \theta} \tag{1}$$

where k, ρ, and c can be position dependent and g''' may depend upon both position and time. There will be no restriction to simple geometrical shapes. The conditions on the boundaries of the region may be combinations of convection, specified heat flux, or specified temperature as shown by equations (2–4).

$$\text{Convection: } -k\frac{\partial t}{\partial n}=h(t_\infty-t) \tag{2}$$

$$\text{Specified heat flux: } -k\frac{\partial t}{\partial n}=q_s'' \tag{3}$$

$$\text{Specified temperature: } t=t_s \tag{4}$$

The convection heat-transfer coefficient may depend upon position but not upon time. The quantities t_∞, q_s'', and t_s may depend upon both position and time. In fact, the primary purpose of this paper is to discuss the problems in which t_∞, q_s'', t_s, and g''' are prescribed functions of time. Since long-time solutions rather than initial transients are of interest, the initial condition given by

$$t(x, y, z, 0)=t^{(0)}(x, y, z) \tag{5}$$

will be unimportant.

[1] On leave from Middle East Technical University, Ankara, Turkey.

Contributed by the Heat Transfer Division for publication in the JOURNAL OF HEAT TRANSFER. Manuscript received by the Heat Transfer Division June 5, 1979.

Finite-difference and finite-element methods for solving this problem both involve using a set of n nodal points to subdivide the region into a finite number of discrete regions. This discretizing process is discussed in [1] and [3] for both finite differences and finite elements. Both methods replace equations (1–4) by a system of first-order ordinary differential equations that can be compactly written in matrix notation as

$$\mathbf{C}\dot{\mathbf{t}} + \mathbf{S}\mathbf{t} = \mathbf{r} \tag{6}$$

The temperature vector $\mathbf{t}$ contains the temperatures at the n nodal points. The capacitance matrix $\mathbf{C}$ describes the thermal capacitance of each discrete region. The conductance matrix $\mathbf{S}$ contains the conductances between the various discrete regions and between the boundary and the ambient. The $\mathbf{C}$ and $\mathbf{S}$ matrices are symmetric and banded. In finite differences $\mathbf{C}$ will be diagonal whereas in finite elements $\mathbf{C}$ will have the same bandwidth as $\mathbf{S}$. The input vector $\mathbf{r}$ contains the values of ambient temperature, specified boundary heat flux, specified boundary temperature, and energy generation. In this paper, $\mathbf{C}$ and $\mathbf{S}$ are constants and $\mathbf{r}$ is a specified function of time. The initial condition, equation (5), is replaced by

$$\mathbf{t}(0) = \mathbf{t}^{(0)} \tag{7}$$

Rather than following the standard Euler or Crank-Nicolson procedure for approximating the solution to equation (6), the exact solution will be used. If the discussion in [3] is generalized to handle time-dependent $\mathbf{r}$ by using an integrating factor or by using Duhamel's theorem, the exact solution to equation (6) may be shown to be

$$\mathbf{t}(\theta) = \mathbf{X}\exp(-\mathbf{\Lambda}\theta)\mathbf{X}^T\mathbf{C}\mathbf{t}^{(0)} + \mathbf{X}\int_{\tau=0}^{\theta}\exp[-\mathbf{\Lambda}(\theta-\tau)]\mathbf{X}^T\mathbf{r}(\tau)d\tau \tag{8}$$

where the diagonal eigenvalue matrix $\mathbf{\Lambda}$ contains the n eigenvalues and the eigenvector matrix $\mathbf{X}$ contains the corresponding n eigenvectors found by solving the generalized eigenvalue problem given by

$$\mathbf{S}\mathbf{X} = \mathbf{C}\mathbf{X}\mathbf{\Lambda} \tag{9}$$

The $\mathbf{C}$ matrix is always positive definite. The $\mathbf{S}$ matrix is also positive definite whenever there is at least one convection or specified-temperature boundary condition. These properties of $\mathbf{C}$ and $\mathbf{S}$ will yield positive eigenvalues [10]. The eigenvalues in $\mathbf{\Lambda}$ are ordered so that $0 < \lambda_1 \leqq \lambda_2 \leqq \ldots \leqq \lambda_n$ and the eigenvectors are normalized so that $\mathbf{X}^T\mathbf{C}\mathbf{X} = \mathbf{I}$. Direct substitution of equation (8) into equation (6) will verify that equation (8) is indeed the exact solution of equation (6). It also satisfies the initial condition given by equation (7).

Two important observations should be made about equation (8). First, for long-time solutions the initial condition $\mathbf{t}^{(0)}$ will drop out of the solution because of the multiplication by the decaying exponential term. Second, although the complete past history of the input vector $\mathbf{r}$ is theoretically required to evaluate the integral that appears on the right-hand side of equation (8), the decaying exponential that also appears in the integrand means that only the most recent history of $\mathbf{r}$ will be important.

Although $\mathbf{r}$ will be an $n \times 1$ vector, if there are n nodal points in the discrete model, the number of specified input functions will normally be much less than n. For example, a plane-wall problem might have many nodes but have only two specified inputs—the ambient temperatures on each face. It will therefore be convenient to express $\mathbf{r}$ in terms of the smaller number of specified input functions. If there are m time-dependent inputs (contained in an $m \times 1$ vector $\mathbf{s}$) and k constant inputs (contained in a $k \times 1$ vector $\mathbf{p}$), the input vector $\mathbf{r}$ can be written as

$$\mathbf{r} = \mathbf{P}\mathbf{s} + \mathbf{Q}\dot{\mathbf{s}} + \mathbf{R}\mathbf{p} \tag{10}$$

where $\mathbf{P}$ and $\mathbf{Q}$ are $n \times m$ matrices and $\mathbf{R}$ is an $n \times k$ matrix. If there are no time-dependent specified temperatures, $\mathbf{Q}$ will be $\mathbf{0}$. Substitution of equation (10) into equation (8), assuming that θ is large enough so that the term containing the initial condition can be neglected, gives

$$\mathbf{t}(\theta) = \mathbf{X}\int_{\tau=0}^{\theta}\exp[-\mathbf{\Lambda}(\theta-\tau)]\mathbf{X}^T[\mathbf{P}\mathbf{s} + \mathbf{Q}\dot{\mathbf{s}} + \mathbf{R}\mathbf{p}]d\tau$$

The term containing $\mathbf{s}$ may be integrated by parts and the term containing $\mathbf{p}$ may be integrated directly. Each of these integrations will produce a term containing $\exp(-\mathbf{\Lambda}\theta)$ which can be dropped for sufficiently large θ. After carrying out these steps it will be convenient to replace the dummy variable of integration τ by $\sigma = \theta - \tau$ so that σ will be 0 at the current time θ and increase until $\sigma = \theta$ at the beginning of the transient. The expression for $\mathbf{t}(\theta)$ then becomes

Nomenclature

$\mathbf{A}$ = defined in equation (13); varies
$\mathbf{B}$ = response coefficient, equation (17); varies
c = specific heat; E/MT
C = response coefficient, equation (17); none
$\mathbf{C}$ = capacitance matrix; E/L^2T, E/LT, or E/T
$\mathbf{D}$ = response coefficient, equation (17); varies
E = dimension of energy; E
$\mathbf{E}$ = defined in equation (13); varies
$\exp(-\mathbf{\Lambda}\Delta\theta)$ = diagonal matrix with $\exp(-\lambda_i\Delta\theta)$ in i^{th} row; none
$[\exp(-\mathbf{\Lambda}\Delta\theta)]^{\mu-1}$ = diagonal matrix with $[\exp(-\lambda_i\Delta\theta)]^{\mu-1}$ in i^{th} row; none
g''' = energy generation rate per unit volume; $E/\Theta L^3$
h = convection heat-transfer coefficient; $E/\Theta L^2\mathrm{T}$
H = Biot number, hL/k; none
$\mathbf{I}$ = identity matrix; none
k = thermal conductivity; $E/\Theta LT$
κ = number of constant inputs; none
ℓ = number of desired outputs; none
L = thickness; L
L = dimension of length; L
m = number of time-dependent inputs; none
M = dimension of mass; M
n = number of nodes; none
n = inward coordinate normal to boundary; L
$\mathbf{p}$ = constant input vector; varies
$\mathbf{P}$ = defined in equation (10); varies
q'' = heat flux; $E/\Theta L^2$
q_s'' = specified heat flux; $E/\Theta L^2$
$\mathbf{Q}$ = defined in equation (10); E/LT
$\mathbf{r}$ = input vector; $E/\Theta L$
$\mathbf{R}$ = defined in equation (10); varies
$\mathbf{s}$ = reduced input vector; varies
$\mathbf{S}$ = conductance matrix; $E/\Theta L^2T$, $E/\Theta LT$, or $E/\Theta T$
t = temperature; T
$\mathbf{t}$ = temperature vector; T
t_L = room temperature; T
t_s = specified temperature; T
t_0 = mean ambient temperature, Fig. 1; T
t_∞ = ambient temperature; T
$t^{(0)}$ = initial temperature distribution, equation (5); T
$\mathbf{t}^{(0)}$ = initial temperature vector, equations (7, 8); T
$\mathbf{t}^{(0)}$ = current temperature vector, equations (11, 12, 27); T
T = dimension of temperature; T
T_0 = amplitude of ambient temperature, Fig. 1; T
$\mathbf{u}$ = output vector; varies
$\mathbf{U}$ = defined in equation (12); varies
$\mathbf{V}$ = defined in equation (12); varies
$\mathbf{W}$ = defined in equation (12); varies
x = position coordinate; L
$\mathbf{X}$ = eigenvector matrix; $L\sqrt{T/E}$, $\sqrt{LT/E}$, or $\sqrt{T/E}$
$\mathbf{X}^T$ = transpose of $\mathbf{X}$; $L\sqrt{T/E}$, $\sqrt{LT/E}$, or $\sqrt{T/E}$
y = position coordinate; L
$\mathbf{Y}$ = defined in equation (12); varies
z = position coordinate; L
α = thermal diffusivity; L^2/Θ
$\delta_{\mu 1}$ = Kronecker delta; none
$\Delta\theta$ = time interval; Θ
θ = time; Θ
Θ = dimension of time; Θ
λ = eigenvalue, equation (9); $1/\Theta$
λ = eigenvalue, equation (24); $1/L$
$\mathbf{\Lambda}$ = diagonal eigenvalue matrix; $1/\Theta$
μ = time-step index; none
ρ = density; M/L^3
σ = dummy variable; Θ
τ = dummy variable; Θ
ω = frequency of ambient temperature, Fig. 1; $1/\Theta$

$$\mathbf{t}(\theta) = \mathbf{X}\boldsymbol{\Lambda}^{-1}\mathbf{X}^T\mathbf{P}\mathbf{s}(\theta) + \mathbf{X}\boldsymbol{\Lambda}^{-1}\int_{\sigma=0}^{\theta}\exp(-\boldsymbol{\Lambda}\sigma)\mathbf{X}^T\mathbf{P}\dot{\mathbf{s}}(\sigma)d\sigma - \mathbf{X}\int_{\sigma=0}^{\theta}\exp(-\boldsymbol{\Lambda}\sigma)\mathbf{X}^T\mathbf{Q}\dot{\mathbf{s}}(\sigma)d\sigma + \mathbf{X}\boldsymbol{\Lambda}^{-1}\mathbf{X}^T\mathbf{R}\mathbf{p}$$

where $\dot{\mathbf{s}}(\sigma)$ denotes differentiation with respect to σ.

To carry out the integrals containing $\dot{\mathbf{s}}(\sigma)$ we will assume that each of the input functions in $\mathbf{s}$ can be adequately represented by continuous, piecewise-linear functions each having the same uniform time interval $\Delta\theta$. The integrals can then be written as the sum of contributions over each time interval. Furthermore, since $\mathbf{s}$ is assumed to be linear within each interval, $\dot{\mathbf{s}}(\sigma)$ will be a constant within the interval and will be given by

$$\dot{\mathbf{s}}(\sigma) = \frac{\mathbf{s}^{(\mu+1)} - \mathbf{s}^{(\mu)}}{\Delta\theta}$$

where μ is a time-step index that is 0 at the present time θ and increases by one for each step $\Delta\theta$ backward in time. Since $\dot{\mathbf{s}}(\sigma)$ is a constant within each time interval, the integrations over each time interval can be quite simply carried out. After integrating, juggling series indices, and combining terms, one obtains the temperature vector at the current time as

$$\mathbf{t}^{(0)} = \{\mathbf{X}\boldsymbol{\Lambda}^{-1}\mathbf{X}^T\mathbf{P} - \mathbf{X}(\boldsymbol{\Lambda}\Delta\theta)^{-1}[\mathbf{I} - \exp(-\boldsymbol{\Lambda}\Delta\theta)] \times [\boldsymbol{\Lambda}^{-1}\mathbf{X}^T\mathbf{P} - \mathbf{X}^T\mathbf{Q}]\}\mathbf{s}^{(0)} + \sum_{\mu=1}\{\mathbf{X}[\exp(-\boldsymbol{\Lambda}\Delta\theta)]^{\mu-1}(\boldsymbol{\Lambda}\Delta\theta)^{-1} \times [\mathbf{I} - \exp(-\boldsymbol{\Lambda}\Delta\theta)]^2[\boldsymbol{\Lambda}^{-1}\mathbf{X}^T\mathbf{P} - \mathbf{X}^T\mathbf{Q}]\}\mathbf{s}^{(\mu)} + \mathbf{X}\boldsymbol{\Lambda}^{-1}\mathbf{X}^T\mathbf{R}\mathbf{p} \quad (11)$$

The summation over μ theoretically runs until the initial time is reached. Practically speaking, however, the series will converge much sooner than this because of the exponential term raised to the power $\mu - 1$.

Generally one is not interested in the internal temperature distribution itself but rather only in one or two outputs (e.g., surface temperatures or heat flows) that can be computed once the temperature distribution has been found. If there are ℓ desired outputs (contained in an $\ell \times 1$ vector $\mathbf{u}$), the current outputs $\mathbf{u}^{(0)}$ can be written in terms of the current temperature distribution $\mathbf{t}^{(0)}$, the current values of the time-dependent inputs $\mathbf{s}^{(0)}$, the current values of the derivatives of the time-dependent inputs $\dot{\mathbf{s}}^{(0)}$, and the values of the constant inputs $\mathbf{p}$ as

$$\mathbf{u}^{(0)} = \mathbf{U}\mathbf{t}^{(0)} + \mathbf{V}\mathbf{s}^{(0)} + \mathbf{W}\dot{\mathbf{s}}^{(0)} + \mathbf{Y}\mathbf{p} \quad (12)$$

where $\mathbf{U}$, $\mathbf{V}$, $\mathbf{W}$, and $\mathbf{Y}$ depend upon what outputs are desired and how they are related to the temperature distribution and to the inputs. If there are no time-dependent specified temperatures $\mathbf{W}$ will be $\mathbf{0}$. Substitution of equation (11) into equation (12) and replacement of $\dot{\mathbf{s}}^{(0)}$ by $[\mathbf{s}^{(0)} - \mathbf{s}^{(1)}]/\Delta\theta$ gives

$$\mathbf{u}^{(0)} = \mathbf{A}_0\mathbf{s}^{(0)} + \sum_{\mu=1}\mathbf{A}_\mu\mathbf{s}^{(\mu)} + \mathbf{E}\mathbf{p} \quad (13)$$

where

$$\mathbf{A}_0 = \mathbf{U}\mathbf{X}\boldsymbol{\Lambda}^{-1}\mathbf{X}^T\mathbf{P} - \mathbf{U}\mathbf{X}(\boldsymbol{\Lambda}\Delta\theta)^{-1}[\mathbf{I} - \exp(-\boldsymbol{\Lambda}\Delta\theta)] \times [\boldsymbol{\Lambda}^{-1}\mathbf{X}^T\mathbf{P} - \mathbf{X}^T\mathbf{Q}] + \mathbf{V} + (\Delta\theta)^{-1}\mathbf{W} \quad (14)$$

$$\mathbf{A}_\mu = \mathbf{U}\mathbf{X}[\exp(-\boldsymbol{\Lambda}\Delta\theta)]^{\mu-1}(\boldsymbol{\Lambda}\Delta\theta)^{-1}[\mathbf{I} - \exp(-\boldsymbol{\Lambda}\Delta\theta)]^2 \times [\boldsymbol{\Lambda}^{-1}\mathbf{X}^T\mathbf{P} - \mathbf{X}^T\mathbf{Q}] - \delta_{\mu 1}(\Delta\theta)^{-1}\mathbf{W} \quad (15)$$

$$\mathbf{E} = \mathbf{U}\mathbf{X}\boldsymbol{\Lambda}^{-1}\mathbf{X}^T\mathbf{R} + \mathbf{Y} \quad (16)$$

Observe that $\mathbf{A}_1$ is not typical of the other $\mathbf{A}_\mu$ when $\mathbf{W} \neq \mathbf{0}$. It can also be shown that as μ increases the $\mathbf{A}_\mu$ will decay to $\mathbf{0}$ as given by

$$\mathbf{A}_\mu = \mathbf{A}_{\mu-1}\exp(-\lambda_1\Delta\theta)$$

Equation (13) says that the desired outputs $\mathbf{u}^{(0)}$ may be computed from current and previous time-dependent inputs $\mathbf{s}^{(0)}$ and $\mathbf{s}^{(\mu)}$ and the constant inputs $\mathbf{p}$, once the coefficient matrices $\mathbf{A}_0$, $\mathbf{A}_\mu$, and $\mathbf{E}$ have been determined from equations (14–16). These coefficient matrices depend upon the time interval used to approximate the time-dependent inputs but not upon the particular values of the input history. Consequently these same coefficient matrices can be used for any input history that can be adequately approximated using the same time interval $\Delta\theta$.

Calculations can be facilitated if previously computed outputs are incorporated into the computation of the current outputs by writing

$$\mathbf{u}^{(0)} = \mathbf{B}_0\mathbf{s}^{(0)} + \sum_{\mu=1}\mathbf{B}_\mu\mathbf{s}^{(\mu)} + \sum_{\mu=1}C_\mu\mathbf{u}^{(\mu)} + \mathbf{D}\mathbf{p} \quad (17)$$

instead of equation (13). The $\mathbf{B}_0$, $\mathbf{B}_\mu$, C_μ, and $\mathbf{D}$ response coefficients must be chosen so that the $\mathbf{u}^{(0)}$ computed from equation (17) will be identical to the $\mathbf{u}^{(0)}$ that would be computed if equation (13) were used. To determine these response coefficients, the previous outputs required in equation (17) are written in terms of $\mathbf{s}^{(\mu)}$ and $\mathbf{p}$ following equation (13) and the resulting coefficients of $\mathbf{s}^{(0)}$, $\mathbf{s}^{(\mu)}$, and $\mathbf{p}$ in equation (17) can then be equated to those in equation (13) by choosing

$$C_1 = \sum_{i=1}^{n}\exp(-\lambda_i\Delta\theta)$$

$$C_2 = -\sum_{i=1}^{n-1}\exp(-\lambda_i\Delta\theta)\sum_{j=i+1}^{n}\exp(-\lambda_j\Delta\theta)$$

$$\vdots$$

$$C_\mu = (-1)^{\mu+1}\sum_{i=1}^{n-\mu+1}\exp(-\lambda_i\Delta\theta) \times \sum_{j=i+1}^{n-\mu+2}\exp(-\lambda_j\Delta\theta)\cdots\sum_{m=\ell+1}^{n}\exp(-\lambda_m\Delta\theta)$$

$$\vdots$$

$$C_n = (-1)^{n+1}\exp\left(-\sum_{i=1}^{n}\lambda_i\Delta\theta\right) \quad (18)$$

$$C_\mu = 0 \qquad (\text{for } \mu > n) \quad (19)$$

$$\mathbf{B}_0 = \mathbf{A}_0 \quad (20)$$

$$\mathbf{B}_\mu = \mathbf{A}_\mu - \sum_{i=1}^{\mu}C_i\mathbf{A}_{\mu-i} \quad (\text{for } 1 \leq \mu \leq n+1) \quad (21)$$

$$\mathbf{B}_\mu = \mathbf{0} \quad (\text{for } \mu > n+1) \quad (22)$$

$$\mathbf{D} = \left(1 - \sum_{\mu=1}^{n}C_\mu\right)\mathbf{E} \quad (23)$$

where n is the number of nodal points in the discrete formulation and consequently also the number of eigenvalues in the solution to equation (9). It should be observed that equations (19) and (22) mean that the $\mathbf{B}_\mu$ and C_μ summations in equation (17) need only go to $n+1$ and n respectively rather than to infinity. It is also interesting to note that the C_μ depend only upon the eigenvalues in $\boldsymbol{\Lambda}$ and $\Delta\theta$ whereas the $\mathbf{B}_\mu$ and $\mathbf{D}$ also depend upon the eigenvectors in $\mathbf{X}$ and the matrices $\mathbf{P}$, $\mathbf{Q}$, $\mathbf{R}$, $\mathbf{U}$, $\mathbf{V}$, $\mathbf{W}$, and $\mathbf{Y}$ defined in equations (10) and (12).

Once all of the response coefficients $\mathbf{B}_0$, $\mathbf{B}_\mu$, C_μ, and $\mathbf{D}$ have been determined, equation (17) can then be used to compute the desired outputs. In order to start computations, it is necessary to be far enough into the transient so that enough previous input history is available to use in equation (17). Furthermore, an assumption regarding the previous outputs required by equation (17) must be made. The effect of this assumption will decay out as time increases.

Illustrative Example

Let us consider the one-dimensional plane wall shown in Fig. 1. The thermal properties k, ρ, and c are uniform and constant. The convection heat-transfer coefficients on each face are equal and constant. The ambient temperature on the left-hand face is a time-dependent input and the ambient temperature on the right-hand face is a con-

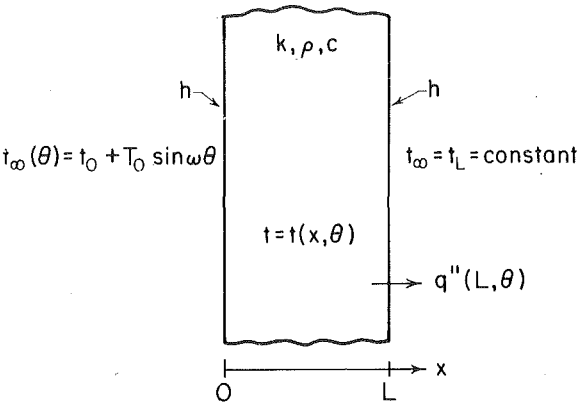

Fig. 1 One-dimensional plane-wall example

stant input. The reason for choosing a periodic input is for ease in obtaining an analytical solution for comparison. The response-coefficient method is in no way restricted to periodic inputs. The desired output will be the heat flux at the right-hand face. Although this example does not reflect the generality of the method and the economy of using it, it will illustrate the basic principles and allow comparison with other solution techniques.

The exact long-time solution of the governing partial differential equation and boundary conditions may be obtained using separation of variables and Duhamel's theorem [1]. The heat flux at $x = L$ is then found to be

$$q''(L,\theta) = \frac{h}{2+H}(t_0 + T_0 \sin\omega\theta - t_L) - hT_0\left(\frac{\omega L^2}{\alpha}\right) \times \sum_{i=1}^{\infty} \frac{[H^2 + (\lambda_i L)^2]\sin(\lambda_i L)\left[(\lambda_i L)^2\cos\omega\theta + \left(\frac{\omega L^2}{\alpha}\right)\sin\omega\theta\right]}{(\lambda_i L)[(\lambda_i L)^2 + 2H + H^2]\left[(\lambda_i L)^4 + \left(\frac{\omega L^2}{\alpha}\right)^2\right]} \quad (24)$$

where $H = hL/k$ and the $(\lambda_i L)$ are the positive roots of

$$\tan(\lambda_i L) = \frac{2H(\lambda_i L)}{(\lambda_i L)^2 - H^2}$$

The method of solution described in this paper begins with a discrete formulation of the problem. For a three-node finite-difference model with node 1 at $x = 0$, node 2 at $x = L/2$, and node 3 at $x = L$, the nodal energy balances result in three first-order ordinary differential equations that may be written in matrix form as

$$\frac{\rho cL}{4}\begin{bmatrix}1&0&0\\0&2&0\\0&0&1\end{bmatrix}\dot{\mathbf{t}} + \frac{2k}{L}\begin{bmatrix}1+\frac{H}{2}&-1&0\\-1&2&-1\\0&-1&1+\frac{H}{2}\end{bmatrix}\mathbf{t} = h\begin{bmatrix}\mathbf{f}t_\infty(\theta)\\0\\t_L\end{bmatrix} \quad (25)$$

This is a three-node example of equation (6). The vector r may be separated into time-dependent inputs and constant inputs following equation (10) by writing

$$\mathbf{r} = \mathbf{Ps} + \mathbf{Rp} = \begin{bmatrix}h\\0\\0\end{bmatrix}[t_\infty(\theta)] + \begin{bmatrix}0\\0\\h\end{bmatrix}[t_L] \quad (26)$$

In this example $\mathbf{Q} = 0$ since there are no specified temperatures. The heat flux at the right-hand face is given by $h(t_3 - t_L)$. This desired output can then be expressed as in equation (12) by writing

$$\mathbf{u}^{(0)} = \mathbf{U}\mathbf{t}^{(0)} + \mathbf{Yp} = [0\ 0\ h]\begin{bmatrix}t_1\\t_2\\t_3\end{bmatrix}^{(0)} + [-h][t_L] \quad (27)$$

In this example $\mathbf{V}$ and $\mathbf{W}$ are both $\mathbf{0}$. We have now identified all of the matrices and vectors needed to solve this example.

Table 1 A_μ coefficients

μ	$n = 3$	$n = 9$
0	0.0081	0.0040
1	0.0522	0.0475
2	0.0728	0.0747
3	0.0647	0.0656
4	0.0509	0.0513
5	0.0386	0.0390
6	0.0291	0.0296
7	0.0218	0.0223
8	0.0163	0.0169
$\mu > 8$	$\mathbf{A}_\mu = 0.7490\,\mathbf{A}_{\mu-1}$	$\mathbf{A}_\mu = 0.7555\,\mathbf{A}_{\mu-1}$

$\mathbf{A}_\mu$ (Btu/hr-ft^2-°F^2)

Table 2 Response coefficients

	$n = 3$	$n = 9$	ASHRAE [10]
$\mathbf{B}_0$	0.0081	0.0040	0.0036
$\mathbf{B}_1$	0.0436	0.0437	0.0438
$\mathbf{B}_2$	0.0194	0.0303	0.0309
$\mathbf{B}_3$	0.0007	0.0018	0.0017
C_1	1.0612	0.9477	0.9441
C_2	−0.2561	−0.1467	−0.1435
C_3	0.0167	0.0011	0.0009
$\mathbf{D}$	−0.0718	−0.0798	−0.0800

$\mathbf{B}_\mu$(Btu/hr-ft^2-°F^2); C_μ(none); $\mathbf{D}$(Btu/hr-ft^2-°F^2)

For comparison to the ASHRAE results [11], we will use the following numerical values: $L = 8.0$ in., $k = 0.6$ Btu/hr-ft-°F, $\rho = 61.0$ lbm/ft^3, $c = 0.2$ Btu/lbm-°F, $h = 1.46$ Btu/hr-ft^2-°F and $\Delta\theta = 1.0$ hr. These data are representative of a concrete wall undergoing a transient in which the input ambient temperature can be approximated using one hr time intervals.

The numerical solution of the eigenvalue problem shown in equation (9) has been carried out using EISPACK [12] subroutines and is given by

$$\mathbf{\Lambda} = \begin{bmatrix}0.2890&&\\&1.6032&\\&&2.1995\end{bmatrix} hr^{-1}$$

and

$$\mathbf{X} = \begin{bmatrix}-0.2770&0.4959&0.4113\\-0.4113&0.0000&-0.2770\\-0.2770&-0.4959&0.4113\end{bmatrix} \text{ft}\sqrt{\text{°F/Btu}} \quad (28)$$

The $\mathbf{A}_\mu$ coefficients may now be computed by carrying out the matrix multiplications in equations (14) and (15). For this example these coefficients will be 1×1 matrices since there is only one time-dependent input and one output. The results are shown in the three-node column of Table 1. Observe the convergence of $\mathbf{A}_\mu$ to $\mathbf{0}$ as μ increases. Using the eigenvalues shown in equation (28), the C_μ coefficients in equation (17) can be computed according to the relations given in equations (18) and (19). The $\mathbf{B}_\mu$ coefficients can then be computed following equations (20–22). Finally, $\mathbf{D}$ may be computed using equations (16) and (23). The results of the computations for the $\mathbf{B}_0$, $\mathbf{B}_\mu$, C_μ, and $\mathbf{D}$ response coefficients are shown in the three-node column of Table 2. The $\mathbf{B}_\mu$ and C_μ coefficients not shown in Table 2 are all zero in this example. This completes the computation of the response coefficients for a three-node model of the problem shown in Fig. 1.

As is the case with all discrete models, the accuracy of the model may be improved by increasing the number of nodes. The results of a nine-node model are also shown in Tables 1 and 2. Observe that as one goes from three nodes to nine nodes the coefficients approach the ASHRAE values [11], which are the exact response coefficients for this example. Although there are theoretically 9 nonzero C_μ coefficients, only the first three are given since the others are essentially

Table 3 Comparison of various methods

Time	Outdoor Temperature	Analytical eq. (24)	ASHRAE	Euler $n = 9$	Crank-Nicolson $n = 9$	Response Coefficients $n = 3$	Response Coefficients $n = 9$
θ	$t_\infty(\theta)$	$q''(L,\theta)$	$q''(L,\theta)$	$q''(L,\theta)$	$q''(L,\theta)$	$q''(L,\theta)$	$q''(L,\theta)$
0	90.00	3.03	3.06	3.00	3.03	3.11	3.06
1	95.18	3.95	3.97	3.92	3.95	4.07	3.98
2	100.00	5.15	5.17	5.13	5.14	5.30	5.18
3	104.14	6.55	6.56	6.53	6.54	6.72	6.58
4	107.32	8.06	8.06	8.05	8.04	8.23	8.07
5	109.32	9.56	9.55	9.56	9.54	9.73	9.57
6	110.00	10.96	10.94	10.97	10.94	11.11	10.96
7	109.32	12.17	12.14	12.18	12.14	12.29	12.16
8	107.32	13.09	13.06	13.11	13.07	13.18	13.07
9	104.14	13.67	13.64	13.70	13.65	13.71	13.65
10	100.00	13.87	13.84	13.90	13.85	13.86	13.84
11	95.18	13.67	13.64	13.71	13.66	13.62	13.65
12	90.00	13.09	13.06	13.13	13.09	12.99	13.07
13	84.82	12.17	12.15	13.20	12.18	12.03	12.15
14	80.00	10.97	10.95	11.00	10.98	10.80	10.95
15	75.86	9.57	9.56	9.59	9.59	9.38	9.55
16	72.68	8.07	8.06	8.08	8.09	7.87	8.06
17	70.68	6.56	6.57	6.57	6.59	6.37	6.56
18	70.00	5.16	5.18	5.16	5.19	4.98	5.17
19	70.68	3.96	3.98	3.94	3.98	3.81	3.97
20	72.68	3.03	3.06	3.01	3.06	2.92	3.06
21	75.86	2.45	2.48	2.42	2.47	2.39	2.48
22	80.00	2.25	2.29	2.22	2.27	2.24	2.28
23	84.82	2.45	2.48	2.42	2.46	2.48	2.48
24	90.00	3.03	3.06	3.00	3.03	3.11	3.06

θ(hr); t_∞(°F); q''(Btu/hr-ft^2)

0. Similarly, although the nonzero $\mathbf{B}_\mu$ coefficients go up to $\mathbf{B}_{10}$ in a nine-node example, the $\mathbf{B}_\mu$ for $\mu > 3$ in this example are essentially **0**.

It is of interest to use equation (17) to carry out a transient solution for the input shown in Fig. 1. As a specific example let us take $t_0 = 90°\text{F}$, $T_0 = 20°\text{F}$, $\omega = \pi/12\ \text{hr}^{-1}$, and $t_L = 70°\text{F}$ to represent a wall exposed to a daily outdoor-temperature cycle oscillating sinusoidally between 70 and 110°F with the room temperature on the other side of the wall maintained at 70°F. The results of several long-time solutions are compared in Table 3. The analytical solution obtained from equation (24) is the exact solution to the partial differential equation for the sinusoidal input. The other solutions all approximate the sinusoidal input by having the correct values at discrete intervals but varying linearly in between rather than sinusoidally. The ASHRAE solution is exact for this piecewise-linear input approximation. The difference between the ASHRAE result and the analytical result is an indication of the error introduced by using a piecewise-linear approximation to the sinusoidal input. The remaining four solutions are all obtained from finite-difference models of the wall. The nine-node Euler solution used $\Delta\theta = 0.05$ hr to be within the critical time step of 0.069 hr. This required 480 time steps for a 24-hr time period to produce the results shown in Table 3. Considerably larger time steps could be used for the Crank-Nicolson solution. The nine-node Crank-Nicolson results in Table 3 used $\Delta\theta = 1$ hr and required the solution of a set of nine linear algebraic equations 24 times during a 24-hr period. The final two solutions in Table 3 are the response-coefficient solutions described in this paper. Although the three-node results are fairly good, noticeable improvement is obtained in going to a nine-node model. The nine-node model results are quite comparable to the ASHRAE results.

In order to start computations in the ASHRAE and the response-coefficient methods, it was necessary to make an assumption regarding the previous outputs. In this example the previous outputs were assumed to be 0. The effect of this assumption decayed out by the end of the second cycle. The long-time solutions presented in Table 3 were attained in the third cycle.

Discussion

Although there are currently several methods that can be used to obtain long-time solutions to heat-conduction transients, each of them has its own practical limitations. The method developed in this paper makes use of the best ideas of each of the previous methods to arrive at a technique that can handle a wide variety of multidimensional composite structures with irregular geometry and time-dependent energy generation. It utilizes the ability of finite-difference or finite-element techniques to model complicated structures. Analytical techniques are used to solve the discrete equations to avoid critical-time-step problems and excessive computations at each time step required by Euler and Crank-Nicolson solutions. Finally, the new technique arrives at a set of response coefficients for the structure that can be used to study different input histories. This is a general technique that can be applied to any problem that can be satisfactorily modeled by a system of first-order ordinary differential equations with constant coefficients and whose input histories can be adequately approximated by continuous, piecewise-linear functions having a uniform time interval.

One of the major costs in obtaining the response coefficients is the solution of the eigenproblem given by equation (9). Since for one-dimensional conduction problems the number of nodes is generally not large and **C** and **S** are at most tridiagonal, finding $\mathbf{\Lambda}$ and **X** is inexpensive. For two-dimensional problems with a large number of nodes and nontridiagonal matrices the cost will be higher. However, this one-time cost for a particular structure and time interval may be justified. The response coefficients described in this paper may be used repeatedly for different input histories without having to recompute $\mathbf{\Lambda}$ and **X**. Furthermore, the cost of carrying a long-time solution using response coefficients is considerably cheaper than other solutions such as Crank-Nicolson which requires the solution of a large system of algebraic equations at each time step.

Although there appears to be considerable computational effort involved in arriving at the response coefficients, past experience has shown that the cost of doing so for one-dimensional problems is a relatively small portion of the total cost of carrying out a long-time solution. The cost of obtaining the response coefficients in the illustrative example was less than obtaining them from the computer program [13] that generated the ASHRAE results [11].

Even though the number of nodes n used to discretize a problem might be large, the response-coefficient matrices will generally be small since the number of inputs and outputs will generally be small. The sizes of $\mathbf{B}_0$ and $\mathbf{B}_\mu$ will be $\ell \times m$ if there are ℓ outputs and m time-dependent inputs and **D** will be $\ell \times k$ if there are k constant inputs. The C_μ coefficients are simply scalars. Once the response

coefficients have been obtained, they are the only information that needs to be stored in the computer. The continued storage of large matrices is unnecessary.

The only errors involved in solving the original heat-conduction problem are due to the spatial discretization of the structure and to the approximation of the time-dependent inputs by continuous, piecewise-linear functions. No additional approximations are made in determining the long-time solutions.

The savings in using equation (17) rather than equation (13) should be pointed out. In the nine-node illustrative example discussed earlier it would be necessary to calculate and use about 30 $\mathbf{A}_\mu$ coefficients in equation (13) to obtain the same degree of accuracy as one obtains by using four $\mathbf{B}_\mu$ and three C_μ coefficients in equation (17). The computation of the four $\mathbf{B}_\mu$ coefficients following equation (21) will require only four $\mathbf{A}_\mu$ coefficients.

The efficiency of using response coefficients in carrying out long-time solutions should be emphasized. In the nine-node illustrative example the response-coefficient technique computes the desired heat-flux output directly from equation (17), using the coefficients from Table 2, as

$$q''^{(0)} = 0.0040\, t_\infty^{(0)} + 0.0437\, t_\infty^{(1)} + 0.0303\, t_\infty^{(2)} + 0.0018\, t_\infty^{(3)} + 0.9477\, q''^{(1)} - 0.1467\, q''^{(2)} + 0.0011\, q''^{(3)} - 0.0798\, t_L$$

None of the nine nodal temperatures is ever computed. The matrix operations required by Euler or Crank-Nicolson at every time step are avoided. Even when the number of inputs and/or outputs is increased, the matrix operations required at each time step by the response-coefficient method involve much smaller matrices and less computer storage than Euler or Crank-Nicolson.

A finite-difference computer program that calculates response coefficients for composite plane walls is available from the authors for a nominal cost.

Acknowledgments

This work was carried out under the sponsorship of the National Science Foundation under Grant No. ENG78-08673 and the Graduate School of the University of Wisconsin-Madison.

References

1 Myers, G. E., *Analytical Methods in Conduction Heat Transfer*, McGraw-Hill, NY, 1971.

2 Carslaw, H. S. and Jaeger, J. C., *Conduction of Heat in Solids*, 2nd ed., Oxford University Press, Fair Lawn, N.J., 1959.

3 Myers, G. E., "Finite-Difference Class Notes," University of Wisconsin-Madison, 1978.

4 Myers, G. E., "The Critical Time Step for Finite-Element Solutions to Two-Dimensional Heat-Conduction Transients," ASME JOURNAL OF HEAT TRANSFER, Vol. 100, 1978, pp. 120–127.

5 Stephenson, D. G. and Mitalas, G. P., "Cooling Load Calculations by Thermal Response Factor Method," *ASHRAE Transactions*, Vol. 73, Part I, 1967, pp. III.1.1–III.1.7.

6 Mitalas, G. P. and Stephenson, D. G., "Room Thermal Response Factors," *ASHRAE Transactions*, Vol. 73, Part I, 1967, pp. III.2.1–III.2.10.

7 Stephenson, D. G. and Mitalas, G. P., "Calculation of Heat Conduction Transfer Functions for Multi-Layer Slabs," *ASHRAE Transactions*, Vol. 77, Part II, 1971, pp. 117–126.

8 *ASHRAE Handbook and Product Directory, 1977 Fundamentals*, pp. 25.27–25.35.

9 Pawelski, M. J., "Development of Transfer Function Load Models and Their Use in Modeling the CSU Solar House I," MS Thesis, University of Wisconsin-Madison, 1976.

10 Franklin, J. N., *Matrix Theory*, Prentice-Hall, Englewood Cliffs, N.J., 1968, p. 106.

11 *ASHRAE Handbook and Product Directory, 1977 Fundamentals*, Table 29, Problem 19, p. 25.34.

12 *Eigensystem Subroutine Package (EISPACK)*, 2nd ed., Argonne National Laboratory, Argonne, Ill., 1977.

13 Mitalas, G. P. and Arseneault, J. G., "Fortran IV Program to Calculate z-Transfer Functions for the Calculation of Transient Heat Transfer through Walls and Roofs," *Proceedings of the Conference on Use of Computers for Environmental Engineering Related to Buildings*, held in Gaithersburg, MD, Nov. 30 to Dec. 2, 1970, NBS Building Science Series 39, Oct. 1971.

S. K. Fraley[1]
Oak Ridge National Laboratory,
Oak Ridge, Tenn 37830

T. J. Hoffman
Oak Ridge National Laboratory,
Oak Ridge, Tenn 37830

P. N. Stevens
The University of Tennessee,
Knoxville, Tenn 37916

A Monte Carlo Method of Solving Heat Conduction Problems[2]

A new approach in the use of Monte Carlo to solve heat conduction problems is developed using a transport equation approximation to the heat conduction equation. A variety of problems is analyzed with this method and their solutions are compared to those obtained with analytical techniques. This Monte Carlo approach appears to be limited to the calculation of temperatures at specific points rather than temperature distributions. The method is applicable to the solution of multimedia problems with no inherent limitations as to the geometric complexity of the problem.

1 Introduction

Monte Carlo methods are particularly useful in the solution of neutron and gamma-ray transport problems which involve complex geometries. Recent work [1] has suggested that the Monte Carlo approach might also be useful in the solution of certain classes of heat conduction problems.

In this paper a new approach to the use of Monte Carlo in the solution of heat conduction problems is developed. This method, which uses a transport equation approximation, will allow the solution of problems with as much geometric complexity as is necessary to adequately describe the physical model. The method is also completely compatible with Monte Carlo radiation transport programs. Thus, nuclear criticality, radiation shielding, and heat transfer calculations can be performed with one geometric description and one computer code. Coupled radiation transport and heat conduction problems can also be performed in a single computer run where the energy generated by nuclear radiation (for example, through fission reactions or by energy absorption) is the heat source for the heat transfer calculation.

There are many ways to solve the basic heat conduction problem; both numerically and analytically. Numerical techniques such as finite difference or finite element will in general provide a much faster solution. The proposed method will, however, be able to solve certain problems for which solutions were not previously feasible. Since the method uses the same random walk logic as existing Monte Carlo radiation transport computer codes, it was not necessary to generate a completely new computer program for its implementation. The solution to the problems solved in this paper were performed using existing computer codes.

Other continuous Monte Carlo techniques for solving heat conduction problems have been reported [1–10], and a summary of these methods is given in [1]. However, all published results using these methods have been limited to single medium problems. Discrete Monte Carlo approaches have also been used [11–14]. These methods are Monte Carlo methods which solve the finite difference equations and have not proven to be competitive with other finite difference techniques. Hybrid Monte Carlo approaches have also been developed [15, 16], but these require the use of both analog and digital systems and appear to be limited in their potential applications.

2 Transport Theory Approximation to the Differential Equation of Heat Conduction

The differential equation of heat conduction through a stationary, isotropic solid is given by [17]:

$$\nabla \cdot K(r, T)\nabla T(\bar{r}, t) + S(\bar{r}, t) = \rho c \frac{\partial T}{\partial t}, \tag{1}$$

where, $K(\bar{r}, T)$ = thermal conductivity, ρ = density, c = specific heat, and $S(\bar{r}, t)$ = internal heat source.

If the thermal conductivity is not a function of position or temperature, this simplifies to:

$$K\nabla^2 T(\bar{r}, t) + S(\bar{r}, t) = \rho c \frac{\partial T}{\partial t}. \tag{2}$$

It is desirable to solve the above differential equation subject to the following types of standard boundary conditions:

1. **Boundary Condition of the First Kind.** The temperature is specified along a boundary surface

$$T = f(\bar{r}_s, t), \tag{3}$$

where $\bar{r}_s$ is on a boundary surface.

2. **Boundary Condition of the Second Kind.** The normal derivative of the temperature is specified along a boundary surface

$$\frac{\partial T}{\partial n} = f(\bar{r}_s, t), \tag{4}$$

where $\bar{r}_s$ is on a boundary surface, $\partial/\partial n$ represents differentiation along the outward normal to the surface.

3. **Boundary Condition of the Third Kind.** A combination of the temperature and normal derivative is specified at a boundary.

$$K\frac{\partial T}{\partial n} + hT = f(\bar{r}_s, t), \tag{5}$$

where $\bar{r}_s$ is on a boundary surface, $\partial/\partial n$ represents differentiation along the outward normal to the surface, K is the thermal conductivity, and h is the convective heat transfer coefficient. This type of boundary condition is normally associated with forced convection and written as

$$K\frac{\partial T}{\partial n} = h(T_\infty - T), \tag{6}$$

where T_∞ is the temperature of the surroundings.

The neutron diffusion equation can be written as [18]

$$D\nabla^2\phi(\bar{r}, t) - \Sigma_a\phi(\bar{r}, t) + S(\bar{r}, t) = \frac{1}{v}\frac{\partial \phi}{\partial t}, \tag{7}$$

where, ϕ = neutron flux, D = diffusion coefficient, Σ_a = absorption cross section, v = neutron's speed.
D is normally given by

$$D = \frac{1}{3(\Sigma - \bar{\mu}\Sigma_s)}, \tag{8}$$

where Σ = total cross section, $\bar{\mu}$ = average cosine of the scattering angle, Σ_s = scattering cross section.
If $\Sigma_a = 0$, then $\Sigma = \Sigma_s$ and

$$D = \frac{1}{3\Sigma(1 - \bar{\mu})}. \tag{9}$$

If the scattering is isotropic, $\bar{\mu} = 0$, and

$$D = \frac{1}{3\Sigma}. \tag{10}$$

---

[1] Present Address: U. S. Arms Control and Disarmament Agency, Room 4953, Washington, D.C. 20451.

[2] Research sponsored by the Office of Nuclear Material Safety and Safeguards, Nuclear Regulatory Commission under Interagency Agreement (DOE-549-75) with the U.S. Department of Energy under contract W-7405-eng-26 with the Union Carbide Corporation.

Contributed by the Heat Transfer Division for publication in the JOURNAL OF HEAT TRANSFER. Manuscript received by The Heat Transfer Division August 8, 1979.

Therefore, under these conditions, the diffusion equation becomes

$$\frac{1}{3\Sigma}\nabla^2\phi + S(\bar{r}, t) = \frac{1}{v}\frac{\partial\phi}{\partial t}, \tag{11}$$

and by comparing the above to the heat conduction equation, i.e., equation (2), the two equations are equivalent if

$$\Sigma = \frac{1}{3K}, \tag{12}$$

and

$$v = \frac{1}{\rho c}. \tag{13}$$

In neutron transport problems, the diffusion equation is frequently used as an approximation to the Boltzmann transport equation. Since Monte Carlo methods are available for solving the transport equation in problems with very complex geometries, these methods may then be used to approximate the solutions to the equivalent heat conduction problems.

Transport theory differs from diffusion theory when scattering is highly anisotropic or the angular distribution of particles (angular flux) is highly anisotropic. Transport theory also differs from diffusion theory in the application of various boundary conditions. For example, diffusion theory allows the specification of a zero flux boundary condition whereas transport theory allows only a zero incoming flux boundary condition.

In trying to adjust neutron diffusion theory to approximate the transport equation, various methods of correction have been developed. For example, a zero flux boundary condition at an extrapolated distance [19] from the boundary is used to simulate a zero incoming flux at the boundary. In optically thin regions (very few mean-free-paths thick), in the vicinity of strong absorbers or sources or when scattering is strongly anisotropic, the differences between the neutron diffusion approximation and transport theory may be significant, and in these cases, the use of neutron diffusion theory is inappropriate. These differences are more easily corrected when transport theory is used to approximate diffusion theory. The diffusion equation with isotropic scattering and the heat conduction equation are equivalent, and the scattering used in the transport solution can always be performed isotropically. To correct for the anisotropic flux which transport theory will give in the vicinity of strong absorbers or sources or in optically thin regions, the actual cross sections used in the transport calculation can be scaled so that the regions of interest are no longer optically thin. An anisotropic flux will, therefore, exist only over a small region of the problem and the transport theory approximation to the diffusion equation will be appropriate.

Scaling of cross sections is accomplished by letting $T = \beta\phi$ where β is a constant and the heat conduction equation becomes

$$K\beta\nabla^2\phi + S(\bar{r}, t) = \beta\rho c\frac{\partial\phi}{\partial t}. \tag{14}$$

The boundary conditions appropriate to a given problem are also modified and assume the following forms:

1. **Boundary Condition of First Kind**

$$\phi = \frac{f(r_s, t)}{\beta}. \tag{15}$$

2. **Boundary Condition of Second Kind**

$$\frac{\partial\phi}{\partial n} = \frac{f(r_s, t)}{\beta}. \tag{16}$$

3. **Boundary of Third Kind**

$$K\beta\frac{\partial\phi}{\partial n} + h\beta\phi = f(r_s, t). \tag{17}$$

Across an interface, the equality of heat fluxes becomes

$$K_1\beta\frac{\partial\phi_1}{\partial n} = K_2\beta\frac{\partial\phi_2}{\partial n}, \tag{18}$$

and the equality of temperatures becomes

$$\beta\phi_1 = \beta\phi_2. \tag{19}$$

Therefore, by letting $T = \beta\phi$ and comparing to the diffusion equation

$$\Sigma = \frac{1}{3K\beta}, \tag{20}$$

and

$$v = \frac{1}{\rho c\beta}. \tag{21}$$

It is noted that the source doesn't change due to the scaling procedure.

The method of solution using the transport equation approximation is then to solve the Boltzmann transport equation for the flux ϕ under conditions of isotropic scattering and no absorption. The actual cross sections and velocities used in the calculation may be scaled using equations (20) and (21) so as to make the differences between the transport equation solution and the diffusion equation solution as small as desired (with a penalty of increasing computation time). The boundary conditions used during the calculation are obtained from equations (15–19). Since the diffusion equation is equivalent to the heat conduction equation under the above conditions, the transport equation approximation of the solution to the heat conduction equation is then obtained from

$$T = \beta\phi. \tag{22}$$

Once the appropriate transport problem has been defined, any of the methods which would normally be used in its solution can be used without additional justification. Monte Carlo methods have been developed for solving transport problems, and the associated existing methodology is thereby appropriate. A mathematical treatment of the application of the Monte Carlo method to solve the Boltzmann transport equation is given in a book by Spanier and Gelbard [20] and a review of the Monte Carlo method as applied to particle transport is given by Carter and Cashwell [21].

Since the boundary conditions associated with heat conduction are different from those normally used in transport theory, it is necessary to develop appropriate methods for applying these boundary conditions during Monte Carlo calculations. The convective boundary condition can be written:

$$K_1\frac{\partial T}{\partial n} = h(T_\infty - T). \tag{23}$$

This can be rewritten as

$$K_1\frac{\partial T}{\partial n} = h\Delta n\left(\frac{T_\infty - T}{\Delta n}\right) \tag{24}$$

If it is assumed that T_∞ is the temperature at a distance Δn away from the surface, then $h\Delta n$ has the form of a conduction coefficient and $(T_\infty - T)/\Delta n$ represents the change in temperature per unit distance. Let $K_2 = h\Delta n$; then, this boundary condition could be approximated in transport theory by adding a layer Δn thick onto the boundary with a cross section Σ given by

$$\Sigma = \frac{1}{3K_2} = \frac{1}{3h\Delta n}. \tag{25}$$

The thickness of this layer in mean-free-paths is given by

$$\Sigma\Delta n = \frac{\Delta n}{3K_2} = \frac{1}{3h}. \tag{26}$$

The thickness in mean-free-paths does not depend upon the Δn used in the approximation. If the limit as Δn approaches 0 is taken, then it is apparent that the convective boundary condition is equivalent to a physically infinitesimally thin layer of material which is $1/3h$ mean-free-paths thick. This type of boundary condition can be treated as an albedo problem. Letting β be the albedo (the ratio of the current returning from the boundary layer to the current entering the

boundary layer) and $\delta = 1/3h$ be the thickness of the boundary layer in mean-free-paths, a simple diffusion theory solution (based on Fick's law) for the albedo gives

$$\beta = \frac{1 - \frac{2}{3\delta}}{1 + \frac{2}{3\delta}}. \tag{27}$$

The convective boundary condition can, therefore, be represented by an equivalent albedo condition.

The fixed temperature boundary condition of heat conduction (which is equivalent to the neutron diffusion theory zero flux condition) does not have an exact equivalent boundary condition in transport theory. The most common method used is to treat the zero flux diffusion theory boundary condition as being represented by a zero incoming flux condition in the transport equation. To account for the differences in the boundary conditions, the diffusion equation flux is assumed to be zero at an extrapolated distance beyond the boundary at which the zero incoming angular flux condition is imposed. The extrapolation distance used (0.71 mean-free-paths) is determined from neutron transport theory. This correction was made in several problems and resulted in excellent agreement with analytical solutions. However, this type of correction is not always practical for problems with complex shapes or with several different types of materials on the external boundaries. The effect of the different boundary conditions can still be minimized in cases where an extrapolation distance correction is not practical by scaling up the cross sections used in the transport calculation (with a resultant penalty of increased computer running time).

A better boundary condition for the transport solution to simulate the diffusion theory zero flux condition is obtained by considering the limit of the convective boundary condition as the thickness of the convective layer (in mean-free-paths) goes to zero. This limit is equivalent to the fixed temperature boundary condition. Taking this limit in equation (27) gives a transport condition of an albedo of minus one on the boundary. Fractional negative albedo conditions can be used in transport solutions, but a negative albedo of minus one on all external boundaries for a problem with $\Sigma_a = 0$ is nonconvergent. To test the negative albedo boundary condition, various negative albedo conditions were applied at the boundary of the Milne problem, and solutions were obtained with ANISN [22]. The Milne problem is a one-dimensional infinite half-space problem (material from 0 to ∞) with a unit source at infinity. The albedo condition was imposed at the boundary $x = 0$. The results of the ANISN calculations for the total flux are given in Fig. 1 for the albedo conditions of 0 and -0.4 and are compared to the diffusion theory solution with a zero flux boundary condition. Based on these calculations, if the change associated with going from a vacuum boundary condition (zero incoming angular flux) to a -0.4 albedo condition is multiplied by 1.89 and added to the vacuum boundary transport solution, the results are the same as the diffusion theory solution at points which are not close to the boundary. The results are also very good even at points close to the boundary. An albedo of -0.4 was chosen because it gave a significant correction (over 50 percent of the difference between the vacuum boundary transport theory solution as compared to the zero flux diffusion theory solution) and is still small enough so as not to prohibitively increase the running time for problem solutions. Test problems with a -0.4 albedo condition ran 1.5 to 2.0 times as long as those with a vacuum boundary condition. This type of boundary condition is easily implemented in Monte Carlo transport codes and can be implemented so as to give the solution with a vacuum boundary condition and the negative albedo boundary condition in the same run.

3 Applications

Problems with known solutions [23] were selected as a means to check out and evaluate the use of the transport equation approximation to the heat conduction equation. Three-dimensional, time-dependent, multimedia problems were investigated. Generally, the adjoint formulation was found to be most suitable for finding temperatures at distinct points. Evaluation of temperature profiles was found to be impractical using this Monte Carlo method. The calculations were performed with the radiation transport code, MORSE-SGC [24]. For more detailed information on these test problems, the reader is referred to [25].

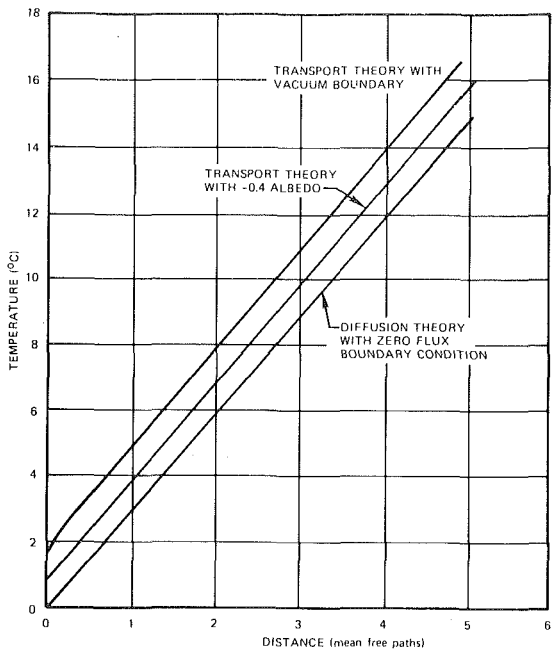

Fig. 1 Diffusion theory versus transport theory with different boundary conditions

One of the major advantages of this method is that solutions can be obtained for heat conduction problems in which the heat source is due to nuclear radiation. The transport of the radiation and the diffusion of the heat deposited by the radiation can be accounted for in a single Monte Carlo calculation. As an example, the Monte Carlo method is applied to a coupled gamma ray radiation and heat conduction problem with the following characteristics (Fig. 2):

1 Outer boundary of the sphere is maintained at a constant temperature
2 Radius of sphere is 10 cm
3 $K = 0.3333$ cal/cm-s-°C
4 Σ_t for gammas (all energies) = 0.1 cm^{-1}
5 Σ_a for gammas = 0.03 cm^{-1}
6 1 cal/cm^2 s energy in the incident gamma radiation
7 Steady-state condition
8 Isotropic scattering of gamma radiation

The values chosen are typical of those for a metal such as aluminum.

To provide a check on the Monte Carlo solution, the average temperature as a function of radius of the sphere is estimated using previously available techniques. For calculating the average gamma flux as a function of radius, Kalos [26] has shown that the incident parallel beam of ϕ_0 particles/cm^2-s can be replaced by an isotropic flux of ϕ_0 particles/cm^2-s over the entire surface of the sphere. Using this transformation, the average gamma flux as a function of radius was solved using the discrete ordinates code ANISN and the average energy deposition was calculated. With an incident gamma radiation beam of 1 cal/cm^2-s, the radius averaged gamma flux was fairly uniform in the sphere varying from a low of 0.685 cal/cm^2-s at the center to a high of 0.848 cal/cm^2-s at the edge. The volume averaged flux was 0.773 cal/cm^2-s. The average heat source in the sphere is then given by $\phi_{avg}\Sigma_a$ and is 0.0232 cal/cm^2-s. Assuming that this heat source is uniform across the sphere, a one-dimensional estimate of the temperature as a function of radius can then be made analytically.

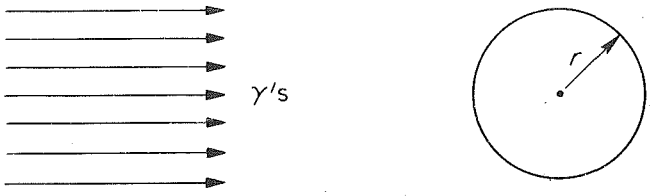

Fig. 2 One-medium sphere with incident gamma beam

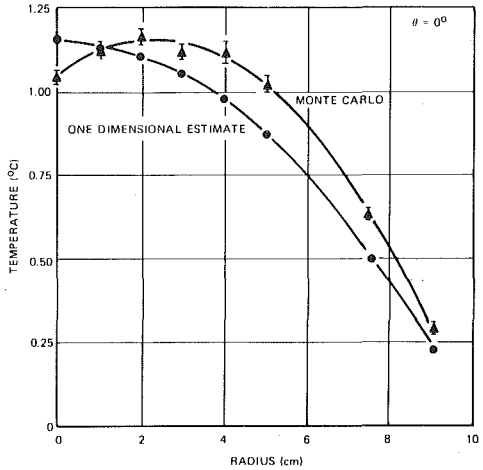

Fig. 3 Temperatures for $\theta = 0$ deg compared to one-dimensional estimates

The Monte Carlo calculation of the coupled gamma-ray and heat conduction problem was performed using MORSE-SGC. The logic used for performing a coupled gamma radiation and heat conduction problem with MORSE-SGC is the same as that used for solving a coupled neutron-gamma problem. For the forward formulation of the problem, a gamma starting location is chosen from the parallel beam distribution; and the gamma particle is tracked until it escapes or until the weight of the particle has been reduced by nonabsorption weighting at collision sites and its survival determined by Russian roulette. At each collision site energy is absorbed and represents an energy source. This heat source was assumed to generate secondary particles. In the actual calculation a secondary particle was generated with a probability of 0.1 at each collision site with particle weighting to maintain a fair game. The secondary particles are then tracked to determine temperatures.

As was expected, an adjoint formulation of the problem was necessary to obtain good statistics. (The adjoint calculation obtained fractional standard deviations of less than 1 percent in the same computation time that the forward calculation obtained fractional standard deviations of over 30 percent. Further reduction in the fractional standard deviation can be obtained by analysis of more histories; the standard deviation is inversely proportional to the square root of the number of histories. However, uncertainties in the physical data restrict the accuracy required for practical problems.) A next event estimator was used in the adjoint formulation at each gamma collision site (the secondary particles in the adjoint formulation) and the probability of the gamma having reached this collision site from the incident beam was scored. By scoring to different detectors, where for each detector a different location of the incoming beam was used, the temperature at a number of points could be calculated with the same computer run. Each of these points will have the same radius but are at locations which have the same relative locations to the incoming beams as was used during the estimator process.

Comparisons of the one-dimensional estimate of the average temperature as a function of radius and the Monte Carlo calculation of the temperature at various locations in the sphere are shown in Figs. 3–5. An adjoint Monte Carlo calculation was performed for each of the eight radii shown in the figures. Each Monte Carlo calculation required 4.2 min of CPU time on the IBM 360/91.

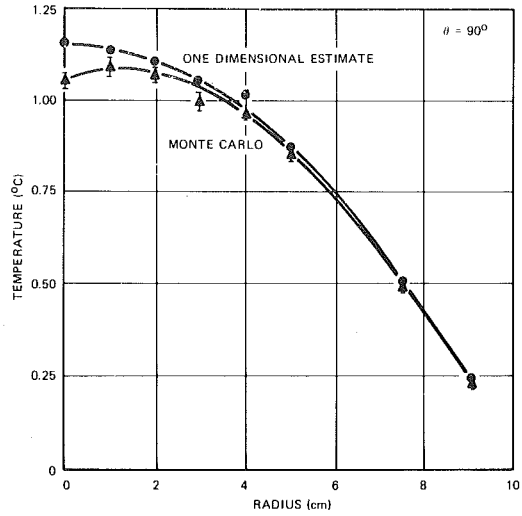

Fig. 4 Temperatures for $\theta = 90$ deg compared to dimensional estimates

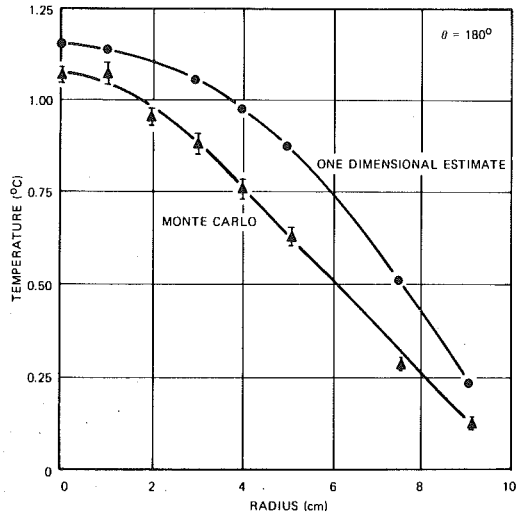

Fig. 5 Temperatures for $\theta = 180$ deg compared to one-dimensional estimates

The Monte Carlo results along various radii show the variation of the temperature over the sphere. As would be expected intuitively, the hottest point in the sphere is not at the center but is several centimeters off center in the direction towards the incident beam of gamma radiation.

4 Conclusions

The transport theory approximation has been shown to be appropriate for use in solving many types of heat conduction problems. The transport approximation is not limited to Monte Carlo methods; however, since most other techniques can be used to solve the heat conduction equation directly, the approximation is not necessary with these other methods.

As is typical with current Monte Carlo methods, other methods of problem solutions appear to be preferable when they may be used. However, there are heat conduction problems for which the solution is not feasible using other methods. The application of the Monte Carlo method to the transport equation approximation will provide solutions to many of these problems. There are no inherent limitations as to the geometric complexity of the heat conduction problems which can be solved using this method. It will also simplify, or make possible, the solution of coupled problems which involve nuclear reactions as the heat source for a heat conduction problem.

The Monte Carlo solution of the transport equation approximation is more suitable for calculating temperatures at individual points within a system rather than calculating complete temperature dis-

tributions. The adjoint formulation appears to be the most suitable mode of solution. The method is not applicable to problems where the thermal conductivity is temperature dependent.

The advantages and disadvantages of the transport equation approximation for performing Monte Carlo solutions of heat conduction problems are illustrated by the following comparison to the surface density walk [1] and floating random walk [2] Monte Carlo techniques:

1 There are no published results on the use of either the surface density walk or floating random walk in multimedia problems.

2 The tracking algorithm used by the floating random walk is difficult since it requires the determination of the nearest boundary point. Both the transport equation approximation and the surface density walk use a simpler method which requires the finding of the intersect point between a surface and a given line.

3 The surface density walk tracks directly to surface points, with the number of tracks for a given walk being determined by the number of terms in the truncated Fredholm series being evaluated. The floating random walk tracks over large distances until the walk approaches a boundary in which case the distances become smaller and smaller. An approximation must then be used to reach the boundary. The transport equation approximation uses relatively small steps throughout the walk with the step size becoming smaller as a scale factor is increased to make the transport equation approximation better.

4 The surface density walk and the transport equation approximation may be used with or readily adapted to existing Monte Carlo radiation transport codes.

5 All three methods may be used to solve heat conduction problems with internal heat sources, given surface temperature distributions and time dependence.

6 The floating random walk and the transport equation approximation may be used to solve problems with convective boundary conditions.

7 The transport equation approximation may be used to solve coupled nuclear radiation and heat conduction problems.

The Monte Carlo solution of the transport equation approximation has been shown to be useful in the solution of many types of heat conduction problems. All of the standard biasing techniques available for use in solving radiation transport problems with Monte Carlo are applicable to this method. The method should also be useful when used in conjunction with deterministic codes as in the adjoint difference method [27].

References

1 Hoffman, T. J., and Banks, N. E., "Monte Carlo Surface Density Solution to the Dirichlet Heat Transfer Problem," *Nuclear Science and Engineering,* Vol. 59, 1976, pp. 205–214.

2 Haji-Sheikh, ., and Sparrow, E. M., "The Solution of Heat Conduction Problems by Probability Methods," ASME JOURNAL OF HEAT TRANSFER, Vol. 89, 121 1967, p. 121.

3 Haji-Sheikh, A., and Sparrow, E. M., "The Floating Random Walk and Its Application to Monte Carlo Solutions of Heat Equations," *Journal SIAM, Applied Mathematics,* Vol. 14, 1966, p. 370.

4 Troubetzkoy, E. S., and Banks, N. E., "Solution of the Heat Diffusion Equation by Monte Carlo," *Transactions of the American Nuclear Society,* Vol. 19, 1974, p. 163.

5 Hoffman, T. J., and Banks, N. E., "Monte Carlo Solution to the Dirichlet Problem with the Double Layer Potential Density," *Transactions of the American Nuclear Society,* Vol. 18, 1974, p. 136.

6 Banks, N. E., and Hoffman, T. J., "Continuous Monte Carlo Solution to the Dirichlet Heat Transfer Problem Using the Double Layer Potential," 20th Army Math. Conf., Boston, Mass., 1974.

7 Banks, N. E., and Hoffman, T. J., "Extension of the Surface Density Monte Carlo Technique to Heat Transfer in Non-Convex Regions," *Transactions of the American Nuclear Society,* Vol. 19, 1974, p. 164.

8 Hoffman, T. J., and Banks, N. E., "Monte Carlo Solutions to Transient Heat Conduction Problems," *Transactions of the American Nuclear Society,* Vol. 21, 1975, p. 204.

9 Hoffman, T. J., "Monte Carlo Solution to Heat Conduction Problems with Internal Sources," *Transactions of the American Society,* Vol. 24, 1976, p. 181.

10 Muller, M. E., "Some Continuous Monte Carlo Methods for the Dirichlet Problem," *Annual Mathematic Statistics,* Vol. 27, 1956, pp. 569–589.

11 Thompson, J. J., and Chen, P. Y. P., "Heat Conduction with Internal Sources by Modified Monte Carlo Method," *Nuclear Engineering and Design,* Vol. 12, 1970, pp. 207–214.

12 Todd, J., "Experiments in the Solution of Differential Equations by Monte Carlo Methods," *Journal of the Washington Academy of Science,* Vol. 44, 1954.

13 Hoshino, S., and Ichida, K., "Solution of Partial Differential Equations by a Modified Random Walk," *Numerical Mathematics,* Vol. 18, 1971, pp. 61–72.

14 Zinsmeister, G. E., and Sawyer, J. A., "A Method for Improving the Efficiency of Monte Carlo Calculation of Heat Conduction Problems," ASME JOURNAL OF HEAT TRANSFER, Vol. 96, 1974, pp. 246–248.

15 Little, W. D., "Hybrid Computer Solutions of Partial Differential Equation by Monte Carlo Method," Ph.D. thesis, University of British Columbia, 1965.

16 Fahrmeir, L., "Extension of the Hybrid Monte Carlo Method for Boundary-Value Problems," *Simulation,* Vol. 21(6), 1973, p. 477.

17 Ozisik, M. N., *Boundary Value Problems of Heat Conduction,* International Textbook, Scranton, 1968.

18 Murray, R. L., *Nuclear Reactor Physics,* Prentice Hall, 1957.

19 Case, K. M., de Hoffman F., and Placzek, G. P., "Introduction to the Theory of Neutron Diffusion," U.S. Government Printing Office, Washington, D.C., 1953.

20 Spanier, J., and Gelbard, E. M. *Monte Carlo Principles and Neutron Transport Problems,* Addison-Wesley, 1969.

21 Carter, L. L., and Cashwell, E. D., "Particle-Transport Simulation with the Monte Carlo Method," USERDA Tech. Info. Center, TID-26607, 1975.

22 Engle, Jr., W. W., "A User's Manual for ANISN, A One-Dimensional Discrete Ordinates Transport Code with Anisotropic Scattering," UCC-ND, K-1693, 1967.

23 Carslaw, H. S., and Jaeger, J. C., *Conduction of Heat in Solids,* Oxford, 2nd ed., 1959.

24 Fraley, S. K., "User's Guide to MORSE-SGC," ORNL/CSD-7, 1976.

25 Fraley, S. K., "A Monte Carlo Method of Solving Heat Conduction Problems," Ph.D. thesis, University of Tennessee, 1977.

26 Kalos, M. H., "ANTE 2, Adjoint Monte Carlo Time-Dependent Neutron Transport Code in Combinatorial Geometry," Appendix G, MAGI, Inc., 1970.

27 Hoffman, T. J., Robinson, J. C., and Stevens, P. N., "The Adjoint Difference Method and Its Application to Deep Penetration Radiation Transport," *Nuclear Science and Engineering,* Vol. 48, 1972, pp. 179–188.

Transient Heat Transfer between a Plate and a Fluid whose Temperature Varies Periodically with Time

J. Sucec
Professor of Mechanical Engineering,
Room 203 Boardman Hall,
University of Maine,
Orono, Maine 04469
Mem. ASME

Using the method of complex temperature in conjunction with the Laplace transformation, an exact analytical solution is found for the transient, conjugate, forced convection problem consisting of a plate, whose base is insulated, interacting with a fluid, moving in a steady slug fashion, whose temperature, at points far from the plate, varies sinusoidally with time. Simple quasi-steady results are derived for comparison. Also presented is a method for determining the qualitative conditions under which one might expect a quasi-steady analysis to be valid in a general problem.

Introduction

The problem of predicting the surface heat flux and surface temperature, as a function of position and time, of a body subjected to a flowing fluid whose temperature, far away from the body, varies periodically with time, has a number of possible applications. For instance, gas turbine blades and vanes must interact with a periodically varying gas temperature as a consequence of processes in the combustor. The thermal response of coatings to this periodic thermal loading may be a factor in coating life. In addition, the storage material in a parallel flow regenerative heat exchanger is subject to a periodically varying fluid inlet temperature, both during the transient start-up and in the ultimate cyclic, or periodic, unsteady state.

Willmott and Burns [1] use finite difference methods to solve the classical regenerator equations for the transient response of a regenerator operating initially in the periodic unsteady state when, suddenly, a step change in either inlet gas temperature or mass flow rate initiates a transient that causes the regenerator to go toward a new periodic unsteady state. Their analysis, in common with most analyses performed specifically for regenerators, employs the quasi-steady assumption which uses, in this case, a constant, both in space and time, surface coefficient of heat transfer. In [2], Kardas solves the case of the unidirectional regenerator with a sinusoidal or cosinusoidal inlet temperature. However, the quasi-steady approximation is employed and the results are only for the ultimate periodic unsteady state and not the transient leading up to this state. Chase, et al. [3] relax the quasi-steady assumption and use the slug flow approximation in a Laplace transform solution for the regenerator wall and bulk mean temperature after a step change in the inlet temperature to a value which is held constant in time thereafter. Sparrow and DeFarias [4] solve, by the method of complex temperature, the problem of slug flow in a parallel plate duct, with both outer plate surfaces insulated, when the fluid inlet temperature varies in a sinusoidal fashion. Their problem, like those of [1–3] is a conjugate one, that is, the temperature distribution within the moving fluid and in the solid wall are mutually coupled. The results of [4] are, however, limited to the periodic unsteady state. In [5] the author presents analytical results for the case of slug flow over a plate, cooled from below, when the fluid flows over it in a slug fashion and the inlet temperature is either a step or ramp function of time. Also presented in [5] is an approximate method for arbitrary fluid inlet temperature variation with time. (Discussion of other works in transient forced convection, both of the conjugated and non-conjugated type, which bear a peripheral relationship to the present work, is given in [5].)

The present work considers a flat plate which is insulated on its lower surface and has a fluid flowing in a steady, laminar, slug fashion over its top surface. Initially both the plate and the fluid are at a constant temperature when, suddenly, at time $t = 0$, the fluid temperature at the leading edge varies sinusoidally with time. It is required to predict both the fluid and wall temperature distributions during the initial transient as well as in the ultimate periodic unsteady state. Use of the slug velocity profile allows an analytic solution to be obtained which, it is felt, displays the essential features to be expected in the actual case in which there is a two-dimensional velocity distribution. Numerical values will differ between the slug and non-slug flow cases, but, as evidenced by the work in [12], the major trends and insights will remain basically unchanged. With this in mind, the physical situation considered here can be used as a first model of an uncooled turbine vane or a thermal entrance region of a parallel flow regenerator. Response functions are presented for the local wall temperature and the local surface heat flux as well as for the local bulk mean temperature of the fluid in the case of the thermal entrance region. Also presented is a method whereby one can determine the qualitative conditions under which one would reasonably expect any quasi-steady solution to yield good results in a general transient forced convection problem.

Theoretically, one should be able to solve the problem at hand by use of Duhamel's Theorem coupled with the results presented in [5]. An attempt to do this, however, did not lead to a solution in terms of elementary (tabulated) functions. Thus it was decided to attempt a solution by the method of complex temperature [6] usually employed, insofar as the author is aware, to find only the eventual periodic unsteady state. In this work it is also employed successfully to find the transient leading up to the periodic unsteady state and to solve for the transient between one periodic unsteady state and a new periodic unsteady state due to a sudden change in the amplitude of the sinusoidal driving function. The linearity of the governing equations for the problem allows the results to be used, via harmonic analysis as in [2], to generate the response to more general periodic fluid temperature variations.

Analysis

Consider steady, laminar, constant property, low speed, two-dimensional planar, thin boundary layer type flow over a flat plate of thickness b units with a perfectly insulated lower surface. Both the plate and the moving fluid have an initial temperature excess of zero when a transient is initiated by a sudden change in the temperature excess of the fluid to $\Delta T \sin\omega t$ at the plate leading edge. Axial conduction in the fluid is neglected, by virtue of a large enough Peclet number, and is also neglected in the plate, as well, due to its thinness. It is assumed that the thermophysical properties of the plate are constant and that the local Biot number is small enough to allow one

Contributed by The Heat Transfer Division for publication in THE JOURNAL OF HEAT TRANSFER. Manuscript received by The Heat Transfer Division, July 27, 1979.

to lump the plate's temperature in the direction perpendicular to the plate. Lastly, a slug flow idealization of the actual velocity field will be utilized.

An energy balance on a volume of the plate, differential in extent to the x direction, yields, after invoking the conjugation condition, that is, equality of the local fluid and plate temperature at their common interface, and using the lumped condition for the plate,

$$t > 0, y = 0, x > 0 \quad \frac{\partial \theta}{\partial y} = r \frac{\partial \theta}{\partial t}. \tag{1}$$

The remainder of the mathematical description of the problem to be solved is as follows.

$$\frac{\partial \theta}{\partial t} + u \frac{\partial \theta}{\partial x} = \alpha \frac{\partial^2 \theta}{\partial y^2} \tag{2}$$

$$t = 0, x > 0, y > 0 \quad \theta = 0 \tag{3}$$

$$t > 0, x = 0, y > 0 \quad \theta = \Delta T \sin \omega t \tag{4}$$

$$t > 0, x > 0, y \to \infty \quad \theta \text{ remains finite} \tag{5}$$

It is proposed to solve equations (1–5) by use of the method of complex temperature [6]. Thus, one defines

$$\phi = \theta^* + i\theta \tag{6}$$

where θ^* is the solution to equations (1–5) for a cosine thermal disturbance function at the inlet. θ itself is eventually found from

$$\theta = Im \{\phi\} \tag{7}$$

Since both the transient response and the ultimate periodic unsteady state are being sought, proper cognizance must be given to the initial condition (3) in the formulation of the problem in terms of ϕ. Using (6) and Euler's expansion formula, one arrives at the problem statement in terms of ϕ.

$$\frac{\partial \phi}{\partial t} + u \frac{\partial \phi}{\partial x} = \alpha \frac{\partial^2 \phi}{\partial y^2} \tag{8}$$

$$t = 0, x > 0, y > 0 \quad \phi = 0 \tag{9}$$

$$t > 0, x = 0, y > 0 \quad \phi = \Delta T e^{i\omega t} \tag{10}$$

$$t > 0, x > 0, y \to \infty \quad \phi \text{ is finite} \tag{11}$$

$$t > 0, x > 0, y = 0 \quad \frac{\partial \phi}{\partial y} = r \frac{\partial \phi}{\partial t} \tag{12}$$

Next, a solution is effected to equations (8–12) by successive application of the Laplace transform to the independent variables x and t.

Defining,

$$\hat{\phi} = \int_0^\infty \phi e^{-sx} \, dx \tag{13}$$

and

$$\hat{\hat{\phi}} = \int_0^\infty \hat{\phi} e^{-pt} \, dt \tag{14}$$

equations (8–12) become, in the second transformed plane,

$$\frac{d^2 \hat{\hat{\phi}}}{dy^2} - \frac{(su + p)}{\alpha} \hat{\hat{\phi}} = -\frac{u \Delta T}{\alpha (p - i\omega)} \tag{15}$$

$$y \to \infty \quad \hat{\hat{\phi}} \text{ is finite} \tag{16}$$

$$y = 0 \quad \frac{d\hat{\hat{\phi}}}{dy} = rp\hat{\hat{\phi}} \tag{17}$$

After solving (15), subject to (16) and (17), one has

$$\frac{\hat{\hat{\phi}}}{\Delta T} = \frac{u}{(su + p)(p - i\omega)} - \frac{rp\sqrt{\alpha/u}\, e^{-y\sqrt{u/a}\,\sqrt{s+p/u}}}{(p - i\omega)(s + p/u)(\sqrt{s+p/u} + rp\sqrt{\alpha/u})} \tag{18}$$

With the aid of tables of transforms [7], as well as the substitution and translation properties, (18) is inverted and its imaginary part is found yielding the solution below.

$$\frac{\theta}{\Delta T} = 0 \quad \text{for} \quad \tau < 0$$

$$\frac{\theta(X, Y, \tau)}{\Delta T} = \text{erf } Y \sin \omega\tau + Im \left\{ e^{i(\omega\tau + 2YX) - X^2} \left[\text{erfc } (Y + iX) - \text{erfc} \left(\frac{\omega\tau}{2X} + Y + iX \right) \right] \right\} \text{ for } \tau > 0 \tag{19}$$

The new independent variables, τ, X, and Y, are given in the Nomenclature. Next, in order to put equation (19) into a more recognizable form, we define σ and γ as follows.

$$\sigma = -X + i \left(\frac{\omega\tau}{2X} + Y \right) \tag{20}$$

$$\gamma = -X + i\, Y \tag{21}$$

Now, from [8], a tabulated function $W(z)$, with z being a complex number, is defined in terms of the error function of complex argument as,

$$W(z) = e^{-z^2} \text{erfc } (-iz) = e^{-z^2} \left[1 + \frac{2i}{\sqrt{\pi}} \int_0^z e^{t^2} \, dt \right] \tag{22}$$

Nomenclature

$b^* = \omega \rho_w C_{pw} bR/k$
b = thickness of plate
C_{pw} = specific heat of plate
h_x = local surface coefficient of heat transfer
$i = \sqrt{-1}$
Im = imaginary part of
j = index
k = thermal conductivity of fluid
p = Laplace transform parameter
q_w = local wall heat flux
Q_w = nondimensional local wall heat flux
$r = \rho_w C_{pw} b/k$
$\mathbf{r}$ = position vector
R = half thickness of channel
Re = real part of
s = Laplace transform parameter
t = time
T = local temperature
T_0 = time averaged fluid inlet temperature
u = fluid velocity in x direction
$W(z)$ = function related to error function of complex argument and defined by equation (22)
x = space coordinate along plate
$X = r\omega \sqrt{\alpha x/u}$ nondimensional x coordinate
y = space coordinate perpendicular to plate
$Y = \frac{y}{2} \sqrt{u/\alpha x}$
α = thermal diffusivity of fluid
β = dummy variable of integration
γ = defined by equation (21)
ΔT = amplitude of fluid inlet temperature variation
$\theta = T - T_0$ temperature excess
λ = dummy variable of integration
ρ_w = mass density of wall material
σ = defined by equation (20)
$\chi = \alpha x/uR^2$
$\tau = t - x/u$
ω = angular frequency
ϕ = complex temperature defined by equation (6)

Subscripts

B = bulk mean condition
qs = quasi-steady condition
w = wall condition

Superscripts

$(\overline{})$ = complex conjugate of
$(\hat{})$ = Laplace transform of

Combining equations (19–22) yields,

$$\frac{\theta}{\Delta T} = 0 \quad \text{for} \quad \tau < 0$$

$$\frac{\theta}{\Delta T} = \text{erf } Y \sin\omega\tau + e^{-Y^2}\{\sin\omega\tau\, Re[W(-X+iY)] + \cos\omega\tau\, Im[W(-X+iY)]\} - e^{-(\omega\tau/2X+Y)^2} Im\left\{W\left[-X + i\left(\frac{\omega\tau}{2X}+Y\right)\right]\right\} \quad \text{for} \quad \tau > 0 \quad (23)^1$$

The last term of equation (23) represents the transient response function which causes the fluid temperature excess to change from its initial value, zero, to the eventual periodic unsteady state which is given by the first two terms of equation (23).

Equation (23), being the exact solution function, allows the determination of all other quantities of interest, such as the wall temperature, surface heat flux and, for the case of a thermal entrance region in a channel, the local bulk mean temperature excess. Equation (23) also serves as a fundamental solution for any form of periodic inlet fluid temperature by applying (23) to each separate harmonic and adding.

Local Wall Temperature. Setting $Y = 0$ and making use of the fact [8] that,

$$W(-x+iy) = \overline{W(x+iy)}$$

allows one to find the wall temperature excess as,

$$\frac{\theta_w}{\Delta T} = e^{-X^2}\sin\omega\tau - \frac{2}{\sqrt{\pi}}\cos\omega\tau\left[e^{-X^2}\int_0^X e^{\lambda^2}\,d\lambda\right] - e^{-\omega^2\tau^2/4X^2}\, Im\{W(-X+i\omega\tau/2X)\} \quad \text{for} \quad \tau > 0 \quad (24)$$

and

$$\frac{\theta_w}{\Delta T} = 0 \quad \text{for} \quad \tau < 0$$

The first bracketed quantity in equation (24) is Dawson's integral for which numerical values can be found in [8].

Local Surface Heat Flux. By Fourier's law of conduction, the local surface heat flux is given by

$$q_w = -k\left(\frac{\partial\theta}{\partial y}\right)_{y=0}$$

Combining this equation with the energy balance on the wall, equation (1), gives the expression which follows for the nondimensional surface heat flux.

$$Q_w = \frac{q_w}{\rho_w C_{pw} b \Delta T \omega} = -\frac{\partial\theta_w/\partial\tau}{\omega\Delta T} \quad (25)$$

Performing the appropriate differentiation of equation (24) leads to the final expression for the nondimensional surface flux as,

$$Q_w = 0 \quad \tau < 0$$

$$Q_w = -\left[e^{-X^2}\cos\omega\tau + 2/\sqrt{\pi}\sin\omega\tau\, e^{-X^2}\int_0^X e^{\lambda^2}\,d\lambda - e^{-\omega^2\tau^2/4X^2}\,\text{Re}\left\{W\left(-X+i\frac{\omega\tau}{2X}\right)\right\}\right] \quad \text{for} \quad \tau > 0 \quad (26)$$

Local Bulk Mean Temperature Excess. Consider the thermal entrance length between two parallel plates spaced a distance $2R$ units apart. In this region of the parallel plate duct, the solution functions (23, 24) and (26) are applicable. An energy balance on a control volume of fluid R by dx by one unit is made, using the bulk mean temperature excess θ_B to characterize the average enthalpy per unit mass of the fluid across the duct at any x and t, and the following equation results.

$$\frac{\partial\theta_B}{\partial t} + u\frac{\partial\theta_B}{\partial x} = \frac{q_w(x,t)}{\rho C_p R} \quad (27)$$

Changing to τ, X coordinates in equation (27), inserting equation (26) for Q_w, and solving, subject to the side condition that at

$$X = 0, \tau > 0 \quad \theta_B = \Delta T \sin\omega\tau,$$

yields the response function for the local bulk mean temperature excess, namely,

$$\frac{\theta_B}{\Delta T} = 0 \quad \text{for} \quad \tau < 0$$

$$\frac{\theta_B}{\Delta T} = \left[1 - \frac{2}{\omega r R\sqrt{\pi}}\left(X - e^{-X^2}\int_0^X e^{\lambda^2}\,d\lambda\right)\right]\times\sin\omega\tau - \frac{(1-e^{-X^2})}{\omega r R}\cos\omega\tau + \frac{2}{\omega r R}\int_0^X e^{-\omega^2\tau^2/4\beta^2}\,\beta\, Re\left\{W\left(-\beta + \frac{i\omega\tau}{2\beta}\right)\right\}d\beta \quad \text{for} \quad \tau > 0 \quad (28)$$

Transient Change from One Periodic Unsteady State to Another. Suppose there exists initially a periodic unsteady state due to the inlet temperature $\Delta T_1 \sin\omega\tau$ and then, at $t = 0$, the inlet temperature's amplitude changes from ΔT_1 to $\Delta T_1 + \Delta T_2$. It is desired to find the response of the wall to this change. By a decomposition of the temperature excess into a periodic component driven by $\Delta T_1 \sin\omega\tau$ before $t = 0$ and a transient component that satisfies equations (1–5) with ΔT set equal to ΔT_2, one finds the following solution.

$$\frac{\theta_w}{\Delta T_1} = e^{-X^2}\sin\omega\tau - 2/\sqrt{\pi}\cos\omega\tau\left[e^{-X^2}\int_0^X e^{\lambda^2}\,d\lambda\right] \quad \text{for} \quad \tau < 0 \quad (29)$$

$$\frac{\theta_w}{\Delta T_1} = \left[1 + \frac{\Delta T_2}{\Delta T_1}\right]\left[e^{-X^2}\sin\omega\tau - 2/\sqrt{\pi}\cos\omega\tau\, e^{-X^2}\int_0^X e^{\lambda^2}\,d\lambda\right] - \frac{\Delta T_2}{\Delta T_1}e^{-\omega^2\tau^2/4X^2}\, Im\{W(-X+i\omega\tau/2X)\} \quad \text{for} \quad \tau > 0 \quad (30)$$

Equation (29) is the original periodic wall response due to the sinusoidal inlet temperature excess variation of amplitude ΔT_1, while equation (30) provides the transient response of the wall, due to a sudden change in inlet temperature amplitude to $\Delta T_1 + \Delta T_2$, including the new ultimate periodic unsteady state.

Quasi-Steady Solution. The x dependent surface coefficient for steady slug flow over an isothermal plate was employed in the quasi-steady solution. For these conditions, one has, from [9],

$$h_x = k\sqrt{u/\pi\alpha x} \quad (31)$$

An energy balance on a segment of wall dx long gives,

$$\rho_w C_{pw} b\frac{\partial\theta_{wqs}}{\partial t} + h_x(\theta_{wqs} - \Delta T\sin\omega t) = 0 \quad (32)$$

Combining equations (31) and (32), solving the result subject to the condition that $\theta_{wqs} = 0$ at $t = 0$, then changing to X, $\omega\tau$ variables gives,

$$\frac{\theta_{wqs}}{\Delta T} = \frac{\sqrt{\pi}Xe^{-[\omega\tau/\sqrt{\pi}X+\omega x/u]\sqrt{\pi}X}}{1+\pi X^2} + \frac{\sin[\omega\tau+\omega x/u]}{1+\pi X^2} - \frac{\sqrt{\pi}X\cos[\omega\tau+\omega x/u]}{1+\pi X^2} \quad (33)$$

for all $\tau > -x/u$.

Conditions for Validity of Quasi-Steady Analyses. Often the line of reasoning advanced for the validity of quasi-steady approaches is to say that good results will be obtained if the term containing the time derivative of the fluid temperature, in the thermal energy equation, is negligible. A common way to assess the size of this term is by comparing characteristic diffusion times in both the fluid and the solid (at least for conjugated problems) and if the diffusion time for the fluid is much smaller than that of the solid it is asserted that the quasi-steady assumption will be a good one. This technique is

[1] The generalization of the solution, equation (23), to a non-zero constant initial temperature excess θ_1 can be shown to be as follows: In equation (23), $\theta/\Delta T = \theta_1/\Delta T$ for $\tau < 0$ and, for $\tau > 0$, one must add $\theta_1/\Delta T$ erfc $[\omega\tau/2x + Y]$ to the result in equation (23).

demonstrated, in some detail, by Dorfman [10]. Sparrow and Gregg [11] show a more quantitative way of investigating conditions for a valid quasi-steady analysis which involves expansions of the instantaneous dependent variables about the quasi-steady state and then seeing what must be true for the quasi-steady solution to be close to the true solution. This procedure is complicated by the necessity to solve ordinary differential equations numerically.

Apparently, conditions for quasi-steadiness based on a small time derivative of the fluid temperature do not give the entire picture. As an example, consider the case of periodically varying fluid temperature as in [1, 2, 4] and the present work. In this case, the fluid temperature is always changing with time, perhaps at a fairly rapid rate, yet there are, even in this case, conditions under which the quasi-steady solution is close to the true solution.

Consider a transient forced convection problem which is governed by the following linear homogeneous partial differential equation.

$$L\,\theta(\mathbf{r}, t) = 0 \tag{34}$$

A quasi-steady solution to the problem, $\theta_{qs} = \theta_{q.s.}(\boldsymbol{r}, t)$, is available which satisfies the linear side conditions on the $\theta(\boldsymbol{r}, t)$ of equation (34). Next, a residual function θ_d is defined by the following decomposition.

$$\theta = \theta_{q.s.} + \theta_d \tag{35}$$

To find the conditions under which $\theta_d \to 0$, when θ is not known, equation (35) is inserted into (34) and gives,

$$L\,\theta_d = -L\,\theta_{q.s.} \tag{36}$$

Since $\theta_{q.s.}$ satisfies the side conditions on θ, it follows that θ_d satisfies homogeneous side conditions and therefore θ_d is expected to approach zero under the conditions that lead to the right side of (36) approaching zero. These will then be the conditions for the quasi-steady solution to approach the true solution.

The procedure will now be illustrated by application to the problem of the present work where a quasi-steady solution for the wall temperature is given by equation (33). First, one needs the quasi-steady solution for all x, y, and t. To find this, equation (2) is solved, with the time derivative set equal to zero, subject to the side conditions (4) and (5) and, at $y = 0$, $\theta_{q.s.} = \theta_w(x, t)$ from equation (33). The result for $\theta_{q.s.}$ $(\mathbf{r}, t)$ is as follows.

$$\theta_{q.s.} = [\theta_w(X, t) - \Delta T \sin\omega t]\,\mathrm{erfc}\; Y + \Delta T \sin\omega t \tag{37}$$

For this problem, the equation which corresponds to (34) is equation (2) with the variables changed to X, Y, t, namely.

$$\frac{\partial^2\theta}{\partial Y^2} + 2Y\frac{\partial\theta}{\partial Y} - 2X\frac{\partial\theta}{\partial X} - \frac{4X^2}{\omega\alpha r^2}\frac{\partial\theta}{\partial(\omega t)} = 0 \tag{38}$$

Replacing θ, in equation (38), by $\theta_{q.s.} + \theta_d$ and operating on the known function $\theta_{q.s.}$ leads to the present problem's equivalent of equation (36), namely,

$$\frac{4X^2}{\omega\alpha r^2}\frac{\partial\theta_d}{\partial(\omega t)} + 2X\frac{\partial\theta_d}{\partial X} - 2Y\frac{\partial\theta_d}{\partial Y} - \frac{\partial^2\theta_d}{\partial Y^2} = -2X\frac{\partial\theta_{q.s.}}{\partial X} - \frac{4X^2}{\omega\alpha r^2}\frac{\partial\theta_{q.s.}}{\partial(\omega t)} \tag{39}$$

Inserting (33) into (37) and using the result in the right side of (39) gives,

$$R.H.S. = -2\left\{\left[-2\pi X^2\sin\omega t + \sqrt{\pi}\,(X - \pi X^3)(e^{-\omega t/\sqrt{\pi}X} - \cos\omega t) + \frac{\omega t e^{-\omega t/\sqrt{\pi}X}}{1 + \pi X^2}\right]\mathrm{erfc}\,Y + \frac{2X^2}{\omega\alpha r^2}\left[\left(\frac{\sqrt{\pi}X\sin\omega t - e^{-\omega t/\sqrt{\pi}X} - \pi X^2\cos\omega t}{1 + \pi X^2}\right)\mathrm{erfc}\,Y + \cos\omega t\right]\right\} \tag{40}$$

Upon study of the right side of (40), one observes that $R.H.S. \to 0$ as $X \to 0$ for all Y and t, therefore it is expected that the quasi-steady solution will approach the true solution for small values of X even though $\partial\theta/\partial t$ is not necessarily small. If one next considers X becoming large due to $r\sqrt{\omega\alpha}$ increasing at finite $\omega x/u$, (40) reduces to

$$R.H.S. = -r\left(\frac{\omega x}{u}\right)\cos\omega t\;\mathrm{erf}\;Y \tag{41}$$

From (41), it is seen that the additional condition of $\omega x/u$ being small is needed, along with X becoming large, for the quasi-steady solution to approach the true solution. The physical reason for this requirement will be dealt with in the discussion section.

Results and Discussion

As mentioned before, the exact analytical solution function (23) and functions found from (23), such as (24, 26) and (28), are also expected to apply in the thermal entrance region of a duct with sinusoidally time varying fluid inlet temperature. The extent, in x, of the thermal entrance region of a parallel plate duct can be roughly assessed by a consideration of the exact solution for the local Nusselt number in steady, laminar, constant property, slug flow through an isothermal duct. Upon examination of the solution to this steady state case as given in Kays [9], it was decided that the thermal entrance region's length, l_e, can be given approximately as,

$$\frac{\alpha l_e}{uR^2} \approx 0.20$$

This nondimensional entrance length estimate does not translate into a single value of X because X also depends upon the thermal capacity of the wall material which is not a factor in a steady state response.

To partially check the integrity of the present results, selected comparisons are made for wall temperature and local bulk mean temperature with the results of Sparrow and DeFarias [4] whose results are for the ultimate periodic unsteady state only. The comparison is made for the following values of the parameters of [4].

$$\chi = \frac{\alpha x}{uR^2} = .10 \text{ and } b^* = 1.0,$$

which correspond to $X = .31622777$ of the present work. Equations (24) and (28) provide θ_w and θ_B, with values for Dawson's integral and the imaginary part of $W(z)$ provided by [8]. The last integral in equation (28) does not appear to be a tabulated function and it was evaluated by graphical integration. The results are presented in Fig. 1 for the transient start-up from a zero temperature excess to the eventual periodic unsteady state which, as can be seen, is achieved within 25 percent of the first cycle. The response of the bulk mean temperature is faster (transient portion over within 15 percent of the first cycle) than that at the wall because the bulk mean temperature is, in effect, a spatial average between $y = 0$ and $y = R$ and its response is expected to be closer to that of the inlet temperature. The actual transient response is given by the dashed curves which eventually, as noted above, coalesce into the solid curves which represent the periodic unsteady state. The solid curves are displayed even at low times to show the approach of the fluid and wall to the periodic unsteady state and also because all cycles beyond the first one shown are exactly like the solid curves of the first cycle. The circled points are for the periodic unsteady state and were extracted from Figs. 1 and 3 of Sparrow and DeFarias [4]. The agreement is good, as it should be in the case of two equivalent exact solutions, with the slight differences between two of the points and the solid curve probably attributable to slight inaccuracies in extracting data from the figures of [4].

Wall Temperature Results. In Fig. 2 is shown, as solid lines, the transient wall temperature, from equation (24), response curves for three representative values of X as well as one cycle of the fluid inlet temperature variation with time which is also the response at $X = 0$. One notes, especially for $X = 2.0$, that the wall temperatures are higher during the initial portion of the transient than they are at the

corresponding time in the periodic unsteady state. This is due to the material, initially, being at a higher temperature than it will be in the periodic unsteady condition at the corresponding time. In evidence, also, is the lag and attenuation of the response as X increases. Physically, this is as expected since the time mean thermal boundary layer thickness increases with increasing X and this increased thickness can be viewed as being roughly analogous to different depths from the surface of a stationary solid with a periodic thermal disturbance function on the surface. The trends of Fig. 2 are also in qualitative agreement, in the periodic unsteady state, with those for duct flow in [4]. The wall is brought to its eventual periodic unsteady state in about 6 and 50 percent of cycle one for $X = .10$ and 1.0, respectively, while it requires about one and one third cycles for the transient to disappear for $X = 2.0$. Thus all cycles beyond the second are exactly like cycle two for $X = .1$ and 1.0 and this is even the case for $X = 2.0$ if an error of a few percent can be tolerated in the first third of the cycle.

Fig. 3 isolates the transient portion of the wall response function in a normalized manner convenient for study. TR is defined as the ratio of the absolute value of the transient term in (24) to the absolute value of $\theta_w/\Delta T$ when $\omega\tau = 0$ in the periodic unsteady state. That is,

$$TR = \frac{\left| e^{-\omega^2\tau^2/4X^2} \, Im\left\{ W\left(-X + i\frac{\omega\tau}{2X} \right) \right\} \right|}{\frac{2}{\sqrt{\pi}} e^{-X^2} \int_0^X e^{\lambda^2} d\lambda} \tag{42}$$

From Fig. 3, one sees that the transient response is over, for all intents and purposes, by the time the abscissa value reaches 2.0 to 2.2. Calling τ_c the value of τ at which $TR \leq .01$, a curve fit of the results yields the following relation, for $.1 \leq X \leq 4$,

$$\frac{\omega\tau_c}{2X} = .0468\,X^2 + .0596X + 1.5936 \tag{43}$$

Equation (43) is useful in estimating the time from start-up to the eventual periodic unsteady state.

Heat Flux and Surface Coefficient of Heat Transfer. Equation (26) is used to plot the nondimensional surface heat flux for two values of X in Fig. 4. One observes the same overall pattern of phase lag and decay of amplitude with X as for θ_w in Fig. 2. The surface heat flux is slightly lower at short times than it is at the equivalent time in the cyclic unsteady state and this is caused by the higher wall temperatures, during the transient startup, noticed in connection with Fig. 2. The local instantaneous surface coefficient of heat transfer, based on the difference between the wall temperature and the fluid temperature far from the wall, was found by combining equations (26) and (24). The overall pattern of the Nusselt number with time is similar to that given in [4], Figs. 5 and 6.

Changes from One Periodic Unsteady State to Another. Considered next is the case where the plate of thickness b is initially in the periodic unsteady state in response to the sinusoidally varying fluid inlet temperature of amplitude ΔT_1, when at a time t taken to be zero, for convenience, the fluid inlet temperature's amplitude is suddenly doubled. The appropriate solution functions here are equations (29) and (30) with $\Delta T_2 = \Delta T_1$. The plot of the solution, for $X = 2.0$, is given in Fig. 5. Cycle 0 represents the wall temperature in the original cyclic state. In cycle 1, the first transient cycle, wall temperatures higher than those in the new cyclic state are reached for the same reason as in Fig. 2. The end of the transient portion of the response occurs in the first third of cycle 2 and equation (43) yields a good estimate of the duration of the transient.

Quasi-Steady Results. As can be seen from the response function, equation (33), the quasi-steady solution will always be out of phase with the exact solution because of the presence of the group $\omega x/u$ that is always adding to $\omega\tau$. Because of the fact that conditions sometimes may be such that $\omega x/u \ll 2\pi$, (see [2] and [4]) it was decided to, intentionally, favorably bias the quasi-steady result by neglecting $\omega x/u$ in the plot of the response. The circles, triangles, and squares in Fig. 2 are the quasi-steady wall temperatures for $X = .1$,

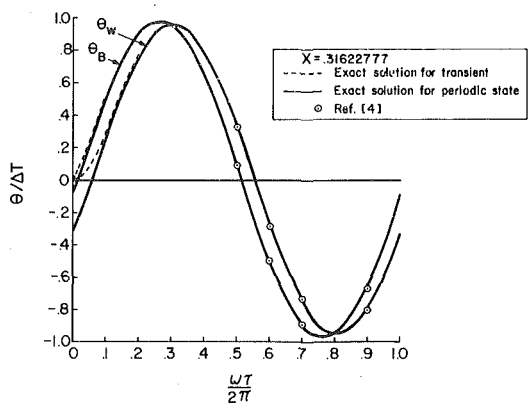

Fig. 1 Bulk mean and wall temperature response to sinusoidal time varying fluid temperature at $x = 0$

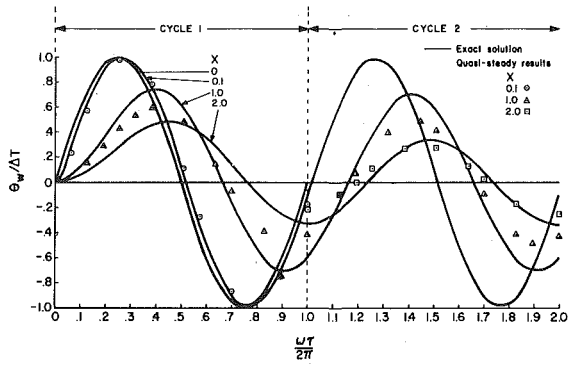

Fig. 2 Wall temperature response and comparison with quasi-steady solution

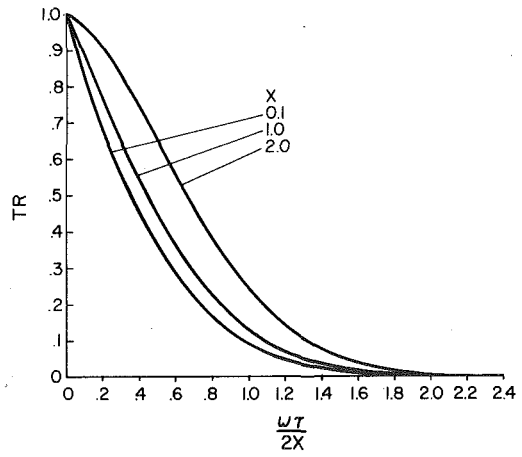

Fig. 3 Transient portion of the wall temperature response function

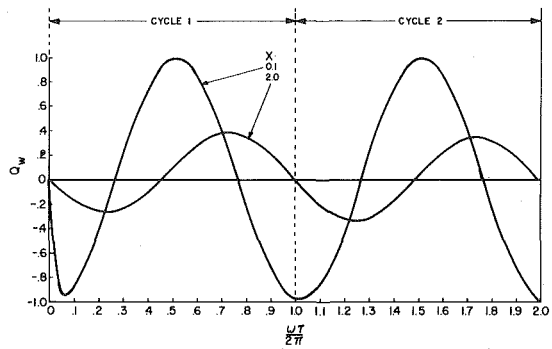

Fig. 4 Surface heat flux response to sinusoidal time varying fluid temperature at $x = 0$

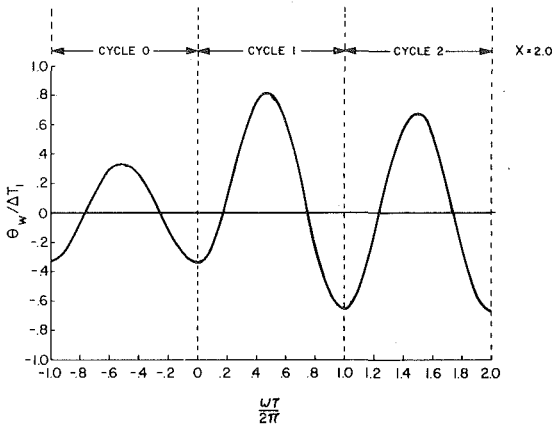

Fig. 5 Wall temperature response when the amplitude of the sinusoidal time varying fluid temperature at $x = 0$ is suddenly doubled at $t = 0$

1.0, and 2.0, respectively. To make the figure easier to read, quasi-steady results are given only for the first cycle at $X = .10$ (results are virtually identical for all succeeding cycles when $X = .10$) and only for the second cycle at $X = 2.0$. It is seen from Fig. 2 that the quasi-steady results provide a reasonably good description at $X = .10$, but display a rather large, unacceptable deviation from the exact wall temperatures at $X = 1.0$. For $X = 2.0$, the quasi-steady results are tending, once again, toward the exact solution but the error, while considerably less than for $X = 1.0$, is still significant.

Turning now to the procedure advanced earlier, in the analysis section, for finding the conditions under which the quasi-steady solution will approach the exact solution, we see, from equation (40) and the comments which follow it, that the two solutions should merge as $X \to 0$ and as X becomes large for small $\omega x/u$. Recalling that $\omega x/u$ was neglected in the quasi-steady results, it is seen that Fig. 2 confirms these conditions. Additional support for this conclusion is found in Figs. 6 and 8 of [4] after noting that the X of this work is equal to $b^*\sqrt{\chi}$ of [4]. The physical reason for $\omega x/u$ needing to be small, as X gets large, stems from the fact that x/u is the lag, or dwell, time before which the material cannot sense a change that occurred at the leading edge. Yet the quasi-steady solution (33) does not predict this and, hence, would be in error, even at long times, (the periodic nature of the disturbance, in effect, makes $\omega\tau = 2\pi$ the "largest" value of nondimensional time that is ever achieved in the ultimate periodic unsteady solution) unless $\omega x/u$ is a very small quantity.

Conclusions

An exact solution has been found for the transient temperature field within a moving fluid which communicates thermally with a plate of finite thermal storage capacity when the fluid temperature at the leading edge varies sinusoidally with time. The solution functions presented can also be used for more general periodic driving temperatures via the vehicle of decomposition into harmonics.

One key element of the analysis was the use of the method of complex temperature not only for the eventual periodic unsteady state, but also for the transient response leading to it. Hopefully this will also be of aid in other transient convection problems where the thermal loading is of a periodic nature.

Comparison of the exact solution with a quasi-steady approach that uses the x dependent surface coefficient of heat transfer for an isothermal plate indicates acceptable agreement at low t, at low X, and at large X provided $\omega x/u$ is small. In general, however, the quasi-steady solution does not provide adequate accuracy in predicting time varying wall temperatures.

A method, which combines the quasi-steady solution and the differential equation of the exact solution, is advanced for finding the circumstances in which the quasi-steady solution is close to the exact solution and is found to work well for the present problem.

Acknowledgment

This material is based upon work supported by the National Science Foundation under Grant No. ENG-77-18268 and the author wishes to express his thanks for their support.

References

1 Willmott, A. J., and Burns, A., "Transient Response of Periodic Flow Regenerators," *International Journal of Heat and Mass Transfer*, Vol. 20, 1977, pp. 753–761.

2 Kardas, A., "On a Problem in the Theory of the Unidirectional Regenerator," *International Journal of Heat and Mass Transfer*, Vol. 9, 1966, pp. 567–579.

3 Chase, Jr., C. A., Gidaspow, D., and Peck, R. E., "A Regenerator—Prediction of Nusselt Numbers," *International Journal of Heat and Mass Transfer*, Vol. 12, 1969, pp. 727–736.

4 Sparrow E. M., and DeFarias, F. N., "Unsteady Heat Transfer in Ducts with Time Varying Inlet Temperature and Participating Walls," *International Journal of Heat and Mass Transfer*, Vol. 11, 1968, pp. 837–853.

5 Sucec, J., "Unsteady Heat Transfer Between A fluid, With Time Varying Temperature, and a Plate: An Exact Solution," *International Journal of Heat and Mass Transfer*, Vol. 18, 1975, pp. 25–36.

6 Arpaci, V. S., *Conduction Heat Transfer*, Addison-Wesley, Reading, Mass., 1966.

7 Roberts, G. E., and Kaufman, H., *Tables of Laplace Transforms*, W. B. Saunders Co., Philadelphia, PA, 1966.

8 Abramowitz, M., and Stegun, I. A., (eds) *Handbook of Mathematical Functions with Formulas, Graphs, and Mathematical Tables*, National Bureau of Standards Appl. Math. Ser. 55, 1964.

9 Kays, W. M., *Convective Heat and Mass Transfer*, McGraw-Hill, New York, 1966.

10 Dorfman, A. S., "Solution of the External Problem of Unsteady State Convective Heat Transfer with Coupled Boundary Conditions" *International Chemical Engineering*, Vol. 17, No. 3, July 1977, pp. 505–509.

11 Sparrow, E. M., and Gregg, J. L., "Nonsteady Surface Temperature Effects on Forced Convection Heat Transfer," *Journal of the Aeronautical Sciences*, Oct. 1957, pp. 776–777.

12 Perlmutter, M., and Siegel, R., "Two Dimensional Unsteady Incompressible Laminar Duct Flow With a Step Change in Wall Temperature," *International Journal of Heat and Mass Transfer*, Vol. 3, 1961, pp. 94–107.

L. W. Florschuetz
Professor,
Mem. ASME

R. A. Berry
Graduate Student,
Student Mem. ASME

D. E. Metzger
Professor,
Mem. ASME

Department of Mechanical Engineering,
Arizona State University,
Tempe, AZ

Periodic Streamwise Variations of Heat Transfer Coefficients for Inline and Staggered Arrays of Circular Jets with Crossflow of Spent Air

Heat transfer characteristics were measured for inline and staggered arrays of circular jets impinging on a surface parallel to the jet orifice plate. The impinging flow was constrained to exit in a single direction along the channel formed by the jet plate and the heat transfer surface. In this configuration the air discharged from upstream transverse rows of jet holes imposes a crossflow of increasing magnitude on the succeeding downstream jet rows. Streamwise heat transfer coefficient profiles were determined for a streamwise resolution of one-third the streamwise hole spacing, utilizing a specially constructed test surface. These profiles are characterized by significant periodic variations. The downstream amplitudes are diminished by the increasing crossflow magnitude, but can persist for at least ten rows of holes. Results were obtained for streamwise hole spacings of 5, 10, and 15 hole diameters; transverse hole spacings of 4, 6, and 8 diameters; and channel heights of 1, 2, and 3 diameters. The number of transverse hole rows was fixed at ten for all configurations. The characteristics of the periodic variations are presented and discussed as a function of the geometric parameters, including the effect of hole pattern.

Introduction

Impingement with high velocity gas jets has become an established method of convectively cooling or heating surfaces in a wide variety of process and thermal control applications. Examples include cooling of gas turbine airfoils and electronic equipment, drying of paper and textiles or other thin layers or films, annealing of metals, and glass tempering operations. The most commonly used jet openings are slots and circular holes. For applications requiring highly localized heating or cooling a single circular jet may suffice. For long, but very narrow areas a single row of circular jets or a single slot jet may be appropriate. The single row or slot may also be adequate, in some cases, for treating sheets of material which can be moved continuously past the row or slot. However, where all portions of a surface of larger expanse must be continuously heated or cooled, multiple slot jets or two-dimensional arrays of jet orifices are required.

For gas turbine airfoils a significant application utilizing a two-dimensional array of jets is the cooling of the midchord region with a trailing edge discharge. In this configuration all of the jet air is constrained to flow toward the rear of the airfoil so that the exhaust from the upstream jets imposes a crossflow on the downstream jets. Gauntner, et al. [1] recently reported results of measurements on a gas turbine vane with the midchord region cooled by a two-dimensional array of circular jets which demonstrated the inadequacy of existing correlations for prediction of heat transfer performance. It appeared also that knowledge of the effect of array configuration on heat transfer characteristics was inadequate for achievement of optimal designs, even for uniformly spaced arrays. In particular, questions remained as to the influence of the crossflow on the downstream heat transfer performance as a function of array configuration.

An investigation, supported by the National Aeronautics and Space Administration, was initiated with the primary objective of determining heat transfer behavior for a variety of uniformly spaced impingement array configurations which model those of interest in current and future gas turbine airfoil cooling. An earlier paper [2] presented results for both mean Nusselt numbers and streamwise Nusselt number profiles resolved to one streamwise hole spacing, for a range of geometric parameters and mean jet Reynolds numbers. An initial higher resolution test result for one configuration was presented which showed that significant periodic variations occurred in the streamwise Nusselt number profile, persisting downstream for at least ten rows of holes. The implications of the characteristics of these periodic variations for the designer should be quite significant, not only for thermal control considerations, but also from the thermal stress standpoint, particularly in applications such as the cooling of gas turbine airfoils.

It is the purpose of the present paper to report extensive additional higher resolution results which show the effect of channel height, hole spacing, hole diameter, and hole pattern (inline versus staggered) on the characteristics of the periodic variations. For these tests, the number of transverse hole rows was fixed at ten for all configurations. Normalized by hole diameter, streamwise hole spacings were 5, 10, and 15; transverse hole spacings were 4, 6, and 8; and the channel heights were 1, 2, and 3. The range of mean jet Reynolds numbers covered was 5×10^3 to 3.5×10^4 for transverse hole spacings of 4 hole diameters, 5×10^3 to 2×10^4 for spacings of 6 diameters, and 5×10^3 to 5×10^4 for spacings of 8 diameters.

Prior heat transfer studies for two-dimensional arrays of circular impinging jets with flow constrained to exit in a single direction parallel to jet hole rows provided either mean heat transfer results or were limited to spatial resolutions greater than or equal to one streamwise hole spacing [3–6]. Therefore, the periodic variations were not observed. High resolution studies of a single impinging jet in the presence of a crossflow were carried out by Bouchez and Goldstein [7] and Sparrow, et al. [8].

Experimental Facility

The test facility consisted basically of a compressed air supply, an air flow metering section, and interchangeable plenum/jet plate assemblies which produced arrays of jets impinging on an instrumented heat transfer test surface. Chordwise and spanwise cross-sectional views of the assembly of the major components are shown in Fig. 1, for one plenum size. A single test plate unit consisting of a segmented copper test plate with individual segment heaters, the necessary thermal insulation, and the test plate support structure, was utilized for all tests. The segmented design provided for control of the chordwise thermal boundary condition at the heat transfer test

Contributed by the Gas Turbine Division and presented at the Winter Annual Meeting, New York, N.Y. December 2–7, 1979 of THE AMERICAN SOCIETY OF MECHANICAL ENGINEERS. Manuscript received by the Heat Transfer Division August 3, 1979. Paper No. 79-WA/GT-11.

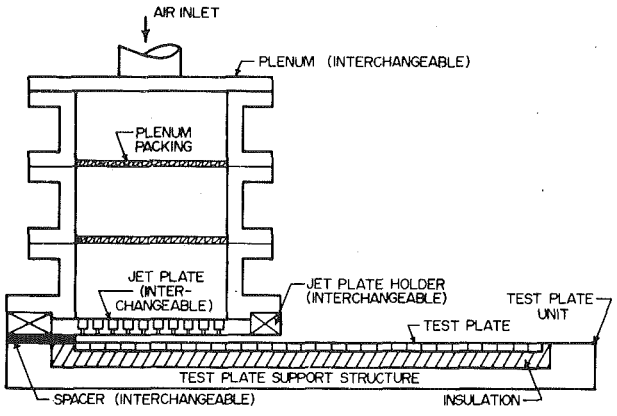

Fig. 1 Test unit assembly

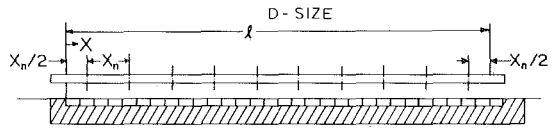

Fig. 2 Chordwise relation of spanwise jet hole rows to test plate segments

surface, as well as for determination of spatially resolved heat transfer coefficients in the chordwise direction. The jet plate lower surface was positioned relative to the heat transfer surface via interchangeable spacers to permit covering the desired range of z/d.

Laboratory compressed air was passed through the plenum packing to provide a uniform flow upstream of the jet plate. After passing through the jet plate the air exhausted to atmospheric pressure by flowing along the channel formed by the jet plate, the test surface, and the spacer.

The plenum/jet plate assembly illustrated in Fig. 1, which was designated as a B-size, had ten spanwise rows of holes, each row centered directly over one of the first ten copper segments of the test plate. For this configuration the maximum chordwise resolution for determination of heat transfer coefficients was equal to one chordwise hole spacing, x_n. Most of the results previously reported [2] were for this plenum size configuration.

The higher resolution results to be reported here were obtained utilizing the largest plenum (designated as D-size), which covered the full length of the test plate. The maximum active chordwise length of the test plate was 38.1 cm (15 in.) (30 segments by 1.27 cm (0.5 in.) per segment), with an additional segment at the downstream end to serve as a guard element. Each D-size jet plate had ten uniformly spaced spanwise rows of holes resulting in one row of holes per three test plate segments, thus providing a chordwise resolution of $x_n/3$. The relationship between the spanwise hole rows and the test plate segments is shown in Fig. 2. Note that each row is centered directly over a test plate segment and that the first row (counted from upstream) is located a distance $x_n/2$ from the upstream end of the channel.

The spanwise width of the test plate and the channel were fixed at 12.2 cm (4.8 in.) and 18.3 cm (7.2 in.), respectively. The excess width of the channel permitted the jet hole pattern to extend beyond the edges of the heat transfer surface, thus minimizing flow pattern edge effects on the heat transfer characteristics (see Fig. 1, spanwise view).

The geometric characteristics of the configurations for which data are reported here are summarized in Table 1. Note that the number of holes across the channel span always exceeds the number across the test surface. In what follows a given configuration will, when convenient, be referred to in abbreviated form such as D(5,4,1)I indicating plenum size-D, $x_n/d = 5$, $y_n/d = 4$, $z/d = 1$, and inline hole pattern. Jet plates with inline jet hole patterns, for which most of the tests were run, had holes located at the intersection points of a uniform rectangular grid. The staggered pattern was identical to its inline counterpart, except that alternating spanwise rows were offset by one-half the spanwise spacing.

The jet plate thickness, b, at each hole location is equal to the jet hole diameter. This was achieved by appropriately counterboring plates of larger overall thickness (Fig. 1). The larger overall thickness was dictated primarily by the need to insure accurate channel heights during test runs, a particularly critical requirement for the narrowest channel heights. The counterbore was three jet hole diameters, except for the narrowest hole spacings where two jet hole diameters were used. In one test with $z/d = 1$, a 2d counterbore plate was used with the counterbored holes subsequently bored out to 3d, and the test repeated. The results were identical to within experimental uncertainty.

The copper test plate segments were 0.635 cm (1/4 in.) thick and 1.19 cm (15/32 in.) wide with 0.079 cm (1/32 in.) balsa wood insulation bonded between adjacent segments to minimize heat leak. The individual heaters were foil-type bonded to the underside of each segment, each with power input controlled by a separate variac. The primary temperature instrumentation in the test plate consisted of copper-constantan thermocouples mounted in the center of each copper segment, with a redundant thermocouple in each segment offset 1.52 cm (0.6 in.) in the spanwise direction. Several segments at intervals along the plate had additional thermocouples mounted out to the edge to verify that the spanwise temperature distributions during testing were essentially uniform. Additional details may be found in [2] and [9].

Nomenclature

b = thickness of jet plate at jet hole locations
c_p = specific heat at constant pressure
d = jet hole diameter
$\overline{G}$ = mean mass flux based on jet hole area
$\overline{G}^*$ = mean mass flux based on heat transfer surface area
h = convective heat transfer coefficient
$\overline{h}$ = convective heat transfer coefficient averaged over entire heat transfer surface
k = thermal conductivity of air
ℓ = chordwise length of heat transfer surface
N_c = number of spanwise rows in chordwise direction
N_s = number of jet holes across span of heat transfer surface
N_s' = number of jet holes across span of channel
Nu = Nusselt number resolved in chordwise direction, averaged across span, hd/k
$\overline{\text{Nu}}$ = Nusselt number averaged over entire heat transfer surface, $\overline{h}d/k$ (where distinction necessary, subscript I refers to inline pattern, S to staggered)
$\overline{\text{Re}}$ = mean jet Reynolds number, $\overline{G}d/\mu$
T_p = plenum air temperature
T_r = adiabatic wall temperature
T_s = heat transfer surface temperature
x = chordwise location along heat transfer surface measured from upstream end of channel
x_n = chordwise jet hole spacing
y_n = spanwise jet hole spacing
z = channel height or jet plate-to-impingement surface spacing
μ = dynamic viscosity

Table 1 Geometric characteristics of configurations tested

Plenum Size	ℓ cm (in.)	d & b cm (in.)	x_n/d	y_n/d	z/d	(1) Hole Patterns	(2) N_s	N_s'	(3) Maximum Chordwise Resolution
D	38.1(15.0)	0.762 (0.300)	5	4	1,2,3	*I*	4	6	1.67*d*
		0.381 (0.150)			1,3	*S*			
			10	4	1,2,3	*I*	8	12	3.33*d*
				8	1,2,3	*I*	4	6	
			15	4	1,2,3	*I*	12	18	5*d*
		0.254 (0.100)		6	1,2,3	*I*	8	12	
				8	1,2,3	*I*	6	9	

Notes: (1) *I* denotes inline hole pattern, *S* denotes staggered.
(2) $N_c = \ell/x_n$ fixed at 10 for all tests.
(3) Maximum chordwise resolution was $x_n/3$ for all tests.

Experimental Procedures and Data Reduction

Details of the experimental procedures and data reduction techniques utilized were identical to those described in [2] and [9] and therefore will not be repeated here. Like the prior results, the present heat transfer coefficients were determined for a nominally uniform heat transfer surface temperature. With the entire test plate active, steady-state overall surface temperature variations were less than 8 percent of the temperature potential used in defining the heat transfer coefficient, and differences between adjacent segments were less than 4 percent. These variations in the thermal boundary condition have no significant effect on the heat transfer coefficients. The heat transfer coefficients for the individual test plate segments are based on a temperature potential defined as the difference between the segment surface temperature, T_s, and the segment adiabatic wall temperature, T_r. This was essential since for the relatively low laboratory pressure levels at which the tests were run, T_r differed significantly from the plenum air temperature, T_p, for the higher flow rates. In the turbine cooling application, which motivated the present study, one may, to a reasonable approximation, take $(T_s - T_p)/(T_s - T_r) = 1$, so that knowledge of heat transfer coefficients and plenum air temperatures is adequate for determination of heat fluxes. For the tests reported here $(T_s - T_r)$ ranged from about 6 to 35K.

Results and Discussion

Higher-resolution Nusselt number profiles for each D-size configuration tested are shown in the series of plots of Figs. 3–8. The overall experimental uncertainty associated with the resolved Nusselt numbers was determined to be about ±5 percent for a confidence level of 95 percent. The resolved values are plotted as ratios to the corresponding mean values for $\overline{\mathrm{Re}} = 1.5 \times 10^4$. Over the range of $\overline{\mathrm{Re}}$ covered (5×10^3 to 5×10^4), some dependence of these normalized higher-resolution Nusselt numbers on $\overline{\mathrm{Re}}$ was observed. However, the basic character of the periodic variations as a function of the geometric parameters remained the same over the entire range of $\overline{\mathrm{Re}}$. Thus, the profiles presented in Figs. 3–8 for $\overline{\mathrm{Re}} = 1.5 \times 10^4$ are representative of the geometric effects over this entire range. Profiles smoothed across the periodic variations are also shown for each case. These curves were drawn through the data points resolved to one chordwise spacing (points omitted for clarity). Each figure is for a given hole spacing combination (x_n/d, y_n/d), with individual plots for each z/d (= 1, 2, and 3). All results shown are for inline hole patterns only, except for configurations D(5,4,1) and D(5,4,3) (Fig. 3) for which results for the staggered pattern were also obtained. The D-size tests were run in the staggered pattern for the (5,4) hole spacing since prior low-resolution results [2, 9] had indicated the hole pattern effect was largest for this spacing.

The vertical arrows along the abscissa of each plot indicate the location of the spanwise rows of holes. The reader may find it helpful to refer again to Fig. 2 which shows the relationship between the spanwise rows of holes and the test plate segments. It should also be borne in mind that while the chordwise resolution was fine enough to clearly show the nature of the periodic variations, the results do not precisely reflect profiles of infinite resolution which would show even larger amplitude variations.

In this connection, the maximum chordwise resolution of heat transfer coefficients relative to hole diameter should be noted. Since $N_c = \ell/x_n$ was fixed at ten for all tests, and ℓ was constant, x_n was also constant. Thus, the parameter x_n/d was varied by changing d. Since the heat transfer surface segment width was fixed, the chordwise resolution relative to hole diameter was different depending on the x_n/d of the jet plate under test, as listed in Table 1. These resolutions relative to hole diameter were independent of all other geometric parameters. Therefore, for a given x_n/d, comparisons made to examine the effects of other geometric parameters reflect identical resolutions relative to hole diameter.

Characteristic of these results are the amplitude attenuation and the increasing displacement of the peak value of Nu for each row of holes as one proceeds in the downstream direction, effects clearly associated with the influence of the increasing crossflow magnitude. These and other characteristics of the results as a function of the geometric parameters are discussed in detail in the following paragraphs.

Values of $\mathrm{Nu}/\overline{\mathrm{Nu}}$ (Figs. 3 to 8) range overall from 0.25 to just over 2. For $z/d = 1$, the peak value associated with the last row of jets is always larger than or equal to the other peak values, with the single exception of the least dense hole array, configuration D(15,8,1)*I*. For $z/d = 2$ and 3, the largest peak values are always associated with the upstream jet rows. In general, the minimum values for each row of a given configuration are more uniform than the peak values.

For the closest spanwise spacing, $y_n/d = 4$, the amplitude attenuation becomes stronger as z/d is increased. The upstream amplitudes are somewhat larger for $z/d = 2$ and 3 than for $z/d = 1$, while downstream the reverse is true. While the high resolution nonuniformity increases with z/d, the smoothed profiles become more nearly uniform. For $y_n/d = 8$, both the upstream and downstream amplitudes, and hence the degree of amplitude attenuation are similar for all z/d. Likewise, the smoothed profiles are all fairly uniform.

Viewed from the standpoint of the effect of y_n/d for a fixed z/d, it may be observed that for $z/d = 1$ the resulting downstream amplitudes are not sensitive to y_n/d, but for $z/d = 2$ and 3 the amplitude is clearly damped out more for $y_n/d = 4$ than 8.

The results clearly indicate that the presence of the crossflow downstream can strongly attenuate the periodic variations. If, in applications, thermal stresses proved to be severe at upstream locations due to the large periodic variations of the heat transfer coefficient, the presence of an initial crossflow would certainly be advantageous in alleviating such a problem.

The effect of varying the chordwise hole spacing for a fixed cooled surface length cannot be determined directly from the present data since the ratio ℓ/x_n was fixed at ten for all tests. However, comparison of results in Figs. 3–8 for the several values of x_n/d (5, 10, and 15) with the other parameters fixed shows that spreading ten rows of holes over a larger surface (i.e., increasing both x_n and ℓ, while holding d, y_n, and z fixed) clearly increases the amplitude of the variations. Indeed,

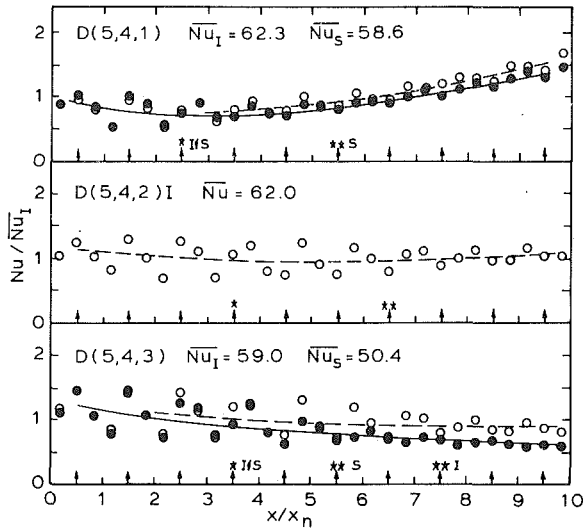

Fig. 3 Normalized chordwise Nusselt number profiles for inline (open points) and staggered (solid points) patterns for D(5,4) configuration

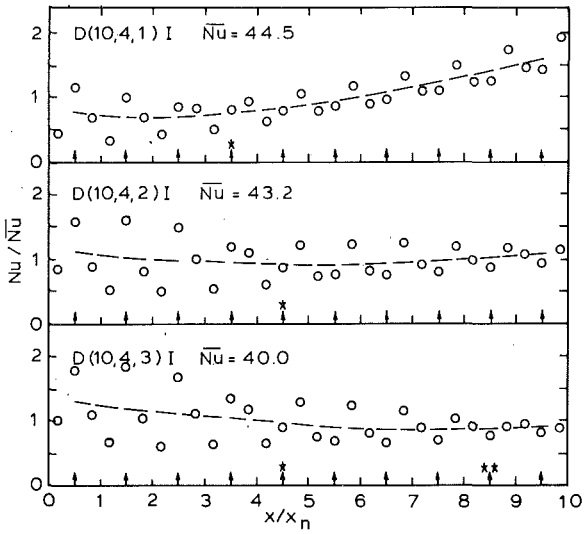

Fig. 4 Normalized chordwise Nusselt number profiles for D(10,4)/ configuration

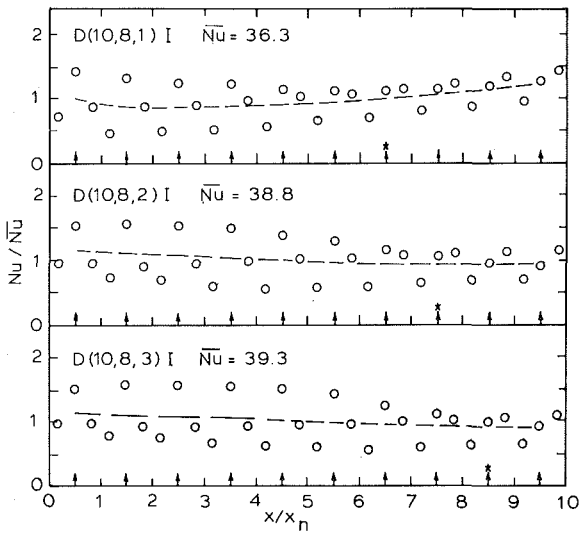

Fig. 5 Normalized chordwise Nusselt number profiles for D(10,8)/ configuration

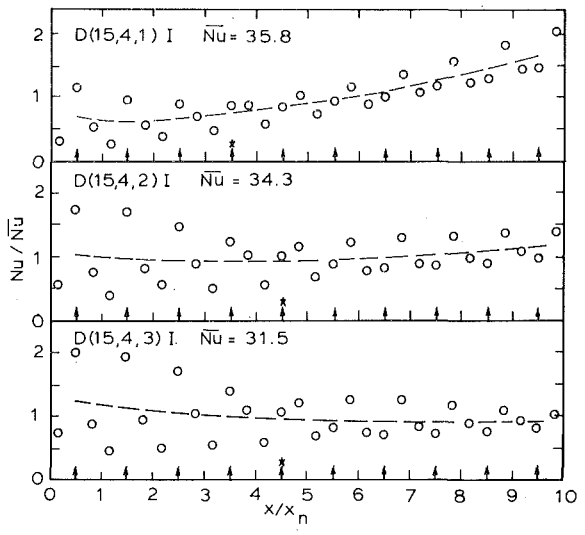

Fig. 6 Normalized chordwise Nusselt number profiles for D(15,4)/ configuration

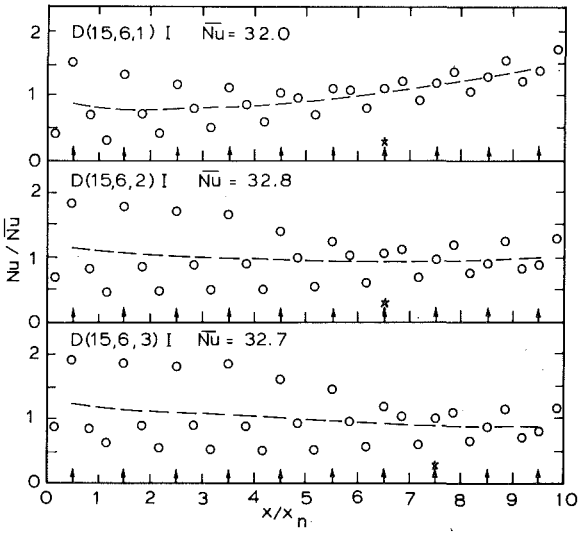

Fig. 7 Normalized chordwise Nusselt number profiles for D(15,6)/ configuration

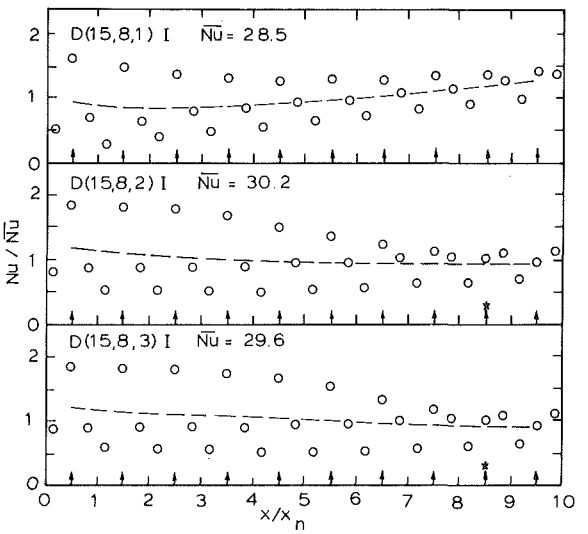

Fig. 8 Normalized chordwise Nusselt number profiles for D(15,8)/ configuration

infinitely resolved chordwise profiles would undoubtedly show this increase to be even more pronounced, since the smallest amplitude data, for $x_n/d = 5$, were obtained with the highest resolution relative to hole diameter, while the largest amplitude results, for $x_n/d = 15$, were obtained with the lowest resolution relative to hole diameter.

Attention is now turned to the increasing displacement of the peak value of Nu for each row of holes which occurs in the downstream direction. It may be observed (Figs. 3–8) that upstream the peak value of $\mathrm{Nu}/\overline{\mathrm{Nu}}$ associated with a spanwise row of holes is always for the heat transfer surface segment centered directly opposite the row, while at some row downstream the peak value shifts to the segment immediately downstream of that row. Since the segment width is $x_n/3$ for the D-size configurations, this means that the local peak value of Nu for that row is displaced by at least $(1/2)(x_n/3) = x_n/6$ downstream of the row location. The row at which this peak shift occurs is marked by a single asterisk in each plot of Figs. 3–8.

In several instances, (D(5,4) at all z/d (Fig. 3) and D(10,4) at $z/d = 3$ (Fig. 4)), the peak value subsequently shifts to the second segment downstream of the row location. These rows are marked by a double asterisk. At these rows the local peak value is displaced by at least $(1.5)(x_n/3) = x_n/2$ downstream of the row location. For other configurations this second peak shift is not observed.

Examination of these peak shift points gives an indication of how rapidly the displacement of the local peak value of Nu increases from row to row depending on the geometric parameters of the configuration. Overall, this displacement appears to be a weak function of z/d over the range covered, but depends more strongly on y_n/d. The trend is for the displacement at a given row to be smaller for the larger y_n/d. There is a similar trend, though not as strong, with x_n/d. For the most dense hole packing in inline pattern, D(5,4)I (Fig. 3), the displacement has reached a value of $x_n/2$ about $\frac{3}{4}$ of the way down the channel, while for the lowest hole density, D(15,8)I (Fig. 8), it is still only approaching $x_n/6$ as the end of the channel is reached.

It is tempting to identify the observed displacement of the local peak values of Nu with the distance by which the jet impingement points are deflected downstream from the centerlines of the jet holes, since the observation of a peak shift from one segment to the next undoubtedly depends strongly on the location of the impingement point relative to the segments. However, the particular row at which a peak shift is observed may also depend somewhat on the local distribution of Nu about the impingement point. Due to the crossflow this distribution presumably becomes flatter and more asymmetrical from row to row in the downstream direction. The presence of crossflow also has some direct contribution to the segment Nu values, since they are averaged over the spanwise direction. Despite these uncertainties, the evidence suggests that the deflection of the jet impingement point itself is primarily dependent on y_n/d, with only a weak dependence on z/d and x_n/d over the range of these parameters covered.

The ratio of the crossflow mass velocity to the jet mass velocity will decrease with both z/d and y_n/d. The observed effect of y_n/d on the displacement of the peak values is consistent with this trend. The fact that the effect of z/d on this displacement is not as strong may be due to a compensating effect. That is, although the crossflow-to-jet velocity ratio decreases with z/d, the path length of the jet from injection point to impingement point increases with z/d.

The effect of hole pattern on the mean values and the chordwise profiles of Nu resolved to one chordwise hole spacing were previously discussed in [2]. The higher-resolution results presented in Fig. 3 provide some additional insight into the effects of the staggered pattern as compared with the inline pattern. It appears that the periodic variations are essentially identical upstream for the two hole patterns, but like the smoothed profiles differ significantly downstream. The amplitude attenuation is more severe for the staggered pattern than for the inline, especially for $z/d = 3$, in which case the variation for the staggered pattern has almost disappeared at the downstream end. The second peak shift (double asterisk) occurs further upstream for the staggered patterns than for the inline. Both of these effects suggest that the crossflow/jet interactions and possible resulting interactions between adjacent jets are stronger for the staggered pattern.

One may speculate as follows. Consider a particular spanwise row, n, for the inline pattern. The jets in row $n + 1$ cause most of the crossflow from fluid injected at row n to be diverted so that it flows between the jets of row $n + 1$. The path of least resistance for this diverted fluid is to continue flowing down imaginary channels between adjacent pairs of chordwise rows. Thus, for the inline pattern the jets of a given spanwise row tend to be deflected downstream and diffused primarily due to crossflow from the row immediately upstream; each row tends to be "protected" from crossflow originating two rows upstream by the jets of the row immediately upstream. The hypothesis that the crossflow for the inline patterns tends to be channelized between adjacent chordwise hole rows is consistent with observations of discoloration patterns on the test surface which suggest such a flow pattern.

In contrast, for the staggered pattern the flow from a jet in, say, spanwise row n first flows directly between two jets in row $n + 1$. It is then diverted to flow around a jet in row $n + 2$, and in so doing joins the crossflow originating from the hole directly upstream in row $n + 1$. This combined flow, along with any existing crossflow already originated upstream, interacts directly with the immediately downstream jet in row $n + 3$. Thus, the direct influence of the crossflow on each jet is larger than for the inline case. Each jet is therefore deflected and diffused more than its inline counterpart would be. This reduces the contribution to the heat rate made by the jet, thus reducing the spanwise average Nu.

Close examination of the inline versus staggered data points for D(5,4,3) (Fig. 3) indicates that as the crossflow effect increases downstream the difference between the inline and staggered peak values for each row is larger than for the minimum values. This observation also suggests that the degradation of the jet impingement heat transfer is greatest for the staggered case, and is a major factor in the reduction of the overall heat transfer rate as compared with the inline pattern. However, it should be emphasized that the differences due to hole pattern become significant only for the denser hole patterns [2, 9].

The effect of hole diameter on the chordwise periodic variations of the heat transfer coefficient is shown in Figs. 9 and 10 under the condition that other geometric parameters as well as the mean flow rate per unit heat transfer surface area ($\overline{G}^*$) are held fixed. This is accomplished in dimensionless form utilizing a Stanton number defined as $h/\overline{G}^* c_p$ rather than a Nusselt number.

The effect of reducing the hole diameter by one-half is shown in Fig. 9, by comparing results for configuration D(5,4,1)I with those for D(10,8,2)I. The effect of this reduction in diameter is to double the mean heat transfer coefficient and provide a more uniform smoothed profile, but significantly increase the amplitude of the periodic variations. Clearly, reducing the hole diameter by one-half for constant $\overline{G}^*$ increases the mean jet mass velocity ($\overline{G}$) by a factor of four. It is therefore not surprising that the mean heat transfer coefficient is significantly increased. Less obvious are the effects of the chordwise flow distribution resulting from the channel pressure gradient on the resolved heat transfer coefficients. Flow distributions for these cases based on chordwise pressure traverse results indicate that for the upstream spanwise row of jets (Row 1), the jet velocity for D(10,8,2)I is about eight times that for D(5,4,1)I, while for the downstream row (Row 10) it is just double. The trends exhibited by both the higher-resolution profiles and the smoothed profiles in Fig. 9 are consistent with these observations. Attempts to correlate the heat transfer coefficients resolved to one chordwise spacing with the individual spanwise row jet and crossflow velocities and with the geometric parameters are currently in progress.

The plot of Fig. 10 represents a case where the diameter is reduced by two-thirds, by comparing configurations D(10,4,2)I and D(15,6,3)I. Here the mean heat transfer coefficient is increased by about 50 percent, the amplitudes of the variations are again increased, but there is not a strong effect on the uniformity of the smoothed profile. It should be emphasized that the increases in amplitude with diameter

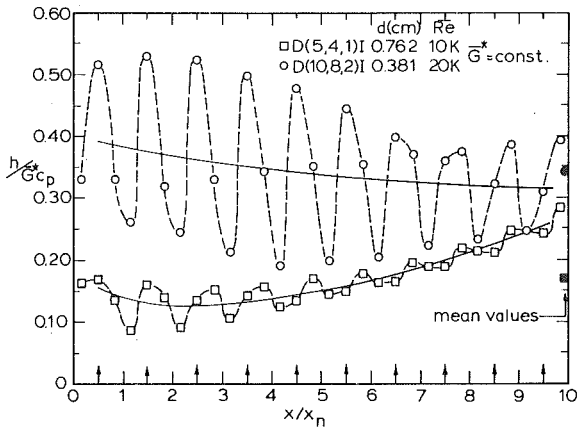

Fig. 9 Effect of hole diameter on chordwise periodic variations, smoothed profiles, and mean values of heat transfer coefficient for fixed $\overline{G}^*$—inline hole pattern

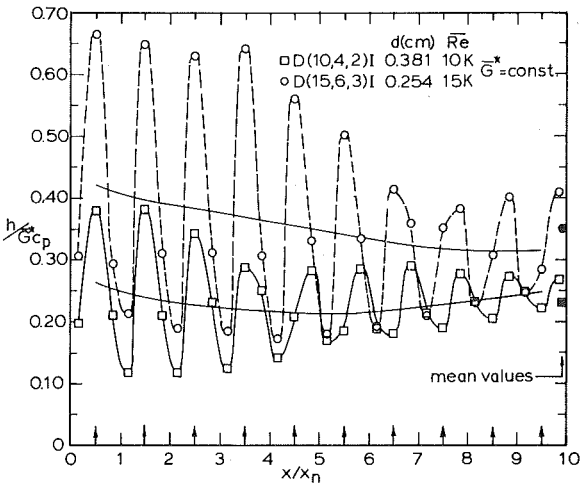

Fig. 10 Effect of hole diameter on chordwise periodic variations, smoothed profiles, and mean values of heat transfer coefficient for fixed $\overline{G}^*$—inline hole pattern

reduction as shown in Figs. 9 and 10 would be even larger if the chordwise resolution were infinitely small. This is because, as already indicated, the resolution relative to hole diameter is better for the larger hole diameters since the heat transfer test plate segment size was fixed for all tests.

Concluding Remarks

The results presented show that the large amplitudes of the upstream periodic variations are significantly reduced downstream by the influence of the crossflow from the upstream jets. However, for the larger hole spacings the amplitudes can remain as large as 30 percent of the smoothed profiles even at the tenth row of holes. As a general trend, the downstream amplitudes are larger for the larger hole spacings and channel heights, though the degree of sensitivity to any one geometric parameter varies depending on the particular values of the other parameters under consideration. Smaller downstream amplitudes are also associated with larger deflections of the jet flow prior to impingement.

The mean heat transfer coefficients, the periodic variations, the smoothed profiles and their inter-relationships, considered as a function of array geometric parameters will take on various degrees of significance, depending on design requirements. For example, for constant $\overline{G}^*$ the mean heat transfer coefficient varies essentially inversely with hole diameter over the parameter ranges covered by these results. From this standpoint, the use of smaller hole diameters for turbine airfoil cooling is quite advantageous. The disadvantages, however, include the significantly increased pressure drop, the increased probability of plugging of holes with foreign matter, and the potential for thermal stress problems associated with the periodic variations of the heat transfer coefficients. The designer must also weigh these factors against the influence of hole diameter on the smoothed chordwise variation of heat transfer coefficients as related to his thermal control requirements.

Acknowledgments

The support of the National Aeronautics and Space Administration, Lewis Research Center, under Grant NSG 3075 is hereby gratefully acknowledged. Mr. J. M. Bitner, graduate assistant, and Mr. C. R. Truman, research associate, provided valuable assistance in the acquisition and reduction of data.

References

1 Gauntner, J. W., Gladden, H. J., Gauntner, D. J., and Yeh, F. C., "Crossflow Effects on Impingement Cooling of a Turbine Vane," NASA TM X-3029, March 1974.

2 Metzger, D. E., Florschuetz, L. W., Takeuchi, D. I., Behee, R. D., and Berry, R. A., "Heat Transfer Characteristics for Inline and Staggered Arrays of Circular Jets with Crossflow of Spent Air," ASME JOURNAL OF HEAT TRANSFER, Vol. 101, 1979, pp. 526–531.

3 Friedman, S. J., and Mueller, A. C., "Heat Transfer to Flat Surfaces," *Proceedings, General Discussion on Heat Transfer,* the Institute of Mechanical Engineers, London, England, 1951, pp. 138–142.

4 Huang, G. C., "Investigations of Heat Transfer Coefficients for Air Flow Through Round Jets Impinging Normal to a Heat Transfer Surface," ASME JOURNAL OF HEAT TRANSFER, Vol. 85, 1963, pp. 237–243.

5 Kercher, D. M., and Tabakoff, W., "Heat Transfer by a Square Array of Round Air Jets Impinging Perpendicular to a Flat Surface Including the Effect of Spent Air," ASME *Journal of Engineering for Power,* Vol. 92, No. 1, Jan. 1970, pp. 73–82.

6 Chance, J. L., "Experimental Investigation of Air Impingement Heat Transfer Under an Array of Round Jets," *Tappi,* Vol. 57, No. 6, 1974, pp. 108–112.

7 Bouchez, J. P., and Goldstein, R. J., "Impingement Cooling From a Circular Jet in a Crossflow," *International Journal of Heat and Mass Transfer,* Vol. 18, 1975, pp. 719–730.

8 Sparrow, E. M., Goldstein, R. J., and Rouf, M. A., "Effect of Nozzle-Surface Separation Distance on Impingement Heat Transfer for a Jet in a Crossflow," ASME JOURNAL OF HEAT TRANSFER, Vol. 97, 1975, pp. 528–533.

9 Florschuetz, L. W., D. E. Metzger, D. I. Takeuchi, and R. A. Berry, *Multiple Jet Impingement Heat Transfer Characteristics—Experimental Investigation of Inline and Staggered Arrays with Crossflow,* NASA Contractor Report, Arizona State University, Tempe (in press).

G. D. Raithby
Mem. ASME

G. E. Schneider
Department of Mechanical Engineering,
University of Waterloo,
Waterloo, Ontario, Canada N2L 3G1

The Prediction of Surface Discharge Jets by a Three-Dimensional Finite-Difference Model

A three-dimensional model is presented which describes the thermal and hydrodynamic behavior of a turbulent heated jet entering at the surface of a receiving body of water. A two-equation turbulence model, together with a semi-empirical description of the preferential attenuation of vertical turbulent exchange due to buoyancy, is used to predict non-isotropic turbulent diffusivities. A finite-difference solution method, involving several novel features, has been used. Predictions are compared with both field and laboratory measurements, for both deep and shallow receiving basins, for the special case of a quiescent ambient fluid. Good agreement is found, indicating that the model can be reliably used as a design tool, or to evaluate the environmental impact of surface discharges.

Introduction

Electric power generation produces large amounts of waste heat which is often discharged into lakes or rivers as condensor cooling water. Environmental concern over both damage to the biota from the heated water, and the dispersion of possible pollutants that may be carried from the plant, has led to extensive study of the problem.

The cooling water may be discharged either at, or beneath, the surface of the receiving water. The present study focuses on the surface discharge configuration illustrated in Fig. 1. On entering the receiving body, the jet spreads in the horizontal direction, driven by buoyancy forces, and may either deepen or contract in the vertical direction, depending on the outlet conditions and location of the bottom. The features which complicate this problem are (1) the important direct effect of buoyancy on the jet behavior, (2) the indirect effect of buoyancy that affects the turbulent exchange, (3) the interaction of the jet with the bottom and shoreline, and (4) the effect of cross-flow which can bend the jet sharply.

Work related to the surface discharge problem up to 1975 has been summarized in two excellent reviews by Dunn, et al. [1], and Jirka, et al. [2]. The modelling has followed three major directions: phenomenological modelling (e.g. [3]), integral modelling (e.g., [4, 5]) and numerical modelling [7, 8], although certain hybrid phenomenological-integral models have been developed (e.g., [6]). Dunn, et al. [2] concluded that the available models were only useful for generalized estimates of plume characteristics, but considered numerical models to hold the greatest promise of the future.

Perhaps the most serious limitation of the numerical models examined by Dunn, et al. [1] was the high computational cost required for a solution even for a coarse grid. This prevented adequate testing to properly evaluate the models. Moreover, should subsequent testing establish that the accuracy of one of these models is adequate, the high cost would also limit its use as a practical predictive tool.

The newer numerical models of McGuirk and Rodi [9] and of the present authors [10, 11] require much less computational effort. This permits extensive comparisons with data to be made, thereby enabling the accuracy of the models to be established. The purposes of the present paper are to present the authors' model for the first time in the open literature, and to provide a sample of the extensive comparisons that have been made between predictions and measurements.

Because the model of McGuirk and Rodi [9] and the present model [10, 11] were developed in parallel, it may be helpful to point out the major differences between the models. The major difference in the formulation is that only the present model solves the vertical momentum equation as part of the equation set. This may result in a slightly higher solution cost, despite the good convergence characteristics of the present model. However, this permits the present model to include bottom interaction effects which are frequently of importance; the McGuirk-Rodi model is directly applicable only to deep-water receiving basins. Even in the absence of bottom effects, neglecting the vertical momentum constraint will be a poor approximation at both very low and very high outlet Froude numbers. A second difference is that a more complete set of turbulent stress and heat transfer terms are retained in the present model which account, it is believed, for the substantial differences in predictions for deep-water receiving basins.

Other significant differences between the two models include the turbulence model adopted, the finite difference discretization and the method of grid expansion.

Mathematical Formulation

The Conservation and Transport Equations. The equations of mean motion used in this study are presented in equations (1–3). The Boussinesq approximation has been made and the turbulent fluxes have been replaced by an eddy-viscosity model to be described later. A Cartesian tensor notation is used in which the index j implies summation in the equation; the exception is the subscript on the 'properties' Γ and μ^t where no summation is implied. Fig. 1 is the definition sketch.

$$\frac{\partial}{\partial x_j}(\rho_0 u_j) = 0 \tag{1}$$

$$\frac{\partial}{\partial x_j}(\rho_0 u_j u_i) = -\frac{\partial p}{\partial x_i} + \frac{\partial}{\partial x_j}\left(\Gamma_{ij}^{u_j}\frac{\partial u_i}{\partial x_j}\right) + (\rho - \rho_{\text{ref}})g\delta_{i3} + \left(\frac{\partial \mu_{ij}^t}{\partial x_j}\right)\left(\frac{\partial u_j}{\partial x_i}\right) \tag{2}$$

$$\frac{\partial}{\partial x_j}(\rho_0 u_j T) = \frac{\partial}{\partial x_j}\left(\Gamma_{jj}^T\frac{\partial T}{\partial x_j}\right) \tag{3}$$

For the density of water, the Gebhart-Mollendorf [12] equation was used, namely

$$\rho = 999.9720(1 - 9.297173 \times 10^{-6}(T - 4.029325)^{1.894816}) \tag{4}$$

where T is in °C and ρ is in Kg/m^3.

To obtain equation (2), a linear relation between turbulent stress and the mean velocity gradients has been assumed (see, for example, [13]), but the proportionality constant, the turbulent viscosity, has been allowed to be a tensor (see Hinze [14]). Using primes to denote fluctuating components, and an overbar to denote a time-average quantity, this relation is

Contributed by The Heat Transfer Division for publication in the JOURNAL OF HEAT TRANSFER. Manuscript received by The Heat Transfer Division March 30, 1979.

$$-\rho_0 \overline{u_i' u_j'} = \frac{2}{3}\rho_0 k \delta_{ij} - \mu_{ij}^t(\partial u_i/\partial x_j + \partial u_j/\partial x_i) \quad (5)$$

where k is the turbulent kinetic energy, and μ^t is the turbulent viscosity. To obtain the correct relation upon contraction, it must also be asserted that $\mu_{11}^t = \mu_{22}^t = \mu_{33}^t$. Replacing the Reynolds stresses in the fundamental mean-flow momentum equations by equation (5) leads to equation (2), where

$$\Gamma_{ij}^{\mu} = \mu + \mu_{ij}^t \quad (6)$$

In addition, the pressure is given by

$$p = \left(P - \int_{z_{\text{ref}}}^{z} \rho_{\text{ref}} g dz - P_{\text{ref}}\right) + \frac{2}{3}\rho_0 k; \quad z = x_3 \quad (7)$$

where P is the actual pressure at any location; the quantity in parenthesis is the pressure relative to a hydrostatic pressure defined by the reference density $\rho_{\text{ref}}(z)$, whose introduction also gives the density difference term in equation (2). The turbulent kinetic energy contributes the apparent pressure of $\frac{2}{3}\rho_0 k$ to the mean motion. In equation (3), the apparent diffusion coefficient is represented by

$$\Gamma_{jj}^T = \lambda/C_p + \mu_{jj}^t/\sigma_j^T \quad (8)$$

where λ is thermal conductivity and σ^T is the turbulent Prandtl number defined in equation (15b).

The turbulent viscosity has been approximated in terms of k and the dissipation of turbulent kinetic energy, ϵ, as proposed by Harlow and Nakayama [15] and widely used by Launder, Spalding and others (e.g., [16, 17]). The equations used for k and ϵ are

$$\frac{\partial}{\partial x_j}(\rho_0 u_j k) = \frac{\partial}{\partial x_j}\left(\Gamma_{jj}^k \frac{\partial k}{\partial x_j}\right) + \rho_0 G(1 - \text{Ri}/\sigma^T) - \rho_0 \epsilon \quad (9)$$

$$\frac{\partial}{\partial x_j}(\rho_0 u_j \epsilon) = \frac{\partial}{\partial x_j}\left(\Gamma_{jj}^{\epsilon} \frac{\partial \epsilon}{\partial x_j}\right) + \frac{\epsilon}{k}(C_1 G - C_2 \epsilon)\rho_0 \quad (10)$$

where G is the generation

$$G = -\overline{u_i' u_j'}\partial u_i/\partial x_j \quad (11)$$

and the apparent diffusion coefficients are defined as

$$\Gamma_{jj}^k = \mu + \mu_{jj}^t/\sigma^k; \quad \Gamma_{jj}^{\epsilon} = \mu + \mu_{jj}^t/\sigma^{\epsilon} \quad (12)$$

Following the recommendations of Launder and Spalding [17],

$$C_1 = 1.44, C_2 = 1.92, \sigma^k = 1.0, \sigma^{\epsilon} = 1.3, C_D = 0.09 \quad (13)$$

Equation (9) can be derived in a fairly rigorous manner; the derivation of equation (10) requires many approximations of questionable validity, in the writers' opinion, and should perhaps better be considered as a general transport equation with empirical coefficients that permits ϵ to be convected, diffused, generated and dissipated.

The generation term in equation (9) contains a dependence on Richardson number, Ri, defined as

$$\text{Ri} = -g\sigma^T \overline{\rho' u_3'}/\rho_0 G \approx g\,\mu_{33}^t(\partial\rho/\partial x_3)/G \quad (14)$$

When ρ locally increases with depth (stable stratification), the generation of turbulent kinetic energy is reduced; unstable stratification, on the other hand, augments k. Thus, the important role of buoyancy on the level of turbulence is directly accounted for in the equation. A similar term should appear in the ϵ-equation, but Gibson and Launder [18] have neglected it because its "effect should be negligible;" this practice has also been followed here.

While stable stratification reduces the level of k, the component of k in the vertical direction, x_3, is more severely damped than those in the horizontal directions. The effect of this damping on the vertical transport of momentum and thermal energy is represented in the present work by a modification to the 'standard' $k-\epsilon$ model [16] in such a way that the conventional equations are recovered when buoyancy effects are absent. The following equations are used.

$$\mu_{ij}^t = \mu_{ji}^t = (\rho_0 C_D k^2/\epsilon)/f_1(\text{Ri}) \quad (15a)$$

$$\sigma_3^T = \sigma^T f_2(\text{Ri}), \sigma^T = 0.7 \quad (15b)$$

The following expressions of Munk and Anderson [19] have been used as tentative approximations of f_1 and f_2 for $\text{Ri} \geq 0$ *and* (i, j) values of (1, 3), (2, 3), (3, 1) and (3, 2):

$$f_1 = \sqrt{1 + 10\text{Ri}} \quad (15c)$$

$$f_2 = (1 + 10\text{Ri}/3)^{3/2} \quad (15d)$$

Otherwise

$$f_1 = f_2 = 1.0 \quad (15e)$$

The sensitivity of predictions to the values of f_1 and f_2 used will be reported later.

This turbulence model is an alternative to the algebraic model employed by McGuirk and Rodi. Its main advantages are that it reduces to the standard k–ϵ model, and that it is somewhat simpler. There is no basis, at present, for assessing the relative accuracy of the models.

It was stated in the Introduction that a parabolic approximation greatly reduces the numerical integration effort. This is implemented by dropping diffusion terms in the $x_2 = y$ direction in equations (2) and (3). A subtle consequence of this approximation is that the pressure gradient $\partial p/\partial x_2$ must be specified. Several alternatives exist:

Nomenclature

b_0 = half-width of the outfall, Fig. 1
$b_{1/2}^T$ = thermal half-width; width from the centerline to the location on the surface where $T = (T_{\text{¢}} + T_\infty)/2$
b^v = velocity full width; distance from centerline to location where $u = 0$ on the surface, and distance along the bottom to outer extremity of jet
$b_{1/2}^v$ = velocity half-width; distance from the centerline to the location on the surface at which $v = 1/2\, v_{\text{¢}}$
C_p = specific heat at constant pressure
f_1, f_2 = factors to account for the vertical attenuation of diffusivities due to buoyancy, equation (15)
$\text{Fr}_0 = v_0/\sqrt{\Delta\rho_0 g h_0/\rho_0}$; outlet Froude number
g = gravitational acceleration
G = generation of turbulent kinetic energy, equation (11)
h_0 = depth of outfall, Fig. 1
$h_{1/2}^T$ = thermal half-depth, depth at which temperature under the centerline is $(T_{\text{¢}} + T_\infty)/2$
$h_{1/2}^v$ = velocity half-depth; depth at which velocity under the centerline is $v_{\text{¢}}/2$
H = water depth (Fig. 4)
k = kinetic energy of turbulence
p = pressure, equation (7)
Ri = Richardson number, equation (14)
T = temperature
$T_{\text{¢}}$ = centerline temperature at the surface; $T_{\text{¢}}(y)$
T_0 = average temperature at the outlet
T_∞ = ambient temperature
u_i = velocity component in the x_i direction. Note that $u_1 = u$, $u_2 = v$ and $u_3 = w$
u, v, w = velocity components in the x, y and z directions
$v_{\text{¢}}$ = centerline velocity at the surface; $v_{\text{¢}}(y)$
v_0 = average velocity at the outlet
x_i = spatial coordinate, Fig. 1. Note that $x_1 = x$, $x_2 = y$ and $x_3 = z$,
x, y, z = spatial coordinates, Fig. 1
Γ_{ij}^{ϕ} = diffusion coefficient for quantity ϕ, equations (6, 8) and (12)
$\Delta T_{\text{¢}} = T_{\text{¢}} - T_\infty$
$\Delta T_0 = T_0 - T_\infty$
ϵ = dissipation of turbulent kinetic energy, equation (10)
λ = thermal conductivity
μ = molecular viscosity
μ_{ij}^t = turbulent viscosity, equation (5)
ρ = local density; $\rho(T)$
ρ_0 = density of the fluid at the outlet
ρ_{ref} = reference density; ρ_∞ for surface jet
ρ_∞ = density of water at T_∞
σ = turbulent Schmidt number, equations (13) and (15b)

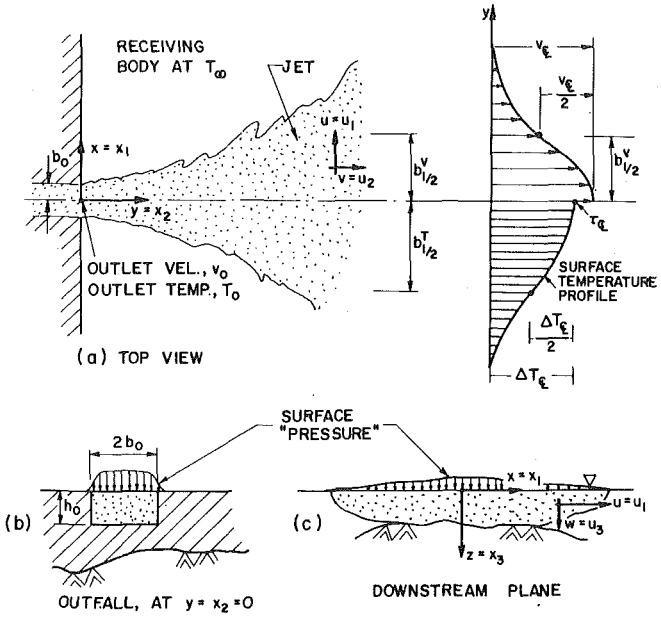

Fig. 1 Schematic of surface jet showing plan view, (*a*), and two cross-sections, (*b*) and (*c*)

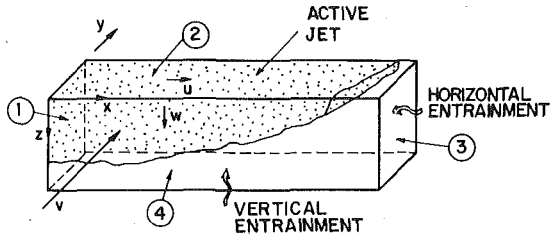

$$\textcircled{1}: u = \frac{\partial v}{\partial x} = \frac{\partial w}{\partial x} = \frac{\partial p}{\partial x} = \frac{\partial k}{\partial x} = \frac{\partial \epsilon}{\partial x} = 0$$

$$\textcircled{2}: \frac{\partial u}{\partial z} = \frac{\partial v}{\partial z} = w = \frac{\partial p}{\partial z} = \frac{\partial k}{\partial z} = \frac{\partial \epsilon}{\partial z} = 0$$

$$\textcircled{3}: \frac{\partial u}{\partial x} = v = \frac{\partial w}{\partial x} = p = k = \epsilon = 0$$

$$\textcircled{4}: \frac{\partial u}{\partial z} = v = \frac{\partial w}{\partial z} = p = k = \epsilon = 0 : \text{FREE JET}$$

$$\textcircled{4}: u = v = w = \frac{\partial p}{\partial z} = \frac{\partial k}{\partial z} = 0 \quad \left.\begin{array}{l} \epsilon - \text{SPECIFIED THROUGH } \mu^t \\ \text{WALL FUNCTION FOR u \& v} \end{array}\right\} \text{SOLID BOUNDARY}$$

Fig. 2 Boundary conditions on dependent variables

it can be ignored altogether, it can be estimated from calculated pressures (from the other momentum equations) on upstream planes, or it can be estimated in terms of density gradient using (for this purpose only) the hydrostatic approximation [1]. The last alternative results in

$$\left(\frac{\partial p}{\partial x_2}\right) - \left(\frac{\partial p}{\partial x_2}\right)_{\text{ref}} \doteq g \int_{z_{\text{ref}}}^{z} \frac{\partial \rho}{\partial x_2}\, dz \tag{16}$$

In the absence of a boundary below the jet, $z_{\text{ref}} = +\infty$ where $\partial p/\partial x_2 = 0$. In the outer extremities of the jet, the pressure gradient given by equation (16) becomes positive, tending to create negative u_2-velocities which violate the parabolic assumption. The treatment of the flow direction pressure gradient will receive further attention in a later section of this paper.

The in-plane pressure distribution in a given y-plane must be calculated such that the velocities obtained through the momentum equations satisfy mass conservation. The slight increase in elevation of the water surface over the jet creates the positive pressure near the jet centerline which drives the rapid horizontal spread. In the present study, the need to compute the free surface elevation was avoided by using the rigid lid approximation [1]. Figs. 1(*b*) and 1(*c*) illustrate the pressure distribution on the bottom of the imaginary lid which approximates the effect of the free surface displacement.

Boundary Conditions. The present paper confines attention to a jet issuing into quiescent water where the receiving basin is either very deep or has a uniform depth. The boundary conditions for these two cases are summarized in Fig. 2.

At the surface, a zero gradient boundary condition on ϵ was employed; a similar constraint was used by McGuirk and Rodi [9]. This, together with the other boundary conditions, treats the surface as a plane of symmetry, and does *not* imply that the turbulent length scale associated with vertical transport near this boundary goes to zero—in contradiction to reality. However, other possible boundary conditions on ϵ also have drawbacks. It is thought that because all other gradients are legitimately zero at this boundary, the results should be very insensitive to the value of μ^t (and therefore ϵ) near the surface.

At a solid lower boundary, wall functions were used to apply the no-slip condition; the calculation of the near-wall generation and the boundary conditions on ϵ also required special treatment. These are described in the next section.

Finite-Difference Analog

A full description of the finite-difference approximation of the mathematical model just described cannot, for the sake of brevity, be given. However, most of the details are available elsewhere in the open literature so that the present description concentrates on providing an overview, with frequent references to these other sources. Detailed discussion will be restricted to facets that are unique to this study. For these discussions, it is convenient to revert to x, y, and z as the spatial co-ordinates, and to u, v and w as the velocity components in each of these directions, respectively (see Fig. 1).

At a given y-station, the solution domain was subdivided into control volumes with uniform Δx, Δz and Δy (see below). The variables were assigned storage locations according to the staggered mesh system of Harlow and Welch [23, 21]. The finite difference equations (FDE's) were formulated using the upstream-weighted approach (scheme V, [25]) except that the exponential expressions, which are costly to compute, were approximated by simple algebraic expressions. The solution method was similar to that used by Patankar and Spalding [21]. The major differences were:

1 Whenever a dependent variable was obtained from its FDE, a sufficient number of iterations on the equation were performed to guarantee a converged solution.
2 An outer iteration loop was established which repeated the solution cycle of each y-station until convergence of the equation *set* was established.
3 The pressure was not updated using p' since the resulting convergence of the set of equations was too slow. The PUMPIN method described in [40] was found to provide faster convergence. Also, because of the staggered grid, the pressure at the exterior grid points need never be calculated, and the pressure under the "rigid lid" does not require the special attention as, for example, in [7].

When solving for the u and v velocities in the presence of a solid bottom, shear stress components in the x and y directions from the previous iteration cycle were applied at the bottom. From the resulting u and v at the grid points adjacent to the boundary, new shear stress components were calculated assuming a Rannie [20] profile very near the wall, followed by a log-law profile [28]. This also permits μ^t at these points to be found. The values of k are determined using a zero-gradient boundary condition (Fig. 2). The corresponding values of ϵ at the near-bottom points were determined from equation (15) and used as boundary conditions. The generation, G, in the k- and ϵ-equations for the control volumes adjacent to the bottom were computed from a closed-form expression based on the von Karman universal velocity profile.

Once the solution to the equation set had been established for a given y-station, the solution plane was advanced distance Δy downstream. The value of Δy was normally increased with increasing distance downstream. To accommodate the varying vertical and hori-

zontal dimensional changes of the active jet region without loss in resolution, a new mesh was constructed, at each new y-station, which was uniform in the x- and z-directions, and which maintained the same number of gridlines. The solution on the upstream plane was interpolated onto the new mesh.

Using this mesh system the grid "appears" to be uniform, resulting in both simplicity and a reduction in computational effort. A disadvantage is the artificial smoothing, or apparent diffusion, which accompanies the interpolation process, and which causes small changes in the calculated streamwise momentum and energy fluxes passing through the plane. These changes were removed in the present work by "antidiffusing" the velocity and temperature profiles to restore the original fluxes. The antidiffusion was accomplished by applying the finite difference form of a transient heat conduction operator to the interpolated v and T profiles through a negative time step. This process should be considered as part of the interpolation process.

This grid expansion method is different from that used by McGuirk and Rodi [9]. They obtained simplicity by ignoring terms arising from the non-orthogonality of their mesh, an approximation which is quite questionable when the jet (and therefore the grid) expands rapidly. The alternative of including the non-orthogonal terms is undesirable because of the increased complexity.

Finite-Difference Predictions

Preliminary Test Results. The preliminary predictions of the model included two-dimensional heat conduction, two-dimensional natural convection in a square cavity [29] and three-dimensional parabolic laminar flow in the entrance region of a square duct. The latter were found [10] to be in excellent agreement with the measurements of Goldstein and Kreid [30].

The maximum density effect for water near 4°C is of interest for thermal discharges under winter conditions [31]. To test the capability of the model to handle this thermal effect, predictions of the simultaneous hydrodynamic and thermal development in the entrance region of a square duct were made first with the wall and inlet water temperatures both above 4°C, and then with the wall temperature at 10°C and the inlet temperature at 0°C. Fig. 3 shows the u and w velocity distributions in one duct cross-section, along with the 4°C isotherm corresponding to maximum density. The fluid is seen to plunge downward along this isotherm with a return flow upward both along the centerline and the wall, in agreement with expectation.

Next, the turbulence model was included, and predictions were made for two-dimensional isothermal jets. Good agreement [10] with measured centerline velocity decay, velocity half-widths, velocity profiles, kinetic energy and dissipation profiles, etc., was obtained. The review of Rodi [32] was particularly helpful in this study. Calculations for two-dimensional buoyant surface jets were in qualitative agreement with the measurements of Vanvari and Chu [33]. Preliminary predictions of both buoyant and sinking heated three-dimensional surface jets also gave reasonable results, and attention was turned to definitively establishing the predictive capabilities of the model when applied to surface discharge problems. These results are now described in some detail.

Surface Jets with Bottom Interaction. Adams, et al. [6] have reported measurements for buoyant surface jets issuing from rectangular outfalls with a wide range of depth to width ratios, and with confinement from below by both uniform and sloping bottoms. Centerline temperature decay in the flow direction at the surface, velocity "full widths," b^v, at both the surface and the bottom, and distance to the observed bottom attachment of the jet (where applicable) were provided. Velocity full width at the surface, measured using dye injection, can be identified with the distance from the jet centerline to the lateral position at which the surface u-velocity reverses direction. It is not so clear how the velocity full width at the bottom should be interpreted; it was taken here as the distance from the centerline to the position near the outer jet boundary where $v = u$.

The inlet velocity profiles for this problem were assumed to vary with the $1/7^{th}$ power of velocity from the nearest duct wall, the inlet

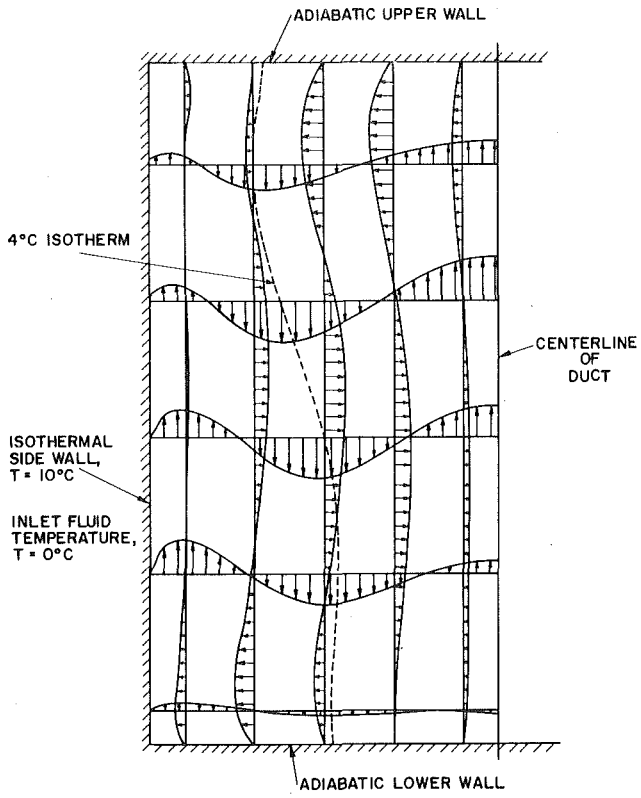

Fig. 3 u and w velocity profiles, and the 4°C maximum-density isotherm, for a cross-section of a square duct in which the flow is thermally and hydraulically developing

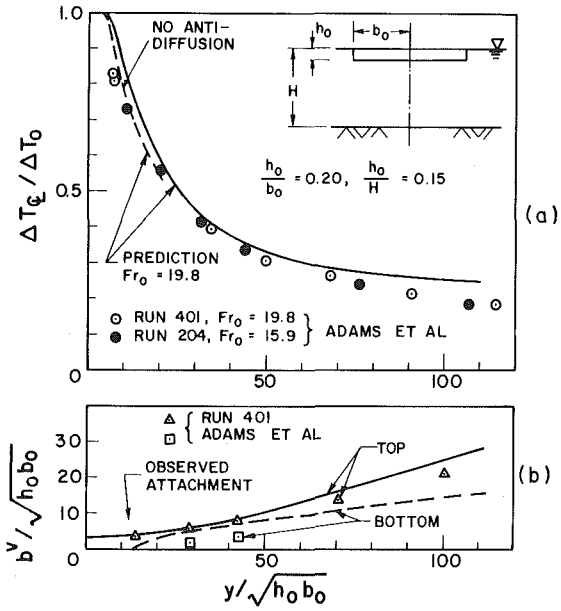

Fig. 4 Centerline temperature decay and velocity full widths: comparison of data for Runs 401 and 204 [5] with prediction

temperature was taken as uniform, and values of k and μ^t typical of channel flow were prescribed, with the corresponding ϵ-distribution obtained using equation (15a). For the first few planes downstream, until the shear layer had grown to a sufficient width to enable accurate numerical computation of the generation, G, shear layer values for k, μ^t (and therefore ϵ) were implanted into the shear layer region. Where the jet did not attach to the bottom very near the outfall, the grid was expanded in the vertical direction using the free-jet boundary conditions in Fig. 2 until the solid bottom was encountered.

The predictions and measurements for a wide and shallow outfall are compared in Fig. 4. The predicted centerline temperature decay

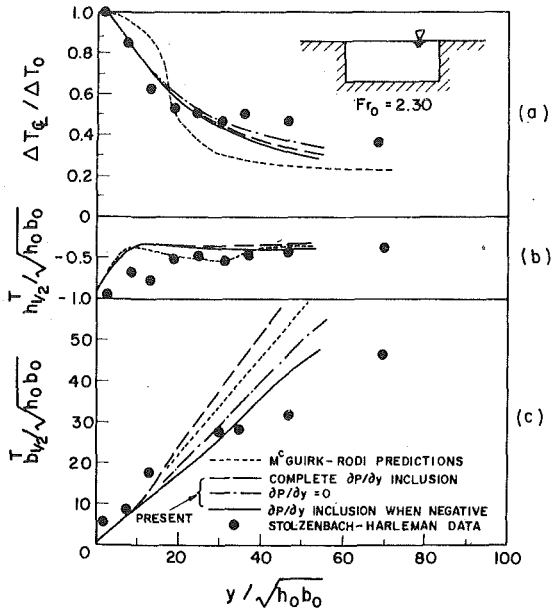

Fig. 5 Comparison of measured downstream development of centerline temperature at the surface (*a*), thermal half-depth (*b*), and thermal half-width (*c*), for Run 3 [4], with prediction

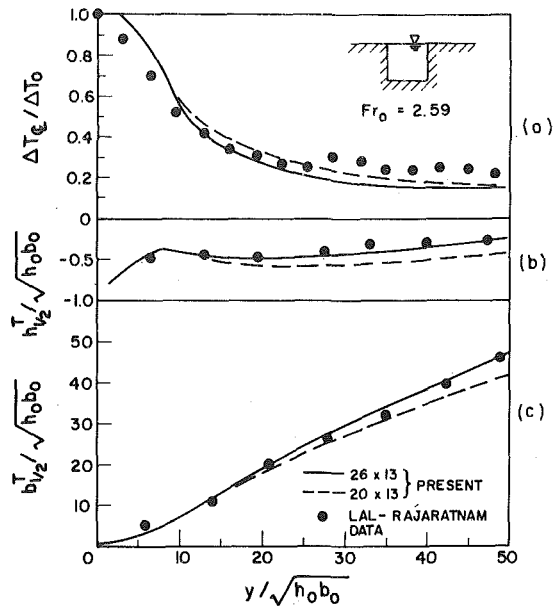

Fig. 6 Comparison of downstream development of centerline temperature at the surface (*a*), thermal half-depth (*b*), and thermal halfwidth (*c*), for Run 1 [37], with prediction

is slightly less rapid than observed (Fig. 4*a*), and the full velocity widths in Fig. 4(*b*) are quite well predicted. The predicted and observed distance from the outfall to the jet attachment location (at 12.1 $\sqrt{h_o b_o}$) were in nearly perfect agreement. It will be seen from Fig. 4(*b*) that, near the outfall, the jet spreads downward very quickly with increasing distance in the flow direction, while the width at the surface stays nearly constant. This seems to be related to the observed rapid adjustment of jets from a high aspect ratio outlet to a nearly axisymmetric shape a short distance downstream [34].

The effect of the antidiffusion operator significantly affected the temperature-decay results in this particular problem. This resulted from the large aspect reatio of the jet which made it necessary near the outlet to place only a few gridlines in the high shear region along the vertical edges of the jet. This, in turn, resulted in significant smoothing of the interpolated profiles. The solid curve in Fig. 4(*a*) is the better solution of the equation set, despite the slightly better agreement between the predictions without antidiffusion and the data.

The solution time for a 13 × 15 grid with 30 planes in the y-directions was about 12 minutes on an IBM 370 computer.

Comparisons using other data of Adams et al at high outlet Froude numbers are not presented because lower Froude numbers are of greater practical interest, but similar results were obtained.

Surface Discharge without Bottom Interaction. *Stolzenbach-Harleman Data.* Fig. 6 shows the data from Run 3 of Stolzenbach and Harleman [4] for a rectangular outlet with $h_0/b_0 = 0.87$ and $Fr_0 = 2.30$. This particular run was chosen because of the low Froude number, and because the data set was comparatively complete.

The inlet conditions for the model were similar to those in the previous section. The model was run many times for this problem to check grid independence of the solution, the suitability of convergence criteria, and the sensitivity of the results to some of the model parameters. A grid with 13 lines in the z-direction by 20 in the x-direction (over the half-width of the jet) was found to be sufficiently fine. Also, failure to achieve a tight convergence on the energy equation was found to have a marked effect on the final predictions. It was found that replacing f_1 and f_2 in equations (15*a*) and (15*b*) by unity had very little effect on any of the predictions. This is particularly significant since the effect of vertical stratification should be most important for jets of low outlet Froude number.

The present predictions, along with the predictions of the McGuirk-Rodi model, are shown together with the data in Fig. 5. The present thermal decay predictions in Fig. 5*a* are in good agreement with measurement out to 30 $\sqrt{h_o b_o}$ where a "bump" occurs in the data which is not reproduced by the model. This bump has been associated with a jet stagnation [6] and seems to be supported by other investigators through field measurements [35, 36]. The decrease in the thermal half-depth (Fig. 5*b*) with downstream distance is somewhat over-predicted but the equilibrium depth agrees well. There is also good agreement with measured $b^T_{1/2}$ out to the location of the bump in the thermal decay. There is generally good agreement with the McGuirk-Rodi predictions except in Fig. 6(*a*), where the present thermal decay predictions are in much better agreement with experiment.

The results of the present model are represented by three curves, corresponding to different methods of handling the flow-direction pressure gradient. In the first case, $\partial p/\partial y$ from equation (16) is used; in the second, $\partial p/\partial y$ is set equal to zero; and in the third, $\partial p/\partial y$ from (16) is again used but set to zero in regions of adverse pressure gradient. The only results that indicate sensitivity to $\partial p/\partial y$ are the $b^T_{1/2}$ values in Fig. 5(*c*). In the first case, the flow direction pressure gradient is adverse in the region well removed from the jet centerline, and this tries to drive negative v-velocities. While such negative velocities are physically reasonable, and are in fact observed, they violate the parabolic assumption and therefore must be replaced by zero before commencing with the next step in the solution algorithm. With zero v-velocities, the energy flux by diffusion in the x-direction cannot be carried through a y-surface but, instead, continues to diffuse outward, causing the jet to be excessively wide. Replacing $\partial p/\partial y$ by zero everywhere, permits v to go asymptotically to zero from the positive side with increasing x. Inclusion of $\partial p/\partial y$ only when it drives the flow forward, results in a jet which is more inertially dominated, causing an increase in vertical penetration, a decrease in horizontal spread, and a more rapid thermal decay.

The solution time for the reported results was about 20 minutes.

Lal-Rajaratnam Data. The most complete set of data for the quiescent ambient problem has been presented by Lal and Rajaratnam [37]; comparison with these data constitutes a more complete and definitive test of the model. Their highest Froude number experiment ($Fr_0 = 2.59$) was chosen for the comparison. The measured centerline temperature decay, the thermal half-depths, and thermal half-widths are plotted in Figs. 6(*a–c*), respectively. Similar quantities for velocity are plotted in Figs. 7(*a–c*). The outfall geometry is shown on the figures.

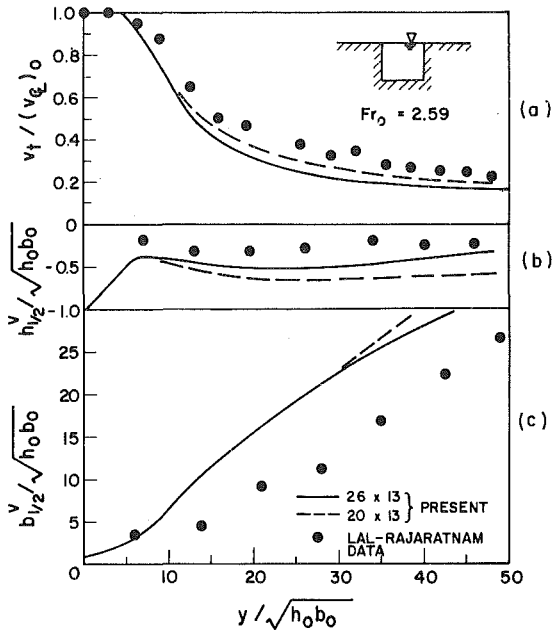

Fig. 7 Comparison of measured downstream development of centerline velocity at the surface (*a*), velocity half-depth (*b*), and velocity half-width (*c*), for Run 1 [37], with prediction

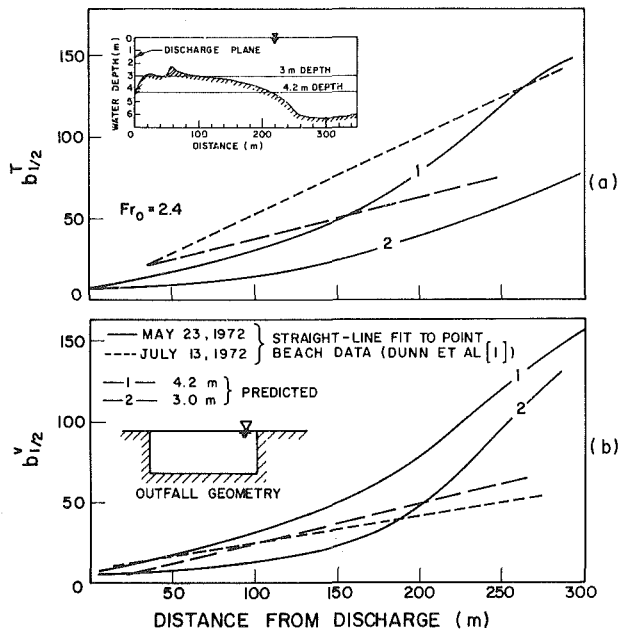

Fig. 8 Comparison of field measurements of the downstream development of thermal half-width and velocity half-width (May 23, 1972 and July 13, 1972, data from [1]) with predictions, using two different uniform depths

The inlet conditions in the model were again treated in a manner similar to that already described. A finer grid was required for this problem (26 lines in the x-direction) and the extreme sensitivity to incomplete convergence of the energy equation was again noted. The flow direction pressure gradient from equation (16) was used where it aided the flow but was otherwise set to zero.

Fig. 6(a) shows that the predicted centerline temperature decay is in good agreement with measurement out to 25 $\sqrt{h_o b_o}$ where a bump occurs in the data; thereafter, the measured thermal decay is somewhat less than predicted. The thermal half-depths and half-widths are both in excellent agreement with measurement. Unlike the Stolzenbach-Harleman data in Fig. 5(c), no bump in the $b^T_{1/2}$ data was observed.

The predicted centerline velocity decay is slightly larger than observed (Fig. 7(a)) and the predicted half-depth is slightly greater (Fig. 7(b)). The predicted velocity half-width in Fig. 7(c) departs rapidly from the measured half-widths between 5 and 15 times $\sqrt{h_o b_o}$, the predicted rate of spread at larger values of $\sqrt{h_o b_o}$ agrees well with experiment, but the curve in Fig. 7(c) is shifted vertically.

The broken lines in Figs. 6 and 7 illustrate the rather sensitive dependence on the grid resolution in the x-direction for this problem. The vertical half-depths were particularly affected.

Comparison with Point Beach (Field) Data. Dunn, et al. [1] have summarized velocity and temperature data collected at the Point Beach Power Station. The depth of the lake along a line extending directly out from the outfall, and the outfall geometry, are shown in inserts in Figs. 8(a) and 8(b), respectively. Data from two dates under nominally the same conditions (quiescent lake) are used in the comparisons. The model assumed that the outfall velocity varied with the $1/7^{th}$ power of distance from the nearest solid surface, that the temperature was uniform, and that k and μ^t values (to enable ϵ to be estimated) were specified from open-channel flow measurements. The model was run for two uniform water depths of 3 m and 4.2 m. Clearly a uniform depth approximation is rather poor, but the two predictions would be expected to include the data between them; insight into the sensitivity to depth is also obtained by this treatment.

The best *straight line* fit to the measured thermal and velocity half-widths, as reported in [1], are plotted for both dates in Figs. 8(a) and 8(b), respectively. Fig. 8(a) suggests that the rate of thermal spread is somewhat underpredicted near the outfall but the data uncertainty, as indicated by the differences between the two data sets, is also large; the straight line fit does not permit the shape of the curves to be checked. The velocity half-widths agree about as well as could be expected for a straight line fit to the data.

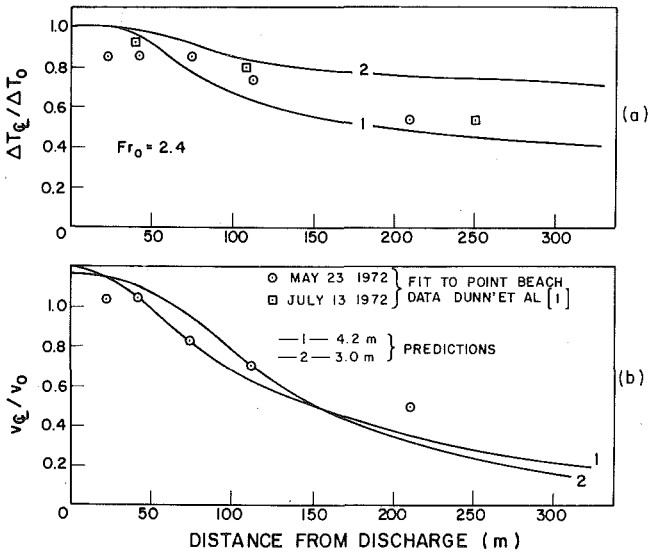

Fig. 9 Comparison of field measurements of the downstream development of centerline temperature (top) and velocity (bottom) near the surface (May 23, 1972, and July 13, 1972, data from [1]) with predictions, using two different uniform depths

The temperature and velocity decay data in Figs. 9(a) and 9(b), respectively, were obtained by correlating all the data and then reporting the results of the correlation at the measurement stations. Except near the outfall, the centerline temperature decay observations fall between the two predictions. There is also good agreement with observed centerline velocity decay.

Dunn, et al. [1] make detailed comparisons between the predictions of five different models and the field data just discussed. The temperature and velocity half-widths from the various models are reproduced in Figs. 10(a) and 10(b), respectively. Also shown are the results of the present model, obtained by averaging the 3.2 m and 4 m predictions. Despite the fact that the previous models have been tuned to fit surface discharge data, the present predictions are in best overall agreement with the straight-line correlations representing the measurements. For larger distances from the outfall, the present model is in good agreement with the Shirazi-Davis predictions. The

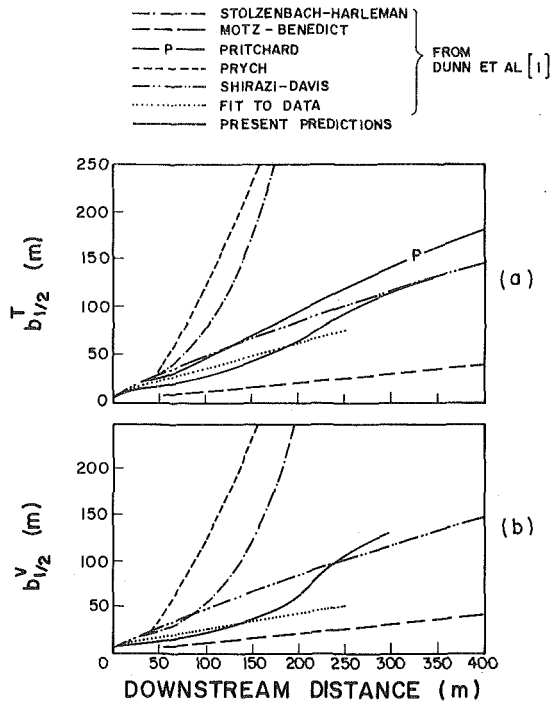

Fig. 10 Comparison of various predictions to the Point Beach field data, from [1], together with the present predictions using the average of results from the 3 m and 4.2 m depths

reason for the relatively poor performance of the integral models in this problem is believed to be the strong bottom interaction.

Extensions of Numerical Model

The predictions already shown were actually made using two entirely different finite-difference models which were verified to give the same results for the quiescent-ambient predictions. The first model [10] is restricted to this problem. The second model [11] solves the equations in a circular cylinder co-ordinate system with angular displacement corresponding to movement in the principal flow direction of the jet. With an infinite radius of curvature, this corresponds to the y-direction. By marching the solution in the angular direction, changing the radius of curvature from plane to plane, a jet which is bent over by a cross-flow can be closely followed. Testing of this model for problems involving cross-flow is currently being conducted.

The second modification is the introduction of a stretched co-ordinate in the z-direction to permit irregular bottom geometries to be treated. The σ-co-ordinate idea of Phillips [38] is being employed. This was first used by Freeman, et al. [39] for lake circulation problems, and applied to the thermal discharge problem by Paul and Lick [7].

Summary

A mathematical model is presented which describes the thermal and hydrodynamic development of a surface jet discharging into a receiving body of water. Turbulent exchange is simulated using a directionally-dependent eddy viscosity, which is in turn estimated using a two equation turbulence model. This model assumes the flow to be parabolic in the flow direction, and is the first such model that includes the solution of the vertical momentum equation. To obtain good convergence characteristics, it was necessary to develop a new method of updating pressure in the solution scheme.

Comparisons with laboratory and field data were made for quiescent receiving-body conditions in both "deep" and shallow reservoirs. The agreement between measurement and prediction has been demonstrated to be very good.

Acknowledgments

The initial work on this project was sponsored through a contract with Supply and Services Canada, with Dr. C. R. Murthy and Dr. T. J. Simons of the Canada Centre for Inland Waters as liaison officers. The remainder of the work was supported by Ontario Hydro, with Dr. R. V. Elliott as liaison officer, and by the Natural Sciences and Engineering Research Council of Canada. Our thanks to Drs. Adams and Rajaratnam for supplying laboratory data.

References

1 Dunn, W. E., Policastro, A. J., Paddock, R. A., "Surface Thermal Plumes: Evaluation of Mathematical Models for the Near and Complete Field," Argonne National Lab Rept. ANL/WR-75-3, 1975.

2 Jirka, G. H., Abraham, G., Harleman, D. R. F., "An Assessment of Techniques for Hydrothermal Prediction," Ralph M. Parson Laboratory for Water Resources and Hydrodynamics, Report 203, Massachusetts Institute of Technology, July, 1975.

3 Asbury, J. G., Frigo, A. A., "A Phenomenological Relationship for Predicting the Surface Areas of Thermal Plumes in Lakes," Argonne National Lab Report ANL/ES-5, Apr. 1971.

4 Stolzenbach, K. D., Harleman, D. R. F., "An Analytical and Experimental Investigation of Surface Discharges of Heated Water," Ralph M. Parsons Laboratory for Water Resources and Hydrodynamics, M. I. T. Report No. 135, Feb. 1971.

5 Adams, E. E., Stolzenbach, K. D., Harleman, D. R. F., "Near and Far Field Analysis of Buoyant Surface Discharges into Large Bodies of Water," Ralph M. Parsons Lab for Water Resources and Hydrodynamics, M. I. T. Report No. 205, Aug. 1975.

6 Elliott, R. V., Harkness, D. G., "A Phenomenological Model for the Prediction of Thermal Plumes in Large Lakes," *Proceedings Fifteenth Conference Great Lakes Research*, 1972, pp. 544–564.

7 Paul, J. F., Lick, W. J., "A Numerical Model for a Three-Dimensional, Variable-Density Jet, School of Engineering," Case Institute of Technology, Case Western Reserve University, Ref. FTAS/TR 73-9, 1974.

8 Waldrop, W. R., Farmer, R. C., "Thermal Plumes from Industrial Cooling Water," 24th Heat Transfer and Fluid Mechanics Inst., 1974.

9 McGuirk, J., Rodi, W., "Calculation of Three-Dimensional Heated Surface Jets," *Proceedings of the 1976 ICHMT Seminar on Turbulent Buoyant Convection*, Dubrovnik, Yugoslavia, Aug. 1976.

10 Raithby, G. D., "Prediction of Dispersion by Surface Discharge," Report of the Basin Investigation and Modelling Section, Canada Centre for Inland Waters, Aug. 1976.

11 Schneider, G. E., Raithby, G. D., "A Finite-Difference Model for the Prediction of Surface Discharges, including Crossflow Effects," Report prepared for Ontario Hydro, Dept. Mechanical Engineering, University of Waterloo, Feb. 1978.

12 Gebhart, B., Mollendorf, J. C., "A New Density Relation for Pure and Saline Water," *Deep-Sea Research*, Vol. 244, 1977, pp. 831–848.

13 Harlow, F. H., Nakayama, P. I., "Turbulent Transport Equations," *Physics of Fluids*, Vol. 10, No. 11, 1967.

14 Hinze, J. O., *Turbulence*, McGraw-Hill, 1975.

15 Harlow, F. H., Nakayama, P. I., "Transport of Turbulence Energy Decay Rate," Los Alamos Sci. Lab, University of California Report LA-3854, 1968.

16 Launder, B. E., Spalding, D. B., *Mathematical Models of Turbulence*, Academic Press, 1972.

17 Launder, B. E., Spalding, D. B., "The Numerical Computation of Turbulent Flows," *Computer Methods in Applied Mechanics and Engineering*, Vol. 3, 1974, pp. 269–289.

18 Gibson, M. M., Launder, B. E., "On the Calculation of Horizontal, Free Shear Flows under Gravitational Influence," ASME JOURNAL OF HEAT TRANSFER, Vol. 98, 1976, pp. 81–87.

19 Munk, W. H., Anderson, E. R., "Notes on the Theory of the Thermocline," *Journal of Marine Research*, Vol. 1, 276, 1948.

20 Reynolds, A. J., *Turbulent Flows in Engineering*, John Wiley & Sons, 1974, p. 189.

21 Patankar, S. V., Spalding, D. B., "A Calculation Procedure for Heat, Mass and Momentum Transfer in Three-Dimensional Parabolic Flows," *International Journal of Heat and Mass Transfer*, Vol. 15, 1972, pp. 1787–1806.

22 Amsden, A. A., Harlow, F. H., "The SMAC Method: A Numerical Technique for Calculating Incompressible Fluid Flows," Los Alamos Scientific Laboratory, Report LA-4370, 1970.

23 Harlow, F. H., Welch, J. E., "Numerical Calculation of Time-Dependent Viscous Incompressible Flow of Fluid with Free Surface," *Physics of Fluids*, Vol. 8, No. 12, 1965, pp. 2182–2189.

24 Roache, P. J., *Computational Fluid Dynamics*, Hermosa Publishers, Albuquerque, New Mexico.

25 Raithby, G. D., Torrance, K. E., "Upstream-Weighted Differencing Schemes and their Applications to Elliptic Problems involving Fluid Flow," *Computers and Fluids*, Vol. 2, 1974, pp. 191–206.

26 Spalding, D. B., "A Novel Finite-Difference Formualtion for Differential Expressions involving both First and Second Derivatives," *International Journal Numerical Methods Engineering*, Vol. 4, 1972, pp. 551–559.

27 Schneider, G. E., Raithby, G. D., Yovanovich, M. M., "Finite Element Solution Procedures for Solving the Incompressible, Navier-Stokes Equations using Equal Order Variable Interpolation," *Numerical Heat Transfer*, Vol. 1, No. 4, 1978, pp. 433–452.

28 Gebhart, B., *Heat Transfer*, McGraw-Hill, Second Edition, 1971, p.

207.
29 Denny, J. E., Clever, R. M., "Comparisons of Galerkin and Finite Difference Methods for Solving Highly Nonlinear Thermally Driven Flows," *Journal Computational Physics,* Vol. 16, 1974, pp. 271–284.
30 Goldstein, R. J., Kreid, D. K., "Measurement of Laminar Flow Development in a Square Duct using a Laser-Doppler Flowmeter," *Journal of Applied Mechanics,* Vol. 34, 1967, pp. 813–818.
31 Sato, G. K., Mortimer, C. H., "Lake Currents and Temperatures Near the Western Shore of Lake Michigan," Center for Great Lakes Studies, The University of Wisconson-Milwaukee, Special Report 22, 1975.
32 Rodi, W., "A Review of Experimental Data of Uniform Density Free Turbulent Boundary Layers," in *Studies in Convection* (B. E. Launder, editor), Academic Press, 1975, pp. 79–164.
33 Vanvari, M. R., Chu, V. H., "Two-Dimensional Turbulent Surface Jets of Low Richardson Number," Dept. of Civil Engineering and Applied Mechanics, McGill University, Technical Report 74-2 (FML), 1974.
34 Sforza, P. M., Stasi, W., "Heated Three-Dimensional Turbulent Jets," ASME JOURNAL OF HEAT TRANSFER, Vol. 101, No. 1, 1979, pp. 353–358.
35 Adams, E. E., Stolzenbach, K. D., Harleman, D. R. F., "Near and Far Field Analysis of Buoyant Surface Discharges into Large Bodies of Water," Ralph M. Parsons Laboratory for Water Resources and Hydrodynamics, Report No. 205, 1975, p. 47.
36 Scarpace, F., Green, T., "On Rapid Changes and Periodic Temperature Structure in Thermal Plumes," University of Wisconsin Inst. for Environmental Studies Remote Sensing Program, Report No. 17, 1972.
37 Lal, P. B. B., Rajaratnam, N., "An Experimental Study of Heated Surface Discharges into Quiescent Ambients," Dept. Civil Engineering Report, University of Alberta, Sept. 1975.
38 Phillips, N. A., "A Coordinate System having some Special Advantages for Numerical Forecasting," *Journal of Meteorology,* Vol. 14, 1957, pp. 184–185.
39 Freeman, N. G., Hale, A. M., Danard, M. B., "A Modified Sigma Equations' Approach to the Numerical Modeling of Great Lakes Hydrodynamics," *Journal of Geophysical Research,* Vol. 77, No. 6, 1972, pp. 1050–1060.
40 Raithby, G. D., Schneider, G. E., "The Numerical Solution of Problems in Incompressible Fluid Flow; Treatment of the Velocity-Pressure Coupling," *Numerical Heat Transfer,* In Press.

F. L. Test
Professor.

R. C. Lessmann
Assoc. Professor.

Department of Mechanical Engineering and Applied Mechanics,
University of Rhode Island,
Kingston, R. I. 02881

An Experimental Study of Heat Transfer During Forced Convection over a Rectangular Body

An experimental investigation has been performed to determine the constant surface temperature heat transfer behavior on the upper surface of a rectangular model with a chord length of 20.3 cm (8 in.) and an aspect ratio of 6/1. Data were obtained for angles of attack from 0 to 50 deg and freestream velocities of 9.1, 15.2, and 21.3 m/s (30, 50 and 70 ft/s). Separation existed on a portion of the upper surface for angles between 0 and 20 deg with the flow being turbulent after reattachment. Above 30 deg the flow was always laminar with the stagnation point on the upper surface. The heat transfer results in the laminar case were strongly influenced by freestream disturbances.

Introduction

The purpose of this investigation is to experimentally determine the convective heat transfer from the upper surface on a body of rectangular cross section in two-dimensional flow. The National Science Foundation is supporting a research project at the University of Rhode Island entitled, "Convection Heat Transfer due to Wind Currents over Inclined Flat Surfaces." One of the goals of this research is to determine whether or not wind tunnel studies can be used to predict behavior in the natural environment. The work reported in this paper discusses the experimental results of the wind tunnel studies only.

The model used had an aspect ratio, C/H, of 6 and a chord length of 20.3 cm (8 in.). This is the same geometry considered in a study of the fluid dynamics of the flow over rectangular bodies as reported by Sam, Lessmann and Test [1]. That study was undertaken first in order to develop an understanding of the flow phenomena that determine the heat transfer behavior.

The flow configurations examined in [1] and in the present study are shown in Fig. 1. If the results of this research are to be applied, for example, to solar collectors, the angle of inclination would be such that Fig. 1(c), where the stagnation point is on the upper surface, would represent the typical flow pattern. However, at small angles a separation bubble will exist on the upper surface and at some particular angle the stagnation point should be at the leading edge with the flow similar to that about an asymmetric wedge. In fact the asymmetrical wedge flow analysis of Morton [2] can predict the angles at which separation will no longer exist on the upper surface [1]. For an aspect ratio of 6, the work presented in [1] indicates that above an angle of attack of 40 deg the pressure coefficient can be predicted by the methods applicable to a flat plate as described by Abernathy [3]. Between angles of attack of 20 and 30 deg for an aspect ratio of 6 a curve fit is given in [1] for the pressure coefficient. At angles of attack less than 20 deg a definite separation bubble exists on the upper surface and analytical techniques are not available to predict the flow.

Ota and Kon [4] experimentally determined local heat transfer coefficients in the separated, reattached and redeveloped regions for flow over a rectangular plate with an aspect ratio of 20. They only studied zero angle of attack and developed an empirical relation for the reattachment point Nusselt No. under these conditions.

Kottke, et al. [5, 6] studied mass transfer for flow over a thick plate with various nose profiles, including a blunt nose at zero angle of attack. In the first paper their plot of Sherwood number exhibits the same characteristics as that reported by Ota and Kon for Nusselt number. They claim the existence of two types of separation regions; but the reported Reynolds number region for which the authors claim the first type of separation should exist is so low that it would not be present on blunt plates thicker than 2.5 cm (1 in.) at velocities greater than 1 m/s (3.3 ft/s). Their second paper presents curves relating to Fig. 5 of this paper and it will be discussed in Discussion and Results.

There are a number of papers that have studied average heat transfer during separation behind a step, and a rather complete discussion of local heat transfer coefficients is given by Filetti and Kays [7]. They also developed a correlation for the heat transfer coefficient at reattachment.

Sparrow and Tien [8] used a sublimation technique to determine average heat transfer coefficients from a square plate when the angle of attack and angle of yaw were varied. The plate had a sharp leading edge so that separation was not present at any angle of attack. Sparrow, et al. [9] extended this work to determine the three dimensional effects of various length to width ratios.

If the angle of attack for the blunt plate is such that there is no separation (as in Fig. 1(b) or 1(c)), the freestream velocity distribution is known analytically, and techniques are available to predict the local heat transfer coefficient for laminar or turbulent flow. Turbulent flow heat transfer can be calculated by a "Law of Wall" integral method presented by White, et al. [10] or an Ambrok method as discussed by Moretti and Kays [11]. Laminar flow predictions can be obtained using the one parameter integral method of Smith and Spalding as explained in White [12].

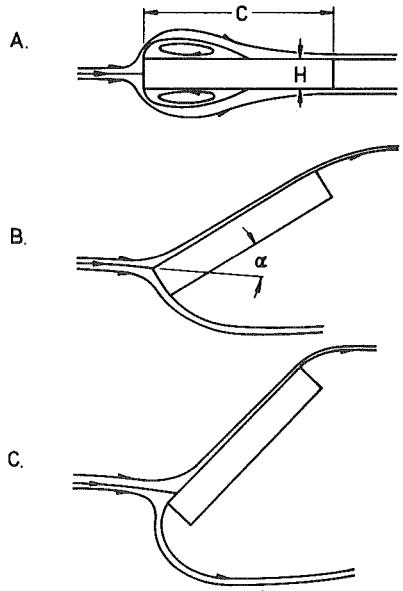

Fig. 1 Flow pattern around model at various angles of attack

Contributed by the Heat Transfer Division for publication in the JOURNAL OF HEAT TRANSFER. Manuscript received by the Heat Transfer Division, March 12, 1979.

Experimental Apparatus and Technique

The measurements were taken in a low speed open circuit wind tunnel having a test section 167.6 cm (66 in.) long, 77.5 cm (30.5 in.) square, and which is divergently tapered to account for wall boundary layer growth. The tunnel side walls were modified to support the model, allowing it to be rotated to any particular angle of attack.

The model, except for the copper heating surfaces, was constructed of plexiglass. The model extended across the full width of the wind tunnel. A sketch of the model is shown in Fig. 2. There are 16 separate heaters and convection surfaces. An enlarged view of one of the 16 units is also shown in Fig. 2. The copper pieces are 4.75 cm (1.87 in.) by 4.45 cm (1.75 in.) with a thickness of 0.635 cm (.25 in.).

An unheated model with seven spanwise pressure taps, spaced 5 cm (2 in.) apart on the top and bottom surfaces was used to check the two dimensionality of the flow. The variation in spanwise pressure recorded from these taps at the mid chord never showed a consistent variation and the variation was less than the uncertainty in the pressure measurements (±.5 percent).

The space between the copper pieces is filled with Stycast 3050, a low viscosity electrical grade epoxy manufactured by Emerson and Cuming, Inc. The thickness of the epoxy is 0.25 cm (0.1 in.) and is carefully controlled during fabrication to a tolerance of ±1 percent. The thermal conductivity of the epoxy is measured after the epoxy has cured between the copper pieces. This measurement was made on the unit before and after the heat transfer experiments. The conductivity values did not change by more than 3 percent.

A copper constantan thermocouple is imbedded by peening it in the copper plates, one on each side of the epoxy. All leads are brought out through small grooves in the copper. A thin 65 ohm heater with a mylar backing is attached with pressure sensitive adhesive to the underside of the lower plate.

Temperature measurements along with knowledge of the thermal conductivity of the epoxy gave the average heat transfer coefficient on a given copper surface which was considered to be the quasi-local value at the mid-point of the surface. For this reason the nomenclature refers to the Stanton number as quasi-local.

A two-dimensional finite difference heat transfer analysis used in the design of these units indicated that at a typical operating condition when there was a 3.6°C (6.5°F) temperature difference across the epoxy there was only a 0.01°C (0.02°F) difference between the upper and lower surfaces of each copper piece. If the heat transfer coefficient changed by a factor of 3 over a given surface, the surface temperature of the upper copper piece would vary by less than 0.28°C (0.5°F) from one edge to the other when the air to surface temperature difference was about 13.9°C (25°F).

The number and size of copper surfaces incorporated in the final model was a compromise between a manageable number of control points and sufficient data points to observe the phenomena of interest. Only the center two rows parallel to the flow in Fig. 2 were used for data on which the results were based and the outer rows were used as guard heaters. However, lateral heat loss was so small that the data on the outer rows fell within the accuracy range for the inner rows.

The center rib between the two inner rows had eight pressure taps. The pressure coefficients for all heated runs agreed within ±5 percent of those for unheated runs and reproduced those reported in [1]. This was taken as evidence that free convection effects were negligible. In addition if one uses the criterion developed by Mucoglu and Chen [13], it is found that the experimental data is well within the region for which buoyancy effects are negligible.

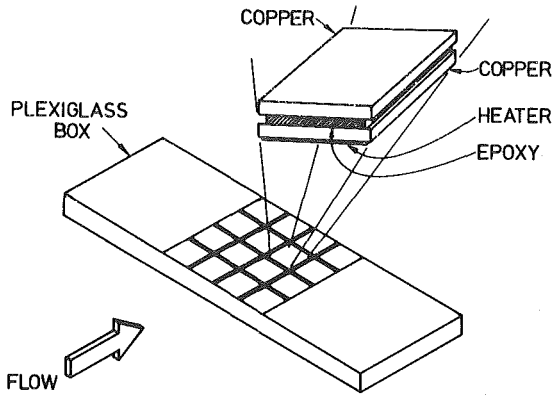

Fig. 2 Construction details of model

Data was recorded for angles of attack from 0 to 50 deg in 10 deg increments with freestream velocities upstream of the plate equal to 9.1, 15.2 and 21.3 m/s (30, 50 and 70 ft/s). For each copper piece the difference between the two copper temperatures and the difference between the top copper and freestream air temperatures were measured with calibrated copper-constantan thermocouples. The thermocouple outputs were recorded on a calibrated multipoint recorder using the most appropriate full scale deflection. The power to the heaters was regulated by variable resistors so as to maintain the same temperature difference between the top surface and air on all copper surfaces. This could be done within ±4 percent in the worse cases and normally was ±2 percent. When the air to surface temperature difference was changed, all other variables remaining unchanged, the heat transfer results were unaffected. For most runs this temperature difference was about 12.2°C (22°F).

The copper surfaces were polished each day to minimize radiation loss from the upper surface. Calculations based on the emissivity of polished copper indicate that such losses were less than 1 percent of the convective heat transfer for the temperatures involved.

The heat flow through the epoxy of the first and last piece of the middle rows must be reduced by the conductive and convective heat loss out the front and back edges before calculating the top surface heat transfer. The error involved in this procedure could cause up to a 2 percent error in the surface heat transfer for these units.

When the possible errors in thermocouple calibration, recorder accuracy, thermal conductivity measurement and heat loss evaluation are considered and combined with a possible 3 percent error in the local freestream velocity, the uncertainty in the evaluation of the Stanton number is ±6 percent. It was found by repeating runs at the same operating conditions that the results for the same location were always within ±8 percent.

Velocity profile and turbulence intensity measurements were also taken at each tenth of a chord position and at each angle and speed. This data was taken with a Disa constant temperature hot wire anemometer connected to a 90 deg upstream facing miniature 5 μm boundary layer probe. Positional accuracy along a surface normal was ±0.02 cm.

Nomenclature

C = chord, model length
C/H = aspect ratio
c = specific heat of air at constant pressure
CP = nondimensional pressure coefficient, $1 - (U/U_0)^2$
f = frequency of wake induced oscillations
H = model thickness
I_t = average turbulence intensity in boundary layer
RE = Reynolds number based on local freestream velocity (U) and distance from stagnation point (X_s)
ST = quasi-local Stanton number based on local freestream velocity (U)
ST_0 = quasi-local Stanton number based on freestream velocity well upstream of the plate (U_0)
U = local freestream velocity
U_0 = freestream velocity well upstream of the plate
X = distance from the leading edge, parallel to the flow, along the top surface of the plate
X_s = distance from the stagnation point, parallel to the flow, along the top surface of the plate. Distance is only applicable when stagnation point is at the leading edge or on the top surface of the plate
α = angle of attack

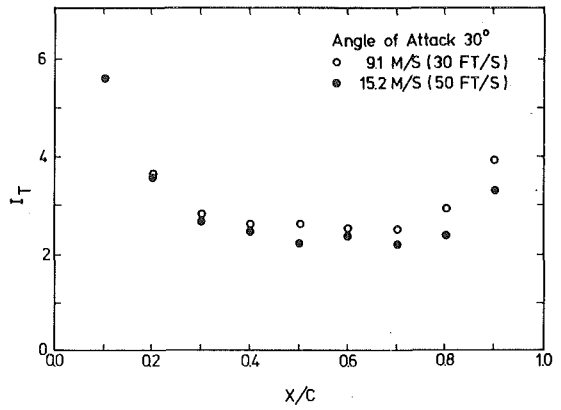

Fig. 3 Average turbulence intensity in boundary layer at 30 deg

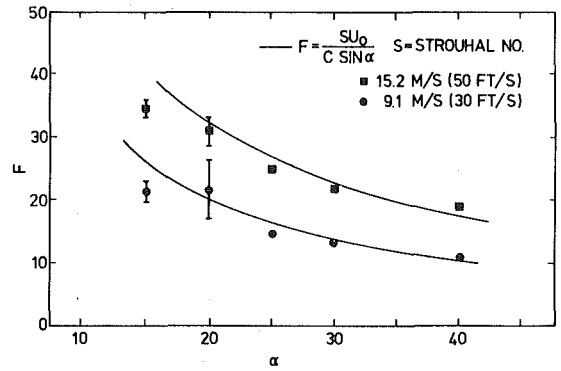

Fig. 4 Frequency of wake induced oscillations

Each probe used for these measurements was fabricated and calibrated in the laboratory. The calibration data were fitted with a King's Law curve in the range 3–30 m/s (10–100 ft/s). Typically this procedure yielded average velocities to better than ±3 percent and turbulence intensities to about ±1 percent of the recorded values.

The only unusual aspect of these measurements involved the determination of the turbulence intensity at the edge of a model's boundary layer. The basic freestream turbulence level of the unobstructed wind tunnel is about 0.5 percent. The readings obtained during any typical traverse of the boundary layer were always well above this, being typically 2.5 percent at mid chord and an angle of 30 deg. The "freestream" turbulence intensity also increased toward the leading and trailing edges of the model and showed some dependence on freestream speed. This behavior is shown in Fig. 3 which plots the average turbulence intensity across the boundary layer against position.

The explanation for this elevated level of freestream disturbance was found to be vortex shedding and wake oscillation behind the model which cause disturbances in the freestream flow upstream of the model.

When the fluctuating hot wire signal was examined on an oscilloscope it was seen to have a relatively long-period harmonic component. The frequency of this component was measured using an electronic counter and the magnitude of its contribution to the rms voltage corresponded to the observed elevation in "freestream turbulence".

Fig. 4 plots the frequency of this component of the signal against plate angle for speeds of 9.1 and 15.2 m/s (30 and 50 ft/s). The curves on this figure are plots of the frequency obtained from a Strouhal Number [14] for vortex shedding behind a plate normal to the stream whose height is the vertical projection of a 20.3 cm (8 in.) inclined surface. The error bands on these data are ±1 standard deviation of the sample taken at each angle and speed. The data are in good agreement with these curves particularly at higher angles.

The wake was also visually observed to be oscillating at all angles and speeds by use of a smoke probe. Vortex shedding was observed with the scale of the separating vortex being approximately equal to the chord of the model.

Results and Discussion

Figs. 5–8 show some of the basic heat transfer results plotted in the form of quasi-local (i.e., average over ¼ chord heaters) Stanton number (ST_0) based on upstream velocity as a function of position on the plate. The use of the freestream velocity upstream of the plate in evaluating the Stanton number rather than the local freestream velocity is appropriate when considering a variety of flow conditions.

Ota and Kon [4] state that for zero angle of attack the reattachment point is four times the plate thickness. For an aspect ratio of 6 this would place the reattachment point at 67 percent of chord. This is shown as point B in Fig. 5(*a*). They also indicate that the heat transfer coefficient is greatest at reattachment and give a prediction correlation for the heat transfer coefficient at this point. This is shown as point A in Fig. 5(*a*). By observation of the deflection of tufts, Sam, et al. [1] were able to develop a correlation for the reattachment point as a function of the angle of attack when the aspect ratio is 6. This is shown as point C in Figs. 5(*a*) and 5(*b*), and is very close to the point of maximum heat transfer. The values of ST_0 at reattachment for 0 deg angle as indicated by A, B, C or the curve maximum are all within ±6 percent for each velocity. The percent of chord at which this occurs is not in such good agreement.

Fig. 5 indicates that Stanton Number increased within the separation region from the leading ledge to reattachment. Ota and Kon [4] indicate that the Stanton number initially decreases from the leading edge to about the mid point of the separation region before starting to increase. They attribute this to a strong shear layer existing at the leading edge. The results reported in the present paper do not reproduce this phenomenon. Filetti and Kays [7] results for the local coefficient behind a step show results similar to Fig. 5(*a*) for a small step but for a large step they have a drop in heat transfer coefficient for a short distance after the leading edge but not of the same magnitude as in [4]. The reasons for this phenomenon occurring in only certain cases is not discussed in [7].

The second paper by Kottke, et al. [6] presents a Fig. 6 which shows the ratio of Sherwood number over maximum Sherwood number for a blunt plate at zero angle of attack, the maximum occurring at reattachment. The ratio of minimum to maximum is 0.4 and the minimum occurs at 0.1 times the distance to reattachment. It can be seen that the author's Fig. 5(*a*) is quite analogous to Kottke's Fig. 6 between minimum and maximum. The authors far left hand point in Fig. 5(*a*) is an average over a distance of $X = 0.25C$ so the resolution is not good enough to state that it is a true minimum, but the ratio of the value of the Stanton number at this point to that at the maximum is 0.38 for all three velocities, which agrees closely with the work of Kottke.

Another possible comparison could be made with Fig. 13 in Cur and Sparrow [15] in which the average value of $ST_0Pr^{2/3}$ is plotted as a function of length Reynolds number for two horizontal in line rectangular plates that are a plate length apart. The lowest length Reynolds number for the current work is 120,000 but the highest in Cur and Sparrow is only 16,000 but $ST_0Pr^{2/3}$ is only falling very slowly with Reynolds number. The highest value of C/H in Cur and Sparrow is 0.12 but it is 0.167 for the authors' study. The value of $ST_0Pr^{2/3}$ is between 0.008 and 0.009 for Cur and Sparrow and 0.005 for the authors at the length Reynolds number of 120,000. This difference is probably due to the much higher Reynolds number for the authors work.

In order to further consider the curves in Figs. 5–8, it is necessary to examine the fluid dynamics of the flow. Results for the pressure coefficient are presented in Fig. 9. The paper by Sam, et al. [1] indicates that separation on the upper surface ceases between an angle of attack of 20 and 30 deg. It is seen that the pressure coefficient for the 30 deg angle should be about 1. at the leading edge. The flow on the upper surface for angles of attack higher than 30 deg show that the stagnation point has started to move up along the top surface. The boundary layers were probed with a hot wire anemometer at several chordal positions to determine whether laminar or turbulent flow existed. Turbulent flow was present for all angles less than 20 deg and

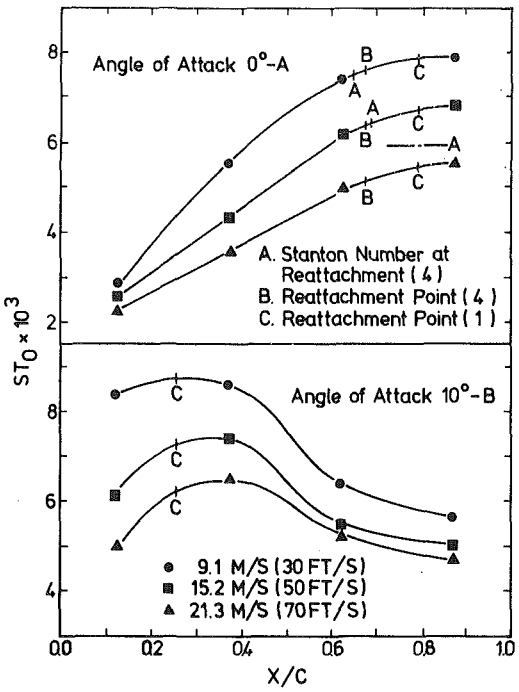

Fig. 5 Quasi-local Stanton number (ST_0) for 0 and 10 deg angles of attack

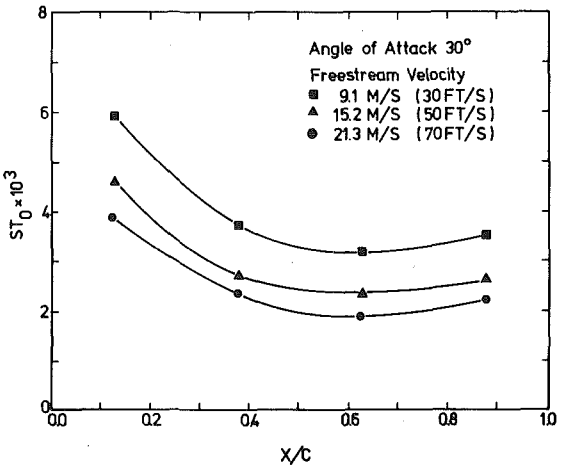

Fig. 6 Quasi-local Stanton number (ST_0) for 30 deg angle of attack

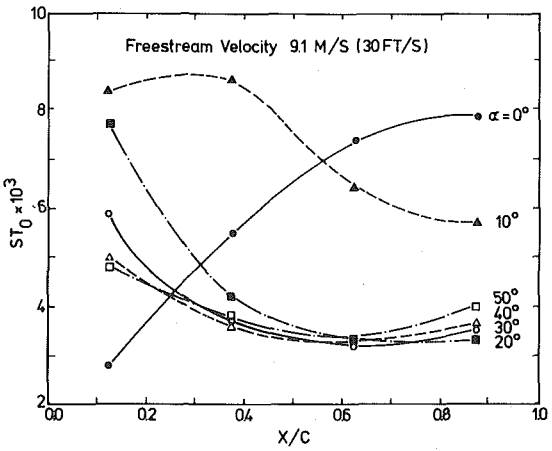

Fig. 7 Quasi-local Stanton number (ST_0) at 9.1 M/s (30 ft/s)

laminar flow for all angles greater than 30 deg. Between 20 and 30 deg the flow appeared basically laminar but occasional turbulent oscillations would appear on an oscilloscope screen. The conclusion is that the formation of a separation bubble will cause the flow downstream of the bubble to be turbulent but if the separation bubble is not present the highly accelerating mainstream flow will keep the boundary layer laminar. It is noted that the pressure coefficient, at all angles of attack greater than 0 deg, drops off at the back edge of the plate as a result of acceleration around the rear edge plus a slight wind tunnel blockage effect. This acceleration will cause an increase in the heat transfer coefficient and it shows clearly in Figs. 7 and 8 for angles of attack greater than 10 deg.

A question might be raised as to the effect of wind tunnel blockage on the heat transfer results. These measurements were made when blockage effects were present but a Smith-Spalding analysis, made using velocity distributions with and without blockage, showed that the heat transfer results differed by no more than 7 percent between these cases with the greatest percentage deviation occurring at the lower Stanton numbers.

Fig. 5(*b*) gives a heat transfer rate in the turbulent flow downstream of the reattachment point that is much higher than one would obtain by analysis using the methods of [10] and [11]. The same phenomenon downstream of a reattachment point was observed in [4] and [7].

A comparison of Figs. 7 and 8 shows that the curve for 20 deg falls within the other laminar curves at 9.1 M/s (30 ft/s) but is well above them at 15.2 M/s (50 ft/s). It was noted earlier that between 20 and 30 deg the formation of a separation bubble and thus turbulent boundary layer was somewhat indeterminate. It evidently was not present at 9.1 M/s (30 ft/s) but was at 15.2 M/s (50 ft/s).

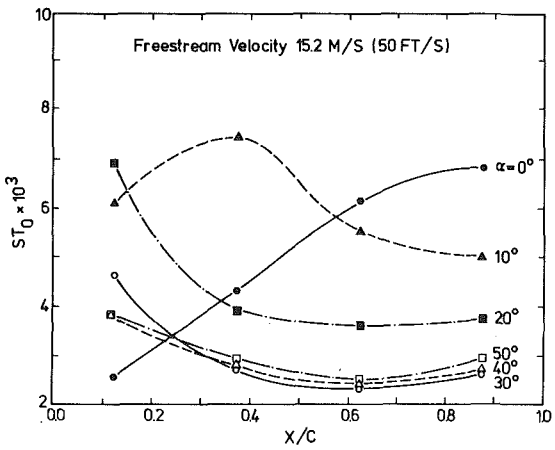

Fig. 8 Quasi-local Stanton number (ST_0) at 15.2 M/s (50 ft/s)

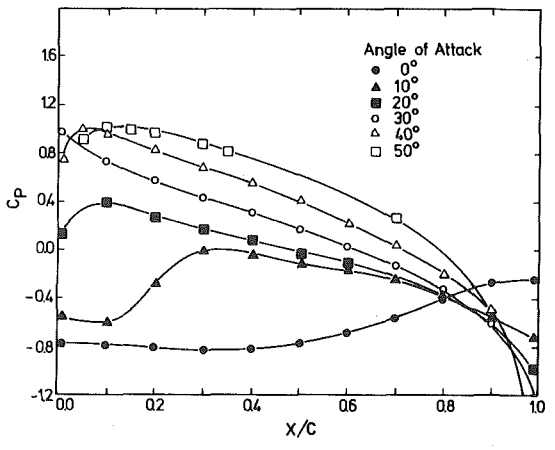

Fig. 9 Pressure coefficient on upper surface of model for various angles of attack

From this point on the discussion will focus on the results for angles of attack of 30 deg and greater. These are the angles that will be of greatest interest if the results are to be applied to the determination of convective heat losses from flat plate solar collectors. In addition, as was mentioned in the introduction, the determination of local heat transfer coefficients when a portion of the flow is separated cannot be readily accomplished from analytical models.

If the flow were to behave as a laminar flow over a symmetrical wedge as analyzed by Eckert [12] it would be expected that ST $\sqrt{RE}$ would be a constant. In this relation and in all further discussion the velocity in the local ST and local RE will be calculated using the local freestream velocity determined from the pressure coefficient in Fig. 9. The Prandtl number is 0.72 in all calculations. The 30 deg angle should be the nearest to wedge flow and Fig. 10 shows the Eckert solution, the Smith-Spalding one-parameter integral solution and the experimental results for this angle. If the velocity distribution over the plate had been exactly that for the symmetrical wedge, the Eckert solution and Smith-Spalding analysis would have agreed.

The primary question to be answered about Fig. 10 is why should the experimental results exceed the Smith-Spalding analysis by at least 50 percent.

Laminar flow heat transfer in the vicinity of a stagnation point can be enhanced by freestream turbulence. Kestin, in his discussion of the paper by Junkhan and Serovy [16] indicates that the heat transfer rate in the vicinity of the stagnation point can be almost doubled by a freestream turbulence intensity of 2.5 percent. The influence of freestream turbulence on laminar heat transfer in a favorable pressure gradient but without a stagnation point is less than 15 percent as discussed in [17] and [18].

At angles of attack equal to 30 deg or greater the flow was laminar and a stagnation point existed on the upper surface. It would be expected that the heat transfer enhancement should be between that reported by [16] and that reported in [17] and [18]. Since the recorded freestream turbulence intensity is about 2.5 percent, a 50 percent improvement in heat transfer does not seem out of the question. However, the freestream turbulence intensity of 2.5 percent is not conventional turbulence but as mentioned earlier is primarily due to a freestream oscillation resulting from disturbances initiated by an oscillating wake shedding from the plate.

It is not clear how the presence of such disturbances actually cause an increase in heat transfer. Miyazaki and Sparrow [19] have suggested an analytical approach in which elevated freestream turbulence gives rise to an effective viscosity and thermal conductivity similar to boundary layer turbulence. However, the measured mean velocity profiles were clearly laminar showing no significant alterations characteristic of earlier transition or turbulent flow. Alternatively, it is possible (even probable) that such disturbances act as a trigger for streamwise directed vortices. Such Taylor-Goertler vortices could arise from instabilities in the curved flow near the stagnation point and have been demonstrated to enhance the heat transfer by McCormack, et al. [20]. No definite evidence exists for the presence of such vortices in the present case as a spanwise study of the flow was not undertaken.

A question might be raised as to whether the heat transfer enhancement might be caused by plate vibration that is induced by the oscillating wake. Studies of heat transfer enhancement with laminar free convection from a plate with transverse vibrations have been made by Schoenhals and Clark [21] and Blankenship and Clark [22]. Nickerson [23] investigated the effect of longitudinal vibrations on the forced convection laminar boundary layer on a flat plate. In all cases studied the heat transfer was either unchanged or slightly decreased. It is therefore concluded that plate vibration is not a significant factor in the 50 percent improvement in laminar heat transfer reported in the present paper.

The conclusion is that freestream disturbances whether conventional turbulence which is stochastic in nature or well behaved oscillations of the freestream contribute to an enhancement of the laminar flow heat transfer and to the recorded freestream turbulence intensity. In the discussion of results the term, turbulence intensity, means the combined effort of conventional turbulence and wake induced freestream oscillations.

Fig. 3, which plots average turbulence intensity through the laminar boundary layer for two of the velocities in Fig. 10, gives further insight into these results. The average boundary layer turbulence is about the freestream value at the center of the plate but increases near the ends. The results for the two velocities agree at the leading edge but diverge with downstream position; the lower velocities having the higher turbulence intensities. It is also seen in Fig. 10 that the experimental heat transfer results diverge somewhat with downstream position. Although this divergence is within the experimental accuracy of the results, there is a systematic behavior to it which could be explained by the divergence in turbulence intensities shown in Fig. 3.

Fig. 11 compares the experimental results for angles of attack greater than or equal to 30 deg with the Smith-Spalding analysis. These theoretical results which are independent of freestream velocity are averaged over the length of a heated segment (¼ of chord) and plotted at the mid point of each segment. The experimental results presented are all for a freestream speed of 15.2 M/S (50 ft/s). Had other speeds been shown on the figure there would have resulted the kind of fanning out of the data as displayed in Fig. 10 which has already been discussed. This figure shows clearly that the elevation in experimentally determined local heat transfer is relatively independent of angle of attack and approximately 50 percent above the analytical result at all chord positions. It should be pointed out that there is an error in Fig. 11. The angle designations of 30 and 40 deg on the experimental curves should be reversed.

The applicability of these results to actual situations in the environment depends primarily on whether or not all free stream disturbances result in the same effect on heat transfer. This would be the case for instance if such disturbances acted only to trigger streamwise

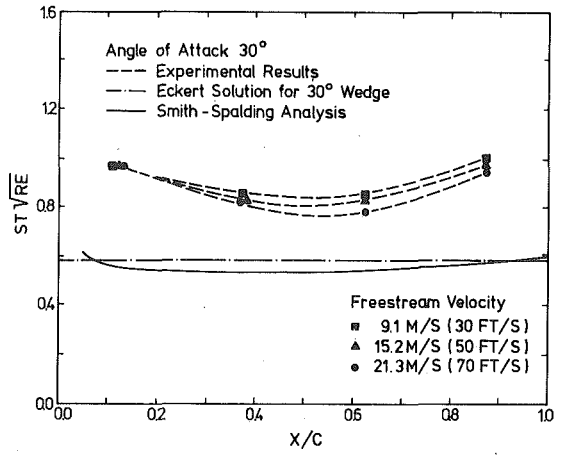

Fig. 10 Comparison with wedge flow theory at 30 deg angle

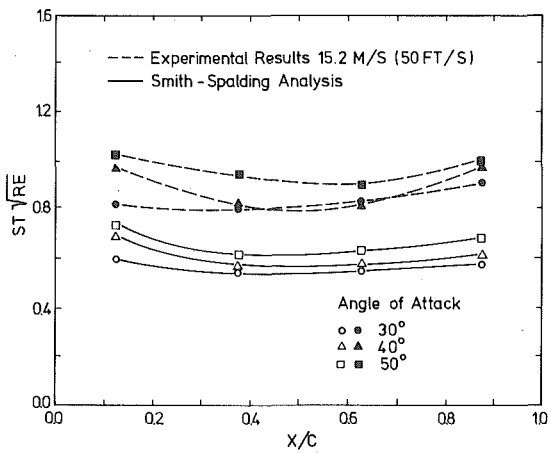

Fig. 11 Comparison of experimental results with Smith-Spalding analysis

vortices and it was these secondary flows which caused the observed enhancement of heat transfer. If some such conclusion were valid then it is conceivable that the variability of a typical real flow situation could be lumped into an effective level of freestream "turbulence" and used to replace the disturbances present in the wind tunnel experiment. This possibility is currently under active investigation.

Conclusions

1 For an aspect ratio of 6 there is a separation bubble on the upper surface of the plate when the angle of attack is less than 20 deg and turbulent flow exists downstream of reattachment. Above an angle of attack of 30 deg there is no separation and flow is laminar on the upper surface with the stagnation point moving slightly downstream from the leading edge with increasing angle.

2 An oscillating wake downstream of the plate causes oscillations of freestream velocity in the vicinity of the plate. One way in which these oscillations manifest themselves is as a significant increase in the apparent freestream turbulence intensity. The velocity profiles in the boundary layer remain laminar in the presence of this elevated disturbance level.

3 In the separation region, the local heat transfer rate increases with downstream position, and reaches a maximum in the vicinity of the reattachment point.

4 In the laminar flow region the experimental heat transfer coefficients are about 50 percent higher than those determined by the Smith-Spalding analysis. This difference appears to be due to freestream disturbances, caused by wake oscillations which have the same effect as freestream turbulence, in the presence of favorable pressure gradient laminar flow following a stagnation point. The variation of heat transfer coefficient at a particular velocity appears to follow the variation in total freestream turbulence intensity.

5 Theoretical analyses are not available for the prediction of local heat transfer coefficients at low angles of attack where a separation bubble exists over a portion of the surface. At angles of attack above 30 deg when laminar flow is present, analyses which do not account for the effects of freestream disturbances will considerably under estimate the heat transfer.

Acknowledgments

This research was performed under the auspices of NSF Grant ENG 16-18379. The authors wish to express their appreciation for the efforts of Prof. Warren M. Hagist in developing the wind tunnel facilities, without which this work would not have been possible. The help of Richard Boeglin and J. Quinn Murphy, students at the University of Rhode Island, is gratefully acknowledged.

References

1 Sam, R. G., Lessmann, R. C. and Test, F. L., "An Experimental Study of Flow over a Rectangular Body," accepted for publication in the ASME *Journal of Fluids Engineering*, 1979.

2 Morton, W. B., "On the Discontinuous Flow of Liquid Past a Wedge," *Philosophical Magazine*, Ser. 6, 1921, pp. 801–808.

3 Abernathy, F. H., "Flow over an Inclined Plate," Pratt and Whitney Research Report No. 151, Aug. 1958.

4 Ota, T. and Kon, N., "Heat Transfer in the Separated and Reattached Flow on a Blunt Flat Plate," ASME JOURNAL OF HEAT TRANSFER, No. 1974, pp. 459–462.

5 Kottke, V., Blenke, H., and Schmidt, K. G., "The Influence of Nose Section and Turbulence Intensity on the Flow around Thick Plates in Parallel Flow," *Warme-und Stoffubertragung*, Vol. 10, 1977, pp. 159–174.

6 Kottke, V., Blenke, H., and Schmidt, K. G., "Determination of the Local and Average Mass Transfer on Thick Plates in Parallel Flow with Flow Separation and Reattachment," *Warme-und Stoffubertragung*, Vol. 10, 1977, pp. 217–232.

7 Filetti, E. G. and Kays, W. M., "Heat Transfer in Separated, Reattached and Redevelopment Regions Behind a Double Step at Entrance to a Flat Duct," ASME JOURNAL OF HEAT TRANSFER, May 1967, pp. 163–167.

8 Sparrow, E. M. and Tien, K. K., "Forced Convection Heat Transfer at an Inclined and Yawed Square Plate—Application to Solar Collectors," ASME JOURNAL OF HEAT TRANSFER, Nov. 1977, pp. 507–512.

9 Sparrow, E. M., Ramsey, J. W. and Moss, E. A., "Effect of Finite Width on Heat Transfer and Fluid Flow about an Inclined Rectangular Plate," ASME JOURNAL OF HEAT TRANSFER, May 1979, pp. 199–204.

10 White, F. M., Lessmann, R. C. and Christoph, G., "Calculation of Turbulent Heat Transfer and Skin Friction," *AIAA Journal*, Vol. 11, No. 7, July 1973, pp. 1046–1048.

11 Moretti, P. M. and Kays, W. M., "Heat Transfer to a Turbulent Boundary Layer with Varying Free-Stream Velocity and Varying Surface Temperature—an Experimental Study," *International Journal of Heat and Mass Transfer*, Vol. 8, 1965, pp. 1187–1202.

12 White, F. M., *Viscous Fluid Flow*, McGraw-Hill, New York, 1974, pp. 326–329.

13 Mucoglu, A. and Chen, T. S., "Mixed Forced and Free Convection on Inclined Surfaces," Paper 78-WA/HT-46, Presented at ASME annual meeting, San Francisco, 1978.

14 Blevins, R. D., *Flow Induced Vibration*, Van Nostrand Reinhold Co., 1977.

15 Cur, N. and Sparrow, E. M., "Experiments on Heat Transfer and Pressure Drop for a Pair of Colinear Interrupted Plates Aligned with the Flow," *International Journal of Heat and Mass Transfer*, Vol. 21, 1978, pp. 1069–1080.

16 Junkhan, G. H. and Serovy, G. K., "Effects of Free Stream Turbulence and Pressure Gradient on Flat Plate Boundary-Layer Velocity Profiles and on Heat Transfer," ASME JOURNAL OF HEAT TRANSFER, May 1967, pp. 164–179.

17 Buyuktur, A. R., Kestin, J. and Maeder, P. F., "Influence of Combined Pressure Gradient and Turbulence on the Transfer of Heat from a Plate," *International Journal of Heat and Mass Transfer*, Vol. 7, 1964, pp. 1175–1186.

18 Dyban, E. P. and Epik, E. Y., "Heat Transfer in a Boundary Layer in Turbulized Air Flow," *Proceedings of the Sixth International Heat Transfer Conference*, Toronto, Canada, 1978, Vol. 2, pp. 507–512.

19 Miyazaki, H. and Sparrow, E. M., "Analysis of Free-Stream Turbulence on Heat Transfer and Skin Friction," ASME JOURNAL OF HEAT TRANSFER, Nov. 1977, pp. 614–619.

20 McCormack, P. D., Walker, H. and Keller, M., "Taylor-Goerther Vortices and Their Effect on Heat Transfer," ASME JOURNAL OF HEAT TRANSFER, Feb. 1970, pp. 101–112.

21 Schoenhals, R. J. and Clark, J. A., "Laminar Free Convection Boundary Layer Perturbations Due to Transverse Wall Vibrations," ASME JOURNAL OF HEAT TRANSFER, 1962.

22 Blankenship, V. D. and Clark, J. A., "Effects of Oscillation on Free Convection From a Vertical Finite Plate," ASME JOURNAL OF HEAT TRANSFER, 1964, pp. 149–158.

23 Nickerson, R. J., "The Effect of Free Stream Oscillation on the Laminar Boundary Layer of a Flat Plate," ScD. Thesis, MIT, 1957.

R. Chandran
Research Asst.,
Student Mem.
ASME

J. C. Chen
Professor,
Mem. ASME
Lehigh University,
Bethlehem, PA

F. W. Staub
General Electric Company,
Schenectady, NY
Fellow, ASME

Local Heat Transfer Coefficients around Horizontal Tubes in Fluidized Beds

The local characteristics of heat transfer from horizontal tubes immersed in fluidized beds were investigated experimentally. Steady-state heat transfer measurements were obtained in air-fluidized beds of glass beads, both for a single tube and a ten-row bare tube bundle. The test results indicated that local heat transfer coefficients are strongly influenced by angular position and gas flow rate, as well as by particle size and system pressure. The heat transfer coefficients, averaged around the circumference of the tube, exhibited a general tendency to increase with decreasing particle size and increasing system pressure. The heat transfer coefficients for a tube in an inner-row position within the bundle were found to be slightly higher than those for a tube in the bottom-row. Comparison of the average heat transfer coefficient data obtained in this study with some of the existing correlations for heat transfer from horizontal tubes showed that the correlations are unsatisfactory.

Introduction

Many applications of fluidized beds involve heat transfer to or from immersed tubes and tube bundles. The rate of heat transfer between a fluidized bed and a submerged tube depends upon a number of factors, including the properties of the bed material and the fluid, bed and tube geometries, and the fluidization state [1, 2]. Measurements of heat transfer between fluidized beds and horizontal tubes have been carried out by many investigators and both experimental data and correlations are reported in the literature [3–6]. Reviews of the work are given in [7–10], and a comparison of the available correlations is presented by Ainshtein and Gel'perin [11]. As pointed out by Chen [12], there is little agreement among the various correlations or between correlations and data. This state is attributed to incorrect or insufficient accounting of the governing parameters/mechanisms as well as to the empiricism that is usually invoked in fitting data. From an applications standpoint, there is a need for improved phenomenological understanding of the mechanisms and appropriate modeling of the transport processes.

The foregoing is especially true for tubes placed *horizontally* in fluidized beds. Since air flow is normal to the tube axis for horizontal tubes, one cannot assume axial symmetry. Local heat transfer coefficients could, in principle, vary with circumferential position on the tube surface. Evaluation of this effect has been hampered by insufficient experimental data on *local* heat transfer coefficients. A few studies [5, 6, 8, 10] have reported local measurements around horizontal tubes. These data were restricted to relatively small particle sizes ($\bar{d}_p < 350$ μm) and were all limited to fluidized beds operating at atmospheric pressure.

This paper presents local heat transfer coefficients obtained in fluidized beds, over a broader range of particle sizes ($125 \leq \bar{d}_p \leq 1580$ μm) and at various system pressures ($100 \leq P \leq 400$ kPa). Data are presented for a single horizontal tube, as well as for tubes at two different locations within a horizontal tube bundle.

Test Apparatus and Experimental Method

Two different fluidized bed test facilities were used in this investigation.

The test facility for single tube experiments consisted of two fluidized beds, one for operation at atmospheric pressure and the other for operation at pressures up to 500 kPa. For this facility the fluidizing air was supplied by a pair of reciprocating compressors, capable of delivering 0.47 m^3/s at a maximum pressure of 860 kPa. The air flow rate was monitored at a specially designed flowboard that used annubar sensors (pitot tube rakes) with associated read-out instruments. The flow metering system was designed to measure air flow rates, from 0.004 to 0.57 m^3/s and at pressures up to 690 kPa, with an accuracy of two percent. The single tube tests were all performed in the pressurized bed of 0.203 m ID. The middle section of the cylindrical vessel was fabricated from acrylic plastic to permit visual observation. Aluminum headers at the top and bottom of the bed were used for air and instrumentation connections. The distributor was a sandwich assembly of a perforated steel plate, a plastic porous sheet and a metal screen.

The tube bundle experiments were carried out in a 0.305 m square, open-loop fluidized bed. The bed was transparent with column walls made out of Lexan sheets. The distributor employed was of the bubble-cap type. Air was supplied to this test facility by a two-stage blower driven by a 75 kW motor. All flow measurements were made by means of ASME flow nozzles and associated instrumentation.

A specially instrumented tube was developed for the measurement of local heat transfer coefficients. Fig. 1 shows the details of the test tube. Eight strips of 50.8 μm thick Inconel foil were bonded to a solid Lexan rod as shown. Each foil strip was heated by an individually controlled AC power supply. Miniature thermocouples (0.25 mm dia wires) were placed in grooves directly beneath the foil strips. The temperature sensed by the thermocouples were corrected (less than 1 percent correction of ΔT) to obtain surface temperatures at the top of the heated foils. All the heat transfer tests were carried out under isothermal wall conditions, wherein the power to individual foil strips were adjusted to obtain a uniform temperature around the circum-

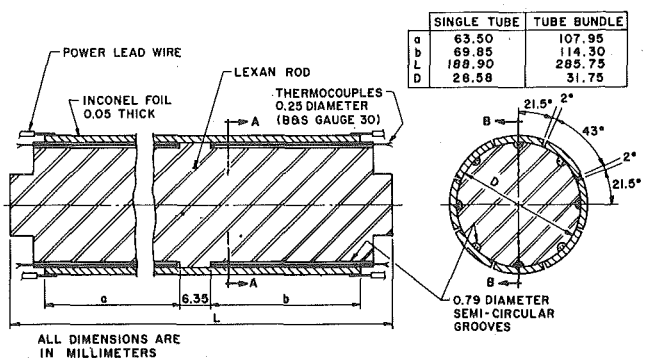

Fig. 1 Heat transfer test section

Contributed by The Heat Transfer Division for publication in the JOURNAL OF HEAT TRANSFER. Manuscript received at ASME Headquarters April 20, 1979.

Table 1 Properties of test particles

Designation	Mean Size $\bar{d}_p(\mu m)$	Size Range (μm)	U_{mf}(m/s) Pressure (kPa) 101.3	202.6	405.3	U_t(m/s) Pressure (kPa) 101.3	202.6	405.3
GT-1	125	105–149	0.024			0.83		
GT-2	245	210–297	0.051	0.051	0.050	1.66	1.32	1.07
GT-3	610	500–707	0.280	0.254	0.231	3.91	3.10	2.46
GT-5	950	707–1190	0.430	0.337	0.267	5.56	4.41	3.37
GT-6	1580	1410–1679	0.801		0.512	9.47		4.74
SG	650	595–707	0.31			4.6		

Material: Soda Lime Glass, *Density* ρ_s: 2480 kg/m^3, *Specific* heat c_{ps}: 753 J/kg K, *Thermal* conductivity k_s: 0.89 w/m K.

ference of the rod. The measured input power to each strip then permitted the determination of the local heat fluxes, $\dot{q}(\beta)$. Thermocouple readings yielded the difference between the foil surface temperature and the bed bulk temperature, ΔT. From these measurements, local heat transfer coefficients could be obtained directly,

$$h(\beta) = \dot{q}(\beta) \div \Delta T \tag{1}$$

The single tube heat transfer studies were carried out in fluidized beds of glass beads over a range of air flow rates (up to 12 times the minimum fluidization flow rate). Data were obtained for five different particle sizes and at pressures of 101.3, 202.6 and 405.3 kPa. In the case of the tube bundle, the experiments were performed with a medium size particle and at atmospheric pressure. Local heat transfer measurements were obtained for a tube at two different positions within a ten-row bare tube bundle and over a range of air flow rates. Geometry of the tube bundle is shown in the inset of Fig. 11. The characteristics of the various test particles are furnished in Table 1. The mean particle diameter ($\bar{d}_p$) was computed on the usual basis of weight fractions [1, 2]. The minimum fluidization velocity (U_{mf}) was determined experimentally by observation of pressure drop behavior. The value for the terminal velocity (U_t) was calculated by standard equations [1] for the smallest particle size in the bed.

In all tests, the static height of the (unfluidized) bed (H_s) was 0.457 m. In the case of single tube experiments, the center-line elevation of the tube above the distributor (H) was held constant at 0.229 m. The tube was 28.58 mm in diameter (D) and 188.9 mm in length. In tube bundle experiments, the instrumented tube was positioned at locations shown in the inset in Fig. 11. The test tube was 285.8 mm long and had a diameter of 31.75 mm. The heat transfer measurements were all made at angular positions 45 deg apart around the circumference of the horizontal test tubes.

Experimental Results

Heat Transfer from a Single Horizontal Tube. The local heat transfer coefficients obtained around a single tube, for a fluidized bed of a medium size particle (GT-3), are shown in Fig. 2. Data are plotted for fluidization at a pressure of 202.6 kPa and at three different gas flow rates. It is seen that the heat transfer coefficients are vertically symmetrical about the axis as expected, confirming the reproducibility of the instrumentation method. Secondly, it is apparent that the coefficients vary significantly with changing gas flow velocity and changing angular position around the tube. At the lowest velocity indicated, the maximum heat transfer coefficient is found at the sides of the tube (90 deg/270 deg positions). A distinct minimum in the coefficient is found at the top of the tube (0 deg position). This result is consistent with the observations reported in [13–15], which indicate the presence of a stagnant cap of solid particles at the top of the tube at low flow rates. An increase in the gas flow rate serves to enhance heat transfer for all positions around the tube and results in a much more uniform distribution of the coefficients. The location of the maximum coefficient remains unchanged and still occurs at the sides of the tube. With further increase in gas velocity, the trend reverses and a decline in the local coefficients occurs at all angular positions. At the higher velocities, the maximum coefficient occurs at the top of the tube. This complex trend was observed for essentially all the runs and is an indication that the local heat transfer mechanisms change significantly with varying fluidization states.

For a given particle, fluidization gas flow velocity range is bounded by minimum fluidization velocity (U_{mf}) and terminal entrainment velocity (U_t). To compare results for different bed particles, it is desirable to select an appropriate generalized velocity parameter. The ratio of the superficial gas velocity to either limiting velocities (i.e., U_{sg}/U_{mf} or U_{sg}/U_t)is awkward to use in comparing results obtained with particles of different sizes, because the range of flow velocities is large for small particles (U_t/U_{mf}) $\sim$ 30 to 80] but small for large particles [(U_t/U_{mf}) $\sim$ 7 to 15). In this study, a normalized velocity parameter $(U_{sg} - U_{mf})/(U_t - U_{mf})$ is used to characterize the fluidization flow. The value of this velocity parameter (U_N) usually lies between 0 and 1. For fine powders, however, the value may exceed unity unless U_t is revised as the terminal velocity for the largest particle in the size range. The magnitude of U_N is indicated for all data shown in Figs. 2–11.

The effect of particle size on the local heat transfer coefficients at atmospheric pressure is shown in Fig. 3. The heat transfer coefficients at the sides and bottom portion of the tube show a continuous decline with increasing particle size. The coefficients at the top of the tube tend to increase for an initial increase in particle size from small to medium, but then decrease with further increase to large particle size. However, the magnitude of variation is less pronounced at the top of the tube, as compared to the sides and bottom. It is also worth noting that the heat transfer coefficients are highly nonuniform around the circumference of the tube for small particles (125 μm) but are rela-

Nomenclature

c_0 = coefficient in equation (2)
c_p = specific heat
D = diameter of tube
$\bar{d}_p$ = mean particle diameter
G = superficial mass velocity of gas
g = acceleration due to gravity
H = center-line elevation of the instrumented tube above distributor
H_s = static height of bed
h = local heat transfer coefficient
$\bar{h}$ = average heat transfer coefficient
k = thermal conductivity
Nu = Nusselt number, $(\bar{h}\bar{d}_p)/k_g$
P = absolute pressure
Pr = Prandtl number, $(c_{pg}\mu_g)/k_g$
$\dot{q}(\beta)$ = local heat flux
Re = Reynolds number, $(G\bar{d}_p)/\mu_g$
Re_G = Reynolds group, $(G\bar{d}_p\rho_s)/(\rho_g\mu_g)$
T = temperature
U_{mf} = superficial gas velocity at minimum fluidization
U_N = normalized velocity parameter, $(U_{sg} - U_{mf})/(U_t - U_{mf})$
U_{sg} = superficial gas velocity
U_t = particle terminal velocity
$\bar{\alpha}$ = average bed void fraction
β = angular position around the circumference of tube, measured from the top of the tube
ΔT = temperature difference
μ = absolute viscosity
ψ_s = particle shape factor
ρ = density

Subscripts

g = gas
mf = minimum fluidization
s = particle/solid

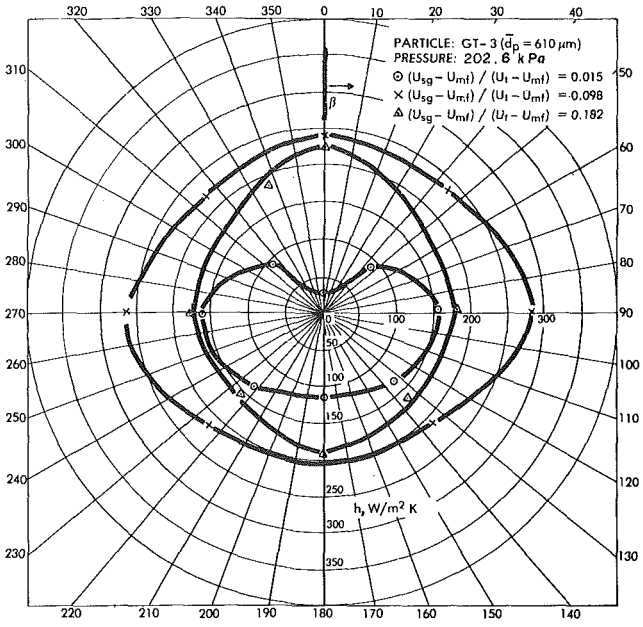

Fig. 2 Local heat transfer coefficients around a single horizontal tube at different gas flow rates

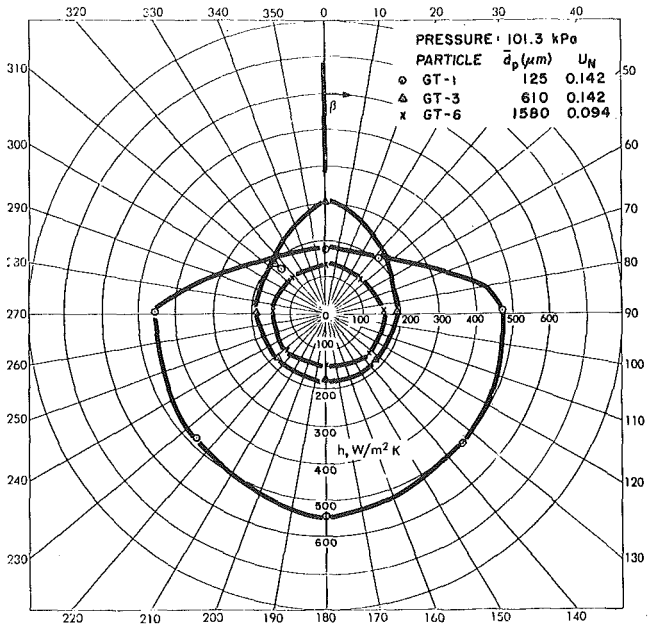

Fig. 3 Local heat transfer coefficients around a single horizontal tube for different particle sizes

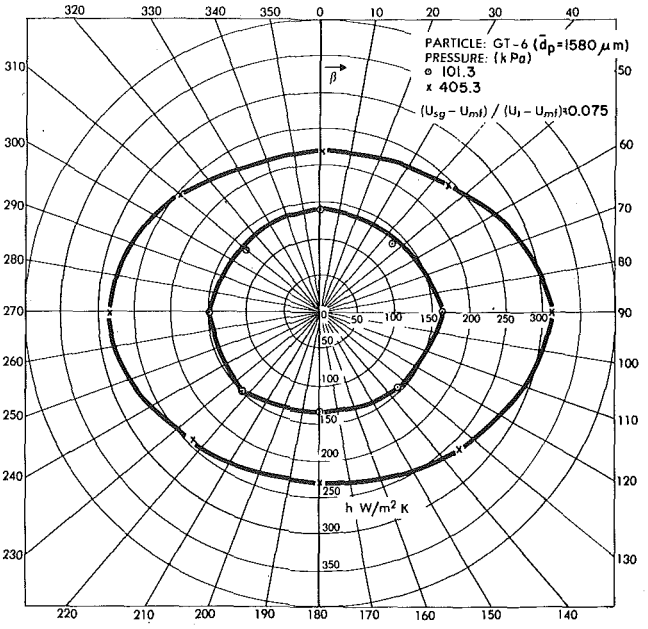

Fig. 4 Effect of pressure on local coefficients for large particles (1580 μm)

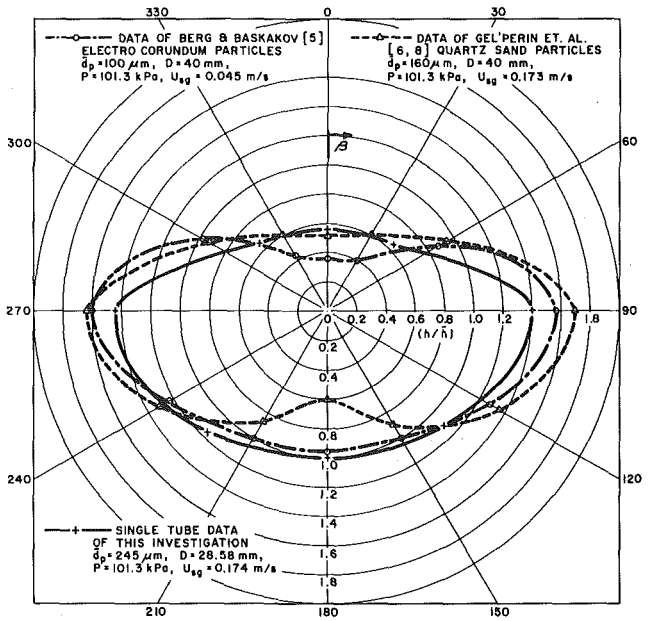

Fig. 5 Relative heat transfer coefficients ($h/\bar{h}$) around a single horizontal tube

tively more uniform for large particles (1580 μm). These data are representative of results for low to moderate fluidization flow rates.

The effect of pressure on the local coefficients for large particles (1580 μm) is exhibited in Fig. 4. It is evident that there is a significant improvement in the heat transfer coefficients with an increase in pressure. It is also apparent that the sides of the tube are more effective in transferring heat at the higher pressure (405.3 kPa). A considerable enhancement in the heat transfer coefficients occurs at higher pressures in the case of small particles (245 μm) as well. The circumferential distribution, however, is different from that for large particles (1580 μm), particularly at the elevated pressure. The top and bottom portions of the tube are better heat transfer locations in the case of small particles (245 μm). This complex effect of pressure on heat transfer for particles of different sizes results from the relative contributions of packet-conduction and dilute-phase convection mechanisms. Increasing pressure tends to increase the gaseous conductivity and convection. However, increasing pressure decreases frequency of packet renewal resulting in a decline in the effectiveness of packet-conduction. Thus the overall effect depends on the relative contributions of conductive and convective mechanisms, which are different at different circumferential locations for particles of various sizes.

Some limited data on local heat transfer coefficients for horizontal tubes are available in the literature [5, 6, 8, 10]. Because of differences in the test parameters, it is difficult to make a direct comparison of the data from the various investigations. But a review of all the test results indicates general qualitative agreement. For the purposes of illustration, a representative sample drawn from the data of Berg and Baskakov [5], Gel'perin, et al. [6, 8] and this study are shown in Fig. 5. The plot gives a measure of the distribution of the relative heat transfer coefficients ($h/\bar{h}$) around the tube. It is seen that the profiles

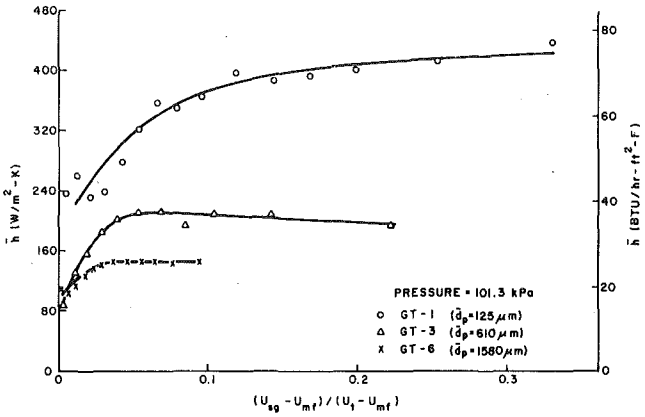

Fig. 6 Average heat transfer coefficients around a single horizontal tube for different particle sizes

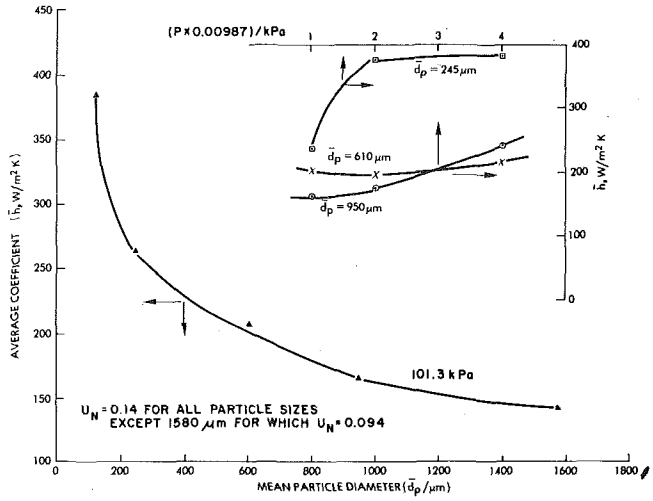

Fig. 7 Effect of particle size and system pressure on average heat transfer coefficients

of the local coefficients around the perimeter are rather similar in nature although the values of the test parameters are quite different. The local fluidization characteristics seem to be the common denominator. Thus, it is plausible that a general relationship between the system parameters and the local fluidization dynamics could be found, and that information in turn could be used to predict the local heat transfer coefficients.

The values of the average heat transfer coefficient around the tube ($\bar{h}$) have been calculated from the measured local coefficients (h), and some sample results are plotted in Figs. 6 and 7. Fig. 6 shows data for three different particle sizes at the same pressure (101.3 kPa). The main part of Fig. 7 shows a cross-plot of $\bar{h}$ versus particle diameter ($\bar{d}_p$) for a constant flow-rate parameter and at a constant pressure. The inset in Fig. 7 shows a cross-plot of $\bar{h}$ versus system pressure (P) for three particle sizes, at the same constant value of the flow-rate parameter.

It is seen that the parameters of particle size and operating pressure both have significant effects on the magnitude of the average heat transfer coefficient. In general, $\bar{h}$ increases with decreasing particle size or increasing system pressure. The strong decrease in the magnitude of $\bar{h}$ with increasing particle size is clearly evident in both figures. The effect of system pressure over the range of 405.3 kPa tested, is shown in the inset. While $\bar{h}$ increases slightly with pressure for the large particles (950 μm), it changes little for the medium size particles (610 μm). With small particles (245 μm), there is a marked increase in the average coefficient for a change in pressure from 101.3 kPa to 202.6 kPa, but little change with further increase to 405.3 kPa. These rather complex trends would argue for a more mechanistic modeling of the heat transfer process in fluidized beds, rather than the conventional attempts to correlate $\bar{h}$ versus operating parameters ($\bar{d}_p$, P, U_{sg}, etc.).

Heat Transfer Results for Tube Bundle. As stated earlier, an instrumented tube was placed at two different positions within a ten-row, bare tube bundle for the measurement of local heat transfer coefficients. The two locations are indicated in the sketch shown in Fig. 11. The locations of thermocouples used to measure bed temperature are also shown in the sketch. Data were obtained with glass particles denoted as *SG* (see Table 1) at a bed pressure of 101.3 kPa.

Figs. 8 and 9 show polar plots of the local heat transfer coefficients measured at locations 1 and 2 within the bundle, respectively. For an internal tube (location 1), the coefficients were found to peak at an

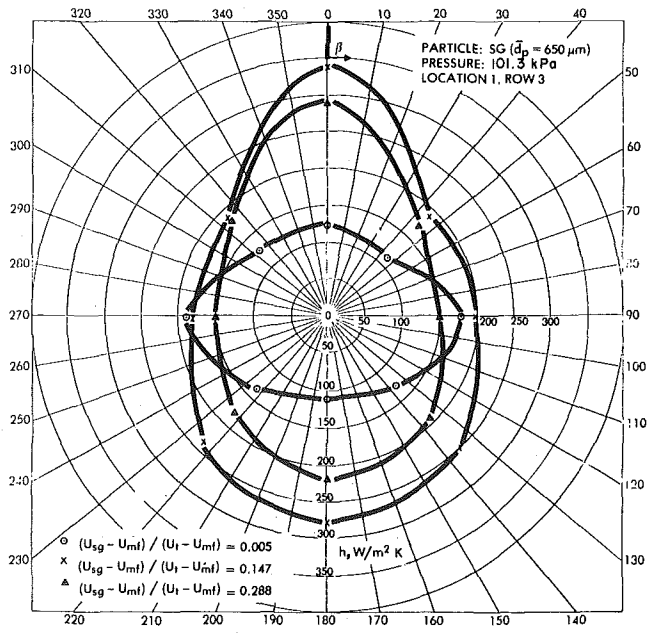

Fig. 8 Local heat transfer coefficients for a tube in the inner-row position within a tube bundle

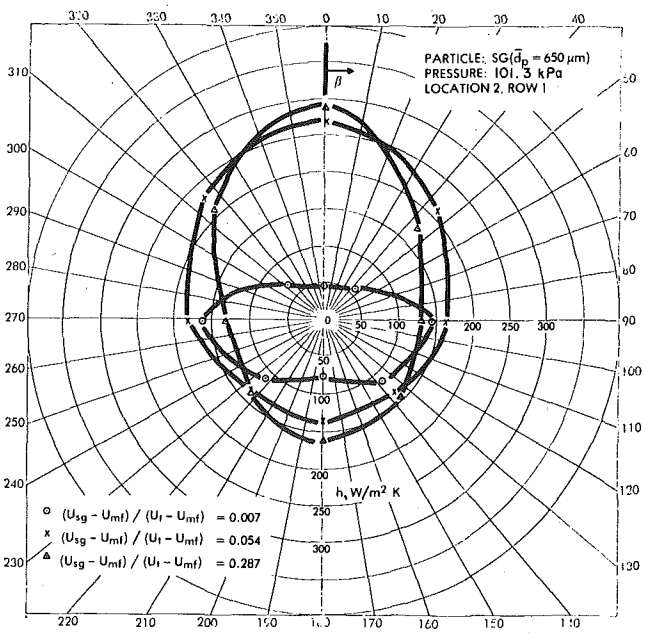

Fig. 9 Local heat transfer coefficients for a tube in the bottom-row position within a tube bundle

intermediate rather than at the highest gas flow rate. For the tube in the bottom-row of the bundle (location 2), the data bear a greater resemblance to the data obtained for a single horizontal tube. For both locations, the coefficients over the top portion of the tube were small for flow rates close to minimum fluidization conditions, but were substantially higher at larger values of the flow parameter. For moderate to high flow rates, the largest local coefficients were found at the top of the tube rather than at the side or bottom positions.

The local coefficients around the tube at two locations in the bundle are compared with those obtained around a single tube in the cylindrical bed in Fig. 10. For the U_N parameter value of ~0.14, the coefficients for the internal tube within the bundle are seen to be slightly higher than those for the tube at the bottom-row and for the single tube.

The circumferentially averaged heat transfer coefficient ($\bar{h}$) for the two locations in the bundle are plotted in Fig. 11 as a function of gas flow rate. For comparison, the average coefficients for a single horizontal tube in the cylindrical bed, with particles of about the same size, are also shown. The coefficients for each of the three configurations were found to exhibit similar trends. Moreover, the $\bar{h}$ values for the single tube are seen to be bounded by those for the bottom-row and inner-row tubes.

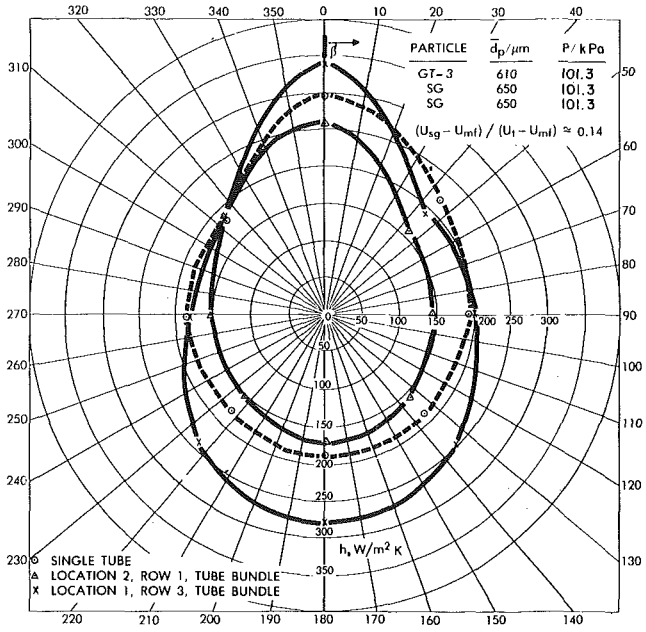

Fig. 10 Comparison of local coefficients around a single tube with those obtained around a test tube at two locations within a tube bundle

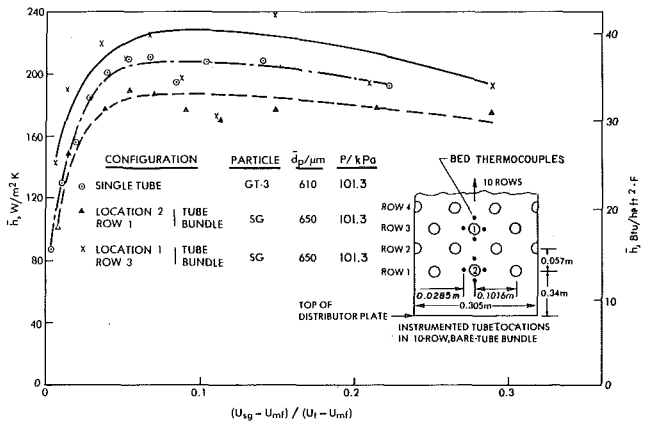

Fig. 11 Comparison of average coefficients around a single tube with those obtained around a test tube at two locations within a tube bundle

Comparisons with Correlations

To our knowledge, correlations for local heat transfer coefficients have not been published to date.

An attempt was made to compare the average heat transfer coefficient ($\bar{h}$) obtained in this study with correlations proposed for heat transfer from single horizontal tubes. Due to space limitations, comparisons could be made with only a few selected correlations which are well-known and find wide use. The three correlations examined are that of Vreedenberg [3], Gel'perin, et al. [11], and modified Vreedenberg as proposed by Andeen and Glicksman [4]. The value of average bed void fraction ($\bar{\alpha}$) is required in these correlations. This quantity could have been measured experimentally during the test runs. However, in design applications, one would normally calculate $\bar{\alpha}$ by some standard correlation since it would not be known a priori. Consistent with this practice, the following equation of Staub and Canada [16] was used to calculate $\bar{\alpha}$ for use in the heat transfer correlations:

$$\frac{U_{sg}}{\bar{\alpha}} = c_0 U_{sg} + \frac{(1-\bar{\alpha}_{mf})}{\bar{\alpha}_{mf}} U_{mf} \tag{2}$$

where c_0 is termed a distribution parameter or slope of velocity plot. The value of c_0 shows a weak dependence on particle size and operating pressure. Based on data for particle sizes of 650 μm and 2600 μm and at pressures of 101.3, 506.5 and 1013 kPa, Staub and Canada suggest a median value of 1.05 for c_0 when the gas velocity (U_{sg}/U_t) does not exceed 0.55. The value of $\bar{\alpha}$ at minimum fluidization ($\bar{\alpha}_{mf}$) was computed from a relation given by Leva, et al. [17]

$$\frac{0.005\,\psi_s{}^2 \bar{\alpha}_{mf}{}^3}{(1-\bar{\alpha}_{mf})} = 0.0007\,\mathrm{Re}_{mf}{}^{-0.0625} \text{ for } \mathrm{Re}_{mf} < 5.0 \tag{3}$$

In cases where Re_{mf} exceeds 5.0, a value of 0.40 was assigned to $\bar{\alpha}_{mf}$, in the absence of a more accurate relationship.

Vreedenberg's Correlation. Vreedenberg [3] proposed the following correlation

$$\left(\frac{\bar{h}D}{k_g}\right) = 0.66 \left(\frac{c_{ps}\mu_g}{k_g}\right)^{0.3} \left[\left(\frac{GD\rho_s}{\rho_g \mu_g}\right) \frac{(1-\bar{\alpha})}{\bar{\alpha}}\right]^{0.44} \text{ for } \mathrm{Re}_G < 2050 \tag{4}$$

$$\left(\frac{\bar{h}D}{k_g}\right) = 420 \left(\frac{c_{ps}\mu_g}{k_g}\right)^{0.3} \left[\left(\frac{GD\rho_s}{\rho_g \mu_g}\right) \left(\frac{\mu_g{}^2}{\bar{d}_p{}^3 \rho_s{}^2 g}\right)\right]^{0.3} \text{ for } \mathrm{Re}_G > 2550 \tag{5}$$

An arithmatic average of $\bar{h}$ calculated from these two equations is recommended for $2050 < \mathrm{Re}_G < 2550$.

In order to encompass all the data in one graph, the results are plotted in terms of the coordinates ($\mathrm{Nu}_{exptal}/\mathrm{Nu}_{Vreedenberg}$) and Re. Comparison of data with correlation is shown in Fig. 12. The predictions are unsatisfactory, with rather large deviations from the experimental data. Examination of numerical results show the disagreement to be especially pronounced for either small particles ($\bar{d}_p$ of 125 μm, 245 μm) or for large particles ($\bar{d}_p$ of 1580 μm).

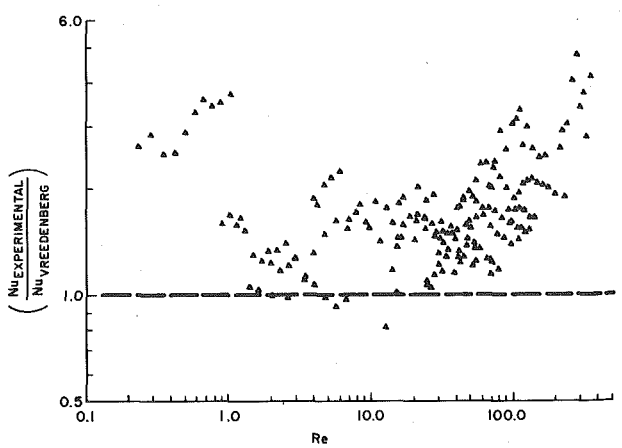

Fig. 12 Comparison of experimental data with Vreedenberg's correlation

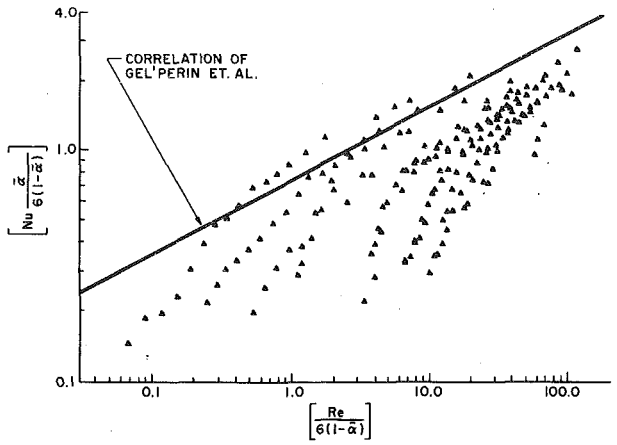

Fig. 13 Comparison of experimental data with the correlation of Gel'perin, et al

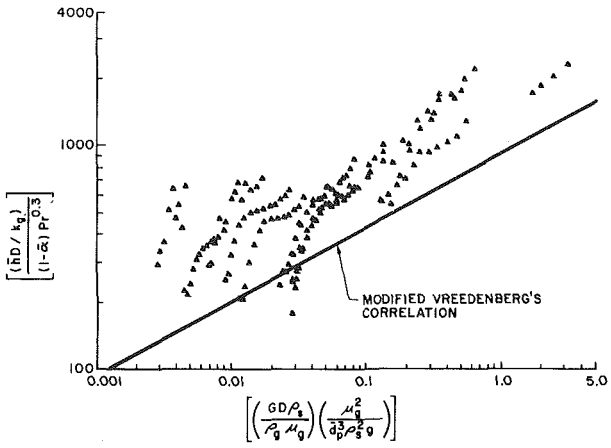

Fig. 14 Comparison of experimental data with modified Vreedenberg's correlation

Correlation of Gel'perin, et al. Gel'perin, et al. [11] proposed a correlation of the form

$$\left[\mathrm{Nu}\frac{\bar{\alpha}}{6(1-\bar{\alpha})}\right] = 0.73\left[\frac{\mathrm{Re}}{6(1-\bar{\alpha})}\right]^{0.32} \tag{6}$$

The experimental data plotted in terms of these two parameters are shown in Fig. 13. Again, the correlation turns out to be unsatisfactory, with a general tendency to overpredict the data. However, for large particles this correlation seems to be in better agreement with these data than the other two correlations.

Modified Vreedenberg's Correlation. Andeen and Glicksman [4] have suggested a modified form of Vreedenberg's correlation

$$\left[\frac{(\bar{h}D/k_g)}{(1-\bar{\alpha})\mathrm{Pr}^{0.3}}\right] = 900\left[\left(\frac{GD\rho_s}{\rho_g\mu_g}\right)\left(\frac{{\mu_g}^2}{{\bar{d}_p}^3{\rho_s}^2 g}\right)\right]^{0.326} \text{ for } \mathrm{Re}_G > 2550 \tag{7}$$

Fig. 14 compares the data with this correlation. Relatively better agreement is observed. Nevertheless, a consistent and significant underprediction exists.

Conclusions

Local heat transfer coefficients around horizontal tubes in fluidized beds were found to be significantly different for different circumferential positions, particularly at low to moderate flow rates. In addition, the magnitude of the local coefficients were affected by both particle size and system pressure, as well as by gas flow rate. Likewise, the circumferentially averaged coefficients were also affected by all these operating parameters, showing a generally increasing trend with decreasing particle size and increasing system pressure.

Some noticeable, though small, differences were found for heat transfer coefficients on tubes at different locations within a horizontal tube bundle. The results indicated a somewhat higher heat transfer coefficient for a tube within the bundle than for a tube in the bottom-row of the bundle. Coefficients found for a single tube, at comparable conditions, were bounded by the coefficients for these two positions.

Comparisons of measured average coefficients with published correlations showed poor agreement, with deviations up to several hundred percent.

The complex trend found for the variation of local heat transfer coefficients with variations in circumferential position, particle size, gas flow rate, and system pressure indicates a need for mechanistic modeling of the heat transfer process. The conventional approach of relating heat transfer coefficients and operating parameters by means of empirical correlations would seem to be inadequate.

Acknowledgment

The authors wish to express their appreciation for the help provided by associates and staff in the Mechanical Engineering and Mechanics Department of Lehigh University. The authors are grateful for the support of, and advise given to, this investigation by the Corporate Research and Development Center of General Electric Company.

References

1 Kunii, D. and Levenspiel, O., *Fluidization Engineering,* John Wiley and Sons, New York, 1969.

2 Botterill, J. S. M., *Fluid-Bed Heat Transfer,* Academic Press, New York, 1975.

3 Vreedenberg, H. A., "Heat Transfer Between a Fluidized Bed and a Horizontal Tube," *Chemical Engineering Science,* Vol. 9, 1958, p. 52.

4 Andeen, B. R. and Glicksman, L. R., "Heat Transfer to Horizontal Tubes in Shallow Fluidized Beds," ASME Paper No. 76-HT-67, ASME-AIChE Heat Transfer Conference, St. Louis, Mo., 1976.

5 Berg, B. V. and Baskakov, A. P., "Investigation of Local Heat Transfer Between a Fixed Horizontal Cylinder and a Fluidized Bed," *International Chemical Engineering,* Vol. 14, No. 3, 1974, p. 440.

6 Gel'perin, N. I., Einstein, V. G., Korotjanskaja, L. A., and Perevozchikova, J. P., *Teoreticheskie Osnovy Khimicheskoi Tekhnologii,* Vol. 2, 1968, p. 430.

7 Zabrodsky, S. S., *Hydrodynamics and Heat Transfer in Fluidized Beds,* MIT Press, Cambridge, MA, 1966.

8 Gel'perin, N. I. and Einstein, V. G., "Heat Transfer in Fluidized Beds," in *Fluidization,* edited by Davidson, J. F. and Harrison, D., Academic Press, London, 1971, p. 471.

9 Gutfinger, C. and Abuaf, N., "Heat Transfer in Fluidized Beds," *Advances in Heat Transfer,* Vol. 10, 1974, p. 167.

10 Saxena, S. C., Grewal, N. S., Gabor, J. D., Zabrodsky, S. S., and Galershtein, D. M., "Heat Transfer between a Gas Fluidized Bed and Immersed Tubes," *Advances in Heat Transfer,* Vol. 14, 1978, p. 149.

11 Ainshtein, V. G. and Gel'perin, N. I., "Heat Transfer Between a Fluidized Bed and a Surface," *International Chemical Engineering,* Vol. 6, No. 1, 1966, p. 67.

12 Chen, J. C., "Heat Transfer to Tubes in Fluidized Beds," ASME Paper 76-HT-75, *ASME-AIChE Heat Transfer Conference,* St. Louis, Mo., 1976.

13 Glass, D. H. and Harrison, D., "Flow Patterns Near a Solid Obstacle in a Fluidized Bed," *Chemical Engineering Science,* Vol. 19, 1964, p. 1001.

14 Botterill, J. S. M., George, J. S., and Besford, H., "Bubble Chains in Gas Fluidized Beds," *Chemical Engineering Progress Symposium Series,* Vol. 62, No. 62, 1966, p. 7.

15 Hager, W. R. and Thomson, W. J., "Bubble Behavior Around Immersed Tubes in a Fluidized Bed," *AIChE Symposium Series,* Vol. 69, No. 128, 1973, p. 68.

16 Staub, F. W. and Canada, G. S., "Effect of Tube Bank and Gas Density on Flow Behavior and Heat Transfer in Fluidized Beds," in *Fluidization,* ed. by Davidson, J. F. and Keairns, D. L., Cambridge University Press, London, 1978, p. 339.

17 Leva, M., Takashi, S., and Wen, C. Y., "Génie Chimique," Supplement to *Chimie et Industrie,* Vol. 75, No. 2, 1956, p. 33.

S. Mochizuki
Associate Professor,
Department of Mechanical Engineering,
Tokyo University of Agriculture and Technology,
Koganei, Tokyo, Japan

T. Shiratori
Graduate Student,
Institute of Space and Aeronautical Science,
University of Tokyo,
Komaba, Tokyo, Japan

Condensation Heat Transfer within a Circular Tube under Centrifugal Acceleration Field

Experimental and analytical investigation has been carried out to determine the effect of centrifugal acceleration on the condensation heat transfer within a circular tube. The experiments were conducted by condensing steam on the inside of a vertical tube rotating about an axis parallel to its own. A physical model was proposed consisting of a laminar filmwise condensation region and a bottom condensate flow region. The results of the present study indicate that the overall coefficient of heat transfer increases substantially with increasing centrifugal acceleration and it is slightly lower than the value for the case of condensation on the outside of circular tube under the same acceleration field.

Introduction

In recent years, consideration has been given to rotary condensers, mainly with the aim of reducing air-cooled condenser dimensions [1–3]. These rotary condensers consist of a rotating core of condenser tubes within which condensation takes place, and are characterized by the rotating condenser cores themselves acting as fans as well as heat exchangers. Due to the influence of strong centrifugal force on the formation of filmwise condensation region and bottom flow region, the condensation process in such condensers is believed to differ significantly from that in the ordinary types of condensers.

For the case of condensation on the outside of tubes, several attempts [4–10] have been made to utilize the centrifugal force on rotating systems, to achieve higher rates of condensation heat transfer. These investigations have demonstrated the effectiveness of centrifugal forces on improving the rate of condensation heat transfer.

However, for condensation on the inside of tubes, as in the previously mentioned condensers, little research has yet been made, resulting in the present lack of information for the performance estimation of such condensers.

In this investigation, a wide range of experiments was performed on a single circular condenser tube rotating about a parallel vertical axis; and a theoretical analysis, based on a mathematical model including bottom flow, has been made.

Experimental Apparatus and Conditions

As shown in Fig. 1, steam generated by boiler A (0.76 m^3 in volume capacity) is led to the test section B with its pressure controlled by regulating valve C. Air, a noncondensable gas, isolated from water within the boiler is removed prior to the experiment by opening valve D for about half an hour, and no fresh water is supplied to the boiler during experiments. The flow rate of cooling water is controlled by valve E and rotameter F. The cooling water temperature is then adjusted by heat-exchangers G and H before being supplied to the test section.

The rotating body is supported by bearings A and B, and is driven by a variable speed motor through shaft C (Fig. 2). Steam entering from top D is led through a mechanical-sealed hollow rotating shaft, a crank bend and honeycomb E for removing flow distortion, to the inlet bell-mouth. Here, trap F is located to remove any condensate that forms prior to this point, letting only pure saturated steam into the condenser tube. The entering steam is completely condensed within the condenser tube and the condensate is freely discharged from the end of tube to separator G. This separator has a three-dimensionally bent tube designed to remain filled with condensate under both stationary and rotating conditions. Thus, only the condensate is released into the annular collector H. The test section consists of a copper tube, I, and heat resistant PVC tube, J, which form a double concentric tube. The tubes are set parallel to the vertical rotating axis (radius of rotation, $R = 0.1$ m). Cooling water flows up-

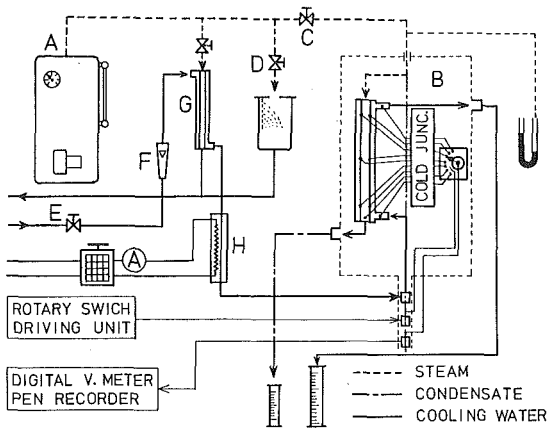

Fig. 1 A schematic diagram of the experimental set-up

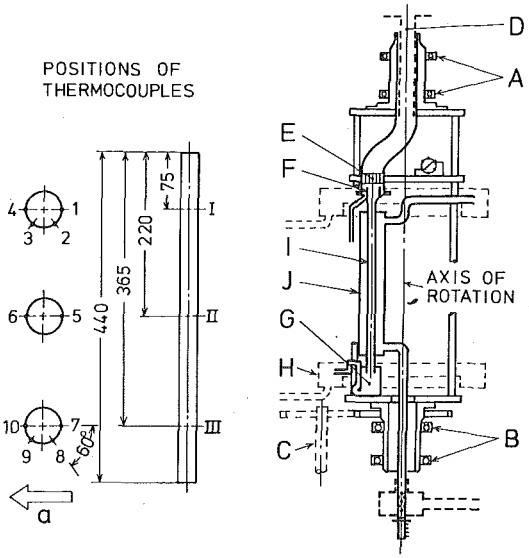

Fig. 2 Rotating section of experimental apparatus

Contributed by the Heat Transfer Division for publication in the JOURNAL OF HEAT TRANSFER. Manuscript received by the Heat Transfer Division January 26, 1979.

Table 1 Condenser tube dimensions and experimental conditions

		1	2	3
Tube Inner Diameter, Length	d, ℓ m	0.010, 0.440	0.0193, 0.440	0.031, 0.452
ℓ/d		44.0	22.8	14.6
Acceleration Ratio	G	0–18.6	0–23.8	0–25.6
Inlet Steam Pressure	KPa	102–104	102–103	102–104
Inlet Steam Velocity	V m/s	27–56	5–20	5–10
$T_s - T_w$	deg K	14.5–29.1	4.1–28.1	4.5–26.1
Pr/H		73–42	250–43	220–45
Ga		$(9.1–7.2) \times 10^7$	$(7.5–5.2) \times 10^8$	$(3.1–2.2) \times 10^9$
Cooling Water Flow Rate	W_c kg/s	0.08–0.13	0.05–0.14	0.07–0.15
Cooling Water Inlet Temperature	T_c K	286–288	288–340	288–338
Overall Heat Transfer Coef.	h_M W/m^{2}K	$(8.6–25.6) \times 10^3$	$(6.7–23.3) \times 10^3$	$(6.2–20.9) \times 10^3$

wards in the annular portion between the two tubes. On the interior surface of the condenser tube, ten sheathed type C-A thermocouples of 0.5 mm OD are located at positions shown in Fig. 2.

Taking the mean value of average wall temperature for each of sections I, II and III as the representative surface temperature, T_w, of the tube, the overall heat transfer coefficient, h_M, is found from

$$h_M = q/(T_s - T_w) \tag{1}$$

where q is the mean heat flux obtained from the measured condensate flow rate.

Table 1 shows the dimensions of the three types of condenser tubes and the range of parameters for which the present experiments were performed.

Experimental Results and Discussion

Fig. 3 shows the effect of centrifugal acceleration of the nondimensional overall heat transfer coefficient. Its vertical scale is taken as the ratio of the overall Nusselt number, Nu_M, obtained from experiment to the theoretical value of Nusselt number, Nu_g, for filmwise condensation in a stationary vertical tube:

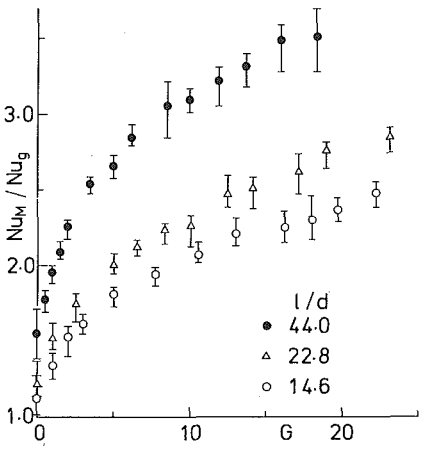

Fig. 3 Effect of centrifugal acceleration on the overall Nusselt number

$$Nu_g = hd/\lambda = 0.943(Ga\,Pr/H)^{1/4} \cdot (d/\ell)^{1/4} \tag{2}$$

Property values at $T = T_w + 0.3\,(T_s - T_w)$ are adopted [11]. From this figure it can be seen that the overall Nusselt number increases definitely with the increase of centrifugal force for all three types of tubes, and that the larger the tube length to diameter ratio, the more apparent this effect becomes.

In order to examine the effect of vapor shear force on the coefficient of heat transfer, the data for stationary conditions were obtained for various inlet steam Reynolds number [12]. From these results and Fig. 3, it was concluded that, within the range of present experiment, the vapor shear force has its effect only at low rotational speeds, and the effect of centrifugal force is dominant at comparatively large rotational speeds.

Fig. 4 shows typical examples of the variation of circumferential wall temperature distribution in section III. For both (a) ID = 10 mm and (b) ID = 31 mm, although the temperatures are almost uniformly distributed for the stationary condition ($G = 0$), the temperature in the vicinity of $\phi = 180$ deg declines sharply as centrifugal acceleration is increased. The same tendency was observed for sections I and II, although the magnitudes of temperature drop differed. This observation is considered to support the view that when there exists a large

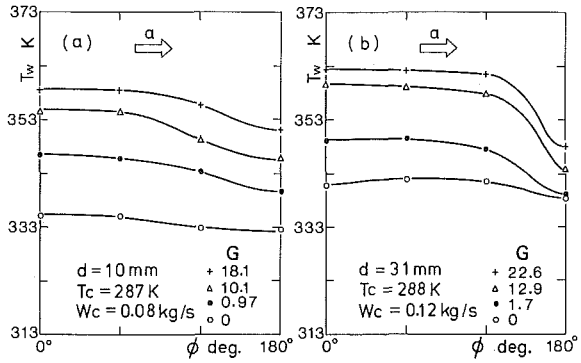

Fig. 4 Typical examples of the variation of circumferential wall temperature distribution in section III (see Fig. 2) for tubes of (*a*) ID = 10 mm and (*b*) ID = 31 mm

Nomenclature

a = centrifugal acceleration at tube axis
A = cross-sectional area of bottom flow
c_p = specific heat of condensate
d = tube diameter
d_h = hydraulic diameter = $4A/\theta d$
f = Fanning's friction factor
F = force on an element of bottom flow
h = heat transfer coefficient
K = factor of f defined in equation (16)
ℓ = tube length
L = latent heat of condensation
Q = volumetric flow rate of bottom flow
r_0 = tube radius
R = radius of rotation
T_s = temperature of saturated vapor
T_w = tube wall temperature
u = local circumferential velocity component of condensate film
U = mean velocity of bottom flow
v = local axial velocity component of condensate film
x = distance along tube axis
z = distance normal to tube interior surface
β = momentum correction factor
δ = thickness of condensate film
λ, ρ, ν = heat conductivity, density, kinematic viscosity of condensate
θ = angle of bottom flow level
ϕ = co-ordinate in circumferential direction
G = acceleration ratio = a/g
$Ga = gd^3/\nu^2$
$H = c_p(T_s - T_w)/L$
Nu = local Nusselt number = $hd/\lambda = \{2Ga\,Pr\,G/(3HZ)\}^{1/4}$
Pr = Prandtl number = $\rho\nu c_p/\lambda$
Re = Reynolds number = $Ud_h/\nu = (Ga/2)^{1/2}(\Gamma/\theta)$
X = dimensionless axial distance = Gx/r_0
Z = dimensionless condensate film thickness = $\{2Ga\,Pr\,G/(3H)\}(\delta/d)^4$

centrifugal force, the condensate film flows along the circumferential direction, and collects at $\phi = 180$ deg, which corresponds to bottom of a tube when viewed along the direction of centrifugal acceleration, resulting in a downward axial flow or bottom flow in this region.

Theoretical Analysis

For condensation within a vertical tube rotating about a parallel axis, forces acting on the condensate film formed over the tube surface are the gravitational force, the centrifugal force and, when the steam flow velocity is large, shear force along the vapor-liquid interface. Schematically, condensate with the film flows along a route over the tube interior surface as shown by the broken line in Fig. 5; a bottom flow represented by the hatched area of the figure forms as a result. This bottom flow region, in general, blocks most of heat flow across itself, and the tube surface covered by it becomes ineffective as a condensation heat transfer surface [13–15]. Therefore, when evaluating the overall heat transfer coefficient of condensation for the whole condenser tube, it is necessary to take into account not only the flow of liquid film over the tube surface, but also the behavior of the bottom flow.

Condensate Film Flow. Analysis is made under assumptions similar to those of Nusselt's well-known basic condensation theory [16] and an assumption that the effect of vapor shear stress is negligible at the vapor-liquid interface, based on the observation of the previous section. On the condensate film act gravitational acceleration, g, in the x-direction and the circumferential component of centrifugal acceleration, $a \sin \phi$, in the ϕ-direction ($a \sin \phi$ can be found from geometrical consideration [5]). The momentum equations for the condensate film become:

$$x: \nu \frac{\partial^2 v}{\partial z^2} + g = 0 \tag{3}$$

$$\phi: \nu \frac{\partial^2 u}{\partial z^2} + a \sin \phi = 0 \tag{4}$$

with the boundary conditions:

$$u = v = 0 \qquad \text{at tube wall, } z = 0$$

$$\partial u/\partial z = 0,\ \partial v/\partial z = 0, \text{ at vapor-liquid interface, } z = \delta$$

Considering the energy balance for an element of volume, $\delta r_0 dx d\phi$, we obtain:

$$\frac{1}{r_0}\frac{\partial}{\partial \phi}\left(\int_0^\delta u dz\right) + \frac{\partial}{\partial x}\left(\int_0^\delta v dz\right) = \frac{\lambda(T_s - T_w)}{\rho \delta L} \tag{5}$$

By substituting solutions u, v of equations (3) and (4) into equation (5) and introducing the following nondimensional variables:

$$X = Gx/r_0 \ (G = a/g)$$

$$Z = \frac{\rho a L \delta^4}{3 r_0 \nu \lambda (T_s - T_w)} = \left(\frac{2Ga\mathrm{Pr}G}{3H}\right)\left(\frac{\delta}{d}\right)^4$$

an equation for the nondimensional film thickness, Z, is obtained:

$$\frac{\partial Z}{\partial X} + \sin \phi \frac{\partial Z}{\partial \phi} = \frac{4}{3}(1 - Z \cos \phi) \tag{6}$$

The boundary conditions can be found from the fact that the film thickness, δ, is zero for $x = 0$ and that it is smooth and continuous for $\phi = 0$, as follows:

$$Z = 0 \quad \text{for } X = 0; \quad \partial Z/\partial \phi = 0 \quad \text{for } \phi = 0$$

The differential equation (6) is of the same form as the equation for nondimensional condensate film thickness under condensation on the outside of an inclined circular cylinder derived by Hassan and Jakob [17], although Z is defined differently. In equation (6), $\partial Z/\partial X = 0$ as $X \to \infty$, and according to Hassan and Jakob's calculations, it is possible to let $\partial Z/\partial X \fallingdotseq 0$ for $X > 3.2$. In this case, Z can easily be obtained as a function of ϕ alone as follows:

$$Z = \frac{4}{3(\sin \phi)^{4/3}} \int_0^\phi (\sin \phi)^{1/3} d\phi \tag{7}$$

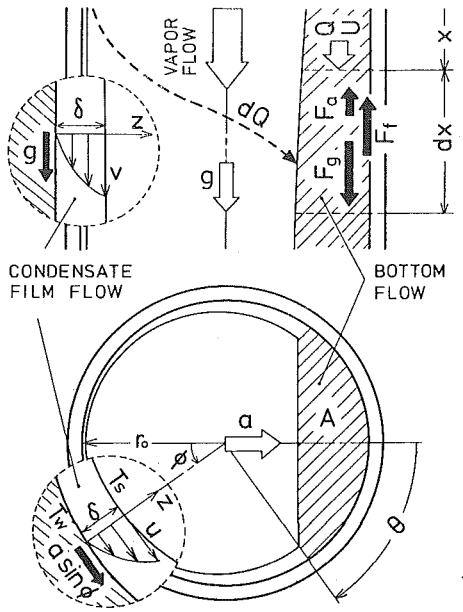

Fig. 5 Analytical model and geometry

The length, x_{st}, such that $X = 3.2$ is extremely small for large acceleration ratio (e.g. $x_{st} = 0.16d$ for $G = 10$), and is negligible compared to the whole length of the actual condenser tube. Hence, in subsequent calculations, equation (7) will be adopted as a good approximate solution of equation (6).

Bottom Flow. We consider the equation of momentum for an element of bottom flow over an infinitesimal length, dx, as shown in Fig. 5. Assuming that the forces in x-direction acting on this element are body force due to gravity, F_g, the viscous friction force at the wall, F_f, and the force due to difference in water pressure over dx resulting from the difference in liquid level of bottom flow under centrifugal acceleration, F_a, the following equation may be written:

$$\beta \frac{d}{dx}(\rho Q U)dx = F_g + F_f + F_a \tag{8}$$

where β is a momentum correction factor to account for the nonuniform flow velocity distribution in bottom flow. Each term on equation (8) may be expressed as follows:

$$\beta \frac{d}{dx}(\rho Q U)dx = \beta\rho\{2Q(dQ/dx)/A - Q^2(dA/d\theta)(d\theta/dx)/A^2\}dx \tag{9}$$

$$F_g = \rho g A dx \tag{10}$$

$$F_f = -\tau_w \theta d dx = -(f\rho Q^2 \theta d/8A^2)dx \tag{11}$$

$$F_a = -\rho a A d \sin \theta (d\theta/dx)dx/2 \tag{12}$$

In equation (11), f is Fanning's friction factor which will be discussed later. From equations (8–12) and introducing the following nondimensional variables:

$$\Psi = A/\pi r_0^2 = (2\theta - \sin 2\theta)/2\pi, \ \Gamma = Q/(g r_0^5)^{1/2}$$

we obtain a differential equation for level angle, θ, of bottom flow:

$$\frac{d\theta}{dX} = \frac{8\pi\beta G \Psi \Gamma (d\Gamma/dX) - 4\pi^3 \Psi^3 + f\Gamma^2\theta}{8\beta G \Gamma^2 \sin^2 \theta - 4\pi^3 G^2 \Psi^3 \sin \theta} \tag{13}$$

Meanwhile, the increase in flow rate of the bottom flow must be a result of condensate inflow from filmwise condensation region. This condition gives:

$$\Gamma = \frac{4 \sin \theta (2Ga)^{1/2}}{3}\left(\frac{3H}{2Ga\mathrm{Pr}G}\right)^{3/4} \int_0^X Z_\theta^{3/4} dX \tag{14}$$

where subscript θ denotes values at $\phi = \pi - \theta$ and Z_θ is a quantity

obtainable from equation (7).

Friction Factor. Friction factor, f, is estimated for each of the three flow regions classified by the bottom flow Reynolds number, Re.

In the laminar flow region (Re $\leq$ 2300), f is assumed to be approximated by the value for a flow through a semi-elliptical cross-section open channel having equal cross-sectional area, A, and wetted perimeter, P. These geometrical relations are

$$\left.\begin{aligned} A &= d^2(2\theta - \sin 2\theta)/8 = \pi bc/2 \\ P &= \theta d = 2b \int_0^{\pi/2} \left[1 - \frac{b^2 - c^2}{b^2} \sin^2 t\right]^{1/2} dt \end{aligned}\right\} \quad (15)$$

Friction factor for flow through a semi-elliptical cross-section channel has been known as:

$$f = K/\mathrm{Re},\ K = 8{d_h}^2(b^2 + c^2)/b^2c^2 \quad (16)$$

Thus, from equations (15) and (16), f can be determined with respect to θ as shown in Fig. 6.

In the turbulent flow region (Re $\geq$ 3000), as it has been experimentally found that f is not significantly affected by flow cross-section [18], Prandtl-Kármán's relation:

$$1/f^{1/2} = 2 \log_{10} (\mathrm{Re} f^{1/2}) - 0.8 \quad (17)$$

may be applied to this investigation.

In the transitional flow region (2300 < Re < 3000), an equation of linear interpolation between the values of equation (16) for Re = 2300, f_ℓ, and of equation (17) for Re = 3000, f_t, is used.

$$f = (f_t - f_\ell)(\mathrm{Re} - 2300)/700 + f_\ell \quad (18)$$

Overall Nusselt Number. As it can be assumed that the tube surface covered by bottom flow loses its effectiveness as heat transfer surface [13], the mean Nusselt number, Nu_m, over the circumference and the overall Nusselt number, Nu_M, for the whole condenser tube become, respectively:

$$\mathrm{Nu}_m = \frac{1}{\pi} \int_0^{\pi-\theta} \mathrm{Nu} d\phi = \frac{1}{\pi} \int_0^{\pi-\theta} \left(\frac{2Ga\,\mathrm{Pr}G}{3HZ}\right)^{1/4} d\phi \quad (19)$$

$$\mathrm{Nu}_M = \frac{1}{\ell} \int_0^{\ell} \mathrm{Nu}_m dx \quad (20)$$

Initial Values for Equation (13) and Procedure of Numerical Calculation. Differential equation (13) cannot be evaluated at the starting point ($X = 0$) of condensation. Hence, the following method has been adopted as a recommended method for obtaining the initial values for equation (13). Since no clear bottom flow region distinguishable from condensate film is formed and flow rate is still very small in the small interval, $X = 0 \sim X_0$, the flow in the bottom region at X_0 is considered to be governed mainly by gravitational force and friction force. Therefore we obtain $F_g + F_f = 0$ or the following equation:

$$f\Gamma_0^2\theta_0 = (2\theta_0 - \sin 2\theta_0)^3/2 \quad (21)$$

determining the initial value, θ_0, for equation (13). Γ_0 is the initial value of bottom flow rate calculated from equation (14), assuming no bottom flow in the interval $X = 0 \sim X_0$.

The procedure to be taken to evaluate the flow level angle for $X > X_0$ is as follows: Initial values, Γ_0 and θ_0, are evaluated from equations (14) and (21), respectively. A suitable tube length increment, ΔX, is selected and equation (14) is used to calculate the change, $\Delta\Gamma$, in Γ. Then, selecting a suitable equation for f from equations (16–18) depending on Re, equation (13) is solved to obtain the change, $\Delta\theta$, in θ in the increment ΔX by finite difference method. Thus the calculations with equations (13) and (14) are repeated for every increment until the given length of condenser tube is reached.

Results of Calculations and Comparisons between Experimental and Theoretical Results

Calculations were conducted for the typical combinations of parameters, G, Ga, Pr/H and ℓ/d corresponding to the conditions of present experiment. The value of β is taken to be 4/3 for Re $\leq$ 2300, and 1.05 for Re $\geq$ 3000 by referring to [19]. For 2300 < Re < 3000, an interpolated value of β is used. According to the results of calculations performed for various values of $X_0(X_0 \fallingdotseq 4 \sim 20)$, little effect on flow-level angle or overall Nusselt number is seen with the exception of the region very close to X_0.

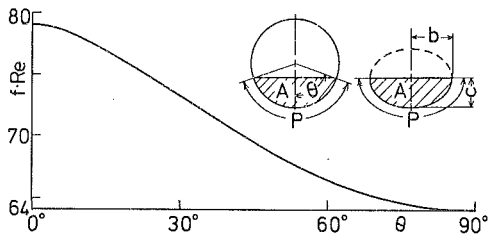

Fig. 6 Friction factor in laminar flow region

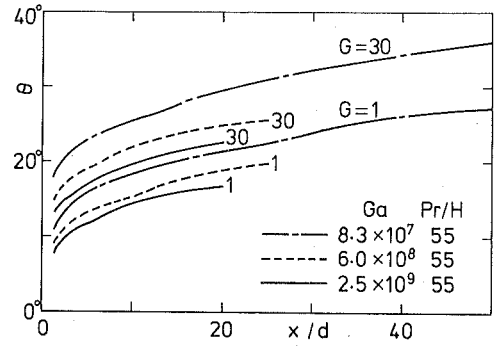

Fig. 7 Flow-level angle of bottom flow

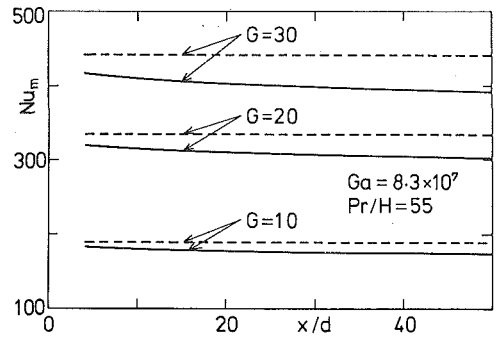

Fig. 8 Mean Nusselt number over circumference

Some typical results of the flow-level angle are shown in Fig. 7. This figure shows that, for a given condenser operating condition, flow-level angle increases in the axial direction and that, for a given axial position, flow-level angle increases as acceleration ratio increases, and Ga decreases. It may also be noted that an apparent discontinuity of slope in the figure indicates the transition from laminar to turbulent flow in the bottom condensate.

An example of the variation along tube axis of the mean Nusselt number over the circumference, Nu_m, is shown in Fig. 8. The broken lines represent cases where all of the tube surface remains effective of filmwise condensation, that is, for the values obtained from equation (19) letting $\theta = 0$. It can be seen from this figure that Nu_m is greater for large values of acceleration ratio, G, and that Nu_m declines slowly along the axial direction for all acceleration ratios. This decline is evidently due to the existence of bottom flow and its tendency could easily be expected from Fig. 7.

Fig. 9 shows the ratio of Nu_M, the overall Nusselt number for the whole condenser tube with bottom flow over Nu_0, without bottom flow, as a function of acceleration ratio. This figure shows that the effect of bottom flow on coefficient of heat transfer becomes more

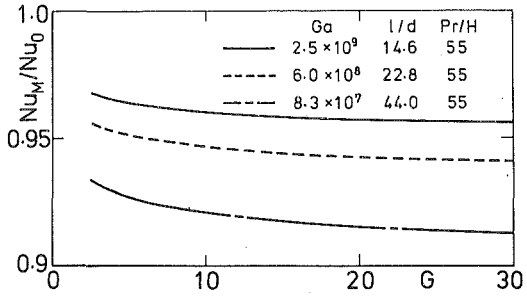

Fig. 9 Ratio of the overall Nusselt number for the whole condenser tube with bottom flow to that without bottom flow, as a function of acceleration ratio

apparent for larger G but the resulting drop in Nu_M is less than ten percent.

Before comparing experimental results with theoretical results, it may be mentioned here that, in obtaining the overall coefficient of heat transfer by experiment, it is customary to use the mean of the measured tube wall temperatures as the representative temperature of the heat transfer surface when the wall temperature is not uniform [20, 21]. The experimental results in Fig. 3 are obtained according to this practice. However, in this experiment as centrifugal acceleration becomes large, a bottom flow forms which is very heat resistant. The portion of the tube wall covered by bottom flow loses its role as the surface of heat transfer and its temperature drops significantly as can be seen in Fig. 4. Therefore, it seems more reasonable to evaluate the representative temperature of the heat transfer surface by excluding the temperatures of this region which does not contribute to heat transfer when comparing the results against theoretical values obtained for a uniform wall temperature.

Based on the above consideration, the experimental results for $G > 1$ are revaluated excluding the temperatures measured at three points for which $\phi = 180$ deg. The results are presented in Fig. 10. The experimental and theoretical values show a good agreement, indicating the appropriateness of the treatment of wall temperature described above. From this figure, it can be safely said that, for a given condenser tube, the overall coefficient of heat transfer increases definitely as the rotational speed increases. However, because of the scatter in experimental values, the drop in Nu_M suggested by theoretical analysis (the difference between the values indicated by a broken line and solid lines, where the broken line is obtained assuming all of the tube surface remains effective of filmwise condensation), due to the existence of bottom flow, cannot be clearly shown by experimental results. The experimental results for $\ell/d = 44.0$, yield larger values for small G's, but this difference is seen to diminish as G increases. This is thought to be caused by the effect of vapor shear being present at relatively small G's, and by the effect of centrifugal acceleration becoming dominant at higher G's. The experimental results of condensation heat transfer on the outside of a tube rotating about a parallel axis [5] are also plotted in Fig. 10. These data show a similar tendency of dependence on centrifugal acceleration but the values are much higher than the present results, which seems to be attributed to the surface waves in the condensate film [5].

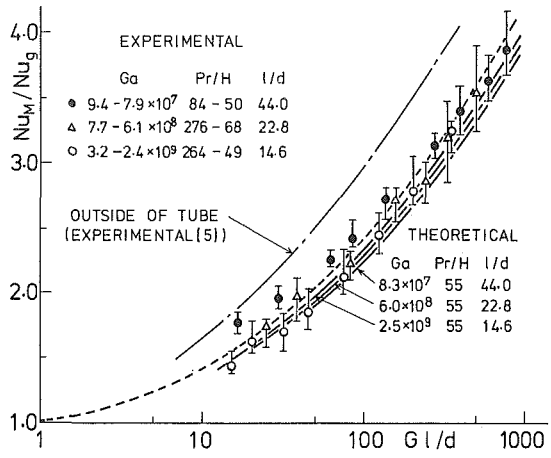

Fig. 10 Comparison of experimental data and theoretical results

Conclusions

1 A significant improvement in the coefficient of condensation heat transfer on the inside of tubes can be expected when the condenser tubes are rotated about an axis parallel to themselves.

2 Flow-level angle of bottom condensate increases in the axial direction and it also increases as acceleration ratio increases and as Ga decreases.

3 Due to the existence of bottom flow, the heat transfer coefficient is slightly lower than the value for a case of condensation of the outside of the tube under the same acceleration field.

Acknowledgments

Part of this study has been made under financial aid from the Japan Automobile Research Institute and Ministry of Education of Japan. Their aid is gratefully acknowledged.

References

1 Doerner, W. A., and Dietz, R. J., "A Rankine Cycle Engine with Rotary Heat Exchangers," SAE Paper, No. 720053, Jan., 1972.

2 Nikolaus, L., "Rotary Heat Exchangers," U.S. Patent 3424234, Jan., 1969.

3 Mochizuki, S., "A Fundamental Research on Rotary Heat Exchangers," (in Japanese), *Proceedings of The Japan Society of Mechanical Engineers*, Autumn Annual Meeting, No. 780-16, 1978, pp. 183–185.

4 Yamanaka, N., "On the Revolving Condenser Tube, its Temperature Distribution and the Coefficients of Heat Transfer," (in Japanese), *Transactions of The Japan Society of Mechanical Engineers*, Vol. 7, No. 26, Feb., pp. II-12–II-27, No. 27, May, pp. II-1–II-13, No. 28, Aug., pp. II-16–II-25, 1941.

5 Suryanarayana, N. V., "Condensation Heat Transfer Under High Gravity Condition," *Proceedings of 5th International Heat Transfer Conference*, Vol. III, Sept., 1974, pp. 279–285.

6 Yeh, L., "The Effect of Surface Speed and Steam Pressure Upon the Transfer of Heat to a Rotating Cylinder," PhD Thesis, Department of Mechanical Engineering, Imperial College of Science and Technology, London, 1953.

7 Singer, R. M., and Preckshat, G. W., "The Condensation of Vapor on a Horizontal Rotating Cylinder," *Proceedings of the Heat Transfer and Fluid Mechanics Institute*, No. 14, 1963, pp. 205.

8 Hoyle, R., and Mathews, D. H., "The Effect of Diameter Size and Speed of Rotation on the Heat Transfer from Steam to Cooled Cylinder," *International Journal of Heat and Mass Transfer*, Vol. 7, 1964, pp. 1223.

9 Nicol, A. A., and Gacesa, M., "Condensation of Steam on a Rotating Vertical Cylinder," ASME JOURNAL OF HEAT TRANSFER, Vol. 92, No. 1, Feb., 1970, pp. 144–152.

10 Sparrow, E. M., and Hartnett, J. P., "Condensation on a Rotating Cone," ASME JOURNAL OF HEAT TRANSFER, Vol. 83, No. 1, Feb., 1961, pp. 101–102.

11 Minkowycz, W. J., and Sparrow, E. M., "Condensation Heat Transfer in the Presence of Noncondensables, Interfacial Resistance, Superheating, Variable Properties and Diffusion," *International Journal of Heat and Mass Transfer*, Vol. 9, 1966, pp. 1125–1144.

12 Shiratori, T., "Condensation Heat Transfer Within a Circular Tube under Centrifugal Acceleration Field," (in Japanese), unpublished MAS. Thesis, Tokyo University of Agriculture and Technology, Tokyo, 1976.

13 Chaddock, J. B., "Film Condensation of Vapor in a Horizontal Tube," *Refrigerating Engineering*, Vol. 65, Apr., 1957, pp. 36–41 and 91–95.

14 Chato, J. C., "Laminar Condensation Inside Horizontal and Inclined Tubes," *ASHRAE, Journal*, Vol. 4, Feb., 1962, pp. 52–60.

15 Rufer, C. E., and Kezios, S. P., "Analysis of Two-Phase One-Component Stratified Flow with Condensation," ASME JOURNAL OF HEAT TRANSFER, Vol. 88, No, 3, Aug., 1966, pp. 265–274.

16 Jakob, M., *Heat Transfer*, John Wiley & Sons, 1949, Vol. 1, pp. 658–680.

17 Hassan, K. E. , and Jakob, M., "Laminar Film Condensation of Pure Saturated Vapor on Inclined Circular Cylinders," *Trans. ASME*, Vol. 80, No. 1, May, 1958, pp. 887–894.

18 Straub, L. G., Silberman, E., and Nelson, H. C., "Open-Channel Flow at Small Reynolds Numbers," *Transactions of the American Society of Civil Engineers*, Paper No. 2935, 1958, pp. 685–714.

19 Chow, V. E., *Open-Channel Hydraulics*, McGraw-Hill, 1959, pp. 27.

20 Fujii, T., et al., "Heat Transfer and Flow Resistance in Condensation of Low Pressure Steam Flowing through Tube Banks," *International Journal of Heat and Mass Transfer*, Vol. 15, 1972, pp. 247–260.

21 Kutateladze, S. S., *Problems of Heat Transfer and Hydraulics of Two-Phase Media*, 1969, Pergamon, Oxford.

Thermal Conductivity of Methane at Atmospheric Pressure in the Temperature Range of 360-1275 K

R. Afshar
A. C. Cogley
S. C. Saxena

Department of Energy Engineering,
University of Illinois at Chicago Circle,
Chicago, IL 60680

Thermal conductivity of a research grade pure methane sample is measured in a hot-wire column instrument in the temperature range 360-1275 K from heat transfer rate data taken in the continuum region. The results are correlated by a quadratic polynomial in temperature viz., $k(T) = -23.35 + 0.1698T + 1.893 \times 10^{-5}T^2$. Here k is in mW/m-K and T in K. The experimental data are compared with the available conductivity values and with the predictions of kinetic theories of polyatomic gases in conjunction with realistic intermolecular potentials. The conductivity data are also employed to compute the diffusion coefficient for vibrational energy. The effect of gaseous radiative transfer on the measured thermal conductivity of methane is estimated by comparing the conductivity coefficients of a slab of gas with and without the presence of the absorption bands.

Introduction

Among alkanes, methane is thermally stable over the widest temperature range though its thermal conductivity is not sufficiently investigated at elevated temperatures. Touloukian, et al. [1] found a large scatter in the available thermal conductivity data of methane and preferred the data of Geier and Schäfer [2] as the basis for recommending the conductivity values above 500 K. The difficulty in measurement primarily arises due to the thermal dissociation of alkanes in the presence of metallic surfaces. Even in the absence of metallic surfaces, thermal decomposition of alkanes is detectable at about 750–1050 K. At about 1270 K, methane is expected to be in equilibrium state with carbon and hydrogen as its decomposition products. However, in actual practice, this equilibrium is never reached and the results of pyrolytic decomposition are hydrogen and free methylene [3]. Winters [4] has investigated in detail the dissociative chemisorption of methane on tungsten. In the present work, thermal conductivity of methane is determined in the temperature range 360–1275 K by steady-state heat transfer measurements at pressures of 39.4 and 94.4 kN/m^2. The conductivity values suggest that the thermal dissociation effect is appreciable at 1000 K and above. The values are therefore considered reliable for methane in the temperature range 360–1000 K only. The present experimental values are in satisfactory agreement with the earlier data of Geier and Schäfer [2] above 500 K but a more recent measurement of Le Neindre, et al. [5] up to a maximum temperature of 723 K are systematically higher than our present results. Thus, these measurements attempt to resolve the discrepancy in the two sets of hitherto available values at high temperatures which differ by as much as five percent. The experimental data are also examined on the basis of kinetic theory of polyatomic gases in conjunction with reasonable choices for intermolecular potentials.

Experimentation

The improved heat transfer column employed for thermal conductivity measurements is described in detail by Jody, et al. [6]. The column was equipped with a 0.3048 mm tungsten wire having a length of 58 cm. The methane gas was supplied by Matheson Gas Products and was of research grade purity. The steady-state heat transfer measurements were taken for test gas pressures of 39.4 and 94.4 kN/m^2. The details of the experimental procedures and of data analysis are similar to those described earlier by Chen and Saxena [7]. The smallness of the convective heat transfer was established by performing calculations on the approximate theoretical expression suggested by Chen and Saxena [8] which revealed that only 0.4 percent of the total energy fed to the wire was transported by molecular convection. The small values of the Knudsen number (0.0003 to 0.002) for this system and operating conditions was interpreted as indicating the negligible contribution of temperature-jump effect. The magnitudes of the small corrections to the conductivity values due to the small temperature drop across the glass column wall, change in the wire diameter due to changes in its length, and fluctuations in the cold wall temperature along its length were calculated. The maximum magnitude of the total correction was 0.85 percent.

The conductivity values thus obtained for the two pressure levels are shown plotted in Fig. 1. The two sets of conductivity values are in good agreement with each other up to about 1000 K but differ from each other above this temperature. This difference is attributed to the onset of appreciable dissociation of methane which will be pressure dependent and therefore the conductivity values will differ because they will refer to mixtures of different compositions. It may be noted that this effect will get particularly amplified in the column instrument due to the cascading effect of thermal diffusion separation. It will therefore follow that such a conductivity apparatus will be particularly sensitive to the detection of onset and degree of dissociation. The experimental data were, consequently, regarded as conclusive only in the temperature range of 360 to 1000 K. The two sets of conductivity values, k, in this temperature range were correlated by the following quadratic polynomial in temperature, T,

$$k = B_0(1 + B_1T + B_2T^2) \tag{1}$$

where B_0, B_1 and B_2 are equal to -23.35 mW/m-K, -7.272×10^{-3}/K, and -8.107×10^{-7}/K^2, respectively. Here k is in mW/m-K and T is in degrees Kelvin.

The above relation of equation (1) for the thermal conductivity of methane reproduces the actual data within an average and maximum absolute deviation of 1.1 and 2.8 percent, respectively. The two data sets are shown compared with the predicted values on the basis of the relation of equation (1) in Fig. 2. Also shown in this figure are the estimates of the random errors obtained according to procedure described by Chen and Saxena [7] and Chen, et al. [9]. It will be noticed from Fig. 2 that the deviations of the two sets of data from each other do not suggest any systematic trend in as much as the low pressure conductivity values which are greater than the high pressure conductivity values by about one to two percent, become more or less identical at high temperatures above about 700 K. Thus, the difference in the two sets cannot be attributed to pure dissociation effect of any appreciable magnitude. Further, the disagreement between the two sets of values and their deviation from the predicted values based on equation (1) is always within the estimated uncertainties of the experiments.

Contributed by the Heat Transfer Division for publication in the JOURNAL OF HEAT TRANSFER. Manuscript received at ASME Headquarters July 7, 1978.

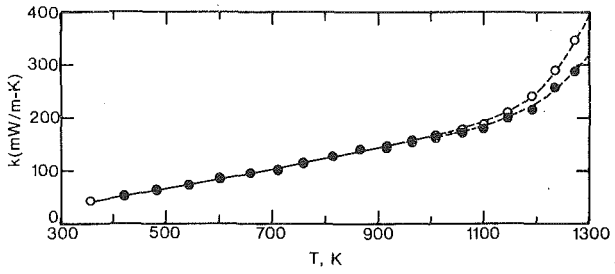

Fig. 1 Experimental thermal conductivity data as a function of temperature. ○ 39.4 kN/m² and ● 94.4 kN/m²

Discussion

The experimental data of Le Neindre, et al. [5], Geier and Schäfer [2] and the recommended values of Touloukian, et al. [1] are compared with the present measurements as given by equation (1) in Fig. 2. The positive deviations in the figure imply that the present values are greater than the comparison set. Touloukian, et al. [1] values are estimated to be uncertain by about 6 percent and their scatter from present results is always less than 1.8 percent. The deviations are both positive and negative and are always within the estimated errors of present measurements. We, therefore, conclude that the present results and recommended values [1] are in good agreement with each other. On the other hand Le Neindre, et al. [5] values are always greater than our present values, and the deviations oscillate between 2.3 to 5.2 percent and are outside the range of estimated errors of our measurements. Le Neindre, et al. estimated a precision of 1.5 percent in their experimental data. Our present results are also in good agreement with those of Geier and Schäfer [2] and a direct comparison is displayed in Fig. 2, curve 2. Both sets of data are, however, appreciably smaller than the data set of Le Neindre, et al. [5]. One possible source of this disagreement may be the presence of convection in Le Neindre, et al. data, though based on Rayleigh number criterion they [5] have discarded this possibility. The present work supports the earlier work of Geier and Schäfer [2] over that of Le Neindre, et al. [5] and values based on equation (1) are recommended for engineering calculations. Hanley, et al. [10] have developed a tabulated set of recommended thermal conductivity of methane in the maximum temperature and pressure ranges of 95–500 K and 0.1 and 75 MPa on the basis of available data, kinetic theory and intermolecular potential. The estimated uncertainty of the recommended values is approximately 5 percent. Their values given at the lowest pressure of 0.1 MPa are shown in Fig. 2 compared with the predictions of equation (1) in the temperature range 420–500 K.

In Fig. 3, we have compared the present results with the predictions of various theories and intermolecular potentials for methane, whose molecules are regarded as quasi-spherical. Positive deviations in Fig. 3 mean that the experimental values are greater than the calculated values. The thermal conductivity, k, viscosity, η, molecular weight, M, and molar heat capacity, C_v, are related as:

$$Mk = f\eta C_v. \tag{2}$$

The values for η and C_v as given by Touloukian, et al. [11] and Svehla

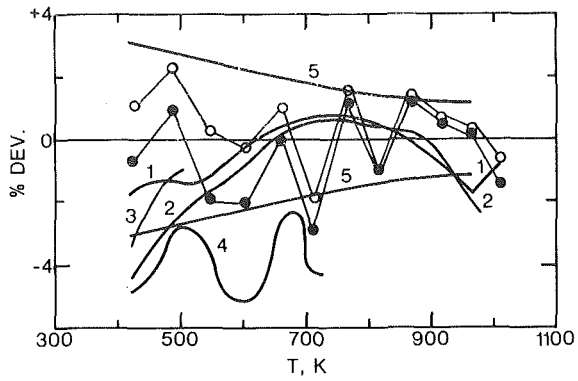

Fig. 2 Comparison of the experimental conductivity values (○ 39.4 kN/m² and ● 94.4 kN/m²) with the smoothed values (equation (1)). Curves 1 to 4 represent the percent deviations of the values of Touloukian, et al. [1], Geier and Schäfer [2], Hanley, et al. [10], and Le Neindre, et al. [5], respectively, from the present results (equation (1)). Curves 5 represent the probable errors of present measurements

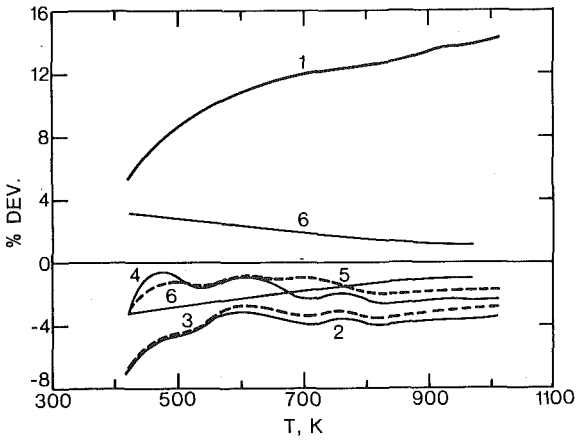

Fig. 3 Comparison of experimental thermal conductivity values with the theoretically calculated values. Curve 1: [13]; Curve 2: [14] and exp-six potential [16]; Curve 3: [14] and (11-6-8) potential [17]; Curve 4: [15] and exp-six potential [16]; Curve 5: [15] and (11-6-8) potential [17]; and Curves 6: represent probable errors of measurement. Percent dev. = [k(equation (1)) − k(calculated)]100/k(equation (1))

Nomenclature

A = total band absorptance, cm^{-1}
$\overline{A}$ = dimensionless band absorptance
A_0 = band width parameter, cm^{-1}
B_ω = Planck's function, erg/cm-s
C_v = total heat capacity at constant volume, erg/gmole-K
d^* = line spacing in the band, cm^{-1}
D = mass diffusion coefficient, cm^2/s
D_{vib} = diffusion coefficient for vibrational energy, cm^2/s
E_n = exponential integral, dimensionless
f = Eucken correction factor, dimensionless
j = bands' index, —
k = thermal conductivity, mW/m-K
L = gas layer thickness, cm
M = molecular weight, g/gmole
N = number of bands, —
P = pressure, dyne/cm^2
q_c = conductive heat flux, mW/m^2
q_R = wall to wall radiation, mW/m^2
q_r = radiative flux, mW/m^2
R = gas constant, erg/gmole-K
S = path length, cm
T = temperature, K
T_H = temperature of the hot surface, K
T_W = temperature of the cold surface, K
T_0 = reference temperature, K
u = pressure path length, dimensionless
u_0 = u based on reference length L
x = physical coordinate, cm
Z_{rot} = number of molecular collisions required for translational-rotational energy equilibrium, —
Z^∞_{rot} = limiting value of Z_{rot} at high temperatures, —
α_0 = band integrated intensity, $cm^{-1}/g\text{-}m^{-2}$
α = steepness of the repulsive limb of the exp-six potential, —
β = line structure parameter, dimensionless
γ = line half-width, cm^{-1}
ΔT = temperature difference between the two walls, K
ζ = a constant which occurs in equation (20), dimensionless
η = gas viscosity, g/cm-s
κ_ω = absorption coefficient, cm^{-1}
ξ = physical coordinate, dimensionless
ρ = gas density, g/cm^3
σ = Stefan-Boltzmann constant, $W/m^2\text{-}K^4$
ω = wave number, cm^{-1}
θ = direction angle, deg

[12], respectively, are used in the present calculations. The expressions for the Eucken correction factor, f, under different assumptions are given by Eucken [13], Hirschfelder [14], and Mason and Monchick [15]. In the two latter cases, the knowledge of intermolecular potential is needed and two such potentials, one by Schamp, et al. [16] and the other by Hanley and Cohen [17], are used.

It is to be noted that the predictions based on Eucken theory [13] underestimate the conductivity values over the entire temperature range, curve 1 of Fig. 3, while the other theories [14, 15] overestimate the values, though the magnitudes differ on the two theories and these also depend on the choice of the interaction potential. These qualitative trends have been observed earlier [18] over a limited temperature range and were explained on the basis of the relaxation of internal energy. Curves 2 and 3 of Fig. 3 are based on Hirschfelder's theory [14] in conjunction with exp-six and (11-6-8) potentials, respectively. The two choices for the steepness of the repulsive limb of the exp-six potential [16] as characterized by the parameter $\alpha = 14$ and 15 are tried. The latter choice is found to give better results and is employed here. The (11-6-8) potential leads to better results than the exp-six potential and further substantiates the earlier conclusion of Nain, et al. [19] regarding the superiority of (11-6-8) potential for correlating the transport properties of gases. Curves 4 and 5 of Fig. 3 are based on Mason and Monchick theory [15] for the two potentials in conjunction with the rotational collision number, Z_{rot}, as given by Brau and Jonkman [20] with $Z_{\text{rot}}^{\infty} = 32.5$ collisions. Here, again the (11-6-8) potential gives a superior reproduction of experimental values of thermal conductivity. However, the agreement between theory and experiment beyond about 750 K is not satisfactory lending support to the widely held view that the thermal conductivity of polyatomic gases is not adequately predicted on the basis of existing theories.

Ahtye [21] proposed a semi-theoretical scheme to take care of the above deficiency by splitting internal energy into rotational and vibrational components. This is particularly appropriate for methane where as much as 25 and 60 percent of the total energy is vibrational at 400 and 1000 K respectively. Ahtye [21], thus, introduced the idea of the diffusion coefficient for vibrational energy, D_{vib}. Computed values of ρD_{vib} from his theory and present conductivity data are shown in Fig. 4 as a function of temperature. ρ is the gas density. D_{vib} is always smaller than the mass diffusion coefficient, D, as is evident from Fig. 4.

Effect of Gaseous Radiative Transfer On Thermal Conductivity

Since methane has three relatively strong absorption bands in the infrared, gaseous radiative heat transfer may cause errors in the conductivity measured in this work. To correct such data, one must theoretically calculate the radiative contribution to the heat flux. Pigal'skaya [22] has solved such a problem for monochromatic radiation in cylindrical slabs with small temperature differences and optical depths. Although this work is an important step, it lacks generality. Band models are needed to allow summation over the spectral frequency and use of these in cylindrical geometry leads to complexity in the solution.

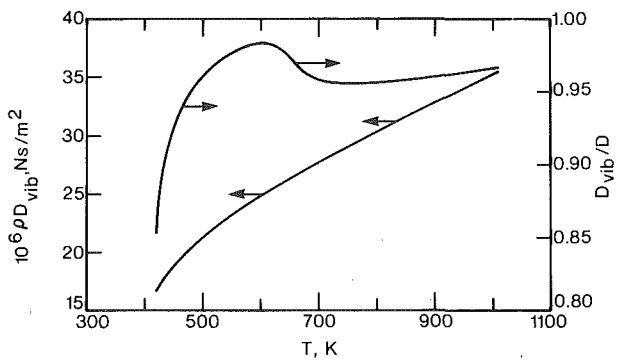

Fig. 4 Variation of ρD_{vib} and D_{vib}/D with temperature

The approach here is to develop an argument that will estimate the order of magnitude of the effect that radiative transfer may have on conductivity measurements. To model this problem, plane-parallel geometry was chosen for its simplicity and because Pigal'skaya's work suggested that results from the plane case would place a lower bound on the error expected in the actual experimental situation of cylindrical geometry. The model is further simplified by assuming the heat transfer modes are not coupled. Conduction is used to find the temperature field which is then used to calculate the gaseous radiative heat flux. This latter calculation is done in detail as described below. The radiative transfer in the plane model is treated precisely since it eventually will be applied to the cylindrical geometry of the experiment.

For the plane-parallel model shown in Fig. 5, the surfaces are black and the temperature profile is linear and given by

$$\frac{T - T_H}{T_W - T_H} = x/L \equiv \xi. \tag{3}$$

The wall-to-wall radiative flux is simply

$$q_R = \sigma\,(T_H{}^4 - T_W{}^4), \tag{4}$$

while the conductive heat flux is given by

$$q_c = L^{-1}\,k(T)\,\frac{dT}{d\xi}. \tag{5}$$

The conductivity coefficients are taken from equation (1). By direct integration, equation (5) can be expressed in the following form:

$$q_c = \overline{k(T)}\,\frac{\Delta T}{L},$$

where $\overline{k(T)} = k_m(1 + \delta)$. k_m is the conductivity coefficients evaluated at the arithmetic mean of the surface temperatures and $\delta = \frac{1}{3}\,B_0B_2(T_m^2 - T_HT_W)/k_m$, which is a substantially small quantity compared to k_m.

The radiative heat flux from the gas is obtained by a formal solution using a band absorptance model and closely follows the approach of Sparrow and Cess [23], and Cess and Tiwari [24]. The important methane bands are centered at 2.37, 3.31, and 7.65 μ, however only the last two are considered here. The 2.37μ band is relative weak, contributing about 15 percent to the total emissivity [25], and its band parameters are not accurately known.

The solution of the radiative transfer equation for a slab of gas with no boundary surfaces gives the monochromatic exiting heat flux $q_{r,\omega}$ as

$$q_{r,\omega} = 2\pi \int_0^L \kappa_\omega B_\omega E_2(\kappa_\omega x)dx. \tag{6}$$

Here ω is the wave number, B_ω the Planck function, κ_ω the linear absorption coefficient and E_2 the exponential integral function. This expression can be written in terms of a band absorptance A which is defined by

$$A = \int_{\text{band}} \{1 - \exp(-\kappa_\omega x)\}\,d\omega. \tag{7}$$

The first step is to take the derivative of equation (7) to obtain

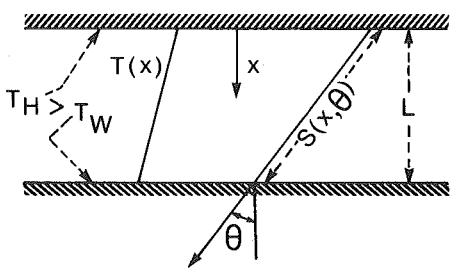

Fig. 5 The physical model of a non-isothermal slab of gas bounded by two parallel plates with black surfaces

$$\frac{dA}{dX} = \int_{\text{band}} \kappa_\omega \exp(-\kappa_\omega x) d\omega \tag{8}$$

and then introduce the following exponential Kernel approximation:

$$E_2(Z) \cong \frac{3}{4} \exp\left(-\frac{3}{2} Z\right). \tag{9}$$

Since the absorbing bands are spectrally narrow with respect to the Planck function, the latter is evaluated at the band centers and can be taken outside the wave number integral. Combining equations (6) and (9), the gaseous radiative heat flux summed over each band j becomes

$$q_r = \pi \sum_{j=1}^{N} \int_0^L B_{\omega j}(x) \left\{ \int_{\text{band}} \frac{3}{2} \kappa_{\omega j} e^{-3/2 \kappa_{\omega j} x} d\omega \right\} dx. \tag{10}$$

The dimensionless pressure path length u is introduced by

$$u = \frac{\alpha_0 P x}{A_0} \tag{11}$$

where α_0 is the band intensity, P the pressure, and A_0 the wave number width of the band. A normalized A is given by

$$\overline{A} = A/A_0 \tag{12}$$

and equation (10) can be written in the form

$$q_r = \pi \sum_{j=1}^{N} \int_0^1 B_{\omega j}(\xi) \frac{3}{2} u_{0j}(\xi) A_{0j}(\xi) \frac{d\overline{A}(3/2u_j, \beta)}{du_j} d\xi, \tag{13}$$

where β is a line-shape parameter.

There are several band absorptance correlations for $\overline{A}$, see Sparrow and Cess [23]. Here the one suggested by Tien and Lowder [26] is used and can be written as

$$\overline{A}(u, \beta) = \ln\left[u f(\beta) \left(\frac{u+2}{u+2f(\beta)} \right) + 1 \right], \tag{14}$$

where

$$f(\beta) = 2.94[1 - e^{-2.6\beta}], \tag{15}$$

$$u(\xi) = PL[\alpha_0(\xi)/A_0(\xi)]\xi = u_0(\xi)\xi, \tag{16}$$

and

$$\beta(\xi) = 4[\gamma(\xi)/d^*(\xi)]. \tag{17}$$

The line half-width γ and line spacing d^* are functions of temperature and from Lee and Hoppel [25] we have

$$\gamma(T) = \gamma(T_0) \left(\frac{T_0}{T} \right)^{1/2} \tag{18}$$

and

$$d^*(T) = d^*(T_0) \left(\frac{T_0}{T} \right)^{\zeta}. \tag{19}$$

The above equations then give the line-shape parameter as

$$\beta(T) = \beta(T_0) \left(\frac{T}{T_0} \right)^{\zeta - 1/2}, \tag{20}$$

where ζ is 1.52 and 2.18 for the 7.65μ and 3.31μ bands, respectively. The correlations for α_0 and A_0 are taken from the work of Edwards [27–29] and are:

$$\alpha_0(T) = K_1/RT \tag{21}$$

and

$$A_0(T) = K_3 \left(\frac{T}{T_0} \right)^{1/2}. \tag{22}$$

The constants K_1 and K_3 along with other band parameters are given in Table 1 for the reference temperature T_0 of 100 K.

With the above correlations, equation (13) is integrated numerically for a linear temperature profile with wall temperatures characteristic of those in the experiment, i.e., 500–1000 K. The effect of the gaseous radiative transfer is to lower the conductivity values. This was found by comparing the conductivity of the slab with and without the absorption bands present. The results give an almost constant error of about 2.5 percent over the temperature range of interest. Since this error is slightly larger than the expected experimental error and represents a lower bound for the error one would experience in cylindrical geometries, the conclusion is that the complete radiative transfer problem must be solved to correct thermal conductivity measurements in methane. Such work is now being carried out.

Table 1 Band parameters used in the calculation of radiative heat flux

Bands	w_0 cm^{-1}	K_1 cm^{-1}/gm^{-1}	K_3 cm^{-1}	ζ	$\beta_0 \times 10^2$
3.31μ	3020	46	55	2.18	6.973
7.65μ	1310	28	23	1.52	86.980

Acknowledgment

This work is supported in part by the National Science Foundation in a collaborative USA-USSR research program under grant number ENG 77-08780.

References

1 Touloukian, Y. S., Liley, P. E., and Saxena, S. C., *Thermal Conductivity: Nonmetallic Liquids and Gases,* IFI/Plenum, New York, 1970.

2 Geier, H., and Schäfer, K., "Heat Conductivity of Pure Gases and Gas Mixtures at 0–1200°C," *Allgemeine Warmetech,* Vol. 10, 1961, pp. 70–75.

3 Whitmore, F. C., *Organic Chemistry,* D. Van Nostrand Co., New York, 1951.

4 Winters, H. F., "The Activated, Dissociative Chemisorption of Methane on Tungsten," *Journal Chemical Physics,* Vol. 62, 1975, pp. 2454–2460.

5 LeNeindre, B., Tufeu, R., Bury, P., Johannin, P., and Vodar, B., "Experimental Study of Thermal Conductivity Coefficients of Methane and Ethane Between 25°C and 450°C at Pressures up to 1000 Bars," *Proceedings of the Eighth Conference on Thermal Conductivity,* Plenum, New York, 1969, pp. 229–243.

6 Jody, B. J., Jain, P. C., and Saxena, S. C., "Determination of Thermal Properties From Steady State Heat Transfer Measurements on a Heated Tungsten Wire in Vacuum and Helium Gas," ASME JOURNAL OF HEAT TRANSFER, Vol. 97, 1975, pp. 605–609.

7 Chen, S. H. P., and Saxena, S. C., "Experimental Determination of Thermal Conductivity of Nitrogen in the Temperature Range 100–2200°C," *High Temperature Science,* Vol. 5, 1973, pp. 206–233.

8 Chen, S. H. P., and Saxena, S. C., "An Analytical Study of Heat Transfer Through Gases Contained Between Two Vertical Coaxial Cylinderical Surfaces at Different Temperatures," Second National Heat Mass Transfer Conference, India, 1973, pp. A.17-A.23.

9 Chen, S. H. P., and Saxena, S. C., "Thermal Conductivity and Effective Diffusion Coefficient for Vibrational Energy: Carbon Dioxide (350–2000K)," *Journal Physics B: Atomic and Molecular Physics,* Vol. 8, 1975, pp. 1962–1972.

10 Hanley, H. J. M., Haynes, W. M., and McCarty, R. D., "The Viscosity and Thermal Conductivity Coefficients for Desne Gaseous and Liquid Methane," *Journal Physical and Chemial Reference Data,* Vol. 6(2), 1977, pp. 597–609.

11 Touloukian, Y. S., Liley, P. E., and Saxena, S. C., *Viscosity,* IFI/Plenum, New York, 1975.

12 Svehla, R. A., "Estimated Viscosities and Thermal Conductivities of Gases at High Temperatures," NASA Technical Report R-32, 1962, pp. 1–140.

13 Eucken, A., "On the Thermal Conductivity, Specific Heat and Viscosity of Gas," *Physik Z.* Vol. 14, 1913, pp. 324–332.

14 Hirschfelder, J. O., "Heat Conductivity in Polyatomic or Electronically Excited Gases. II," *Journal Chemical Physics,* Vol. 26, 1957, pp. 282–285.

15 Mason, E. A. and Monchick, L., "Heat Conductivity of Polyatomic and Polar Gases," *Journal Chemical Physics,* Vol. 36, 1962, pp. 1622–1639.

16 Schamp, H. W., Mason, E. A., Richardson, A. C. B., and Altman, A., "Compressibility and Intermolecular Forces in Gases: Methane," *Physics of Fluids,* Vol. 1, 1958, pp. 329–337.

17 Hanley, H. J. M., and Cohen, E. G. D., "Analysis of the Transport Coefficients for Simple Dense Fluids: The Diffusion and Bulk Viscosity Coefficients," *Physica,* Vol. 83A, 1976, pp. 215–232.

18 Saxena, S. C., and Agrawal, J. P., "Thermal Conductivity of Polyatomic Gases and Relaxation Phenomena," *Journal Chemical Physics,* Vol. 35, 1961, pp. 2107–2113.

19 Nain, V. P. S., Aziz, R. A., Jain, P. C., and Saxena, S. C., "Interatomic Potentials and Transport Properties for Neon, Argon and Krypton," *Journal*

Chemical Physics, Vol. 65, 1976, pp. 3242–3249.
20 Brau, C. A., and Jonkman, R. M., "Classical Theory of Rotational Relaxation in Diatomic Gases," *Journal Chemical Physics,* Vol. 52, 1970, pp. 477–484.
21 Ahtye, W. F., "Thermal Conductivity in Vibrationally Excited Gases," *Journal Chemical Physics,* Vol. 57, 1972, pp. 5542–5555.
22 Pigal'skaya, L. A., "Temperature Fields and Effective Thermal Conductivity in Cylindrical Layer of an Absorbing Medium," *High Temperature,* Vol. 7, 1969, pp. 628–633.
23 Sparrow, E. M. and Cess, R. D., *Radiation Heat Transfer,* Brooks/Cole, Belmont, California, 1978.
24 Cess, R. D., and Tiwari, S. N., "Infrared Radiation Energy Transfer in Gases," *Advances in Heat Transfer,* Vol. 8, Academic Press, New York, 1972, pp. 229–284.
25 Lee, R. H. C., and Hoppel, J., "Thermal Radiation of Methane Gas," *Industrial and Engineering Chemistry Fundamentals,* Vol. 12, pp. 167–176.
26 Tien, C. L. and Lowder, J. E., "A Correlation for Total Band Absorptance of Radiating Gases," *International Journal of Heat and Mass Transfer,* Vol. 9, 1966, pp. 698–701.
27 Edwards, D. K., and Menard, W. A., "Correlations for Absorption by Methane and Carbon Dioxide Gases," *Applied Optics,* Vol. 3(7), 1964, pp. 847–852.
28 Edwards, D. K., Glassen, L. K., Hauser, W. C., and Tuchscher, J. S., "Radiation Heat Transfer in Non-isothermal Nongray Gases," ASME JOURNAL OF HEAT TRANSFER, Vol. 89, 1967, pp. 219–229.
29 Edwards, D. K., and Balakrishnan, A., "Thermal Radiation By Combustion Gases," *International Journal of Heat and Mass Transfer,* Vol. 16, 1973, pp. 25–40.

Journal of Heat Transfer

Technical Notes

This section contains shorter technical papers. These shorter papers will be subjected to the same review process as that for full papers.

Prediction of Combined Free and Forced Convective Heat Transfer along a Vertical Plate with Uniform Blowing

S. Tsuruno[1] and I. Iguchi[2]

Nomenclature

$f(\xi, \eta)$ = dimensionless stream function, $\psi(x, y)/\sqrt{u_\infty \nu x}$
g = gravitational acceleration
Gr = Grashof number, $g\beta(T_w - T_\infty)x^3/\nu^2$
Nu = Nusselt number, hx/k
Pr = Prandtl number, ν/α
Re = Reynolds number, $u_\infty x/\nu$
T = temperature
u = velocity component in x-direction
v = velocity component in y-direction
α = thermal diffusivity
β = volumetric expansion
$\psi(x, y)$ = stream function
ν = kinematic viscosity

Subscripts

w = wall condition
∞ = ambient fluid condition

Introduction

The present paper is concerned with laminar combined free and forced convective heat transfer with blowing along an isothermal vertical wall. So far, convective heat transfer with the effect of blowing has been studied many investigators [1–5]. Eichhorn [1] gave a similar solution and Merkin [2] and Parikh, et al. [3] presented their numerical solutions for the free convective heat transfer with blowing along an isothermal vertical flat plate. Hartnett, et al. [4] and Sparrow, et al. [5] reported the characteristics of heat transfer and skin friction for the pure forced convection with blowing; the former dealt with a similar solution and the latter a nonsimilar one. According to these studies, the blowing effect on convective heat transfer has been well defined; however, there may still be a shortage of information on combined free and forced convective heat transfer with blowing.

Therefore, the purpose of this paper is to clarify the characteristics of the combined convective heat transfer with blowing; especially, attention is paid to clarify the limit between the combined convection and the effectively pure (either forced or free) convection.

2 Analysis

The field of flow discussed in this paper is that of flow along an isothermal porous wall with uniform blowing. The porous wall is vertical, where the x-coordinate is measured along the wall surface and the y-coordinate is measured normal to the x-axis. Under the assumption of constant fluid properties and no dissipation energy, the governing equations employed here are identical to those given by equation (3) of [3]. The boundary condition is given as $u = 0$, $v = v_w$ (=constant), $T = T_w$ at $y = 0$ and $u = u_\infty$, $T = T_\infty$ at $y = \infty$. These equations, being systems of the x-y coordinate, are transformed to nondimensional equations of a new coordinate system, η and ξ, as the first step in this analysis:

$$\frac{\partial^3 f}{\partial \eta^3} + f\frac{\partial^2 f}{\partial \eta^2} - 2\xi\left(\frac{\partial f}{\partial \eta}\frac{\partial^2 f}{\partial \xi \partial \eta} - \frac{\partial^2 f}{\partial \eta^2}\frac{\partial f}{\partial \xi}\right) + 8\xi\theta = 0 \tag{1}$$

$$\frac{\partial^2 \theta}{\partial^2 \eta} + \Pr\left\{f\frac{\partial \theta}{\partial \eta} - 2\xi\left(\frac{\partial f}{\partial \eta}\frac{\partial \theta}{\partial \xi} - \frac{\partial \theta}{\partial \eta}\frac{\partial f}{\partial \xi}\right)\right\} = 0 \tag{2}$$

$$f = C_0\sqrt{\xi}\,, \frac{\partial f}{\partial \eta} = 0, \theta = 1 \text{ at } \eta = 0$$
$$\frac{\partial f}{\partial \eta} = 2, \theta = 0 \text{ at } \eta = \infty \tag{3}$$

where the nondimensional variables employed are:

$$\xi = \frac{g\beta(T_w - T_\infty)x}{u_\infty^2} \quad (4) \qquad \eta = \frac{u_\infty}{2}\sqrt{\frac{u_\infty}{\nu x}} \tag{5}$$

$$\theta = T - T_\infty/T_w - T_\infty \quad (6) \qquad C_0 = \frac{v_w}{u_\infty}\sqrt{\mathrm{Re}}/\sqrt{\xi} \tag{7}$$

Equations (1) and (2) were solved by a numerical procedure in which the nonlineality of those equations was avoided by the use of a method similar to the Terril's [6]. The parameter, C_0, is the ratio of the blowing rate, $v_w/u_\infty\sqrt{\mathrm{Re}}$, and $\sqrt{\xi}$, prescribing the flow conditions.

3 Numerical Results and Discussion

The numerical solutions were carried out for Pr = 0.72 and 10 and the values of C_0 were varied for $C_0 = 0 - 1$. The predicted Nusselt numbers were compared with those for pure forced and pure free convection, by which the limits of the effectively pure convective heat transfer were derived. The standard employed for judging those limits is whether the Nusselt numbers obtained deviate more than five percent from the value associated with the completely pure convective flow or not. Figs. 1 and 2 demonstrate the limits of each effectively pure convection by plotting the relation between ξ and C_0 for Pr = 0.72 and 10. As illustrated by Fig. 1, the region regarded as the combined convective flow depends mainly on C_0. The more C_0 increases, the closer the mixed region starts and ends to the position of smaller ξ with increasing C_0. Fig. 2 shows the limit of the effectively pure convection for Pr = 10. But in regions of $C_0 > 0.3$, it is difficult to predict the limit of the free convection because the Nusselt number corresponding to the limit of the free convection is so small that it means very little to estimate the differences between those of mixed

[1] Lecturer, Department of Mechanical Engineering, The National Defense Academy, Hashirimizu, Yokosuka, Japan
[2] Professor, Department of Mechanical Engineering, The National Defense Academy, Hashirimizu, Yokosuka, Japan.
Contributed by the Heat Transfer Division for publication in the JOURNAL OF HEAT TRANSFER. Manuscript received by the Heat Transfer Division May 8, 1978.

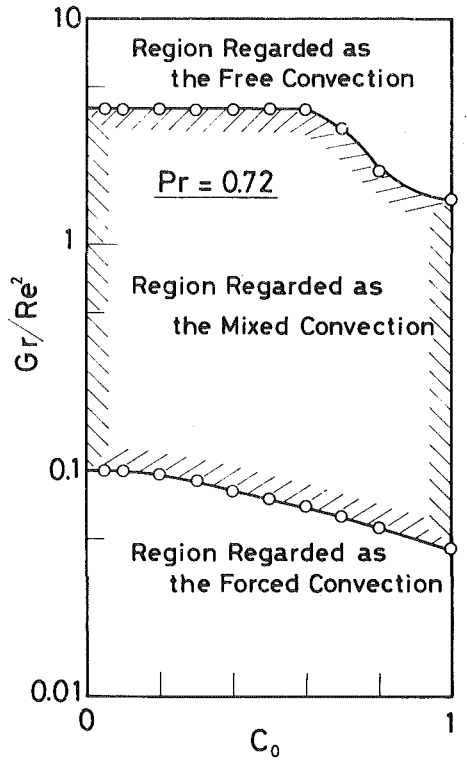

Fig. 1 Division of convective heat transfer from forced to free convection for Pr = 0.72

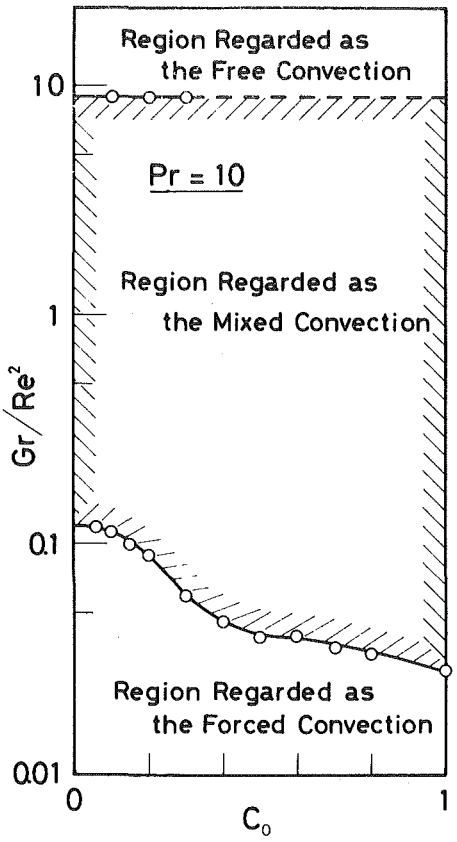

Fig. 2 Division of convective heat transfer from forced to free convection for Pr = 10

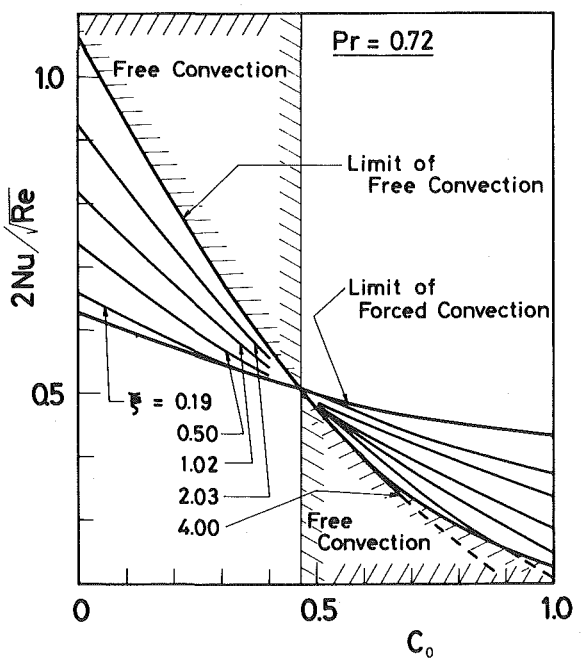

Fig. 3 Heat transfer in combined convection for Pr = 0.72

flow and pure free convection. The tendency of the limit of forced convection is similar to the case in Fig. 1, but the limit decreases accelerratively passing through the point of $C_0 = 0.2$ as compared with the case in Fig. 1.

Figs. 3 and 4 show the characteristic of heat transfer in the mixed flow and the division of convection from forced to free convection for Pr = 0.72 and 10, where the ordinate is the Nusselt number and the abcissa is C_0. The former is drawn on the graph of a usual real axis; the latter is plotted on the log-log graph. In Figs. 3 and 4, the limits of effectively pure convection are described by thick rigid lines. The other rigid lines show the characteristics of the heat transfer for the regions regarded as mixed flow. The regions enclosed by oblique lines correspond to those considered to be effectively free convection. The regions enclosed by two thick rigid lines, which describe the limit of the effectively pure convection, are those of the combined convective heat transfer, the width of which describes heat transfer that can vary in flow conditions corresponding to the values of C_0. Accordingly, one should note that no variations of the heat transfer occur as a result of the buoyancy force at the intersection of two thick rigid lines. Furthermore, the manner of action of the buoyancy force changes at the point of intersection, in the left side of which the buoyancy force causes the increase of the heat transfer, whereas it causes the decrease of those in the right side of that point. Moreover, it should be noted that the phenomenon of heat transfer with blowing is strongly dependent on C_0 and the Prandtl number. By comparing Figs. 3 and 4, it can be proved that the position of the intersection moves in the direction of the smaller C_0 as the Prandtl number increases; thereby, the area of the left side of the intersection decreases. Since this tendency seems to accelerate with the increase of the Prandtl number, the buoyancy force will hardly act on the increase of the heat transfer but will only act on the decrease of heat transfer at a high Prandtl number.

Finally, the transformation of variables employed in making Figs. 1–4 are:

$$\frac{\mathrm{Nu}}{\sqrt{\mathrm{Re}}} = \sqrt{2}\xi^{1/4}\frac{\mathrm{Nu}}{\sqrt[4]{\mathrm{Gr}}} \tag{8}$$

$$\xi = \left\{\frac{v_w x}{\nu}\left(\frac{4}{\mathrm{Gr}}\right)^{1/4} \Big/ \sqrt{2}C_0\right\}^4 \tag{9}$$

Equation (8) was used to transform the heat transfer of pure free convection into the form of forced convection. Equation (9) shows the relation between the variable of ξ and $v_w x/\nu\ (4/\mathrm{Gr})^{1/4}$.

Acknowledgment

The authors are deeply indebted to Professor N. Seki of the Department of Mechanical Engineering, University of Hokkaido, for many helpful suggestions and guidance during the course of the investigation.

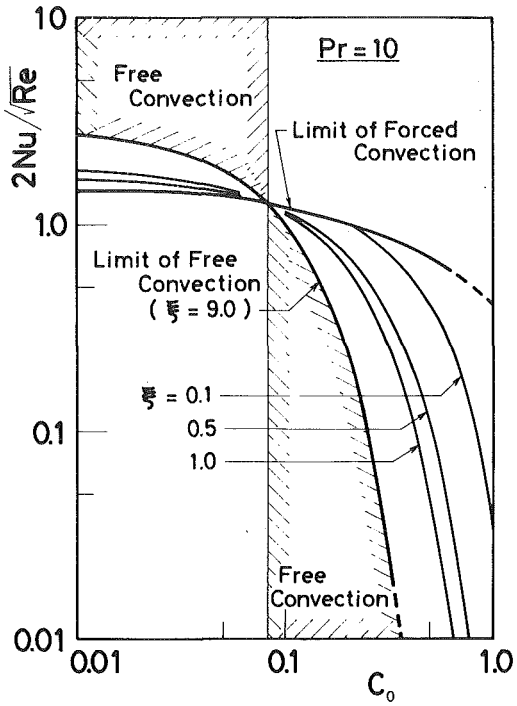

Fig. 4 Heat transfer in combined convection for Pr = 10

References

1 Eichhorn, R. "The Effect of Mass Transfer on Free Convection," ASME JOURNAL OF HEAT TRANSFER, Vol. 82, 1960, pp. 260–263.

2 Merkin, J. H, "Free Convection with Blowing and Suction," *International Journal of Heat and Mass Transfer*, Vol. 15, 1972, pp. 989–999.

3 Parikh, P. G., Moffat, R., J., Kays, W., M. and Bershader, D., "Free Convection over a Vertical Porous Plate with Transpiration," *International Journal of Heat and Mass Transfer*, Vol. 17, 1974, pp. 1465–1474.

4 Hartnett, J. P. and Eckert, E. R. G., "Mass Transfer Cooling in a Laminar Boundary Layer with Constant Fluid Properties," ASME JOURNAL OF HEAT TRANSFER, Vol. 79, 1957, pp. 247–254.

5 Sparrow, E. M. and Starr, J. B., "The Transpiration-Cooling Flat Plate with Various Thermal and Velocity Boundary Conditions," *International Journal of Heat and Mass Transfer*, Vol. 9, 1966, pp. 508–510.

6 Terill, R. M., "Laminar Boundary-Layer Flow near Separation with and without Suction," *Philosophy Transaction of The Royal Society*, Vol. 253, a, 1960, pp. 55–100.

Buoyancy Effects in Boundary Layer Adjacent to a Continuous, Moving Horizontal Flat Plate

T. S. Chen[1] and F. A. Strobel[2]

Introduction

Very recently, Chen et al. [1] re-examined the problem of mixed convection in laminar boundary layer flow over a stationary, horizontal flat plate and provided new heat transfer results for the intermediate range of buoyancy force intensities by the local similarity and local nonsimilarity methods of solution. In the present study, the same solution methods are applied to analyze the effects of buoyancy-induced streamwise pressure gradient on the momentum and heat transfer characteristics in laminar boundary layer adjacent to a continuous, moving horizontal flat plate. Such an analysis has not been performed in the past.

Analysis

Consider a continuous horizontal flat plate that is maintained at a constant temperature T_w and is moving with a velocity u_s through an otherwise quiescent fluid at temperature T_∞. The x coordinate is measured along the moving plate from the point where the plate originates and the y coordinate is measured normal to the plate. Positive y is taken to be vertical upward for fluid above the moving plate and vertical downward for fluid below the moving plate. With the Boussinesq approximation, the conservation equations for the problem under consideration are exactly identical to equations (1–3) of [1]. However, the boundary conditions for the velocity field are now different and changed to $u = u_s$ and $v = 0$ at $y = 0$ and $u \to 0$ as $y \to \infty$. Thus, with u_∞ replaced by u_s, $F'(\xi, 0) = 0$ by $F'(\xi, 0) = 1$, and $F'(\xi, \infty) = 1$ by $F'(\xi, \infty) = 0$, the nomenclature and equations (5–24) for the problem treated in [1] apply to the present problem as well, even though the two problems are physically different. It suffices to mention here that the local friction factor C_f and the local Nusselt number Nu_x are given, respectively, by

$$C_f \mathrm{Re}_x^{1/2} = 2F''(\xi, 0), \ \mathrm{Nu}_x \mathrm{Re}_x^{-1/2} = -\theta'(\xi, 0) \tag{1}$$

where $\mathrm{Re}_x = u_s x/\nu$ is the Reynolds number, $\theta(\xi, \eta) = (T - T_\infty)/(T_w - T_\infty)$ is the dimensionless temperature, $F(\xi, \eta) = \psi/(\nu u_s x)^{1/2}$ is the reduced stream function, and the primes stand for partial derivatives with respect to $\eta = y(u_s/\nu x)^{1/2}$. The buoyancy parameter ξ is defined by

$$\xi = |\mathrm{Gr}_x|/\mathrm{Re}_x^{5/2} \tag{2}$$

with $\mathrm{Gr}_x = g\beta(T_w - T_\infty)x^3/\nu^2$ denoting the local Grashof number. With the exception of the changes in the boundary conditions to $F'(\xi, 0) = 1$ and $F'(\alpha, \infty) = 0$, it is noted that $F(\xi, \eta)$ and $\theta(\xi, \eta)$ satisfy equations (8–10) of [1].

In addition to the local quantities, it is of interest to determine the average Nusselt number $\overline{\mathrm{Nu}} = \bar{h}L/k$, where L is the plate length and $\bar{h}$ is the average heat transfer coefficient. From the definition of $\bar{h}$,

$$\bar{h} = \frac{1}{L}\int_0^L h(x)dx \tag{3}$$

the average Nusselt number can be expressed as

$$\overline{\mathrm{Nu}}\mathrm{Re}_L^{-1/2} = \frac{2}{\xi_L}\int_0^{\xi_L} [-\theta'(\xi, 0)]d\xi \tag{4}$$

where

$$\xi_L = |\mathrm{Gr}_L|/\mathrm{Re}_L^{5/2}, \ \mathrm{Gr}_L = g\beta(T_w - T_\infty)L^3/\nu^2, \ \mathrm{Re}_L = u_s L/\nu \tag{5}$$

Results and Discussion

The numerical solution of the governing system of equations follows that outlined in [1]. Results were obtained for Prandtl numbers of 0.7 and 7 over a range of values of the buoyancy force parameters $\mathrm{Gr}_x/\mathrm{Re}_x^{5/2}$. To conserve space, only the results for $F''(\xi, 0)$ and $\theta'(\xi, 0)$ from the local nonsimilarity solution are listed in Table 1. It is noted that the present results are in excellent agreement with those of the previous investigations in which $\mathrm{Gr}_x/\mathrm{Re}_x^{5/2} = 0$; that is, when the buoyancy force effect was neglected in the analysis (see, for example, [2]).

The variations of the local friction factor and the local Nusselt number with the buoyancy force parameter $\mathrm{Gr}_x/\mathrm{Re}_x^{5/2}$ are shown, respectively, in Figs. 1 and 2. The trends exhibited by the curves are consistent with the expected effects of favorable and adverse pressure gradients in the boundary layer. A positive buoyancy force parameter (i.e., $\mathrm{Gr}_x/\mathrm{Re}_x^{5/2} > 0$) induces a favorable pressure gradient that enhances the fluid motion, which in turn increases the local friction factor and hence the local Nusselt number. On the other hand, a negative buoyancy force parameter (i.e., $\mathrm{Gr}_x/\mathrm{Re}_x^{5/2} < 0$) induces an

[1] Department of Mechanical and Aerospace Engineering, University of Missouri-Rolla, Rolla, MO.

[2] Department of Mechanical and Aerospace Engineering, University of Missouri-Rolla, Rolla, MO. Presently with Naval Weapons Center, China Lake, CA.

Contributed by the Heat Transfer Division for publication in the JOURNAL OF HEAT TRANSFER. Manuscript received at ASME Headquarters May 31, 1979.

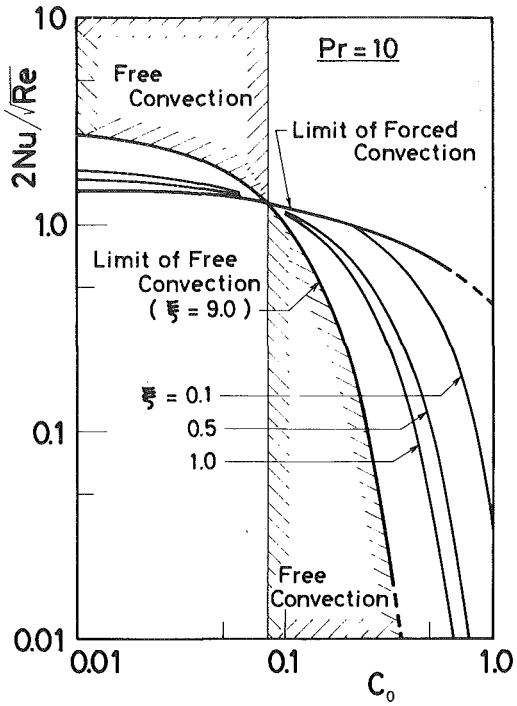

Fig. 4 Heat transfer in combined convection for Pr = 10

References

1 Eichhorn, R. "The Effect of Mass Transfer on Free Convection," ASME JOURNAL OF HEAT TRANSFER, Vol. 82, 1960, pp. 260–263.

2 Merkin, J. H, "Free Convection with Blowing and Suction," *International Journal of Heat and Mass Transfer*, Vol. 15, 1972, pp. 989–999.

3 Parikh, P. G., Moffat, R., J., Kays, W., M. and Bershader, D., "Free Convection over a Vertical Porous Plate with Transpiration," *International Journal of Heat and Mass Transfer*, Vol. 17, 1974, pp. 1465–1474.

4 Hartnett, J. P. and Eckert, E. R. G., "Mass Transfer Cooling in a Laminar Boundary Layer with Constant Fluid Properties," ASME JOURNAL OF HEAT TRANSFER, Vol. 79, 1957, pp. 247–254.

5 Sparrow, E. M. and Starr, J. B., "The Transpiration-Cooling Flat Plate with Various Thermal and Velocity Boundary Conditions," *International Journal of Heat and Mass Transfer*, Vol. 9, 1966, pp. 508–510.

6 Terill, R. M., "Laminar Boundary-Layer Flow near Separation with and without Suction," *Philosophy Transaction of The Royal Society*, Vol. 253, a, 1960, pp. 55–100.

Buoyancy Effects in Boundary Layer Adjacent to a Continuous, Moving Horizontal Flat Plate

T. S. Chen[1] and F. A. Strobel[2]

Introduction

Very recently, Chen et al. [1] re-examined the problem of mixed convection in laminar boundary layer flow over a stationary, horizontal flat plate and provided new heat transfer results for the intermediate range of buoyancy force intensities by the local similarity and local nonsimilarity methods of solution. In the present study, the same solution methods are applied to analyze the effects of buoyancy-induced streamwise pressure gradient on the momentum and heat transfer characteristics in laminar boundary layer adjacent to a continuous, moving horizontal flat plate. Such an analysis has not been performed in the past.

Analysis

Consider a continuous horizontal flat plate that is maintained at a constant temperature T_w and is moving with a velocity u_s through an otherwise quiescent fluid at temperature T_∞. The x coordinate is measured along the moving plate from the point where the plate originates and the y coordinate is measured normal to the plate. Positive y is taken to be vertical upward for fluid above the moving plate and vertical downward for fluid below the moving plate. With the Boussinesq approximation, the conservation equations for the problem under consideration are exactly identical to equations (1–3) of [1]. However, the boundary conditions for the velocity field are now different and changed to $u = u_s$ and $v = 0$ at $y = 0$ and $u \to 0$ as $y \to \infty$. Thus, with u_∞ replaced by u_s, $F'(\xi, 0) = 0$ by $F'(\xi, 0) = 1$, and $F'(\xi, \infty) = 1$ by $F'(\xi, \infty) = 0$, the nomenclature and equations (5–24) for the problem treated in [1] apply to the present problem as well, even though the two problems are physically different. It suffices to mention here that the local friction factor C_f and the local Nusselt number Nu_x are given, respectively, by

$$C_f \mathrm{Re}_x^{1/2} = 2F''(\xi, 0), \ \mathrm{Nu}_x \mathrm{Re}_x^{-1/2} = -\theta'(\xi, 0) \tag{1}$$

where $\mathrm{Re}_x = u_s x/\nu$ is the Reynolds number, $\theta(\xi, \eta) = (T - T_\infty)/(T_w - T_\infty)$ is the dimensionless temperature, $F(\xi, \eta) = \psi/(\nu u_s x)^{1/2}$ is the reduced stream function, and the primes stand for partial derivatives with respect to $\eta = y(u_s/\nu x)^{1/2}$. The buoyancy parameter ξ is defined by

$$\xi = |\mathrm{Gr}_x|/\mathrm{Re}_x^{5/2} \tag{2}$$

with $\mathrm{Gr}_x = g\beta(T_w - T_\infty)x^3/\nu^2$ denoting the local Grashof number. With the exception of the changes in the boundary conditions to $F'(\xi, 0) = 1$ and $F'(\alpha, \infty) = 0$, it is noted that $F(\xi, \eta)$ and $\theta(\xi, \eta)$ satisfy equations (8–10) of [1].

In addition to the local quantities, it is of interest to determine the average Nusselt number $\overline{\mathrm{Nu}} = \bar{h}L/k$, where L is the plate length and $\bar{h}$ is the average heat transfer coefficient. From the definition of $\bar{h}$,

$$\bar{h} = \frac{1}{L}\int_0^L h(x)dx \tag{3}$$

the average Nusselt number can be expressed as

$$\overline{\mathrm{Nu}}\mathrm{Re}_L^{-1/2} = \frac{2}{\xi_L}\int_0^{\xi_L} [-\theta'(\xi, 0)]d\xi \tag{4}$$

where

$$\xi_L = |\mathrm{Gr}_L|/\mathrm{Re}_L^{5/2}, \ \mathrm{Gr}_L = g\beta(T_w - T_\infty)L^3/\nu^2, \ \mathrm{Re}_L = u_s L/\nu \tag{5}$$

Results and Discussion

The numerical solution of the governing system of equations follows that outlined in [1]. Results were obtained for Prandtl numbers of 0.7 and 7 over a range of values of the buoyancy force parameters $\mathrm{Gr}_x/\mathrm{Re}_x^{5/2}$. To conserve space, only the results for $F''(\xi, 0)$ and $\theta'(\xi, 0)$ from the local nonsimilarity solution are listed in Table 1. It is noted that the present results are in excellent agreement with those of the previous investigations in which $\mathrm{Gr}_x/\mathrm{Re}_x^{5/2} = 0$; that is, when the buoyancy force effect was neglected in the analysis (see, for example, [2]).

The variations of the local friction factor and the local Nusselt number with the buoyancy force parameter $\mathrm{Gr}_x/\mathrm{Re}_x^{5/2}$ are shown, respectively, in Figs. 1 and 2. The trends exhibited by the curves are consistent with the expected effects of favorable and adverse pressure gradients in the boundary layer. A positive buoyancy force parameter (i.e., $\mathrm{Gr}_x/\mathrm{Re}_x^{5/2} > 0$) induces a favorable pressure gradient that enhances the fluid motion, which in turn increases the local friction factor and hence the local Nusselt number. On the other hand, a negative buoyancy force parameter (i.e., $\mathrm{Gr}_x/\mathrm{Re}_x^{5/2} < 0$) induces an

[1] Department of Mechanical and Aerospace Engineering, University of Missouri-Rolla, Rolla, MO.

[2] Department of Mechanical and Aerospace Engineering, University of Missouri-Rolla, Rolla, MO. Presently with Naval Weapons Center, China Lake, CA.

Contributed by the Heat Transfer Division for publication in the JOURNAL OF HEAT TRANSFER. Manuscript received at ASME Headquarters May 31, 1979.

Table 1 Results for $F''(\xi, 0)$ and $-\theta'(\xi, 0)$ from the local nonsimilarity solution.

	Pr = 0.7		Pr = 7	
$Gr_x/Re_x^{5/2}$	$F''(\xi, 0)$	$-\theta'(\xi, 0)$	$F''(\xi, 0)$	$-\theta'(\xi, 0)$
−0.05			−0.44980	1.38548
−0.02			−0.44643	1.38686
−0.01			−0.44503	1.38693
0	−0.44375	0.34924	−0.44375	1.38702
0.1	−0.32890	0.37951	−0.43126	1.38918
0.2	−0.23865	0.39625	−0.41886	1.39165
0.3	−0.15998	0.40880	−0.40754	1.39372
0.4	−0.08777	0.41909	−0.39625	1.39605
0.5	−0.02204	0.42773	−0.38511	1.39823
0.6	0.04144	0.43556	−0.37502	1.40021
0.7	0.10110	0.44250	−0.36415	1.40247
0.8	0.15745	0.44874	−0.35340	1.40446
0.9	0.21194	0.45457	−0.34289	1.40658
1.0	0.26503	0.45994	−0.33347	1.40876

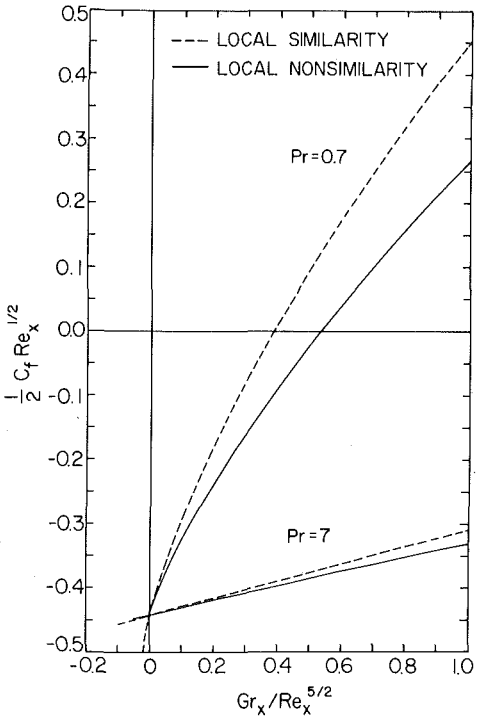

Fig. 1 The local friction factor results for Pr = 0.7 and 7

adverse pressure gradient which retards the fluid motion and hence reduces the surface heat transfer rate. It is seen from Fig. 1 that for $Gr_x/Re_x^{5/2} > 0$, the local friction factor increases from a negative value at zero buoyancy force to a less negative value as the buoyancy force increases. For the case of Pr = 0.7, for example, the local friction factor increases to zero at a buoyancy force parameter $Gr_x/Re_x^{5/2}$ of about 0.53 from the local nonsimilarity solution and becomes positive with a further increase in the buoyancy force intensity. The reason for this will be explained later when the velocity profiles are presented. The average Nusselt number plot, Fig. 3, exhibits trends that are similar to those of the local Nusselt number curves. As has been shown [1] that the results from the local nonsimilarity solution are more accurate than those from the local similarity solution.

The extent the buoyancy-induced pressure gradient affects the local Nusselt numbers and the local friction factors can be determined from the Nu_x/Nu_{x0} and C_f/C_{f0} ratios, where Nu_{x0} and C_{f0} are the local Nusselt number and friction factor without the buoyancy force effects, by employing equation (1) along with the use of $F''(\xi, 0)$ and $-\theta'(\xi, 0)$ values listed in Table 1. The departure of these ratios from unity is then a direct measure of the influence of the buoyancy forces. Simple calculations will show that for $Gr_x/Re_x^{5/2} = 1.0$, for example, the Nu_x/Nu_{x0} ratios are about 1.317 and 1.016, respectively, for Pr = 0.7 and 7. This corresponds to an increase in the respective local

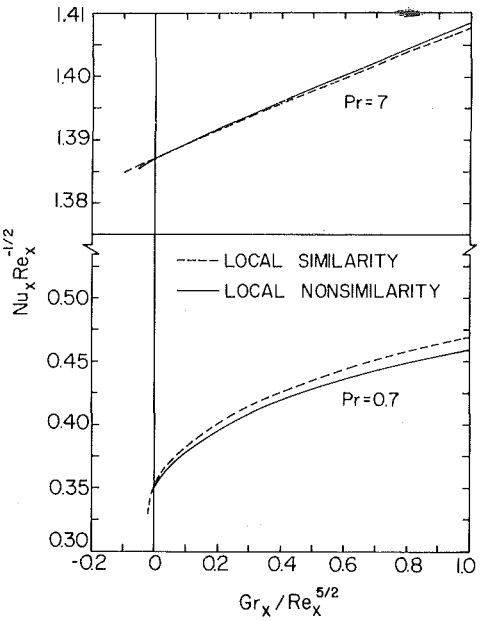

Fig. 3 The average Nusselt number results for Pr = 0.7 and 7

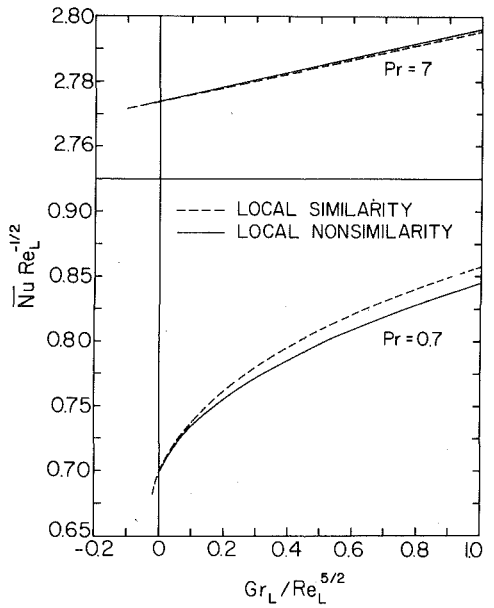

Fig. 2 The local Nusselt number results for Pr = 0.7 and 7

Nusselt numbers of 31.7 percent and 1.6 percent. Thus, it is evident that fluids having a Prandtl number of 0.7 (such as air) are much more responsive to the buoyancy force than fluids with a Prandtl number of 7 (such as water).

The reason the buoyancy force effect is larger in a fluid with Pr = 0.7 is due to the lower density of the fluid, which makes it more sensitive to the buoyancy-induced streamwise pressure gradients. This causes a larger change in the velocity gradients at the wall and hence a larger effect on the wall shear stress and surface heat transfer results. To illustrate this, representative velocity profiles are shown in Fig. 4. It can be seen that for fluids with Pr = 0.7, the velocity gradient at the wall increases from a negative value at zero buoyancy force to a positive value for $Gr_x/Re_x^{5/2} \geq 0.53$ as the buoyancy force increases. This is accompanied by an increase in the velocitieis near the wall, until finally there exists an overshoot and the velocities become greater than the plate velocity. For example, at $Gr_x/Re_x^{5/2} = 1.0$ the overshoot is about 6 percent. For a fluid with Pr = 7, the velocity gradient at the wall increases only slightly with an increase in the buoyancy force, even at $Gr_x/Re_x^{5/2} = 1.0$. This is because of the

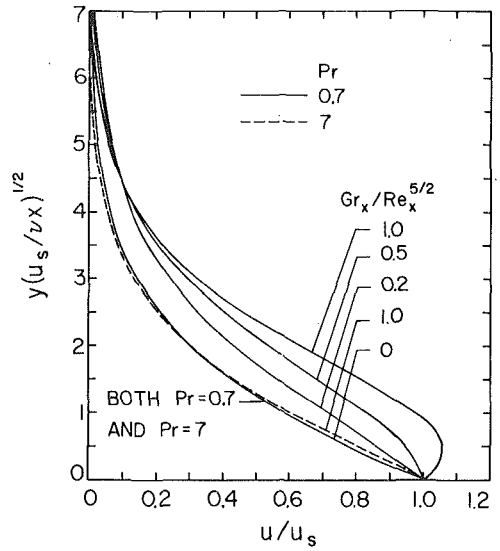

Fig. 4 Representative velocity profiles for Pr = 0.7 and 7

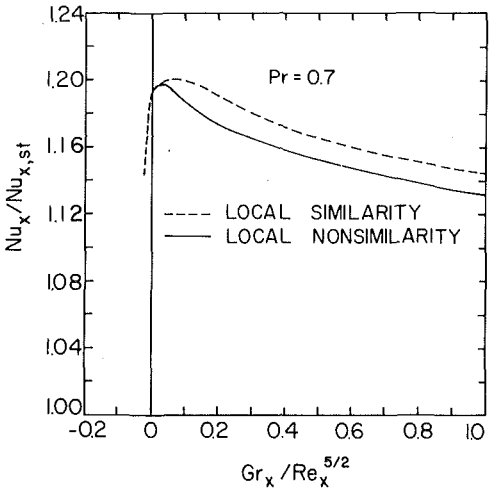

Fig. 5 A comparison of the local Nusselt numbers between the moving and stationary plates for Pr = 0.7

greater density of the fluid, which makes it less susceptible to the buoyancy force effects.

A comparison of the local Nusselt numbers between the moving plate and the stationary plate is illustrated in Fig. 5. The reference quantity $Nu_{x,st}$ denotes the local Nusselt number for a stationary plate [1]. As can be seen from the figure, the local Nusselt number ratio $Nu_x/Nu_{x,st}$ is larger than one. This is because the fluid particles near the plate surface have larger velocities and will carry away heat at a faster rate for the continuous, moving plate than for the stationary plate. For example, at $Gr_x/Re_x^{5/2} = 0$ the local Nusselt number is about 19.4 percent higher. When the buoyancy force assists the fluid motion, as the buoyancy force increases the Nusselt number ratio increases to a maximum of about 1.197 at $Gr_x/Re_x^{5/2} = 0.025$ and then decreases for $Gr_x/Re_x^{5/2} > 0.025$. When the buoyancy force opposes the fluid motion, as illustrated by the local similarity results, there is a sharp decrease in the local Nusselt number ratio, signifying a rapid decrease in the local Nusselt number as a result of the more pronounced bouyancy force effect on the continuous, moving plate.

References

1 Chen, T. S., Sparrow, E. M., and Mucoglu, A., "Mixed Convection in Boundary Layer Flow on a Horizontal Plate," ASME JOURNAL OF HEAT TRANSFER, Vol. 99, 1977, pp. 66–71.

2 Tsou, F. K., Sparrow, E. M., and Goldstein, R. J., "Flow and Heat Transfer in the Boundary Layer on a Continuous Moving Surface," *International Journal of Heat and Mass Transfer*, Vol. 10, 1967, pp. 219–235.

Cell Merging and Its Effect on Heat Transfer in Thermo-Solutal Convection

C. S. Reddy[1]

1 Introduction

Horizontal convecting layers are formed spontaneously under supercritical conditions if a stably stratified solution is subjected to steady horizontal temperature gradients. The wave number of the initially formed layered system depends upon the solute Rayleigh number. The adjacent layers of such a system merge with each other giving rise to layered systems of larger and larger wave lengths until a quasi-steady state is reached. This process is a subset of "diffusive" instability. Here heat, the higher diffusivity component, is destabilizing whereas solute, the lower diffusivity component, is stabilizing. On the other hand, if the faster diffusing component has a gravitationally stable density distribution and the slower diffusing one an unstable distribution, a phenomenon known as "salt fingering" takes place. Both the instabilities come under thermosolutal or double-diffusive convection and are discussed in detail by Turner [1]. Double-diffusive convection is a phenomenon that deals with the natural convection resulting from the diffusion of two (or more) components having different molecular diffusivities in a fluid. It has a number of applications in diverse fields ranging from oceanography to various engineering problems as described in [2].

Although double-diffusive convection has been studied extensively, the mechanism of layer merging, which is very important in the initial stages of layered convection, and its effect on heat transfer have remained almost unexplored. The objective of the present study, therefore, is to investigate these two aspects. Section 2 describes the mathematical formulation. The results are discussed in Section 3 and conclusions presented in Section 4.

2 Mathematical Formulation

The physical model and coordinate system are shown in Fig. 1. It is a two-dimensional slot having isothermal, infinitely long, vertical walls maintained at temperatures T_0 and $T_0 + \Delta T$. The region of interest has a width L and height H. The mathematical solution is assumed to be periodic over this height, which is so chosen that H is an even integer multiple of the expected layer thickness. The slot is filled with a two component fluid of T and S in such a way that the concentration S and density ρ increase with depth.

For the present physical model, the governing equations in the nondimensional form, subject to the Boussinesq approximation, are given by

$$\nabla^2\psi = -\omega \tag{1}$$

$$\frac{\partial\omega}{\partial t} = -J(\omega, \psi) + Pr\nabla^2\omega + PrRa\frac{\partial Tp}{\partial x} - \frac{PrRs}{Le}\frac{\partial Sp}{\partial x} \tag{2}$$

$$\frac{\partial Tp}{\partial t} = -J(Tp, \psi) + \nabla^2 Tp - \frac{\partial\psi}{\partial y} \tag{3}$$

$$\frac{\partial Sp}{\partial t} = -J(Sp, \psi) + \frac{1}{Le}\nabla^2 Sp - \frac{\mathrm{Ra}Le}{Rs}\frac{\partial\psi}{\partial y} + \frac{\partial\psi}{\partial x} \tag{4}$$

where

$$\mathrm{Pr} = \frac{\nu}{D_T}; \quad Le = \frac{D_T}{D_S} \tag{5}$$

$$\mathrm{Ra} = \frac{g\alpha\Delta TL^3}{\nu D_T}; \quad Rs = \frac{g\beta\phi L^4}{\nu D_s} \tag{6}$$

[1] Assistant Professor, Department of Mechanical Engineering and Mechanics, Old Dominion University, Norfolk, VA.

Contributed by the Heat Transfer Division for publication in the JOURNAL OF HEAT TRANSFER. Manuscript received by the Heat Transfer Division, September 1, 1979.

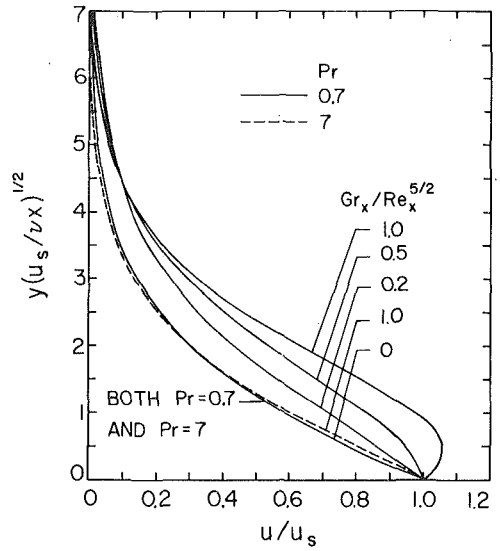

Fig. 4 Representative velocity profiles for Pr = 0.7 and 7

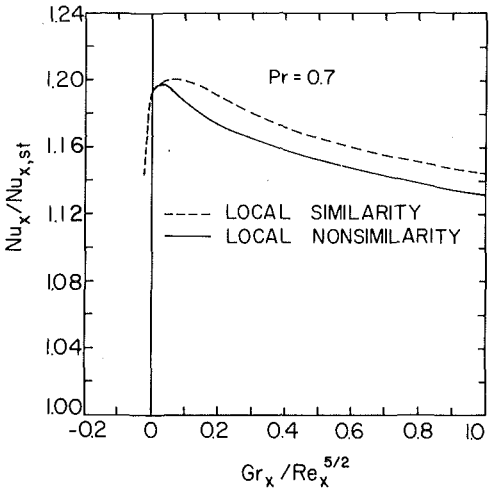

Fig. 5 A comparison of the local Nusselt numbers between the moving and stationary plates for Pr = 0.7

greater density of the fluid, which makes it less susceptible to the buoyancy force effects.

A comparison of the local Nusselt numbers between the moving plate and the stationary plate is illustrated in Fig. 5. The reference quantity $Nu_{x,st}$ denotes the local Nusselt number for a stationary plate [1]. As can be seen from the figure, the local Nusselt number ratio $Nu_x/Nu_{x,st}$ is larger than one. This is because the fluid particles near the plate surface have larger velocities and will carry away heat at a faster rate for the continuous, moving plate than for the stationary plate. For example, at $Gr_x/Re_x^{5/2} = 0$ the local Nusselt number is about 19.4 percent higher. When the buoyancy force assists the fluid motion, as the buoyancy force increases the Nusselt number ratio increases to a maximum of about 1.197 at $Gr_x/Re_x^{5/2} = 0.025$ and then decreases for $Gr_x/Re_x^{5/2} > 0.025$. When the buoyancy force opposes the fluid motion, as illustrated by the local similarity results, there is a sharp decrease in the local Nusselt number ratio, signifying a rapid decrease in the local Nusselt number as a result of the more pronounced bouyancy force effect on the continuous, moving plate.

References

1 Chen, T. S., Sparrow, E. M., and Mucoglu, A., "Mixed Convection in Boundary Layer Flow on a Horizontal Plate," ASME JOURNAL OF HEAT TRANSFER, Vol. 99, 1977, pp. 66–71.

2 Tsou, F. K., Sparrow, E. M., and Goldstein, R. J., "Flow and Heat Transfer in the Boundary Layer on a Continuous Moving Surface," *International Journal of Heat and Mass Transfer*, Vol. 10, 1967, pp. 219–235.

Cell Merging and Its Effect on Heat Transfer in Thermo-Solutal Convection

C. S. Reddy[1]

1 Introduction

Horizontal convecting layers are formed spontaneously under supercritical conditions if a stably stratified solution is subjected to steady horizontal temperature gradients. The wave number of the initially formed layered system depends upon the solute Rayleigh number. The adjacent layers of such a system merge with each other giving rise to layered systems of larger and larger wave lengths until a quasi-steady state is reached. This process is a subset of "diffusive" instability. Here heat, the higher diffusivity component, is destabilizing whereas solute, the lower diffusivity component, is stabilizing. On the other hand, if the faster diffusing component has a gravitationally stable density distribution and the slower diffusing one an unstable distribution, a phenomenon known as "salt fingering" takes place. Both the instabilities come under thermosolutal or double-diffusive convection and are discussed in detail by Turner [1]. Double-diffusive convection is a phenomenon that deals with the natural convection resulting from the diffusion of two (or more) components having different molecular diffusivities in a fluid. It has a number of applications in diverse fields ranging from oceanography to various engineering problems as described in [2].

Although double-diffusive convection has been studied extensively, the mechanism of layer merging, which is very important in the initial stages of layered convection, and its effect on heat transfer have remained almost unexplored. The objective of the present study, therefore, is to investigate these two aspects. Section 2 describes the mathematical formulation. The results are discussed in Section 3 and conclusions presented in Section 4.

2 Mathematical Formulation

The physical model and coordinate system are shown in Fig. 1. It is a two-dimensional slot having isothermal, infinitely long, vertical walls maintained at temperatures T_0 and $T_0 + \Delta T$. The region of interest has a width L and height H. The mathematical solution is assumed to be periodic over this height, which is so chosen that H is an even integer multiple of the expected layer thickness. The slot is filled with a two component fluid of T and S in such a way that the concentration S and density ρ increase with depth.

For the present physical model, the governing equations in the nondimensional form, subject to the Boussinesq approximation, are given by

$$\nabla^2\psi = -\omega \tag{1}$$

$$\frac{\partial\omega}{\partial t} = -J(\omega, \psi) + Pr\nabla^2\omega + PrRa\frac{\partial Tp}{\partial x} - \frac{PrRs}{Le}\frac{\partial Sp}{\partial x} \tag{2}$$

$$\frac{\partial Tp}{\partial t} = -J(Tp, \psi) + \nabla^2 Tp - \frac{\partial\psi}{\partial y} \tag{3}$$

$$\frac{\partial Sp}{\partial t} = -J(Sp, \psi) + \frac{1}{Le}\nabla^2 Sp - \frac{\mathrm{Ra}Le}{Rs}\frac{\partial\psi}{\partial y} + \frac{\partial\psi}{\partial x} \tag{4}$$

where

$$\mathrm{Pr} = \frac{\nu}{D_T}; \quad Le = \frac{D_T}{D_S} \tag{5}$$

$$\mathrm{Ra} = \frac{g\alpha\Delta TL^3}{\nu D_T}; \quad Rs = \frac{g\beta\phi L^4}{\nu D_s} \tag{6}$$

[1] Assistant Professor, Department of Mechanical Engineering and Mechanics, Old Dominion University, Norfolk, VA.

Contributed by the Heat Transfer Division for publication in the JOURNAL OF HEAT TRANSFER. Manuscript received by the Heat Transfer Division, September 1, 1979.

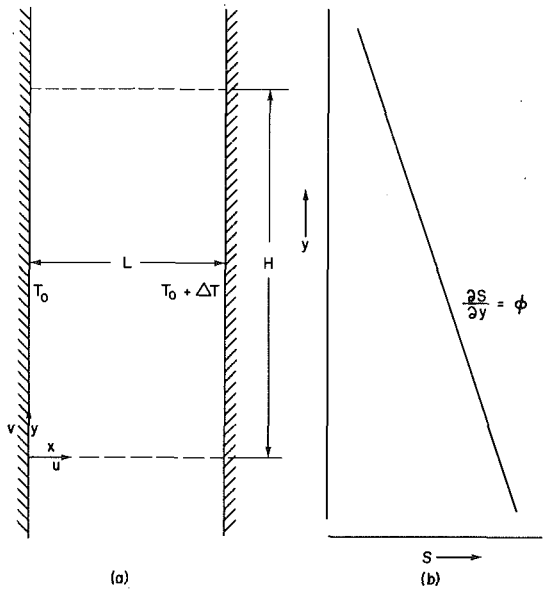

Fig. 1(*a*) Schematic diagram of slot containing linearly stratified fluid (*b*) initial solute profile

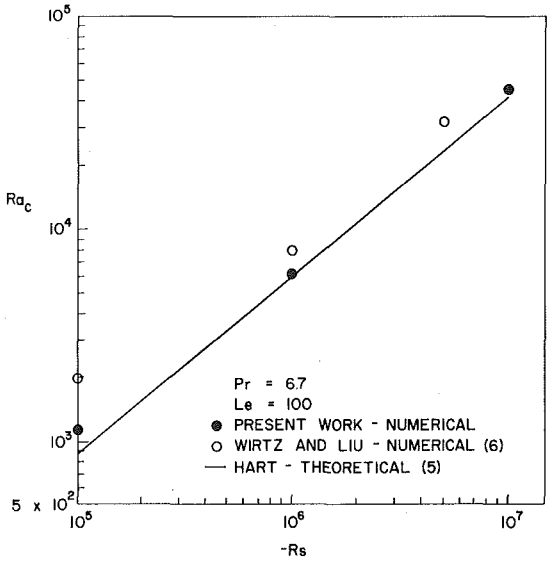

Fig. 2 Comparison of critical Rayleigh numbers

$$J(f, g) = \frac{\partial f}{\partial x}\frac{\partial g}{\partial y} - \frac{\partial f}{\partial y}\frac{\partial g}{\partial x} \tag{7}$$

and ψ is stream function and ω vorticity; α and β are the thermal and solute expansion coefficients; and D_T and D_S thermal and solute molecular diffusivities, respectively; and subscript p refers to perturbation quantities.

The above equations together with the appropriate initial and boundary conditions are numerically solved. (For details of the derivation and numerical solution, one may refer to Reddy [3, 4].)

3 Results and Discussion

In order to assess the accuracy of the numerical code developed and used, the predicted critical Rayleigh numbers are compared with the previous work [5, 6], as shown in Fig. 2, and found to agree favorably.

The evolution of the flow is depicted in the contour maps shown in Fig. 3. This figure corresponds to Rs = -10^6, Ra = 5×10^4, Pr = 6.7 and Le = 100 and time levels $t = 0.17$, and $t = 0.24$. The numerically

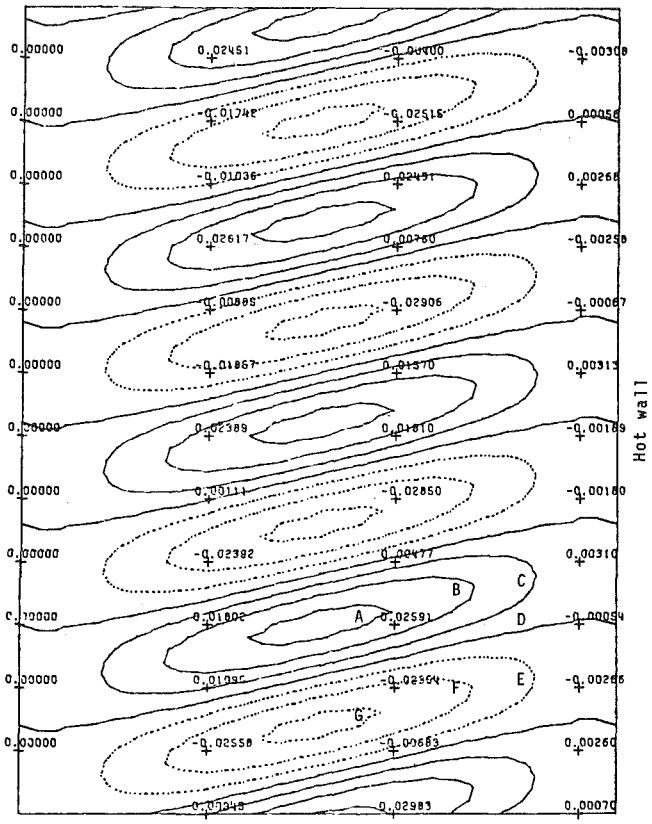

A = 0.03; B = 0.02; C = 0.01; D = 0.0; E = -0.01; G = -0.03.

Fig. 3(*a*) Contour map of stream function at $t = 0.17$

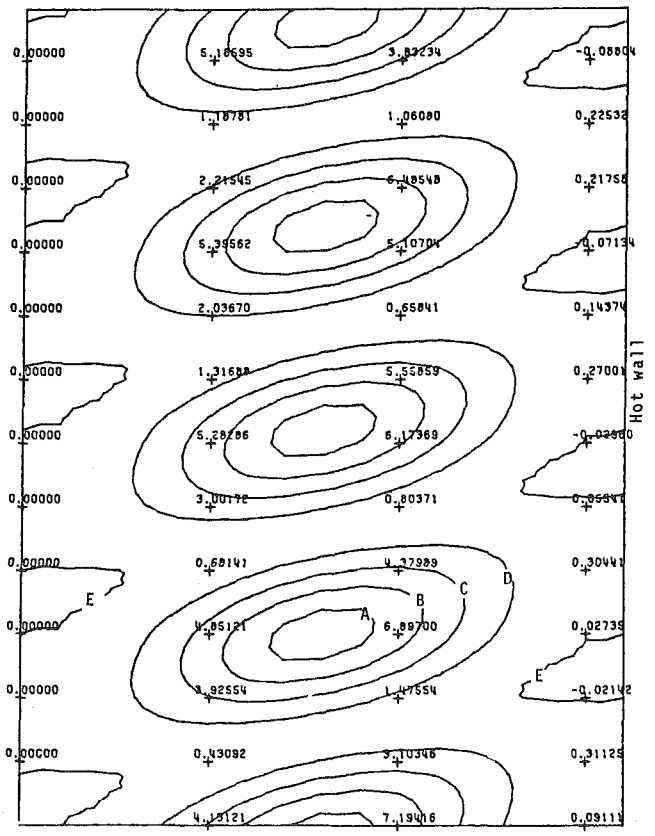

A = 8; B = 6; C = 4; D = 2; E = 0.

Fig. 3(*b*) Contour map of stream function at $t = 0.24$

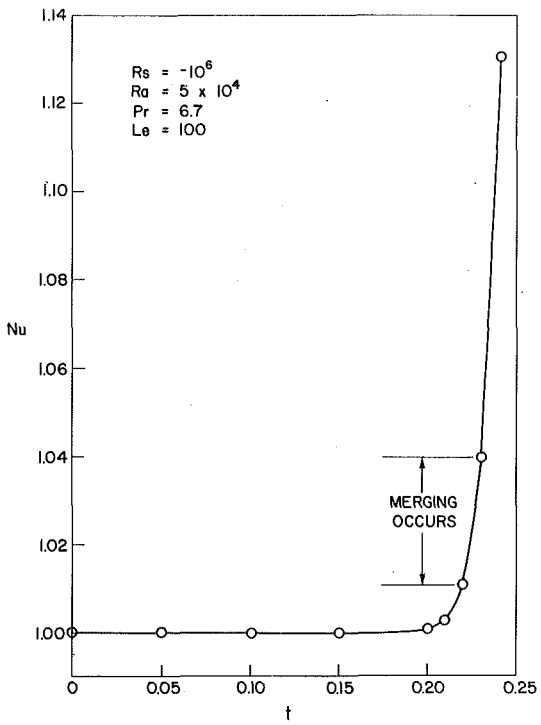

Fig. 4 Variation of Nusselt number with time showing the jump when merging of cells occurs

obtained critical thermal Rayleigh number corresponding to these conditions is 6.25×10^3. The nondimensional values of stream function at selected points are indicated by the numbers in the figures. The hot vertical boundary is on the right hand side and the cold one on the left.

Fig. 3(a) shows cells of almost equal size and strength but alternatingly rotating in opposite directions. They are inclined to the horizontal owing to the buoyancy effect. At this point the flow is less energetic as can be seen from the figure. The heated particles rise as high as their buoyancy permits and then turn away from the hot wall carrying with them some particles immediately above them because of viscous effects. The opposite happens on the cold wall (left hand side). As a result the clockwise rotating cells also exist in the early stages of flow development. However, this may appear at first "unnatural" given the fact that the hot wall is on the right. As the time progresses and the flow becomes more energetic, the counterclockwise rotating cells become stronger and stronger. The clockwise rotating cells, shown by dotted lines, become thinner and weaker as they are against the natural fluid motion and are finally annihilated as shown in Fig. 3(b). By this time, the first merging of cells is complete and well developed counter-clockwise rotating layers separated by the interfaces are formed. By looking at these figures, it can be visualized how the flow becomes more and more energetic as the time progresses. For example the absolute maximum dimensional velocity (calculated by assuming L = 2cm and $D_T = 1.5 \times 10^{-3}$ cm^2/s) has increased from 1.57×10^{-4} cm/s at t = 0.17 to 1.96×10^{-2} cm/s at t = 0.24. By examining Fig. 3(b) it can also be found that the horizontal velocity changes its direction in the interfaces between the cells.

As can be seen from Fig. 3, the counter-clockwise rotating cells are growing at the expense of the clock-wise rotating cells. This growth may be due to viscous interaction between the cells rotating in the opposite directions, and the boundary layer flow may not be a significant factor in bringing about the merging. It appears at this stage that no such flow exists as indicated by the contour maps of stream function (Fig. 3). Had there been a boundary layer, the contour lines would have been bunched up near the vertical boundary. However, there should be a boundary layer flow for any finite value of Rs. Probably it is extremely weak and confined to a very narrow layer, and so the numerical scheme might not be able to resolve it.

The Nusselt number increases with time as shown in Fig. 4. The increase is very little until the merging takes place as indicated by the curve. When the merging occurs, the Nusselt number increases very rapidly. The merging is almost complete by t = 0.23. By looking at the stream function contour maps produced at every time step, it is found that the merging has begun at about t = 0.22 when the clockwise rotating cells began to weaken. The rate of change of the Nusselt number dNu/dt has increased from 0.08 just before merging to 0.9 just after merging, thus registering an order of magnitude increase. An increase in the Nusselt number during merging is also observed in the experimental work of Reddy [4] at higher Rayleigh numbers.

4 Conclusions

The initially formed layers have pairs of cells rotating in opposite directions. These cells merge relatively quickly to form layers of double the original wave length. The sense of rotation of newly (after merging) formed layers is dictated by the location of the heat source causing the horizontal mean temperature gradients. It seems the mechanism that is responsible for bringing about the merging of the adjacent cells rotating in the mutually opposite directions is viscous interaction at the boundaries of the involved cells. There is no identifiable boundary layer flow at this stage of merging. The effect of merging is to rapidly increase the heat transfer.

Acknowledgment

This work was funded by the NSF under grant ENG 75-05337 and the Research Division of Clarkson College of Technology. The author gratefully acknowledges this support, and the help from Dr. R. A. Wirtz.

References

1 Turner, J. S., *Buoyancy Effects in Fluids*, Cambridge University Press, 1973.

2 Turner, J. S., "Double-Diffusive Phenomena," *Annual Review of Fluid Mechanics*, Vol. 6, 1974, pp. 37–56.

3 Reddy, C. S., "Double-Diffusive Convection in an Infinitely Tall Slot—A Numerical Study," ASME Paper 78-WA/HT-8, 1978.

4 Reddy, C. S., "Numerical and Experimental Investigation of Layer Merging in Double-Diffusive Convection in a Slot," *MIE Report 020*, Clarkson College of Technology, Potsdam, New York, 1976.

5 Hart, J. E., "On Sideways Diffusive Instability," *Journal of Fluid Mechanics*, Vol. 49, pp. 279–288, 1971.

6 Wirtz, R. A. and Liu, L. H., "Numerical Experiments on the Onset of Layered Convection in a Narrow Slot Containing a Stably Stratified Fluid," *International Journal Heat and Mass Transfer*, Vol. 18, 1975, pp. 1299–1305.

Periodic Vortex Formation in Combined Free and Forced Convection

P. A. Sandborn[1] and V. A. Sandborn[1]

Nomenclature

a = distance from potential source to stagnation point
R = radius of the heat source, approximately 2 mm
r = radial coordinate
θ = angular coordinate

Introduction

An experimental study of the heat transfer from horizontal cylinders in the region of equal opposed free and forced convection by Nayak and Sandborn [1] showed the existence of a low frequency,

[1] Department of Civil Engineering, Colorado State University, Fort Collins, CO 80523.

Contributed by the Heat Transfer Division for publication in the JOURNAL OF HEAT TRANSFER. Manuscript received by the Heat Transfer Division April 19, 1979.

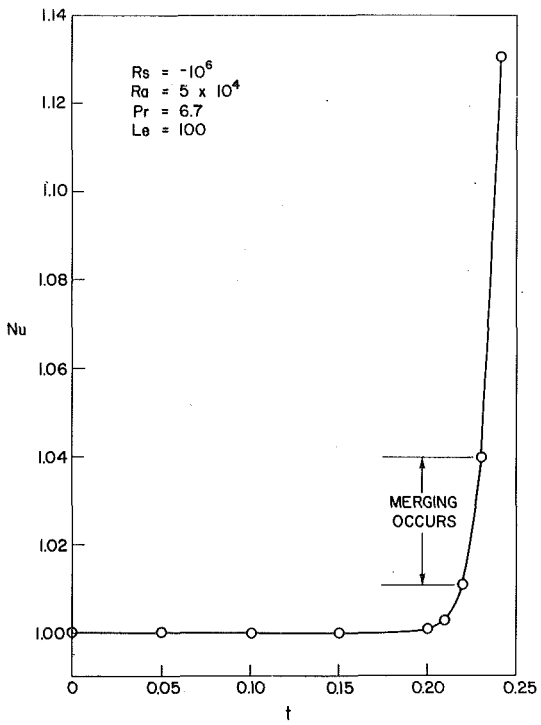

Fig. 4 Variation of Nusselt number with time showing the jump when merging of cells occurs

obtained critical thermal Rayleigh number corresponding to these conditions is 6.25×10^3. The nondimensional values of stream function at selected points are indicated by the numbers in the figures. The hot vertical boundary is on the right hand side and the cold one on the left.

Fig. 3(a) shows cells of almost equal size and strength but alternatingly rotating in opposite directions. They are inclined to the horizontal owing to the buoyancy effect. At this point the flow is less energetic as can be seen from the figure. The heated particles rise as high as their buoyancy permits and then turn away from the hot wall carrying with them some particles immediately above them because of viscous effects. The opposite happens on the cold wall (left hand side). As a result the clockwise rotating cells also exist in the early stages of flow development. However, this may appear at first "unnatural" given the fact that the hot wall is on the right. As the time progresses and the flow becomes more energetic, the counterclockwise rotating cells become stronger and stronger. The clockwise rotating cells, shown by dotted lines, become thinner and weaker as they are against the natural fluid motion and are finally annihilated as shown in Fig. 3(b). By this time, the first merging of cells is complete and well developed counter-clockwise rotating layers separated by the interfaces are formed. By looking at these figures, it can be visualized how the flow becomes more and more energetic as the time progresses. For example the absolute maximum dimensional velocity (calculated by assuming L = 2cm and $D_T = 1.5 \times 10^{-3}$ cm^2/s) has increased from 1.57×10^{-4} cm/s at t = 0.17 to 1.96×10^{-2} cm/s at t = 0.24. By examining Fig. 3(b) it can also be found that the horizontal velocity changes its direction in the interfaces between the cells.

As can be seen from Fig. 3, the counter-clockwise rotating cells are growing at the expense of the clock-wise rotating cells. This growth may be due to viscous interaction between the cells rotating in the opposite directions, and the boundary layer flow may not be a significant factor in bringing about the merging. It appears at this stage that no such flow exists as indicated by the contour maps of stream function (Fig. 3). Had there been a boundary layer, the contour lines would have been bunched up near the vertical boundary. However, there should be a boundary layer flow for any finite value of Rs. Probably it is extremely weak and confined to a very narrow layer, and so the numerical scheme might not be able to resolve it.

The Nusselt number increases with time as shown in Fig. 4. The increase is very little until the merging takes place as indicated by the curve. When the merging occurs, the Nusselt number increases very rapidly. The merging is almost complete by t = 0.23. By looking at the stream function contour maps produced at every time step, it is found that the merging has begun at about t = 0.22 when the clockwise rotating cells began to weaken. The rate of change of the Nusselt number dNu/dt has increased from 0.08 just before merging to 0.9 just after merging, thus registering an order of magnitude increase. An increase in the Nusselt number during merging is also observed in the experimental work of Reddy [4] at higher Rayleigh numbers.

4 Conclusions

The initially formed layers have pairs of cells rotating in opposite directions. These cells merge relatively quickly to form layers of double the original wave length. The sense of rotation of newly (after merging) formed layers is dictated by the location of the heat source causing the horizontal mean temperature gradients. It seems the mechanism that is responsible for bringing about the merging of the adjacent cells rotating in the mutually opposite directions is viscous interaction at the boundaries of the involved cells. There is no identifiable boundary layer flow at this stage of merging. The effect of merging is to rapidly increase the heat transfer.

Acknowledgment

This work was funded by the NSF under grant ENG 75-05337 and the Research Division of Clarkson College of Technology. The author gratefully acknowledges this support, and the help from Dr. R. A. Wirtz.

References

1 Turner, J. S., *Buoyancy Effects in Fluids*, Cambridge University Press, 1973.

2 Turner, J. S., "Double-Diffusive Phenomena," *Annual Review of Fluid Mechanics*, Vol. 6, 1974, pp. 37–56.

3 Reddy, C. S., "Double-Diffusive Convection in an Infinitely Tall Slot—A Numerical Study," ASME Paper 78-WA/HT-8, 1978.

4 Reddy, C. S., "Numerical and Experimental Investigation of Layer Merging in Double-Diffusive Convection in a Slot," *MIE Report 020*, Clarkson College of Technology, Potsdam, New York, 1976.

5 Hart, J. E., "On Sideways Diffusive Instability," *Journal of Fluid Mechanics*, Vol. 49, pp. 279–288, 1971.

6 Wirtz, R. A. and Liu, L. H., "Numerical Experiments on the Onset of Layered Convection in a Narrow Slot Containing a Stably Stratified Fluid," *International Journal Heat and Mass Transfer*, Vol. 18, 1975, pp. 1299–1305.

Periodic Vortex Formation in Combined Free and Forced Convection

P. A. Sandborn[1] and V. A. Sandborn[1]

Nomenclature

a = distance from potential source to stagnation point
R = radius of the heat source, approximately 2 mm
r = radial coordinate
θ = angular coordinate

Introduction

An experimental study of the heat transfer from horizontal cylinders in the region of equal opposed free and forced convection by Nayak and Sandborn [1] showed the existence of a low frequency,

[1] Department of Civil Engineering, Colorado State University, Fort Collins, CO 80523.

Contributed by the Heat Transfer Division for publication in the JOURNAL OF HEAT TRANSFER. Manuscript received by the Heat Transfer Division April 19, 1979.

periodic variation in heat transfer rate. Based on the measured heat transfer rate and visual observations of the smoke from a burning stick of incense, three specific flow regimes were identified:

1 A dominant free convection region at the lowest flow velocities; In this region, the heated plume, made visable by the smoke, rises above the heat source. As the downward velocity is increased, the motion of the plume becomes unsteady, but still maintains an upward motion near the heat source.
2 A region of equal free and forced convection; In this region the downward flow stagnates the free convection plume, and a "shroud" of heated air is produced around the heat source. This shroud increases in volume and temperature with time, and finally develops sufficient buoyancy to move upward against the downward forced flow. The development of the shroud of smoke and its rise above the source corresponds closely to the measured periodic variation in heat transfer rate measured for circular cylinders. The frequency of the periodic heat transfer rate was of the order of 0.1 to 1 cycle per minute for small (0.01 to 0.03 mm) cylinders.
3 A dominant forced convection region at higher opposed flow velocities; A critical point was found for the cylinder heat transfer rate where the fluctuations in the heat transfer rate ceased. At this critical point the average heat transfer rate was minimum. The downward flow then holds the shroud of heated fluid in a fixed position around the source, once the critical flow point is exceeded. The heat transfer through the shroud to the downward flow is sufficient to prevent the buildup of buoyant forces within the shroud.

The present study examines the shape of the heated air shroud as it develops in the periodic "bubbling" process. Turner [2] proposed that buoyant thermals could be modeled with an "expanding spherical vortex." Although Turner developed this model to explain the flow patterns of thermals created by different density fluids, the present note shows that it is also a useful model for the present observations of periodic shroud formation.

Flow Visualization

A low speed vertical wind tunnel with a 22.4 cm diameter test section was used for the study. Air was drawn into the tunnel through a small mesh screen. Velocities in the test section were of the order of 5 to 10 cm/s. A burning stick of incense, 4 mm in diameter, was placed vertically in the test section as shown in Fig. 1. A slide projector was used to produce a slit of light, which passed through the test section directly in front of the incense stick. Fig. 1(*a*) shows a typical periodic smoke pattern observed soon after the shroud forms around the heat source. Once a shroud of heated air obtains sufficient buoyant force, it rises above the heat source. When the shroud reaches a point where the main vortex motion is above the heat source, the pattern becomes distorted and appears to quickly lose its upward motion. The distorted vortex is carried downstream with the flow and a new shroud begins to form around the heat source. The new shroud develops as an elongated, nearly symmetrical, spherical vortex ring around the heat source. The stagnation of the rising buoyant fluid produces a vortex motion, which in turn draws cooler fluid into the region downstream of the heat source. For the periodic case, which corresponds to the flow conditions of Fig. 1(*a*), the spherical vortex expands with time until its buoyant force is sufficient to allow it to rise. The slight nonsymmetry of the spherical vortex in Fig. 1 is due to the development of ash and the nonuniform burning of the incense.

Fig. 1(*a*) depicts the general development of the shroud during the initial time period. If the forced convection is strong enough, the shroud is stretched in the downstream direction. It appears that for flows in the dominant forced convection region, the vortex system is "shed" in the downstream direction. This downstream shedding can result in a spiral vortex pattern, as demonstrated in Fig. 1(*b*). Note that the photograph of Fig. 1(*b*) was taken with total illumination rather than a slit of light. It is also possible for the shroud to develop an instability, which appears as a "rocking" motion. This rocking instability will also produce a spiral vortex pattern downstream of the heat source.

Fig. 2 shows the vortex patterns developed when the forced flow is not vertical, but at an angle with respect to the vertical. Fig. 2(*a*) shows the shroud just after it has formed, for the case where the forced flow makes an angle of 20 deg with the vertical. Fig. 2(*b*) was taken just after the shroud had risen above the heat source. Once the vortex system rises above the heat source, the upstream vortex side quickly stretches and becomes distorted. As the angle increases vortex motion on the lower side of the heat source ceases. Fig. 2(*c*), for an angle of 50 deg, shows the vortex system developing as an instability of the plume. The vortex systems of Fig. 2 all appear as noncircular rings. As the angle between the free and forced convection approaches 90 deg, the instability of the plume begins well downstream of the heat source. Thus, the periodic variation in heat transfer rate from an approximate point source will occur only when the angle between the

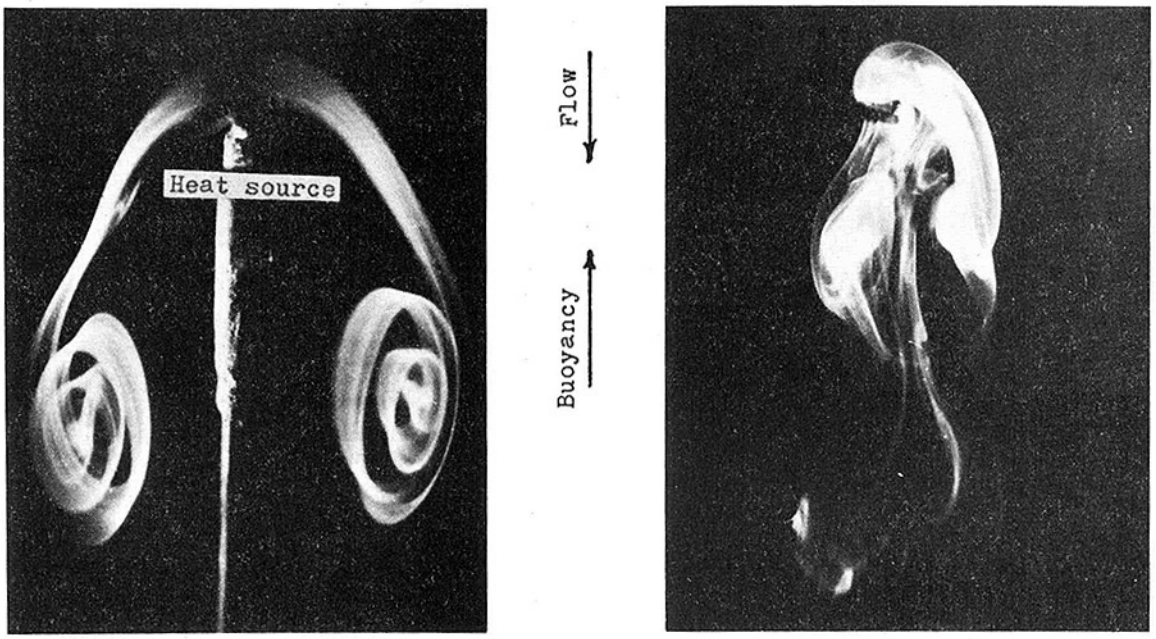

Fig. 1 (*a*) Periodic formed spherical vortex, air velocity 21.5 cm/s

Fig. 1 (*b*) Spiral vortex shedding, air velocity 25.5 cm/s

Fig. 1 Smoke visualization of the shroud of heated air around a point heat source in directly opposed flow

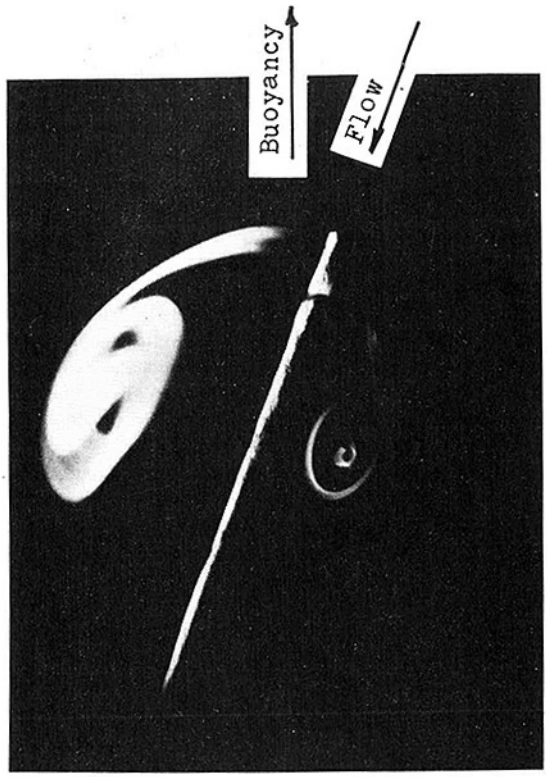

Fig. 2 (*a*) Periodic formed vortex, flow angle 20 deg, air velocity 30.7 cm/s

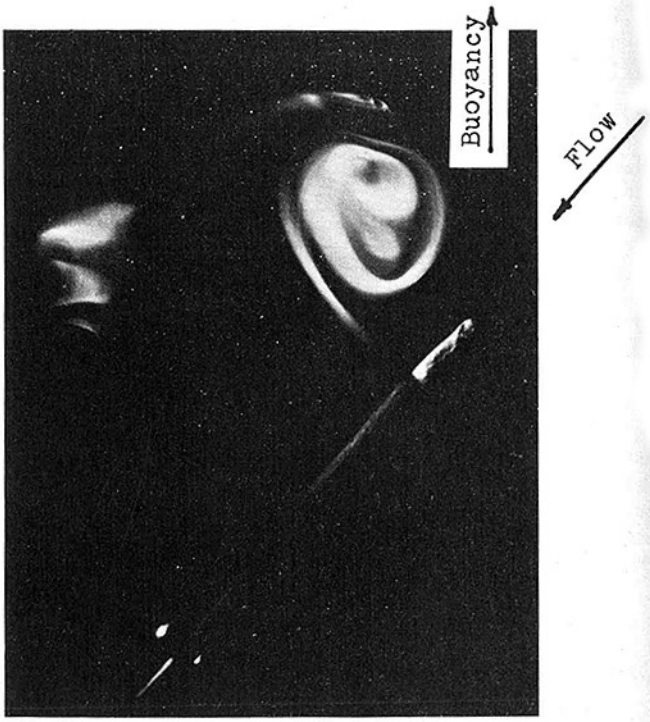

Fig. 2 (*c*) Unstable vortex formed in the plume, flow angle 50 deg, air velocity 17.6 cm/s

Fig. 2 Smoke visualization of the heat shroud formed when the forced convection is at an angle to the free convection

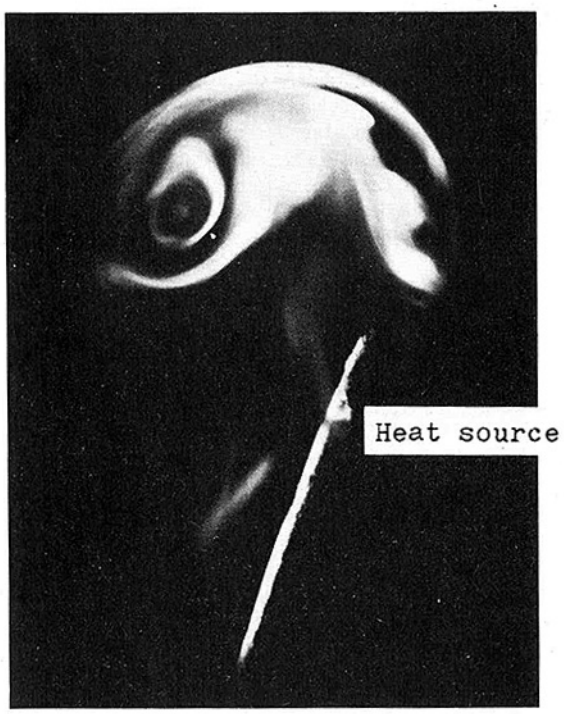

Fig. 2 (*b*) Vortex rising above the source, flow angle 20 deg, air velocity 22.4 cm/s

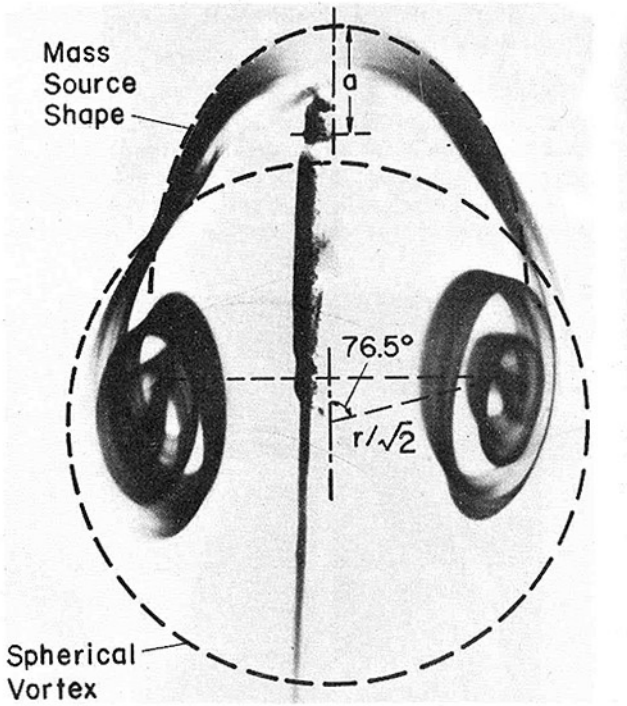

Fig. 3 Comparison of the directly opposed flow spherical vortex with Turner's expanding spherical vortex

free and forced convection is within approximately 45 deg of the vertical.

Expanding Spherical Vortex

The symmetrical vortex shown in Figure 1(*a*) appears to be similar to the ideal expanding spherical vortex proposed by Turner [2]. Fig. 3 compares the observed spherical vortex, Fig. 1(*a*), with the outline of Turner's expanding spherical vortex. The radius, r, of the expanding spherical vortex was defined from the location of the vortex eyes, as noted on Fig. 3. With the exception of the region very close to the heat source, the pattern defined by the smoke agrees closely with Turner's spherical vortex. The accuracy of the comparison is limited due to uncertainties in the location of the light "slice" with respect to the true center of the spherical vortex.

Near the heat source the flow is distorted, since the burning incense is both a heat and a mass source. An estimate of the equivalent "source" body obtained by a fit of the smoke outline with the source in a uniform stream, where the dividing streamline relation is

$$[r \sin(180\text{-}\theta)]^2 = 2a^2(1 + \cos\theta) \quad (1)$$

gives a value $2a/R = 10.88$, where $2a$ is the equivalent radius of the source body and R is the radius of the heat source.

Conclusions

The shroud of heated air formed around an approximate point heat source was found to be modeled by an expanding spherical vortex proposed by Turner. The expanding spherical vortex model can be used to explain the existence of time dependent heat transfer rates from bodies such as spheres, in the region of equal free and forced convection. Although the present visualization was limited to point heat sources, a similar two-dimensional vortex sheet pattern may be envisioned for heated cylinders.

The flow visualization method used in this work required the development of smoke (or mass flow) from the heat source. This mass flow may distort the thermal shroud slightly, so that a potential mass source flow shape is noted close to the heat source.

References

1 Nayak, S. K. and Sandborn, V. A., "Periodic Heat Transfer in Directly Opposed Free and Forced Convection Flow," *International Journal Heat and Mass Transfer*, Vol. 20, 1977, pp. 189–194.

2 Turner, J. S., "The Flow into an Expanding Spherical Vortex," *Journal Fluid Mechanics*, Vol. 18, 1964, pp. 195–208.

Conjugate Heat Transfer for Laminar Flow over a Plate with a Nonsteady Temperature at the Lower Surface

B. T. F. Chung[1] and S. A. Kassemi[2]

Introduction

In a recent paper, Wang et al. [1] presented an analysis for the transient conjugate heat transfer for a steady incompressible flow over a thick plate with a uniform heat flux at the bottom. However, the counter part of the problem with a prescribed surface temperature boundary condition has not yet been investigated. Complementary to [1], the present study considers a nonsteady step change in temperature at the lower surface of the plate. The physical situation is described in Fig. 1 of [1]. The notations of [1], except dimensionless temperatures, are also applicable to the present paper. The analysis parallels are given in [1]. To conserve space, its details are omitted here.

Analysis

Consider a system in which an incompressible fluid flows laminarly and steadily over a long plate with a finite thickness, w. Initially, both fluid and solid are at a temperature of T_∞. At an instant ($t = 0$) the lower surface of the solid plate is suddenly brought to a uniform temperature, T_w which is greater than T_∞. The heat is transferred from the bottom of the plate reaching the fluid-solid interface after a time t_0 which is referred to as penetration time. To find this penetration time, we apply the thermal penetration concept [2] and assume a third order temperature profile in the solid. Integrating the unsteady heat conduction equation with respect to space from 0 to δ, the thermal thickness, we obtain $t_0 = w^2/8\alpha_s$, which represents the time when the heat starts to affect the fluid temperature. The second time domain, therefore, begins at $t_2 = t - t_0$, at which time the fluid starts to "feel" the heat wave originating from the bottom of the plate. The governing equations describing the conjugate system in the second time domain are identical to those given by equations (5–13) of [1] except that the uniform wall heat flux condition (equation (11b)) is now replaced by the uniform wall temperature, $T_s = T_w$ at $y = -w$. Following the same approach presented in [1], we obtain the integral equations of the form

$$\left.\frac{\partial P_s}{\partial Y}\right|_{Y=0} - \left.\frac{\partial P_s}{\partial Y}\right|_{Y=-1} = \frac{1}{R}\frac{\partial}{\partial \tau_2}\int_{Y=-1}^{0} P_s dY \quad (1)$$

$$\frac{\partial}{\partial \tau_2}\int_0^\Delta P dY + \frac{\partial}{\partial X}\int_0^\Delta UP dY = -\left.\frac{\partial P}{\partial Y}\right|_{Y=0} \quad (2)$$

where the dimensionless temperatures for fluid and solid, P and P_s are defined as $(T - T_\infty)/(T_w - T_\infty)$ and $(T_s - T_\infty)/(T_w - T_\infty)$ respectively and $R = \alpha/\alpha_s$. They may be in terms of interfacial temperature, P_0 and thermal boundary layer, Δ as

$$P = P_0\left(1 - \frac{Y}{\Delta}\right)^2 \quad (3)$$

and

$$P_s = P_0 - \frac{2KP_0}{\Delta}Y + \left[1 - \left(1 + \frac{2K}{\Delta}\right)P_0\right]Y^2 \quad (4)$$

where K is conductivity ratio, k/k_s. Equations (3) and (4) satisfy the boundary conditions: $P_s = 1$ at $Y = -1$, $P = \partial P/\partial Y = 0$ at $Y = \Delta$, $P = P_s = P_0$ at $Y = 0$ and $K\partial P/\partial Y = \partial P_s/\partial Y$ at $Y = 0$. Solutions to equations (1–4) depend on the velocity of the flow, U. Three different types of velocity are considered. They are in terms of uniform, linear and third order polynomial in Y.

Uniform Velocity Profile. Substituting equations (3–4) into equation (2) along with slug flow assumption, $U = 1$, we arrive at

$$\frac{\partial}{\partial \tau_2}(P_0\Delta) + \frac{\partial}{\partial X}(P_0\Delta) = \frac{6P_0}{\Delta} \quad (5)$$

Using equation (1) along with its boundary conditions and substituting for P_s from equation (4) results:

$$\frac{\partial}{\partial \tau_2}\left(\frac{P_0}{\Delta}\right) + \frac{2}{K}\frac{\partial P_0}{\partial \tau_2} + 12R\left(\frac{P_0}{\Delta}\right) + \frac{6R}{K}P_0 = \frac{6R}{K} \quad (6)$$

Integrating equation (6) gives

$$\frac{P_0}{\Delta} = \frac{1}{2K}[1 - \mathrm{EXP}(-12R\tau_2)] - \frac{2P_0}{K} + \frac{18R}{K} \times \mathrm{EXP}(-12R\tau_2)\int_0^{\tau_2} P_0(X,\xi)\,\mathrm{EXP}(12R\xi)d\xi \quad (7)$$

To obtain an expression for the interfacial temperature P_0, equation (7) is combined with equation (5) to eliminate Δ. The final result becomes

$$\left(\frac{2G}{P_0} + \frac{2}{K}\right)\frac{\partial P_0}{\partial \tau_2} + \left(\frac{2G}{P_0} + \frac{2}{K}\right)\frac{\partial P_0}{\partial X} - 18\frac{R}{K}\mathrm{EXP}(-12R\tau_2)\int_0^{\tau_2}\frac{\partial P_0}{\partial X} \times \mathrm{EXP}(12R\xi)\,d\xi = -12RG - \frac{6RP_0}{K} + \frac{6R}{K} + \frac{6G^3}{P_0^2} \quad (8)$$

where

$$G = \frac{P_0}{\Delta} = \frac{1}{2K}[1 - \mathrm{EXP}(-12R\tau_2) - \frac{2P_0}{K} + 18R\frac{\mathrm{EXP}(-12\tau_2)}{K}\int_0^{\tau_2} P_0(X,\xi)\,\mathrm{EXP}(12R\xi)\,d\xi \quad (9)$$

The above integral differential equation is solved using a finite difference scheme with the aid of conditions $P_0(0,\tau_2) = P_0(X,0) = 0$.

[1] Associate Professor, Department of Mechanical Engineering, The University of Akron, Akron, Ohio 44325. Mem. ASME.

[2] Graduate Assistant, Department of Mechanical Engineering, The University of Akron, Akron, Ohio 44325, presently with J. T. Associate Inc., Akron, Ohio.

Contributed by the Heat Transfer Division for publication in the JOURNAL OF HEAT TRANSFER. Manuscript received by the Heat Transfer.

Near the heat source the flow is distorted, since the burning incense is both a heat and a mass source. An estimate of the equivalent "source" body obtained by a fit of the smoke outline with the source in a uniform stream, where the dividing streamline relation is

$$[r \sin(180\text{-}\theta)]^2 = 2a^2(1 + \cos\theta) \quad (1)$$

gives a value $2a/R = 10.88$, where $2a$ is the equivalent radius of the source body and R is the radius of the heat source.

Conclusions

The shroud of heated air formed around an approximate point heat source was found to be modeled by an expanding spherical vortex proposed by Turner. The expanding spherical vortex model can be used to explain the existence of time dependent heat transfer rates from bodies such as spheres, in the region of equal free and forced convection. Although the present visualization was limited to point heat sources, a similar two-dimensional vortex sheet pattern may be envisioned for heated cylinders.

The flow visualization method used in this work required the development of smoke (or mass flow) from the heat source. This mass flow may distort the thermal shroud slightly, so that a potential mass source flow shape is noted close to the heat source.

References

1 Nayak, S. K. and Sandborn, V. A., "Periodic Heat Transfer in Directly Opposed Free and Forced Convection Flow," *International Journal Heat and Mass Transfer*, Vol. 20, 1977, pp. 189–194.

2 Turner, J. S., "The Flow into an Expanding Spherical Vortex," *Journal Fluid Mechanics*, Vol. 18, 1964, pp. 195–208.

Conjugate Heat Transfer for Laminar Flow over a Plate with a Nonsteady Temperature at the Lower Surface

B. T. F. Chung[1] and S. A. Kassemi[2]

Introduction

In a recent paper, Wang et al. [1] presented an analysis for the transient conjugate heat transfer for a steady incompressible flow over a thick plate with a uniform heat flux at the bottom. However, the counter part of the problem with a prescribed surface temperature boundary condition has not yet been investigated. Complementary to [1], the present study considers a nonsteady step change in temperature at the lower surface of the plate. The physical situation is described in Fig. 1 of [1]. The notations of [1], except dimensionless temperatures, are also applicable to the present paper. The analysis parallels are given in [1]. To conserve space, its details are omitted here.

Analysis

Consider a system in which an incompressible fluid flows laminarly and steadily over a long plate with a finite thickness, w. Initially, both fluid and solid are at a temperature of T_∞. At an instant ($t = 0$) the lower surface of the solid plate is suddenly brought to a uniform temperature, T_w which is greater than T_∞. The heat is transferred from the bottom of the plate reaching the fluid-solid interface after a time t_0 which is referred to as penetration time. To find this penetration time, we apply the thermal penetration concept [2] and assume a third order temperature profile in the solid. Integrating the unsteady heat conduction equation with respect to space from 0 to δ, the thermal thickness, we obtain $t_0 = w^2/8\alpha_s$, which represents the time when the heat starts to affect the fluid temperature. The second time domain, therefore, begins at $t_2 = t - t_0$, at which time the fluid starts to "feel" the heat wave originating from the bottom of the plate. The governing equations describing the conjugate system in the second time domain are identical to those given by equations (5–13) of [1] except that the uniform wall heat flux condition (equation (11b)) is now replaced by the uniform wall temperature, $T_s = T_w$ at $y = -w$. Following the same approach presented in [1], we obtain the integral equations of the form

$$\left.\frac{\partial P_s}{\partial Y}\right|_{Y=0} - \left.\frac{\partial P_s}{\partial Y}\right|_{Y=-1} = \frac{1}{R}\frac{\partial}{\partial \tau_2}\int_{Y=-1}^{0} P_s dY \quad (1)$$

$$\frac{\partial}{\partial \tau_2}\int_0^\Delta P dY + \frac{\partial}{\partial X}\int_0^\Delta UP dY = -\left.\frac{\partial P}{\partial Y}\right|_{Y=0} \quad (2)$$

where the dimensionless temperatures for fluid and solid, P and P_s are defined as $(T - T_\infty)/(T_w - T_\infty)$ and $(T_s - T_\infty)/(T_w - T_\infty)$ respectively and $R = \alpha/\alpha_s$. They may be in terms of interfacial temperature, P_0 and thermal boundary layer, Δ as

$$P = P_0\left(1 - \frac{Y}{\Delta}\right)^2 \quad (3)$$

and

$$P_s = P_0 - \frac{2KP_0}{\Delta}Y + \left[1 - \left(1 + \frac{2K}{\Delta}\right)P_0\right]Y^2 \quad (4)$$

where K is conductivity ratio, k/k_s. Equations (3) and (4) satisfy the boundary conditions: $P_s = 1$ at $Y = -1$, $P = \partial P/\partial Y = 0$ at $Y = \Delta$, $P = P_s = P_0$ at $Y = 0$ and $K\partial P/\partial Y = \partial P_s/\partial Y$ at $Y = 0$. Solutions to equations (1–4) depend on the velocity of the flow, U. Three different types of velocity are considered. They are in terms of uniform, linear and third order polynomial in Y.

Uniform Velocity Profile. Substituting equations (3–4) into equation (2) along with slug flow assumption, $U = 1$, we arrive at

$$\frac{\partial}{\partial \tau_2}(P_0\Delta) + \frac{\partial}{\partial X}(P_0\Delta) = \frac{6P_0}{\Delta} \quad (5)$$

Using equation (1) along with its boundary conditions and substituting for P_s from equation (4) results:

$$\frac{\partial}{\partial \tau_2}\left(\frac{P_0}{\Delta}\right) + \frac{2}{K}\frac{\partial P_0}{\partial \tau_2} + 12R\left(\frac{P_0}{\Delta}\right) + \frac{6R}{K}P_0 = \frac{6R}{K} \quad (6)$$

Integrating equation (6) gives

$$\frac{P_0}{\Delta} = \frac{1}{2K}[1 - \mathrm{EXP}(-12R\tau_2)] - \frac{2P_0}{K} + \frac{18R}{K} \times \mathrm{EXP}(-12R\tau_2)\int_0^{\tau_2} P_0(X,\xi)\,\mathrm{EXP}(12R\xi)d\xi \quad (7)$$

To obtain an expression for the interfacial temperature P_0, equation (7) is combined with equation (5) to eliminate Δ. The final result becomes

$$\left(\frac{2G}{P_0} + \frac{2}{K}\right)\frac{\partial P_0}{\partial \tau_2} + \left(\frac{2G}{P_0} + \frac{2}{K}\right)\frac{\partial P_0}{\partial X} - 18\frac{R}{K}\mathrm{EXP}(-12R\tau_2)\int_0^{\tau_2}\frac{\partial P_0}{\partial X} \times \mathrm{EXP}(12R\xi)\,d\xi = -12RG - \frac{6RP_0}{K} + \frac{6R}{K} + \frac{6G^3}{P_0^2} \quad (8)$$

where

$$G = \frac{P_0}{\Delta} = \frac{1}{2K}[1 - \mathrm{EXP}(-12R\tau_2) - \frac{2P_0}{K} + 18R\frac{\mathrm{EXP}(-12\tau_2)}{K}\int_0^{\tau_2} P_0(X,\xi)\,\mathrm{EXP}(12R\xi)\,d\xi \quad (9)$$

The above integral differential equation is solved using a finite difference scheme with the aid of conditions $P_0(0,\tau_2) = P_0(X,0) = 0$.

[1] Associate Professor, Department of Mechanical Engineering, The University of Akron, Akron, Ohio 44325. Mem. ASME.

[2] Graduate Assistant, Department of Mechanical Engineering, The University of Akron, Akron, Ohio 44325, presently with J. T. Associate Inc., Akron, Ohio.

Contributed by the Heat Transfer Division for publication in the JOURNAL OF HEAT TRANSFER. Manuscript received by the Heat Transfer.

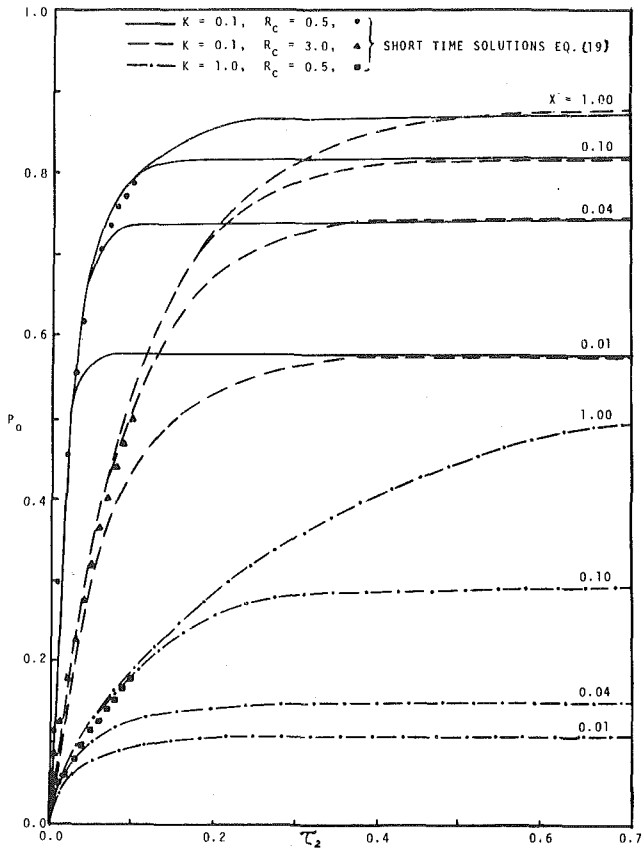

Fig. 1 Transient fluid-solid interfacial temperature of a slug flow

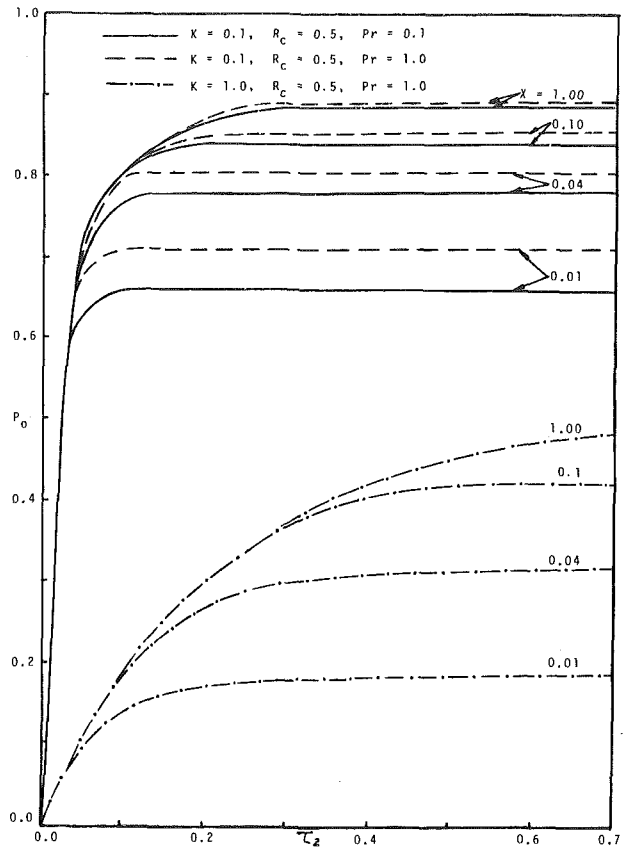

Fig. 2 Transient fluid-solid interfacial temperature of a boundary layer flow with a third order velocity profile

Third and Linear Order Velocity Profiles. To study a more general case, the following profile is considered:

$$U = \frac{3A}{2}\left(\frac{Y}{c\sqrt{X}}\right) - \frac{B}{2}\left(\frac{Y}{c\sqrt{X}}\right)^3 \tag{10}$$

where $A = B = 1$ are applicable for moderate Prandtl numbers and $A = 1.1067$, $B = 0$ for flow with higher Prandtl numbers. Note c in equation (10) is a function of Prandtl number only, i.e., $c = 5\sqrt{\text{Pr.}}$ $\delta_h = c\sqrt{X}$ represents hydrodynamic boundary layer thickness. Combining equations (2, 3, 9) and (10) and rearranging, we obtain

$$\left(\frac{2}{3}P_0G^4 + \frac{2}{3K}P_0^2G^3\right)\frac{\partial P_0}{\partial \tau_2} + \left(\frac{3A}{8C\sqrt{X}}\right)P_0^2G^3 + \frac{A}{2CK\sqrt{X}}P_0^3G^2 - \frac{B}{24C^3X^{3/2}}GP_0^4 - \frac{B}{15C^3KX^{3/2}}P_0^5\Bigg)\frac{\partial P_0}{\partial X} + \frac{18R}{K}\left(-\frac{A}{4C\sqrt{X}}P_0^3G^2 + \frac{B}{30C^3X^{3/2}}P_0^5\right)\text{EXP}\,(-12R\tau_2) \times \int_0^{\tau_2}\frac{\partial}{\partial X}P_0(X,\xi)\,\text{EXP}\,(12R\xi)\,d\xi = 2G^6 - 4RG^4P_0^2 + \left(\frac{A}{16CX^{3/2}} - \frac{2R}{K}\right)P_0^3G^3 - \frac{BG}{80C^3X^{5/2}}P_0^5 + \frac{2R}{K}G^3P_0^2 \tag{11}$$

The finite difference representation of equation (11) leads to a sixth order polynomial algebraic equation in terms of P_0 and fourth order in P_0, if $B = 0$ [3].

Case of Arbitrary Temperature at the Lower Surface. Above analyses are restricted to the case of a uniform step temperature input at the bottom. A more general boundary condition at the lower surface is considered which is an arbitrary function of time. Using Duhamel's integral theorem, the numerical results in the previous sections can be used directly to give a corresponding result for the case of an arbitrary time dependent temperature change, i.e., the new fluid-solid interfacial temperature, $S_0(X, \tau_2)$ can be obtained from the following relation:

$$S_0(X,\tau_2) = \int_0^{\tau_2} F(\lambda)\frac{\partial}{\partial \tau_2}P_0\,(X, \tau_2 - \lambda)\,d\lambda \tag{12}$$

where $F(\tau_2)$ is any time variant disturbance introduced at the bottom of the solid plate. For an example, when $F(\tau_2) = \tau_2$, equation (12) gives

$$S_0(\tau_2) = \int_0^{\tau_2} P_0(\xi)\,d\xi \tag{13}$$

Results and Discussion

Numerical results based on the above analysis are illustrated graphically. Details of the associated computer program have been well documented in [3]. It is noted that, although the solutions of equations (8) and (11) require the use of digital computers, the present approach is much simpler as compared with the direct finite difference solution of the original partial differential equations.

Interfacial Temperature. The predicted transient local interfacial temperature based on the slug flow and the general boundary layer flow models are shown in Figs. 1 and 2, respectively, for given values of K and R_c where $R_c = (\rho C_p)_s/\rho C_p$. For a given capacity ratio, the higher the values of conductivity ratio, the lower the interfacial temperature. For a fixed conductivity ratio, as the capacitance ratio increases the interfacial temperature decreases. In the case of higher wall capacitance, more time is required for the system to reach steady state. The same trends are found in the earlier work [1].

Local Nusselt Numbers and Comparison of Results Under Two Extreme Boundary Conditions. Numerical calculations of local Nusselt number for slug flow is shown in Fig. 3. The case with uniform heat flux boundary condition at the bottom of the plate reproduced from [1] is also shown on the same figure for comparison purposes. Note that we can only compare Nusselt numbers but not the dimensionless interfacial temperatures since the former are defined identically in both cases, i.e., $\text{Nu}_w = hw/k = -(\partial P/\partial Y)_{Y=0}/P_0$ while the latter are defined differently.

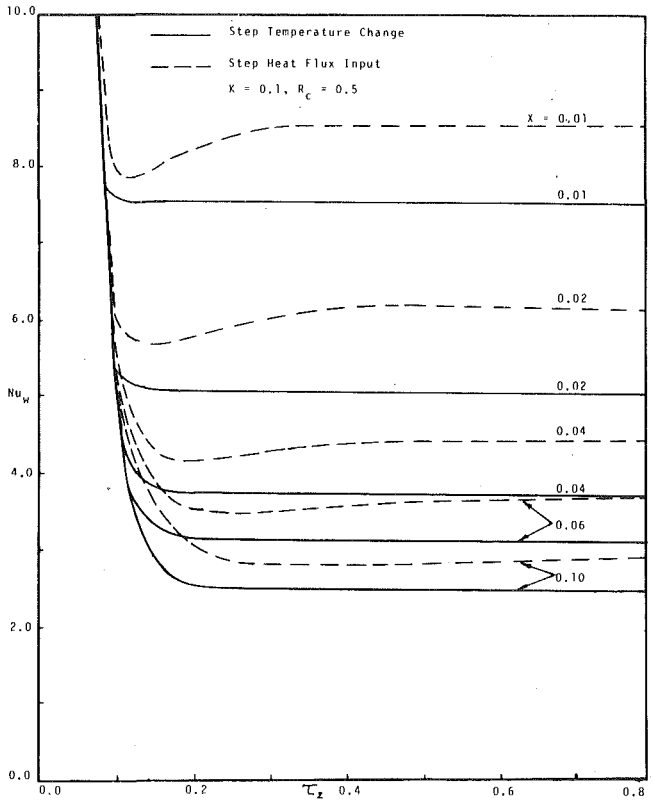

Fig. 3 Local nusselt number for slug flow as compared with its counterpart with a step heat flux input

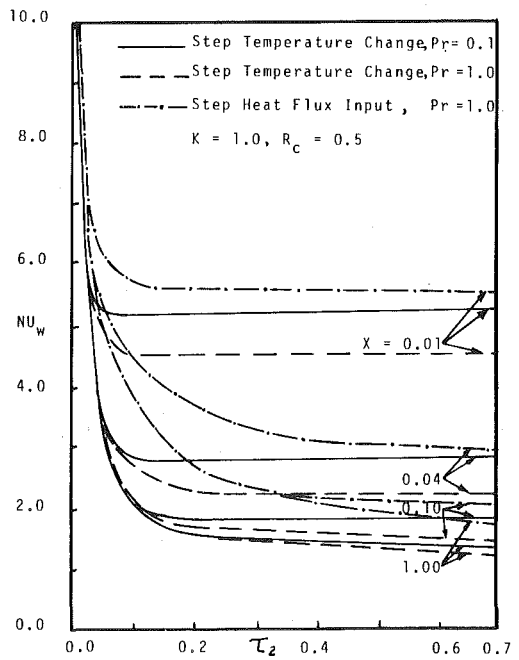

Fig. 4 Local nusselt number for a boundary layer flow with a third order velocity profile

It can be seen that under the same physical parameters the values of Nusselt number for the case of a step heat flux are always greater than the corresponding ones with uniform wall temperature condition. As time becomes large a fixed ratio between the Nusselt numbers is detected. Under steady state and slug flow condition, this ratio, r can be obtained in closed form by solving the pertaining differential equations. The result is

$$r = \frac{\mathrm{Nu}_{\textcircled{q}}}{\mathrm{Nu}_{\textcircled{T}}} = \frac{\sqrt{\pi}/2\ \mathrm{Re}_x^{0.5}\mathrm{Pr}^{0.5}}{(\mathrm{Pr}^{0.5}\mathrm{Re}_x^{0.5}\, z e^{z^2}\,\mathrm{erfc}\, z)/(1 - e^{z^2}\,\mathrm{erfc}\, z)} \tag{14}$$

where $z = \sqrt{X}/K$. The denominator of equation (14) agrees with Luikov's [4][3] solution. As a limit, when z in equation (14) approaches infinity, r becomes $\pi/2$. Numerical calculations show that equation (14) agrees well with the present approximate solutions shown in Fig. 3. Fig. 4 illustrates Nusselt number versus time based on the third order velocity profile. Comparisons to the case of a step heat flux input is made in all cases. In Figs. 3 and 4, the Nusselt number appears to decrease as Pr increases for given X. This is due to the dependence of X on Re and Pr in the first degree, i.e., $X = 4x/(w\mathrm{Re}_w\mathrm{Pr})$.

Limiting Solutions. It is of interest to compare present limiting solutions with the exact analytical solutions available in the literature [4–6]. All of them are for slug flow situation. We consider the following three cases, (1) steady interfacial temperature with wall resistance, (2) unsteady heat transfer without wall resistance and capacitance, and (3) same as case (2) except that the wall surface temperature is a linear function of time.

The steady interface temperature for slug flow model can be solved from equations (5) and (6) analytically by setting $\partial/\partial\tau_2 = 0$. There is obtained

$$z^2 = \frac{X}{K^2} = \frac{1}{3}\left[\left(\frac{P_0}{1-P_0}\right)^2 + \frac{2P_0}{1-P_0} + 2\,\ell\mathrm{n}(1-P_0)\right] \tag{15}$$

The corresponding exact analytical solution is available in [4]

$$P_0 = 1 - z^2\,\mathrm{erfc}\, z$$

It is found that equation (15) agrees excellently with the above equation with a maximum error of 3.4 percent.

When both the resistance and the capacitance of the solid plate approach zero, P_0 becomes independent of τ_2 and X. The resulting equation (5) can be solved exactly. It gives the ratio of Nusselt numbers at transient and steady states:

$$\frac{q_w}{q_{ws}} = \frac{\mathrm{Nu}_w}{\mathrm{Nu}_{ws}} = \frac{\Delta_s}{\Delta} = \begin{cases} \left(\dfrac{\tau_2}{X}\right)^{-1/2} & \text{for } \dfrac{\tau_2}{X} \le 1 \\ 1 \text{ for } \dfrac{\tau_2}{X} \ge 1 \end{cases} \tag{16}$$

where the subscript s implies steady state. Equation (16) compares well with the results of Chao and Cheema [5] for small Prandtl number (Pr = 0.01).

For the case where a linear time variant temperature disturbance, $F(\tau_2) = \tau_2$, is introduced to the lower surface of the plate with negligible wall resistance and capacitance, equation (5) reduces to

$$\frac{\partial}{\partial\tau_2}(\tau_2\Delta) + \frac{\partial}{\partial X}(\tau_2\Delta) = \frac{6\tau_2}{\Delta} \tag{17}$$

Laplace transform is employed and the following expression is obtained

$$\frac{q_w}{q_{ws}'} = \begin{cases} \sqrt{3}\,(X/\tau_2)^{0.5} & \text{for } \tau_2/X \le 1 \\ 1\Big/\left[1 - \dfrac{\dot{X}}{\tau_2} + \dfrac{1}{3}\left(\dfrac{X}{\tau_2}\right)^2\right]^{0.5} & \text{for } \tau_2/X \ge 1 \end{cases} \tag{18}$$

where q_{ws}' is quasi-steady solution, i.e., the steady wall heat flux when a uniform wall temperature is imposed. Equation (18) agrees reasonably well with the analytical solution obtained by Cess [6] for Pr = 0.01.

Short Time Solution. When time is very small, the convective effect is insignificant. The terms $u\partial T/\partial X$ and $v\partial T/\partial y$ can be neglected as compared with $\partial T/\partial t$. The problem is reduced to the unsteady heat conduction in two-layer composite media. Under this condition, the solution for the interfacial temperature is obtained from Laplace transform

[3] A typographical error appears in equation (3.15) of [4], π should be replaced by $\sqrt{\pi}$ on the right hand side of this equation.

$$P_0 = \frac{2}{1+\sqrt{K/R_c}} \sum_{n=0}^{\infty} \left\{ \left[\frac{\sqrt{\frac{K}{R_c}} - 1}{\sqrt{\frac{K}{R_c}} + 1} \right]^n \times \operatorname{erfc} \frac{(2n+1)\sqrt{R_c K}}{2\sqrt{\tau_2 + KR_c/8}} \right\} \quad (19)$$

Numerical computations show a good agreement between equation (19) and the present numerical solution for small time, ($\tau_2 < 0.1$) as illustrated in Fig. 1.

References

1 Wang, R. C. C., Chung, B. T. F., and Thomas, L. C., "Transient Convective Heat Transfer for Laminar Boundary Layer Flow with Effects of Wall Capacitance and Resistance," ASME JOURNAL OF HEAT TRANSFER, Vol. 89, 1977, p. 513.

2 Arpaci, V. S., *Conduction Heat Transfer,* Addison-Wesley Publishing Company, Mass., 1966, p. 78.

3 Kassemi, S. A., "Conjugate Heat Transfer for Laminar Flow over a Plate with A Nonsteady Temperature at the Lower Surface," M.S. Thesis University of Akron, Akron, Ohio, 1979.

4 Luikov, A. V., "Conjugate Convective Heat Transfer Problems," *International Journal of Heat and Mass Transfer,* Vol. 17, 1974, p. 257.

5 Chao, B. T. and Cheema, L. S., "Unsteady Heat Transfer in Laminar Boundary Layer Over a Plat Plate," *International Journal of Heat and Mass Transfer,* Vol. 11, 1968, p. 1311.

6 Cess, R. D., "Heat Transfer to Laminar Flow Across a Flat Plate With a Non-Steady Surface Temperature," ASME JOURNAL OF HEAT TRANSFER, *83,* 1961, p. 274.

The Effects of Dimensions on the Heat Flowrate through Extended Surfaces

P. J. Heggs[1] and P. R. Stones[1]

Nomenclature

$Q1$, $Q2$ = one and two-dimensional heat flows
B11, B21, B22 = assembly Biot numbers = $h_w W/k_1$, $h_A W/k_1$ and $h_A W/k_2$, respectively
H, W, S = fin height, thickness and spacing, respectively
h_A, h_w = finned and unfinned side heat transfer coefficients
k_1, k_2 = wall and fin material thermal conductivities
r, x, y = system coordinates
Ti, Tii = wall and fin temperatures
T_A, T_w = finned and unfinned side fluid temperatures
WT = wall thickness
$X2$, YSW, XW = dimensionless fin height, fin spacing and wall thickness = H/W, S/W and WT/W
θi (θii) = $(Ti(ii) - T_A)/(T_w - T_A)$

Introduction and Background

Finned surfaces are presently designed on the assumption that the temperature distribution is one-dimensional. Investigations [1, 2] have shown however that temperature depressions occur at the fin base. Further studies of the temperature depression in multi-fin arrays [3, 4] have revealed that fin heat fluxes can be lower by 80 percent than those predicted by the one-dimensional approach. These studies covered a somewhat restricted range of system parameters for longitudinal fins either attached to a wall or a pipe of like material. Suryanaryana [4] concludes that a one-dimensional analysis overestimates the heat flowrate. In addition the error increases as the wall thickness and fin height increase and as the fin spacing and ratio of unfinned to finned side heat transfer coefficients decrease. The one-dimensional analysis gives satisfactory values for fin height equal to the fin semi-thickness. This contradicts Klett and McCulloch [2] whose results indicate that the temperature depression at the fin base may be substantial for small fin height to thickness ratios. Sparrow and Lee [3] conclude that increasing the spacing between longitudinal fins on a tube increases the error, again this is contrary to the observations of [4].

This study compares one and two-dimensional heat flows through longitudinal and annular fin assemblies for a wide range of system parameters: fin height (1.5 − 240 mm), interfin spacing (1.5 − 75 mm), wall thickness (1.5 − 150 mm), materials ranging from stainless steel to copper and heat transfer conditions ranging from free convection to condensation.

Analysis

Fig. 1 is a cross-section through an assembly where x and y are cartesian coordinates for longitudinal fins on a plane wall, whereas r and y are cylindrical coordinates for annular fins on a tube. The heat flow through an assembly is evaluated from temperature distributions in the two regions ABCE and DEFG with perfect contact at the interface DE. All exposed surfaces; AB, CD, DG and GF are subjected to convective transfer.

One-Dimensional Analysis. The temperature distribution within both regions is represented by the following equation:

$$\frac{d^2\theta}{dN^2} + a\frac{d\theta}{dN} + b\theta = 0$$

with N, a and b taking the following values.

		LONGITUDINAL			ANNULAR		
		N	a	b	N	a	b
WALL	ABCE	x/W	0	0	r/W	W/r	0
FIN	DEFG	x/W	0	−2B22	r/W	W/r	−2B22

The boundary conditions are:

AB $$\mathrm{B11}(\theta i - 1) = \frac{d\theta i}{dN}$$

CE $$(1 + YSW)\frac{d\theta i}{dN} = \frac{k_2}{k_1}\frac{d\theta ii}{dN} - \mathrm{B21}\,YSW\theta i$$

and DE $$\theta i = \theta ii$$

FG $$\mathrm{B22}\,\theta ii = -\frac{d\theta ii}{dN}$$

The analytical solution of these equations provides the heat flow through the complete assembly and for the longitudinal case is given by:

$$Q1 = (T_W - T_A)/\left[\frac{WT}{k_1(W+S)} + \frac{1}{h_W(W+S)} + \frac{1}{h_A S + k_2 W m\left(\dfrac{\sinh mH + \dfrac{h_A}{k_2 m}\cosh mH}{\cosh mH + \dfrac{h_A}{k_2 m}\sinh mH}\right)}\right]$$

where $m^2 = 2\,h_A/k_2 W$. This expression is identical to the commonly used concept of overall heat transfer coefficient which employs the total efficiency of the finned surface [5] i.e., the third term in the denominator. A similar expression is obtained for the annular situation.

Two-Dimensional Analysis. The Laplace equation now describes the temperature distributions in all regions:

$$\frac{\partial^2\theta}{\partial N^2} + c\frac{\partial\theta}{\partial N} + \frac{\partial^2\theta}{\partial M^2} = 0$$

[1] Chemical Engineering Department, Leeds University, Leeds LS2 9JT, United Kingdom.

Contributed by the Heat Transfer Division for publication in the JOURNAL OF HEAT TRANSFER. Manuscript received by the Heat Transfer Division February 8, 1979.

$$P_0 = \frac{2}{1+\sqrt{K/R_c}} \sum_{n=0}^{\infty} \left\{ \left[\frac{\sqrt{\frac{K}{R_c}} - 1}{\sqrt{\frac{K}{R_c}} + 1} \right]^n \times \operatorname{erfc} \frac{(2n+1)\sqrt{R_c K}}{2\sqrt{\tau_2 + KR_c/8}} \right\} \quad (19)$$

Numerical computations show a good agreement between equation (19) and the present numerical solution for small time, ($\tau_2 < 0.1$) as illustrated in Fig. 1.

References

1 Wang, R. C. C., Chung, B. T. F., and Thomas, L. C., "Transient Convective Heat Transfer for Laminar Boundary Layer Flow with Effects of Wall Capacitance and Resistance," ASME JOURNAL OF HEAT TRANSFER, Vol. 89, 1977, p. 513.

2 Arpaci, V. S., *Conduction Heat Transfer,* Addison-Wesley Publishing Company, Mass., 1966, p. 78.

3 Kassemi, S. A., "Conjugate Heat Transfer for Laminar Flow over a Plate with A Nonsteady Temperature at the Lower Surface," M.S. Thesis University of Akron, Akron, Ohio, 1979.

4 Luikov, A. V., "Conjugate Convective Heat Transfer Problems," *International Journal of Heat and Mass Transfer,* Vol. 17, 1974, p. 257.

5 Chao, B. T. and Cheema, L. S., "Unsteady Heat Transfer in Laminar Boundary Layer Over a Plat Plate," *International Journal of Heat and Mass Transfer,* Vol. 11, 1968, p. 1311.

6 Cess, R. D., "Heat Transfer to Laminar Flow Across a Flat Plate With a Non-Steady Surface Temperature," ASME JOURNAL OF HEAT TRANSFER, *83,* 1961, p. 274.

The Effects of Dimensions on the Heat Flowrate through Extended Surfaces

P. J. Heggs[1] and P. R. Stones[1]

Nomenclature

$Q1$, $Q2$ = one and two-dimensional heat flows
B11, B21, B22 = assembly Biot numbers = $h_w W/k_1$, $h_A W/k_1$ and $h_A W/k_2$, respectively
H, W, S = fin height, thickness and spacing, respectively
h_A, h_w = finned and unfinned side heat transfer coefficients
k_1, k_2 = wall and fin material thermal conductivities
r, x, y = system coordinates
Ti, Tii = wall and fin temperatures
T_A, T_w = finned and unfinned side fluid temperatures
WT = wall thickness
$X2$, YSW, XW = dimensionless fin height, fin spacing and wall thickness = H/W, S/W and WT/W
θi (θii) = $(Ti(ii) - T_A)/(T_w - T_A)$

Introduction and Background

Finned surfaces are presently designed on the assumption that the temperature distribution is one-dimensional. Investigations [1, 2] have shown however that temperature depressions occur at the fin base. Further studies of the temperature depression in multi-fin arrays [3, 4] have revealed that fin heat fluxes can be lower by 80 percent than those predicted by the one-dimensional approach. These studies covered a somewhat restricted range of system parameters for longitudinal fins either attached to a wall or a pipe of like material. Suryanaryana [4] concludes that a one-dimensional analysis overestimates the heat flowrate. In addition the error increases as the wall thickness and fin height increase and as the fin spacing and ratio of unfinned to finned side heat transfer coefficients decrease. The one-dimensional analysis gives satisfactory values for fin height equal to the fin semi-thickness. This contradicts Klett and McCulloch [2] whose results indicate that the temperature depression at the fin base may be substantial for small fin height to thickness ratios. Sparrow and Lee [3] conclude that increasing the spacing between longitudinal fins on a tube increases the error, again this is contrary to the observations of [4].

This study compares one and two-dimensional heat flows through longitudinal and annular fin assemblies for a wide range of system parameters: fin height (1.5 − 240 mm), interfin spacing (1.5 − 75 mm), wall thickness (1.5 − 150 mm), materials ranging from stainless steel to copper and heat transfer conditions ranging from free convection to condensation.

Analysis

Fig. 1 is a cross-section through an assembly where x and y are cartesian coordinates for longitudinal fins on a plane wall, whereas r and y are cylindrical coordinates for annular fins on a tube. The heat flow through an assembly is evaluated from temperature distributions in the two regions ABCE and DEFG with perfect contact at the interface DE. All exposed surfaces; AB, CD, DG and GF are subjected to convective transfer.

One-Dimensional Analysis. The temperature distribution within both regions is represented by the following equation:

$$\frac{d^2\theta}{dN^2} + a\frac{d\theta}{dN} + b\theta = 0$$

with N, a and b taking the following values.

		LONGITUDINAL			ANNULAR		
		N	a	b	N	a	b
WALL	ABCE	x/W	0	0	r/W	W/r	0
FIN	DEFG	x/W	0	−2B22	r/W	W/r	−2B22

The boundary conditions are:

AB $$\mathrm{B11}(\theta i - 1) = \frac{d\theta i}{dN}$$

CE $$(1 + YSW)\frac{d\theta i}{dN} = \frac{k_2}{k_1}\frac{d\theta ii}{dN} - \mathrm{B21}\,YSW\theta i$$

and DE $$\theta i = \theta ii$$

FG $$\mathrm{B22}\,\theta ii = -\frac{d\theta ii}{dN}$$

The analytical solution of these equations provides the heat flow through the complete assembly and for the longitudinal case is given by:

$$Q1 = (T_W - T_A)/\left[\frac{WT}{k_1(W+S)} + \frac{1}{h_W(W+S)} + \frac{1}{h_A S + k_2 W m\left(\dfrac{\sinh mH + \dfrac{h_A}{k_2 m}\cosh mH}{\cosh mH + \dfrac{h_A}{k_2 m}\sinh mH}\right)}\right]$$

where $m^2 = 2\,h_A/k_2 W$. This expression is identical to the commonly used concept of overall heat transfer coefficient which employs the total efficiency of the finned surface [5] i.e., the third term in the denominator. A similar expression is obtained for the annular situation.

Two-Dimensional Analysis. The Laplace equation now describes the temperature distributions in all regions:

$$\frac{\partial^2\theta}{\partial N^2} + c\frac{\partial\theta}{\partial N} + \frac{\partial^2\theta}{\partial M^2} = 0$$

[1] Chemical Engineering Department, Leeds University, Leeds LS2 9JT, United Kingdom.

Contributed by the Heat Transfer Division for publication in the JOURNAL OF HEAT TRANSFER. Manuscript received by the Heat Transfer Division February 8, 1979.

with $N = x/W$, $c = 0$ and $M = y/W$ for the longitudinal case and $N = r/W$, $c = W/r$ and $M = y/W$ for the annular situation. The boundary conditions are:

AB $$B11(\theta i - 1) = \frac{\partial \theta i}{\partial N}$$

BC, AE and EF $$\frac{\partial \theta}{\partial M} = 0$$

CD $$-B21\theta i = \frac{\partial \theta i}{\partial N}$$

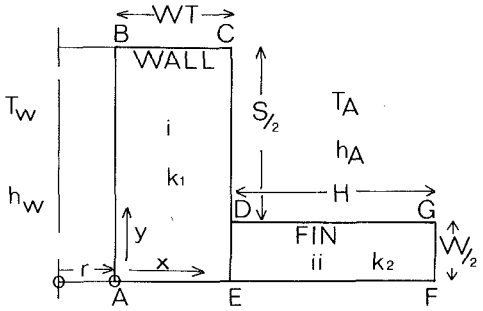

Fig. 1 Nomenclature for longitudinal and annular assemblies

DE $$\frac{\partial \theta i}{\partial N} = \frac{k_2}{k_1}\frac{\partial \theta ii}{\partial N}$$

and $$\theta i = \theta ii$$

DG $$-B22\theta ii = \frac{\partial \theta ii}{\partial M}$$

GF $$-B22\theta ii = \frac{\partial \theta ii}{\partial N}$$

Numerically derived temperature distributions provided the heat flow ($Q2$) through the assemblies.

Results and Conclusions

The heat flow through the assembly, $Q1$ (one-dimensional) and $Q2$ (two-dimensional) are both functions of B11, B11/B21 ($=h_W/h_A$), B21/B22 ($=k_2/k_1$), $X2$, YSW and XW. To investigate all combinations of these six parameters is beyond the scope of this report, however a detailed study for a fixed B11 = 2 has been accomplished for both longitudinal and annular systems. The parameter ranges investigated were B11/B21: 2–20000, B21/B22: 1–25, $X2$: 1–160, YSW: 1–50 and XW: 1–100. Only for B11/B21 of 20 or less were the differences between $Q1$ and $Q2$ greater than 4 percent for both geometrical arrangements. Figs. 2 and 3, respectively, show the percentage differences in $Q1$ and $Q2$ for longitudinal and annular systems for

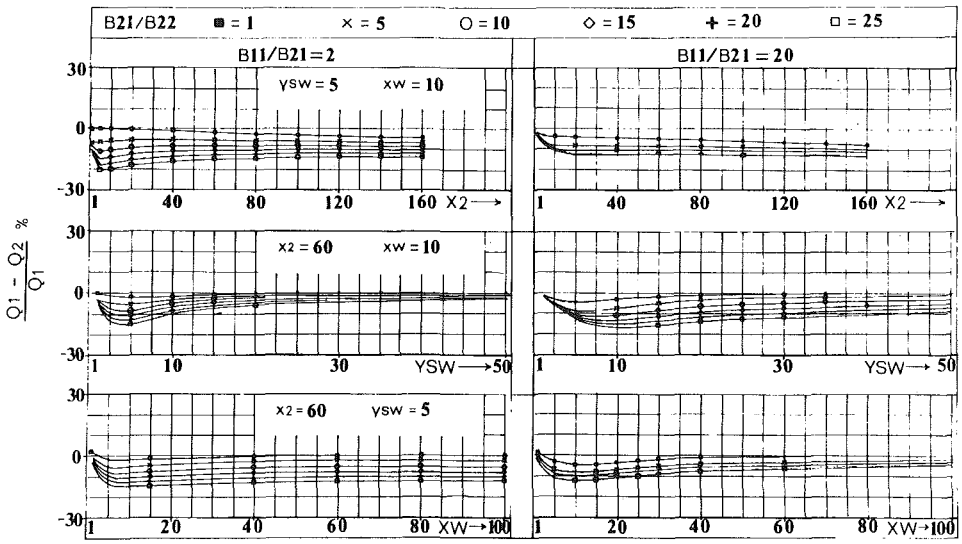

Fig. 2 The effects of dimensions on longitudinal fin assemblies

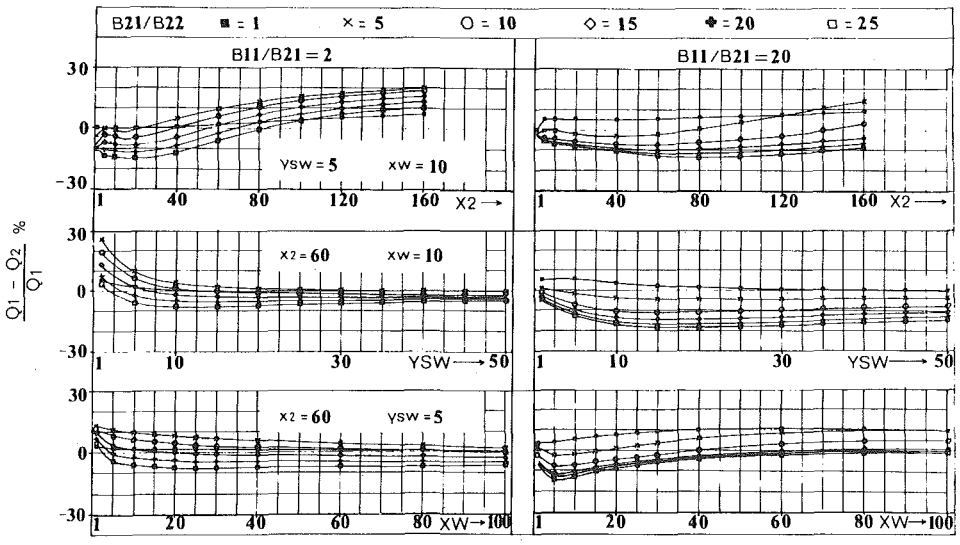

Fig. 3 The effects of dimensions on annular fin assemblies

B11/B21 = 20 and 2 for various combinations of the other parameters.

In the longitudinal situation, the maximum difference is −20 percent for B11/B21 = 2, YSW = 5, XW = 10, B21/B22 = 25 and $X2$ = 5. The two-dimensional representation always predicts larger heat flows and so present design techniques for this configuration always predicts conservative transfer areas. This overestimation is more pronounced the greater B21/B22, the shorter the fins, the closer the spacing and the thinner the wall. For the annular arrangement, the maximum difference is +26 percent for B11/B21 = 2, $X2$ = 60, XW = 10, YSW = 5 and B21/B22 = 5. In fact the two-dimensional representation predicts either lower or higher heat flows. Hence present design techniques for annular systems can result in either under- or over-design depending upon the parameter values.

For B11/B21 = 2, $Q1 > Q2$ for long fins ($X2 > 80$), the difference increasing for decreasing B21/B22. Conversely $Q1 < Q2$ for short fins ($X2 < 40$). $Q1 > Q2$ for closely spaced fins ($YSW < 10$) conversely $Q1 < Q2$ for widely spaced fins ($YSW > 20$). Finally $Q1 > Q2$ for fins attached to a thin wall ($XW < 40$), conversely $Q1 < Q2$ for fins attached to a thick wall ($XW > 60$).

Fig. 2 shows that for longitudinal assemblies as YSW is increased the magnitude of the error between heat flowrates first increases, reaches a maximum at YSW = 5 for B11/B21 = 2 (YSW = 10 for B11/B21 = 20), and then steadily decreases. However these results cannot be used to resolve the contradictory conclusions mentioned earlier in [3] and [4] because both present separate expressions for the heat flowrates through the fin and through the unfinned surface. Neither [3] nor [4] combine the fin and unfinned heat flowrate errors to show the effects on the total heat flowrate through the complete assembly. Fig. 2 shows that as YSW, $X2$ and XW are increased there is a maximum in the magnitude of the total heat flowrate error. If the starting point lies to the left or the right of the maximum, increasing YSW, $X2$ or XW can result in either an increase or decrease in the error.

References

1 Sparrow, E. M. and Hennecke, D. K. "Temperature Depression at the Base of a Fin," ASME JOURNAL OF HEAT TRANSFER, Vol. 92, 1970, pp. 204–206.

2 Klett, D. E. and McCulloch, J. W. "The Effect of Thermal Conductivity and Base-Temperature Depression on Fin Effectiveness," ASME JOURNAL OF HEAT TRANSFER, Vol. 94, 1972, pp. 333–334.

3 Sparrow, E. M. and Lee, L. "Effects of Fin Base Temperature Depression in a Multi-Fin Array," ASME JOURNAL OF HEAT TRANSFER, Vol. 97, 1975, pp. 463–465.

4 Suryanarayana, N. V. "Two-Dimensional Effects on Heat Transfer Rates from an Array of Straight Fins," ASME JOURNAL OF HEAT TRANSFER, Vol. 99, 1977, pp. 129–132.

5 Kreith, F. *Principles of Heat Transfer*, Third edition, Intext Press, 1973.

Heat Transfer through Irradiated, Semi-transparent Layers at High Temperature

R. Viskanta[1] and D. M. Kim[1]

Nomenclature

D_n = function defined as $\int_0^1 \mu^{n-2} \exp(-t/\mu)\beta(\mu)d\mu$
$E_{b\lambda}$ = Planck's black body distribution function
E_n = exponential integral defined as $\int_0^1 \mu^{n-2} \exp(-t/\mu)d\mu$
$\mathcal{F}$ = radiative flux in the y-direction
F_i = external flux incident on gas-material interface
k = thermal conductivity of material
n = index of refraction
q = total (conductive + radiative) heat flux in y-direction
R_n = function defined as $\int_0^1 r_i(\mu)\mu^{n-2} \exp(-t/\mu)\beta(\mu)d\mu$
r_i = reflectivity of gas-material interface
T = temperature
t_i = transmissivity of gas-material interface
T_n = function defined as $\int_0^1 t_i(\mu')(\mu')^{n-2} \exp(-t/\mu')\beta(\mu)d\mu'$
y = distance measured from the opaque wall
β = function defined as $[1 - \rho_w r_i \exp(-2\tau_0/|\mu|)]^{-1}$
ϵ = emissivity of opaque wall
κ = absorption coefficient
λ = wavelength
ρ = reflectance of opaque wall
τ = optical depth, $\int_0^y \kappa dy$
τ_0 = optical thickness of layer, $\int_0^L \kappa dy$

Subscripts

i = refers to interface
λ = refers to wavelength
w = refers to wall

[1] Heat Transfer Laboratory, School of Mechanical Engineering, Purdue University, West Lafayette, Ind. 47907.

Contributed by the Heat Transfer Division for publication in The JOURNAL OF HEAT TRANSFER. Manuscript received by The Heat Transfer Division June 21, 1979.

Introduction

Slag layers are known to form on tubes and walls of utility boilers [1], exhaust gas recuperators associated with glass melting tanks, MHD plant components [2, 3], black liquor boilers [4] and many other slagging combustion systems. For example, slag layers are expected to form in the combustor, channel, diffuser, radiant boiler, and seed recovery components of an MHD plant [3]. Dense, stable slag layers can protect structural materials from high temperature gases, corrosive products and large transient heat loads. However, the presence of slag layers on surfaces also increases thermal resistance to heat transfer thus necessitating a larger and costlier piece of equipment. The fact that a coal-ash slag is not opaque but is semitransparent to thermal radiation is not recognized [1, 5]. The semi-transparency of the slag is expected to have serious implications in the design of some MHD plant components [2]. For example, as a result of the semi-transparency, the slag will lose some of its heat protection capability, and the total heat transfer by conduction and radiation through the layer will be increased. Also, one possible reason for the failure ("burnout") of utility boiler tubes can be attributed to the melting of the slag because of changes in the system operating conditions such as use of coal having different composition and ash content. In view of the serious consequences of a tube failure in a large utility boiler, the understanding of heat transfer through an irradiated, coal-ash slag layer is of considerable practical and economic significance not only to the designer but also to the operator of a power plant.

The purpose of this note is to present a model for predicting conduction and radiation heat transfer across an irradiated layer of semitransparent material at high temperature. A model for analyzing gravity flow and heat transfer in a slag layer has been recently given [2], but the prediction of radiative transfer is too complicated for design calculations. The validity and accuracy of the model is established by comparing the predictions with those reported in the literature. Results of sample calculations are included for the purpose of determining the relative importance of radiation in comparison to the total heat transfer across the layer.

Analysis

Consider a layer of an amorphous, semi-transparent substance of uniform thickness L which is bounded on one side by an opaque wall and on the other by gases. The material may be solid, liquid or both simultaneously and be capable of absorbing, and emitting but not scattering thermal radiation. Heat transfer in the layer is predominantly in the y-direction perpendicular to the layer. The radiation

B11/B21 = 20 and 2 for various combinations of the other parameters.

In the longitudinal situation, the maximum difference is −20 percent for B11/B21 = 2, YSW = 5, XW = 10, B21/B22 = 25 and $X2$ = 5. The two-dimensional representation always predicts larger heat flows and so present design techniques for this configuration always predicts conservative transfer areas. This overestimation is more pronounced the greater B21/B22, the shorter the fins, the closer the spacing and the thinner the wall. For the annular arrangement, the maximum difference is +26 percent for B11/B21 = 2, $X2$ = 60, XW = 10, YSW = 5 and B21/B22 = 5. In fact the two-dimensional representation predicts either lower or higher heat flows. Hence present design techniques for annular systems can result in either under- or over-design depending upon the parameter values.

For B11/B21 = 2, $Q1 > Q2$ for long fins ($X2 > 80$), the difference increasing for decreasing B21/B22. Conversely $Q1 < Q2$ for short fins ($X2 < 40$). $Q1 > Q2$ for closely spaced fins ($YSW < 10$) conversely $Q1 < Q2$ for widely spaced fins ($YSW > 20$). Finally $Q1 > Q2$ for fins attached to a thin wall ($XW < 40$), conversely $Q1 < Q2$ for fins attached to a thick wall ($XW > 60$).

Fig. 2 shows that for longitudinal assemblies as YSW is increased the magnitude of the error between heat flowrates first increases, reaches a maximum at YSW = 5 for B11/B21 = 2 (YSW = 10 for B11/B21 = 20), and then steadily decreases. However these results cannot be used to resolve the contradictory conclusions mentioned earlier in [3] and [4] because both present separate expressions for the heat flowrates through the fin and through the unfinned surface. Neither [3] nor [4] combine the fin and unfinned heat flowrate errors to show the effects on the total heat flowrate through the complete assembly. Fig. 2 shows that as YSW, $X2$ and XW are increased there is a maximum in the magnitude of the total heat flowrate error. If the starting point lies to the left or the right of the maximum, increasing YSW, $X2$ or XW can result in either an increase or decrease in the error.

References

1 Sparrow, E. M. and Hennecke, D. K. "Temperature Depression at the Base of a Fin," ASME JOURNAL OF HEAT TRANSFER, Vol. 92, 1970, pp. 204–206.

2 Klett, D. E. and McCulloch, J. W. "The Effect of Thermal Conductivity and Base-Temperature Depression on Fin Effectiveness," ASME JOURNAL OF HEAT TRANSFER, Vol. 94, 1972, pp. 333–334.

3 Sparrow, E. M. and Lee, L. "Effects of Fin Base Temperature Depression in a Multi-Fin Array," ASME JOURNAL OF HEAT TRANSFER, Vol. 97, 1975, pp. 463–465.

4 Suryanarayana, N. V. "Two-Dimensional Effects on Heat Transfer Rates from an Array of Straight Fins," ASME JOURNAL OF HEAT TRANSFER, Vol. 99, 1977, pp. 129–132.

5 Kreith, F. *Principles of Heat Transfer*, Third edition, Intext Press, 1973.

Heat Transfer through Irradiated, Semi-transparent Layers at High Temperature

R. Viskanta[1] and D. M. Kim[1]

Nomenclature

D_n = function defined as $\int_0^1 \mu^{n-2} \exp(-t/\mu)\beta(\mu)d\mu$
$E_{b\lambda}$ = Planck's black body distribution function
E_n = exponential integral defined as $\int_0^1 \mu^{n-2} \exp(-t/\mu)d\mu$
$\mathcal{F}$ = radiative flux in the y-direction
F_i = external flux incident on gas-material interface
k = thermal conductivity of material
n = index of refraction
q = total (conductive + radiative) heat flux in y-direction
R_n = function defined as $\int_0^1 r_i(\mu)\mu^{n-2} \exp(-t/\mu)\beta(\mu)d\mu$
r_i = reflectivity of gas-material interface
T = temperature
t_i = transmissivity of gas-material interface
T_n = function defined as $\int_0^1 t_i(\mu')(\mu')^{n-2} \exp(-t/\mu')\beta(\mu)d\mu'$
y = distance measured from the opaque wall
β = function defined as $[1 - \rho_w r_i \exp(-2\tau_0/|\mu|)]^{-1}$
ϵ = emissivity of opaque wall
κ = absorption coefficient
λ = wavelength
ρ = reflectance of opaque wall
τ = optical depth, $\int_0^y \kappa dy$
τ_0 = optical thickness of layer, $\int_0^L \kappa dy$

Subscripts

i = refers to interface
λ = refers to wavelength
w = refers to wall

[1] Heat Transfer Laboratory, School of Mechanical Engineering, Purdue University, West Lafayette, Ind. 47907.

Contributed by the Heat Transfer Division for publication in The JOURNAL OF HEAT TRANSFER. Manuscript received by The Heat Transfer Division June 21, 1979.

Introduction

Slag layers are known to form on tubes and walls of utility boilers [1], exhaust gas recuperators associated with glass melting tanks, MHD plant components [2, 3], black liquor boilers [4] and many other slagging combustion systems. For example, slag layers are expected to form in the combustor, channel, diffuser, radiant boiler, and seed recovery components of an MHD plant [3]. Dense, stable slag layers can protect structural materials from high temperature gases, corrosive products and large transient heat loads. However, the presence of slag layers on surfaces also increases thermal resistance to heat transfer thus necessitating a larger and costlier piece of equipment. The fact that a coal-ash slag is not opaque but is semitransparent to thermal radiation is not recognized [1, 5]. The semi-transparency of the slag is expected to have serious implications in the design of some MHD plant components [2]. For example, as a result of the semi-transparency, the slag will lose some of its heat protection capability, and the total heat transfer by conduction and radiation through the layer will be increased. Also, one possible reason for the failure ("burnout") of utility boiler tubes can be attributed to the melting of the slag because of changes in the system operating conditions such as use of coal having different composition and ash content. In view of the serious consequences of a tube failure in a large utility boiler, the understanding of heat transfer through an irradiated, coal-ash slag layer is of considerable practical and economic significance not only to the designer but also to the operator of a power plant.

The purpose of this note is to present a model for predicting conduction and radiation heat transfer across an irradiated layer of semitransparent material at high temperature. A model for analyzing gravity flow and heat transfer in a slag layer has been recently given [2], but the prediction of radiative transfer is too complicated for design calculations. The validity and accuracy of the model is established by comparing the predictions with those reported in the literature. Results of sample calculations are included for the purpose of determining the relative importance of radiation in comparison to the total heat transfer across the layer.

Analysis

Consider a layer of an amorphous, semi-transparent substance of uniform thickness L which is bounded on one side by an opaque wall and on the other by gases. The material may be solid, liquid or both simultaneously and be capable of absorbing, and emitting but not scattering thermal radiation. Heat transfer in the layer is predominantly in the y-direction perpendicular to the layer. The radiation

characteristics of the opaque wall are assumed to be known, and the radiation characteristics of the free (gas-material) surface are predicted from Fresnel equations. The external radiation flux incident on the free surface is considered to be given. Since the interest here is to develop an approximate radiation and not the total heat transfer model, the temperatures of the opaque wall and of the gas-material interface are taken as known.

If heat transfer by convection in the liquid layer is neglected in comparison to conduction and radiation as can be readily justified [2], the energy equation becomes

$$q = -k\frac{dT}{dy} + \mathcal{J}(y) \tag{1}$$

The first term on the right-hand-side of equation (1) represents the conductive and the second the radiative fluxes, respectively. For a plane layer of semi-transparent material, either in a liquid or a solid phase, in direct contact with an opaque, diffusely reflecting wall maintained at a constant temperature T_w, the local radiative flux $\mathcal{J}(y)$ can be expressed as [2]

$$\mathcal{J}(y) = 2\int_0^\infty [\epsilon_{w\lambda} n_\lambda^2 E_{b\lambda}(T_w) f_1(\tau_\lambda) - F_{i\lambda} f_2(\tau_\lambda) + \int_0^{\tau_{0\lambda}} n_\lambda^2 E_{b\lambda}(t) G(\tau_\lambda, t) dt] d\lambda \tag{2}$$

where

$$f_1(\tau_\lambda) = [D_3(\tau_\lambda) - R_3(2\tau_{0\lambda} - \tau_\lambda)] \tag{3}$$

$$f_2(\tau_\lambda) = [T_3(\tau_{0\lambda} - \tau_\lambda) - \rho_{w\lambda} T_3(\tau_{0\lambda} + \tau_\lambda)] \tag{4}$$

and

$$G(\tau_\lambda, t) = \text{sign}(\tau_\lambda - t) E_2(|\tau_\lambda - t|) + \rho_{w\lambda} D_2(\tau_\lambda + t) + \rho_{w\lambda} R_2(2\tau_{0\lambda} + \tau_\lambda - t) - R_2(2\tau_{0\lambda} - \tau_\lambda - t) - \rho_{w\lambda} R_2(2\tau_{0\lambda} - \tau_\lambda + t) \tag{5}$$

The first term on the right-hand-side of equation (2) represents the contribution to the net radiative flux due to the emission by the wall, the second term denotes the contribution to the flux due to the external radiation flux $F_{i\lambda}$ incident on the free boundary ($y = L$) of the layer, and the final (integral) term represents the net contribution from the emission and partial absorption of radiation by the material. In deriving equation (2) all possible interreflections between the opaque wall and the transparent outer boundary at $y = L$ were taken into account.

The optical thicknesses $\tau_{0\lambda}$ of slag layers under slagging conditions are expected to be such that the Planck's function will vary slowly over the distance by which the local radiation effects will attenuate, that is,

$$\frac{dE_{b\lambda}}{dt} = \frac{dE_{b\lambda}}{dT}\frac{dT}{dt} \simeq \frac{dE_{b\lambda}}{dT}\frac{dT}{d\tau_\lambda} \tag{6}$$

for $|\tau_\lambda - t| \leq \delta$. This is equivalent to saying that the attenuation of the integro-exponential functions [$E_n(t)$, $D_n(t)$, $R_n(t)$ and $T_n(t)$] is very rapid. If the third term in equation (2) is integrated by parts and the above approximation is made in the evaluation of the integral over the optical thickness ($\int_0^{\tau_{0\lambda}} \ldots dt$), the equation can be expressed as

$$\mathcal{J}(y) = \int_0^\infty \left[\mathcal{J}_{s\lambda}(y) - H_\lambda(y)\frac{dT}{dy}\right] d\lambda \tag{7}$$

where

$$\mathcal{J}_{s\lambda}(y) = 2[\epsilon_{w\lambda} n_\lambda^2 E_{b\lambda}(T_w) f_i(\tau_\lambda) - F_{i\lambda} f_2(\tau_\lambda)] + 2[n_\lambda^2 E_{b\lambda}(T_w)[-E_3(\tau_\lambda) + \rho_{w\lambda} D_3(\tau_\lambda) + \rho_{w\lambda} R_3(2\tau_{0\lambda} + \tau_\lambda) + R_3(2\tau_{0\lambda} - \tau_\lambda) - \rho_{w\lambda} R_3(2\tau_{0\lambda} - \tau_\lambda)] + n_\lambda^2 E_{b\lambda}(T_L)[E_3(\tau_{0\lambda} - \tau_\lambda) - \rho_{w\lambda} D_3(\tau_{0\lambda} + \tau_\lambda) + \rho_{w\lambda} R_3(\tau_{0\lambda} + \tau_\lambda) - R_3(\tau_0 - \tau_\lambda) + \rho_{w\lambda} R_3(3\tau_{0\lambda} - \tau_\lambda)]] \tag{8}$$

and

$$H_\lambda(y) = -2\{[-\tfrac{2}{3} + E_4(\tau_\lambda) - E_4(\tau_{0\lambda} - \tau_\lambda) - \rho_{w\lambda}[D_4(\tau_{0\lambda} + \tau_\lambda) - D_4(\tau_\lambda)] - \rho_{w\lambda}[R_4(\tau_{0\lambda} + \tau_\lambda) - R_4(2\tau_{0\lambda} + \tau_\lambda)] + [R_4(\tau_{0\lambda} + \tau_\lambda) - R_4(2\tau_{0\lambda} - \tau_\lambda)] + \rho_{w\lambda}[R_4(3\tau_{0\lambda} - \tau_\lambda) - R_4(2\tau_{0\lambda} - \tau_\lambda)]\}\left(\frac{n_\lambda^2}{\kappa_\lambda}\right)\left(\frac{dE_{b\lambda}}{dT}\right)_T \tag{9}$$

The first term on the right-hand-side of equation (7) represents the net contribution to the radiative flux due to the "long-range" effects of radiation emitted from the wall and external radiation transmitted into the layer of material across the free surface. The second term represents the contribution to the net flux resulting from the local emission of radiation by the material and its "diffusion" in the layer.

Substitution of the expression for the local radiative flux, equation (7), into equation (2) gives

$$q = -\left[k + \int_0^\infty H_\lambda(y) d\lambda\right]\frac{dT}{dy} + \int_0^\infty \mathcal{J}_{s\lambda}(y) d\lambda = -(k + \tilde{k}_r)\frac{dT}{dy} + \mathcal{J}_s(y) \tag{10}$$

Thus, according to equation (10) the local radiative flux can be considered as consisting of diffusion and source contributions. Clearly, the basic difference between the present model and Rosseland diffusion approximation [6] is that in the analysis $\tau_{0\lambda}$ is finite and the presence of boundaries and external radiation sources are accounted for.

Equation (1) was solved numerically by imposing the temperature boundary conditions: $T = T_w$ at $y = 0$ and $T = T_L$ at $y = L$. The integro-exponential functions, except $E_n(t)$, were evaluated numerically. To reduce the computational time the functions were approximated accurately by a sum of exponentials, i.e., $D_n(t) \simeq \Sigma_i^N a_i e^{b_i t}$. The coefficients a_i and b_i were determined from a least-square fit.

Results and Discussion

A comparison of temperature distributions predicted using the exact expression for the local radiative flux, equation (2), as reported in [2] with those determined employing the approximate expression, equation (7), is given in Fig. 1. The calculations were carried out on a gray basis for a given thickness and a temperature difference across the layer. As expected, the results show that the approximate expression for the radiative flux becomes more accurate as the optical thickness of the layer is increased. The total (conductive plus radiative) fluxes predicted by the present model are 11, 6 and 3 percent higher than those reported in [2] for cases 1, 2 and 3, respectively. In agreement with results reported elsewhere [2], heat transfer by conduction was predominant only in the immediate vicinity of the opaque wall, but for $y/L > 0.2$ heat transfer was mostly (~90 percent) by radiation.

The importance of semitransparency and spectral effects on heat transfer across high temperature, irradiated layers is clearly evident from the results presented in Fig. 2 and Table 1. The sample results reported have been obtained using gray calculations based on a Planck

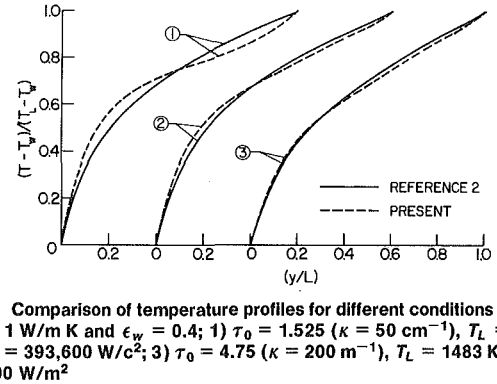

Fig. 1 Comparison of temperature profiles for different conditions T_w = 810 K, k = 1 W/m K and ϵ_w = 0.4; 1) τ_0 = 1.525 (κ = 50 cm^{-1}), T_L = 1444 K, and F_i = 393,600 W/c^2; 3) τ_0 = 4.75 (κ = 200 m^{-1}), T_L = 1483 K and F_i = 377,300 W/m^2

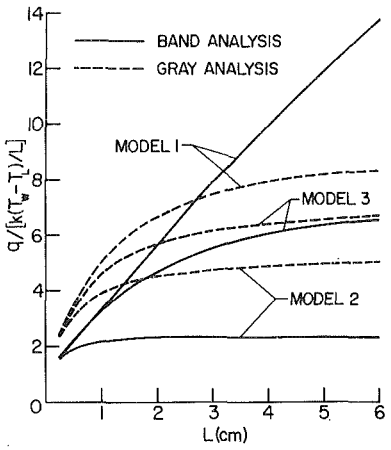

Fig. 2 Dependence of dimensionless heat flux on the layer thickness, T_w = 800 K, T_L = 1500 K, K = 1 W/mK, ϵ_w = 0.4 and F_i = 246,000 W/m²

mean absorption coefficient and band approximation. The spectral absorption coefficient models used in the calculations were:

Model 1: $\kappa_\lambda = 0.12\ \text{cm}^{-1}$ for $0 \le \lambda < 2.75\ \mu\text{m}$; $\kappa_\lambda = 4.5\ \text{cm}^{-1}$ for $2.75 \le \lambda < 4.7\ \mu\text{m}$; $\kappa_\lambda = \infty$ for $\lambda \ge 4.7\ \mu\text{m}$

Model 2: $\kappa_\lambda = 4.0\ \text{cm}^{-1}$, $0 \le \lambda < 2.75\ \mu\text{m}$; $\kappa_\lambda = 5.0\ \text{cm}^{-1}$ for $2.75 \le \lambda < 4.7\ \mu\text{m}$; $\kappa_\lambda = \infty$ for $\lambda \le 4.7\ \mu\text{m}$

Model 3: $\kappa_\lambda = 1.0\ \text{cm}^{-1}$ for $0 \le \lambda < 1\ \mu\text{m}$; $\kappa_\lambda = 0.8\ \text{cm}^{-1}$ for $1.0 \le \lambda < 2.75\ \mu\text{m}$; $\kappa_\lambda = 5\ \text{cm}^{-1}$ for $2.75 \le \lambda < 4.7\ \mu\text{m}$; $\kappa_\lambda = \infty$ for $\lambda \ge 4.7\ \mu\text{m}$

Models 1 and 2 are intended to approximate the absorption coefficient of window and green glass and Model 3 that of slag formed as a result of coal combustion. The spectral radiation flux incident on the layer, $F_{i\lambda}$, was assumed to have a Planckian distribution with a total flux F_i = 246,000 W/m². This value is representative of the radiant flux expected in some components of an open-cycle, coal-fired MHD plant [2].

The sample results reported show that treatment of the slag as if it were an opaque substance could result in large underpredictions of the total heat transfer in comparison to the situation where the material of the layer is semitransparent to radiation. The findings have practical implications to the design of components of coal-fired combustion systems. Data on the spectral absorption coefficient and transport properties are required for realistic design calculations of heat transfer in combustion systems in which slag is formed on heat transfer surfaces.

Table 1 Effects of temperature level and difference on heat transfer $[q/(k\Delta T/L)]$ across the layer: F_i = 246,000 W/m², L = 1 cm, k = 1 W/m K, and ϵ_w = 0.4

$T_w(K)$	$\Delta T(K)$	Model 1	Model 2	Model 3
		a) T_L = 1500 K		
1100	400	4.55	2.74	4.42
900	600	3.67	2.33	3.50
700	800	3.14	2.05	3.05
500	1000	2.80	1.85	2.70
		b) T_L = 1800 K		
1400	400	5.42	2.78	4.55
1200	600	4.78	2.65	4.17
1000	800	4.19	2.45	3.73
800	1000	3.73	2.24	3.34

References

1 Reid, W. T., *External Corrosion and Deposits,* American Elsevier Publishing Co., New York, 1971.

2 Chow, L. S. H., Viskanta, R. and Johnson, T. R., "Slag Transport Models for Radiant Heater of an MHD System," ASME Paper No. 78-WA/HT-21.

3 Postlethwaite, A. W. and Sluyter, M. M., "MHD Heat Transfer Problems—An Overview," *Mechanical Engineering,* Vol. 100, No. 3, March 1978, pp. 32–39.

4 Sheth, P. R., Lawit, R. L. and Klett, M. G., "Application of Black-Liquor Boiler Technology to MHD Heat and Seed Recovery Equipment Design," in *18th Symposium Engineering Aspects of Magnetohydrodynamics,* Butte, Montana, June 18–20, 1979, pp. C1.1–C.1.6.

5 Smith, V. L., "Coal Firing and Industrial Boiler Design—the Modern Approach," ASME *Journal of Engineering for Power,* Vol. 98, No. 3, 1976, pp. 297–304.

6 Viskanta, R. and Anderson, E. E., "Heat Transfer in Semitransparent Solids," in *Advances in Heat Transfer,* Edited by T. F. Irvine, Jr. and J. P. Hartnett, Academic Press, 1975, Volume 11, pp. 317–441.

Journal of Heat Transfer

Discussion

An Efficient Algorithm for Evaluating Arrays of Extended Surface[1]

P. Razelos.[2] The evaluation of the thermal performance of extended surface arrays is an important complicated engineering problem. The authors have provided us with a very interesting method, which simplifies it considerably. They have shown that each regular fin in the arry is characterized by a 2×2 thermal transmission matrix $[\Gamma]$, while singular fins (zero tip area) are characterized by a single thermal transmission ratio μ. They have further shown how these results can be applied to analyze a general array; and a second example is given to demonstrate the usefulness of their method to problems where the heat input at the most remote fins is given.

The reader, however, would have expected an algorithm from the authors, as the title suggests. The characterization of the array and the accompanying demonstration (authors' equations (34–43)) lack suitability for computer calculations; and the second example is far too simple to be used as a guide for general cases. We would like to offer a modification and extend their method by providing algorithms which are more suitable for computer or hand calculations.

Consider the array depicted by the authors' Fig. 2 and let us name the connecting fins 1, 4, 7, and 10 *rods* and the rest fins. To make the problem more general, consider that the array consist of N *rods,* and that at the end of each *rod* there are J fins attached. We may also consider that J is not necessarily the same for all *rods*. Given the configuration and the thermal parameters, the authors have considered the following two problems:

1 Given the temperature excess θ_{b1} determine the heat dissipated by the array (or the ratio q_{b1}/θ_{b1}) and

2 Given q_{b1} and q_{aN} determine the temperatures θ_{b1} and θ_{aN} (or any other temperature θ_{ai}).

Using their matrix notation, for each *rod* i we write

$$\begin{bmatrix}\theta_{bi}\\ q_{bi}\end{bmatrix} = [G_i]\begin{bmatrix}\theta_{ai}\\ q_{ai}\end{bmatrix} \quad 1 \le i \le N \tag{1}$$

where the matrix $[G]$ is obtained exactly as the matrix (Γ) with the functions $\lambda_1(x)$, $\lambda_2(x)$ satisfying the initial conditions

$$\lambda_1(a) = 1; \frac{d\lambda_1(a)}{dx} = 0 \tag{2}$$

$$\lambda_2(a) = 0; \frac{d\lambda_2(a)}{dx} = \frac{1}{k(a)A(a)} \tag{3}$$

Note that neither the *rod* nor the computer know which end is a or b, and that for each *rod,* $A(a) \neq 0$. Actually, in the examples cited by the authors, one may obtain the matrix $[G]$ from the matrix $[\Gamma]$ by simply replacing a for b and vice versa.

Following the authors' procedure for Problem 1, we obtain from equation (1) the expression

$$\frac{q_{bi}}{\theta_{bi}} = \frac{g^i_{21} + g^i_{22}\,(q_{ai}/\theta_{ai})}{g^i_{11} + g^i_{12}(q_{ai}/\theta_{ai})} \tag{4}$$

The above equation is identical with the authors' equation (34), if we make the substitutions $g_{11} = -\gamma_{22}, g_{12} = \gamma_{12}, g_{21} = \gamma_{21}$ and $g_{22} = -\gamma_{11}$. Equation (4) is also applicable for each fin (authors' equation (34)). However, in order to determine q_{b1}/θ_{b1} only the ratios

$$\frac{q_{bf}}{\theta_{bf}} = \mu \text{ (the subscript } f \text{ refers to fins)} \tag{5}$$

are needed, and these are readily obtained from (4) if one eliminates the ratio q_a/θ_a by virtue of the relationship $q_a = h_a\delta_a\theta_a$ (authors' equations (35–37)). Utilizing further the energy equation at the end of each *rod* i, and the equality of temperatures $\theta_{ai} = \theta_{bfi} = \theta_{bi+1}$, we obtain the equation

$$\frac{q_{ai}}{\theta_{ai}} = \sum_1^J \mu_{ij} + \frac{q_{bi+1}}{\theta_{bi+1}} \tag{6}$$

where J can be written as J_i if J is not the same for all rods. The combinations of equations (4) and (6) result in the following algorithm:

$$\frac{q_{bi}}{\theta_{bi}} = \frac{g^i_{21} + g^i_{22}\left\{\sum_1^J \mu_{ij} + \dfrac{q_{bi+1}}{\theta_{bi+1}}\right\}}{g^i_{11} + g^i_{21}\left\{\sum_1^J \mu_{ij} + \dfrac{q_{bi+1}}{\mu_{bi+1}}\right\}} \tag{7}$$

with

$$\frac{q_{bN}}{\theta_{bN}} = \frac{g^N_{21} + g^N_{22}\sum_1^J \mu_{Ni}}{g^N_{11} + g^N_{12}\sum_1^J \mu_{Nj}} \tag{7a}$$

The total array is characterized by the matrices (G_i) (or (Γ)), and the ratios μ's. This is essentially the authors' conclusion stated differently. Once the parameters g's and μ's have been computed, equations (7) provide a very simple algorithm for the solution of the first problem.

The solution of Problem 2 is obtained by substituting q_{ai} from (6) into the equation (1) and using the equality of temperatures $\theta_{ai} = \theta_{bfi} = \theta_{bi+1}$. The resulting equations are

$$\begin{bmatrix}\theta_{bi}\\ q_{bi}\end{bmatrix} = [G_i]\begin{bmatrix}\theta_{bi+1}\\ q_{bi+1} + \sum_J^J \mu_{ij}\theta_{bi+1}\end{bmatrix}$$

$$= [G_i]\begin{bmatrix}\theta_{bi+1}\\ q_{bi+1}\end{bmatrix} + \sum_J^J \mu_{ij}\,[G_i]\begin{bmatrix}0\\ \theta_{bi+1}\end{bmatrix} \tag{8}$$

where equation (1) for the N^{th} *rod* remains

$$\begin{bmatrix}\theta_{bN}\\ q_{bN}\end{bmatrix} = [G_N]\begin{bmatrix}\theta_{aN}\\ q_{aN}\end{bmatrix} \tag{8a}$$

The above relationships constitute a set of $2N$ linear algebraic equations that can be solved exactly, though it may be simpler to use an iterative technique. In the latter case one starts the calculations

[1] By A. D. Kraus, A. D. Snider and L. F. Doty, published in the May 1978 issue of the JOURNAL OF HEAT TRANSFER, Vol. 100, May 1978, pp. 288–293.

[2] Applied Sciences Department, The College of Staten Island, The City University of New York, St. George, Campus, 130 Stuyvesant Place, Staten Island, NY 10301.

by assuming a value for θ_{aN}, and determines θ_{bN-1}, q_{bN-1} until eventually obtaining θ_{b1}, q_{b1}. If q_{b1} does not agree with the given value modify θ_{aN} and repeat the calculations. For the case where there are only two *rods* with two similar fins and two similar *rods* as in the example given by the authors, we can make an additional substitution to obtain

$$\begin{bmatrix}\theta_{bi}\\ q_{bi}\end{bmatrix} = [G][G]\begin{bmatrix}\theta_{a2}\\ q_{a2}\end{bmatrix} + 2\mu\,[G][g_{11} + g_{12}]\begin{bmatrix}\theta_{a2}\\ q_{a2}\end{bmatrix} \tag{9}$$

We notice that the second of the above equations determines directly the temperature θ_{a2}.

The authors' discussion of singular fins is not complete; with the exception of two specific examples where the results were known *a priori*, they do not offer any method for generally obtaining these ratios. However, these relationships are required for some idealized fins. In practice there are no fins with zero tip area, and one can simply use for the calculations a very small δ_a. We have made extensive calculations for triangular profile circular fins with $\delta_a = \delta_b \times 10^{-6}$,[3] which is much smaller than any real tip thickness and we have never encountered any computational difficulties.

Finally, one may recognize that the ratio q_{bf}/θ_{bf} for any fin is by definition proportional to the efficiency η. This is particularly helpful for hand calculations since the efficiencies for many profiles and tip conditions are extensively tabulated (authors' [2]). For the same assumptions that these efficiencies have been tabulated, one may obtain μ from the expression

$$\mu = 2h(b - a)\eta \tag{10}$$

We may also point out that in the same manner, the authors' method determines the overall passage efficiency expressed as

$$\eta_{\text{pass}} = \frac{q_{bi}}{\theta_{b1}}\frac{1}{\int h ds} \tag{11}$$

There is an obvious typographical error in the author's matrice (17), where in the denominator of the element γ_{12}, σ should be replaced by δ.

Authors' Closure

The authors are grateful to Dr. Rezelos for his interest and commentary on their work. Most of the points that he raises are well taken, and they provide an enhancement of the original exposition. In particular, his equations (6) and (7) do, indeed, give explicit formulations for the algorithm implied in the paper. Some comments on particular features in the Razelos discussion are in order.

The classification of fins into "rods" and "fins" according to whether or not they are mounted with tip attachments could be very helpful, as long as one does not lose sight of the fact that this *a posteriori* partitioning is not the same as the *a priori* categorization as "regular fins" and "singular fins," based on intrinsic fin properties. Razelos acknowledges this.

As mentioned, the basic algorithm for solving the "first problem" is neatly expressed by equations (6) and (7), and the authors endorse this methodology. Moreover, the formulation expressed in equation (8) for the second problem arises quite naturally from Razelos' perspective; compare the somewhat contrived treatment leading to equation (48) in the original paper.

As regards the use of the matrix G instead of the original Γ: G is no more difficult to compute, and has the very slight advantage of introducing no negative signs into the induced bilinear transformation equation (4); compare with the original equation (34). G offers no advantage in equation (8) for the second problem, because either the G or the Γ formulation ultimately produces the solution indirectly, in terms of a system of linear equations. Of course there are six different, equivalent, ways of expressing the two linear relationships which exist among q_b, θ_b, q_a, and θ_a. Subsequent work by the authors has shown that other formulations are appropriate to some circumstances; in fact, in the most general situation when there are loops in the array (a case that cannot be treated by the method discussed herein!), it is convenient to express q_a and q_b in terms of θ_a and θ_b, utilizing the "thermal admittance" matrix. With no clear choice at hand, the authors have continued to tabulate Γ, and to express rules for obtaining other matrices from it.

G is, of course, Γ^{-1}, and Razelos' statement that one may obtain G from Γ by switching a and b is true; but this rule is treacherous for some of the more exotic fins because it requires that one also switch *all* variables referring to tip dimensions such as thickness, height and taper angle with the corresponding base parameters. Notice that G is not the same as Γ for the fin operated in reverse, because when the "base" and "tip" *designations* are switched, the reference direction for q is changed; additional minus signs are called for. In this regard, the authors are puzzled by Razelos' disclaimer of any distinction between base and tip on the part of the rod or the computer. One of the authors (Kraus) has developed a computer program that handles an array of any number of fins, and this orientation information is an essential part of the package.

Two other points bear mentioning. In the authors' opinion there is no need of employing an iterative technique to solve the linear equations which result from the second problem; direct solution is easily implemented. But Razelos' criticism of the singular fin discussion is valid. A "complete" treatment involves some highly technical mathematics—in particular, the theory of singular Sturm-Liouville equations. The authors are disinclined to get into this, and will continue to tabulate μ only for the solvable cases. In this regard the Razelos-Imre paper should prove interesting.

The typographical correction is appropriate. There are two others; h should be replaced with k in equation (11), and there is an obvious β missing in equation (28). Again the authors would like to express their gratitude to Dr. Razelos for his discussion. Papers substantiating the authors' statements herein have been submitted to the Journal.

[3] Razelos, P. and Imre, K., "The Optimum Dimensions of Circular Fins with Variable Thermal Parameters," presented at the 1979 ASME Winter annual meeting.

Condensation on an Extended Surface[1]

J. Ernest Wilkins, Jr.[2] In this very interesting paper the authors are led to a consideration of the differential equations

$$\eta F' = 8(F - \Theta), \quad \Theta'' = F^{-1/4}\Theta, \ (' = d/d\eta), \tag{1}$$

and the boundary conditions

$$\Theta(0) = 1, \quad \Theta(\infty) = F(\infty) = 0. \tag{2}$$

They assert that "an analytic solution . . . is out of reach," carry out a numerical integration, and conclude, among other things, that

$$\Theta'(0) = -1.080. \tag{3}$$

In fact, an analytic solution can be found, and the numerical constant in (3) is $(7/6)^{1/2} = 1.08012$.

The authors implicitly assumed that $F > 0$. It is not physically possible that $F < 0$, and if $F = 0$, then $\Theta = 0$ also. Therefore, we may write the differential equations in the form

$$\eta F' = 8(F - \Theta), \quad F^{1/2}\Theta'' = \Theta, \tag{4}$$

that is valid even if $F = 0$. A solution consists of a pair of functions $F(\eta)$, $\Theta(\eta)$ defined when $\eta \geq 0$, such that F, Θ and Θ' are continuous

[1] By S. V. Patankar and E. M. Sparrow, published in the August 1979 issue of the ASME JOURNAL OF HEAT TRANSFER, Vol. 101, No. 3, pp. 434–440.

[2] Associate General Manager, EG&G Idaho, Inc., P.O. Box 1625, Idaho Falls, Idaho 83415. Associate Member ASME.

by assuming a value for θ_{aN}, and determines θ_{bN-1}, q_{bN-1} until eventually obtaining θ_{b1}, q_{b1}. If q_{b1} does not agree with the given value modify θ_{aN} and repeat the calculations. For the case where there are only two *rods* with two similar fins and two similar *rods* as in the example given by the authors, we can make an additional substitution to obtain

$$\begin{bmatrix}\theta_{bi}\\ q_{bi}\end{bmatrix} = [G][G]\begin{bmatrix}\theta_{a2}\\ q_{a2}\end{bmatrix} + 2\mu\,[G][g_{11}+g_{12}]\begin{bmatrix}\theta_{a2}\\ q_{a2}\end{bmatrix} \tag{9}$$

We notice that the second of the above equations determines directly the temperature θ_{a2}.

The authors' discussion of singular fins is not complete; with the exception of two specific examples where the results were known *a priori*, they do not offer any method for generally obtaining these ratios. However, these relationships are required for some idealized fins. In practice there are no fins with zero tip area, and one can simply use for the calculations a very small δ_a. We have made extensive calculations for triangular profile circular fins with $\delta_a = \delta_b \times 10^{-6}$,[3] which is much smaller than any real tip thickness and we have never encountered any computational difficulties.

Finally, one may recognize that the ratio q_{bf}/θ_{bf} for any fin is by definition proportional to the efficiency η. This is particularly helpful for hand calculations since the efficiencies for many profiles and tip conditions are extensively tabulated (authors' [2]). For the same assumptions that these efficiencies have been tabulated, one may obtain μ from the expression

$$\mu = 2h(b-a)\eta \tag{10}$$

We may also point out that in the same manner, the authors' method determines the overall passage efficiency expressed as

$$\eta_{\text{pass}} = \frac{q_{bi}}{\theta_{b1}}\frac{1}{\int h ds} \tag{11}$$

There is an obvious typographical error in the author's matrice (17), where in the denominator of the element γ_{12}, σ should be replaced by δ.

Authors' Closure

The authors are grateful to Dr. Rezelos for his interest and commentary on their work. Most of the points that he raises are well taken, and they provide an enhancement of the original exposition. In particular, his equations (6) and (7) do, indeed, give explicit formulations for the algorithm implied in the paper. Some comments on particular features in the Razelos discussion are in order.

The classification of fins into "rods" and "fins" according to whether or not they are mounted with tip attachments could be very helpful, as long as one does not lose sight of the fact that this *a posteriori* partitioning is not the same as the *a priori* categorization as "regular fins" and "singular fins," based on intrinsic fin properties. Razelos acknowledges this.

As mentioned, the basic algorithm for solving the "first problem" is neatly expressed by equations (6) and (7), and the authors endorse this methodology. Moreover, the formulation expressed in equation (8) for the second problem arises quite naturally from Razelos' perspective; compare the somewhat contrived treatment leading to equation (48) in the original paper.

As regards the use of the matrix G instead of the original Γ: G is no more difficult to compute, and has the very slight advantage of introducing no negative signs into the induced bilinear transformation equation (4); compare with the original equation (34). G offers no advantage in equation (8) for the second problem, because either the G or the Γ formulation ultimately produces the solution indirectly, in terms of a system of linear equations. Of course there are six different, equivalent, ways of expressing the two linear relationships which exist among q_b, θ_b, q_a, and θ_a. Subsequent work by the authors has shown that other formulations are appropriate to some circumstances; in fact, in the most general situation when there are loops in the array (a case that cannot be treated by the method discussed herein!), it is convenient to express q_a and q_b in terms of θ_a and θ_b, utilizing the "thermal admittance" matrix. With no clear choice at hand, the authors have continued to tabulate Γ, and to express rules for obtaining other matrices from it.

G is, of course, Γ^{-1}, and Razelos' statement that one may obtain G from Γ by switching a and b is true; but this rule is treacherous for some of the more exotic fins because it requires that one also switch *all* variables referring to tip dimensions such as thickness, height and taper angle with the corresponding base parameters. Notice that G is not the same as Γ for the fin operated in reverse, because when the "base" and "tip" *designations* are switched, the reference direction for q is changed; additional minus signs are called for. In this regard, the authors are puzzled by Razelos' disclaimer of any distinction between base and tip on the part of the rod or the computer. One of the authors (Kraus) has developed a computer program that handles an array of any number of fins, and this orientation information is an essential part of the package.

Two other points bear mentioning. In the authors' opinion there is no need of employing an iterative technique to solve the linear equations which result from the second problem; direct solution is easily implemented. But Razelos' criticism of the singular fin discussion is valid. A "complete" treatment involves some highly technical mathematics—in particular, the theory of singular Sturm-Liouville equations. The authors are disinclined to get into this, and will continue to tabulate μ only for the solvable cases. In this regard the Razelos-Imre paper should prove interesting.

The typographical correction is appropriate. There are two others; h should be replaced with k in equation (11), and there is an obvious β missing in equation (28). Again the authors would like to express their gratitude to Dr. Razelos for his discussion. Papers substantiating the authors' statements herein have been submitted to the Journal.

[3] Razelos, P. and Imre, K., "The Optimum Dimensions of Circular Fins with Variable Thermal Parameters," presented at the 1979 ASME Winter annual meeting.

Condensation on an Extended Surface[1]

J. Ernest Wilkins, Jr.[2] In this very interesting paper the authors are led to a consideration of the differential equations

$$\eta F' = 8(F-\Theta), \quad \Theta'' = F^{-1/4}\Theta, \ (' = d/d\eta), \tag{1}$$

and the boundary conditions

$$\Theta(0) = 1, \quad \Theta(\infty) = F(\infty) = 0. \tag{2}$$

They assert that "an analytic solution . . . is out of reach," carry out a numerical integration, and conclude, among other things, that

$$\Theta'(0) = -1.080. \tag{3}$$

In fact, an analytic solution can be found, and the numerical constant in (3) is $(7/6)^{1/2} = 1.08012$.

The authors implicitly assumed that $F > 0$. It is not physically possible that $F < 0$, and if $F = 0$, then $\Theta = 0$ also. Therefore, we may write the differential equations in the form

$$\eta F' = 8(F-\Theta), \quad F^{1/2}\Theta'' = \Theta, \tag{4}$$

that is valid even if $F = 0$. A solution consists of a pair of functions $F(\eta)$, $\Theta(\eta)$ defined when $\eta \geq 0$, such that F, Θ and Θ' are continuous

[1] By S. V. Patankar and E. M. Sparrow, published in the August 1979 issue of the ASME JOURNAL OF HEAT TRANSFER, Vol. 101, No. 3, pp. 434–440.

[2] Associate General Manager, EG&G Idaho, Inc., P.O. Box 1625, Idaho Falls, Idaho 83415. Associate Member ASME.

F is nonnegative and F and Θ satisfy not only the differential equations (4) for all positive η but also the boundary conditions (2). This implies that F' and F'' are also continuous when $\eta > 0$.

Suppose that there is a solution $F(\eta)$, $\Theta(\eta)$. If F were identically zero, then Θ would also be identically zero, contradicting the boundary condition that $\Theta(0) = 1$. Therefore, there exists a number η' such that $F(\eta') > 0$, $0 < \eta' < \infty$. If there are any points η'' such that $F(\eta'') = 0$, $\eta'' > \eta'$, let b be the greatest lower bound of the set of all such η''. Otherwise, let $b = \infty$. Then $F(\eta) > 0$ if $\eta' \leq \eta < b$, $F(b) = 0$, and we shall now prove that $F(\eta) > 0$ if $0 < \eta < b$.

If this last assertion were false, there would be a number a' such that $0 < a' < \eta'$, $F(a') = 0$. Let a be the least upper bound of the set of all such a'. Then $0 < a < \eta'$, $F(a) = 0$, and $F(\eta) > 0$ if $a < \eta \leq \eta'$, so that $F(\eta) > 0$ if $a < \eta < b$. It is clear that $F'(a) = 0$, $F''(a) \geq 0$ because $F(a) = 0$ and $F(\eta) \geq 0$ in some (two-sided) neighborhood of a.

On the open interval (a, b), or on any interval where $F(\eta) > 0$, we see from (4) that

$$\eta^7(\eta^{-6}F^{3/4})' = -6\{F^{3/4} - (\eta/8)F^{-1/4}F'\}$$

$$= -6F^{-1/4}\Theta = -6\Theta'',$$

$$\eta^7(\eta^{-6}F'')' = -8\{F - (\eta/8)F'\}'' = -8\Theta''.$$

It follows that $\{\eta^{-6}(3F'' - 4F^{3/4})\}' = 0$, and that there exists a constant α such that

$$3F'' = 4F^{3/4} + \alpha\eta^6 \tag{5}$$

if $a < \eta < b$. Because F and F'' are continuous when $\eta = a$, we see that $\alpha = 3F''(a)a^{-6} \geq 0$, so that $F'' > 0$ when $a < \eta < b$. This is, however, incompatible with $F(a) = F(b) = 0$, $F(\eta) > 0$ when $a < \eta < b$. We conclude that $F(\eta) > 0$ when $0 < \eta < b$, that the differential equation (5) holds when $0 \leq \eta \leq b$, and that b is the least upper bound of the set of points η at which $F(\eta) > 0$.

Suppose that $b = \infty$. Because $F(\infty) = 0$, there exists a number η_1 such that $28F^{3/4}(\eta) < 1$ if $\eta \geq \eta_1$. If we integrate (5) from η_1 to η it follows that

$$0 < 21\{F'(\eta) - F'(\eta_1)\} - \alpha(\eta^7 - \eta_1^7) < \eta - \eta_1 \tag{6}$$

if $\eta > \eta_1$. Because $F'(\infty) = 0$ when (4) and (2) hold, we see, upon dividing (6) by η^7 and letting η approach ∞, that $\alpha = 0$, i.e.,

$$3F'' = 4F^{3/4} \tag{7}$$

when $0 \leq \eta < \infty$. If b is finite, then $F \equiv 0$ and (7) surely holds if $b \leq \eta < +\infty$. The function $\eta^{-6}(3F'' - 4F^{3/4})$ is continuous when $\eta = b$, is equal to zero if $\eta > b$, and is equal to α if $\eta < b$. Therefore, $\alpha = 0$ and (7) holds when $0 \leq \eta < +\infty$, whether b is finite or infinite.

In view of (7) the derivative of the function $21F'^2 - 32F^{7/4}$ vanishes identically. The function itself is therefore a constant, and that constant is zero because $F(\infty) = F'(\infty) = 0$. It follows that

$$F^{-7/8}F' = \pm(32/21)^{1/2}$$

if $0 < \eta < b$, whence an integration shows that

$$8F^{1/8} = \pm (32/21)^{1/2}(\eta - \eta_0),$$

$$F = (\eta - \eta_0)^8/(42)^4$$

for some constant η_0. Because $F'(0)$ is finite, it follows from (4) and (2) that $F(0) = 1$; i.e., $\eta_0 = (42)^{1/2} = 6.48074$, and that $F = \{1 - (\eta/\eta_0)\}^8$ if $0 \leq \eta \leq b$.

It is impossible that $\eta_0 < b$ because in that case $F(\eta_0) = 0$, whereas we have already proved that $F(\eta) > 0$ if $\eta < b$ (this shows in particular that b is finite). It is also impossible that $\eta_0 > b$ because in that case $F(b-) > 0 = F(b+)$, contradicting the continuity of F at b. Therefore, $\eta_0 = b$. We conclude that if there is a solution, then

$$F(\eta) = \{1 - (\eta/\eta_0)\}^8 \text{ if } 0 \leq \eta \leq \eta_0 = (42)^{1/2},$$

$$= 0 \text{ if } \eta_0 \leq \eta < +\infty,$$

and, from (4),

$$\Theta(\eta) = \{1 - (\eta/\eta_0)\}^7 \text{ if } 0 \leq \eta \leq \eta_0,$$

$$= 0 \text{ if } \eta_0 \leq \eta < +\infty.$$

This pair of functions is easily seen to be a solution, and is, therefore, the solution. We observe that

$$\Theta'(0) = -7/\eta_0 = -(7/6)^{1/2} = -1.08012.$$

The numerical constants in the authors' equations (41) and (42) are, respectively, $(6/7)^{1/2} = 0.92582$ and $(8/21)^{1/2} = 0.61721$.

Authors' Closure

The authors welcome Dr. Wilkins' contribution to the paper and regard it as an important enhancement of the work.